materials

Special Issue Reprint

Advances in Material Structural Analysis

Finite Element Analysis and Numerical Modelling

Edited by
Wei Li, Haijian Su, Xiaochen Wang and Chenyang Ma

mdpi.com/journal/materials

MDPI

Advances in Material Structural Analysis: Finite Element Analysis and Numerical Modelling

Advances in Material Structural Analysis: Finite Element Analysis and Numerical Modelling

Guest Editors

Wei Li
Haijian Su
Xiaochen Wang
Chenyang Ma

MDPI

Basel • Beijing • Wuhan • Barcelona • Belgrade • Novi Sad • Cluj • Manchester

Guest Editors

Wei Li
China University of Mining and Technology
Xuzhou
China

Haijian Su
China University of Mining and Technology
Xuzhou
China

Xiaochen Wang
School of Civil Engineering
Shandong Jianzhu University
Jinan
China

Chenyang Ma
Institute of Geotechnical and Underground Engineering
Shandong University
Jinan
China

Editorial Office
MDPI AG
Grosspeteranlage 5
4052 Basel, Switzerland

This is a reprint of the Special Issue, published open access by the journal *Materials* (ISSN 1996-1944), freely accessible at: https://www.mdpi.com/journal/materials/special_issues/2E151MM271.

For citation purposes, cite each article independently as indicated on the article page online and as indicated below:

Lastname, A.A.; Lastname, B.B. Article Title. *Journal Name* **Year**, *Volume Number*, Page Range.

ISBN 978-3-7258-9185-6 (Hbk)
ISBN 978-3-7258-9186-3 (PDF)
https://doi.org/10.3390/books978-3-7258-9186-3

© 2026 by the authors. Articles in this reprint are Open Access and distributed under the Creative Commons Attribution (CC BY) license. The reprint as a whole is distributed by MDPI under the terms and conditions of the Creative Commons Attribution-NonCommercial-NoDerivs (CC BY-NC-ND) license (https://creativecommons.org/licenses/by-nc-nd/4.0/).

Contents

About the Editors . . . . . **vii**

Zhipeng Zhang, Chenyang Ma, Chen Zhao, Zhuo Zheng, Wei Li, Rentai Liu, et al.
Diffusion Mechanism in Running-Water and CFD-DEM Numerical Simulation of Expandable Particulate Grouting Material
Reprinted from: *Materials* **2025**, *18*, 1681, https://doi.org/10.3390/ma18071681 . . . . . **1**

Zhihao Gao, Shihao Guo, Xiaoyong Yang, Shanchao Hu, Junhong Huang, Yafei Cheng, et al.
Failure and Energy Evolution Characteristics of Saturated Natural Defective Material Under Different Confining Pressures
Reprinted from: *Materials* **2025**, *18*, 2027, https://doi.org/10.3390/ma18092027 . . . . . **23**

Yalin Luan, Runan Wang, Changxin Huang, Andrey Jivkov and Lianzhen Zhang
Transport Properties of Solutions in γ–FeOOH/CSH Pores of Steel Fiber-Reinforced Concrete (SFRC) Derived Using Molecular Dynamics
Reprinted from: *Materials* **2025**, *18*, 2176, https://doi.org/10.3390/ma18102176 . . . . . **43**

Xiao Feng, Shilei Zhang, Zhenzhong Shi, Qingsong Zhang, Meiling Li, Wenda Yang, et al.
Evolution Mechanism of Filtration Characteristics of Cement Grouting Materials in Sandy Medium
Reprinted from: *Materials* **2025**, *18*, 2385, https://doi.org/10.3390/ma18102385 . . . . . **65**

Hengjie Luan, Qingzhai Shi, Changsheng Wang, Yujing Jiang, Sunhao Zhang, Jianrong Liu and Kun Liu
Experimental Study on Shear Characteristics of Filled Joints Anchored by Basalt Fiber-Reinforced Polymer Materials
Reprinted from: *Materials* **2025**, *18*, 2393, https://doi.org/10.3390/ma18102393 . . . . . **82**

Lu Han, Weiliang Gao, Yaping Tao and Lulu Liu
Meso-Scale Breakage Characteristics of Recycling Construction and Demolition Waste Subgrade Material Under Compaction Effort
Reprinted from: *Materials* **2025**, *18*, 2439, https://doi.org/10.3390/ma18112439 . . . . . **102**

Shanchao Hu, Lei Yang, Shihao Guo, Chenxi Zhang, Dawang Yin, Jinhao Dou and Yafei Cheng
Study on Similar Materials for Weakly Cemented Medium and Indoor Excavation Test
Reprinted from: *Materials* **2025**, *18*, 2948, https://doi.org/10.3390/ma18132948 . . . . . **119**

Chaowen Hu, Xiaojie Yang, Feng Zhang, Bo Pan, Ruifeng Huang, Bing Hu, et al.
Experimental Study on the Preparation of Paste Filling Materials from Coal-Based Solid Wastes
Reprinted from: *Materials* **2025**, *18*, 3244, https://doi.org/10.3390/ma18143244 . . . . . **139**

Keyong Wang, Zhenhua Zang, Jie Li, Zhenyue Shi, Mingcai Liu, Zhipeng Li, et al.
Experimental Study and Application of TPO Waterproofing Membrane Lapping Process Parameters
Reprinted from: *Materials* **2025**, *18*, 3313, https://doi.org/10.3390/ma18143313 . . . . . **166**

Zhipeng Li, Deming Wang, Kai Wang, Qingsong Zhang, Lianzhen Zhang, Yang Gao and Yongqi Dai
Development of Fault Similar Material for Model Test of Fault Water Inrush Disaster
Reprinted from: *Materials* **2025**, *18*, 3745, https://doi.org/10.3390/ma18163745 . . . . . **188**

Deming Wang, Zhipeng Li, Qingsong Zhang, Lianzhen Zhang, Yang Gao, Hongzhen Dong, et al.
Experimental Study on the Filtration of Seawater Bentonite Slurry Under the Cutting Influence of Shield Cutterhead
Reprinted from: *Materials* **2025**, *18*, 4025, https://doi.org/10.3390/ma18174025 . . . . . **205**

Yalin Luan, Yongmei Wu, Runan Wang, Dongbo Cai, Lianzhen Zhang and Pengxiang Luan
Research on Optimizing the Steel Fiber/CSH Interface Performance Based on Ca/Si Ratio
Reprinted from: *Materials* **2025**, *18*, 4049, https://doi.org/10.3390/ma18174049 . . . . . **227**

Xinghui Wu, Peng Li, Meifeng Cai, Tingting Jiang, Bolin Mu, Wanlei Su, et al.
Material Behavior and Computational Validation of Deep CO_2 Closed-Loop Geothermal Systems in Carbonate Reservoirs
Reprinted from: *Materials* **2025**, *18*, 5144, https://doi.org/10.3390/ma18225144 . . . . . **247**

Shukun Zhang, Peng Jiang, Haohao Wang, Dianzhi Feng and Hao Wang
Research on Mechanical Properties of Nano-Modified Foam Concrete Improved by Micro-inCorporated Carbon Nanotubes
Reprinted from: *Materials* **2026**, *19*, 1681, https://doi.org/10.3390/ma19010184 . . . . . **266**

Guanmei Niu, Wei Li, Kaidi Jiang, Yang Yang, Guojun Wang, Cheng Liu and Linzhong Zhuang
Simulation Analysis of Thermal Deformation and Extruded Profile Formability of Al–10Mg–3Zn Aluminum Alloy
Reprinted from: *Materials* **2026**, *19*, 375, https://doi.org/10.3390/ma19020375 . . . . . **288**

Michał Paduchowicz, Tomasz Dobosz and Artur Górski
The Durability Assessment Methodology of Power Engineering Equipment Under Thermo-Mechanical Fatigue Using the Example of the HR6W Alloy
Reprinted from: *Materials* **2026**, *19*, 891, https://doi.org/10.3390/ma19050891 . . . . . **315**

Zhigang Yang, Fansheng Zhang, Yong Chang, Xihao Yang, Jianjian Li, Qiang Feng, et al.
Research and Development of Cement-Based Dynamic Water Grouting Material for the CSM Construction Method
Reprinted from: *Materials* **2026**, *19*, 1167, https://doi.org/10.3390/ma19061167 . . . . . **341**

Yifan Xie, Haitao Liu, Hao Wen, Chuangui Sun, Yong Chang, Qiang Feng, et al.
Research on Material Optimization of CSM Method Structures in Highly Weathered Strata
Reprinted from: *Materials* **2026**, *19*, 1287, https://doi.org/10.3390/ma19071287 . . . . . **358**

Yue Xu, Tao You and Qizhi Zhu
A Hybrid-Dimensional Iterative Coupled Modeling of Lubrication Flow in Deformable Geological Media with Discrete Fracture Networks
Reprinted from: *Materials* **2026**, *19*, 1444, https://doi.org/10.3390/ma19071444 . . . . . **385**

Qinglin Shan, Changrui Shao, Hengjie Luan, Sunhao Zhang, Chuming Pang, Yujing Jiang and Lujie Wang
Response and Failure of Pillar–Backfill Composite Materials Under Cyclic Loading: The Role of Pillar Width
Reprinted from: *Materials* **2026**, *19*, 1625, https://doi.org/10.3390/ma19081625 . . . . . **415**

About the Editors

Wei Li

Wei Li is an Associate Professor at the State Key Laboratory of Intelligent Construction and Healthy Operation and Maintenance of Deep Underground Engineering, China University of Mining and Technology. He received his Ph.D. in Disaster Prevention, Mitigation and Protection Engineering from the School of Civil Engineering and Water Conservancy, Shandong University. His research focuses on disaster prevention and control in tunnel and underground engineering. In recent years, he has presided over several vertical research projects, including the National Natural Science Foundation of China (Youth Program), the Key Project of Jiangsu Province Basic Research Program, and the Xuzhou Municipal Natural Science Foundation (Youth Program). He has also led multiple enterprise-oriented technological research projects. As the first author or corresponding author, he has published over 20 SCI/EI papers in prestigious journals such as *Cement and Concrete Research* (CCR), *Tunnelling and Underground Space Technology* (TUST), *Physics of Fluids* (POF), and *Journal of China Coal Society*. He has been granted more than ten national invention patents and four software copyrights and published one monograph. He participated in the formulation of four local standards of Shandong Province and one group standard. His research achievements have led to him winning two first prizes and one second prize in scientific and technological awards.

Haijian Su

Haijian Su received his Ph.D. degree in Geotechnical Engineering from the China University of Mining and Technology, Xuzhou, China, in 2015. He is currently a professor at the State Key Laboratory of Intelligent Construction and Healthy Operation and Maintenance of Deep Underground Engineering, China University of Mining and Technology, Xuzhou, China. His current research interests include damage and fracture of civil engineering materials, intelligent prevention and control of underground engineering hazards. He has received seven scientific research awards, including the Second Prize of Henan Provincial Science and Technology Award (China) and the Second Prize of Shandong Provincial Science and Technology Award (China). He has published over 40 academic papers in journals such as *Rock Mechanics and Rock Engineering*, *Engineering Fracture Mechanics*, and *Theoretical and Applied Fracture Mechanics*.

Xiaochen Wang

Xiaochen Wang is an Associate Research Professor in the School of Civil Engineering at Shandong Jianzhu University. He received his Ph.D. from Shandong University, during which he spent a period as a visiting scholar at RMIT University in Australia. His research focuses on disaster prevention and control in tunnel and underground engineering, in addition to novel grouting materials and technologies. Dr. Wang has served as Principal Investigator for a project supported by the Young Scientists Fund of the National Natural Science Foundation of China (NSFC), a Young Scientists Fund project of the Shandong Provincial Natural Science Foundation, and the Doctoral Research Foundation of Shandong Jianzhu University. As a core research member, he has contributed to four additional NSFC projects and five industry-sponsored projects. He has published 20 SCI/EI-indexed papers, including 11 as first or corresponding author, with 7 of them appearing in JCR Q1 journals. He holds 5 invention patents (granted or pending). He also participated in drafting a provincial standard for Shandong Province. His research achievements have been recognized with the Third Prize of the 18th Jinan Excellent Natural Science Academic Achievement Award. In

2024/2025, he was named a Top 5% Highly Cited Scholar by CNKI (China National Knowledge Infrastructure).

Chenyang Ma

Chenyang Ma works at the School of Future Technology, Shandong University. His research focuses on the development of novel grouting materials, mechanisms of adverse geological hazards, and key technologies for underground engineering disaster control. His work centers on the mitigation of water inrush disasters in extremely complex geological environments. To address the industry-wide challenge that conventional grouting materials are easily diluted by high-pressure, high-flow water inrush and fail to gel and solidify effectively, he introduces recent advances from the field of medical polymers to achieve interdisciplinary innovation. He creatively transforms the principle from ”chemical reaction” to ”physical water absorption and swelling”—utilizing the osmotic pressure difference between the material and its surroundings to draw water into the material, achieving a swelling ratio of 150 to 300 times and a blocking volume 100 times that of ordinary materials. This process enables rapid sealing of wide water inrush channels such as faults and karst conduits. He has been deeply involved in on-site scientific research work for the nationally key project of the Yunnan Central Yunnan Water Diversion Project and has successfully extended the research outcomes to water inrush disaster control in underground projects including Qingdao Metro, Jinan Metro, and the CZ Railway. As a guest editor of this Special Issue, he is committed to promoting interdisciplinary innovation in the fields of smart materials and disaster prevention and mitigation, soliciting high-quality research contributions with theoretical breakthroughs and engineering application value, and contributing academic insights to solving the challenges of safe construction of major national infrastructure.

materials

MDPI

Article

Diffusion Mechanism in Running-Water and CFD-DEM Numerical Simulation of Expandable Particulate Grouting Material

Zhipeng Zhang [1], Chenyang Ma [1,*], Chen Zhao [1], Zhuo Zheng [1], Wei Li [2], Rentai Liu [1], Xiuhao Li [1] and Hongyan Wang [3]

[1] School of Civil Engineering, Institute of Geotechnical and Underground Engineering, Shandong University, Jinan 250061, China; 202315052@mail.sdu.edu.cn (Z.Z.); 202222201112@mail.sdu.edu.cn (C.Z.); zhengzhuo22@sdjzu.edu.cn (Z.Z.); rentailiu@163.com (R.L.); lixiuhao@mail.sdu.edu.cn (X.L.)
[2] State Key Laboratory of Intelligent Construction and Healthy Operation and Maintenance of Deep Underground Engineering, China University of Mining and Technology, Xuzhou 221116, China; tbh259@cumt.edu.cn
[3] Jinan Urban Construction Group Co., Ltd., Jinan 250013, China; liyong250014@163.com
* Correspondence: machenyang@sdu.edu.cn; Tel.: +86-15969676922

Abstract: In order to study the diffusion and sealing mechanism of an innovative grouted material tentatively called "expandable particulate grout material", the diffusion process was simulated by the numerical method of CFD-DEM coupling. A numerical model was established for a grouting process in an individual fracture based on the basic physical parameters of expandable particles. The numerical model of the expandable particulate slurry flow was established. The interaction between particles and water in different conditions, such as different grouting times, different volume fractions of the particle, and different velocities, was investigated. The differences in the diffusion process and in the running-water sealing mechanism of expandable particles, cement slurry, and cement-sodium silicate slurry in the crack (in a, in b, and in c) were analyzed. The influence of expandable particles on the streamline of the grout and the drag force in the interaction process under the fracture were analyzed. This is summarized The influence of the velocity ratio of grout to water on different physical quantities, such as diffusion opening degree, diffusion velocity, and diffusion distance, was summarized. It is of significant theoretical and practical value to further develop and improve the grouting technology.

Keywords: CFD-DEM; numerical model; grout material; expandable particulate

1. Introduction

There are plenty of natural defects such as fracture structural planes in the rock mass. During the bearing process, the instability of the fractured rock mass will start to break from weak places such as the fracture structural plane, from part to the whole, and finally destroy the entire rock mass. Grouting is an important means to ensure safe construction [1–4]. In recent years, through the cross innovation with computational fluid dynamics, materials science, and other emerging disciplines, the theoretical system of grouting technology has achieved significant development, and a variety of anti-dispersion grouting materials in running water and corresponding diffusion theories have been developed [5–7].

In terms of materials science: related scholars have developed a large number of grouting materials for different engineering problems. According to the gel particles, it can be divided into granular slurry and chemical slurry. Among them, the granular slurry

mainly includes portland cement, sulfoaluminate cement, and cement-sodium silicate. The chemical slurry mainly includes polyurethane, epoxy resin, polyacrylic acid, lignin, and various types of modified grouting material on this basis [8–13]. However, for the sealing of rapid water inrush (>1 m/s), the current traditional Portland cement grouting materials have a long setting time (6–8 h), so the effect is poor. The cement-sodium silicate slurry is highly sensitive to setting time, and it is easy to block the drilling and damage to the grouting machine. Acrylate and lignin grouting materials are highly toxic and cause environmental damage. Therefore, how to resist the adverse effects of the scouring of running water on the grouting material, contrary, to developing a grouting material that relies on the running-water scouring force to achieve effective slurry transport, diffusion, and sealing is the key to the treatment of water inrush on the fractured structural surface in the water-rich zone.

In terms of computational fluid dynamics: in order to carry out more in-depth calculation and evaluation research on fractured rock mass grouting, a stepwise numerical calculation method is proposed, which takes into account the viscosity change caused by chemical reaction and the decrease in soil porosity caused by the deposition of grout particles and describes the process of cement-based grouting material entering porous media [14]. In addition, different grout constitutive equations, such as Newtonian fluid, Bingham fluid, and power law fluid, are used in the theoretical analysis. Many numerical methods, such as FEM/VOF and time-step calculation methods, are used to describe the grouting process [15–18]. According to the morphological characteristics of the slurry-water interface in the process of slurry diffusion, theoretical and experimental research are carried out, and the relevant mathematical characterization methods are established [19]. Carried out the fracture dynamic water grouting test and analyzed the influence relationship between the pressure field, the grouting method, and the effect [20]. A lot of work has also been conducted on the fissure running-water grouting test system, and the theoretical model research of dynamic water diffusion has been carried out [21]. Furthermore, many scholars have used the CFD-DEM [22–24] numerical calculation method to simulate particle flow and present a coupled model based on computational fluid dynamics (CFD) and discrete element method (DEM) to simulate sediment bed erosion by viscous shear flow at various shear flow velocities [21]. Present, the field in geotechnical engineering has made a series of beneficial progress in studying particle-loaded flows through CFD-DEM coupling.

Aiming at the problem that the slurry is easy to disperse and lose its coagulation ability under running water, Li et al.'s team developed a new type of expandable particle grout material, which is suitable for large-flow water inrush sealing [25,26]. The material is composed of special gel particles and carrier fluid, which are configured in a certain proportion. After entering the groundwater environment, the gel particles use the capillary action of the internal cross-linking network of the material to quickly absorb water and expand (up to 300 times their own volume); the free water is bound inside the material so as to slow down the flow rate of groundwater or directly transform the groundwater environment into a static state. Because the expansion of the expandable particle grouting material does not depend on the chemical reaction, the material will not fail due to the action of flowing water, avoiding the damage of high-pressure and large-flow water inrush to the material reaction process. Its physical and chemical properties have unique advantages in many grouting materials [21]. However, the research on this type of grouting material is very limited, and there is a lack of corresponding grout rheological model and flow calculation theory. Regarding the coupling of particle migration and expansion during dynamic water grouting, no relevant research has been carried out yet. When applying the theory of fluid mechanics to the calculation of slurry flow, it is necessary to follow the assumption of a constant flow pattern. The sealing problem of grouting under running

water involves the whole process of gradual transformation of slurry from fluid to solid, which leads to difficulties in calculation and analysis. In this paper, the CFD-DEM method is used to study the slurry diffusion under running water and the plugging mechanism of the expandable particulate grouting material. The structure of this article is as follows. First, the expandable particle grouting material was used as the research object to test its working performance. Then, the CFD-DEM coupling principle is analyzed. Finally, a numerical simulation was carried out for the problem of grouting with dynamic water in a single plate fissure, and a numerical model of expandable particle grouting material flow was established. The interaction between particles and fluid and the flow field changes during particle expansion and migration are studied in detail. The differences between the expandable particle grouting material and the cement grouting material and cement-sodium silicate grouting material under running water in the fissure grouting material diffusion law and sealing mechanism have been analyzed, compared, and revealed.

2. Physical and Chemical Properties of Expandable Particles Grouting Material

2.1. Introduction to Expandable Particulate Material

Expandable granular material is a kind of ultra-high-expansion granular grouting material suitable for water inrush sealing of karst pipelines and consists of polyacrylic resin with water absorption and expansion characteristics. Specifically, the material is composed of gel particles and carrier fluid. Gel particles are a kind of high molecular polymer formed by cross-linking copolymerization of acrylic acid and acrylamide (see Figure 1) [25,26]. This polymer contains a large number of strong hydrophilic groups (see the molecular synthesis diagram of the material); the molecular structure shows a three-dimensional crosslinked network (see Figure 1, the bottom three-dimensional mesh structure schematic); through the hydration effect, it can quickly absorb hundreds of times its own mass of water; the morphology of the gel (see Figure 1, the bottom before and after the expansion of the material) is gel-like. Gel particles have the advantages of strong water-absorbing capacity, fast water absorption, and strong water retention capacity and are non-toxic and odorless. Gel particles have the appearance of solid powder and cannot be used directly in the grouting process, so they have to be used together with the carrier liquid. The carrier liquid consists of ethanol and glycerin, which play the role of suspending and transporting the gel particles. When the gel particles are exposed to water, the water molecules are hydrated with hydrophilic groups through hydrogen bonding, and the hydrophilic groups begin to dissociate, causing osmotic pressure to build up in the material and water molecules to penetrate into the mesh structure. Therefore, the water absorption process of the gel particles is a physical process and is not affected by scouring. During the grouting process, it is not necessary for the material to resist the disturbance of flowing water. Instead, the material is expected to diffuse with the groundwater, absorbing it and slowing its flow as it migrates until it is sealed.

2.2. Material Performance

The size of the gel particle has an important influence on the expansion performance. To this end, >100 mesh, 100–50 mesh, and 50–30 mesh gel particles (2 g) are wrapped in tea bags, put into water, and taken out every 30 s. A centrifuge (speed 1000 r/min, time 1 min) was used to remove residual moisture. By measuring the mass change of the gel particles before and after water absorption, the expansion ratio can be calculated. The calculation formula is shown in Equation (1).

$$S_w = \frac{m_i - m_0}{m_0} \tag{1}$$

In the formula, m_0 and m_i are the mass of the gel particle before and after swelling; S_W stands for Expansion Rate. The expansion ratio of gel particles with different meshes is measured as shown in Figure 2. As mentioned, gel particles have superior water absorption properties; the expansion ratio was as high as 320, and the particle size has little effect on the expansion ratio. In addition, the smaller the particle, the larger the specific surface area and the faster the water absorption rate. The time required for the super absorbent polymer (subsequently abbreviated to SAP) >100 mesh particles to fully expand was half that of the 30–50 mesh particles upon water exposure. Therefore, the expansion rate can be adjusted according to the engineering requirements.

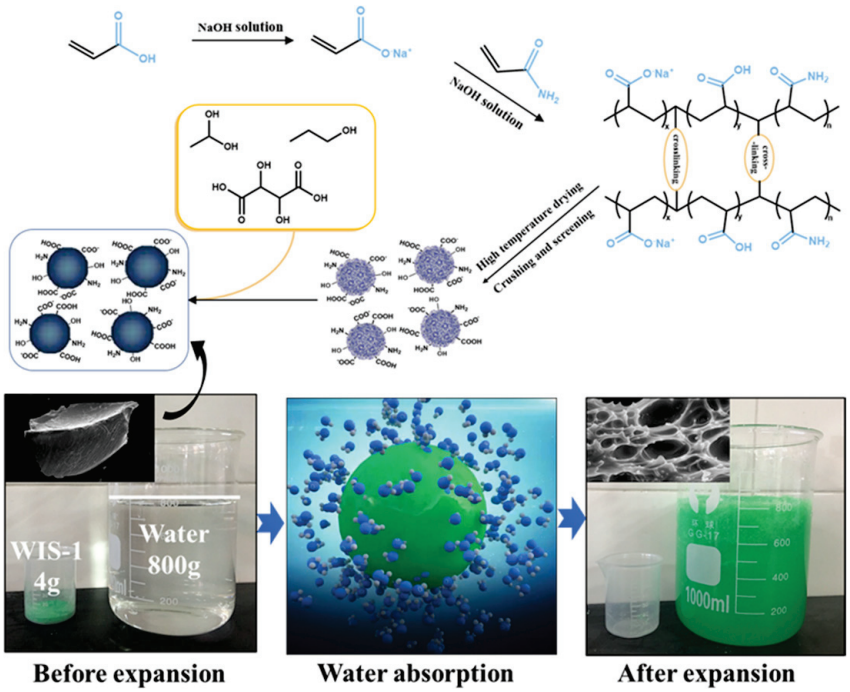

Figure 1. Gel particle synthesis principle, expansion effect, and water absorption mechanism.

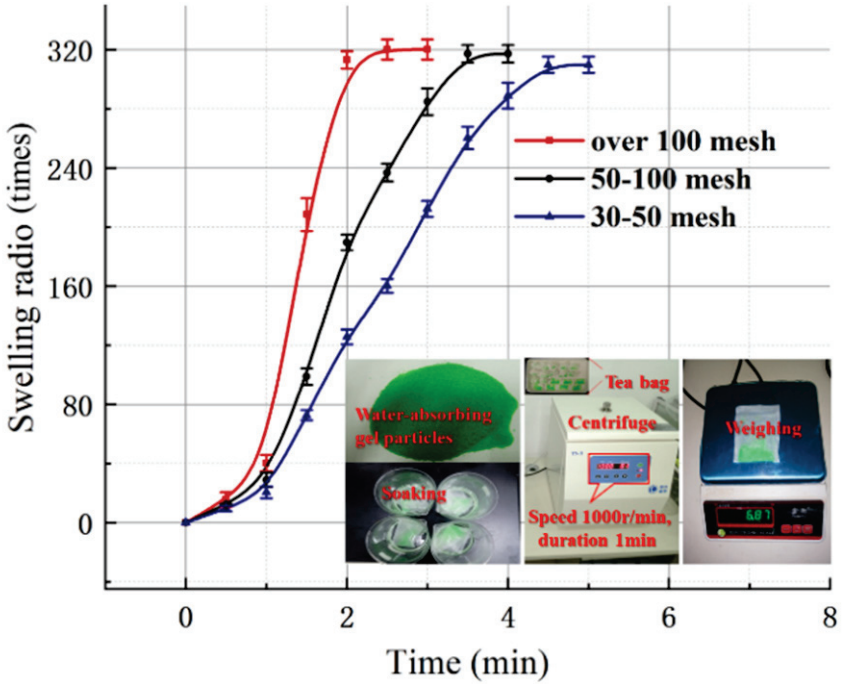

Figure 2. The swelling ratio of gel particles with different meshes.

3. CFD-DEM Coupling

3.1. CFD-DEM Coupling Principle

3.1.1. Grid Division and Calculation of Flow Field Information

In order to ensure the accuracy of calculation, when discretizing the flow field, the divided fluid grid unit should not be too coarse. At the same time, the length of the grid unit should be large enough relative to the particle size to ensure that the particle unit has a sufficiently long time interval in each grid unit. For this reason, the mesh element length should meet the following constraints when building the model:

$$6r < \Delta x_{cfd} < \frac{1}{5} d_{\min} \tag{2}$$

$$\Delta x_{cfd} > 3|\mathbf{u}|t_c \tag{3}$$

In the Formulas (2) and (3), Δx_{cfd} is the length of the grid unit, d_{min} is the minimum side length dimension of the calculation area, $\boldsymbol{u}$ is the gel particle velocity, and t_c is the fluid-structure coupling calculation time step.

Since the stiffness of the gel particles will gradually decrease after absorbing water; there will be a large overlap when the particles collide with the wall boundary. When the length of the overlapping part exceeds the radius of the particle, the particle will pass through the wall and escape. Therefore, in the calculation process, the stiffness of the particles needs to meet the following constraints (4):

$$\frac{2}{3}\pi r^3 \rho_p |\mathbf{u}_{\max}|^2 < \frac{k_n r^2}{8} \tag{4}$$

where, ρ_p is the particle density and k_n is the normal contact stiffness of the particle.

3.1.2. Calculation Method of Particle-Fluid Interaction

The fluid force on the gel particles is determined by calculating the following formula:

$$\frac{\partial \mathbf{u}}{\partial t} = \frac{\mathbf{f}_m + \mathbf{f}_l}{m} + \mathbf{g} \tag{5}$$

$$\frac{\partial \boldsymbol{\omega}}{\partial t} = \frac{\mathbf{M}}{I} \tag{6}$$

In the Formulas (5) and (6), $\boldsymbol{u}$ is the velocity of the gel particles, $\boldsymbol{m}$ is the mass of gel particles, f_l is the total force of the fluid on the gel particles, and f_m is all forces on the particles except fluid force (such as contact force between particles, gravity, etc.), $\boldsymbol{g}$ is the acceleration of gravity, ω is the angular velocity of the gel particles, $\mathbf{M}$ is the momentum received by the particles, and $\boldsymbol{I}$ is the moment of inertia of the particles. The specific expression of f_l is:

$$\mathbf{f}_l = \mathbf{f}_{drag} + \frac{4}{3}\pi r^3 (\nabla p - \rho_l \mathbf{g}) \tag{7}$$

From Equation (7), shows that the force of the fluid on the particles consists of two parts. The first term is the drag force f_{drag} caused by the velocity difference between the fluid and the particles, and the second term represents the fluid pressure caused by the pressure gradient. In order to obtain the specific expression of $\mathbf{f}_{drag}$, the velocity difference between the fluid and the particles must be determined firstly. If ignoring the influence of

gel particles on fluid flow and the interaction between particles, the drag force on a single particle in the flow field can be expressed as:

$$\mathbf{f}_0 = \frac{1}{2} C_d \rho_l \pi r^2 |\mathbf{u} - \mathbf{v}| (\mathbf{u} - \mathbf{v}) \tag{8}$$

In the Formula (8), C_d is the drag force coefficient, ρ_l is the fluid density, $\boldsymbol{r}$ is the particle radius, $\boldsymbol{v}$ is the fluid velocity, and $\boldsymbol{u}$ is the particle velocity.

The specific expression of the drag coefficient C_d is shown in the Formula (9).

$$C_d = \left(0.63 + \frac{4.8}{\sqrt{\mathrm{Re}_p}} \right)^2 \tag{9}$$

Re_p is the Reynolds number of the suspension shown in the Formula (10).

$$\mathrm{Re}_p = \frac{2\rho_l r |\mathbf{u} - \mathbf{v}|}{\mu_l} \tag{10}$$

As the particles continuously absorb water and expand during the slurry flow process, the volume occupied by the particles in the fluid unit continues to increase, and the fluid porosity continues to decrease. At the same time, as the particle spacing keeps getting smaller, the interaction between the particles keeps increasing, and the Reynolds number of the suspension keeps changing. Therefore, it is necessary to add a correction factor to the fluid drag force of a single particle. The drag force of any particle in the slurry flow process can be expressed as the Formula (11).

$$\mathbf{f}_{drag} = \mathbf{f}_0 \varepsilon^{-\chi} \tag{11}$$

ε is the instantaneous porosity of the fluid unit. χ is an empirical parameter, and specifically expressed as (12):

$$\chi = 3.7 - 0.65 \exp\left[-\left(1.5 - \log_{10} \mathrm{Re}_p\right)^2 / 2 \right] \tag{12}$$

At the same time, it should be pointed out that within the same fluid unit, the fluid velocity at different spatial positions is the same, but there are certain differences in the flow velocity in different fluid units. Since particles will continue to traverse from one fluid unit to other units during the migration process, the drag force components of different units on the particle need to be calculated according to the volume percentage of the overlap between the particle and different units. At the same time, when calculating the resultant force, the point of action of each component force is located at the center of the particle, and the drag force will not produce a rotational effect on the particle. Therefore, the resultant force of the drag force exerted by different fluid units on the gel particles can be expressed as (13):

$$\mathbf{f}_b = \frac{\Sigma_j \mathbf{f}^j_{drag}}{V} \tag{13}$$

3.2. Calculation Model

The shape of the fracture is a regular cuboid, which conforms to the basic assumption of a single flat crack: the inclination angle of the crack is set to zero; that is, the influence of gravity on the spread of grout and the flow of groundwater is ignored. The upper and lower walls of the crack are parallel plates with smooth surfaces, and the crack opening at any point inside the crack is a constant value.

The geometric model and boundary conditions of the fracture grouting diffusion simulation are shown in Figure 3. Set the crack aperture to 0.2 dm and the distance between the two sides of the crack to 80 dm. The fluid grid size is a rectangular parallelepiped with a length of 2 dm, a width of 2 dm, and a height of 0.2 dm. Set the groundwater on the inlet boundary as a vertical inflow, and set it as a constant velocity boundary with 1 dm/s. Set the groundwater on the outlet boundary to be in a vertical outflow state, and its groundwater pressure is zero. The boundary on both sides of the fracture is set as an impervious boundary; that is, there is no flow in the direction perpendicular to the boundary. The grouting hole is located on the bisector of the boundary on both sides, and the grouting flow is 2 L/s, 4 L/s, 6 L/s, 8 L/s, and 10 L/s. Assuming that the shape of the expandable particle material is a regular sphere with the same particle size, the calculation uses a spherical element to approximate the expanded particles and simulate the mechanical behavior during the flow process. The initial content of expanded particles in the slurry is 1%. In the actual calculation, the distance between the entrance boundary and the grouting hole is three times the maximum counter-current diffusion of the slurry, and the distance between the export boundary and the grouting hole is 50 dm longer than the maximum along-water diffusion distance of the slurry. The various parameters of fluid and particle properties in the calculation are shown in Table 1.

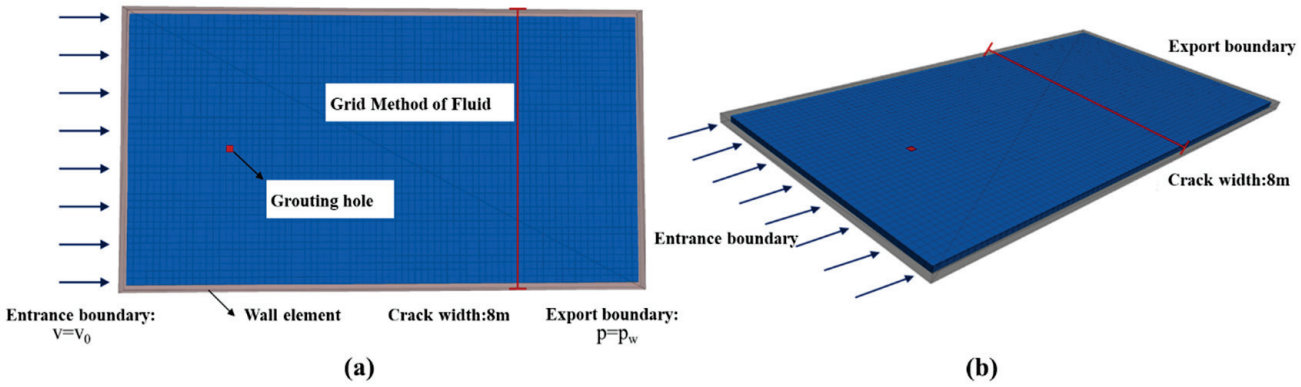

Figure 3. Geometric model and boundary condition. (**a**) Geometric model, (**b**) Boundary conditions.

Table 1. Calculation parameters.

	Fluid Properties		**Wall Properties**		**Particle Properties**		
Name	Density	Viscosity	Stiffness	Stiffness	Density	Particle size	Expansion rate
Unit	kg/m^3	Pa·s	Pa	Pa	kg/m^3	mm	s^{-1}
Value	1000	1×10^{-3}	1×10^{9}	1×10^{3}	1000	1	1

4. Analysis on Slurry Diffusion and Sealing Mechanism of Fracture

4.1. Diffusion Law of Fissure Grouting in Running Water

4.1.1. Diffusion Morphology of Different Types of Slurry

In previous studies, a series of experiments and numerical studies have been carried out on the running-water diffusion law of common cement slurry and cement sodium silicate slurry [27,28]. The diffusion pattern and numerical simulation results of cement slurry in a running-water test are shown in Figure 4. In the early stage, the diffusion shape of cement slurry is an asymmetric ellipse, and in the later stage, the shape of diffusion is oval in the counter-current direction, and the diffusion range along water is obviously larger than that of counter to the water. It is considered that the flow plays a dominant role in the initial stage of diffusion due to the small amount of slurry entering. With the

increase in grouting time, the slurry begins to deposit continuously along the flow direction from the grouting hole, and the slurry diffusion shape gradually changes from a closed ellipse shape to a U shape. After reaching stability, with the increase in grouting time, the diffusion pattern basically does not change. It can be inferred that the diffusion of slurry is blocked by groundwater and more slurry is transported downstream due to the scouring effect of water flow.

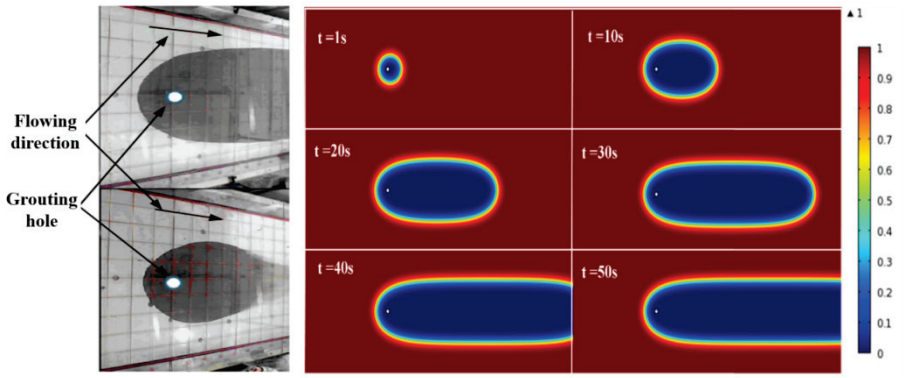

Figure 4. (**a**) The diffusion pattern and (**b**) numerical simulation results of cement slurry in running water.

Some literature also points out that under dynamic water conditions, the early diffusion of cement slurry is easily affected by water flow, and the diffusion range along the water flow is larger than that against the water flow, which is consistent with the results of this study and verifies the dominant role of water flow in the early stage of diffusion. The inference in this study is that the diffusion morphology of the slurry is affected by the blockage of the reverse water flow and the transportation along the water flow, lacking consideration for the dynamic changes in the physical and chemical properties of the slurry itself. For example, the dynamic changes of the slurry under dynamic water conditions can also affect the diffusion morphology, which has not been fully reflected in previous studies. [29,30] In addition, this study suggests that even if the diffusion morphology remains basically unchanged after stabilization, the internal structure of the slurry may still undergo slow adjustment, thereby affecting the overall diffusion effect.

The experimental morphology and the numerical simulation morphology of cement-sodium silicate slurry under running-water conditions are shown in Figure 5. During the diffusion of quick-setting slurry, the slurry diffusion trace forms an asymmetric ellipse that changes over time, with variations influenced by the model boundary. When the slurry solidifies faster and the velocity of flow is not large, the grout reaches the final pressure of grouting and does not spread to the boundary of the model and forms the asymmetric elliptical diffusion in the whole process. See Figure 5a, when the slurry injection rate is fast, the slurry curing time is moderate, and the hydrodynamic velocity is small, the slurry diffusion will reach the solid wall boundary, move along the solid wall boundary to the outflow boundary, form an asymmetric ellipse, and diffuse to the fracture side boundary, as shown in Figure 5b. When the slurry injection rate is slow, the hydrodynamic flow rate is fast, and the slurry solidification time is long, the slurry reaches the outlet boundary, and in this process, the slurry does not diffuse to the solid wall boundary, forming an asymmetric ellipse, which diffuses to the export boundary, as shown in Figure 5c.

Figure 6 shows the diffusion range of expandable particle slurry and the front profile of the slurry diffusion at different times. Observing the slurry diffusion in Figure 6, the slurry diffusion shape is approximately circular at the initial time of grouting, and then

it is approximately elliptical. The reason is as follows: at first, the flow of gel particles is mainly controlled by the injection velocity at the grouting hole, and the initial velocity of slurry entering into the fracture near the grouting hole is much higher than that of groundwater, so the slurry diffusion along all directions is approximately equal. With the increase in grouting time, the diffusion range of slurry gradually increases. The influence of grouting pressure on the particles near the slurry front decreases gradually, and the influence of groundwater flow on the slurry diffusion increases gradually. The slurry mainly diffuses along the direction of groundwater flow, and the diffusion form gradually changes from round to oval. If the slurry diffusion shape is regarded as an irregular ellipse, the major axis of the ellipse coincides with the central axis. The ellipse is symmetrically distributed along its long axis; the velocity, pressure, and expansion volume of the slurry are symmetrically distributed on both sides. While on both sides of the short axis, the physical field information is not symmetrical. Under the influence of groundwater flow, the position of the short axis moves backward along the direction of groundwater flow with the increase in grouting time.

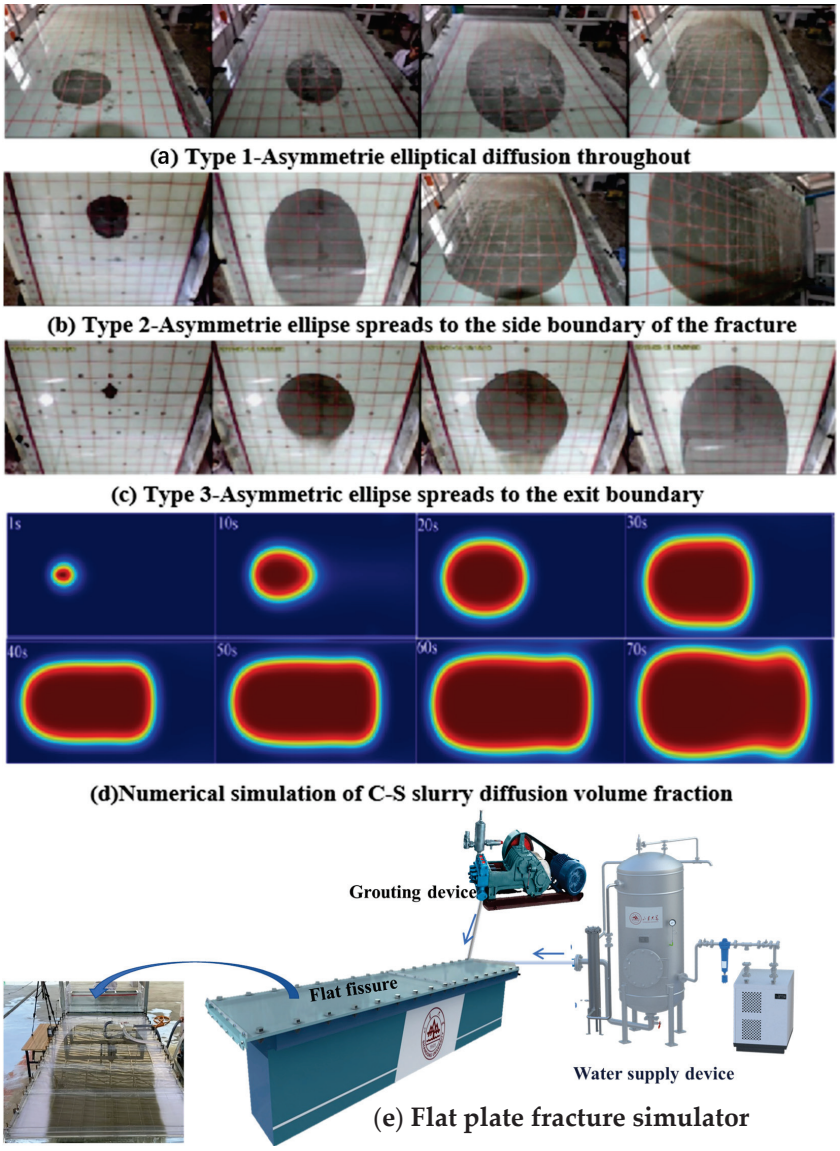

Figure 5. (**a**–**c**) Experimental morphology of cement-sodium silicate slurry in running water, (**d**) is the numerical simulation morphology, and (**e**) Flat plate fracture simulator.

It can be seen from Figure 6g,h that the gel particles entering the fracture at the same time are always in a closed curve during the diffusion process; that is, the particles that enter the fracture first are always in the outermost layer of the slurry diffusion range. At the same time, the water absorption time of the gel particles entering into the fracture in the early stage is longer. Therefore, the closer to the outside of the slurry diffusion range, the larger the particle expansion volume, the higher the resistance in the process of gel particle migration, and the faster the diffusion rate attenuation. Comparing the particle diffusion profiles at different times, it can be found that in Figure 6g, the interval length of the profile gradually decreases from the grouting hole to the outside and tends to be stable. The reason is that with the increase in particle diffusion range, the velocity of gel particles finally approaches the velocity of groundwater. In Figure 6h, when the effect of particle volume expansion on the velocity is considered, the velocity at any point in the fracture decreases continuously with time. The particle outside the diffusion region has a higher degree of water absorption ratio, which leads to a greater attenuation of the diffusion rate, so the contour interval length decreases continuously from the inside to the outside.

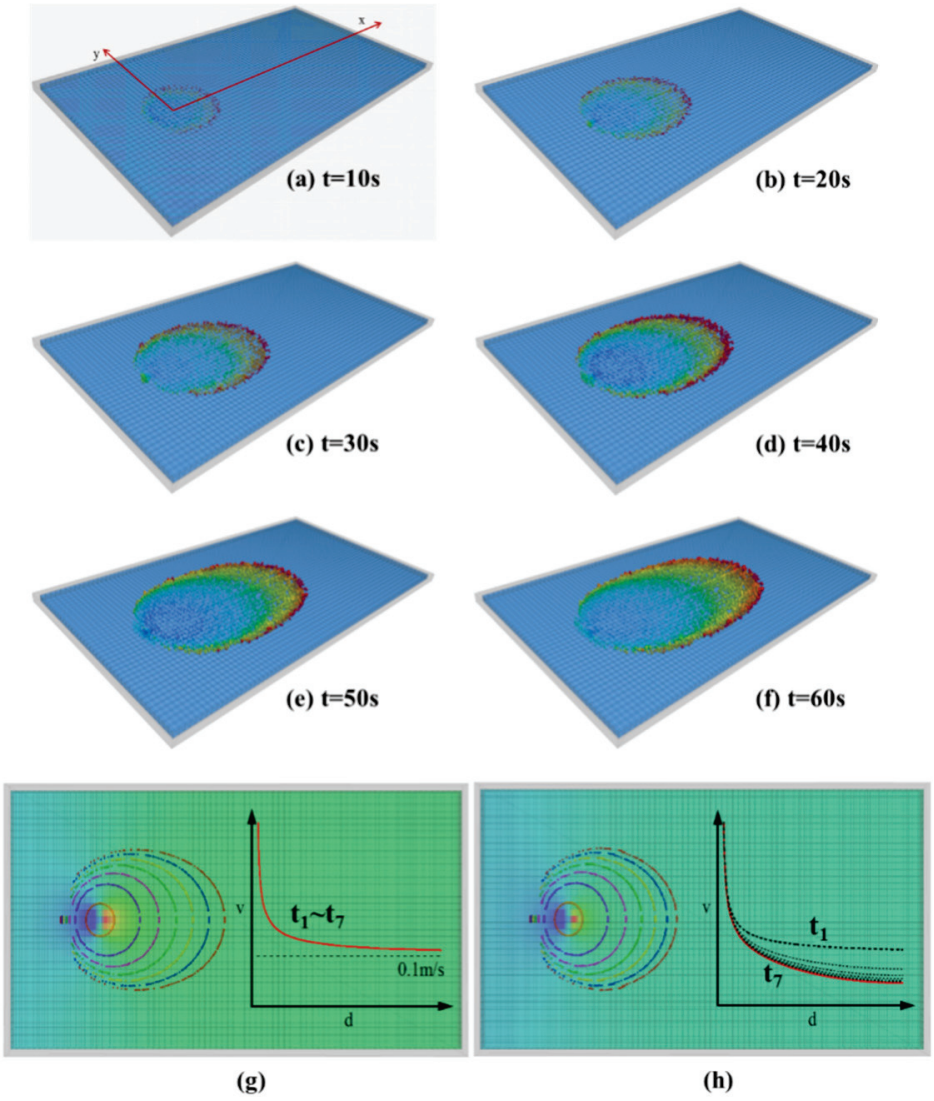

Figure 6. (**a**–**f**) Diffusion range of expanded particle slurry and the expanded state of particles with grouting time. (**g**) The diffusion profile of the gel particles when the flow field in the fracture remains unchanged and the velocity along the water diffusion direction on the central axis of the fracture changes with time. (**h**) The diffusion profile and velocity change obtained when the groundwater velocity gradually decreases under the influence of the gel particles.

By comparing the dynamic water grouting of expanded particle slurry, cement slurry, and cement-sodium silicate slurry, it can be found that the diffusion patterns of the three have similar rules. Among them, cement slurry diffuses in the model under the joint action of hydraulic transportation, scouring, and concentration gradient. Affected by factors such as grouting rate, dynamic water flow rate, slurry solidification rate, and other factors, the diffusion process of cement sodium silicate slurry has different forms. According to the shape characteristics of the irregular ellipse in the process of slurry diffusion, the space-time change equation describing the slurry diffusion shape was established by the curve-fitting method. However, under the influence of many factors, such as fracture shape, groundwater velocity, grouting rate, and slurry viscosity, it is difficult to establish a theoretical model of slurry diffusion covering all factors. The CFD-DEM method is used to calculate the slurry diffusion form more accurately, which can directly reflect the process of particle water absorption and expansion and fully consider the interaction between fluid and suspended particles so as to avoid the difficulty of defining the slurry macro viscosity. The calculation results are more in line with reality and reflect the rheological characteristics of expanded particle slurry more truly.

4.1.2. The Effect of Expandable Particles on Fluid Flow Field

Take the flow field in the fissure at the initial moment of grouting as the benchmark. Calculate the particle movement on the circle with the grouting hole as the center and the radius is 0.3 m. In this way, the particle migration trajectory at different moments and the streamline distribution in the flow field are obtained, and the calculation results are shown in Figure 7. The starting position of the particles is located on a circle with a grouting hole as the center and a radius of 0.3 m. The spatial arrangement of particles with the same starting position represents a streamline.

By observing the distribution of streamlines, it is found that the shapes of streamlines with different initial angles are different. The streamline with the initial angle pointing to the downstream diffusion zone always extends along the downstream direction; that is, the horizontal velocity component of gel particles is always greater than zero. The closer the initial angle is to the horizontal streamline, the larger the horizontal velocity component is and the smaller the vertical velocity component is, the faster the gel particles diffuse along the horizontal direction. The streamline in the counter-water diffusion zone first extends a distance in the counter-water direction and then gradually turns to the downstream direction. The closer the initial angle is to the horizontal streamline, the farther the backwater diffusion distance can be. That is, the horizontal velocity component of the gel particles first gradually attenuates from a certain value to zero and then continues to increase. Because the horizontal velocity component of the gel particles first decreases and then increases, and the migration trajectory of the particles is longer, the displacement of the gel particles that initially diffuse to the upstream area after entering the downstream area always lags behind the particles that diffuse to the downstream area at the same initial time. Therefore, the gel particles entering the fracture at the same time gradually form an oval shape in the diffusion process.

If the angle between the initial position of the gel particles and the line connecting the grouting hole and the y-axis is taken as the parameter, and the clockwise direction is taken as the angle-increasing direction. The relationship curves between the horizontal and vertical velocity components of the streamline with different initial angles and times can be obtained. In Figure 8a, since the streamline distribution is symmetrical about the x-axis, the streamline with initial angles of $\pi/6$, $\pi/3$, $7\pi/6$, and $4\pi/3$, respectively, coincides with the streamline with angles of $5\pi/6$, $2\pi/3$, $11\pi/6$, and $5\pi/6$, respectively. In Figure 8c, the vertical velocity components of the x-axis symmetric streamline are equal in value and

opposite in sign, so only the streamline distribution with a positive velocity component is shown in the figure. In Figure 8b,d, the graphics connected by the velocity components of different initial angles at any time is a closed curve. In Figure 8b, the grouting time corresponding to the curve from outside to inside on the coordinate line with the initial angle of 90° is 0 s, 2 s, 4 s, 6 s, 8 s, 10 s, 20 s, and 30 s, respectively. In Figure 8d, the times corresponding to the outside-in curve on the 0° and 180° coordinate lines are 0 s, 2 s, 4 s, 6 s, 8 s, 10 s, 20 s, and 30 s, respectively.

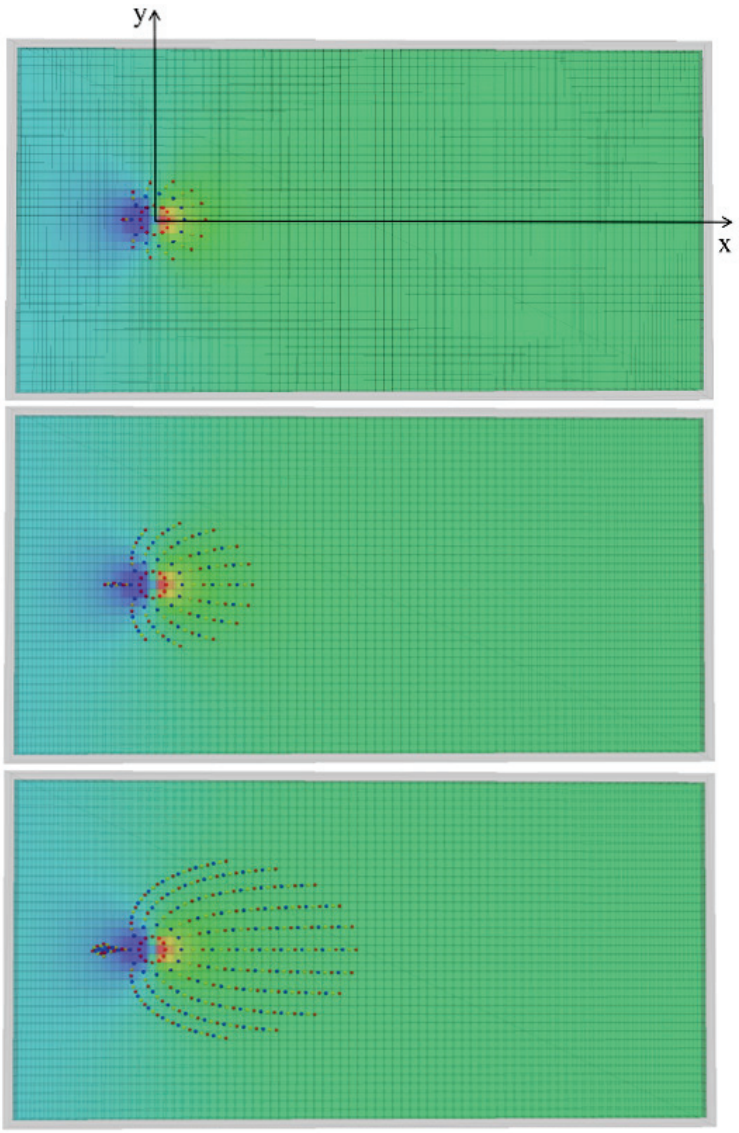

Figure 7. The transport trajectory of gel particles at different times under constant flow conditions.

It can be seen from Figure 8a that the initial velocity of gel particles corresponding to streamlines with different initial angles is different. When the initial angle is $\pi/2$, the initial horizontal velocity component has the maximum value, while the vertical velocity component is zero. It can be seen from Figure 8b that with the increase in grouting time, except for the horizontal velocity component of the streamline with an initial angle of $3\pi/6$, the horizontal velocity component of each streamline gradually approaches 0.1 m/s, that is, the groundwater velocity. The initial velocity of some streamlines with an initial angle between 0 and π is greater than 0.1 m/s and continues to decrease, while the velocity of other streamlines first increases and then decreases. Figure 8b further shows the change trend of velocity distribution with time at different angles. The curve at the initial time

is an irregular ellipse, and its centroid deviates greatly from the origin. At this time, the velocity of gel particles is highly asymmetric, and the slurry flow is highly affected by the incident velocity of the grouting hole. With the increase in time, the shape of the curve gradually changes into a circle centered on the origin, which indicates that the influence of the incident velocity of the grouting hole gradually decreases, and the flow of the gel particles is gradually controlled by the flow.

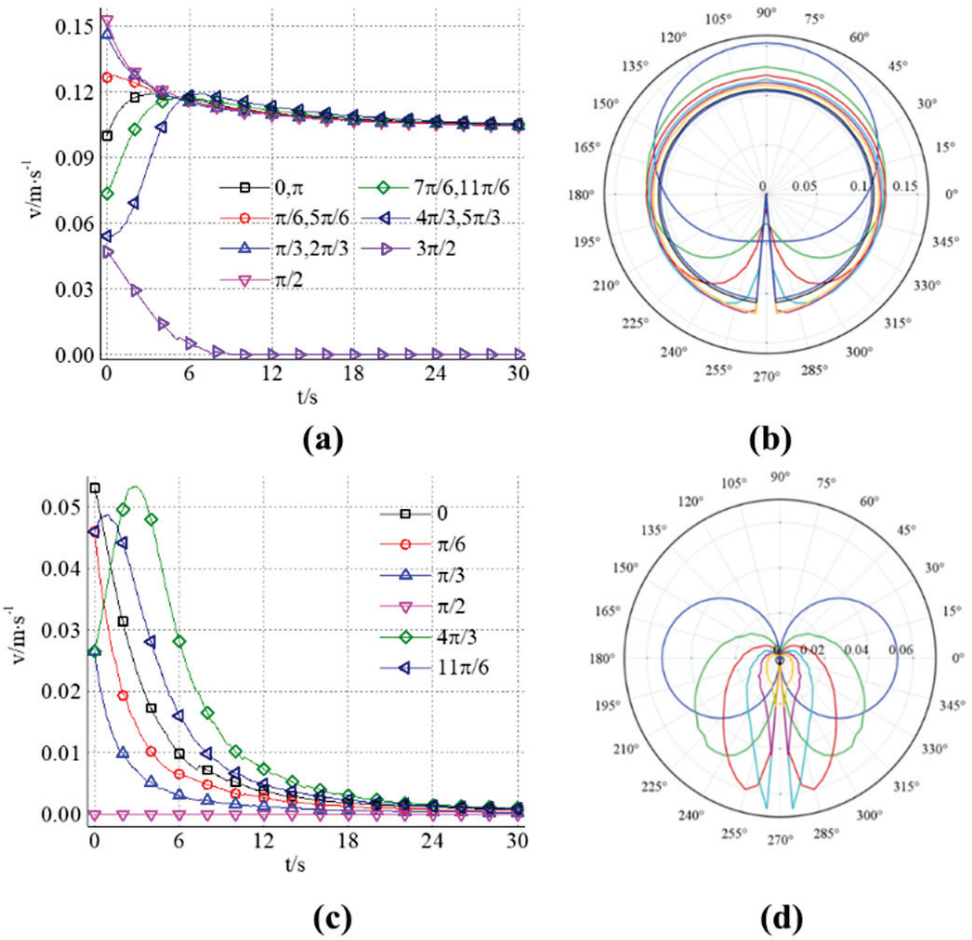

Figure 8. (**a**,**b**) shows the horizontal component of the grout particle velocity changes with the initial angle and grouting time. (**c**,**d**) the vertical component of the grout particle velocity changes with the initial angle and grouting time. Among them, (**a**–**c**) is the change of the streamline velocity with time with different initial angles, and (**b**–**d**) is the change of the velocity of each streamline with the initial angle at different moments.

It can be seen from Figure 8c that with the increase in grouting time, the vertical component of velocity in different streamlines eventually decays to zero. When the initial angle of the streamline is in the range of 0 to $\pi/2$, the initial value decreases with the increase in the angle and continues to decay with the increase in the grouting time. When the initial angle of streamline is in the range of $\pi/2$ to π, the vertical component of particle velocity first increases and then decreases with grouting time and finally approaches zero. By analyzing Figure 8d, it can be further known that the vertical velocity component of the streamline with an initial angle in the range of π to 2π is generally higher than that in the range of 0 to π. With the increase in grouting time, the vertical velocity component of the streamline with an initial angle near $\pi/2$ will reach a certain maximum, and the higher the maximum is when the angle is close to $\pi/2$, the more it indicates that the vertical diffusion distance of the gel particles on the streamline is larger.

4.1.3. The Effect of Expanding Particles on Fluid Drag

Figure 9 shows the distribution of drag force between gel particles and fluid in fractures during slurry diffusion. Because the direction of groundwater flow is positive, except for a small part of the area near the grouting hole, the drag force exerted by the gel particles on the fluid is negative, that is, the gel particles hinder the flow of groundwater. In any fluid unit, the drag force of the gel particles on the fluid is determined by the number of particles contained in the fluid unit, the expansion volume, and the velocity difference between the fluid and the gel particles. As the gel particles continue to absorb water and expand, the drag force between particles and fluid will continue to increase. Because the particle expansion affects the flow field distribution in the fracture, and the particle expansion leads to the increase in the interaction between particles and the constant change of their own motion state, the drag force in the fluid unit is not a simple positive correlation with the particle expansion volume but changes with the increase in grouting time and the expansion of slurry diffusion range.

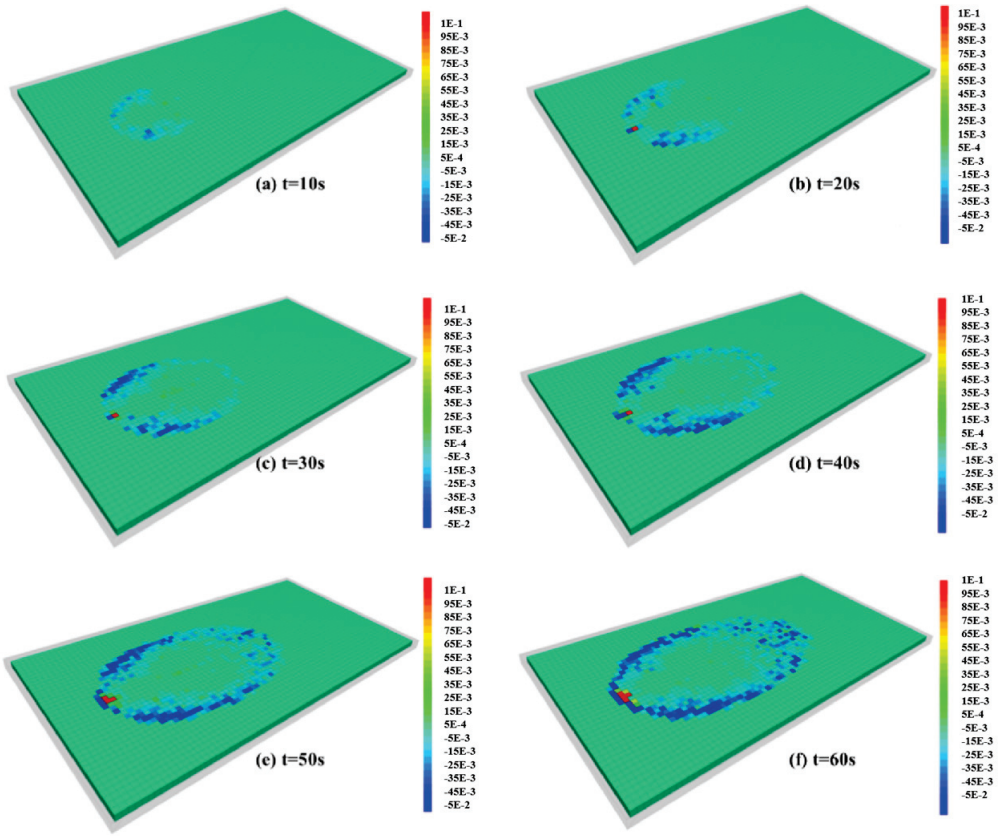

Figure 9. The distribution of the drag force between the gel particles and the fluid in the fracture during the slurry diffusion process: (**a**) t = 10 s, (**b**) t = 20 s, (**c**) t = 30 s, (**d**) t = 40 s, (**e**) t = 50 s, (**f**) t = 60 s.

By analyzing the spatial distribution of the drag force, it can be found that the effect of the drag force on the groundwater remains zero beyond the diffusion range of the slurry. In the range of slurry diffusion, the drag force in different fluid units varies greatly due to the expansion volume of gel particles, particle density, and the spatial heterogeneity of the velocity field in fractures. Comparing the spatial distribution of drag force at different times, it can be found that the area with a larger drag force is always concentrated in the periphery of the slurry diffusion area, while the drag force on the fluid in the inner area is always smaller. At the same time, the maximum drag force is distributed in the first half of the perimeter of the slurry diffusion area.

Combining the slurry diffusion morphology (Figure 5) and the gel particle velocity distribution curve (Figure 8) At different times, it can be seen that in this region, the horizontal velocity of the gel particles changes from a negative value to a positive value. Diffusion in the upstream direction rapidly changes to the downstream direction. This shows that there is a strong interaction between gel particles and groundwater, and there is a large velocity difference between them. However, in the second half of the peripheral perimeter, there is almost no direct interaction between the gel particles and the groundwater; the velocity of the gel particles in the horizontal direction has changed from spreading in the counter-water direction to in the along-water direction. With the increase in diffusion distance, the influence of jet velocity on gel particles disappears gradually, and the movement of gel particles is completely controlled by groundwater. At this time, the velocity of gel particles along the horizontal direction gradually approaches groundwater, and the velocity along the vertical direction gradually approaches zero. The gel particles diffuse with the groundwater under the action of inertia. There is almost no velocity difference between them, so the drag force of gel particles on groundwater is very small.

Considering the interaction between the expansion of particle volume and the change of flow field, the "two-fluid model" in the traditional continuum theory cannot analyze the fluid particle interaction in the flow process. The CFD-DEM method adopts the fluid grid method, which can solve the problem of "fluid-solid phase transition" when the finite element software (COMSOL Multiphysics® 5.6) is used alone. Therefore, the CFD-DEM method is more in line with reality, which provides good guidance for the application of grouting and plugging of expandable particulate materials.

4.2. Plugging Mechanism of Fracture Grouting in Running Water

4.2.1. Different Types of Slurry Plugging Mechanisms

After the cement-sodium silicate slurry is injected; it follows the asymmetric elliptic diffusion law until it diffuses to the boundary section, as shown in Figure 10a. Then, the slurry diffuses into the pseudo-steady state stage. With the progress of the reaction, the slurry changes into a solidified plugging body, thus completing the dynamic water plugging, as shown in Figure 10b,c. Therefore, the running-water plugging mechanism of cement-sodium silicate slurry under constant grouting factor is essentially the process of slurry diffusion and slurry phase transformation. According to Figure 10, the most favorable time period for the formation of a solidified plugging body is t3–t5. When the formation time of the slurry plugging solidified body is less than t3, the grouting resistance may be too large, and the slurry cannot diffuse to the boundary, so the plugging cannot be formed. When the formation time of the solidified plugging body is greater than or equal to t6, the slurry plugging body will not be able to expand to form the plugging area, and the slurry will be washed out of the rock and soil under the action of groundwater, resulting in waste.

During the grouting process of expandable particulate materials, the slurry migration mechanism is obviously different. Expandable particulate materials mainly rely on the particles continuously absorbing water and expanding to increase their own volume. After the slurry enters the groundwater environment, the carrying liquid is dissolved and diluted rapidly by the groundwater. Therefore, in the process of slurry diffusion, the influence of the physical and chemical properties of the carrier fluid on the micromechanical action and macro migration characteristics of the expandable particles in the groundwater environment can be ignored. Dynamic water grouting can be understood as a process in which the solid particles are continuously injected into the fracture, and then the solid particles and groundwater diffuse together.

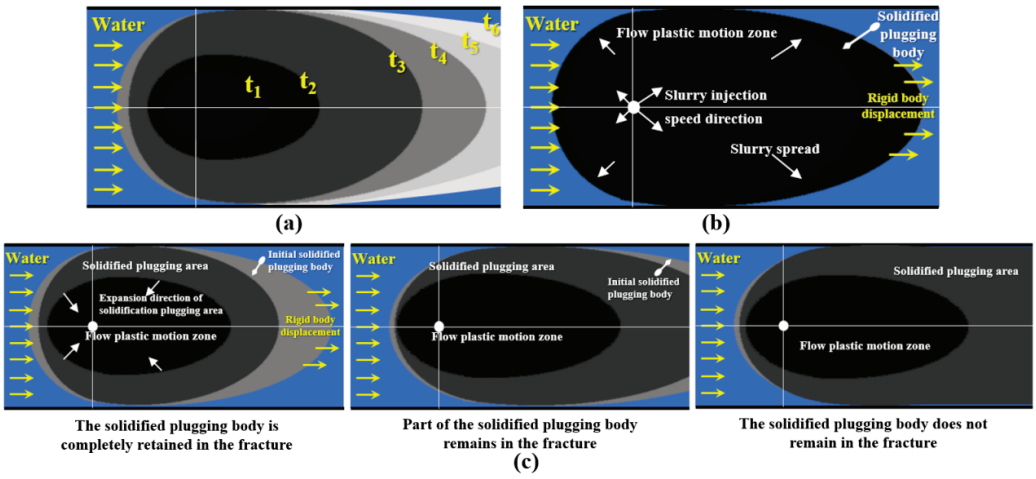

Figure 10. The diffusion process of the cement-sodium silicate slurry in fracture. (**a**) The slurry spreads to the boundary. (**b**) The slurry does not spread to the boundary. (**c**) The three states of the solidified plugging body in fracture.

The maximum diffusion the opening of gel particles in the diffusion process is the key parameter of dynamic water grouting plugging, which directly determines the plugging area formed after grouting, the residual flow size in the fracture, and the retention rate of grouting materials in the fracture. In the process of grouting, the slurry diffusion opening is affected by the groundwater velocity and grouting rate. When analyzing the slurry diffusion process under the influence of dynamic water, the concept of "slurry water velocity ratio" can be used to characterize the joint influence of groundwater velocity and grouting rate. Its physical meaning is the ratio of grouting flow and the product of groundwater velocity and gap width, as shown in Formula (14).

$$\xi = \frac{Q}{U \cdot d} \tag{14}$$

In the Formula (14), U is the velocity of groundwater, d is the width of the gap, and Q is the grouting flow.

4.2.2. The Effect of Slurry-Water Velocity Ratio on the Diffusion Distance of Expandable Particles

Figure 11 shows the time-dependent variation of slurry diffusion distance along water and counter-water under the influence of different slurry water velocity ratios. The solid line is the actual slurry diffusion distance in the calculation, and the corresponding dotted line is the slurry diffusion distance calculated when ignoring the gel particle volume expansion. Except for the part close to the origin, the curve shows almost linear growth, and the slope of the curve (groundwater) velocity corresponding to different slurry water velocity ratios is the same. At the same grouting time, the larger the slurry-water velocity ratio is, the larger the slurry diffusion distance is. When considering the effect of particle volume expansion, there is an obvious inflection point in the calculated slurry diffusion distance curve. The curve before the inflection point almost coincides with the curve obtained by neglecting the particle volume expansion, which indicates that the gel particle movement is controlled by the flow and grouting rate in the fracture, and the particle volume expansion has little effect on the flow field in the fracture. With the continuous water absorption and expansion of particles, the volume content of particles in the fracture increases, and the interaction strength between particles increases. When the volume fraction of particles is close to 50%, the interaction between particles increases significantly and the resistance to the flow increases rapidly. At this time, the particle migration velocity

at the slurry front decreases rapidly, and the curve of diffusion distance forms an inflection point. After the inflection point, the growth rate of the curve decays rapidly and approaches zero, and the slurry diffusion distance hardly increases.

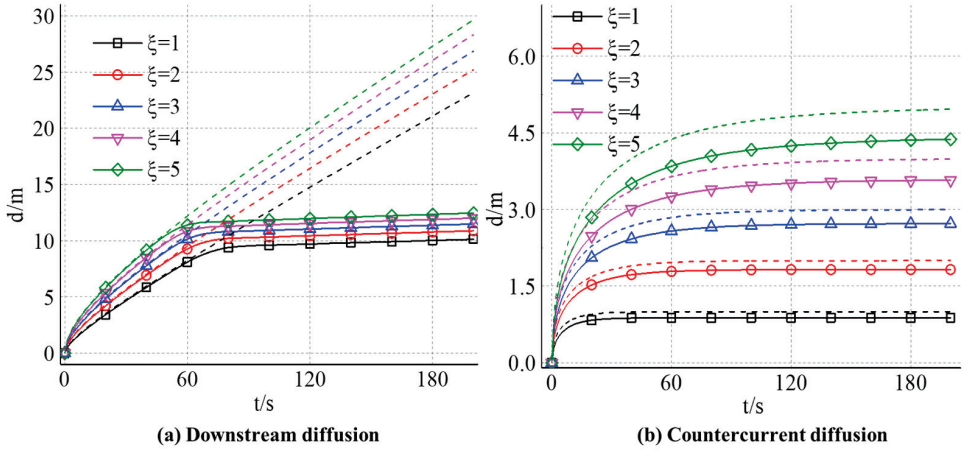

Figure 11. Maximum diffusion distance with different velocity ratio between grout and groundwater (**a**) along the downstream and (**b**) countercurrent direction.

By comparing the slurry diffusion distance curves corresponding to different slurry water speed ratios, with the increase in slurry water speed ratio, the inflection point of the curve is gradually advanced. By observing the curve of slurry diffusion distance with time, it can be found that the curve obtained by considering the effect of particle expansion has a similar growth trend with the curve corresponding to ignoring the effect of particle expansion. The diffusion distance of slurry increases nonlinearly with time, and its growth rate decreases gradually and finally tends to be stable. Compared with the diffusion pattern in the downstream region, there is still a limited diffusion distance in the upstream direction, a stagnation point in the flow field, even without considering the effect of particle volume expansion on the flow. The distance between the stagnation point and the grouting hole is the maximum distance that the slurry can reach along the upstream direction.

The reason for the stagnation point is that the flow field in the fracture can be regarded as the result of the interaction between the parallel flow of groundwater and the point source flow field at the grouting hole. The flow field intensity of a point source decreases with distance, while the field intensity of the parallel flow of groundwater is equal everywhere. In the vicinity of the grouting hole, the flow field strength of the point source is higher than that of the parallel flow field. With the increase in the slurry diffusion distance, the influence of the point source gradually decreases and finally reaches equilibrium, forming a stagnation point in the flow field. By observing the curves corresponding to different slurry water velocity ratios, with its increase, the limit diffusion distance along the upstream direction is increasing, the distance between the stagnation point and the grouting hole is getting farther and farther, and the relationship between them is approximately linear.

When the effect of particle volume expansion is considered; the growth rate of the curve decreases and the limit diffusion distance decreases. Compared with the diffusion distance in the downstream zone, there is no obvious inflection point in the curve, which indicates that the velocity change of gel particles in the upstream diffusion zone is mainly controlled by the flow field in the fracture, and the effect of particle volume expansion on its flow is small. By comparing the curves corresponding to different slurry water velocity ratios, it can be found that the larger the slurry water velocity ratio is, the more obvious the blocking effect of particle volume expansion on flow is and the larger the attenuation range of slurry limiting diffusion distance is.

4.2.3. The Effect of Slurry-Water Velocity Ratio on the Diffusion Velocity of Expandable Particles

Figure 12 shows the variation of slurry diffusion velocity with time along the downstream and countercurrent direction of the grouting hole axis under the influence of different slurry-water velocity ratios. The solid line is the actual diffusion velocity of the slurry in the calculation, and the corresponding dotted line is the diffusion velocity of the slurry when the volume expansion of the gel particles is ignored. It can be seen from the analysis in Figure 12a that the diffusion velocity of gel particles along the water direction gradually decreases with time. At the beginning of grouting, when the effect of particle volume expansion is not considered, the diffusion velocity decays logarithmically, and the decay rate decreases gradually. Finally, the diffusion velocity approaches 0.1 m/s (the groundwater velocity). When the effect of particle volume expansion is considered, the trend of velocity change is almost the same at the initial stage of grouting. With the increase in grouting time, the volume of gel particles expands continuously, and the sealing effect of particles on the flow gradually appears. When the grouting time exceeds 40 s, the diffusion velocity begins to decrease obviously. Moreover, the larger the slurry water velocity ratio is, the faster the attenuation rate is and the larger the amplitude is. When the volume of particles in the fracture is large enough, the diffusion velocity will eventually decay to zero.

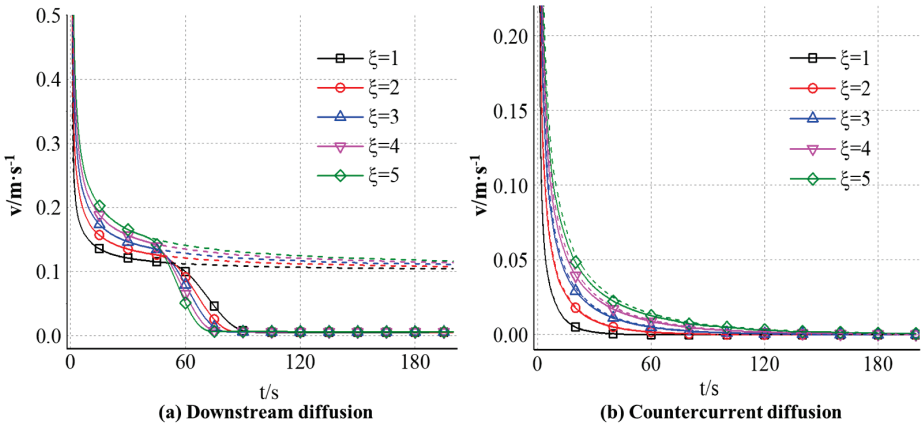

Figure 12. (**a**) The slurry diffusion distance along the downstream and (**b**) countercurrent direction under the influence of different slurry-water velocity ratios.

It can be seen from Figure 12b that the diffusion speed of gel particles along the upstream direction gradually decreases with time. At the initial time of grouting, the diffusion speed of slurry is very fast. With the increase in grouting time, the diffusion distance increases and the decay rate decreases. The curve of velocity change obtained by considering the effect of particle volume expansion is almost the same as that without considering it; the effect of particle volume expansion on its velocity change is small. Compared with the velocity curve in Figure 12a, it can be found that the decay rate of gel particles in the counter-water diffusion zone is faster, and the diffusion rate is more significantly affected by the slurry-water velocity ratio. When the grouting time reaches 30 s, the diffusion rate of gel particles under different slurry-water velocity ratios in the downstream area is maintained between 0.1 m/s and 0.2 m/s, and the maximum difference between different slurry-water velocity ratios is about 30%. However, in the counter-water diffusion region, the diffusion rate has decreased to less than 0.05 m/s, and the diffusion rate corresponding to the slurry-water velocity ratio of 1 is almost zero. When the grouting time reaches 60 s, the particle diffusion rate is still maintained at about 0.1 m/s in the downstream area, while in the upstream area, the diffusion rates corresponding to different slurry-water velocity ratios have declined to zero.

4.2.4. The Effect of Slurry-Water Velocity Ratio on the Opening Degree of Expandable Particles

Figure 13 shows the change of diffusion opening degree with time and different slurry water velocity ratios. It can be seen from Figure 12 that the slurry diffusion opening degree increases nonlinearly with the grouting time, and its growth degree gradually slows down and finally tends to be stable. Combined with the previous analysis, it can be seen that the slurry diffusion shape at any grouting time can be regarded as an irregular ellipse, and the length of its short axis represents the slurry diffusion opening degree at that time. In the initial stage of grouting diffusion, the minor axis of the ellipse is near the grouting hole, and the velocity component of gel particles along the vertical direction is larger, so the growth rate of slurry diffusion opening degree is faster. With the increase in grouting time, the position of the short axis continues to move along the water diffusion direction, the distance between the gel particles and the grouting hole becomes farther, and the volume of the gel particles increases, which leads to the decrease in the velocity component in the vertical direction and the decrease in the growth rate of the slurry diffusion opening. At the same time, because the distance between the gel particles and the boundary on both sides of the fracture gradually shortens, the influence of the fracture boundary on the flow field gradually increases. When the vertical velocity component of the gel particles decreases to zero or the particles diffuse to the side boundary, the slurry diffusion opening degree reaches its maximum. Further analysis of the growth trend of the diffusion opening degree curve shows that when the grouting time exceeds 40 s, the growth rate begins to decrease significantly, and when the grouting time reaches 90 s, the diffusion opening degree basically reaches its maximum. By comparing the diffusion opening degree curves corresponding to different slurry-water velocity ratios, it can be found that with the increase in the slurry-water velocity ratio, the growth rate of the slurry diffusion opening degree increases gradually.

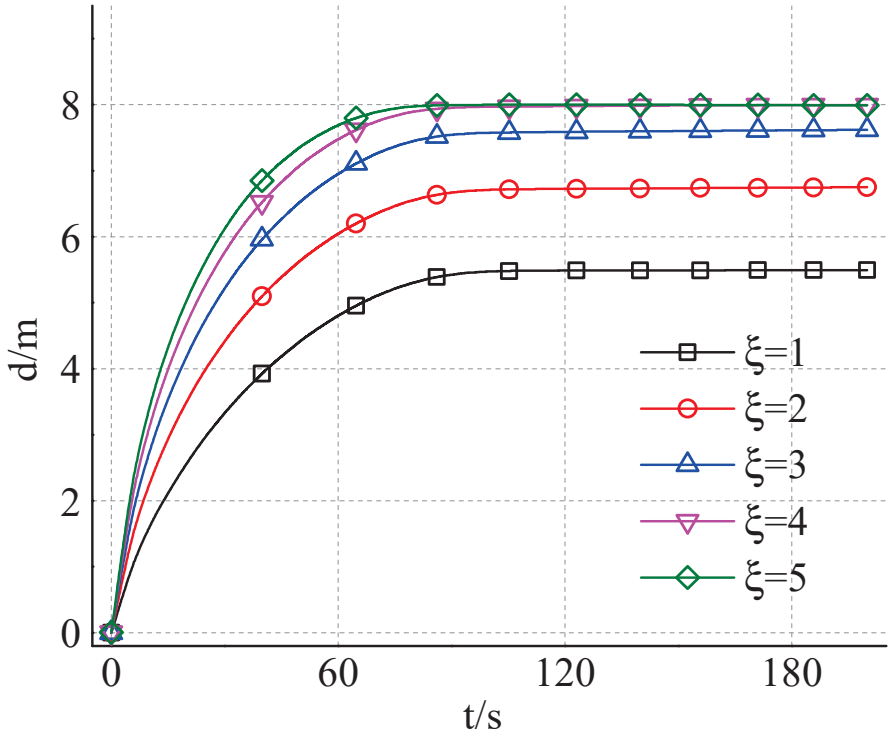

Figure 13. The change of diffusion opening degree with time and different slurry-water velocity ratios.

5. Conclusions

(1) Based on the CFD-DEM method, a numerical model of grouting diffusion in running water of expandable particulate slurry is established. Compared with the calculation method based on continuum theory, the CFD-DEM method can directly reflect the process of gel particle water absorption and expansion and fully consider the interaction between fluid and suspended particles so as to truly reflect the rheological characteristics of expandable particle slurry.

(2) During the grouting process in running water, the cement slurry initially forms an asymmetric ellipse, later becoming elliptical in the counter-water direction. The downstream diffusion range is significantly greater than that of the counter-water diffusion. In the diffusion of cement-sodium silicate slurry, the traces are asymmetric ellipses and different characteristics will be shown by the boundary of the model. For the expandable particulate slurry, the diffusion is approximately elliptical in the fracture with running water. In the counter-water diffusion region, the migration of the gel particles is mainly affected by flow field control, and the attenuation of its speed is mainly caused by a reduction in slurry pressure. In downstream diffusion, the particle is simultaneously influenced by the flow field and its own volume, and its maximum diffusion distance is determined by both. In grouting engineering, adjusting the grout injection rate and the water absorption rate of gel particles can help control the sealing range.

(3) Cement slurry mainly relies on particle deposition to achieve dynamic water sealing, and the work efficiency is relatively low. Cement-sodium silicate slurry has a rapid solidification effect, which is substantially the process of slurry transition from liquid to solid state. The expandable particulate material is mainly based on gel particles that absorb water into the sealing slurry. For expandable particulate materials, if the sealing area is small after grouting, the remaining gel particles will continue to flow and bypass the agglomeration sealing area. At the same time, the original sealing zone expanded particles may also re-flow underwater erosion, eventually resulting in complete loss of the grouting material and not successfully sealing the flow in the fracture. In grouting engineering, the relationship between the diffusion opening degree and the diffusion distance of the slurry is taken, thereby achieving the best grouting sealing effect.

(4) In the actual hydrodynamic grouting process, the water conduction structure in the formation usually has a more complex geometry, which cannot be reduced to a pipeline with a regular contour or a single slab fracture. The diffusion range and plugging effect of the slurry are significantly affected by the spatial morphology of the water conduction structure. Therefore, it is of great significance to construct a more accurate three-dimensional geological model and establish an accurate and efficient grouting diffusion calculation method on this basis for the theory of hydrodynamic grouting plugging.

Author Contributions: Conceptualization, Z.Z. (Zhipeng Zhang) and Z.Z. (Zhuo Zheng); methodology, C.M. and X.L.; data curation, W.L. and C.Z.; writing—original draft preparation, H.W. and X.L.; writing—review and editing, C.M. and R.L.; Experiment: R.L. All authors have read and agreed to the published version of the manuscript.

Funding: This study was financially supported by the China Postdoctoral Science Foundation General Fund (2024M761809) and the Postdoctoral Innovation Talent Support Program (BX20240209).

Institutional Review Board Statement: Not applicable.

Informed Consent Statement: Not applicable.

Data Availability Statement: The original contributions presented in this study are included in the article. Further inquiries can be directed to the corresponding author.

Acknowledgments: The authors thank the editors and two anonymous reviewers for their careful work and thoughtful suggestions.

Conflicts of Interest: Author Hongyan Wang was employed by the Jinan Urban Construction Group Co., Ltd. The remaining authors declare that the research was conducted in the absence of any commercial or financial relationships that could be construed as a potential conflict of interest.

References

1. Li, X.; Zhong, D.; Ren, B.; Fan, G.; Cui, B. Prediction of curtain grouting efficiency based on ANFIS. *Bull. Eng. Geol. Environ.* **2019**, *78*, 281–309. [CrossRef]
2. Han, C.; Xu, J.; Zhang, W.; Wei, J.; Yang, F.; Yin, H.; Xie, D. Assessment and Grouting of Water Inrush Induced by Shaft-Freezing Holes in the Yingpanhao Coal Mine, Inner Mongolia, China. *Mine Water Environ.* **2021**, *41*, 16–29. [CrossRef]
3. Zhou, Z.; Zhao, J.; Tan, Z.; Zhou, X. Mechanical responses in the construction process of super-large cross-section tunnel: A case study of Gongbei tunnel. *Tunn. Undergr. Space Technol.* **2021**, *115*, 104044. [CrossRef]
4. Li, W.; Yu, L.Y.; Tan, Y.Z.; Wu, L.R.; Qian, J.Y. Mechanical properties and impact behavior of frozen clay: Insights from static mechanical tests, fly-plate tests, and split-Hopkinson pressure bar analysis. *Phys. Fluids* **2024**, *36*, 057138. [CrossRef]
5. Wang, M.; Zhu, Z.; Liu, R.; Li, S.; Zhang, C.; Liu, Y.; Zhang, L.; Bai, J. Influence of extreme high-temperature environment and hydration time on the rheology of cement slurry. *Constr. Build. Mater.* **2021**, *295*, 123684. [CrossRef]
6. Shi, J.; Wang, F.; Zhang, D.; Huang, H. Refined 3D modelling of spatial-temporal distribution of excess pore water pressure induced by large diameter slurry shield tunneling. *Comput. Geotech.* **2021**, *137*, 104312. [CrossRef]
7. Zhang, B.; Wang, B.; Zhong, Y.; Li, X.; Zhang, Y.; Li, S. Damage characteristics and microstructures of low-exothermic polymer grouting materials under F–T cycles. *Constr. Build. Mater.* **2021**, *294*, 123390. [CrossRef]
8. Cui, C.; Guo, C.; Lu, Q.; Wang, F.; Fang, H. Fatigue Performance of Concrete–Polyurethane Composite Materials under Compression. *J. Transp. Eng. Part B Pavements* **2021**, *147*, 04021030. [CrossRef]
9. Li, H.; Liu, J.; Wu, J.; Xu, Z.; Zhang, X.; Zhang, L.; Li, Z. Grouting sealing method of flow-control speed-down in karst pipelines and its engineering application. *Tunn. Undergr. Space Technol.* **2021**, *108*, 103695. [CrossRef]
10. Lu, C.; Zhang, Z.; Shi, C.; Li, N.; Jiao, D.; Yuan, Q. Rheology of alkali-activated materials: A review. *Cem. Concr. Compos.* **2021**, *121*, 104061. [CrossRef]
11. Wang, C.; Liu, Q.; Guo, C.; Xia, Y.; Hao, Y.; Shi, M.; Zhao, P. An Experimental Study on the Reinforcement of Silt with Permeable Polyurethane by Penetration Grouting. *Adv. Civ. Eng.* **2020**, *2020*. [CrossRef]
12. Zhang, H.; Zhou, R.; Liu, S.; Zhu, Y.; Wang, S.; Wang, J.; Guan, X. Enhanced toughness of ultra-fine sulphoaluminate cement-based hybrid grouting materials by incorporating in-situ polymerization of acrylamide. *Constr. Build. Mater.* **2021**, *292*, 123421. [CrossRef]
13. Li, Z.Q.; Nie, L.C.; Xue, Y.G.; Li, W.; Fan, K.R. Model Testing on the Processes, Characteristics, and Mechanism of Water Inrush Induced by Karst Caves Ahead and Alongside a Tunnel. *Rock Mech. Rock Eng.* **2025**. [CrossRef]
14. Kim, J.S.; Lee, I.M.; Jang, J.H.; Choi, H. Groutability of cement-based grout with consideration of viscosity and filtration phenomenon. *Int. J. Numer. Anal. Methods Geomech.* **2009**, *33*, 1771–1797. [CrossRef]
15. Pantuso, D.; Jiang, L.; Shankar, S.; Skokov, S. A FEM/VOF hybrid formulation for underfill encapsulation modeling. *Comput. Struct.* **2003**, *81*, 879–885. [CrossRef]
16. Mashayek, F.; Ashgriz, N. A hybrid finite-element–volume-of-fluid method for simulating free surface flows and interfaces. *Int. J. Numer. Methods Fluids* **1995**, *20*, 1363–1380. [CrossRef]
17. Gantois, R.; Cantarel, A.; Dusserre, G.; Félices, J.N.; Schmidt, F. Numerical Simulation of Resin Transfer Molding Using BEM and Level Set Method. *Int. J. Mater. Form.* **2010**, *3*, 635–638. [CrossRef]
18. Chen, T.-l.; Zhang, L.-y.; Zhang, D.-l. An FEM/VOF hybrid formulation for fracture grouting modelling. *Comput. Geotech.* **2014**, *58*, 14–27. [CrossRef]
19. Funehag, J.; Gustafson, G. Design of grouting with silica sol in hard rock—New methods for calculation of penetration length, Part I. *Tunn. Undergr. Space Technol.* **2008**, *23*, 1–8. [CrossRef]
20. Li, S.; Qi, Y.; Li, Z.; Li, H.; Zhang, J. A novel treatment method and construction technology of the pipeline gushing water geohazards in karst region. *Tunn. Undergr. Space Technol.* **2021**, *113*, 103939. [CrossRef]
21. Li, S.; Pan, D.; Xu, Z.; Lin, P.; Zhang, Y. Numerical simulation of dynamic water grouting using quick-setting slurry in rock fracture: The Sequential Diffusion and Solidification (SDS) method. *Comput. Geotech.* **2020**, *122*, 103497. [CrossRef]
22. Chen, H.; Ding, W.; Wei, H.; Saxén, H.; Yu, Y. A Coupled CFD-DEM Study on the Effect of Basset Force Aimed at the Motion of a Single Bubble. *Materials* **2022**, *15*, 5461. [CrossRef] [PubMed]

23. Cheng, J.; Dou, Y.; Zhang, N.; Li, Z.; Wang, Z. A New Method for Predicting Erosion Damage of Suddenly Contracted Pipe Impacted by Particle Cluster via CFD-DEM. *Materials* **2018**, *11*, 1858. [CrossRef]
24. Zhang, S.; Liu, Y.; Li, W.; Cao, J.; Huang, J.; Zhu, L.; Guan, Z. Numerical Analysis of the Effect of Retaining Ring Structure on the Chemical Mechanical Polishing Abrasive Motion State. *Materials* **2023**, *16*, 62. [CrossRef] [PubMed]
25. Ma, C.; Li, S.; Liu, R.; Pei, Y.; Zhang, C.; Liu, Y.; Xu, F.; Feng, X.; Chen, M. Evaluation of a Superabsorbent Polymer for Plugging Karst Pipe Type Water Inrushes. *Mine Water Environ.* **2021**, *41*, 252–264. [CrossRef]
26. Li, W.; Zhang, Q.S.; Wang, X.C.; Yu, L.Y.; Li, Z.Q. Synergistic effect of particle size, carboxymethyl starch and Na_2CO_3 on rheological and filtration property of bentonite-based material. *Case Stud. Constr. Mat.* **2024**, *21*, e03537. [CrossRef]
27. Zhang, Q.S.; Zhang, L.Z.; Liu, R.T.; Han, W.W.; Zhu, M.T.; Li, X.H.; Zheng, D.Z.; Xu, X.H. Laboratory experimental study of cement-silicate slurry diffusion law of crack grouting with dynamic water. *Rock Soil Mech.* **2015**, *36*, 2159–2168. [CrossRef]
28. Li, S.; Liu, R.; Zhang, Q.; Zhang, X. Protection against water or mud inrush in tunnels by grouting: A review. *J. Rock Mech. Geotech. Eng.* **2016**, *8*, 753–766. [CrossRef]
29. Pal, R. Rheological constitutive equation for bubbly suspensions. *Ind. Eng. Chem. Res.* **2004**, *43*, 5372–5379. [CrossRef]
30. Brouwers, H.J.H. Viscosity of a concentrated suspension of rigid monosized particles. *Phys. Rev. E* **2010**, *81*, 051402. [CrossRef]

Disclaimer/Publisher's Note: The statements, opinions and data contained in all publications are solely those of the individual author(s) and contributor(s) and not of MDPI and/or the editor(s). MDPI and/or the editor(s) disclaim responsibility for any injury to people or property resulting from any ideas, methods, instructions or products referred to in the content.

materials

MDPI

Article

Failure and Energy Evolution Characteristics of Saturated Natural Defective Material Under Different Confining Pressures

Zhihao Gao [1], Shihao Guo [1,*], Xiaoyong Yang [2], Shanchao Hu [1], Junhong Huang [1], Yafei Cheng [1], Dawang Yin [1] and Jinhao Dou [1]

[1] College of Energy and Mining Engineering, Shandong University of Science and Technology, Qingdao 266590, China; 19862869727@163.com (Z.G.); skd994527@sdust.edu.cn (S.H.); qaz1253466914@126.com (J.H.); 15726495680@163.com (Y.C.); m15285817719@163.com (D.Y.); djh15092318906@163.com (J.D.)
[2] Shandong Energy Group Xibei Mining Company Limited, Xi'an 710018, China; hjmskd2021@163.com
* Correspondence: skd996359@sdust.edu.cn; Tel.: +86-17852152311

Abstract: In nature, many brittle materials contain natural defects such as microcracks or joints, for example, rocks. Under water-saturated conditions, the strength of defective materials undergoes varying degrees of attenuation, leading to material failure and even structural instability in engineering contexts. Moreover, the deformation and failure of defective brittle materials are essentially the result of the accumulation and dissipation of energy. Studying the energy evolution of defective brittle materials under load is more conducive to reflecting the intrinsic characteristics of strength changes and overall failure of brittle materials under external loading. Natural defective brittle rock materials were firstly water saturated and triaxial compression tests were performed to determine the mechanical properties of water-saturated materials. The energy evolution patterns of water-saturated materials under varying confining pressures were also obtained. Using the discrete element method, the macro- and micro-failure characteristics of water-saturated materials were investigated, revealing the mesoscopic mechanisms of deformation and failure evolution in these materials. The results indicate that confining pressure significantly enhances the peak compressive strength and elastic modulus of water-saturated defective materials. When the confining pressure increased from 0 MPa to 20 MPa, the peak strength and elastic modulus of the water-saturated materials increased by 126.8% and 91.9%, respectively. Confining pressure restricts the radial deformation of water-saturated materials and dominates the failure mode. As confining pressure increases, the failure mode transitions from tensile splitting (at 0 MPa confining pressure) to shear failure (at confining pressures $\geq$ 10 MPa), with the failure plane angle gradually decreasing as confining pressure rises. Confining pressure significantly alters the energy storage–release mechanism of water-saturated defective brittle materials. At peak load, the total energy, elastic energy, and dissipated energy increased by 347%, 321%, and 1028%, respectively. The ratio of elastic energy storage to peak strain ratio shows a positive correlation, and the elastic storage ratio of water-saturated defective brittle materials under confining pressure is always higher than that without confining pressure. When the strain ratio exceeds 0.94, a negative correlation between confining pressure and the rate of elastic storage ratio is observed. From the perspective of mesoscopic fracture evolution in water-saturated defective brittle materials, the crack propagation path shifts from the periphery to the center of the material, and the fracture angle decreases linearly from 89° to 58° as confining pressure increases. The dominant direction of crack development is concentrated within the 45–135° range. The findings elucidate the mechanisms by which water saturation and confining pressure influence the strength degradation of natural defective brittle materials from both mesoscopic

and energy perspectives, providing theoretical support for the stability control of related engineering structures.

Keywords: natural defective brittle materials; saturated experiment; confinement effect; damage characteristics; energy evolution

1. Introduction

Naturally defective materials, as the most common engineering media in underground construction [1–3], undergo significant changes in mechanical properties due to the combined effects of in situ stress and groundwater as underground projects extend to greater depths [4–6]. These changes often lead to engineering hazards, making it crucial to understand the deformation-failure characteristics and energy evolution mechanisms of water-saturated defective materials under varying confining pressures to ensure the stability of deep underground structures [7,8].

In recent years, extensive research has been conducted on the mechanical behavior of naturally defective materials under different moisture conditions. Colback et al. [9] investigated the mechanical properties of quartz sandstone with varying moisture contents, revealing that the strength of saturated quartz sandstone is approximately 50% of that in its dry state. Li et al. [10] demonstrated through mechanical tests that specimens with higher initial strength exhibit greater compressive resistance under the same initial density and moisture content. Song et al. [11] conducted uniaxial compression tests on fractured sandstone in both natural and hydrochemical environments, finding that water significantly influences crack initiation and failure modes. Chen et al. [12] observed that water accelerates crack propagation in shale under varying moisture conditions. Zhao Yanlin et al. [13] demonstrated through permeability tests that pore water pressure negatively correlates with rock strength and elastic modulus. Existing studies confirm that rock failure is fundamentally driven by energy release [14–18]. Xie Heping et al. [19] proposed that rock damage results from the interplay between energy accumulation and dissipation during deformation. Meng Zhaoping et al. [20] investigated the influence of moisture content on elastic strain energy in sedimentary rocks under uniaxial compression. Lai Xingping et al. [21] explored the patterns of energy release in coal-rock masses with varying moisture contents. Liu Wanli et al. [22] analyzed the energy transformation characteristics of saturated mudstone through uniaxial compression tests. Liu Yunsi et al. [23] conducted Brazilian splitting tests on saturated slate using an SHPB system, showing that the dissipated energy density of saturated slate exceeds that of dry slate at higher loading rates. Guo Jiaqi et al. [24] revealed that saturated karst limestone exhibits faster energy release rates compared to dry samples. Gao et al. [25] established a damage evolution model for freeze–thaw cycled sandstone based on energy dissipation ratios. Yang Yongjie et al. [26] developed a damage variable model for coal samples by studying energy evolution under different loading-unloading paths. Zhao Yixin et al. [27] examined the effects of moisture on energy density and damage variables in coal through Brazilian splitting tests. Huang Ming et al. [28] investigated the energy dissipation characteristics of water-bearing siltstone under impact loading. Peng et al. [29] found that the energy absorption efficiency of CASS materials decreases with increasing strain rates. Jiang Jingdong et al. [30] quantified the relationships between total energy, elastic stored energy, and moisture content in triaxial compression tests.

Although previous research has emphasized the significant influence of moisture content on the mechanical properties and energy damage characteristics of rocks, studies

addressing the combined effects of confining pressure and water saturation on the failure behavior and energy evolution of naturally defective materials remain limited. To bridge this gap, the present study conducts uniaxial and triaxial compression experiments on dry and saturated defective materials under varying confining pressures. Specifically, the study systematically examines the following: (i) the variation in mechanical parameters under different confining pressures and saturation conditions; (ii) the macro-failure patterns and meso-damage evolution mechanisms of saturated defective materials subjected to varying confining pressures; and (iii) the mechanisms of energy accumulation and dissipation in water-saturated materials under confining pressure gradients. This research aims to provide theoretical foundations for the stability assessment and disaster mitigation of deep underground engineering projects.

2. Water-Saturated Test Material Preparation and Programs

2.1. Water-Saturated Defective Brittle Material Specimen Preparation

The natural defective brittle material used in the test was sourced from the western Ordos mining area in Inner Mongolia, extracted from middle sandstone at a burial depth of approximately 600 m. The samples exhibited no obvious surface cracks and were gray in their natural state. The natural defective brittle material specimens are shown in Figure 1. The surface of the material was rough, and the specimens were cylindrical with a diameter of 89 mm and a column length between 10 and 70 cm. The engineering drilling core is shown in Figure 1a. According to the "engineering rock test method standard", the retrieved core was subjected to secondary processing, including cutting, polishing, and shaping into standard cylindrical specimens with a height of 100 mm and a diameter of 50 mm, as shown in Figure 1b. The height error of the standard specimen was controlled within 2 mm, and the unevenness of the two end surfaces was maintained within 0.05 mm.



(**a**) (**b**)

Figure 1. Natural defective brittle material specimen: (**a**) engineering drill core; (**b**) indoor test samples.

First, the processed specimens were placed into the drying box shown in Figure 2. The temperature of the drying box was set to 110 °C, and the specimens were weighed every 6 h. If the difference in mass between two consecutive weighings was no more than 0.1 g, the specimens were considered to have reached a completely dry state. The water-saturated specimens were prepared in accordance with the Standard for Test Methods of Engineering Rock Masses. The procedure involved rapid water absorption of dried samples using a free immersion method, followed by 48 h immersion. Subsequently, a vacuum saturation process was implemented for 6 h to ensure complete bubble elimination. After a 4 h stabilization period, the specimens were weighed to confirm full saturation.

2.2. Characterization of the Basic Mineral Composition and Microstructure of Natural Defective Materials

To analyze the mineral composition of defective rock brittle material, powder sample from the core retrieved at the site was manually ground until the particle size was smaller than a 325-mesh sieve. The powder sample was then evenly spread on a glass sample tank to form a specimen, which was placed into the test instrument for X-ray diffraction analysis. By utilizing the different lattice spacings between the mineral components and comparing them with the corresponding reference cards and diagrams, the mineral composition and content of the specimen were determined. As illustrated in Figure 3, the experimental results reveal that the medium sandstone specimen contains seven mineral compositions: quartz, plagioclase feldspar, potassium feldspar, clay minerals, calcite, pyrite, and gypsum. The primary component of clay minerals is chlorite.



Figure 2. Constant temperature and humidity maintenance box.

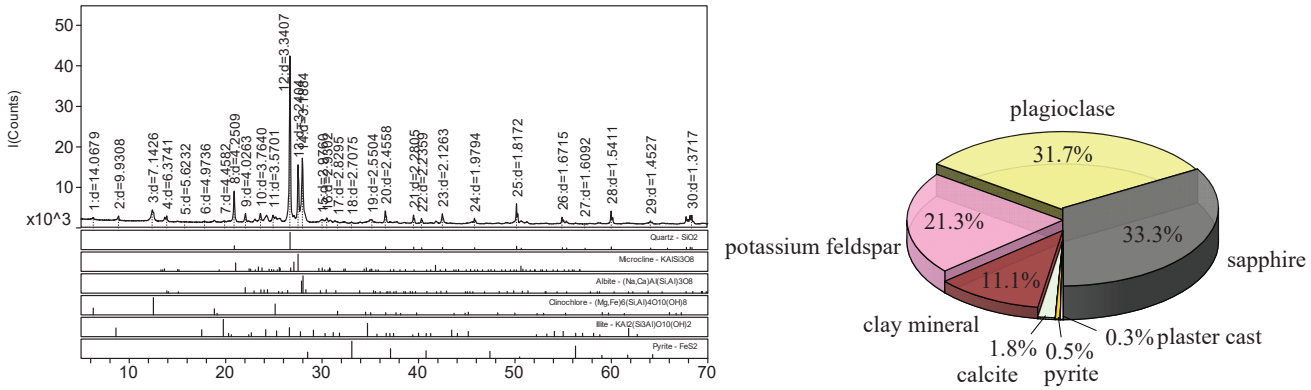

Figure 3. XRD diffraction and mineralogical composition content map.

Based on the complex composition of the mineral components in the natural defective rock brittle materials, and combined with the micro-morphological structure tests, the analysis was conducted using thermal field emission scanning electron microscopy. The micro-morphological structure of the materials is shown in Figure 4. Figure 4a shows that the surface of the defective rock material is flat, with particles tightly bound to each other, although a small number of cracks and pores are still present. Figure 4b reveals the presence of clay minerals such as calcite, potassium feldspar, etc., which react and expand in contact with water, making the pore cracks in the rock material to further expand.

2.3. Test Setup and Test Program

The buried depth of the defective brittle material used in the test is about 600 m, with the confining pressure around 13.8 MPa. For the test, a confining pressure of 10 MPa is selected as the initial value. The test loading instrument adopts the ZST series rock triaxial system, which includes an axial loading system, a confining pressure loading system, and a digital control and data acquisition system. The axial loading system, along with the radial deformation-induced gauge, can employ either displacement or force loading methods. The confining pressure loading system utilizes a hydraulic oil pump for loading, with the loading process and data collection controlled by a computer control system. The test loading device is shown in Figure 5 below. The force loading method is adopted, with a loading accuracy of 1%, and the loading termination condition is set as the destruction of the specimen. To study the effect of confining pressure on the mechanical properties and energy evolution of the materials in a water-saturated state, the confining pressures were set to 0, 10, 15, and 20 MPa, resulting in four different confining pressure conditions. The specific test program is shown in Table 1. To ensure low test dispersion, three groups of tests under the same confining pressure conditions were conducted as controls.

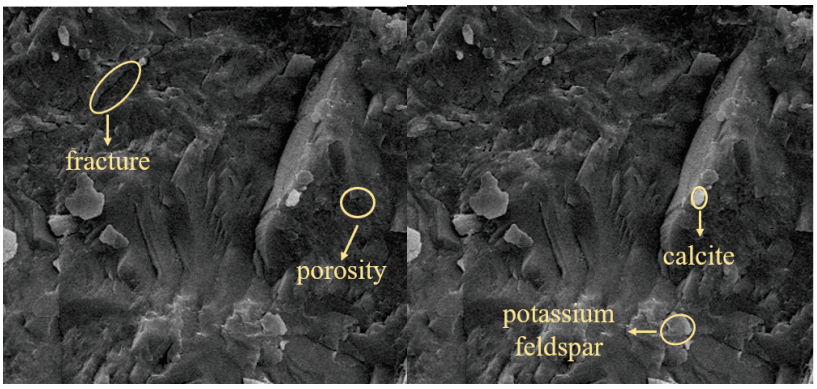

(**a**) (**b**)

Figure 4. Microstructure of defective sandstone materials: (**a**) fine structure of defective sandstone materials; (**b**) defective sandstone material components.

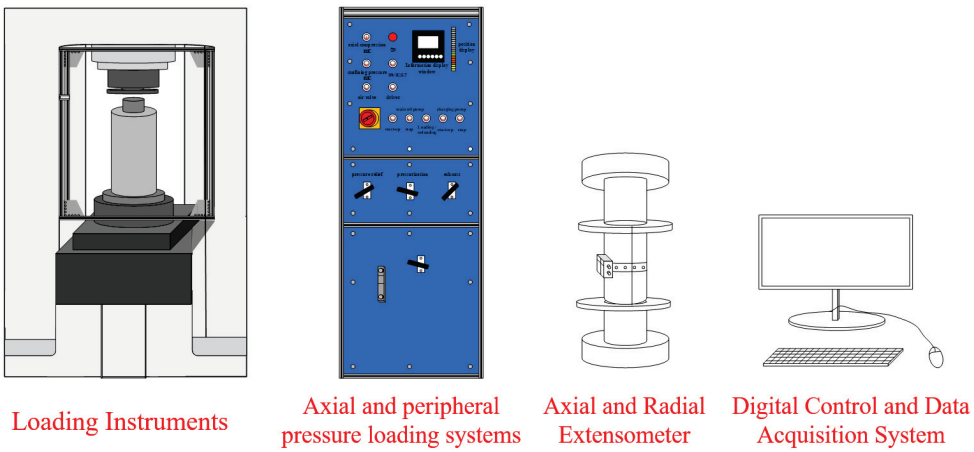

Figure 5. ZST rock triaxial test system.

Table 1. Triaxial test program.

Pressurization/MPa	Waterlogged State		Dry State	
	Test Number	Loading Rate MPa/s	Test Number	Loading Rate MPa/s
0	BS-0	0.01	GZ-0	0.01
10	BS-10		GZ-10	
15	BS-15		GZ-15	
20	BS-20		GZ-20	

3. Mechanical Properties and Deterioration Law of Water-Saturated Natural Defective Materials

3.1. Stress–Strain Analysis

Based on the analysis of the test results in Figures 6 and 7, the bias stress–strain curves of both dry defective brittle material specimens and water-saturated material specimens under different confining pressure conditions exhibit the same trend. These curves can be divided into four typical deformation phases: the compaction phase, the elastic deformation phase, the crack stabilization phase, and the crack accelerated expansion phase. Under the combined effect of confining pressure and axial pressure, the natural defective specimen first experiences the compaction stage. During this stage, the original pores and microcracks are gradually closed under the action of stress, and the curve displays nonlinear characteristics. As the axial load continues to increase, the curve enters the elastic deformation stage, where no new cracks are formed internally, and the stress and strain exhibit a linear relationship. When the axial load reaches the yield strength, the specimen enters the stable crack development stage, during which new cracks start to develop internally. As the axial load continues to increase towards the yield strength, the specimen transitions into the accelerated crack expansion stage. At this point, cracks penetrate through the material, and main cracks form on the surface. The load-carrying capacity decreases rapidly, and the curve shows decay characteristics.

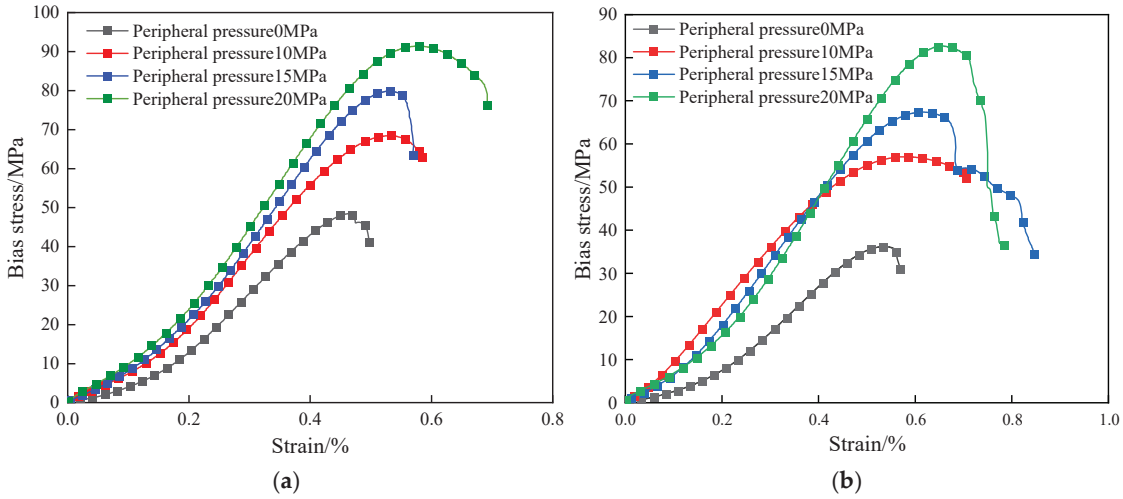

Figure 6. Bias stress–strain curve: (**a**) drying of natural defective specimens; (**b**) water-saturated natural defect specimens.

3.2. Analysis of the Law of Change of Mechanical Parameters of Natural Defective Materials

The evolution pattern of conventional triaxial mechanical parameters of defective brittle material under different confining pressures is shown in Figure 8. As the confining pressure increases from 0 MPa to 20 MPa, the peak strength of water-saturated materials increases from 36.18 MPa to 82.17 MPa, a 126.8% increase; the elastic modulus improves

from 8.7 GPa to 16.7 GPa, a 91.9% increase. In contrast, the peak strength of dry materials increases from 48.23 MPa to 91.39 MPa, an 89.34% increase, and the elastic modulus increases from 13.13 GPa to 20.09 GPa, a 52.55% increase. Linear regression analysis based on the test data shows that the peak strength and modulus of elasticity of the material under water-saturated conditions are lower than those under dry conditions. The increase in the level of confining pressure has a significant effect on the mechanical parameter of the defective brittle rock material under water-saturated conditions. The confining pressure compacts the cracks within the material, effectively increasing the density of the rock. Additionally, the confining pressure restricts the radial deformation of the material, reducing the tendency for volumetric expansion, and strengthens the normal stresses between rock particles, which improves the particle density. The increase in normal stress between the material particles enhances friction between the particles, further contributing to the overall strength of the material.

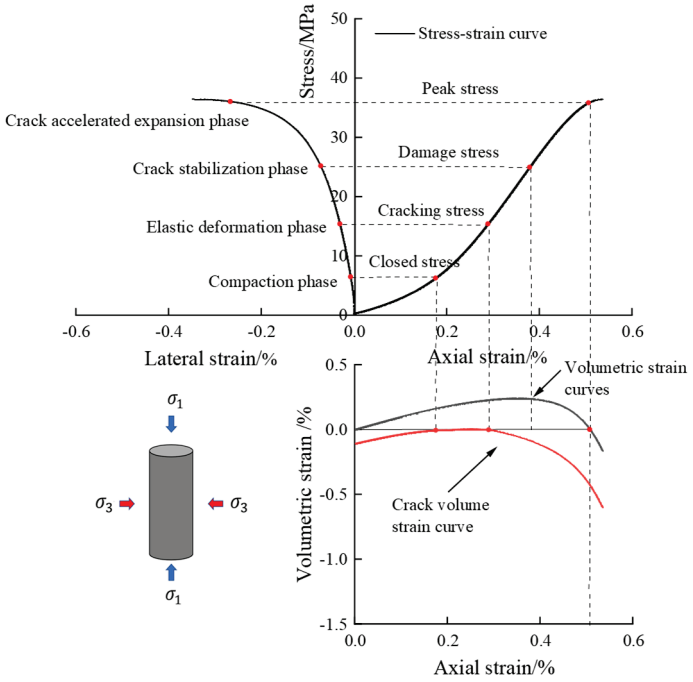

Figure 7. Stress–strain diagram of the damage process of natural defective materials (water-saturated uniaxial).

The evolution of critical stresses in natural defective brittle materials under different enclosing pressures is shown in Figure 9. The defective rock materials in both dry and water-saturated states exhibited the same growth trend under varying enclosure pressures. However, the critical stresses of dry materials were higher than those of water-saturated materials due to changes in the microstructure of the materials caused by water immersion. When the confining pressure of the water-saturated material was increased from 0 MPa to 20 MPa, the closure stress increased from 8.65 MPa to 12.34 MPa, an increase of 42.7%; the crack initiation stress increased from 15.42 MPa to 30.42 MPa, an increase of 98.7%; and the damage stress increased from 25.07 MPa to 56.21 MPa, an increase of 124.2%. The increase in confining pressure level showed a similar trend for both dry and water-saturated defective rock materials, but the critical stresses of dry material were higher than those of water-saturated materials due to change in the material's microstructure under the effect of water immersion. The increase in pressure levels strengthens the critical stresses in the water-saturated material in two ways. On the one hand, the increase in confining pressure enhances the internal density of the material, which reduces the extensibility of primary

cracks. On the other hand, it enhances the normal force at the particle contact surfaces and strengthens the anti-slip ability of the particles, thereby improving the strength required for the initiation of nascent cracks. The four key stresses—crack closure stress, crack initiation stress, damage stress, and peak stress—represent the complete process of progressive damage in rock materials and exhibit a significant positive correlation with the level of surrounding pressure.

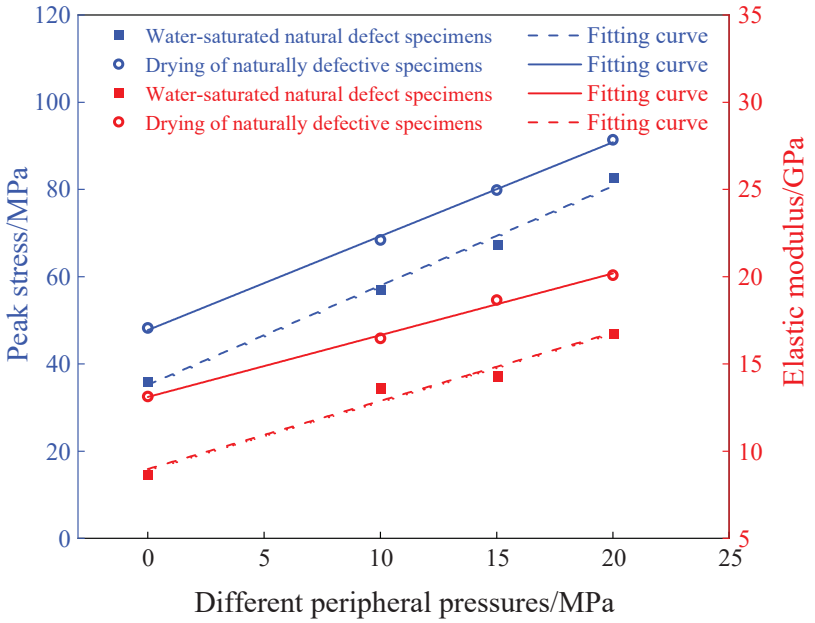

Figure 8. Variation in mechanical parameters of defective brittle materials with increasing confining pressure.

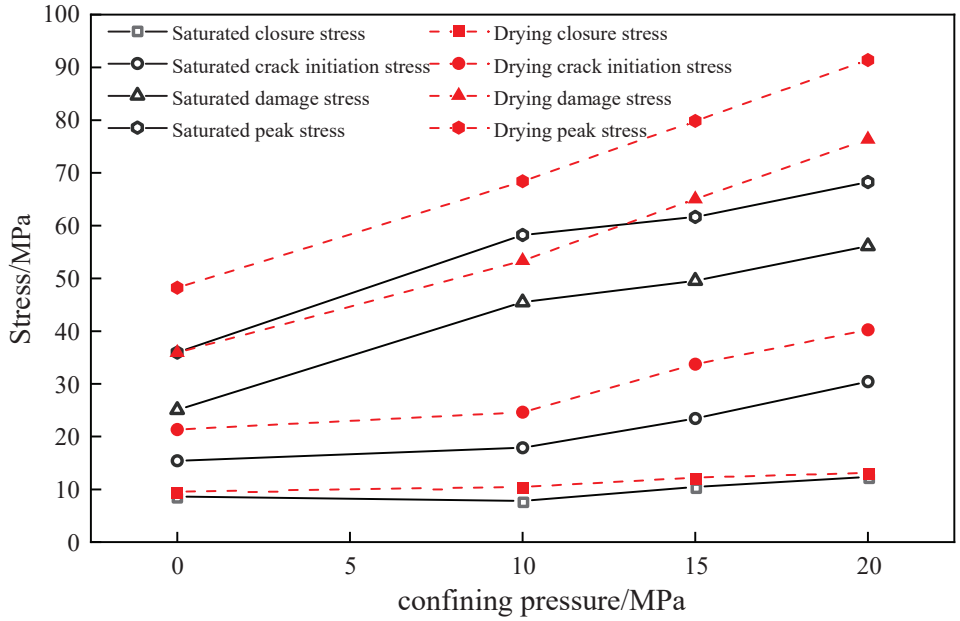

Figure 9. Variation in critical stress with confining pressure for natural defective materials.

3.3. Damage Characteristics of Water-Saturated Natural Defective Rock Materials Under Different Confining Pressures

Figure 10 shows the damage characteristics of the water-saturated material under different confining pressure conditions in the triaxial compression test. It is observed that the damage modes of the water-saturated defective rock materials under different confining

pressures primarily manifest in two modes: tensile damage (the main cracks are nearly vertical to the horizontal direction) and shear damage (the angle between the main cracks and the horizontal direction is acute). When the confining pressure is 0 MPa, the specimen shows typical longitudinal tensile damage, with the inclination angle of the main cracks around 89°. When the confining pressure increases to 10 MPa, the damage mode transitions to single-slope shear damage, with the main crack inclination angle approximately 77.7°; at 15 MPa, the damage mode remains shear damage, with the main crack inclination angle around 62.2°; and when the confining pressure increases to 20 MPa, the damage mode continues to be shear damage, with the main crack inclination angle around 50.3°. The confining pressure dominates the crack extension path and damage characteristics. In the absence of confining pressure, the material is not affected by the annular constraint force, and stress concentration due to the maximum principal stress direction forms radial tensile stress, leading to a damage mode dominated by tensile damage. However, with the application of confining pressure, the annular constraint force enhances the friction force between the particles, causing the crack extension direction to deviate from the direction of the maximum principal stress. This shift results in a damage mode dominated by shear damage. Therefore, there is a negative correlation between confining pressure and crack inclination angle: as confining pressure increases, the crack inclination angle decreases.

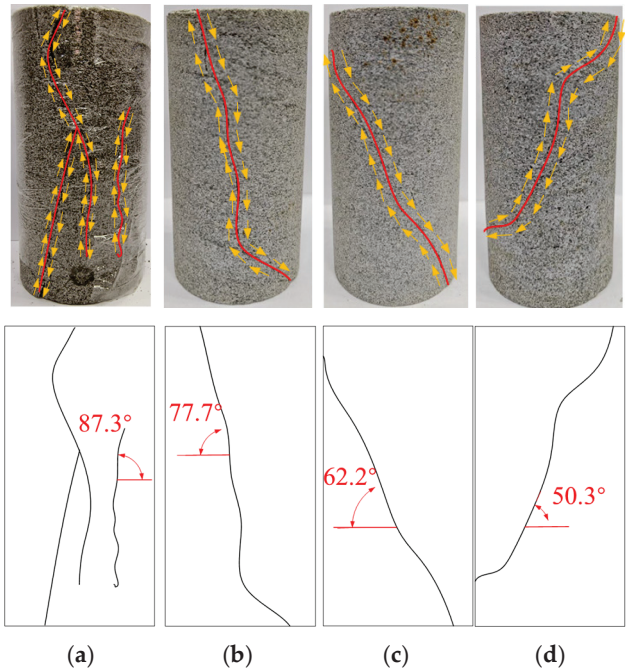

Figure 10. Damage pattern of specimen under different confining pressures: (**a**) confining pressure 0 MPa; (**b**) confining pressure 10 MPa; (**c**) confining pressure 15 MPa; (**d**) confining pressure 20 MPa.

4. Numerical Simulation Based on Discrete Element Method

4.1. Principle and Parameter Calibration

The core of the discrete element method is to map the microscopic mechanical behavior of the material through the mechanical behavior of the particles. This approach allows for the visual demonstration of the dynamic processes of crack generation, expansion and energy conversion, enabling cross-scale mechanical analysis from micro to macro levels. In the indoor experiments, water-saturated material with a density of about 2250 kg·m^{-3} was used, with cylindrical specimens having a diameter of 50 mm and a height of 100 mm. In PFC2D, the specimens were generated with the same dimensions as those in the indoor tests. The minimum particle radius was set at 0.9 mm, with a particle size ratio (maximum

radius to minimum radius) of 1.66. The parallel bonding model was applied between the particles, as shown in Figure 11. Based on the loading method of the indoor test, the model was loaded by displacement control, with the loading rate of the upper and lower loading plates set at 0.01 m·s^{-1}.

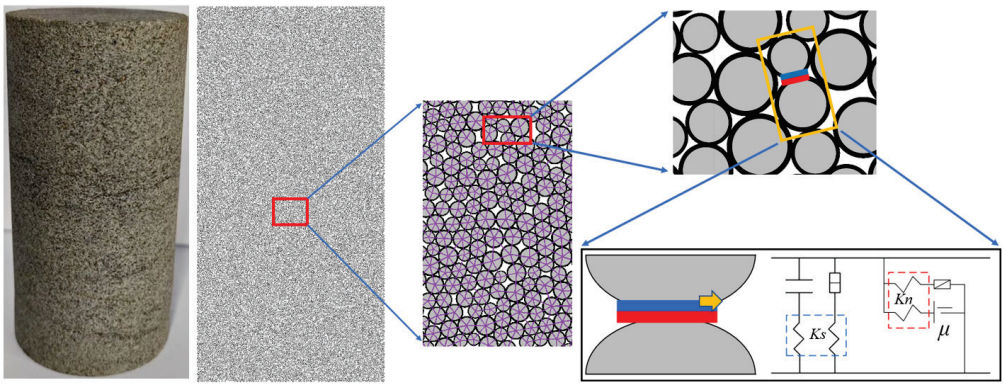

Figure 11. Numerical specimen.

To ensure the accuracy of the numerical simulation results, based on the experimental data of uniaxial compressive strength of the specimen, the micro-parameters of the model were systematically calibrated using the trial-and-error method. The destructive characteristics and stress–strain process of the calibration results are shown in Figure 12, and the finalized values of the micro-parameters are shown in detail in Table 2.

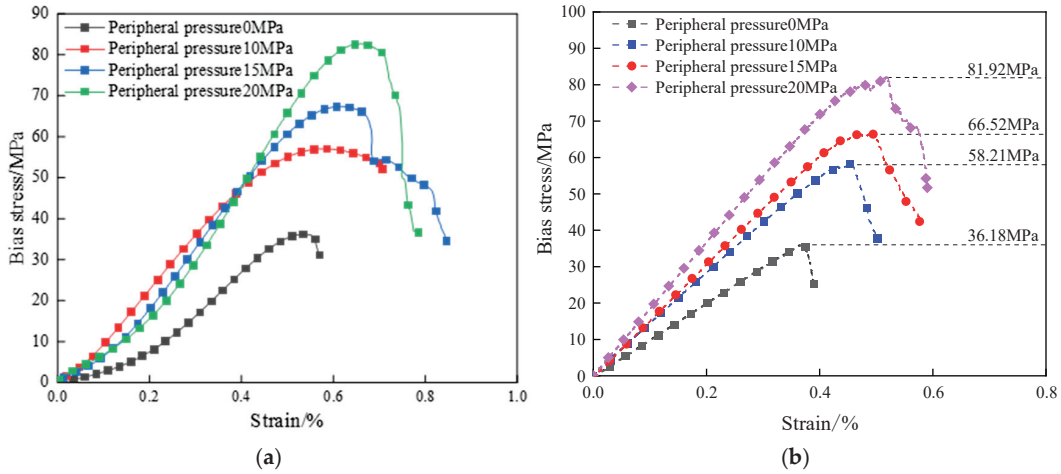

Figure 12. PFC parameter calibration results: (**a**) indoor test curves; (**b**) numerical simulation curves.

Table 2. Simulated fine view parameters.

Type	R_{min}/mm	R_{max}/R_{min}/(mm)	E_c/GPa	μ	σ_c/MPa	c/MPa	Ø	k_s/k_n
water-saturated defective brittle material	0.9	1.66	5.1	0.3	10.9	22.2	38	1.5

Note: R_{min} is the minimum particle radius; R_{max}/R_{min} is the particle radius ratio; E_c is the particle contact modulus; k_n/k_s is the particle stiffness ratio; μ is the particle friction factor; Ø is the angle of internal friction; σ_c is the parallel bond tensile strength; and c is the strength of parallel bond cohesion.

4.2. Spatio-Temporal Evolution Law of Rift Network

The macroscopic damage nature of defective rock materials under uniaxial and triaxial loading conditions is characterized by the generation, expansion, and penetration of cracks at the microscopic scale. The discrete element method can effectively capture the dynamic

development and spatial distribution characteristics of these cracks. As shown in Figure 13, with the increase in bias stress, internal damage in the specimen begins to occur, forming a micro rupture surface with a certain angle to the horizontal direction. The angle between the macro rupture surface and the horizontal plane is the breakage angle. As the confining pressure increases from 0 MPa to 20 MPa, the number of fissures increases, with the fracture angles measured at about 89°, 69°, 63°, and 53°, respectively.

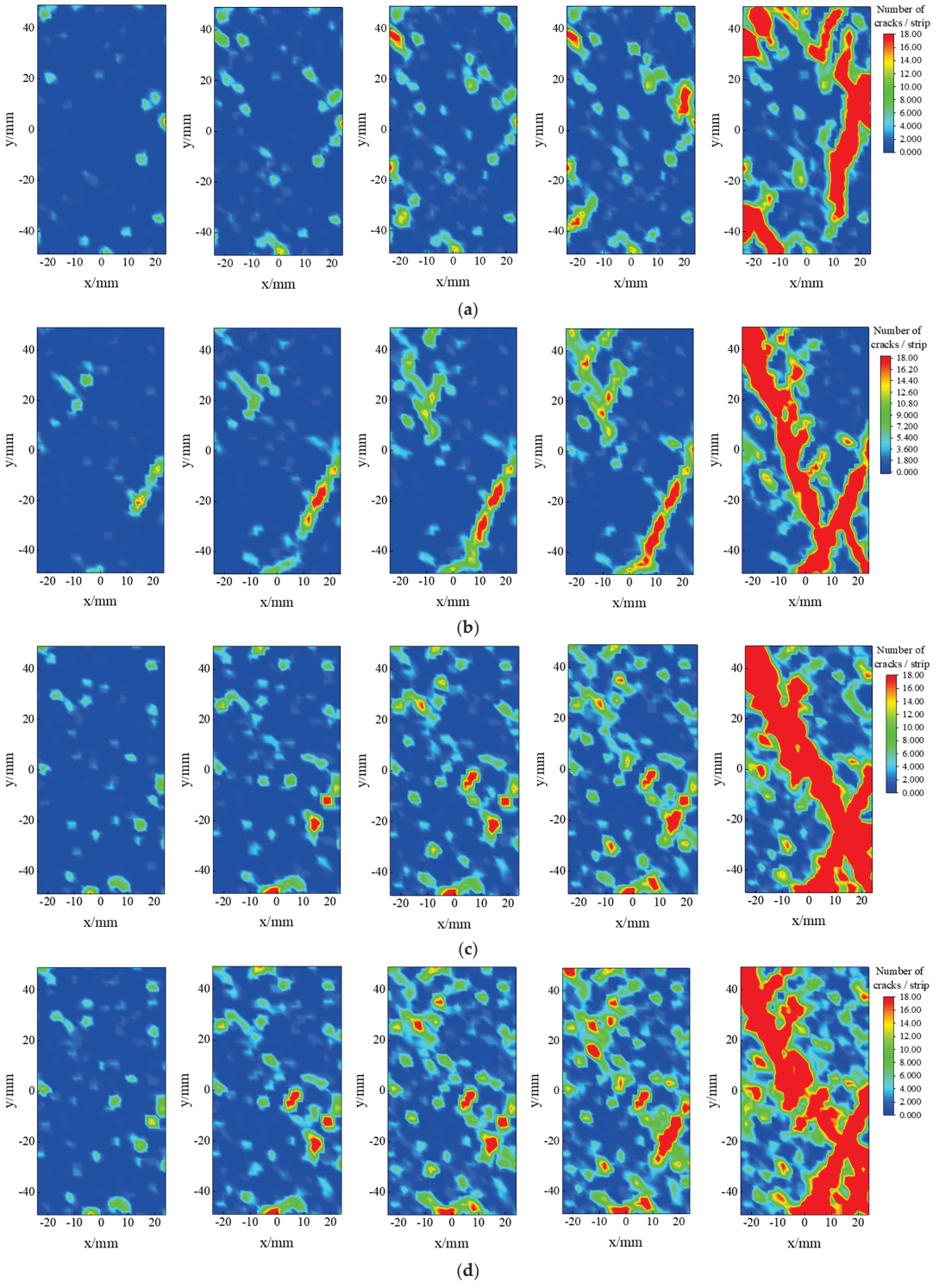

Figure 13. Cracking hotspot map of water-saturated natural defective material under different circumferential pressure conditions: (**a**) confining pressure 0 MPa; (**b**) confining pressure 10 MPa; (**c**) confining pressure 15 MPa; (**d**) confining pressure 20 MPa.

The influence of the surrounding pressure environment on the damage pattern of the defective rock material shows a clear and consistent trend. As the surrounding pressure increases, the crack concentration area (yellow-red area) at the end of the specimen and the boundary area gradually shifts toward the middle of the specimen. Numerical simulation results indicate that, as the confining pressure increases from 0 MPa to 20 MPa, the crack expansion path shifts notably from the free surface to the interior. This suggests that the inhibitory effect of the confining pressure on the internal damage of the material is closely related to the stress redistribution mechanism. Under the influence of confining pressure and stress, the crack tip continues to experience stress concentration, which dominates the direction of crack expansion. Comparative experiments show that, under no confining pressure, the boundary crack hotspot appears early in the axial pressure loading, and the damage area expands rapidly along the free surface. In contrast, under confining pressure, the damage initiation point exhibits multi-point distribution characteristics, and the breakage angle decreases as the confining pressure increases.

4.3. Mechanism of Fine-Scale Evolution of Water-Saturated Natural Defective Materials

Based on the type and number of microcracks generated in the water-saturated material during triaxial loading, as recorded by PFC2D, the evolution of cracks is analyzed under different circumferential pressure conditions. As shown in Figure 14, no cracks are generated inside the water-saturated material during the early stage of loading. As the load increases, tensile cracks are the first to appear, while shear cracks lag behind the tensile cracks before the load reaches the peak value. Therefore, the total cracking trend is similar to that of the tensile cracks. Both shear and tension cracks showed an increasing trend, with the growth rate of tension cracks consistently higher than that of shear cracks. When the confining pressure is 0, 10, 15 and 20 MPa, the ratio of peak strength corresponding to shear cracks to total cracks is 12.1%, 16.3%, 20.8% and 27.7%, respectively. As the confining pressure increases, the ratio of cracks gradually increases, and the peak damage morphology shifts from tension damage to shear damage predominantly. The existence of surrounding pressure has an inhibitory effect on the generation of tension cracks, which in turn leads to a change in the post-peak damage morphology of the water-saturated defective rock material, from tension damage to shear damage.

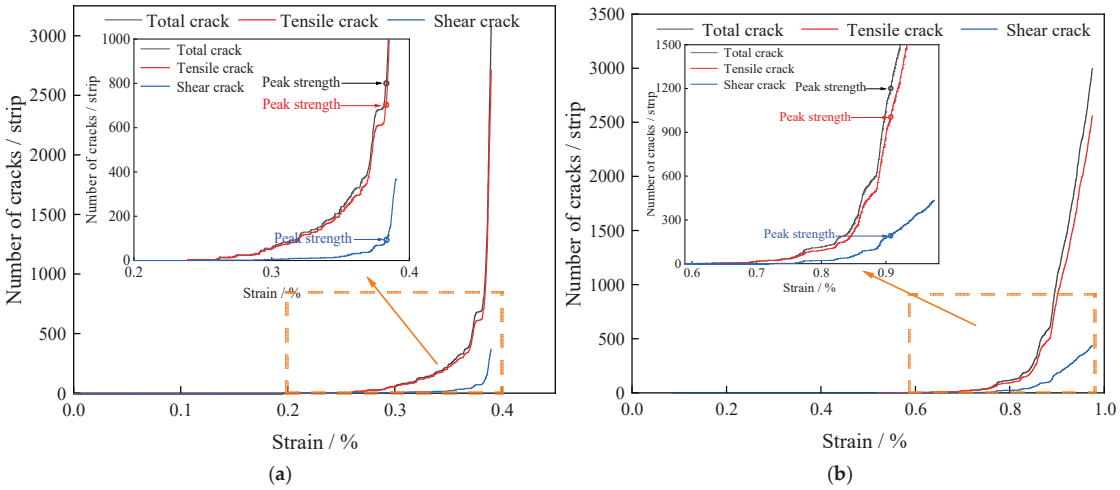

Figure 14. *Cont.*

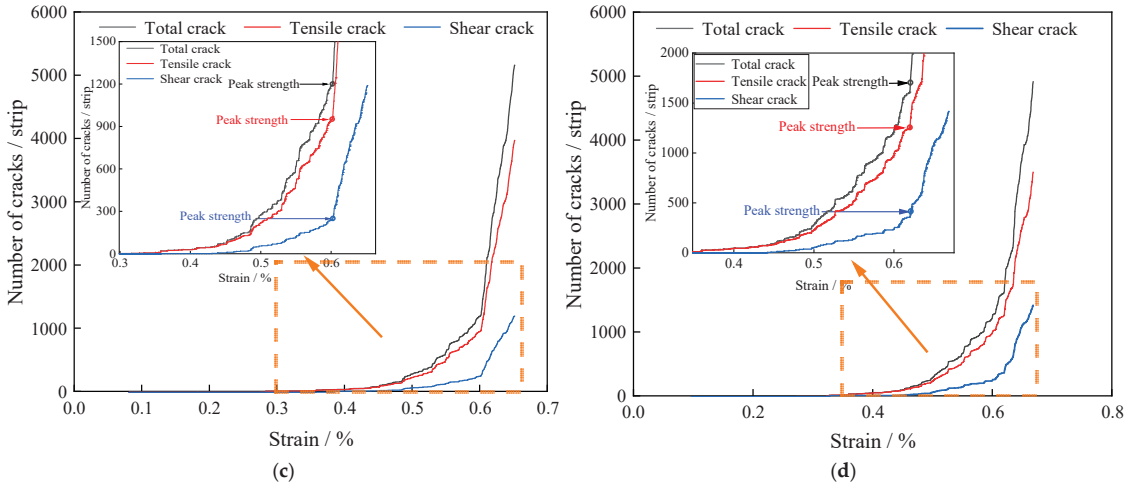

Figure 14. Crack evolution law of water-saturated materials under different confining pressures: (**a**) confining pressure 0 MPa; (**b**) confining pressure 10 MPa; (**c**) confining pressure 15 MPa; (**d**) confining pressure 20 MPa.

To reveal the evolution mechanism of microcracks in water-saturated materials under triaxial compression, the orientation of cracks in the specimens was counted, as shown in Figure 14, where the horizontal coordinate represents the crack direction and the vertical coordinate represents the number of cracks. As seen in Figure 15, the crack azimuth angle mainly ranges from 60 to 135°, with the highest number of cracks occurring 75–105°. This indicates that, before the peak strength, the peak strength is primarily dominated by internal tension cracks in the water-saturated material. As the circumferential pressure increases, the number of cracks in the 45 to 75° increases, suggesting that the circumferential pressure changes the crack opening angle. This change affects the failure characteristics of the water-saturated material, shifting from vertical damage to inclined damage.

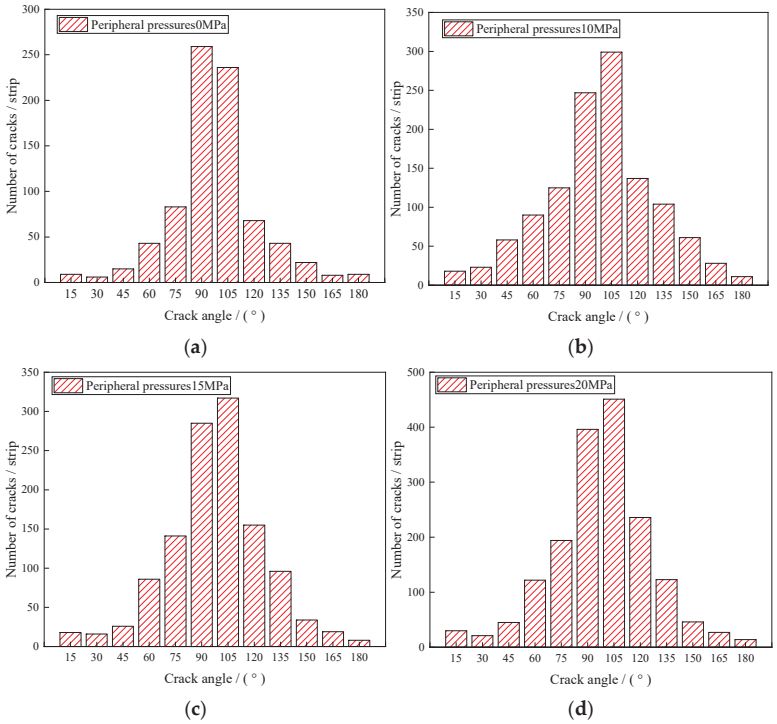

Figure 15. Crack azimuthal distribution under different circumferential pressures: (**a**) confining pressure 0 MPa; (**b**) confining pressure 10 MPa; (**c**) confining pressure 15 MPa; (**d**) confining pressure 20 MPa.

5. Mechanisms of Energy Evolution in Water-Saturated Natural Defective Materials

5.1. Principles of Energy Calculation

Assuming that the entire test process was a closed system with thermal energy exchange with the external environment, the energy relationship of the defective brittle rock material was derived based on the first law of thermodynamics:

$$U = U_e + U_d \tag{1}$$

where U is the mechanical energy input by the external force during the test; U_e is the elastic energy generated by the elastic deformation; U_d is the dissipated energy generated by the plastic deformation and destruction.

In a conventional triaxial compression test ($\sigma_2 = \sigma_3$), the total mechanical energy U of the specimen in this closed system is the sum of the work performed on the specimen by the axial and circumferential pressures, viz:

$$U = U_1 + U_3 \tag{2}$$

where U_1 is the work performed by axial pressure on the specimen; U_3 is the work performed by circumferential pressure on the specimen.

The equations for work performed by axial pressure U_1, work performed by circumferential pressure U_3 and elastic strain energy U_e during triaxial compression are given below, respectively [31]:

$$\left.\begin{aligned} U_1 &= \int \sigma_1 d\varepsilon_1 = \frac{1}{2}\sum_{1}^{n}\left(\varepsilon_{1_{i+1}} - \varepsilon_{1_i}\right)\left(\sigma_{1_i} + \sigma_{1_{i+1}}\right) \\ U_3 &= 2\int \sigma_3 d\varepsilon_3 = \sum_{1}^{n}\left(\varepsilon_{3_{i+1}} - \varepsilon_{3_i}\right)\left(\sigma_{3_i} + \sigma_{3_{i+1}}\right) \\ U_e &= \frac{1}{2E}\left[\left(\sigma_1^2 + 2\sigma_3^2\right) - 2\mu\left(2\sigma_1\sigma_3 + \sigma_3^2\right)\right] \end{aligned}\right\} \tag{3}$$

where E is the modulus of elasticity in the linear elastic phase during triaxial compression; μ is the Poisson's ratio in the linear elastic phase during triaxial compression.

5.2. Characterization of Energy Evolution

The deformation process of water-saturated materials was accompanied by the accumulation and dissipation of energy, and the nature of their destruction was driven by an energy-driven destabilization phenomenon. Therefore, the use of the energy analysis method to study the deformation and damage process of water-saturated materials had significant practical significance. Based on the energy calculation formula, the energy curve was derived, as shown in Figure 16. According to the stress–strain curve, the energy curve can be divided into four stages. In the compression stage, the elastic energy and dissipation energy of the specimen begin to show a nonlinear growth trend. As the pore cracks are compacted and closed, the dissipation energy decreases, while the elastic energy rises. In the elastic deformation stage, the water-saturated specimen is pressurized to pressure, causing elastic deformation, which results in continuous increases in elastic energy and axial strain energy. During this stage, no cracks are produced, so the dissipation energy remains largely unchanged. As the specimen continues to deform, transitioning from the elastic stage to the plastic stage, some of the elastic deformation turns into plastic deformation. The growth rate of elastic energy decreases, while dissipation energy gradually increases due to the generation and expansion of new fissures and the expansion of natural defects in the water-saturated specimen. This leads to an increase in circumferential strain. In the

plastic deformation stage, deformation continues until the destruction stage, where the bias stress decreases rapidly. This is accompanied by continuous increases in both axial and circumferential strains. The elastic energy is rapidly released, leading to intensified fissure expansion in the specimen, and the dissipation energy rises rapidly.

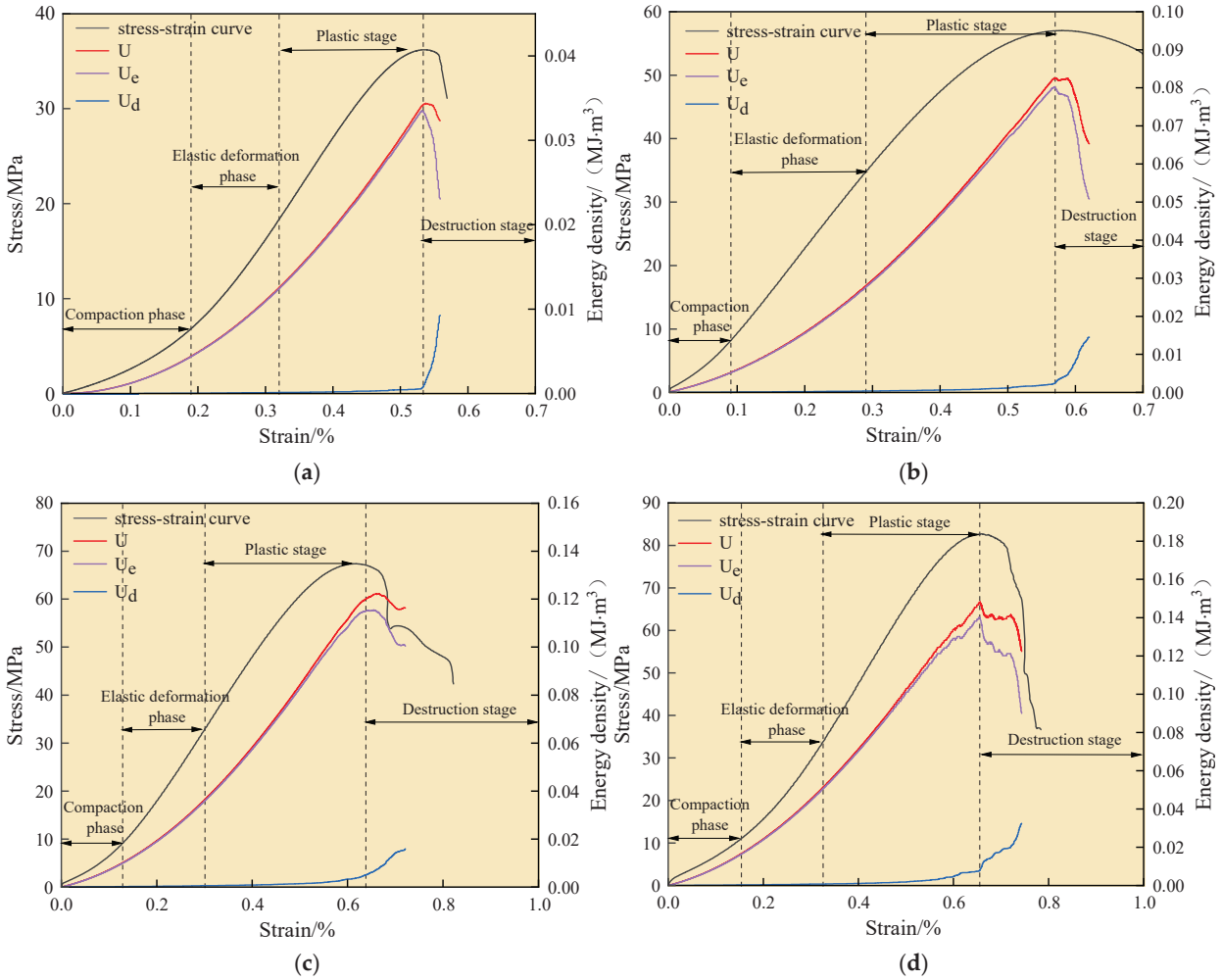

Figure 16. Triaxial compression energy evolution characteristics: (**a**) confining pressure 0 MPa; (**b**) confining pressure 10 MPa; (**c**) confining pressure 15 MPa; (**d**) confining pressure 20 MPa.

The environment of the confining pressure for the water-saturated material shows a significant pattern in the accumulation and dissipation of energy. In the compression stage, when the confining pressure increases from 0 MPa to 20 MPa, the total energy increases by 277%, with elastic energy increasing by 271% and dissipated energy increasing by 401%. This significant increase is due to the relatively small energy consumption during the compression stage, leading to a greater increase in energy. In the elastic stage, when the confining pressure increases from 0 to 20 MPa, the total energy increases by 237%, elastic energy increases by 236%, and dissipated energy remains unchanged, as there is minimal energy dissipation in the elastic stage. In the plastic stage, up to peak strength, when the confining pressure increases from 0 to 20 MPa, the total energy increases by 347%, elastic energy increases by 321%, and dissipated energy increases dramatically by 1028%. On the one hand, the existence of the surrounding pressure strengthens the density of the water-saturated material, thereby enhancing its energy storage capacity. On the other hand, the increase in surrounding pressure also leads to the extension of cracks in the water-saturated material, which requires the consumption of more energy.

5.3. Characterization of Energy Accumulation and Dissipation

To quantitatively analyze the energy storage and dissipation characteristics of water-saturated defective rock materials, the elastic storage ratio is defined as the ratio of elastic energy to the maximum total energy, the dissipation ratio as the ratio of dissipated energy to the maximum total energy, and the displacement ratio as the ratio of the actual strain to the strain corresponding to the peak load. The variation in the elastic storage ratio with the strain ratio for water-saturated materials without confining pressure and with confining pressure of 20 MPa is illustrated in Figure 17, with the corresponding fitted functions provided in Equations (4) and (5). Therefore, the velocity of elastic storage ratio with strain ratio can be obtained as shown in Figure 18.

$$y = 0.85183x^2 + 0.05236x - 0.00698 \tag{4}$$

$$y = 0.41505x^2 + 0.54946 - 0.04138 \tag{5}$$

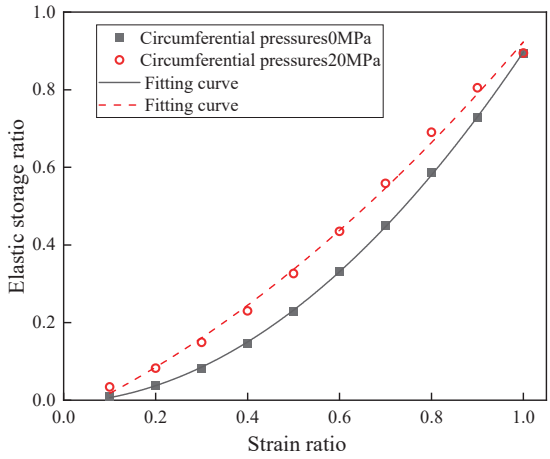

Figure 17. Variation curve of water-saturated defective material with strain ratio.

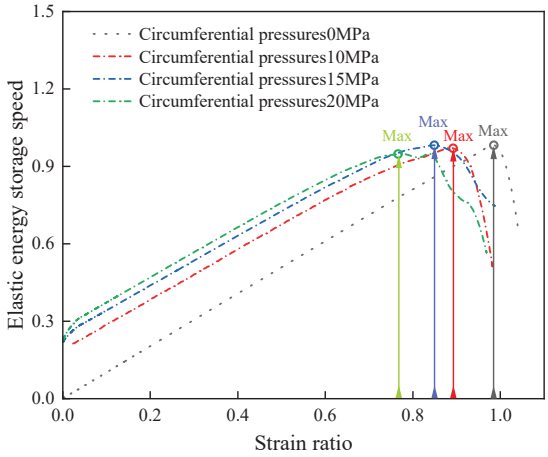

Figure 18. Characteristics of energy evolution rate change of water-saturated defective materials.

This can be obtained through Figures 17 and 18:

(1) The elastic energy storage ratios of defective rock materials with and without pressure enclosure and water saturation show nonlinear changes. Specifically, the elastic energy storage ratio increases with the strain ratio prior to reaching the peak load.

(2) The elastic energy storage ratios of materials with and without confining pressure are essentially similar during the compression stage. However, in the elastic and

plastic phases, the elastic energy storage ratios of materials with confining pressure are higher than those without confining pressure. In the peak phase, the elastic energy storage ratios of both materials reach their maximum values and are comparable.

(3) The elastic storage ratio of water-saturated materials with confining pressure is larger than that of water-saturated materials without confining pressure at any stage. When the strain ratio is <0.94, the elastic storage rate of water-saturated materials with higher confining pressure is the largest. However, when the strain ratio is >0.94, the elastic storage ratio of water-saturated materials with higher confining pressure is progressively smaller than that of materials with lower confining pressure.

The above analysis demonstrates that the presence of confining pressure enhances the energy storage performance of water-saturated materials. At strain ratios close to 1, the enclosing pressure reduces the storage ratio rate. This is due to the fact that the presence of enclosing pressure increases the dissipated energy required for the destruction of water-saturated materials, which in turn leads to the timing of energy release when the material is destroyed.

6. Discussion

This study investigates the influence of confining pressure on the mechanical properties, failure modes, and energy evolution mechanisms of water-saturated brittle materials with natural defects through triaxial compression experiments and discrete element numerical simulations. The findings exhibit both connections to and extensions of previous research, with specific discussions as follows:

(1) Energy Accumulation and Release Under Confining Pressure

Experimental results reveal that confining pressure significantly alters the magnitude of energy accumulation and release in water-saturated defective materials. When the confining pressure increases from 0 to 20 MPa, the elastic energy, dissipated energy, and total energy increase by 321%, 1028%, and 347%, respectively. This phenomenon challenges the established understanding from Meng et al. [20], who reported reduced elastic energy storage under uniaxial compression in water-bearing conditions. The results highlight a unique energy evolution mechanism driven by the combined effects of confining pressure and water saturation.

(2) Nonlinear Relationship Between Elastic Energy Storage Ratio and Strain Ratio

The nonlinear relationship between the elastic energy storage ratio and strain ratio demonstrates that the energy storage rate decreases under high confining pressure when the strain ratio exceeds 0.94. This observation contrasts with the findings of Huang et al. [28], who observed rapid energy dissipation under high confining pressure. The delayed energy release during quasi-static loading, caused by confining pressure prolonging the plastic deformation stage, provides critical insights for early warning systems in deep engineering projects.

(3) Structural Stability and Limitations

Confining pressure enhances structural stability by improving the material's energy storage capacity. However, attention must be paid to the critical threshold of abrupt energy changes under high confining pressure. The use of a single lithology in this experiment limits the generalizability of the conclusions. Subsequent studies should expand the research to diverse lithological systems to validate and broaden these findings.

This discussion underscores the dual role of confining pressure in stabilizing materials while necessitating caution in energy-critical engineering applications. Future work ad-

dressing multi-lithology systems and coupled field effects will further refine the theoretical framework for deep geomechanical engineering.

7. Conclusions

Through triaxial compression tests conducted on water-saturated natural defective rock materials, the following conclusions are drawn from the investigation into the influence mechanism of confining pressure on the mechanical properties, damage characteristics, and energy evolution of these materials:

(1) The peak stress and elastic modulus of defective rock materials under dry conditions are higher than those under water-saturated conditions. Under different confining pressures, the compressive strength and elastic modulus of water-saturated materials exhibit a positive correlation with the level of confining pressure, while the Poisson's ratio shows a negative correlation with the level of confining pressure. Specifically, as the confining pressure is raised from 0 MPa to 20 MPa, the compressive strength increases by 126.8%, the elastic modulus increases by 91.9%, and the Poisson's ratio decreases by 39%.

(2) The critical stresses of defective rock materials in dry conditions are higher than those in water-saturated conditions. In the gradual process of damage of water-saturated materials, the crack closure stress, crack initiation stress, and damage stress exhibit a positive correlation with the level of confining pressure. Specifically, as the confining pressure increases from 0 MPa to 20 MPa, the crack closure stress grows by 42.7%, the crack initiation stress grows by 98.7%, and the damage stress grows by 124.2%. Furthermore, the confining pressure slows down the crack initiation and damage processes of water-saturated materials.

(3) The damage mode of water-saturated material shifted from tensile damage mode to shear damage mode under different confining pressures. Additionally, the level of confining pressure exhibited a negative correlation with the crack inclination angle. The angle of rupture of the material decreased from 87° to 50.3° as the confining pressure was raised from 0 MPa to 20 MPa.

(4) Under varying pressures, cracks in water-saturated materials initiated from the vertical direction around to the middle tilt direction. The crack extension direction was concentrated in the interval of 45~135°. Furthermore, the formation of shear cracks exhibited a strong positive correlation with the level of confining pressure. Specifically, the ratio of shear cracks increased from 12.1% to 27.7% as the confining pressure rose from 0 MPa to 20 MPa.

(5) The energy characteristics of water-saturated materials exhibit a significant positive correlation with the level of confining pressure. When the confining pressure increases from 0 MPa to 20 MPa, the total energy increases by 277%, the elastic energy increases by 271%, and the dissipation energy increases by 401%. Furthermore, the elastic storage rate generally displays a positive correlation with the level of confining pressure. However, a negative correlation appeared when the strain ratio was greater than 0.94.

Author Contributions: Conceptualization, Z.G.; software, Z.G.; writing—original draft, Z.G.; supervision, S.G.; funding acquisition, S.H. and S.G.; writing—review and editing, S.G., S.H. and J.H.; data curation, X.Y., D.Y. and J.D.; formal analysis, D.Y., J.H. and Y.C. All authors have read and agreed to the published version of the manuscript.

Funding: The research described in this paper was financially supported by the National Natural Science Foundation of China (No. 52274087).

Institutional Review Board Statement: Not applicable.

Informed Consent Statement: Not applicable.

Data Availability Statement: The data are not publicly available due to privacy or ethical restrictions.

Conflicts of Interest: Author Xiaoyong Yang was employed by the company Shandong Energy Group Xibei Mining Company Limited. The remaining authors declare that the research was conducted in the absence of any commercial or financial relationships that could be construed as a potential conflict of interest.

References

1. Li, W.; Zhang, Q.; Wang, X.; Yu, L.; Li, Z. Synergistic effect of particle size, carboxymethyl starch and Na_2CO_3 on rheological and filtration property of bentonite-based material. *Case Stud. Constr. Mater.* **2024**, *21*, e03537. [CrossRef]
2. Xu, R.; Zhao, Y.; Dou, B.; Hou, R.; Li, Z.; Dong, J. Experimental investigation of the effect of strain rate on the cracking behaviour and acoustic emission characteristics of red sandstone containing orthogonal cross flaws under quasistatic uniaxial compression. *Eng. Fail. Anal.* **2025**, *170*, 109323. [CrossRef]
3. Li, W.; Yu, L.; Zhang, T.; Su, H.; Mi, X.; Fan, D.; Jin, B. Quantitative analysis of grain size effect on tensile mechanical behavior of granite based on multi-level force chain networks. *Comput. Part. Mech.* **2024**, *11*, 2245–2266. [CrossRef]
4. Xu, R.; Gao, L.; Jin, Y.; Wang, Y.; Li, Z.; Hu, S. Influence of strain measurement methods on crack initiation and crack damage thresholds of shale. *Geomech. Geophys. Geo Energy Geo Resour.* **2025**, *11*, 34. [CrossRef]
5. Xie, H.; Zhang, R.; Zhang, Z.; Gao, M.; Li, C.; He, Z.; Li, C.; Liu, T. Reflections and explorations on deep earth science and deepearth engineering technology. *J. China Coal Soc.* **2023**, *48*, 3959–3978.
6. Tao, M.; Wu, X.; Zhao, R. Advancements and future prospects of mechanical characteristics of rock stress gradients. *J. Cent. S. Univ. (Sci. Technol.)* **2024**, *55*, 4473–4492. [CrossRef]
7. Han, J.; Hu, S.; Gao, Z.; Huang, J.; Cheng, Y.; Guo, S.; Yang, L. A discrete element study of the fracture propagation of rock-like materials under directional sleeve fracturing. *Theor. Appl. Fract. Mech.* **2024**, *130*, 104317. [CrossRef]
8. Guo, S.; Hu, S.; Huang, J.; Gao, Z.; Cheng, Y.; Han, J.; Yang, L. Stability control technology for surrounding rocks in gob-side entry driving with small coal pillars under dynamic pressure. *Energies* **2023**, *16*, 7887. [CrossRef]
9. Colback, P.S.B.; Wild, B.L. Influence of moisture content on the compress strength of rock. In Proceedings of the 3rd Canadian Rock Mechanics Symposium, Toronto, ON, Canada, 15–16 January 1965; Society of Exploration Geophysicists: Houston, TX, USA, 1965; pp. 385–391.
10. Li, W.; Yu, L.; Tan, Y.; Wu, L.; Qian, J. Mechanical properties and impact behavior of frozen clay: Insights from static mechanical tests, fly-plate tests, and split-Hopkinson pressure bar analysis. *Phys. Fluids* **2024**, *36*, 057138. [CrossRef]
11. Song, C.; Feng, G.; Bai, J.; Cui, J.; Wang, K.; Shi, X.; Qian, R. Progressive failure characteristics and water-induced deterioration mechanism of fissured sandstone under water–rock interaction. *Theor. Appl. Fract. Mech.* **2023**, *128*, 104151. [CrossRef]
12. Chen, X.; Eichhubl, P.; Olson, J.E. Effect of water on critical and subcritical fracture properties of Woodford shale. *J. Geophys. Res. Solid Earth* **2017**, *122*, 2736–2750. [CrossRef]
13. Zhao, Y.; Tang, J.; Wang, W.; Cheng, G.; Luo, S.; Fu, C. Study on failure behavior of fluid-solid coupling under conventional triaxial compression for Maokou limestone. *J. Min. Saf. Eng.* **2018**, *35*, 205–212.
14. Luo, S.; Yan, P.; Lu, W.; Dong, Z.; Zhou, C.; Yang, Z.; Hu, Y. Stability index of surrounding rock during deep rock excavation considering energy release speed. *Appl. Sci.* **2023**, *13*, 3000. [CrossRef]
15. Vardar, O.; Zhang, C.; Canbulat, I.; Hebblewhite, B. Numerical modelling of strength and energy release characteristics of pillar-scale coal mass. *J. Rock Mech. Geotech. Eng.* **2019**, *11*, 935–943. [CrossRef]
16. Zhang, W.; Feng, J.; Ma, J.; Shi, J. The revealed mechanism of rock burst based on an Innovative calculation method of rock mass released energy. *Int. J. Environ. Res. Public Health* **2022**, *19*, 16636. [CrossRef] [PubMed]
17. Hu, S.; Zhang, C.; Ru, W.; Han, J.; Guo, S.; Zhou, X.; Yang, L. Creep properties and energy evolution characteristics of weakly cemented rock under step loading. *Int. J. Rock Mech. Min. Sci.* **2023**, *170*, 105428. [CrossRef]
18. Zhang, J.; Song, Z.; Wang, S. Experimental investigation on permeability and energy evolution characteristics of deep sandstone along a three-stage loading path. *Bull. Eng. Geol. Environ.* **2021**, *80*, 1571–1584. [CrossRef]
19. Xie, H.; Gao, F.; Yang, J. Research and exploration of rock mechanics in deep ground engineering. *Chin. J. Rock Mech. Eng.* **2015**, *34*, 2161–2178. [CrossRef]
20. Meng, Z.P.; Pan, J.N.; Liu, L.L.; Meng, G.X.; Zhao, Z.H. Influence of moisture contents on mechanical properties of sedimentary rock and its bursting potential. *Chin. J. Rock Mech. Eng.* **2009**, *28* (Suppl. 1), 2637–2643.
21. Lai, X.; Zhang, S.; Cui, F.; Wang, Z.; Xu, H.; Fang, X. Energy release law during the damage evolution of water-bearing coal and rockand pick-up of AE signals of key pregnancy disasters. *Chin. J. Rock Mech. Eng.* **2020**, *39*, 433–444. [CrossRef]
22. Liu, W.; Yan, E.; Dai, H.; Du, Y.; Xiao, W.B.; Zhao, S. Study on characteristic strength and energy evolution law of Badong formationmudstone under water effect. *Chin. J. Rock Mech. Eng.* **2020**, *39*, 311–326. [CrossRef]

23. Liu, Y.; He, C.; Fu, H.; Wang, S.; Lei, Y.; Peng, Y. Study on tensile mechanical properties and energy consumption law of saturatedslate under impact loads. *Chin. J. Rock Mech. Eng.* **2020**, *39*, 2226–2233. [CrossRef]
24. Guo, J.; Liu, X.; Qiao, C. Experimental study of mechanical properties and energy mechanism of karst limestone under natural and saturated states. *Chin. J. Rock Mech. Eng.* **2014**, *33*, 296–308. [CrossRef]
25. Gao, F.; Cao, S.; Zhou, K.; Lin, Y.; Zhu, L. Damage characteristics and energy-dissipation mechanism of frozen–thawed sandstone subjected to loading. *Cold Reg. Sci. Technol.* **2020**, *169*, 102920. [CrossRef]
26. Yang, Y.; Ma, D. Experimental research on energy evolution properties of coal sample failure under triaxial unloading testing. *J. Min. Saf. Eng.* **2018**, *35*, 1208–1216. [CrossRef]
27. Zhao, Y.; Gong, S.; Huang, Y. Experimental study on energy dissipation characteristics of coal samples under impact loading. *J. China Coal Soc.* **2015**, *40*, 2320–2326. [CrossRef]
28. Huang, M.; Zhang, J.; Hu, L.; Zhang, X. SplitHopkinson pressure bar test and energy dissipationcharacteristics of argillaceous siltstone in Three Gorgesreservoir region. *J. Eng. Geol.* **2015**, *23*, 1175–1181. [CrossRef]
29. Peng, Y.; Yu, L.; Qian, J.; Li, W.; Zhang, T.; Zhou, L. Dynamic tensile behavior and crack propagation in coral aggregate seawater shotcrete: Experimental investigation and numerical simulation. *Cem. Concr. Compos.* **2025**, *159*, 106010. [CrossRef]
30. Jiang, J.; Chen, S.; Xu, J.; Liu, Q. Mechanical properties and energy characteristics of mudstone under different containing moisture states. *J. China Coal Soc.* **2018**, *43*, 2217–2224. [CrossRef]
31. Ru, W.; Hu, S.; Li, D.; Ma, J.; Zhang, C.; Luo, P.; Gong, H.; Zhou, A. Energy evolution of unloading confining pressure and dissipative energy damage constitutive model of coal-rock combination. *J. Rock Soil Mech.* **2023**, *44*, 3448–3458. [CrossRef]

Disclaimer/Publisher's Note: The statements, opinions and data contained in all publications are solely those of the individual author(s) and contributor(s) and not of MDPI and/or the editor(s). MDPI and/or the editor(s) disclaim responsibility for any injury to people or property resulting from any ideas, methods, instructions or products referred to in the content.

materials

MDPI

Article

Transport Properties of Solutions in γ–FeOOH/CSH Pores of Steel Fiber-Reinforced Concrete (SFRC) Derived Using Molecular Dynamics

Yalin Luan [1], Runan Wang [1], Changxin Huang [2], Andrey Jivkov [3] and Lianzhen Zhang [1,*]

[1] College of Pipeline and Civil Engineering, China University of Petroleum, Qingdao 266580, China; luanyalin@upc.edu.cn (Y.L.); 19862857721@163.com (R.W.)
[2] School of Civil Engineering, Shandong University, Jinan 250014, China; 202320792@mail.sdu.edu.cn
[3] School of Engineering, The University of Manchester, Manchester M13 9PL, UK; andrey.jivkov@manchester.ac.uk
* Correspondence: zhanglianzhen@upc.edu.cn; Tel.: +86-18265328519

Abstract: Steel fiber-reinforced concrete structures designed for marine environments can become compromised by the ingress of water and ions. Water and ion transport through the pores between steel fibers and concrete gels significantly affects the durability of such structures, but the mechanisms of this transport are not sufficiently understood. Reported here is a molecular dynamics-based investigation of the transport of water, NaCl, Na_2SO_4, and mixed solutions of NaCl and Na_2SO_4 through γ–FeOOH/CSH pores. The effect of pore width on the capillary transport of NaCl + Na_2SO_4 solutions was also investigated and reported. It is shown that the depth of water penetration in NaCl solution increases parabolically with time. It is further shown that the CSH surface forms bonds with different ions to form Na–O_{CSH}, Cl–Ca_{CSH}, and S–Ca_{CSH} compounds, which results in reduced rates of solution transport. The mixed NaCl + Na_2SO_4 solution was found to have the lowest transport rate. A reduction in pore width was found to reduce the transport rate of water molecules and diminish the transport of ions. In pores smaller than 2.5 nm in width, the immobilized ions aggregate into clusters, occupying pore inlets and blocking more ions from entering the channels. Compared with the matrix on both sides, solutions are transported significantly faster along the CSH side than along the γ–FeOOH side, indicating that the addition of steel fibers can effectively slow down the transport of water molecules and ions in concrete. These data on the difference in the transport of solutions along the two sides of the matrix may provide molecular-level insights to support studies on the durability of concrete materials.

Keywords: steel fiber-reinforced concrete; molecular dynamics simulations; γ–FeOOH/CSH; transport behavior; atomic density distribution

1. Introduction

Improving the durability of concrete structures will contribute substantially to the sustainable development goals of modern societies [1]. This is a challenging problem requiring urgent solutions [2]. One approach involves the incorporation of steel fibers to produce steel fiber-reinforced concrete (SFRC) [3]. This has become widespread in engineering applications [4], particularly in materials for use in marine environments [5]. The number of port construction projects has been increasing year by year. In China alone, the ocean engineering manufacturing industry generated an added value of CNY 103.2 billion by 2024, an increase of 9.1% over the previous year [6]. Compared to conventional concrete,

SFRC composites have superior strength [7,8], crack resistance [9,10], and load–bearing capacity, making them excellent structural materials [11]. However, the interfaces between concrete and steel fibers are weak points in the composite microstructure [12,13] and significantly impact the durability of concrete materials [14]. First, they are pathways for the faster transport of water and ions compared to the rest of the concrete body. Second, they are mechanically weaker and are further weakened by erosion/corrosion by water and ions, making them the likely locations for mechanical damage and crack initiation [15]. Third, the appearance of cracking patterns in SFRC during failure [16] has a strong impact on the nanomechanical properties of local specimen regions [17].

The detrimental effects of water and ion ingress on the mechanical behavior and interfacial properties of SFRC have been investigated via macroscopic-scale experiments [18–20]. Hwang et al. [18] employed an electrically accelerated method to examine the corrosion at the interface between steel fibers and concrete matrices. Their findings showed that the porosity of the interface is higher than the porosity of the matrix and that this porosity facilitates chloride ion transport and leads to steel fiber corrosion. Their conclusion is that SFRC is at higher risk of corrosion than is classical reinforced concrete. Yoo et al. [19] studied the corrosion of SFRC exposed to a 3.5% chloride salt solution and reported a direct correlation between the degree of fiber corrosion and surface roughness. Their results show that when the steel loss due to corrosion ranges from 4% to 6%, the tensile properties of SFRC improve. However, exceeding this threshold results in fiber breakage and the subsequent deterioration of concrete performance. Tai et al. [20] compared the performance degradation of SFRC subjected to chloride erosion to that of SFRC subjected to combined carbonation and chloride erosion. Their results show that corrosion progresses faster under the coupled effect of carbonation and chloride erosion. After 360 wet–dry–wet cycles of chloride exposure, steel fibers within approximately 10 mm of the surface were severely corroded, while deeper fibers remained unaffected despite chloride ion penetration exceeding 40 mm.

The macroscopic experimental results show that water and ions gradually infiltrate SFRC [21] and cause structural damage [22]. However, the exact mechanisms of the transport of water and ions within pores cannot be fully elucidated through macroscopic experiments alone. A better understanding can be obtained by the investigation of transport at the microscopic level, specifically focusing on the steel fiber/concrete interface. Molecular dynamics (MD) simulations have been used to study the structure [23], kinetics [24], and interfacial behavior [25,26] of harmful ions in gel pores, providing insights into the mechanisms of transport of water and ions. Calcium silicate hydrate (CSH) [27], formed by the hydration of cement clinker [28], is the primary component of concrete-based materials [29]. Hou et al. [25] simulated the transport of NaCl, Na_2SO_4, and mixed NaCl + Na_2SO_4 solutions in CSH gel pores. Their finding was that different ions interact with sulfate ions during transport, inhibiting the movement of chloride ions. Large Na–SO_4 clusters block nanochannels, slowing the entry of water into gel pores. Yang et al. [26] simulated the capillary transport of chloride salts in the CSH gel pores of varying sizes. Their findings were that reduced pore size affects water–ion bonding and that channel narrowing inhibits penetration by larger ions. These studies provide valuable microscopic-level information and a theoretical foundation for understanding the intrusion of water and ions into CSH gel pores. However, the transport and bonding mechanisms of water and ions in the pores formed between concrete and steel fibers in SFRC have not been investigated to date.

The present work aimed to better understand the transport behavior and microscopic mechanisms of water and ions within the pores of SFRC. The investigation was performed by molecular dynamics. Initially, a transport model was developed for water, NaCl solution, Na_2SO_4 solution, and a composite NaCl + Na_2SO_4 solution within the pores of SFRC. The

differences in transport characteristics across these solution environments were examined. Subsequently, four distinct pore widths (3.5 nm, 2.5 nm, 1.5 nm, and 1 nm) were considered to analyze the transport process of the NaCl + Na_2SO_4 composite solution. Through the analysis of local structures and intrusion behaviors, the results elucidated the migration mechanisms of water and ions within the pores of SFRC under varying solution types and pore dimensions. These findings provide valuable insights into the degradation mechanisms of SFRC in marine environments.

This article was organized as follows: In Section 2, we provide a detailed introduction to the modeling and simulation processes based on MD. In Section 3, the simulation results are analyzed and discussed. First, the transport process was demonstrated by snapshots, and the invasion depth differences in different solutions in the pores were compared. Second, by calculating the density distribution and RDF of each particle, the bonding differences between different solutions and matrices were revealed. Third, the transport process of NaCl + Na_2SO_4 mixed solution at different pore sizes was analyzed. Fourth, the influence mechanism of different pore sizes on solution transport was studied. Finally, the conclusion is followed up in Section 4.

2. Experiment and Model

2.1. Experiment

Steel fiber-reinforced concrete (SFRC) specimens with dimensions of 100 mm × 100 mm × 100 mm were prepared using steel molds. The concrete mix proportions are listed in Table 1 [30]. After casting, the specimens were stored indoors at a temperature of 293 K for 48 h before demolding, followed by standard curing for 28 days to ensure proper hydration and strength development.

Table 1. Mix proportion of steel fiber-reinforced concrete (kg/m^3).

Cement	Silica Fume	Fly Ash	Water	Superplasticizer	Steel Fiber	Quartz Sand	Coarse Aggregate
559.68	79.95	159.908	127.9264	15.9908	157	799.54	600

After curing, the specimens were subjected to uniaxial compression at a uniform loading rate until failure. To investigate the interfacial microstructure, the steel fiber-containing samples were extracted from the surface layer (within 5 mm depth) of the fractured specimens. These samples were then immersed in anhydrous ethanol to terminate further hydration and subsequently dried in an oven for 24 h until a constant weight was achieved. The dried samples were examined using a JSM–6490LV scanning electron microscope (SEM) to characterize their microstructural features. Key observations from the SEM analysis are shown in Figure 1.

SEM imaging at 500× magnification, shown in Figure 1a, revealed the presence of abundant CSH, which served as the primary binding phase in cementitious materials. Higher-magnification image at 5000× in Figure 1b showed that the CSH exhibited diverse morphologies, including fibrous, flocculent, granular, and densely packed structures. These microstructural features effectively interconnected cement particles and hydration products, contributing to the overall compactness of the matrix. A rough passivation layer was observed in an image at 2000× in Figure 1c, indicating possible surface oxidation or chemical interaction between the steel fibers and the surrounding cementitious matrix.

The region between the steel fibers and the concrete matrix, known as the interfacial transition zone (ITZ), exhibited a looser microstructure with higher porosity and fewer hydration products compared to the bulk matrix. This structural heterogeneity resulted in

reduced bond strength and increased permeability, making the ITZ a critical weak point for the ingress of aggressive solutions.

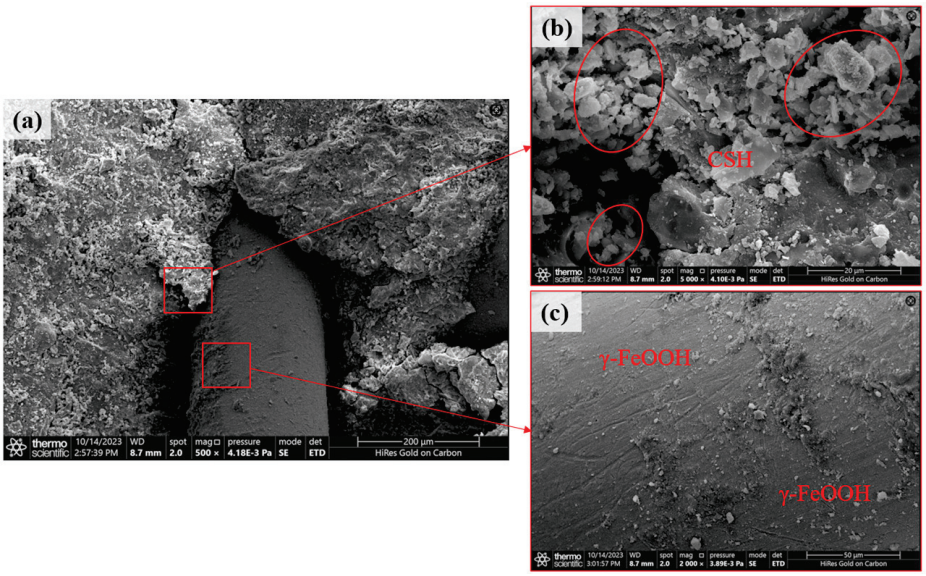

Figure 1. SEM imaging of (**a**) the γ–FeOOH/CSH interface at 500× magnification, (**b**) CSH at 5000× magnification, and (**c**) γ–FeOOH at 2000× magnification.

While SEM provided valuable insights into the microstructural characteristics of SFRC, its resolution and method limited the ability to analyze solution transport mechanisms within micropores. To address this gap, an MD model was built to better understand the penetration behavior of corrosive media in the ITZ and optimize the durability performance of SFRC.

2.2. Model Construction

The transport model consisted of a pore channel of approximately 9.5 nm width in contact with the environment of different solutions at the bottom. A fraction of the cement hydration product was calcium hydroxide, which made the concrete a strongly alkaline environment [31]. In such environments, a passive film was formed on the surface of the steel fibers [32,33]. The main component of the passive film was γ–FeOOH [34]. Figure 2a shows the pore channel model with one wall representing the steel fiber passivation film (γ–FeOOH) and the other wall the calcium silicate hydrate (CSH). The interlayer distances of 1 nm, 1.5 nm, 2.5 nm, and 3.5 nm are chosen by the following SEM-derived measurements of the interfacial pores between steel fibers and the CSH matrix and supported by previous simulations of comparable systems [26]. The passive film wall was constructed by cleaving the bulk crystal of γ–FeOOH along the [0 1 0] direction as shown in Figure 2b [35]. The crystal structure of γ–FeOOH was expanded in every direction by corresponding multiples, and the γ–FeOOH supercell model with dimensions 22.6 Å × 95 Å ×15 Å was built. For the creation of the CSH wall, the initial crystal structure was tobermorite with Ca/Si = 1.7, as depicted in Figure 2c. A realistic hydration product model was built by removing the H_2O molecules and randomly deleting some of the bridging Si–O tetrahedra in the silicon chains [36,37]. Thus, the CSH supercell model with dimensions 22.6 Å × 95 Å × 20 Å was constructed. To elucidate the fundamental mechanisms of solution transport within nanopores, simplified models were employed without considering the roughness and heterogeneity of the interfaces [38]. Four different water solutions were selected as shown in Figure 2d: pure water, 5% NaCl solution, 5% Na_2SO_4 solution, and 5% NaCl + 5% Na_2SO_4 solution, which approximated the actual seawater environment [39]. The real environment

of seawater, such as the marine pH, is also influenced by various factors such as temperature, salinity, atmospheric CO_2 partial pressure, and biological activities. However, the influences of the concentration changes of Ca^{2+} ions, Cl^- ions, and $SO_4{}^{2-}$ ions on the overall pH value of seawater were relatively small. The number of atoms and ions in the four solutions is given in Table 2. A graphene sheet was placed at the bottom of the solutions to set a rigid body condition.

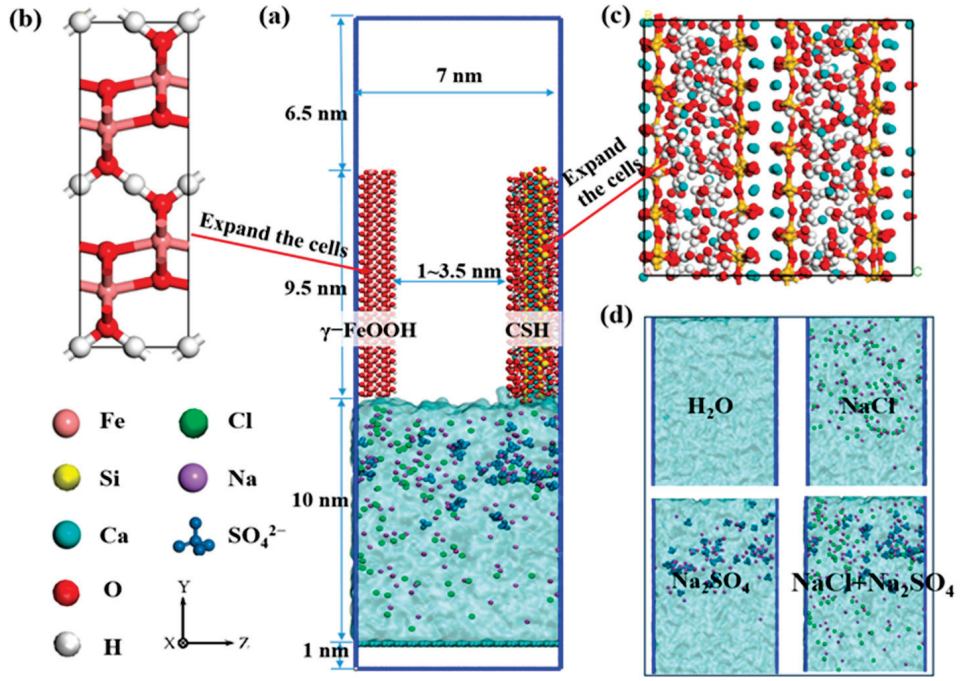

Figure 2. (**a**) Model setup for solution transport through γ–FeOOH/CSH channel; (**b**) structure of γ–FeOOH; (**c**) structure of CSH; (**d**) solution cases: H_2O, NaCl solution, Na_2SO_4 solution, and mixed NaCl + Na_2SO_4 solution.

Table 2. Number of particles in solutions.

	H_2O	Na^+	Cl^-	$SO_4{}^{2-}$
Water	5290	0	0	0
NaCl	5223	84	84	0
Na_2SO_4	5223	68	0	34
NaCl + Na_2SO_4	4948	152	84	34

2.3. Force Field and Molecular Dynamics Procedure

Molecular dynamics (MD) simulations of the model were carried out using the Large-scale Atomic/Molecular Massively Parallel Simulator 8Feb2023 (LAMMPS 8Feb2023) [40] free software package. The visualization of the processes was realized in Visual Molecular Dynamics (VMD) [41]. The ClayFF force field [42] was used in the simulation due to its general applicability for simulating various cement hydration products, interfaces between minerals and solutions, adsorption of anions and cations on hydroxide surfaces, and its success in simulating the interatomic potentials between the atoms in the solution and the calcium silicate calcium skeleton.

The truncation distances for van der Waals (vdW) and short-range electrostatic interactions were set at 10 Å, whereas the long-range electrostatic interactions were calculated using the Particle–Particle–Particle–Mesh (PPPM) method [43]. The simulations were performed as follows: First, both the CSH and γ–FeOOH walls were set as rigid bodies, i.e., a "frozen" state. This setting avoided simulation errors caused by the deformation

of nanopores, enabling the simulation to focus more on the interaction between fluid molecules and nanopore walls [44]. An invisible wall was placed between the entrance of the pore channel and the bottom solution to prevent water molecules and ions from entering the pore. Second, the simulation was performed under NVT ensemble at 300 K via the Nose–Hoover thermostat, and the solution was relaxed for 200 ps to reach equilibrium [35,45]. Third, the "frozen" walls were released, and the simulation was performed under the NVT ensemble to achieve the equilibrium state of the substrates and the surface groups. Finally, the invisible wall at the entrance of the pore channel was removed to allow water and ions to enter freely through the channel under the NVT ensemble for 2000 ps. The flowchart of the simulation process is shown in Figure 3. During the simulation, the atomic trajectories from 0 to 2000 ps were detected and recorded with an interval of every 10 fs with a time step of 1 fs [46]. Periodic boundary conditions were applied in all directions to eliminate the size effect, simulating an infinite system and making the simulation results more accurate, reliable, and closer to the behavior of real physical systems [47].

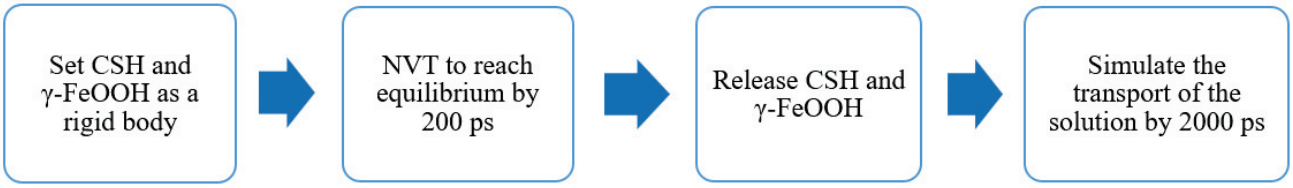

Figure 3. Flowchart of the simulation process.

3. Results and Discussion

3.1. Water and Ions Transport in the γ–FeOOH/CSH Pore

Figure 4 shows the transport of the four solutions at different times. It can be seen that the solution produced capillary adsorption in all four models. Among them, the water molecules were the fastest, driving the Na^+ ions, Cl^- ions, and SO_4^{2-} ions forward in the pore. The water and ions gradually filled the entire pore of γ–FeOOH/CSH within 2000 ps. The contact angles of the NaCl + Na_2SO_4 mixed solution on the solid surfaces were calculated to examine the morphology of the interfacial meniscus. The contact angle θ was calculated by Formula (1):

$$\theta = \tan^{-1}\left(\frac{r^2 - h^2}{2rh}\right) \quad (1)$$

where r is the radius of the nanopore, and h is the height of the meniscus, as shown in Figure 4. The contact angles between the solution and both interfaces were less than 90°, confirming the hydrophilicity of both γ–FeOOH and CSH. The transport of water and ions was significantly faster on the surface of CSH than on the surface of γ–FeOOH. At t = 100 ps, the CSH surface was completely covered by water molecules, while only 30% of the γ–FeOOH surface was covered with water. This confirmed that CSH was more hydrophilic than γ–FeOOH and had a greater adsorption effect on water molecules. During the transport in the mixed solution shown in Figure 4d, the contact angles on the surface of γ–FeOOH gradually decreased from 44.7°, 38.1°, 31.5° to 27.6° over time, while the contact angles on the surface of CSH gradually decreased from 39.7°, 35.8°, 38.3° to 23.7°. The reduction in the contact angles as the solution gradually migrated into the γ–FeOOH/CSH pore conformed to the capillary transport law of water and ions [48].

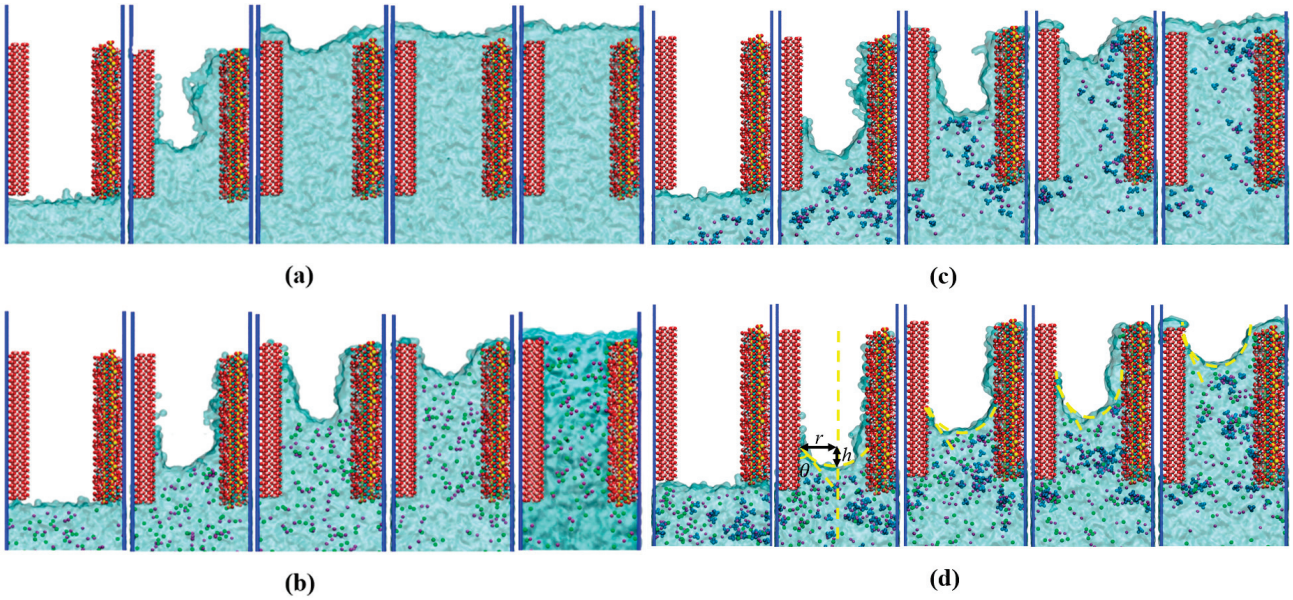

Figure 4. Snapshots of capillary flow of water and ions in 3.5 nm pore at t = 0, 100, 600,1000, and 2000 ps in (**a**) water; (**b**) NaCl; (**c**) Na_2SO_4; (**d**) NaCl + Na_2SO_4. (Color codes for atoms were pink: Fe; yellow: Si; cyan: Ca; red: O; white: H; green: Cl; purple: Na; blue: SO_4^{2-}).

Figure 4a–d show that the water molecules migrate the fastest in a pure water environment compared with the solutions containing ions. At t = 600 ps in a water environment, the water molecules had filled the pore, and the meniscus-like shape between the solution and the pore matrix had disappeared. In contrast, at t = 600 ps in the other solutions, the water molecules migrated between 1/2 and 2/3 of the entire pore. It can be inferred that the addition of ions slowed down the capillary transport rate of the water molecules. It can be further seen in Figure 4b,c that the water and ions migrated slightly faster in the NaCl solution than in the Na_2SO_4 solution. At t = 100 ps, the water molecules in the Na_2SO_4 solution had migrated to about 25% of the entire pore on the γ–FeOOH wall, while in the NaCl solution, they had migrated to nearly 35%. The reason for the slower ingress of the water and ions in the Na_2SO_4 solution was mainly due to the aggregation of Na^+ ions and large SO_4^{2-} ions on the CSH surface as shown in Figure 4c. Furthermore, the aggregation of the Na^+ ions and large SO_4^{2-} ions into clusters at the entrance of the nanopore hindered the migration of the water and ions. The figure also shows that the transport of the water and ions was the slowest in the mixed NaCl + Na_2SO_4 environment. This was due to enhanced ion absorption on the CSH wall. Different types of ions, including the Na^+ ions, Cl^- ions, and SO_4^{2-} ions, agglomerated and blocked the solution flow.

The capillary transport of solutions in the γ–FeOOH/CSH pore was quantified by recording the penetration depths of water molecules and ions along both pore surfaces and was presented in Figure 5. By comparing Figure 5a,b, it was observed that the surface of CSH was fully covered by the water molecules at t = 70 ps, whereas the surface of γ–FeOOH was fully covered at t = 1500 ps. This clearly showed that the water molecules traveled much faster on the CSH surface than on the γ–FeOOH surface. The penetration depths of water molecules in different solutions at any given time can be ordered as follows: water > NaCl > Na_2SO_4 > NaCl + Na_2SO_4. In addition, the penetration depths of water molecules in the NaCl solution on both the γ–FeOOH and CSH surfaces exhibited approximately parabolic dependence on time, which is consistent with the Lucas–Washburn equation in the capillary adsorption theory [49].

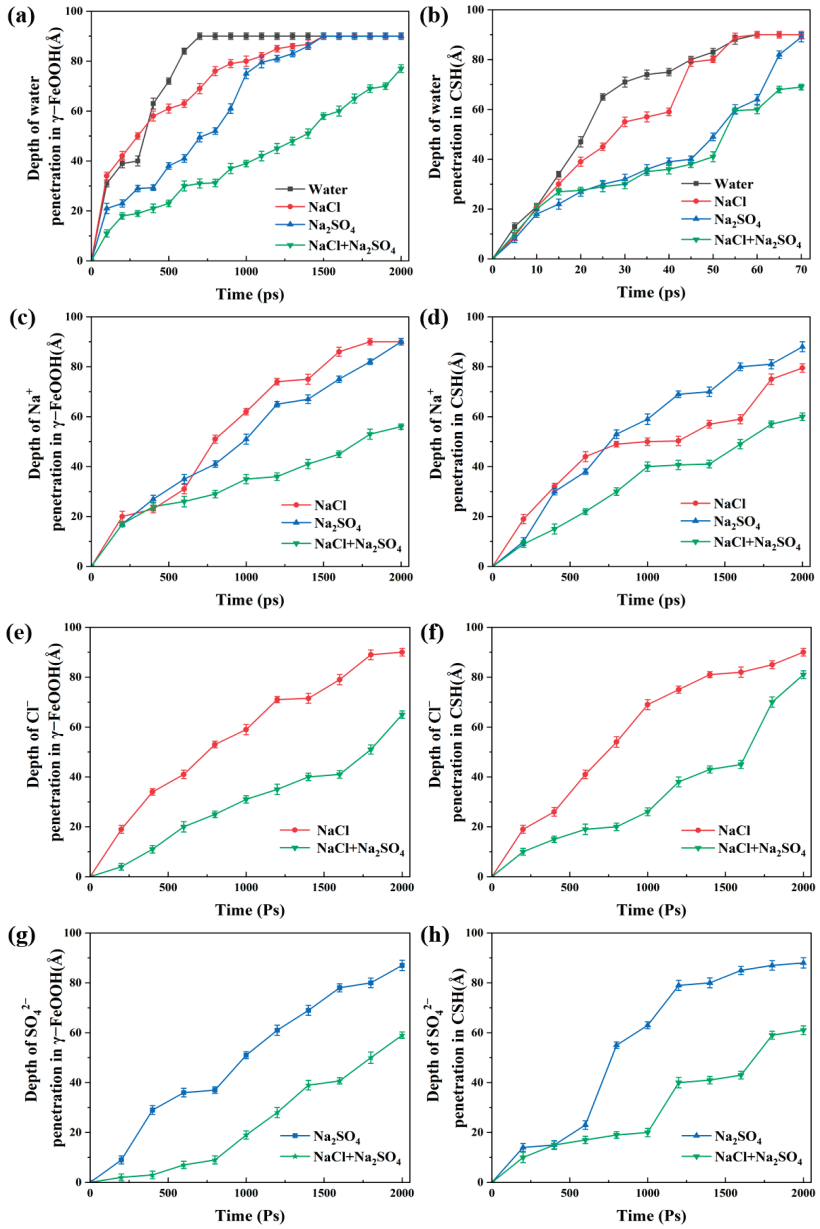

Figure 5. Penetration depths of (**a**) water, (**c**) Na^+, (**e**) Cl^-, and (**g**) SO_4^{2-} along the γ–FeOOH surface and penetration depths of (**b**) water, (**d**) Na^+, (**f**) Cl^-, and (**h**) SO_4^{2-} along the CSH surface under different solutions.

The penetration depths of the Na^+ ions, Cl^- ions, and SO_4^{2-} ions in different solutions on both sides of the pore are depicted in Figure 5c–h. The penetration depth of the ions in the mixed NaCl + Na_2SO_4 solution was smaller than that in the NaCl or Na_2SO_4 solution. At t = 2000 ps, the penetration depth of the Na^+ ions reached 90 Å in the NaCl or Na_2SO_4 solution on both sides of the pore, which was much greater than that of about 60 Å in the mixed solution of NaCl + Na_2SO_4. The transport rate of the Na^+ ions was significantly slower in the mixed solution than in the NaCl or Na_2SO_4 solution. The transport rate was obtained as the ratio of the distance increment to the time increment, which is the slope of the curve. It can be derived from Figure 5c,d that Na^+ ions were significantly slower in the mixed solution than in the NaCl or Na_2SO_4 solution. An analysis of the instantaneous transport rates revealed a consistent temporal trend characterized by an initially elevated rate followed by subsequent attenuation. The maximum observed transport rates in NaCl and Na_2SO_4 solutions reached 0.095 Å/ps and 0.1 Å/ps, respectively, while the minimum

rates decreased to 0.0015 Å/ps and 0.005 Å/ps. The mean transport rates were calculated as 0.044 Å/ps for NaCl and 0.04 Å/ps for Na_2SO_4 solution. In contrast, the mixed solution of NaCl + Na_2SO_4 exhibits a maximum rate of 0.05 Å/ps, a minimum rate of 0.0035 Å/ps, and an average rate of 0.03 Å/ps. Notably, the single-component solutions demonstrate significantly faster mean transport rates compared to the mixed solution, with an average rate enhancement of 233.3%. The same was observed for Cl^- and SO_4^{2-} ions. These results indicated that the coupling of these ions slows down the transport of water and ions. On the surfaces of γ–FeOOH and CSH, the time required for the ions to pass through the 9 nm nanopore was always longer than for the water molecules. In the NaCl or Na_2SO_4 solution environment, ions could completely pass through the pore within 2000 ps. This confirmed that the ion transport rate was lower than the water molecule transport rate and that the ions were carried forward by water molecules.

From the water penetration depth perspective, there was no clear difference between the surfaces of the γ–FeOOH and CSH substrates. To clarify the adsorption difference in the water molecules on the substrates, the interaction energy per unit area between each substrate and the water molecules was calculated by Formula (2):

$$E_{1/2} = \frac{E_{total} - (E_1 + E_2)}{A_{1/2}} \quad (2)$$

where $A_{1/2}$ is the cross-sectional area of components 1 and 2; $E_{1/2}$ represents the interaction energy per unit area between components 1 and 2; E_{total} is the total energy of the system containing components 1 and 2; and E_1 and E_2 are the energies of components 1 and 2, respectively. The calculated interaction energies are shown in Figure 6. It can be seen that the interaction energy between the substrates and the water molecules can be ordered as follows: water > NaCl > Na_2SO_4 > NaCl + Na_2SO_4. This is consistent with the order of transport rates of water shown in Figure 4. $E_{\text{CSH–H2O}} = -12.66$ kcal/mol/Å^2 in a water environment was 50.3% lower than $E_{\text{CSH–H2O}}$ −6.3 kcal/mol/Å^2 in NaCl + Na_2SO_4 solution. In these two different environments, $E_{\text{γ–FeOOH–H2O}}$ decreased from −1.5 kcal/mol/Å^2 to −1.26 kcal/mol/Å^2, i.e., by 16.7%. This showed that the high transport rate of the water molecules in the nanopore was due to their mutual attraction with the substrates. Considering that $E_{\text{CSH–H2O}}$ was much larger than $E_{\text{γ–FeOOH–H2O}}$, and that the water molecules migrated faster on the surface of CSH than on the surface of γ–FeOOH, it can be inferred that the higher the interaction energy, the higher the transport rate. The addition of ions decreased the interaction energy between the substrates and the water molecules, leading to a reduction in the transport rate. In addition, the γ–FeOOH substrate slowed the water transport, thereby inhibiting the corrosion of the steel fibers.

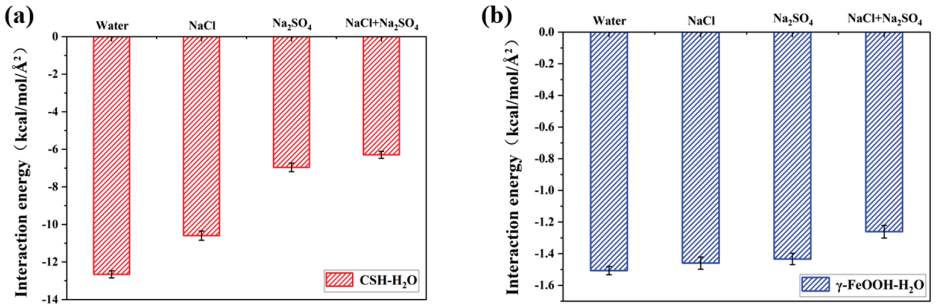

Figure 6. Interaction energy per unit contact area of (**a**) CSH–H_2O and (**b**) γ–FeOOH–H_2O.

3.2. Local Structure of Different Solutions in the γ–FeOOH/CSH Pore

The distribution of the water molecules and ions on the interfaces was investigated by an analysis of the density distributions. Figure 7a shows the density distribution of

water molecules in the nanopore in the Z direction. Multiple peaks of H_w and O_w (H and O atoms in water molecules) were present on both surfaces of the γ–FeOOH and CSH substrates. On the CSH side, H_w had four peaks at Z = 45.5, 49.5, 51.5, and 52.5 Å. The highest density of H_w was 0.042 atoms/Å^3, found at the third peak, Z = 51.5 Å. On the γ–FeOOH side, H_w had also four peaks at Z = 14.5, 16.5, 18.5, and 20.5 Å. The highest density of H_w was 0.035 atoms/Å^3, found at the third peak, Z = 18.5 Å. The distribution of O_w showed a similar trend. Multiple peaks in the density of these elements on the pore surfaces implied a layered accumulation of water molecules [50,51]. H_w was denser than O_w at the surfaces, indicating that the hydrogen atoms in water molecules occupied more sites on the surface of γ–FeOOH and CSH, forming hydrogen bond linkages. This confirmed the hydrophilicity of the two substrates. Compared with γ–FeOOH, the peak densities of H_w and O_w were larger and closer to the CSH surface. The results indicate that CSH has stronger hydrophilicity. Snapshots of water molecules at the substrate surfaces are shown in Figure 7b,c. It can be seen that H_w formed hydrogen bonds with O atoms exposed on the surface of the substrate. H_w points to the substrate, which affected the orientation of water molecules by the formation of hydrogen bonds.

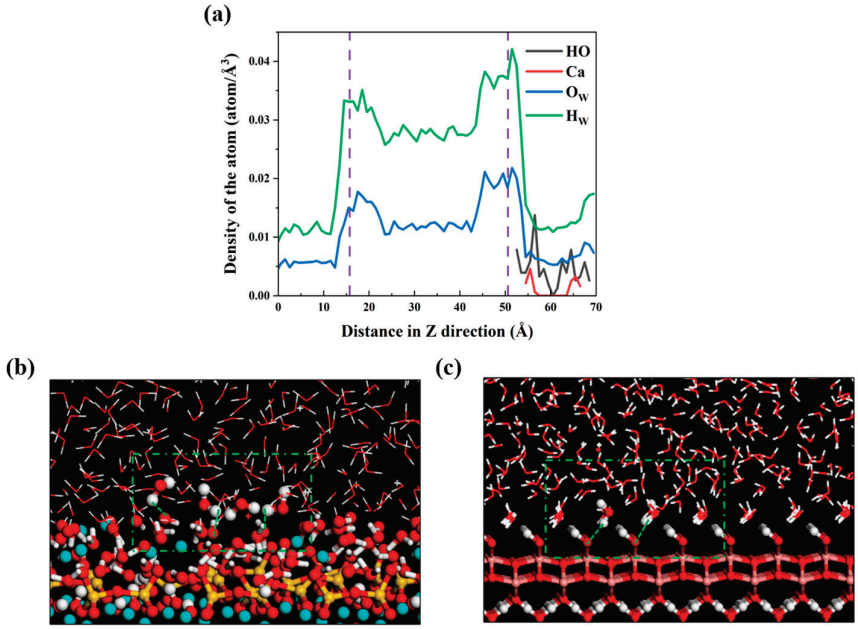

Figure 7. (**a**) Atomic density distribution of H_w and O_w across the γ–FeOOH/CSH channel, and snapshots of the water molecules on the surface of (**b**) CSH and (**c**) γ–FeOOH. (Color codes for atoms were pink: Fe; yellow: Si; cyan: Ca; red: O; white: H; green: Cl; purple: Na; blue: SO_4^{2-}).

The density distribution of ions in the studied solutions is shown in Figure 8. It can be seen in Figure 8a that distinct peaks appeared in the density distribution of both the Na^+ and Cl^- ions in the NaCl solution. Compared to the peaks of the Cl^- ions, the peaks of the Na^+ ions were higher and narrower. The distance between the Na^+ ions and the CSH surface was 0.5 Å, while the distance between the Cl^- ions and the CSH surface was 2.5 Å. Similar trends were observed on the surface of γ–FeOOH: Na^+ was closer to γ–FeOOH than Cl^-, which indicates that the γ–FeOOH and CSH surfaces were attractive to cations and repulsive to anions. The Na^+ ions were denser on the CSH surface than on the γ–FeOOH surface. The adsorption of the Cl^- ions was different, and a larger density distribution peak appeared only on the surface of CSH. From the snapshots of ions on the surfaces of the substrates shown in Figure 9a,b, it could be seen that the Na^+ ions bind to the hydroxyl oxygen atoms and aggregate on the surfaces of γ–FeOOH and CSH, while the Cl^- ions bonded with the Ca^{2+} ions in CSH [52].

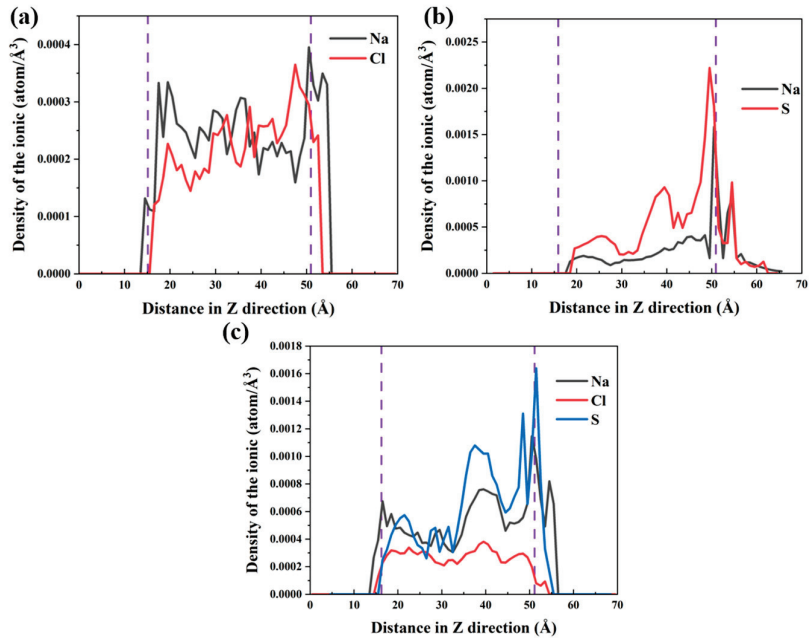

Figure 8. Atomic density distributions of ions across γ–FeOOH/CSH channel: (**a**) NaCl (Na, Cl), (**b**) Na_2SO_4 (Na, SO_4^{2-}), and (**c**) NaCl + Na_2SO_4 (Na, Cl, SO_4^{2-}). (The left dashed line in the figure represents the surface of γ–FeOOH, while the right dashed line represents the surface of CSH).

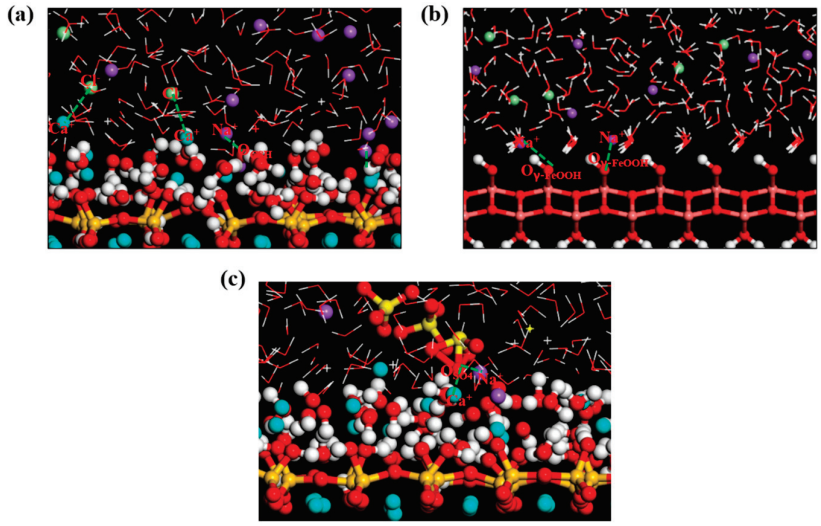

Figure 9. Snapshots of ions in NaCl solution on (**a**) CSH and (**b**) γ–FeOOH surfaces, and (**c**) snapshots of ions in Na_2SO_4 solution on the surface of CSH. (Color codes for atoms were, pink: Fe; yellow: Si; cyan: Ca; red: O; white: H; green: Cl; purple: Na; blue: SO_4^{2-}).

It can be seen in Figure 8b that the Na^+ and SO_4^{2-} ions in the Na_2SO_4 solution were concentrated at the surface of CSH. The density distribution of both the Na^+ and SO_4^{2-} ions had sharp peaks, different from the wide peaks of the Cl^- ions, indicating that CSH had a strong adsorption effect on these ions. The maximum density of the Na^+ ions was at 1 Å from the surface of the substrate, and that of the SO_4^{2-} ions was at 2 Å from the substrate, indicating that the Na^+ ions were adsorbed more strongly than the SO_4^{2-} ions. Compared to the NaCl solution, Na^+ ions in the Na_2SO_4 solution tended to aggregate mostly on the CSH surface, indicating that the adsorption of the SO_4^{2-} ions affected the distribution of the Na^+ ions. From the snapshots in Figure 9c, it was observed that a Ca–SO_4–Na bond was formed after the oxygen atoms in the SO_4^{2-} ions bonded with the Ca^{2+} ions and adsorbed the Na^+ ions on the surface of CSH. This inhibited the aggregation of the Na^+ ions on the γ–FeOOH surface.

The density distribution of ions in a mixed solution of NaCl + Na_2SO_4, given in Figure 8c, showed several peaks of Na^+ ions on both the γ–FeOOH and CSH surfaces as well as several peaks of SO_4^{2-} ions on the CSH surface. This implied that CSH strongly attracts Na^+ ions and SO_4^{2-} ions under different ion coupling. On the contrary, there were no significant density peaks of Cl^- ions on the CSH surface, indicating that the addition of sulfate weakened the interaction between CSH and Cl^- ions. As the sites of the Ca^{2+} ions on the CSH surface were occupied by the SO_4^{2-} ions, the binding of the Cl^- ions to the Ca^{2+} ions was inhibited, which promotes the stripping of Cl^- from the substrate.

To further understand the effect of the chemical environment on the transport in γ–FeOOH/CSH pores and the interactions between the environmental components, the radial density function (RDF) was calculated, and the results are shown in Figure 10. Figure 10a,b show the RDF curves of O_{CSH}–H_{Water} and $O_{\gamma-FeOOH}$–H_{Water}. The first peaks of the two curves were at 1.75 Å and 1.95 Å, respectively, which were less than the distance required for the formation of hydrogen bonds between oxygen and hydrogen (2.45 Å). This indicated that the transport of water molecules was promoted by the hydrogen bonds formed between the two substrates and the water molecules in the solutions. Comparing the RDFs of all solutions, the peaks were lowest in the NaCl + Na_2SO_4 solution, indicating that the hydrogen bonds in this solution were the weakest, resulting in the slowest migration rate of water molecules. The RDF peak of O_{CSH}–H_w was significantly higher than that of $O_{\gamma-FeOOH}$–H_w in the same solution. Taking NaCl + Na_2SO_4 as an example, the RDF peak of O_{CSH}–H_w was 1.21, twice the peak of $O_{\gamma-FeOOH}$–H_w, which was 0.6. This implied that the surface of CSH was more likely to form hydrogen bonds with water molecules. Therefore, the transport rate of water molecules on the surface of CSH was much faster than that on the surface of γ–FeOOH.

As shown in Figure 10c, there were RDF peaks of Na–Ow, Cl–$O_{W,}$ and S–Ow at 2.25 Å, 3.15 Å, and 3.65 Å, respectively. This indicated that the Na^+ ions, Cl^- ions, and sulfates interacted strongly with the surrounding water molecules and were prone to aggregate. The position of the RDF peak represented the optimal radius between the ion and the O_{Water} atom. The RDF peak of Na–O_w was the first to appear at 2.35 Å and was the largest. This showed that the interaction between the Na^+ ions and water molecules was the strongest, and the distribution distance was the shortest.

The RDF of Na–O_{CSH} presented in Figure 10d had a first peak at 2.25 Å, indicating that the hydroxyl oxygen on the CSH surface attracted positively charged Na^+ ions, and the Na–O_{CSH} bond length was 2.25 Å. Figure 10e, f depict the RDFs of Cl–Ca_{CSH} and S–Ca_{CSH}, respectively. The first peaks of the two curves were at 2.95 Å and 3.15 Å, respectively, implying the Cl^- ions and SO_4^{2-} ions had significant spatial correlations with the Ca^{2+} ions exposed on the CSH surface so that Cl–Ca and SO_4–Ca pairs were easily formed. Compared with the single-salt solutions, the RDF peaks of Cl–Ca_{CSH} and S–Ca_{CSH} in the mixed solution were substantially lower, which indicated that the Cl^- ions and SO_4^{2-} ions occupied the binding sites of the Ca^{2+} ions on the CSH surface in the mixed solution, leading to a smaller number of Cl–Ca and SO_4–Ca ion pairs. The effect of multiple ions was that the CSH interface and ions were prone to form large cluster ion pairs such as O_{CSH}–Na–SO_4, O_{CSH}–Na–Cl, SO_4–Ca–Cl–Ca, etc., which was consistent with the observation in Figure 4c,d. The formation of large clusters of ion pairs blocked the transport of water and ions through the gel pores to some extent. In contrast, the exposed part of γ–FeOOH was a hydroxyl group, which had an adsorption effect on the Na^+ ions. Although Na–$O_{\gamma-FeOOH}$ was easy to form, it was difficult to form Cl–$O_{\gamma-FeOOH}$ and SO_4–$O_{\gamma-FeOOH}$. As a result, it was more difficult to form a large cluster of ion pairs on the γ–FeOOH surface, and the adsorption of the Cl^- ions and SO_4^{2-} ions was weak.

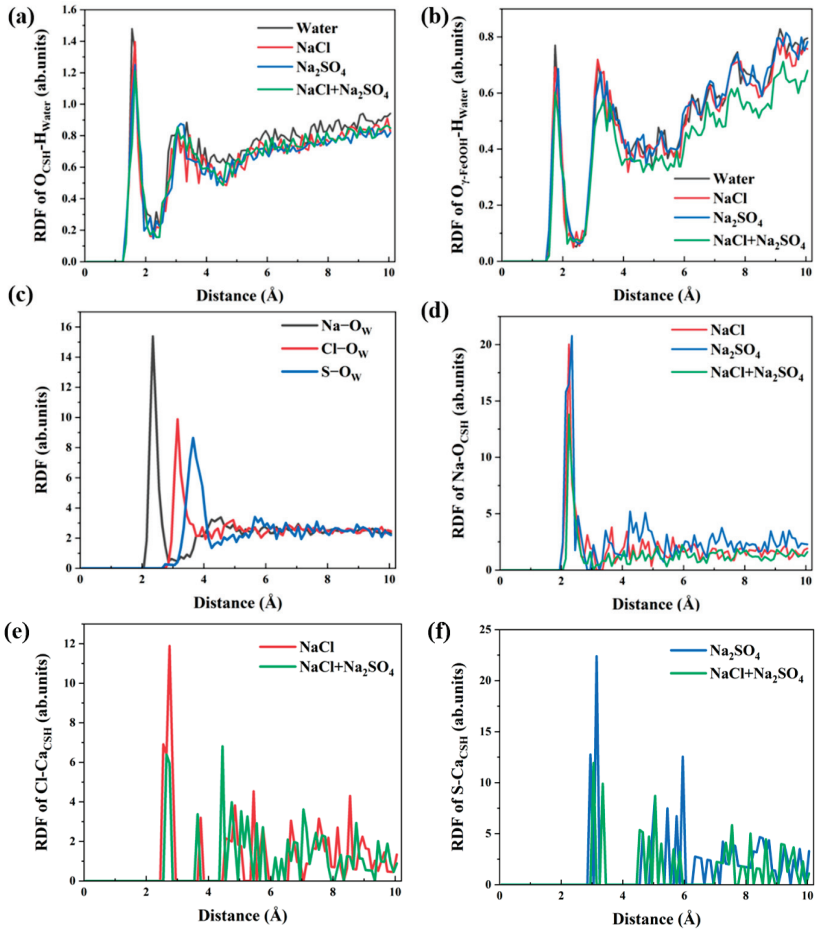

Figure 10. RDF of (**a**) O_{CSH}–H_{Water}, (**b**) $O_{\gamma\text{–FeOOH}}$– H_{Water}, (**c**) Na, Cl, S–O_W, (**d**) Na– O_{CSH}, (**e**) Cl–Ca_{CSH}, and (**f**) S–Ca_{CSH}.

3.3. Water and Ions Transport in Different Pore Widths

The results presented in the previous subsections showed that the rate of transport in the γ–FeOOH/CSH pore was the smallest for the NaCl + Na_2SO_4 solution. To further analyze the effect of pore size on the transport rate, simulations of the transport of the NaCl + Na_2SO_4 solution in the γ–FeOOH/CSH nanopores were performed with four pore widths of 3.5 nm, 2.5 nm, 1.5 nm, and 1 nm.

Snapshots of the capillary flow of the NaCl + Na_2SO_4 solution in these pores at t = 2000 ps are shown in Figure 11. As the pore width decreased from 3.5 nm to 1 nm, the penetration depths of the NaCl + Na_2SO_4 solution along both sides of the γ–FeOOH/CSH nanopore decreased. Furthermore, the penetration rate of all the ions, the Na^+, Cl^-, and SO_4^{2-} ions, were smaller than that of the water molecules, and were further reduced with decreasing pore width. In the 1.5 nm and 1 nm pores, when the water molecules had migrated along the entire CSH surface, the ions had only migrated 30% to 40% of that surface. Pores of small width filtered water and ions effectively. This will be discussed in detail in the next subsection.

Further quantification of the migration of the NaCl + Na_2SO_4 solution in pores of different widths is given in Figure 12, where the positions of ions and water molecules on the substrates' surfaces are plotted as functions of time. Comparing Figure 12a,b, it can be observed that the intrusion depth of water molecules on the surface of CSH was higher than that on γ–FeOOH, which is consistent with the results presented in Section 3.1. With the decrease in pore widths, the intrusion depths of water molecules on both substrate surfaces decrease. The "filtration" of water molecules was most evident for the 1 nm pore.

At t = 1400 ps, the transport of water molecules on the γ–FeOOH was nearly halted. At 2000 ps, less than 50% of the γ–FeOOH surface was covered by the water.

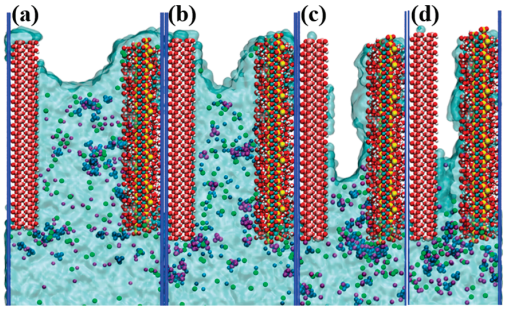

Figure 11. Snapshots of the capillary flow of the water molecules, Na^+, Cl^-, and SO_4^{2-} ions in (**a**) 3.5 nm, (**b**) 2.5 nm, (**c**) 1.5 nm, and (**d**) 1.0 nm pores at 2000 ps. (Color codes for atoms were pink: Fe; yellow: Si; cyan: Ca; red: O; white: H; green: Cl; purple: Na; blue: SO_4^{2-}).

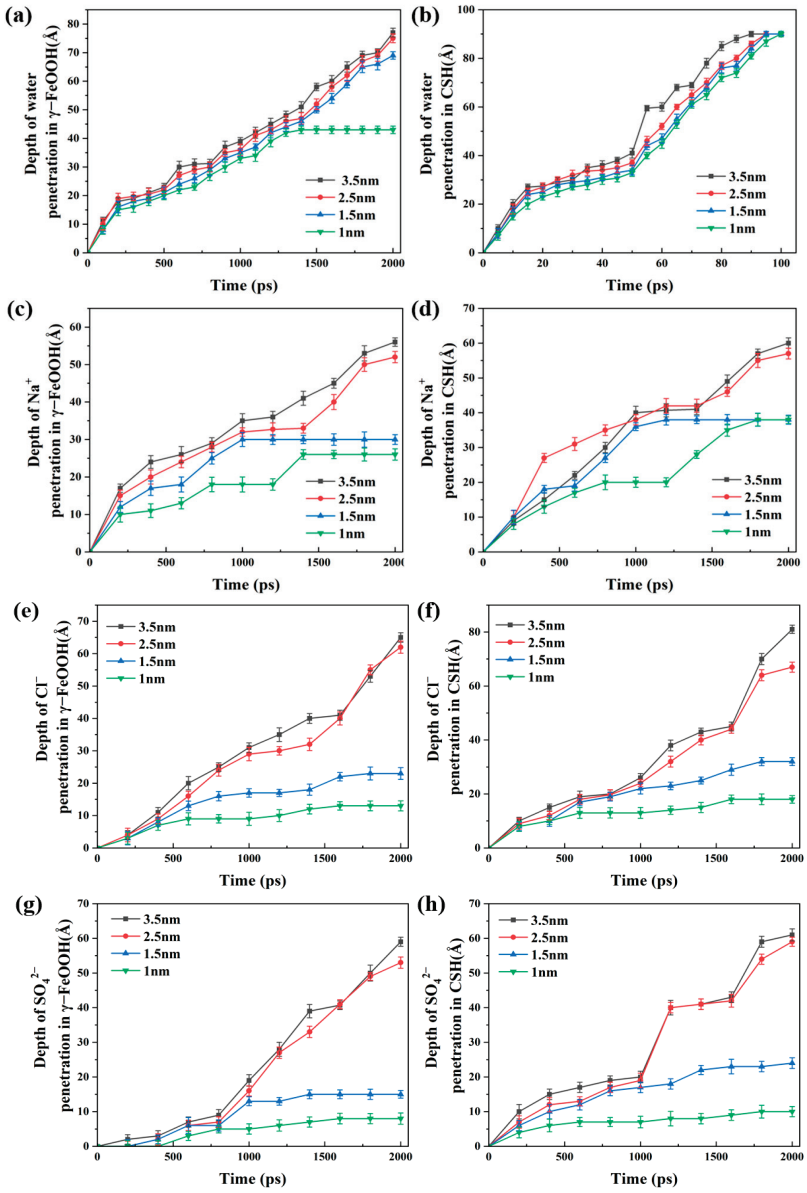

Figure 12. Penetration depths of (**a**) water, (**c**) Na^+, (**e**) Cl^-, and (**g**) SO_4^{2-} along the γ–FeOOH surface and penetration depths of (**b**) water, (**d**) Na^+, (**f**) Cl^-, and (**h**) SO_4^{2-} along the CSH surface at different pore sizes.

Figure 12c–h depict the intrusion depths of the Na^+, Cl^-, and SO_4^{2-} ions on both surfaces of pores with different widths. The intrusion depths of the three ions were smaller than that of the water molecules at any time, i.e., the migration of the ions was not synchronized with water. The curves in the 1.5 nm and 1 nm were lower than those in the 2.5 nm and 3.5 nm pores. At t = 2000 ps, the penetration depths of the Na^+ ions on the γ–FeOOH surface were 5.6 nm, 5.2 nm, 3 nm, and 2.6 nm for the four pore widths, while those on the CSH surface were 6 nm, 5.7 nm, 3.8 nm, and 3.8 nm, respectively. This indicated that the blocking effect of the substrate surfaces on ion transport became stronger with decreasing pore size. The blocking effect was most pronounced for pore widths smaller than 2.5 nm. This observation also applied to the Cl^- and SO_4^{2-}. At t =1000 ps, the rate of penetration of the Cl^- and SO_4^{2-} ions reduced, indicating that the blocking effect of small pore sizes on the Cl^- and SO_4^{2-} ions was more pronounced than on the Na^+ ions. The difference in the blocking effect of γ–FeOOH/CSH nanopore on ions and water molecules was mainly due to the differences between the interface of CSH(γ–FeOOH)/water and the interface C–S–H(γ–FeOOH)/ions.

The different transport rates of NaCl + Na_2SO_4 solution in different pore widths signified the strong effect of the width on the mobility of water and ions. Pores with smaller widths inhibited the penetration of water and ions, especially the diffusion of ions. The mechanism by which this happened required further investigation.

3.4. Local Structures of Water and Ions in Nano–Pores with Different Widths

To understand the obstructing effect of pores with small widths on the solution transport, the density distribution of each constituent was calculated at t = 2000 ps. Figure 13a shows the density distributions of HO, Ca, O_w, and H_w calculated with the 1.5 nm pore width.

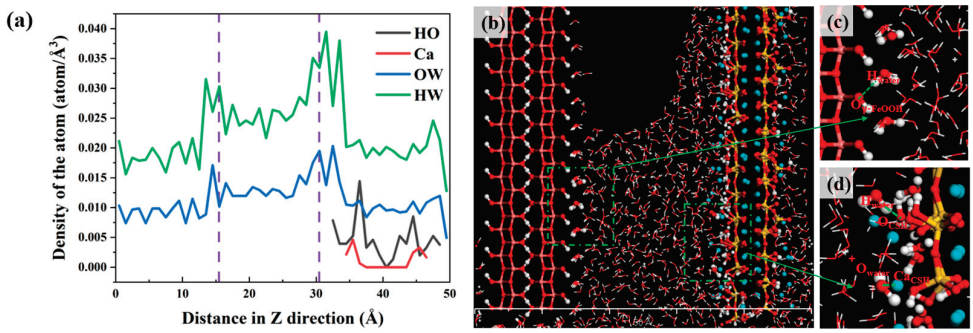

Figure 13. (**a**) Atomic density distribution perpendicular to the γ–FeOOH/CSH slit. Snapshot of the water molecule was (**b**) embedded in a 1.5 nm slit of γ–FeOOH/CSH and on the surface of (**c**) γ–FeOOH and (**d**) CSH. (Color codes for atoms were pink: Fe; yellow: Si; cyan: Ca; red: O; white: H; green: Cl; purple: Na; blue: SO_4^{2-}).

Multiple peaks in the densities of the O_w and H_w atoms could be observed at and between the γ–FeOOH and CSH substrates, which indicated that the water molecules aggregated on the surface of γ–FeOOH and CSH and formed a layered structure. The distribution of H_w on the CSH surface had clear peaks at Z = 27.5, 29.5, 31.5, and 33.5 Å, with the largest peak at Z = 31.5 Å. On the γ–FeOOH surface, the density peaks of H_w were at Z = 13.5 Å and 15.5 Å. The density peaks of H_w and O_w on the γ–FeOOH surface were much smaller, which was explained by the stronger interaction between water molecules and the hydrophilic groups on the surface of CSH, including silicate chains and intra- and interlayer calcium ions. The first density peak of H_w was closer to the two substrates than that of O_w. This is consistent with the results presented in Section 3.2 and indicates that the change in pore width does not affect the orientation distribution of the water

molecules at the substrates. Figure 13b–d show that the water molecules were adsorbed on the substrates by forming hydrogen bonds with the hydroxyl groups in the outer layers of the CSH and γ–FeOOH. Furthermore, the water molecules also formed ionic bonds with the calcium ions on the surface of CSH. As a result, the hydroxyl hydrogen was always oriented towards the substrate, which indicated that the change in pore width does not affect the orientation distribution of water molecules. In summary, a series of changes in atomic density near the substrate were due to the hydrophilicity of γ–FeOOH and CSH and the formation of bonds with water molecules.

To explain the blocking effect of smaller pore widths on the ions, the density distributions of the Na^+, Cl^-, and SO_4^{2-} ions in the Z direction were calculated for the four pore widths and are shown in Figure 14.

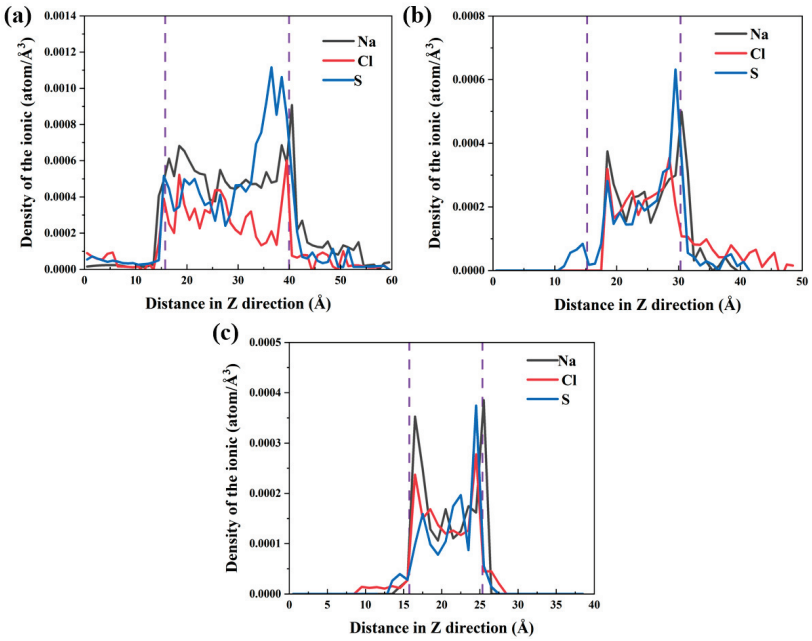

Figure 14. Density distribution of Na^+, Cl^-, and SO_4^{2-} ions in the NaCl + Na_2SO_4 solution in (**a**) 2.5 nm, (**b**) 1.5 nm, and (**c**) 1 nm pores. (The left dashed line in the figure represents the surface of γ–FeOOH, while the right dashed line represents the surface of CSH).

Compared with the Cl^- and SO_4^{2-} ions, the density peaks of the Na^+ ions were closer to the surface of CSH and γ–FeOOH in the pores with four different widths. This shows that the change in pore width has no effect on the adsorption of the Na^+ ions on the surfaces of CSH and γ–FeOOH, and the adsorption of cations on these surfaces is stronger than that of anions. All the ions were gathered on the surface of both substrates. However, fewer ions were accumulated on the γ–FeOOH surface compared to CSH; the density difference of the SO_4^{2-} ions between the two substrates was most pronounced. This can be illustrated by the following example: In the pore with 2.5 nm width, the peak density of the SO_4^{2-} ions on the CSH surface was up to 0.001 atom/Å^3, whereas the peak density on the γ–FeOOH surface was only 0.0005 atom/Å^3. When the pore width decreased, the SO_4^{2-} ions entering the nanopore were mainly attracted by the Ca^{2+} ions on the CSH surface and attached to the CSH surface. On the contrary, the SO_4^{2-} ions near the γ–FeOOH surface were not easily attracted. By comparing the density peaks of the same ion at different pore widths, it can be observed that the density peak of the ion decreased as the pore width decreased. In the four pore widths, the density peaks of Na^+ ions on the CSH surface were 0.0011, 0.0009, 0.0005, and 0.0004 atom/Å^3, respectively. These values represented 18%, 54%, and 63% reductions from those at 3.5 nm. The density peaks on the γ–FeOOH surface exhibited a

similar trend, decreasing from 0.0007 atom/Å^3 to 0.0006 atom/Å^3, 0.0004 atom/Å^3, and finally to 0.00035 atom/Å^3 as the widths decreased. This indicated that the width reduction effectively blocked ions from entering the nanopores and impeded their transport. Notably, when the pore width was less than 2.5 nm, the ion density showed the most significant decrease, suggesting a more pronounced blocking effect.

Further analysis of the pore width effect on the interaction between ions and water molecules was performed by studying the radial distribution functions (RDFs). The RDFs for water–water and water–ion interactions are shown in Figure 15. The first peak of the RDF for O_{water}–O_{water} was observed at 2.75 Å, representing the closest interaction distance between water molecules. As pore width decreased, the peak diminished, indicating that smaller pore widths hindered water molecule interactions. The first peaks for Na–O_{water}, Cl–O_{water}, and S–O_{water} interactions in Figure 15b–d appeared at 2.35 Å, 3.15 Å, and 3.65 Å, respectively. Additionally, the Na–O_{water} RDF exhibited a second broadened peak at 4.45 Å, while Cl–O_{water} and S–O_{water} lacked significant secondary peaks. The peaks signified the radii of the first and the second hydration shells around each ion, and the hydration shell of Na–O_{water} had the smallest radius and the highest peak, suggesting stronger water–ion interactions. Decreasing pore width reduced the RDF peaks of Na–O_{water}, Cl–O_{water}, and S–O_{water}, with the most pronounced differences occurring for widths smaller than 2.5 nm. These findings suggested that smaller widths weakened the water–ion attraction, leading to slower ion transport.

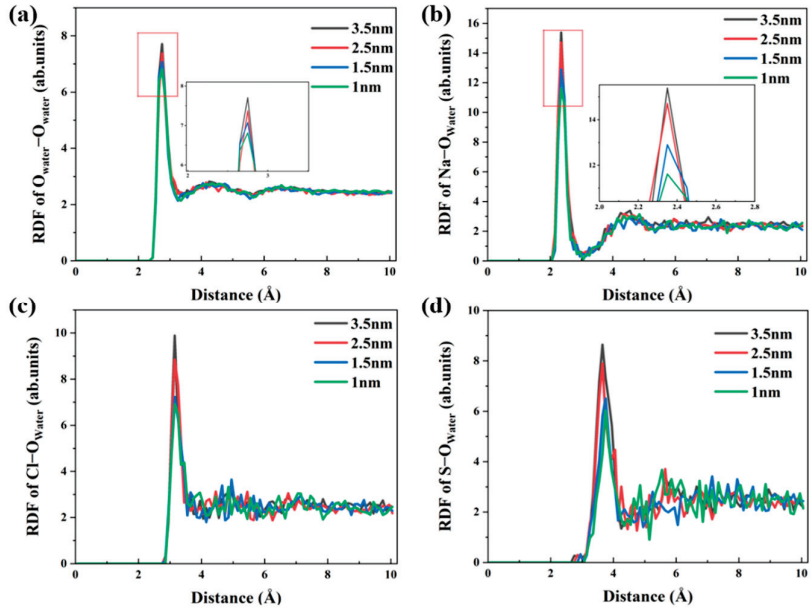

Figure 15. RDF of (**a**) O_{water}–O_{water}, (**b**) Na–O_{water}, (**c**) Cl–O_{water}, and (**d**) S–O_{water}.

In addition to the interaction with solvated water molecules, aqueous species could form chemical bonds with CSH and γ–FeOOH. As depicted in Figure 16a,b, the RDFs for O_{CSH}–H_{water} and $O_{\gamma–FeOOH}$–H_{water} exhibited first peaks at 1.65 Å and 1.75 Å, respectively, indicating that hydrogen bonds formed between substrate surfaces and the adsorbed water molecules. With decreasing pore widths and diminishing peaks, the hydrogen bonds between the substrates and water molecules were weakened, which led to slower water molecules. The RDF peak of O_{CSH}–H_{water} was much higher than that of $O_{\gamma–FeOOH}$–H_{water} at the same pore width, indicating greater CSH affinity for water molecules compared to γ–FeOOH at all pore widths.

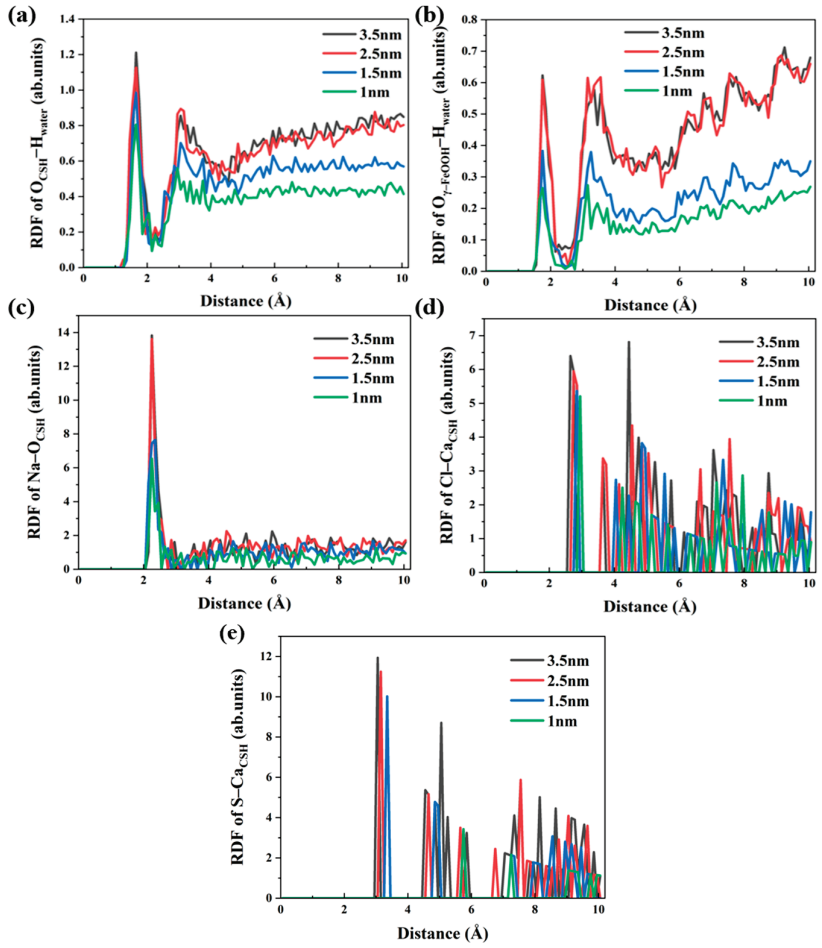

Figure 16. RDF of (**a**) O_{CSH}–H_{water}, (**b**) $O_{\gamma-FeOOH}$–H_{water}, (**c**) Na–O_{CSH}, (**d**) Cl–Ca_{CSH}, and (**e**) S–Ca_{CSH}.

Figure 16c–e present RDFs for the Na^+, Cl^-, and SO_4^{2-} ions interacting with the substrates at various pore widths. As pore width decreased, the RDF peaks of Na–O_{CSH}, Cl–Ca_{CSH}, and S–Ca_{CSH} decreased, suggesting weakened ion–CSH interactions. Their peaks were notably larger than those of O_{CSH}–H_{water}, indicating a stronger immobilization of ions by CSH. The hydroxyl groups on γ–FeOOH surfaces also adsorbed Na^+ ions, forming Na–$O_{\gamma-FeOOH}$ ion pairs. Reduced pore width decreased the distance between ion pairs on CSH surfaces and Na–$O_{\gamma-FeOOH}$, promoting the formation of larger ion clusters such as $O_{\gamma-FeOOH}$–Na–SO_4–Ca and $O_{\gamma-FeOOH}$–Na–Cl–Ca, which obstructed pore channels. Combining the RDF trends for ions and O_{water}, it could be concluded that the reduction in the ion transport rate was due to weakened water molecule-driven ion motion. Moreover, the hydroxyl groups and Ca^{2+} ions on the CSH surface adsorbed the Na^+, Cl^-, and SO_4^{2-} ions, retaining them for extended periods.

4. Conclusions

Molecular dynamics simulations were performed to clarify the transport mechanisms of water, NaCl, Na_2SO_4, and a composite solution of NaCl + Na_2SO_4 in γ–FeOOH/CSH nanopores. The effect of pore width on the transport of NaCl + Na_2SO_4 composite solution was also investigated. The following conclusions could be drawn:

(1) The transport of solutions in nanopores was meniscus-shaped with contact angles less than 90° on both substrates, which was consistent with capillary transport and confirms the hydrophilic nature of both CSH and γ–FeOOH.

(2) The penetration depths of different solutions were ordered as follows: D(water) > D(NaCl) > D(Na_2SO_4) > D(NaCl + Na_2SO_4). In all the solutions, water molecules penetrated along the CSH side faster than along the γ–FeOOH side. Ions penetrated more slowly than water molecules on both sides.

(3) Water molecules in the solution formed hydrogen bonds with γ–FeOOH and CSH, facilitating transport and driving ion movement. The nanopores immobilized different ions via distinct adsorption mechanisms: the Na^+, Cl^-, and SO_4^{2-} ions formed Na–O_{CSH}, Cl–Ca_{CSH}, and S–Ca_{CSH} ion pairs with CSH, while Na–$O_{\gamma–FeOOH}$ ion paired with γ–FeOOH. In the mixed solution of NaCl + Na_2SO_4, water and ion transport were inhibited by the formation of large clusters of ion pairs and their adsorption onto the CSH side.

(4) The transport rate of water and ions reduced with decreasing pore width, and the difference between the penetration depths of the water molecules and ions increased due to capillary action. For pores with less than 2.5 nm width, the Na^+, Cl^-, and SO_4^{2-} ions tended to remain in the entry region of the nanopore.

(5) The Na–O_{CSH}, Cl–Ca_{CSH}, and S–Ca_{CSH} ion pairs formed by CSH with the Na^+, Cl^-, and SO_4^{2-} ions were significantly stronger than the hydrogen bonds between CSH and water molecules. As a result, water transport continued while the ions were retained on the CSH surface for extended periods. This led to the separation of ions from water. For pores with less than 2.5 nm width, the proximity of the substrate surfaces caused the ion pairs adsorbed on the two surfaces to interact, forming a large cluster of ion pairs such as $O_{\gamma–FeOOH}$–Na–SO_4–Ca and $O_{\gamma–FeOOH}$–Na–Cl–Ca. This partially blocked the pore entrance and hindered the transport of water molecules and ions.

In conclusion, this study focused on the transport process of γ–FeOOH/CSH interface nanopores under different erosion ions and different pore sizes, rather than solely the CSH nanopores, by MD simulation. The different mechanisms of solution invasion on the surfaces of two different matrices were revealed at the molecular level. Although the simulation results were limited to nanosecond and nanometer, the laws were applicable to engineering that the addition of steel fibers could effectively slow down the transmission of seawater in the concrete matrix, thereby enhancing the impermeability of port engineering structures. Furthermore, the idealized model was applied in a simulation as the initial exploration and research of this new type of material. More in-depth research on the durability of concrete is expected to be conducted, such as temperature, interface roughness, more comprehensive corrosive ions in seawater, and pore size effects. At present, steel fiber-reinforced concrete is widely used in port construction. It is believed that conducting research from a microscopic perspective will help us understand the working mechanism of this material in solutions, clarify the mechanism of enhancing the durability of SFRC, and hopefully provide support for better predicting its durability in the future.

Author Contributions: Conceptualization, Y.L. and L.Z.; methodology, C.H. and A.J.; software, R.W.; formal analysis, Y.L.; data curation, R.W.; writing—original draft preparation, Y.L. and R.W.; writing—review and editing, A.J. and L.Z.; visualization, C.H. All authors have read and agreed to the published version of the manuscript.

Funding: This research was funded by the National Key Research and Development Project (2022YFB2603000), the National Natural Science Foundation of China (52179120, 52171267, 51909270 and 51909147), and the Fundamental Research Funds for the Central Universities (23CX07013A).

Institutional Review Board Statement: Not applicable.

Informed Consent Statement: Not applicable.

Data Availability Statement: The original contributions presented in this study are included in the article. Further inquiries can be directed to the corresponding author.

Acknowledgments: The authors thank the editors and two anonymous reviewers for their careful work and thoughtful suggestions.

Conflicts of Interest: The authors declare no conflicts of interest.

References

1. Faella, C.; Lima, C.; Martinelli, E.; Pepe, M.; Realfonzo, R. Mechanical and durability performance of sustainable structural concretes: An experimental study. *Cem. Concr. Comp.* **2016**, *71*, 85–96. [CrossRef]
2. Peng, Y.; Yu, L.; Qian, J.; Li, W.; Zhang, T.; Zhou, L. Dynamic tensile behavior and crack propagation in coral aggregate seawater shotcrete: Experimental investigation and numerical simulation. *Cem. Concr. Comp.* **2025**, *159*, 06010. [CrossRef]
3. Li, Z.Q.; Nie, L.; Xue, Y.; Li, W.; Fan, K. Model Testing on the Processes, Characteristics, and Mechanism of Water Inrush Induced by Karst Caves Ahead and Alongside a Tunnel. *Rock. Mech. Rock. Eng.* **2025**, *58*, 1–18. [CrossRef]
4. Liu, H.; Li, K.; Li, Y.; Liu, S.; Dong, Z.; Cui, H.; Liu, W. Corrosion behavior of steel fiber reinforced concrete under ambipolar stray current interference. *Constr. Build. Mater.* **2024**, *411*, 134302. [CrossRef]
5. Li, W.; Zhang, Q.; Wang, X.; Yu, L.; Li, Z. Synergistic effect of particle size, carboxymethyl starch and Na_2CO_3 on rheological and filtration property of bentonite-based material. *Case. Stud. Constr. Mat.* **2024**, *21*, e03537. [CrossRef]
6. Xu, L.; Zhu, X. Detection model for key nodes of manufacturing industry chain stability under complex networks: A naval architecture and marine engineering equipment industry chain example. *Kybernetes* **2025**, *54*, 2892–2915. [CrossRef]
7. Gholamhoseini, A.; Khanlou, A.; MacRae, G.; Scott, A.; Hicks, S.; Leon, R. An experimental study on strength and serviceability of reinforced and steel fibre reinforced concrete (SFRC) continuous composite slabs. *Eng. Struct.* **2016**, *114*, 171–180. [CrossRef]
8. Li, W.; Yu, L.; Zhang, T. Quantitative analysis of grain size effect on tensile mechanical behavior of granite based on multi-level force chain networks. *Comp. Part. Mech.* **2024**, *11*, 2245–2266. [CrossRef]
9. Xiang, D.; Liu, S.; Li, Y.; Liu, Y. Improvement of flexural and cyclic performance of bridge deck slabs by utilizing steel fiber reinforced concrete (SFRC). *Constr. Build. Mater.* **2022**, *329*, 127184. [CrossRef]
10. Song, W.; Yin, J. Hybrid effect evaluation of steel fiber and carbon fiber on the performance of the fiber reinforced concrete. *Materials* **2016**, *9*, 704. [CrossRef]
11. Li, W.; Yu, L.Y.; Tan, Y.Z.; Wu, L.R.; Qian, J.Y. Mechanical properties and impact behavior of frozen clay: Insights from static mechanical tests, fly-plate tests, and split-Hopkinson pressure bar analysis. *Phys. Fluids* **2024**, *36*, 057138. [CrossRef]
12. Zhang, P.; Wang, C.; Gao, Z.; Wang, F. A review on fracture properties of steel fiber reinforced concrete. *J. Build. Eng.* **2023**, *67*, 105975. [CrossRef]
13. Abbass, W.; Khan, M.I.; Mourad, S. Evaluation of mechanical properties of steel fiber reinforced concrete with different strengths of concrete. *Constr. Build. Mater.* **2018**, *168*, 556–569. [CrossRef]
14. Sharma, S.; Arora, V.V.; Kumar, S.; Daniel, Y.N.; Sharma, A. Durability study of high-strength steel fiber-reinforced concrete. *ACI. Mater. J.* **2018**, *115*, 219–225. [CrossRef]
15. Tian, J.; Wu, X.; Zuo, Y.; Yuan, J.; Wang, W.W. Interface behaviors between smart-functional ECC and steel rebar under coupling effect of sustained load and chloride ion erosion: Corrosion resistance, mechanical and self-sensing properties. *Constr. Build. Mater.* **2024**, *438*, 137205. [CrossRef]
16. Li, H.; Wu, Y.; Zhou, A.; Lu, F.; Lei, Z.; Zeng, B.; Zhu, K. Cracking pattern and bearing capacity of steel fiber-reinforced concrete single-layer tunnel lining. *Sustainability* **2023**, *13*, 10665. [CrossRef]
17. Magazzù, A.; Marcuello, C. Investigation of soft matter nanomechanics by atomic force microscopy and optical tweezers: A comprehensive review. *Nanomaterials* **2023**, *13*, 963. [CrossRef]
18. Hwang, J.P.; Jung, M.S.; Kim, M.; Ann, K.Y. Corrosion risk of steel fibre in concrete. *Constr. Build. Mater.* **2015**, *101*, 239–245. [CrossRef]
19. Yoo, D.Y.; Shin, W.; Chun, B. Corrosion effect on tensile behavior of ultra–high–performance concrete reinforced with straight steel fibers. *Cem. Concr. Comp.* **2020**, *109*, 103566. [CrossRef]
20. Tai, Y.; Yang, L.; Gao, D.; Kang, K.; Cao, Z.; Zhao, P. Properties evolution and deterioration mechanism of steel fiber reinforced concrete (SFRC) under the coupling effect of carbonation and chloride attack. *J. Build. Eng.* **2024**, *95*, 110275. [CrossRef]
21. Marcos–Meson, V.; Fischer, G.; Edvardsen, C.; Skovhus, T.L.; Michel, A. Durability of Steel Fibre Reinforced Concrete (SFRC) exposed to acid attack—A literature review. *Constr. Build. Mater.* **2019**, *200*, 490–501. [CrossRef]
22. Feng, G.; Zhu, D.; Guo, S.; Rahman, M.Z.; Jin, Z.; Shi, C. A review on mechanical properties and deterioration mechanisms of FRP bars under severe environmental and loading conditions. *Cem. Concr. Comp.* **2022**, *134*, 104758. [CrossRef]
23. Arnittali, M.; Rissanou, A.N.; Harmandaris, V. Structure of biomolecules through molecular dynamics simulations. *Procedia Comput. Sci.* **2019**, *156*, 69–78. [CrossRef]

24. Hou, D.; Lu, C.; Zhao, T.; Zhang, P.; Ding, Q. Structural, dynamic and mechanical evolution of water confined in the nanopores of disordered calcium silicate sheets. *Microfluid. Nanofluid.* **2015**, *19*, 1309–1323. [CrossRef]
25. Hou, D.; Jia, Y.; Yu, J.; Wang, P.; Liu, Q.F. Transport properties of sulfate and chloride ions confined between calcium silicate hydrate surfaces: A molecular dynamics study. *J. Phys. Chem. C* **2018**, *122*, 28021–28032. [CrossRef]
26. Yang, J.; Jia, Y.; Hou, D.; Wang, P.; Jin, Z.; Shang, H.; Li, S.; Zhao, T. Na and Cl immobilization by size controlled calcium silicate hydrate nanometer pores. *Constr. Build. Mater.* **2019**, *202*, 622–635. [CrossRef]
27. Maddalena, R.; Li, K.; Chater, P.A.; Michalik, S.; Hamilton, A. Direct synthesis of a solid calcium-silicate-hydrate (CSH). *Constr. Build. Mater.* **2019**, *223*, 554–565. [CrossRef]
28. Scrivener, K.L.; Kirkpatrick, R.J. Innovation in use and research on cementitious material. *Cem. Concr. Res.* **2008**, *38*, 128–136. [CrossRef]
29. Hashim, A.A.; Al-Mosawi, A.I.; Abdulsada, S.A. Investigating the mechanical properties, durability, microstructure, and embodied CO_2 emissions of silica fume-infused sustainable concrete. *Int. J. Appl. Ceram. Technol.* **2025**, e15136. [CrossRef]
30. Li, S.; Jensen, O.M.; Yu, Q. Influence of steel fiber content on the rate-dependent flexural performance of ultra-high performance concrete with coarse aggregates. *Constr. Build. Mater.* **2022**, *318*, 125935. [CrossRef]
31. Yang, K.H.; Cho, A.R.; Song, J.K.; Nam, S.H. Hydration products and strength development of calcium hydroxide–based alkali–activated slag mortars. *Constr. Build. Mater.* **2012**, *29*, 410–419. [CrossRef]
32. Farges, F.; Lefrère, Y.; Rossano, S.; Berthereau, A.; Calas, G.; Brown, G.E., Jr. The effect of redox state on the local structural environment of iron in silicate glasses: A combined XAFS spectroscopy, molecular dynamics, and bond valence study. *J. Non. Cryst. Solids* **2004**, *344*, 176–188. [CrossRef]
33. Leung, C.K.Y.; Wan, K.T.; Chen, L. A novel optical fiber sensor for steel corrosion in concrete structures. *Sensors* **2008**, *8*, 1960–1976. [CrossRef] [PubMed]
34. Vayer, M.; Reynaud, I.; Erre, R. XPS characterisations of passive films formed on martensitic stainless steel: Qualitative and quantitative investigations. *J. Mater. Sci.* **2000**, *35*, 2581–2587. [CrossRef]
35. Hou, D.; Xu, X.; Ge, Y.; Wang, P.; Chen, J.; Zhang, J. Molecular structure, dynamics and adsorption behavior of water molecules and ions on [0 1 0] surface of γ-FeOOH: A molecular dynamics approach. *Constr. Build. Mater.* **2019**, *224*, 785–795. [CrossRef]
36. Hamid, S.A. The crystal structure of the 11Å natural tobermorite $Ca_{2.25}[Si_3O_{7.5}(OH)_{1.5}]1H_2O$. *Z. Kristallogr. Cryst. Mater.* **1981**, *154*, 189–198. [CrossRef]
37. Manzano, H.; Moeini, S.; Marinelli, F.; Van Duin, A.C.; Ulm, F.J.; Pellenq, R.J. Confined water dissociation in microporous defective silicates: Mechanism, dipole distribution, and impact on substrate properties. *J. Am. Chem. Soc.* **2012**, *134*, 2208–2215.
38. Zhang, W.; Zhang, M.; Hou, D. Nanoscale insights into the anti-erosion performance of concrete: A molecular dynamics study. *Appl. Surf. Sci.* **2022**, *593*, 153403. [CrossRef]
39. Hou, D.; Yang, Q.; Wang, P.; Jin, Z.; Wang, M.; Zhang, Y.; Wang, X. Unraveling disadhesion mechanism of epoxy/CSH interface under aggressive conditions. *Cem. Concr. Res.* **2021**, *146*, 106489. [CrossRef]
40. Thompson, A.P.; Aktulga, H.M.; Berger, R.; Bolintineanu, D.S.; Brown, W.M.; Crozier, P.S.; Plimpton, S.J. LAMMPS—A flexible simulation tool for particle–based materials modeling at the atomic, meso, and continuum scales. *Comput. Phys. Commun.* **2022**, *271*, 108171. [CrossRef]
41. Humphrey, W.; Dalke, A.; Schulten, K. VMD: Visual molecular dynamics. *J. Mol. Graph. Model.* **1996**, *14*, 33–38. [CrossRef]
42. Pouvreau, M.; Greathouse, J.A.; Cygan, R.T.; Kalinichev, A.G. Structure of hydrated kaolinite edge surfaces: DFT results and further development of the ClayFF classical force field with metal–O–H angle bending terms. *J. Phys. Chem. C* **2019**, *123*, 11628–11638. [CrossRef]
43. Luty, B.A.; van Gunsteren, W.F. Calculating electrostatic interactions using the particle–particle particle–mesh method with nonperiodic long–range interactions. *J. Phys. Chem.* **1996**, *100*, 2581–2587. [CrossRef]
44. Hou, D.; Li, T.; Wang, P. Molecular dynamics study on the structure and dynamics of NaCl solution transport in the nanometer channel of CASH gel. *ACS Sustain. Chem. Eng.* **2018**, *6*, 9498–9509. [CrossRef]
45. Zehtab, B.; Tarighat, A. Molecular dynamics simulation to assess the effect of temperature on diffusion coefficients of different ions and water molecules in CSH. *Mech. Time-Depend. Mat.* **2018**, *22*, 483–497. [CrossRef]
46. Wang, P.; Jia, Y.; Li, T.; Hou, D.; Zheng, Q. Molecular dynamics study on ions and water confined in the nanometer channel of Friedel's salt: Structure, dynamics and interfacial interaction. *Phys. Chem. Chem. Phys.* **2018**, *20*, 27049–27058. [CrossRef]
47. Hou, D.; Gao, L.; Chen, D.; Wang, P.; Wang, J.; Zhou, Y.; Zhang, J. Molecular-scale insights on structure-efficiency relationship of silane-based waterproofing agents. *Constr. Build. Mater.* **2022**, *327*, 126985. [CrossRef]
48. Hou, D.; Li, T. Influence of aluminates on the structure and dynamics of water and ions in the nanometer channel of calcium silicate hydrate (C–S–H) gel. *Phys. Chem. Chem. Phys.* **2018**, *20*, 2373–2387. [CrossRef]
49. Suwito, A.; Cai, X.C.; Xi, Y. Parallel finite element methods for coupled chloride penetration and moisture diffusion in concrete. *Int. J. Numer. Anal. Mod.* **2006**, *3*, 481–503.

50. Hou, D.; Li, Z. Molecular dynamics study of water and ions transport in nano–pore of layered structure: A case study of tobermorite. *Micropor. Mesopor. Mater.* **2014**, *195*, 9–20.
51. Li, D.; Zhao, W.; Hou, D.; Zhao, T. Molecular dynamics study on the chemical bound, physical adsorbed and ultra–confined water molecules in the nano–pore of calcium silicate hydrate. *Constr. Build. Mater.* **2017**, *151*, 563–574. [CrossRef]
52. Khaleel Ibrahim, S.; Abbas Hadi, N.; Movahedi Rad, M. Experimental and numerical analysis of steel-polypropylene hybrid fibre reinforced concrete deep beams. *Polymers* **2023**, *15*, 2340. [CrossRef]

Disclaimer/Publisher's Note: The statements, opinions and data contained in all publications are solely those of the individual author(s) and contributor(s) and not of MDPI and/or the editor(s). MDPI and/or the editor(s) disclaim responsibility for any injury to people or property resulting from any ideas, methods, instructions or products referred to in the content.

materials

MDPI

Article

Evolution Mechanism of Filtration Characteristics of Cement Grouting Materials in Sandy Medium

Xiao Feng [1,*], Shilei Zhang [2], Zhenzhong Shi [1], Qingsong Zhang [3], Meiling Li [2], Wenda Yang [1], Wen Sun [1] and Benao Hou [1]

[1] School of Transportation Engineering, Shandong Jianzhu University, Jinan 250101, China; 2024155112@stu.sdjzu.edu.cn (Z.S.); 2024155129@stu.sdjzu.edu.cn (W.Y.); 2023155138@stu.sdjzu.edu.cn (W.S.); 2023155140@stu.sdjzu.edu.cn (B.H.)
[2] Inner Mongolia Yin Chao Ji Liao Water Supply Co., Ltd., Xing'an League 137400, China; 13783654050@163.com (S.Z.); meiling250629@163.com (M.L.)
[3] Institute of Geotechnical and Underground Engineering, Shandong University, Jinan 250061, China; zhangqingsong@sdu.edu.cn
* Correspondence: fengxiao19@sdjzu.edu.cn

Abstract: The seepage diffusion of cement grouting materials into a sandy medium is influenced by the skeleton's adsorption and the pore channels' tortuosity, resulting in heterogeneous retention of cement particles during migration. This study established a theoretical model for the filtration coefficient based on the mass balance equation and linear filtration law. Grouting tests were conducted to determine the density of the cement slurry at various diffusion positions, and the filtration coefficient was calculated using the theoretical model. Results indicate that the filtration coefficient varies dynamically along the diffusion distance rather than remaining constant. The surface filtration range of Grade 42.5 Portland Cement slurry in sample S1 is approximately 30 cm, with a final diffusion distance of 190 cm. In contrast, the surface filtration ranges for the 800 mesh superfine cement in S2 and the 1250 mesh superfine cement in S3 are less than 10 cm, resulting in final diffusion distances of 69 cm and 87 cm, respectively. This demonstrates that a longer surface filtration range in the sand sample corresponds to a farther final diffusion distance of the slurry. Additionally, a larger ratio of sand pore diameter to cement particle size results in a smaller filtration coefficient and a greater slurry diffusion distance. Under a constant water–cement ratio, smaller cement particle sizes are associated with decreased slurry fluidity, which reduces the diffusion of cement slurry within the sandy medium. The research findings provide valuable insights for designing borehole spacing in grouting treatment for sandy media.

Keywords: cement materials; sandy medium; grouting; darcy percolation; filtration effect; slurry diffusion

1. Introduction

The design depth of urban rail transit lines is predominantly situated within shallow or sub-shallow layers, with subway tunnels frequently intersecting sandy strata, particularly in riverbanks and coastal cities [1–3]. The fragmented and water-saturated characteristics of the Quaternary sandy layer, combined with deteriorating groundwater seepage during construction, can lead to disasters, such as surface collapse and water–sand inrushes [4,5].

In the study of grouting within porous media, such as soft sandy layers, it is often assumed that the slurry disperses uniformly throughout the injected medium. When

cement slurry (a suspended slurry) is employed for penetration grouting in porous media, the medium's skeleton will intercept and adsorb cement particles. Larger particles encounter greater difficulty penetrating the pores and tend to accumulate in the surface layer, forming a "filter cake", a phenomenon known as surface filtration. Smaller particles can penetrate the pores; however, due to skeleton adsorption and pore tortuosity, these particles experience non-uniform filtration retention during migration, a process called deep filtration.

Y.S. Yu et al. [6] examined the effects of filter layer height and particle size on filtration efficiency and fluid properties, concluding that an increase in filter layer height and a decrease in particle size enhance filtration efficiency but adversely affect pressure gradient reduction. Menghuo Chen et al. [7] investigated the angular variation of the seepage field in anisotropic porous media and analyzed the influence of anisotropy on the migration and deposition of nanoparticles. Zilong Zhou et al. [8] assert that when the mass fractal dimension of the porous medium is high, the deposition rate of cement particles decreases significantly with increasing diffusion distance. Binbin Ding et al. [9] proposed a strain-based deep filtration model and investigated the lattice type, lattice ratio, and particle trapping mechanisms associated with deep filtration. Y. Thomas Carraro et al. [10], Juncheng Qiao et al. [11], and Fei Ye et al. [12] investigated the external boundary effective pressure and the permeability empirical equation of porous media under filtration effects, yielding substantial experimental results. Jenchen Fan et al. [13] analyzed the results of indoor sand column tests using the rank correlation coefficient method and stepwise regression analysis, elucidating the effects of sand particle effective diameter and slurry viscosity on grouting time, grouting rate, and water output rate. H. Bayesteh et al. [14] conducted prototype tests on low-water-content clay, thoroughly discussing the influence of grouting technical parameters on slurry diffusion distance and revising the existing estimation formula for slurry diffusion distance. Xiaoli Liu et al. [15] simulated the diffusion process of Bingham fluid in fine sand layers under varying grouting pressure conditions using the discrete element method, establishing the relationship among grouting pressure, diffusion radius, and initial breakdown pressure. Almir Draganovic et al. [16] investigated the injectivity of three cement-based grouting materials, concluding that the maximum allowable opening for fracture injection is 75 μm. Fanlu Min et al. [17] employed a self-developed penetration device to conduct grouting tests and established a theoretical model for sealing the voids of the injected medium. Mohamed Shousha et al. [18] investigated the effects of grouting curtains on the seepage characteristics of small hydraulic structures, establishing a seepage equation influenced by these curtains through regression analysis, and found that the filtration reduction effect of the grouting curtain is 20% more effective than that of the upstream covering layer. Fang Hongyuan et al. [19] took sand layer particle size, dynamic water pressure, grouting pressure, and clay content as factors to study the dominant controlling conditions for the transportation and diffusion of polymer slurry in water-rich sand layers. Deng Fucheng et al. [20] revealed the permeability evolution laws of gravel-pack layers under sand intrusion and hydrate formation conditions based on the synergistic plugging mechanism of medium sand and hydrate within the gravel-pack layer. Ying Cui et al. [21] prepared a DS grouting material for water-rich, silty, fine sand strata using sodium silicate as the base material and diacid ester as the curing agent, featuring an adjustable setting time, high strength, durability, and exemplary performance in tunnel reinforcement. Sun Xu et al. [22] conducted filtration loss tests with different bentonite–ultrafine cement slurry mixtures and performed a microstructural analysis of the filtration cakes, concluding that the bentonite content and the distribution of its hydrated colloids determine the filtration performance. Tongqiang Xiao et al. [23] analyzed the effects of water-reducing agent content on ultrafine cement

slurry's viscosity and bleeding rate. Dongyue Zhang et al. [24] prepared grouted specimens with two water–cement ratios and four superfine cement contents using mercury intrusion tests, fragment fractal dimension analysis, and SEM, finding that increasing the content enhances strength and reduces porosity and fractal dimension. Yuya Sakai et al. [25] used mercury intrusion porosimetry to conduct a three-dimensional diffusion simulation of the pore structure in cementitious materials, and they evaluated the diffusion coefficient of cement paste within these materials. Huang Liwei et al. [26] conducted pressure filtration grouting tests, tested the strengthening strength of the consolidated body under different water–cement ratios and pressure filtration intensities, and established a strengthening strength model for ultrafine cement. Abou-Chakra et al. [27] proposed a multiscale model based on microstructural characteristics for cement-based materials with recycled rubber aggregates to predict diffusion properties considering the interface transition zone (ITZ), which was validated by experiments. Chuen-Ul Juang et al. [28] developed a green grouting material using a low water-to-binder ratio, 20% slag/fly ash, 2–3% water reducer, and 60–70% sand. The material exhibited excellent durability, and the regression analysis was reliable. Li Zhipeng et al. [29] addressed the issue of the lack of a theoretical basis for grouting design in sand layers, proposing a design method to quantitatively determine the grouting mode, the grouting range, and the reinforcement effect and establishing a theoretical model for fracture–compaction grouting. Feng Xiao et al. [30] prepared a novel slurry by adding expansion agents, water reducers, and accelerating agents. Tests showed that its fluidity, strength, and expansion rate improved, and field application significantly enhanced the stratum's impermeability.

Based on the above research, existing studies have predominantly focused on the injectability assessment of cement slurry, often utilizing the ratio of cement particle size to that of the medium skeleton particles. However, the surface filtration effect and final diffusion distance of cement slurry in the sandy medium have been neglected. Additionally, in the experimental studies, particle filtration quality was determined solely by calculating the mass difference before and after grouting, concluding that the filtration coefficient is a constant value. However, the variation of the filtration coefficient along the diffusion distance was not investigated.

Therefore, this study establishes a time-dependent filtration–diffusion coupling model to quantitatively characterize grout performance degradation in sandy media. The model is grounded in the following assumptions: complete saturation of the sand sample, Newtonian fluid behavior of the cement slurry, and a planar laminar flow regime of the grout. The proposed framework dynamically links time-varying filtration parameters to grout diffusion behavior by combining the mass balance equation and the linear filtration law. Through grouting tests, the density values of the cement slurry at various diffusion distances were obtained, the filtration coefficient was calculated based on the coupling model, and the variation trend of the filtration coefficient was analyzed. The research results can be used to obtain the surface plugging time and the final diffusion distance of the slurry in the sandy medium, thereby guiding the design of the borehole spacing in the grouting treatment of sandy strata.

2. Establishment of the Mathematical Model

In this study, the sandy medium is assumed to be fully saturated, and the ordinary Portland Cement slurry, as a particle suspension, exhibits the characteristics of a Newtonian fluid. The essence of grouting pressure lies in its influence on the slurry flow rate (i.e., slurry velocity). Because grouting pump equipment typically uses the flow rate as a control parameter, this study selects slurry velocity as the control indicator. Furthermore, by setting the Reynolds number (which is closely related to slurry velocity), the slurry is ensured to

exhibit plane parallel laminar flow in the sandy medium, thereby satisfying the Darcy flow condition (Re $\leq$ 1).

A particle (with mass but no size or shape) with mass m_i is selected for analysis in the Cartesian coordinate system. At time t_1, the particle is at point x_1 and has a mass m_i (x_1, t_1). After a time interval of Δt, the particle moves to point $x_2 = x_1 + v\Delta t$ with a velocity of v, and its mass is expressed as m_i (x_2, t_2) = m_i ($x_1 + v\Delta t$, $t_1 + \Delta t$).

Thus, the material derivative of mass m_i is given by

$$\frac{\mathrm{d}m_i}{\mathrm{d}t} = \lim_{\Delta t \to 0} \frac{m_i(x_2, t_2) - m_i(x_1, t_1)}{\Delta t} = \lim_{\Delta t \to 0} \frac{m_i(x_1 + v\Delta t, t_1 + \Delta t) - m_i(x_1, t_1)}{\Delta t} \quad (1)$$

Expanding using the Taylor series yields

$$m_i(x_1 + v\Delta t, t_1 + \Delta t) = m_i(x_1, t_1) + \frac{\partial m_i}{\partial t} \cdot \Delta t + (v \cdot \nabla) m_i \cdot \Delta t + \frac{1}{2}\left[\frac{\partial^2 m_i}{\partial t^2} + 2v \cdot \nabla\left(\frac{\partial m_i}{\partial t}\right) + (v \cdot \nabla)^2 m_i\right] \cdot \Delta t^2 + O\left(\Delta t^3\right) \quad (2)$$

$$\frac{\mathrm{d}m_i}{\mathrm{d}t} = \frac{\partial m_i}{\partial t} + (v \cdot \nabla) m_i \quad (3)$$

To investigate the influence of the filtration effect on the movement of cement particles in the sandy medium, we assume that the retained cement particles become part of the medium skeleton, which means that the filtered cement particles participate in its formation. Consequently, filtration can be regarded as a process in which the cement slurry loses the cement particles, and the medium skeleton obtains them.

Based on the mass balance Equation (3), the mass balance expression for cement particles is as follows

$$-\mu = \frac{\partial(\rho_c n_c)}{\partial t} + (v_c \cdot \nabla)(\rho_c n_c) \quad (4)$$

The mass balance Equation for water can be expressed as

$$0 = \frac{\partial(\rho_w n_w)}{\partial t} + (v_w \cdot \nabla)(\rho_w n_w) \quad (5)$$

The mass balance Equation for the sandy medium skeleton is expressed as

$$\mu = \frac{\partial(\rho_s n_s)}{\partial t} + (v_s \cdot \nabla)(\rho_s n_s) \quad (6)$$

In the Equations, ρ_c represents the density of cement particles (2.80–3.15 g/cm^3); ρ_w denotes the density of water (g/cm^3); ρ_s represents the density of the sandy medium skeleton (2.65–2.76 g/cm^3); n_c indicates the volume percentage content of cement particles per unit volume (dimensionless); n_w denotes the volume percentage content of water per unit volume (dimensionless); n_s is the volume percentage content of the sandy medium skeleton per unit volume (dimensionless); t represents time (s); v_c denotes the velocity of cement particles (cm/s); v_w denotes the velocity of water (cm/s), where $v_w = v_c$; v_s refers to the velocity of the medium skeleton (cm/s), where $v_s = 0$; and μ denotes the mass exchange coefficient, representing the mass of cement particles filtered out per unit time and unit volume (g·cm^{-3}·s^{-1}).

Assuming that the pores of the sandy medium are saturated with cement slurry and that the skeleton density of the medium is approximately equal to the density of the cement particles ($\rho_s = \rho_c$), we can express the medium porosity as

$$n = n_w + n_c = 1 - n_s \quad (7)$$

In the Equation, n represents the porosity of the sandy medium (dimensionless).

Because v_s = 0 cm/s, this can be derived by integrating Equation (7) with Equation (6).

$$\frac{\partial[\rho_s n_s]}{\partial t} = \mu \tag{8}$$

$$\frac{\partial(1-n)}{\partial t} = \frac{\mu}{\rho_s} \tag{9}$$

$$\frac{\partial n}{\partial t} = -\frac{\mu}{\rho_c} \tag{10}$$

By the linear filtration law [31,32],

$$\mu = \rho_c n_0 \lambda f(\delta) \tag{11}$$

In the Equation, the scalar μ denotes the mass exchange coefficient, representing the mass of cement particles filtered out per unit time and unit volume, and δ indicates the volume fraction of cement particles within the pores, $\delta = \frac{n_c}{n_0}$.

Function f should comply with the physical condition f (0) = 0. Observing that, generally, δ << 1, Equation (11) may be simplified by adopting the first order of the Taylor expansion of f concerning δ [31,32]

$$f(\delta) \approx \delta, \mu = \rho_c n_0 \lambda \delta \tag{12}$$

$$\delta(x,t) = \frac{\rho_g - \rho_w}{\rho_c - \rho_w} = \begin{cases} \frac{1}{1+\left(\frac{1}{\varphi}-1\right)\exp\left(\frac{\lambda x}{n_0 v_0}\right)} & (0 \le x \le v_0 t) \\ 0 & (x > v_0 t) \end{cases} \tag{13}$$

In the Equation, λ denotes the filtration coefficient (s^{-1}); n_0 represents the initial porosity of the sandy medium (dimensionless); δ indicates the volume fraction of cement particles within the pores (dimensionless); ρ_g represents the density of the cement slurry (g/cm^3); φ denotes the volume fraction of cement particles within the cement slurry (dimensionless); x indicates the slurry diffusion distance (cm); and v_0 refers to the velocity of the cement slurry (cm/s).

From Equations (12) and (13), it can be inferred that

$$\lambda = \frac{\mu}{\rho_c n_0 \delta} = \ln\left[\left(\frac{\rho_c - \rho_w}{\rho_g - \rho_w} - 1\right) \times \frac{\varphi}{1-\varphi}\right] \times \frac{n_0 v_0}{x} \qquad (0 \le x \le v_0 t) \tag{14}$$

Consequently, using Equation (14), one can calculate the filtration coefficient at various diffusion distances by utilizing the density of the cement slurry, the volume fraction of cement particles within the slurry, the initial porosity of the sandy medium, and the flow velocity of the cement slurry.

The boundary condition for the porosity of the sandy medium is as follows

$$n(x,t) = n_0 \text{ at } t = 0 \tag{15}$$

$$n(x,t) = n_0 \text{ at } x > v_0 t \tag{16}$$

Substituting Equations (12) and (13) into Equation (10) and combining with Equations (15) and (16), it can be derived that

$$n = \begin{cases} n_0 - \lambda\left(t - \frac{x}{v_0}\right)\left[\frac{1}{1+\left(\frac{1}{\varphi}-1\right)\exp\left(\frac{\lambda x}{n_0 v_0}\right)}\right] & (0 \le x \le v_0 t = L) \\ n_0 & (x > v_0 t) \end{cases} \tag{17}$$

At x = 0 cm (the initial interface of the slurry entering the sandy medium), when n = 0, it indicates that the pore channels of the sandy medium are entirely obstructed, resulting in

$$n = n_0 - \lambda\left(t - \frac{x}{v_0}\right)\left[\frac{1}{1+\left(\frac{1}{\varphi}-1\right)\exp\left(\frac{\lambda x}{n_0 v_0}\right)}\right] = n_0 - \lambda t\varphi = 0 \tag{18}$$

Therefore, we arrive at

$$\lambda = \frac{n_0}{t\varphi} \tag{19}$$

Consequently, Equation (19) can be used to derive the filtration coefficient of the sand medium's initial interface by utilizing the sandy medium's initial porosity, the volume fraction of cement particles within the cement slurry, and the time when the sand medium's initial interface (x = 0 cm) is completely blocked.

3. Grouting Model Experiment

3.1. Purpose of the Experiment

The grouting test of plane parallel laminar flow is designed to study the change in slurry density along the diffusion distance when the cement slurry flows in parallel in different sand mediums.

3.2. Test Materials

3.2.1. Sandy Medium

According to Sand for Construction, natural sand is defined as rock particles that are naturally formed and artificially mined and screened with a particle size smaller than 4.75 mm. This includes river sand, lake sand, mountain sand, and desalted sea sand, excluding soft and weathered rock particles. The fineness modulus M_x can classify natural sand into three categories, coarse sand (M_x = 3.1–3.7), medium sand (M_x = 2.3–3.0), and fine sand (M_x = 1.6–2.2), calculated according to Equation (20) [33]

$$M_x = \frac{(A_2 + A_3 + A_4 + A_5 + A_6) - 5A_1}{100 - A_1} \tag{20}$$

Specifically, A_1, A_2, A_3, A_4, A_5, and A_6 denote the cumulative sieve residue percentages for 4.75 mm, 2.36 mm, 1.18 mm, 0.60 mm, 0.30 mm, and 0.15 mm sieves, respectively.

According to the Standard for Geotechnical Testing Method, three sand samples were selected for sieve analysis. The particle gradation of the sand samples is presented in Table 1, and the structural parameters of the sand samples are detailed in Table 2.

Table 1. Particle size distribution of sand.

Sand Sample	Mass of Particles with Different Graded Particle Sizes (g)						Fineness Modulus	Type
	4.75–2.36 mm	2.36–1.18 mm	1.18–0.6 mm	0.6–0.3 mm	0.3–0.15 mm	<0.15 mm		
S1	0	251.8	181.8	61.2	3.0	2.2	3.4	Coarse sand
S2	0	151.7	167.8	171.5	4.8	4.2	2.9	Medium sand
S3	0	102.6	131.8	246.2	9.4	10.0	2.6	Medium sand

Table 2. Structural parameters of the sand samples.

Sand Sample	n_0	D_0/mm	d_{01}/mm	d_{02}/mm	d_{03}/mm
S1	0.388	1.27	0.70	0.62	0.54
S2	0.338	0.99	0.48	0.42	0.41
S3	0.329	0.83	0.38	0.34	0.36

Note: (1) D_0 represents the effective diameter of the particles, defined as the average value of all particle diameters [33]

$$D_0 = \sum_{i=1}^{n} \frac{D_i q_i}{100} \tag{21}$$

In the Equation, D_0 denotes the effective diameter of the sandy medium (mm), D_i represents the screening diameter of the sandy medium (mm), and q_i signifies the percentage associated with the screening diameter (dimensionless).

(2) d_0 is the pore diameter [33]:

For a homogenized spherical granular medium

$$d_{01} = 0.855 D_0 \frac{{n_0}^{0.725}}{(1-n_0)^{0.5}} \tag{22}$$

For a uniform sand medium

$$d_{02} = 1.25 n_0 D_0 \tag{23}$$

For quartz sand with a particle size ranging from 1 mm to 3.15 mm

$$d_{03} = 0.84 n_0 D_0 + 0.13 \tag{24}$$

3.2.2. Cement Slurry

The grouting test used Grade 42.5 Portland Cement, 800 mesh superfine cement, and 1250 mesh superfine cement. The average particle size d_{50} of Grade 42.5 Portland Cement measured using the TZC-2 automatic particle size analyzer is 17 μm, while the 800 mesh superfine cement is 7 μm, and the 1250 mesh superfine cement is 4 μm. The performance parameters of each cement slurry are presented in Table 3.

Table 3. Performance parameters of cement grout.

Material Type	Water–Cement Ratio	ρ_g (g/cm^3)	Viscosity μ_1 (mPa·s)	Initial Setting Time (min)	φ	Bleeding Rate (%)
P. O. 42.5	1:1	1.45	4.53	896	0.275	26.0
800 mesh superfine cement		1.46	5.87	763	0.270	9.0
1250 mesh superfine cement		1.48	6.96	630	0.260	2.0

Note: The test temperature is maintained at 20 °C, and all measurement data are averaged.

3.3. Test Scheme

To investigate the variation in slurry density and diffusion distance of cement slurry within a sandy medium under filtration effects and elucidate the interaction mechanism between surface filtration and deep filtration, grouting tests utilizing different types of cement slurries were conducted on three distinct sand samples. The testing scheme is presented in Table 4.

Table 4. Grouting test scheme.

Number	Sand Sample	Cement Type	Water–Cement Ratio of Slurry
1	S1	P. O. 42.5	1:1
2	S2	800 mesh superfine cement	
3	S3	1250 mesh superfine cement	

3.4. Test Process

The grouting test system comprises a grout input system, a planar parallel flow device, and a monitoring system. The planar parallel flow device includes an inlet chamber, cylindrical steel pipes, and an outlet chamber. Each single cylindrical steel pipe has an inner diameter of 100 mm, a height of 200 mm, and a wall thickness of 5 mm, and 20 such pipes were designed. The cylindrical steel pipes are illustrated in Figure 1, while the overall grouting test system is depicted in Figure 2.



Figure 1. Cylindrical steel pipes.



Figure 2. Grouting test system.

The single cylindrical steel pipe is divided into symmetrical sections to facilitate disassembly and coring. The inner wall of each steel pipe is abraded and uniformly coated with a lubricant to eliminate edge effects. A small hole is opened in the middle of the steel pipe, and a sealing joint and a one-way valve are installed to collect the slurry flowing out through the small hole. The single cylindrical steel pipes exhibit high strength and rigidity, preventing deformation.

In each group of grouting tests, the effluent slurry was collected at different positions of the parallel flow device. The volume and mass of the slurry were measured to determine its density. Then, the cement slurry with the same density was prepared in the laboratory,

and the water–cement ratio of the effluent slurry could be obtained through the inverse method so that the mass fraction and volume fraction of cement particles in the slurry at different positions could be calculated.

3.5. Experimental Results

When the Reynolds number (Re) of the cement grout flowing in a sandy medium is $\mathrm{Re} \leq 1$, it indicates that the cement grout exhibits plane parallel flow [33], which satisfies the application premise of the established mathematical model.

$$\mathrm{Re} = 100 \times \frac{\rho_g v_0 d_{10}}{\mu_1} \tag{25}$$

In the equation, v_0 refers to the velocity of the cement slurry (cm/s); d_{10} is the effective particle size of solid particles in a sandy medium (cm); and μ_1 is the dynamic viscosity of cement slurry (mPa·s).

For the S1 sand sample, n_0 = 0.388 and d_{10} = 0.037 cm; the density of Grade 42.5 Portland Cement with a water–cement ratio of 1:1 is ρ_g = 1.45 g/cm^3, φ = 0.275, and μ_1 = 4.53 mPa·s; and the initial velocity of the slurry is 0.85 cm/s, with a sampling duration of 20 s at each point. Through Equation (25), the Reynolds number is calculated to be 1.0, indicating that the Grade 42.5 Portland Cement slurry exhibits plane parallel flow in the S1 sand sample. In addition, the grouting test lasts about 224 s, and the slurry's initial setting time is about 53,760 s (Table 3, 896 min), indicating that the slurry is a Newtonian fluid during the test. Detailed test results are presented in Table 5 and Figure 3.

Table 5. S1 sand sample—Grade 42.5 Portland Cement experimental results.

Position /cm	m_{TTL} /g	v_{TTL} /cm^3	ρ_g g/cm^3	w:c	m_w /g	m_c /g	v_c /cm^3	φ	λ $10^{-3}\cdot s^{-1}$
10	102.9	76.2	1.35	1.18:1.00	55.7	47.2	20.5	0.269	18.17
30	102.1	76.2	1.34	1.21:1.00	55.9	46.2	20.3	0.266	6.27
50	101.5	76.4	1.33	1.25:1.00	56.4	45.1	20.0	0.262	3.86
70	98.0	76.2	1.29	1.43:1.00	57.6	40.4	18.6	0.244	3.03
90	94.7	76.1	1.24	1.74:1.00	60.2	34.5	15.9	0.209	2.42
110	94.5	76.2	1.24	1.74:1.00	60.0	34.5	16.2	0.213	2.06
130	94.0	76.2	1.23	1.88:1.00	61.4	32.6	14.8	0.194	1.56
150	93.0	76.8	1.21	2.03:1.00	62.3	30.7	14.5	0.189	1.51
170	92.3	76.2	1.21	2.03:1.00	61.8	30.5	14.4	0.189	1.24

Note: (1) m_{TTL} is the total mass of the effluent slurry; v_{TTL} is the total volume of the effluent slurry. (2) λ is calculated using Equation (14).

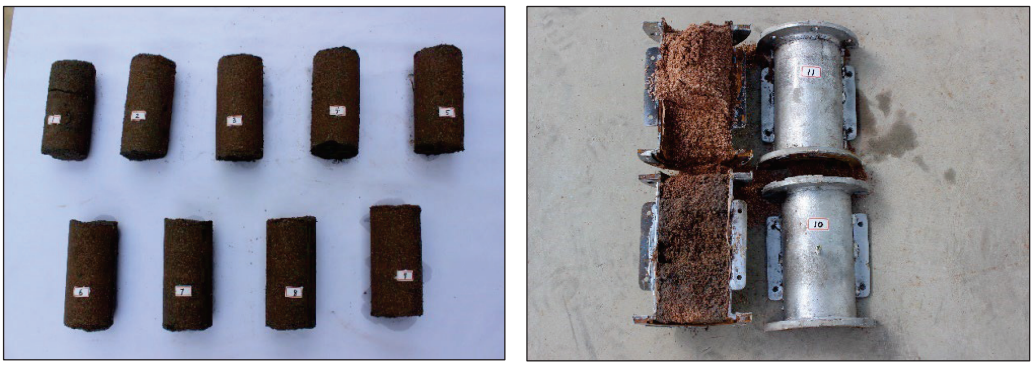

Figure 3. S1 sand sample—Grade 42.5 Portland Cement experimental results.

For the S2 sand sample, n_0 = 0.338 and d_{10} = 0.037 cm; the density of 800 mesh superfine cement with a water–cement ratio of 1:1 is ρ_g = 1.46 g/cm^3, φ = 0.27, and μ_1 = 5.87 mPa·s; and the initial velocity of the slurry is 0.85 cm/s. The sampling time of each point is 20 s, but the sampling time at 50 cm is 10 s. Through Equation (25), the Reynolds number is calculated to be 0.79, indicating that the 800 mesh superfine cement slurry exhibits plane parallel flow in the S2 sand sample. In addition, the grouting test lasts about 82 s, and the slurry's initial setting time is about 45,780 s (Table 3, 763 min), indicating that the slurry is a Newtonian fluid during the test. Detailed experimental results can be found in Table 6 and Figure 4.

Table 6. S2 sand sample—800 mesh superfine cement experimental results.

Position /cm	m_{TTL} /g	v_{TTL} /cm^3	ρ_g g/cm^3	w:c	m_w /g	m_c /g	v_c /cm^3	φ	λ $10^{-3}\cdot s^{-1}$
10	91.6	66.4	1.38	1.22:1.00	50.3	41.3	16.1	0.242	8.86
30	84.1	66.2	1.27	1.87:1.00	54.8	29.3	11.4	0.172	2.74
50	39.5	33.2	1.19	2.43:1.00	28.0	11.5	5.2	0.157	3.29

Note: (1) m_{TTL} is the total mass of the effluent slurry; v_{TTL} is the total volume of the effluent slurry. (2) λ is calculated using Equation (14).

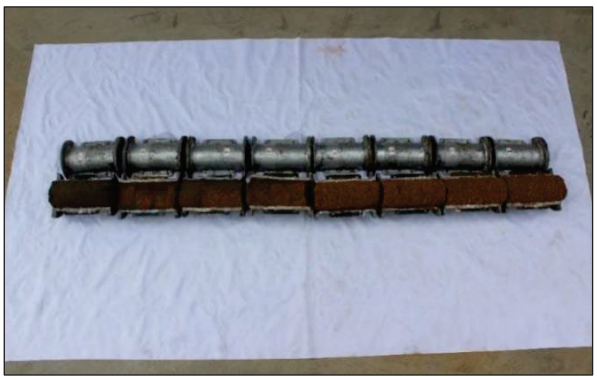

Figure 4. S2 sand sample—800 mesh superfine cement experimental results.

For the S3 sand sample, n_0 = 0.329 and d_{10} = 0.034 cm; the density of 1250 mesh superfine cement with a water–cement ratio of 1:1 is ρ_g = 1.48 g/cm^3, φ = 0.26, and μ_1 = 6.98 mPa·s; and the initial velocity of the slurry is 0.85 cm/s, with a sampling duration of 20 s at each point. Through Equation (25), the Reynolds number is calculated to be 0.61, indicating that the 1250 mesh superfine cement slurry exhibits plane parallel flow in the S3 sand sample. In addition, the grouting test lasts about 103 s, and the slurry's initial setting time is about 37,800 s (Table 3, 630 min), indicating that the slurry is a Newtonian fluid during the test. Detailed experimental results can be found in Table 7 and Figure 5.

Table 7. S3 sand sample—1250 mesh superfine cement experimental results.

Position /cm	m_{TTL} /g	v_{TTL} /cm^3	ρ_g g/cm^3	w:c	m_w /g	m_c /g	v_c /cm^3	φ	λ $10^{-3}\cdot s^{-1}$
10	87.5	64.6	1.35	1.38:1.00	50.7	36.8	13.9	0.215	7.15
30	84.4	64.4	1.31	1.57:1.00	51.6	32.8	12.8	0.20	2.89
50	79.0	64.6	1.22	2.19:1.00	54.2	24.8	10.4	0.161	2.46
70	76	64.6	1.18	2.76:1.00	55.8	20.2	8.8	0.136	1.86

Note: (1) m_{TTL} is the total mass of the effluent slurry; v_{TTL} is the total volume of the effluent slurry. (2) λ is calculated using Equation (14).

Comprehensive analysis of Tables 5–7 summarizes the filtration coefficients (λ) for S1, S2, and S3 sand samples, measured as λ = 1.24–18.17 × 10^{-3} s^{-1}, 3.29–8.86 × 10^{-3} s^{-1}, and 1.86–7.15 × 10^{-3} s^{-1}, respectively. These ranges reflect the dynamic evolution of filtration characteristics under varying particle gradation and cement slurry penetration depths. Specifically, S1 exhibits the widest λ range (1.24–18.17 × 10^{-3} s^{-1}), attributed to its heterogeneous particle size distribution, which amplifies localized clogging effects during grout diffusion. S2 and S3 show narrower λ ranges due to their more uniform gradation, aligning with the model's prediction of reduced filtration variability in homogeneous media.

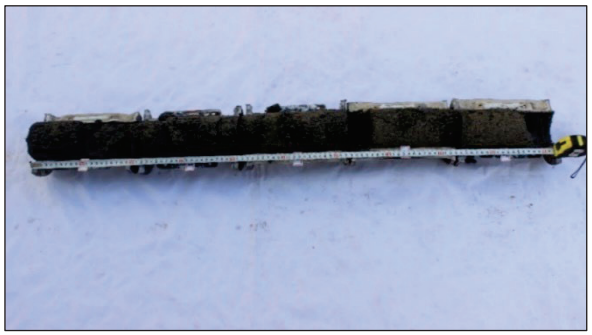

Figure 5. S3 sand sample—1250 mesh superfine cement experimental results.

4. Test Data Analysis

4.1. Variation of Filtration Coefficient Along Slurry Diffusion Distance

Analysis of Tables 5–7 indicates that the density of the cement slurry decreases with increasing diffusion distance within the sandy medium, suggesting that the filtration coefficient diminishes from a higher to a lower value along this distance. However, previous studies have concluded that the filtration coefficient remains constant, as detailed in Table 8.

Table 8. Filtration coefficient of previous studies [34–38].

Literature	Suspended Particles		Porous Media		Particle Size Ratio	Filtration Coefficient λ $10^{-3}\cdot s^{-1}$
	Type	Particle Size /μm	Type	Particle Size /μm		
[34]	Polyvinyl chloride	1.3	Glass microspheres	460	353.8	2.90
				425	326.9	6.60
			Sand	600	461.5	6.16
[35]	Polystyrene	900	Plastic balls	12500	13.9	0.99
		1060			11.8	1.48
[36]	Corner quartz	<20	Glass microspheres	2000	<100	3.70
	Polystyrene	65		2000	30.8	17.20
		90			22.2	35.00
		125			16	47.88
[37]	Colibacillus	1	Sand	104	104	2.74
				227	227	0.52
	Seaweed	15		829	55.3	3.10
[38]	Iron hydroxide	4–25	Sand	700	28–175	0.84

Note: The particle size ratio is the porous media particle size divided by the suspended particle size.

Based on the data presented in Table 8, the following can be concluded.

(1) Most previous studies have used artificial suspended particles and porous media with uniform particle sizes and smooth surfaces. In contrast, this study employs natural

sand samples, Portland Cement, and superfine cement, and there is an essential difference between this study and previous studies regarding the experiment's subjects.

(2) Previous studies determined the corresponding filtration coefficient λ by measuring the mass difference of the porous media before and after the experiment. This study monitored parameters like slurry density and flow rate at various diffusion distances of sand samples, with Equation (14) employed to calculate the theoretical value of λ.

(3) The average filtration coefficient for each sand sample is adopted as the evaluation standard; specifically, the average filtration coefficient of the S1 sand sample is $\lambda = 4.46 \times 10^{-3}s^{-1}$, the S2 sand sample is $\lambda = 4.96 \times 10^{-3}s^{-1}$, and the S3 sand sample is $\lambda = 3.59 \times 10^{-3}s^{-1}$. Although the experimental materials in this study differ from those used in previous research, both sets of test results fall within the same order of magnitude and exhibit a high degree of similarity. This suggests that it is reasonable to quantitatively calculate the filtration coefficient based on the model of the filtration coefficient under the condition of plane parallel laminar flow.

(4) According to the grouting test, the filtration coefficient of the S1 sand sample is $\lambda = 1.24$–$18.17 \times 10^{-3}s^{-1}$, the S2 sand sample is $\lambda = 3.29$–$8.86 \times 10^{-3}s^{-1}$, and the S3 sand sample is $\lambda = 1.86$–$7.15 \times 10^{-3}s^{-1}$. The overall filtration coefficient range in this study spans 1.24–$18.17 \times 10^{-3}s^{-1}$. Existing studies report values like $\lambda = 0.99 \times 10^{-3}s^{-1}$ [35], $\lambda = 35.0$–$47.88 \times 10^{-3}s^{-1}$ [36], $\lambda = 0.52 \times 10^{-3}s^{-1}$ [37], and $\lambda = 0.84 \times 10^{-3}s^{-1}$ [38], which differ from our findings. However, most existing data fall within the range identified in this study. Notably, previous experiments employed porous media and suspensions containing plastic balls [35], glass microspheres [36], colibacillus [37], and iron hydroxide [38]. This contrast highlights the critical role of particle morphology (roughness, angularity) in filtration evolution, as idealized media lack the inherent mechanisms of filtration, adsorption, and deposition in natural sand–cement systems.

4.2. Variation Law of Surface Filtration

Based on the sandy medium's original porosity n_0, the volume fraction φ of cement particles in the slurry, and the grouting time t, the filtration coefficient λ when all of the pore channels on the surface of the sand medium are fully obstructed can be calculated through Equation (19). For the S1 sand sample, the total grouting duration of 224 s results in a filtration coefficient of $6.3 \times 10^{-3}s^{-1}$, indicating that at this value, all pores at the surface of the sand medium are obstructed. Similarly, for the S2 sand sample with a total grouting time of 82 s, the filtration coefficient upon complete blockage is $15.27 \times 10^{-3}s^{-1}$. Additionally, for the S3 sand sample with a total grouting duration of 103 s, its corresponding filtration coefficient when entirely blocked is $12.29 \times 10^{-3}s^{-1}$.

Surface filtration occurs when the pore channel of the sandy medium is fully obstructed at a specific position. The cement slurry continues to enter the sand medium under grouting pressure and squeezes the medium skeleton, resulting in excessive siltation of cement particles. This phenomenon is illustrated in Figure 6. For instance, the filtration coefficient of the S1 sand sample at which all pore channels are fully obstructed is $6.3 \times 10^{-3}s^{-1}$, corresponding to a diffusion depth of approximately 30 cm; consequently, the surface filtration range extends from 0 to 30 cm. In contrast, for the S2 sand sample, when pore channels are entirely blocked, the filtration coefficient is $15.27 \times 10^{-3}s^{-1}$, with a surface filtration range extending from 0 to 10 cm. Similarly, for the S3 sand sample, its filtration coefficient upon complete blockage of pore channels is $12.29 \times 10^{-3}s^{-1}$, and it also exhibits a surface filtration range from 0 to 10 cm.

Furthermore, the range of surface filtration for the S1 sand sample extends from 0 to 30 cm, with a slurry diffusion distance of 190 cm. In contrast, the ranges of surface filtration for the S2 and S3 sand samples are from 0 to 10 cm, corresponding to slurry diffusion

distances of 69 cm and 87 cm, respectively. It is concluded that the longer the distance of surface filtration in the sand sample, the farther the final diffusion distance of the slurry.



Figure 6. Schematic diagram of surface filtration.

4.3. The Influence of the Ratio of Pore Diameter to Cement Particle Size on Filtration Performance

The average particle size d_{50} of Grade 42.5 Portland Cement is 17 μm, while the average particle sizes d_{50} for 800 mesh superfine cement and 1250 mesh superfine cement are 7 μm and 4 μm, respectively. By referencing Table 2, the ratio of the pore diameter of the sand medium to the cement particle size can be obtained. Additionally, values for the filtration coefficient at various locations are presented in Table 9 for comprehensive analysis.

Table 9. The ratio of pore diameter to cement particle size.

Sand Sample	d_{01}/Cement Particle Size	d_{02}/Cement Particle Size	d_{03}/Cement Particle Size	Filtration Coefficient λ ($10^{-3}s^{-1}$)		
				10 cm	30 cm	50 cm
S1	41	36	32	18.17	6.27	3.86
S2	69	60	59	8.86	2.74	3.29
S3	95	85	90	7.15	2.89	2.46

Analysis of Table 9 indicates that at specific diffusion locations, the filtration coefficient of the S1 sand sample is the highest, followed by the S2 sand sample. In contrast, the S3 sand sample exhibits the lowest value. For instance, at a distance of 10 cm, the λ for the S1 sand sample is $18.17 \times 10^{-3}s^{-1}$, for the S2 sand sample, it is $8.86 \times 10^{-3}s^{-1}$, and for the S3 sand sample, it is $7.15 \times 10^{-3}s^{-1}$.

Analysis indicates that the S1 sand sample's pore diameter ratio to cement particle size is the smallest. This hinders the migration of Grade 42.5 Portland Cement particles through its pore channels, resulting in a maximum filtration coefficient. In contrast, the S3 sand sample exhibits the largest pore diameter ratio to cement particle size. It facilitates more efficient migration of 1250 mesh superfine cement particles through its pore channels, leading to a minimum filtration coefficient. It suggests that as the ratio of pore diameter to cement particle size increases, fewer cement particles are filtered and retained, resulting in a lower filtration coefficient.

4.4. Influence of Slurry Density

When the water–cement ratio is 1:1, the density ρ_g of Grade 42.5 Portland Cement slurry is 1.45 g/cm^3, and the volume fraction of cement particles φ is 0.275; for the 800 mesh superfine cement slurry, the density is 1.46 g/cm^3 and φ = 0.27; and for the 1250 mesh superfine cement, the density reaches 1.48 g/cm^3 and φ = 0.26. This suggests that under an identical water–cement ratio, the smaller the cement particle size, the larger the specific surface area, and the prepared cement slurry shows higher density but lower fluidity. This

is why the slurry diffusion distance in the S2 and S3 sand samples is shorter under the same grouting conditions.

5. Discussion

1. This study establishes a time-dependent filtration–diffusion coupling model to characterize grout performance degradation in sandy media quantitatively. The feedback effect between particle filtration and slurry diffusion reveals the mechanism of nonlinear attenuation of slurry density along the diffusion distance, which cannot be realized by the static λ model [35–38].
2. We experimentally verified the grout density attenuation law under filtration through grouting experiments. The results demonstrate that the filtration coefficient dynamically varies with cement slurry diffusion distance rather than remaining constant.
3. The emergence of flow instabilities—characterized by the amplification rather than the attenuation of minor disturbances over time—significantly governs filtration efficiency. In our experiments, these instabilities manifest as localized preferential flow channels and intermittent channel clogging. This phenomenon primarily stems from particle retention during filtration, which reduces slurry viscosity through shear-thinning behavior, consequently lowering the Reynolds number and delaying turbulence onset. Furthermore, the heterogeneous pore structure of natural sand amplifies disturbances, while narrow pore throats alter the slurry's velocity gradient.
4. This study has limitations in both theoretical modeling and experimental design. Firstly, the theoretical framework relies on Darcy's laminar flow assumption and excludes complex scenarios involving non-Newtonian fluid behavior or unsaturated sand layers. Secondly, experiments were conducted under constant flow rate conditions, which deviate from the dynamic groundwater environments encountered in real-world engineering applications. Future work will investigate slurry diffusion mechanisms under multifactor coupling effects and validate the model's applicability using field-collected data.

6. Conclusions

1. Along the diffusion distance of the cement slurry, the filtration coefficient in the S1 sand sample decreased from $18.17 \times 10^{-3}s^{-1}$ to $1.24 \times 10^{-3}s^{-1}$; in the S2 sand sample, it declined from $8.86 \times 10^{-3}s^{-1}$ to $3.29 \times 10^{-3}s^{-1}$; and, in the S3 sand sample, it reduced from $7.15 \times 10^{-3}s^{-1}$ to $1.86 \times 10^{-3}s^{-1}$. This illustrates that the filtration coefficient varies dynamically along the diffusion distance of the cement slurry rather than remaining constant. Based on the time-dependent filtration–diffusion coupling model and the maximum filtration coefficient, the time when the pores on the surface of the sand layer are completely blocked can be inverted to control the grouting process in the sand layer reinforcement project.
2. When the pore channel of the S1 sand sample is fully obstructed, the filtration coefficient is $6.3 \times 10^{-3}s^{-1}$, corresponding to a surface filtration range of 0–30 cm; for the S2 sand sample, with its pore channel fully obstructed, the filtration coefficient is $15.27 \times 10^{3}s^{-1}$, and the surface filtration range is 0–10 cm; similarly, for the S3 sand sample, where its pore channel entirely blocked, the filtration coefficient measures $12.29 \times 10^{-3}s^{-1}$ alongside a corresponding surface filtration range of 0–10 cm.
3. Under a water–cement ratio of 1:1, the diffusion distance of the Grade 42.5 Portland Cement slurry in the S1 sand sample is measured at 190 cm. In contrast, the diffusion distances for the 800 mesh superfine cement slurry in the S2 sand sample and the 1250 mesh superfine cement slurry in the S3 sand sample are recorded as 69 cm and 87 cm, respectively. The longer the range of surface filtration in the sand sample,

the farther the final diffusion distance of the slurry. At the same time, the spacing of boreholes in the sand layer reinforcement project can be optimized based on the surface filtration range and the final diffusion distance.

4. As the ratio of sand pore diameter to cement particle size increases, the adsorption and obstruction effects of the medium skeleton on cement particles diminish, leading to a reduced amount of retained particles and a smaller filtration coefficient. Under a constant water–cement ratio, smaller cement particle sizes result in a higher density of the prepared cement slurry but lower fluidity. These factors significantly affect the diffusion of cement slurry within the sandy medium.

Author Contributions: Conceptualization, X.F. and Q.Z.; Methodology, S.Z. and M.L.; Validation, X.F.; Investigation, X.F., S.Z. and M.L.; Resources, Q.Z.; Data curation, Z.S., W.Y., W.S. and B.H.; Writing—original draft, X.F.; Writing—review and editing, X.F., Z.S., W.Y., W.S. and B.H.; Supervision, Q.Z.; Funding acquisition, X.F. All authors have read and agreed to the published version of the manuscript.

Funding: The authors gratefully acknowledge the financial support from the National Natural Science Foundation of China (Grant No. 52009075), the Natural Science Foundation of Shandong Province (Grant Nos. ZR2020QE262 and ZR2024ME119), and the Doctoral Research Fund of Shandong Jianzhu University (Grant Number X19018Z).

Institutional Review Board Statement: Not applicable.

Informed Consent Statement: Not applicable.

Data Availability Statement: The raw data supporting the conclusions of this article will be made available by the authors upon request.

Acknowledgments: The authors would like to express their sincere appreciation to the reviewers for their valuable comments and suggestions, which helped improve the quality of the paper.

Conflicts of Interest: Authors Shilei Zhang, Meiling Li were employed by the company Inner Mongolia Yin Chao Ji Liao Water Supply Co., Ltd. The authors declare that there are no conflicts of interest regarding the publication of this paper.

References

1. Li, W.; Yu, L.; Zhang, T. Quantitative analysis of grain size effect on tensile mechanical behavior of granite based on multi-level force chain networks. *Comp. Part. Mech.* **2024**, *11*, 2245–2266. [CrossRef]
2. Liu, P.; Wang, H.; Liu, Q.; Li, X.; Dong, Y.; Xie, X. FDEM numerical study on the large deformation mechanism of layered rock mass tunnel under excavation-unloading disturbance. *Tunn. Undergr. Space Technol.* **2025**, *159*, 106497. [CrossRef]
3. Li, W.; Zhang, Q.; Wang, X.; Yu, L.; Li, Z. Synergistic effect of particle size, carboxymethyl starch and Na_2CO_3 on rheological and filtration property of bentonite-based material. *Case Stud. Constr. Mat.* **2024**, *21*, e03537. [CrossRef]
4. Peng, Y.; Yu, L.; Qian, J.; Li, W.; Zhang, T.; Zhou, L. Dynamic tensile behavior and crack propagation in coral aggregate seawater shotcrete: Experimental investigation and numerical simulation. *Cement Concrete Comp.* **2025**, *159*, 106010. [CrossRef]
5. Li, W.; Yu, L.; Tan, Y.; Wu, L.; Qian, J. Mechanical properties and impact behavior of frozen clay: Insights from static mechanical tests, fly-plate tests, and split-Hopkinson pressure bar analysis. *Phys. Fluids* **2024**, *36*, 057138. [CrossRef]
6. Yu, Y.; Tao, Y.; Ma, Z.; He, Y. Experimental study and optimization on filtration and fluid flow performance of a granular bed filter. *Powder Tech.* **2018**, *333*, 449–457. [CrossRef]
7. Chen, M.; Salama, A.; Sun, S. The transport of nanoparticles in subsurface with fractured, anisotropic porous media: Numerical simulations and parallelization. *J. Comput. Appl. Math.* **2019**, *350*, 1–18. [CrossRef]
8. Zhou, Z.; Cai, X.; Du, X.; Wang, S.; Ma, D.; Zang, H. Strength and filtration stability of cement grouts in porous media. *Tunn. Undergr. Space Technol.* **2019**, *89*, 1–9. [CrossRef]
9. Ding, B.; Li, C.; Wang, Y.; Xu, J. Effects of pore size distribution and coordination number on filtration coefficients for straining-dominant deep bed filtration from percolation theory with 3D networks. *Chem. Eng. Sci.* **2018**, *175*, 1–11. [CrossRef]
10. Carraro, T.; Eduard, M.P.; Andro, M. Effective pressure boundary condition for the filtration through porous medium via homogenization. *Nonlinear Anal. Real World Appl.* **2018**, *44*, 149–172. [CrossRef]

11. Qiao, J.; Zeng, J.; Jiang, S.; Ma, Y.; Feng, S.; Xie, H.; Wang, Y.; Hu, H. Role of pore structure in the percolation and storage capacities of deeply buried sandstone reservoirs: A case study of the Junggar Basin, China. *Mar. Petrol. Geol.* **2020**, *113*, 104129. [CrossRef]
12. Ye, F.; Yang, T.; Mao, J.; Qin, X.; Zhao, R. Half-spherical surface diffusion model of shield tunnel back-fill grouting based on infiltration effect. *Tunn. Undergr. Space Technol.* **2019**, *83*, 274–281. [CrossRef]
13. Fan, J.; Liu, W.; Liu, C.; Huang, C.; Tan, Y.; Guo, J. Evaluating permeability and efficiency of substrates by using permeation grouting sand column test. *KSCE J. Civ. Eng.* **2018**, *22*, 2843–2855. [CrossRef]
14. Bayesteh, H.; Sabermahani, M. Field study on performance of jet grouting in low water content clay. *Eng. Geol.* **2020**, *264*, 105314. [CrossRef]
15. Liu, X.; Wang, F.; Huang, J.; Wang, S.; Zhang, Z.; Nawnit, K. Grout diffusion in silty fine sand stratum with high groundwater level for tunnel construction. *Tunn. Undergr. Space Technol.* **2019**, *93*, 103051. [CrossRef]
16. Draganovic, A.; Stille, H. Filtration of cement-based grouts measured using a long slot. *Tunn. Undergr. Space Technol.* **2014**, *43*, 101–112. [CrossRef]
17. Min, F.; Song, H.; Zhang, N. Experimental study on fluid properties of slurry and its influence on slurry in filtration in sand stratum. *Appl. Clay Sci.* **2018**, *161*, 64–69. [CrossRef]
18. Shousha, M.; Basha, A.; Elenany, M.; Hoghazy, H. Effect of using grouted vertical barrier on seepage characteristics under small hydraulic structures. *Alex. Eng. J.* **2020**, *59*, 441–455. [CrossRef]
19. Fang, H.; Liu, K.; Du, X.; Wang, F. Experimental and numerical simulation study on water plugging law of permeable polymer in water-rich sand layer. *Sci. China Technol. Sci.* **2023**, *53*, 457–472.
20. Deng, F.; Wang, Y.; Li, X.; Li, G.; Wang, Y.; Huang, B. A model-based study of the evolution of gravel layer permeability under the synergistic blockage effect of sand particle transport and secondary hydrate formation. *Appl. Energy* **2024**, *355*, 122209. [CrossRef]
21. Cui, Y.; Tan, Z.; Han, D.; Song, J. Investigation and application of a high performance grouting material in water-rich silty fine sand stratum. *Construct. Build. Mater.* **2022**, *329*, 127100. [CrossRef]
22. Sun, X.; Li, J.; Huang, S.; Gao, Y. Study on filtration characteristics of bentonite-superfine cement grout in completely weathered granite stratum. *Sci. Technol. Eng.* **2022**, *22*, 8812–8820.
23. Xiao, T.; Yu, Z.; Liu, F.; Dai, X.; Sun, J. Study on Slurry Flow Characteristics and Diffusion Law of Superfine Cement-Based Composite Grouting Material. *Processes* **2023**, *11*, 1906. [CrossRef]
24. Zhang, D.; Ma, Z.; Zou, Y.; Xie, H.; Guan, R. Study on the Strength and Micro Characteristics of Grouted Specimens with Different Superfine Cement Contents. *Materials* **2021**, *14*, 6709. [CrossRef]
25. Sakai, Y. Evaluation of the diffusion coefficient of cement paste from pore size distribution using three-dimensional simulation. *Mater. Today Commun.* **2024**, *411*, 134451. [CrossRef]
26. Huang, L.; Wang, K.; Huang, J.; Xing, Z. Study on slurry properties of double (super) fine cement under pressure filtration. *J. Water Resour. Archit. Eng.* **2021**, *19*, 155–171.
27. Abou-Chakra, A.; Blanc, G.; Turatsinze, A.; Escadeillas, G. Prediction of Diffusion Properties of Cement-Based Materials Incorporating Recycled Rubber Aggregates: Effect of Microstructure on Macro Diffusion Properties. *Constr. Build. Mater.* **2023**, *35*, 105750. [CrossRef]
28. Juang, C.-U.; Kuo, W.-T. Engineering Properties of Green and Ecofriendly Grouting Materials with Different Sand Filling Ratios. *Materials* **2023**, *16*, 837. [CrossRef]
29. Li, Z.; Zhang, L.; Sun, D.; Zhang, Q.; Wang, D.; Wang, L. Quantitative Design Method for Grouting in Sand Layers: Practice in Qingdao Metro Line 2. *Processes* **2022**, *10*, 840. [CrossRef]
30. Feng, X.; Cao, X.; Li, L.; Li, Z.; Zhang, Q.; Sun, W.; Hou, B.; Liu, C.; Shi, Z. Study on Performance and Engineering Application of Novel Expansive Superfine Cement Slurry. *Materials* **2024**, *17*, 5597. [CrossRef]
31. Kim, J.; Lee, I.; Jang, J.; Choi, H. Grouting of cement-based grout with consideration of viscosity and filtration phenomenon. *Int. J. Numer. Anal. Methods Geomech.* **2009**, *33*, 1771–1797. [CrossRef]
32. Herzig, J.; Leclerc, D.; Legoff, P. Flow of suspensions through porous media-new differential equation for clogged beds is derived. *Ind. Eng. Chem. Res.* **1970**, *62*, 8–35. [CrossRef]
33. Geotechnical Grouting Theory and Engineering Practice Group. *Theory and Engineering Example of Rock-Soil Grouting*; Science Press: Beijing, China, 2001.
34. Ives, K. Deep filters. *Filtr. Sep.* **1967**, *3*, 25–135.
35. Sakthivadivel, R.; Rushton, K. Numerical analysis of large diameter wells with a seepage face. *J. Hydrol.* **1989**, *107*, 43–55. [CrossRef]
36. Maroudas, A.; Eisenklam, P. Clarification of suspension: A study of particle deposition in granular filter media: Part I—Some observation on particle deposition. *Univ. Lond.* **1961**, *20*, 867–873.

37. Iwasaki, T. Molecular dynamics study of adhesion strength and diffusion at interfaces between interconnect materials and underlay materials. *Comp. Mech.* **2000**, *25*, 78–86. [CrossRef]
38. Fox, D.; Bryan, R.; Price, A. The role of soil surface crusting in desertification and strategies to reduce crusting. *Environ. Monit. Assess.* **2004**, *99*, 149–159. [CrossRef]

Disclaimer/Publisher's Note: The statements, opinions and data contained in all publications are solely those of the individual author(s) and contributor(s) and not of MDPI and/or the editor(s). MDPI and/or the editor(s) disclaim responsibility for any injury to people or property resulting from any ideas, methods, instructions or products referred to in the content.

materials

MDPI

Article

Experimental Study on Shear Characteristics of Filled Joints Anchored by Basalt Fiber-Reinforced Polymer Materials

Hengjie Luan [1,2], Qingzhai Shi [1,2], Changsheng Wang [1,2,*], Yujing Jiang [1,2,3], Sunhao Zhang [3,4], Jianrong Liu [2] and Kun Liu [1,2]

[1] State Key Laboratory of Mining Disaster Prevention and Control Co-Founded by Shandong Province, Ministry of Science and Technology, Shandong University of Science and Technology, Qingdao 266590, China; luanjie0330@126.com (H.L.); 202282010062@sdust.edu.cn (Q.S.); jiangyjcn@gmail.com (Y.J.); lkun0311@163.com (K.L.)
[2] Academician (Expert) Workstation, Inner Mongolia Shanghaimiao Mining Co., Ltd., Ordos 016299, China; 15048745086@163.com
[3] Graduate School of Engineering, Nagasaki University, Nagasaki 852-8521, Japan; 17854262633@163.com
[4] School of Civil and Environmental Engineering, Nanyang Technological University, Singapore 639798, Singapore
* Correspondence: cswang0635@163.com

Abstract: Filled joints are widely found in natural rock masses and are one of the main factors causing rock mass engineering instability. The use of bolts can effectively control the shear slip of filled joints, research on bolts filled joints in the filling degree, and other key parameters of the influence of the law, to ensure the stability of the engineering rock body is of great significance. This paper presents shear experiments on bolted filled joints of Basalt Fiber-Reinforced Polymer (BFRP) materials with different joint roughness and filling degrees, while acoustic emission technology monitors the shear failure process of the specimens. The results show that the peak shear strength decreases with the increase in filling degree, and the peak shear strength decreases by 23.9% when the filling degree changes from 0 to 2.0 at 4 MPa and J2 conditions, while the normal stress, the Joint Roughness Coefficient (*JRC*) and the peak shear strength both show a positive correlation. The normal deformation of bolted filled joints exhibits three distinct evolutionary patterns depending on the filling degree, while both *JRC* and normal stress significantly influence the magnitude of shear dilatancy-shrinkage deformation. The shear resistance of BFRP bolts is mainly reflected in the post-peak plastic stage, and some of the fibers break during its shear deformation to form controlled yielding, with vertical and horizontal deformation controlled within 15.5~22.3 mm and 4.7~6.9 mm, respectively. The Acoustic Emission (AE) results show that the AE events are mainly in the post-peak plasticity stage, and the proportion is about the sum of the proportion of the other two phases, and this proportion increases with the increase in the filling degree.

Keywords: mechanics experiment; rock joints; shear properties; filling degree; basalt fiber-reinforced polymer materials; acoustic emission; normal stress

1. Introduction

The existence of joint surfaces in the natural rock mass significantly reduces the mechanical properties of the rock mass, leading to the weakening of its deformation resistance and bearing capacity, which makes it more prone to instability destruction. A large number of engineering practices [1–3] show that, under the synergistic effect of ground stress and mining stress, the roadway surrounding rock is very easy to shear slip

along the joint surface, which leads to the shear failure of the bolt and large deformation of the roadway surrounding rock and other phenomena. In recent years, with the increasing intensity and depth of coal resources mining, the instability of roadway surrounding rock induced by rock mass joints has become more and more prominent [4,5]. The bolt support is an effective means to control the roadway surrounding rock, and one of its main mechanisms is to limit the shear slip of the joint surface, which is fully affirmed by many support theories [6–8].

At present, the more commonly used type of bolt in roadway bolt support is steel material bolt, and many scholars at home and abroad have carried out a lot of research on its shear mechanical properties and bolt mechanism, etc. [9–11]. In terms of theoretical studies, researchers have investigated the bolting conditions [12], bolt types [13,14], *JRC* [12,15], bolting angles [16], and boundary conditions [17,18], respectively. In the field application of steel material bolts, Tao et al. [19] investigated the control of large deformation hazards of tunnel peripheral rock under different complex geological conditions by the active support method based on steel materials in engineering applications. Wang et al. [20] comprehensively verified the working performance of the synergistic bolting technique through field tests. The above exploratory studies on the shear properties and bolting mechanisms of steel material bolts in bolted joints have been fruitful. However, both these research results and practical engineering applications reveal a common phenomenon: steel material bolts are subjected to tensile-shear composite stresses and fracture is still frequent under small shear deformation [11,21]. Given this, systematic research on the key technology to improve the shear-breaking displacement of the bolt and in-depth discussion of its action mechanism is of great theoretical significance and engineering application value for improving the stability control effect of the joint rock mass [22,23].

In order to avoid the breakage of the bolt, which may cause a steep drop in shear stress and consequent instability of the surrounding rock, experts and scholars have carried out extensive research on new material bolts. Some researchers have optimized the traditional steel bolt materials; He et al. [24] carried out a study on the shear performance of joints bolted by NPR bolts, and it was found that NPR bolts can well balance the high strength and high ductility of conventional steel, and the tensile shear resistance is greatly improved. Wu et al. [25] investigated the shear characteristics of energy-absorbing bolts reinforcing rock mass under cyclic loading conditions by indoor shear experiments, and the results showed that the shear performance of the bolts in rock mass was strongly affected by cyclic shear loading, and the shear performance of energy-absorbing bolts was better than that of fully encapsulated bolts under cyclic shear loading conditions. Han et al. [26] conducted shear experiments on rock joints bolted by energy-absorbing bolts, and the results showed that energy-absorbing bolts have good ductility and can quickly respond to external load changes in the surrounding rock through their deformation or interaction with the surrounding rock to "absorb the energy" to inhibit the occurrence of bolt breakage.

In addition, basalt fiber-reinforced polymer (BFRP) bolt, as a new type of composite bolt, has the advantages of good tensile performance, corrosion resistance, fire resistance, and light weight, which is a better reinforcement material instead of steel reinforcement bolt for geotechnical engineering reinforcement [27–29]. Cao et al. [30] studied the mechanical properties of basalt fibers through experiments, and the results showed that the tensile strength of BFRP bar is more than twice that of ordinary steel bars, and the shear strength is only slightly less than that of steel bars, and the BFRP bar has better corrosion resistance. Zhang et al. [31,32] used an indoor direct shear experiment to compare and analyze the shear performance of BFRP bar and traditional steel bar bolted joint rock mass, BFRP bolt has low shear stiffness in elastic section and higher peak shear displacement, but higher residual shear strength compared with steel bar bolt. Xie et al. [33] carried out a double

shear experiment on joint rock mass bolted by BFRP bolts to investigate the effect of bolting angle and preload on the shear capacity of bolted joints. Although a few scholars have carried out studies on the shear performance of bolted joints of BFRP bolts, the objects of their studies are all non-filled joints. In filled joints, the presence of soft fill significantly enhances the shear deformation and sliding tendency of the rock mass, which not only leads to a significant increase in the axial tensile force exerted on the bolts, but also greatly increases the likelihood of fracture of the bolts [34]. Unfortunately, there are still few reports on the research on the shear performance of BFRP bolts in bolted filled joints and their bolting mechanism, which seriously restricts the engineering application and promotion of BFRP bolts under complex geological conditions [35,36].

In view of the above understanding, the traditional steel material bolt breakage displacement is small and difficult to adapt to more complex surrounding rock conditions, while the BFRP bolts have the advantages of high tensile strength, corrosion resistance, and better coordination with the surrounding rock deformation ability. Therefore, this paper investigates the shear characteristics of bolted filled joints of BFRP bolts and the effects of normal stress, filling degree and joint roughness on their shear performance by carrying out the BFRP bolt bolted filled joint shear experiment. At the same time, acoustic emission technology is utilized to conduct dynamic nondestructive monitoring of the failure characteristics of bolted joint-filled specimens, thus elucidating the mechanism of interaction between BFRP materials and filled joints and breaking through the limitations of the bolting theory of the traditional steel material bolts. The research results not only provide theoretical basis for the bolting design of deep jointed rock projects but also provide technical support for the engineering application of new BFRP materials.

2. Shear Experiment

2.1. Specimen Preparation

In order to investigate the shear characteristics of BFRP bolted filled joints and the effects of normal stress, degree of filling and joint roughness on their shear performance, joint specimens with the same surface morphology are required. Therefore, this paper uses super-strong gypsum-like rock materials to prepare the specimens. First, the granite raw rock was cut into specimens with dimensions of 200 mm × 100 mm × 100 mm, and then it was split to obtain joint surface morphology, and the joint surfaces were reproduced on a silicone mold to cast rock-like specimens with the same joints. The nodal surfaces of the three different JRCs are shown in Figure 1. The joint roughness coefficients were calculated using the root mean square method of slope [37], where 50 profile lines were taken at equal intervals along the shear direction (x-direction) on the 3D rough joint surfaces, and the 2D *JRC* values of each curve were first calculated according to the following equation [15,26,38]:

$$JRC = 32.2 + 32.47\log Z_2 \tag{1}$$

$$Z_2 = \left[\frac{1}{M}\sum\left(\frac{z_{i-1} - z_i}{x_{i-1} - x_i}\right)^2\right]^{\frac{1}{2}} \tag{2}$$

where Z_2 is the root mean square of the slope; M is the number of points on the curve; x_i and z_i are the coordinates of the points on the curve; the subscript i section is the number of times of selection, which is taken as 50.

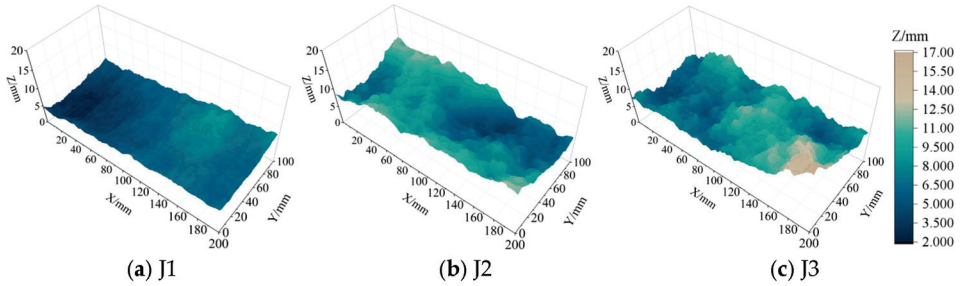

Figure 1. Surface topographies of rock joints with different *JRC*s.

Then, the average value of *JRC* of 50 curves is taken as the *JRC* value of the joint surface, and the calculation results yielded that the joint roughness coefficients of J1, J2, and J3 are JRC_1 = 3.68, JRC_2 = 6.18, and JRC_3 = 9.86.

The complete specimen consists of three parts, which are the upper block, the lower block and the filling layer, and the specimen casting process is shown in Figure 2. Firstly, the upper and lower blocks were cast using silicone molds with replicated nodules surfaces; then, the cast upper and lower blocks were placed in the mold box to cast the bolted filled joints. Finally, after 2 weeks of maintenance of the cast specimens, circular bolt holes with a diameter of 10 mm were drilled and installed, and gypsum slurry was used as the bolting agent. After the specimens of bolted filled joints were made, they were further maintained for a fortnight and then experimented on.

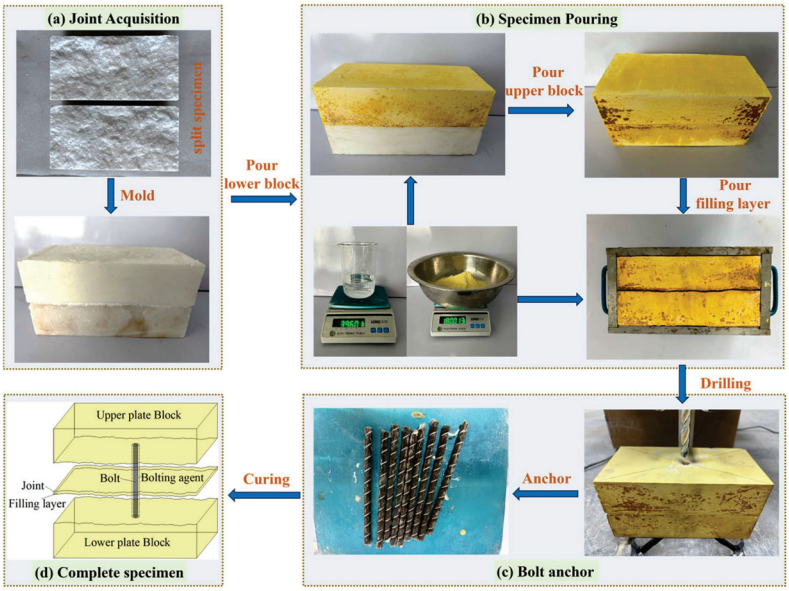

Figure 2. Preparation process of bolted filled joint specimens.

Ladanyi et al. [39] proposed the concept of filling degree (Δ) to quantitatively describe the effect of filling thickness, which is numerically equal to the ratio of the filling thickness t to the difference in the surface relief of the rock joints h. The thickness of the filling layer during the casting of the specimen was obtained by calculating the degree of filling Δ and the difference in nodule surface undulation h.

The experiment ratio of the upper and lower blocks of the bolted filled joint specimen is high strength gypsum–water–retarded =1:0.22:0.0025, and the experiment ratio of the filled layer is high strength gypsum–water = 1:0.4. To experiment the basic mechanical parameters of the upper and lower blocks of rock materials and filling layer materials, cylindrical standard specimens were prepared according to the same ratios for uniaxial compression experiments, and their stress–strain curves and failure characteristics are

shown in Figure 3. The uniaxial compressive strength and modulus of elasticity of the upper and lower blocks were 45.37 MPa and 5.11 GPa; the uniaxial compressive strength and modulus of elasticity of the filling layer specimens were 19.67 MPa and 2.96 GPa. The experiment bolts were made of 6 mm diameter basalt fiber composite bars with a tensile strength of 850 MPa, a modulus of elasticity of 58 GPa, an elongation of 2.6% and a density of 2.1 g/cm^3, and ultimate shear strength of more than 150 MPa. BFRP bolts have excellent corrosion resistance to chloride ions, acid, and alkali and salt spray erosion; its coefficient of thermal expansion (6~8 $\times$ 10^{-6}/°C) is close to that of concrete, which can effectively reduce structural damage caused by temperature stress.

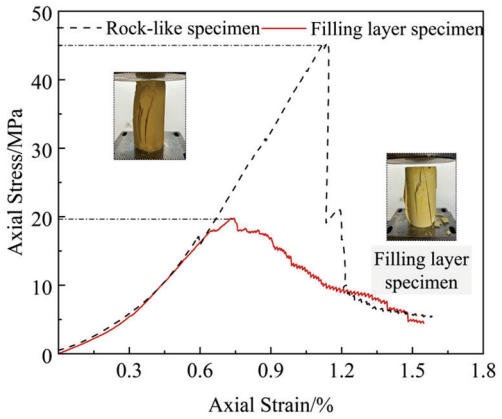

Figure 3. Mechanical property curves of similar materials in rock-like and filling layers.

2.2. Experimental Equipment

The bolted filled joint shear experiment was carried out using the normal stiffness rock joint shear experiment system independently developed by Shandong University of Science and Technology, as shown in Figure 4. The experiment system consists of a shear mainframe, control system, oil source system, and manipulation system. The experiment system uses a hydraulic servo system to provide the working power, and the normal and tangential loading can reach a maximum of 600 kN. Real-time monitoring was performed using high-precision sensors with ±0.5% F.S. accuracy for both loading force and displacement measurements (normal and tangential directions), with data acquired at variable frequencies (5–50 Hz). During the experiment, the specimen was firstly placed in the shear box of the shear experimental system and the normal stress was applied to a constant value, and the normal stress was applied in a load-controlled mode with a rate of 0.1 kN/s; then the normal stress was kept constant, and the lower shear box was subjected to the shear stress, and the displacement-controlled mode was adopted, with a loading rate of 0.01 mm/s, and the test ended when the shear displacement was 10 mm.

The DS5-16B full-information acoustic emission signal analyzer from Beijing Soft Island Times Technology Co Ltd. (Beijing, China) was used to monitor the acoustic emission signals of the bolt-filled joint specimens during the test process when they were subjected to shear damage, so as to realize the visual analysis of the cracks generated and expanded inside the specimens. Before the start of the experiment, four acoustic emission sensors were arranged on each of the two sides of the bolted filled joint specimen as shown in Figure 5, and the sensors were all arranged on the upper and lower blocks at a distance of 20 mm from the edge. The amplification of the acoustic emission front-end amplifier and the threshold of the system were set to 40 dB.

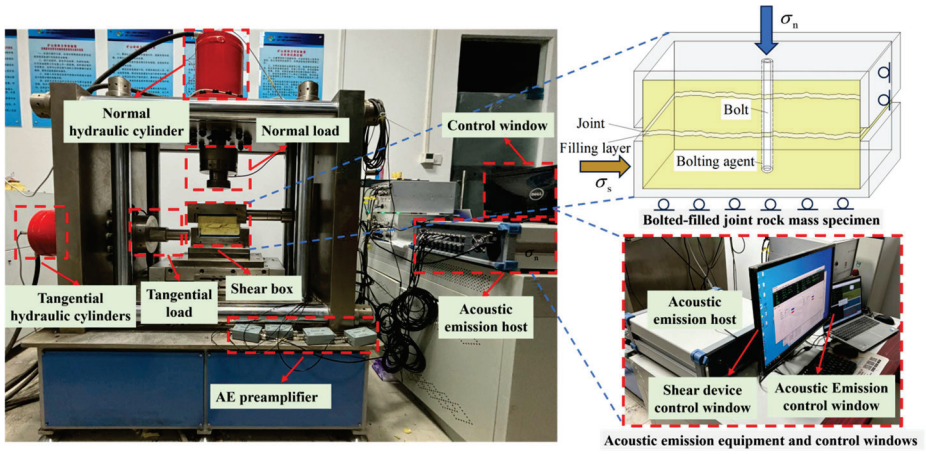

Figure 4. Shear experiment equipment.

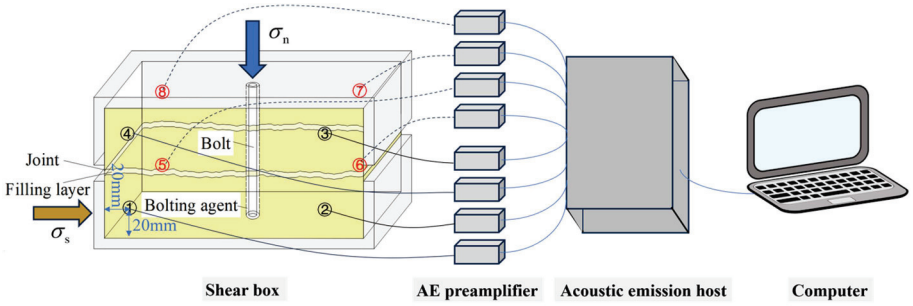

Figure 5. Acoustic emission connection schematic: The numbers 1–8 in the figure represent one AE sensor each, and the red font indicates the AE sensor on the reverse side of the specimen.

2.3. Experimental Scheme

The influence of filling degree is particularly significant among the factors affecting the shear mechanical properties of the rock mass of the filled joints [40]. Referring to the study by Song et al. [38], Δ = 0, 0.5, 1.0, 1.5, and 2.0 were determined, and the difference in the surface undulation of the J1, J2, and J3 joints, *h*, was derived from the surface morphology scanning data of the joints as 5 mm, 8 mm, and 11 mm. Generally, shear failure may occur when the normal stress (σ_n) is higher than 13% of the uniaxial compressive strength of the rock [41], so σ_n was selected as 2 MPa, 4 MPa, and 6 MPa. The finalized scheme for the shear experiments of the bolted filled joint specimens is shown in Table 1.

Table 1. Bolted filled joint shear experiment scheme.

Specimens	Normal Stress/MPa	Filling Degree	*JRC*
1~5	2	0.0, 0.5, 1.0, 1.5, 2.0	J2
6~10	4	0.0, 0.5, 1.0, 1.5, 2.0	J1
11~15	4	0.0, 0.5, 1.0, 1.5, 2.0	J2
16~20	4	0.0, 0.5, 1.0, 1.5, 2.0	J3
21~25	6	0.0, 0.5, 1.0, 1.5, 2.0	J2

3. Results of the Experiment

3.1. Shear Stress–Shear Displacement Curves

Limited to an extent, only the shear stress–shear displacement curves of the bolted filled joint specimens bolted by BFRP bolts under the condition of σ_n = 4 MPa shown in Figure 6 are analyzed as an example. From the figure, it can be seen that the shear–stress

displacement curve can be divided into three stages, which is essentially the same as the study of Zhang et al. [31], including the pre-peak elastic Stage (I), the post-peak plastic Stage (II), and the residual strength Stage (III).

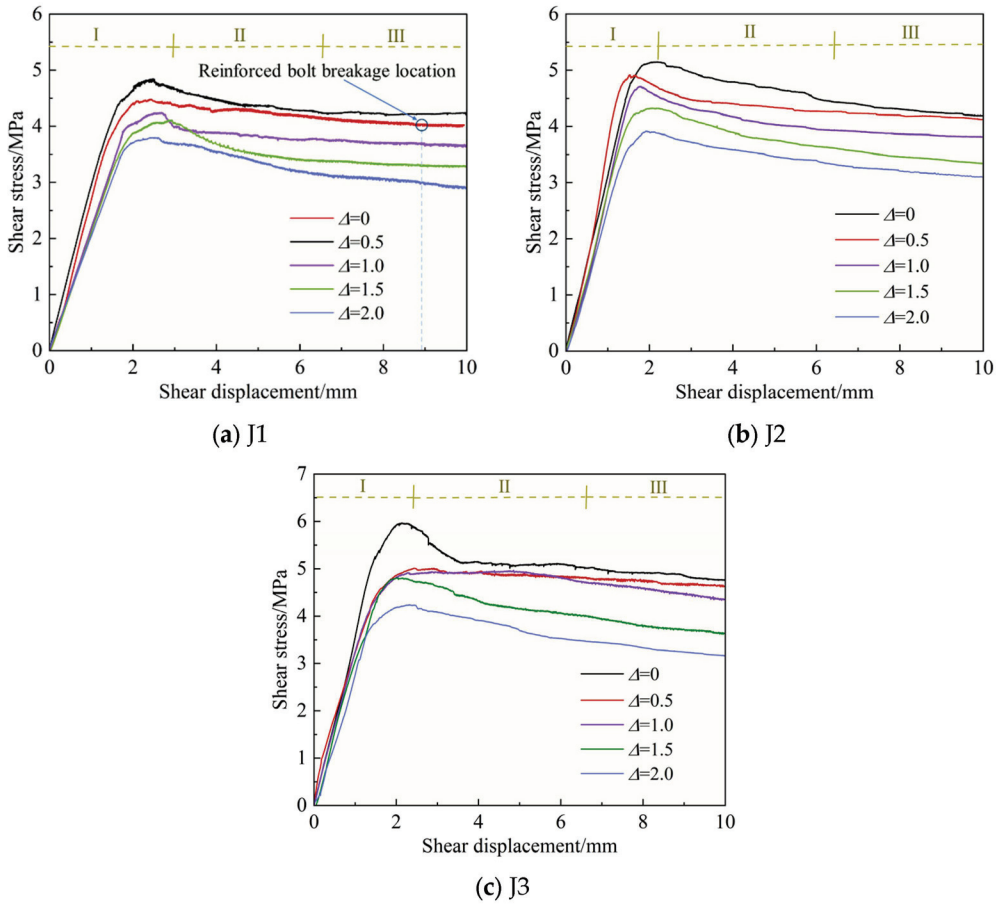

Figure 6. Shear stress–shear displacement curves: (I) Pre-peak elasticity Stage; (II) Post-peak plasticity Stage; (III) Residual strength Stage.

Pre-peak elasticity Stage (I): This is the stage where the shear stress is approximately linearly related to the shear displacement, and the shear displacement is roughly in the range of 0~2 mm. In this stage, the specimen undergoes elastic deformation, the curve shape is approximately straight line, and the slope of the line is negatively correlated with the filling degree. The shear stress increases rapidly to the peak shear stress within a short range of shear displacement. As can be seen from Figure 6, the rougher the joint surface and the lower the degree of filling, the greater the peak shear stress, indicating that the magnitude of the peak stress is affected by the combination of multiple factors, such as the normal stress, the characteristics of the joint surface and the degree of filling.

Post-peak plasticity Stage (II): This is the stage at which the joint surface enters irreversible plastic deformation, and the shear displacement is roughly in the range of 2~6 mm. This phase starts with the shear stress rising to a peak value until the stress no longer changes significantly. Except for the specimen with $\Delta = 0$, the peaks of the curves corresponding to the rest of the specimens are not obvious, which is due to the presence of the soft filling layer producing a significant buffering effect, making the bolted filled joint shear curves gentler. After the shear stress reaches the peak value, the bolted filled joint specimen has also reached the critical point of elastic and plastic deformation, and the curve enters the plastic deformation stage. With the increase in shear displacement, joint surface bulge and filling layer surface friction and extrusion failure, the bolt began

to occur part of the basalt fiber breakage, to achieve the effect of "letting change", but the whole still played the role of shear; bolted filled joint specimen bearing capacity decreased rapidly and, at the same time, the slope of the curve decreases, indicating that the shear stress tends to be gradually stabilized.

Residual strength Stage (III): This is the stage where the stress is stabilized at the residual strength, and the shear displacement is roughly in the range of 6~10 mm. At this stage, the shear stress no longer varies significantly with increasing shear displacement until the end of shear. In particular, the same gypsum slurry was used to prepare the bolted filled joint specimens for the shear experiment as in this paper, and the material ratios were similar, and Wu et al. [42] derived a breaking displacement of 8.891 mm for a reinforced bolt with *JRC* = 3.5 and a filling layer thickness of 3 mm, as shown in Figure 6a. In this paper, the similar J1, Δ = 0.5 BFRP bolt bolted filled joint specimens for the shear experiment, BFRP bolt at the end of the experiment dismantled found that only part of the basalt fiber breakage, still maintains better overall integrity, with a certain shear capacity.

3.2. Peak Shear Strength

Peak shear strength is an important parameter for analyzing the shear characteristics of bolted joints, which is affected by the combined effects of normal stress, joint surface roughness, rock and soft fill properties and other parameters. The specific values of the peak shear strength of the anchorage-filled joint specimens are shown in Tables 2 and 3.

Table 2. Peak shear strength at different normal stresses (J2).

	0	**0.5**	**1**	**1.5**	**2**
2 MPa	3.51	3.37	3.16	2.80	2.52
4 MPa	5.15	4.91	4.71	4.33	3.92
6 MPa	6.65	6.47	6.30	5.60	5.15

Table 3. Peak shear strength at different *JRC* (4 MPa).

	0	**0.5**	**1**	**1.5**	**2**
J1	4.85	4.48	4.24	4.11	3.80
J2	5.15	4.91	4.71	4.33	3.92
J3	5.97	5.01	4.97	4.80	4.24

In order to more intuitively reflect the variation in peak shear strength with normal stress and *JRC*, respectively, the data were summarized and presented in the form of 3D waterfall diagrams, as shown in Figure 7.

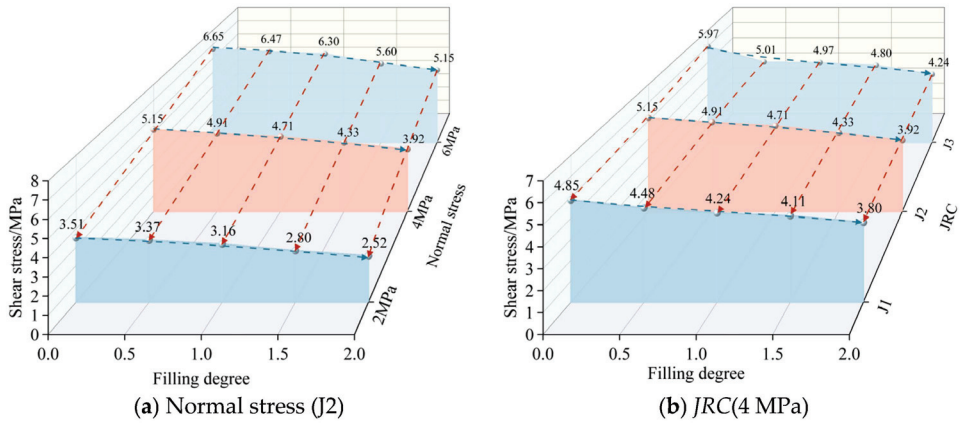

(**a**) Normal stress (J2) (**b**) *JRC*(4 MPa)

Figure 7. Characteristics of peak shear strength change.

As can be seen in Figure 7, the peak shear strength exhibits a decreasing trend with increasing filling degree. Taking the J2 filled joint specimen in Figure 7b as an example, the peak shear strengths were 5.15 MPa, 4.91 MPa, 4.71 MPa, 4.33 MPa, and 3.92 MPa for the change in filling degree from 0 to 2.0. The strength of the filling layer is lower than that of the rock-like specimens, and with the increase in the filling degree, the contact between joint surfaces is gradually replaced by the filling material, resulting in a decrease in the overall shear strength; at the same time, the shear capacity of the filling layer is weaker, especially at high filling degrees, and the shear failure mainly occurs in the interior of the filling layer rather than the contact surface of the rock-like material and the filling layer.

Figure 7a shows the peak shear strength of the specimens of bolted filled joints under the condition of joint roughness J2. By comparing the peak shear strengths with the same filling degree, it can be seen that the increase in normal stress can significantly enhance the peak shear strength of bolted filled joints. σ_n increased from 2 MPa to 4 MPa, the growth rates of peak shear strength were 46.7%, 45.7%, 49.1%, 54.6%, and 55.6% for the five filling degrees; σ_n increased from 4 MPa to 6 MPa, the growth rates of peak shear strength were 29.1%, 31.8%, 33.8%, 29.3%, and 31.4% for the five filling degrees. It can also be seen that the promotion effect of normal stress on peak shear strength is more obvious at low normal stress when the growth is the same. This is due to the fact that the compaction effect of the filling layer is more significant at low normal stresses, and increasing the normal stress significantly improves the compactness and shear capacity of the filling layer; at high normal stresses, the filling layer is close to being fully compacted, and the effect of further increasing the normal stress is limited.

Figure 7b shows the peak shear strength of the bolted filled joint specimen at 4 MPa normal stress. As can be seen from the figure, the rougher the joint surface, the greater the peak shear strength of the bolted filled joint specimens, which is the same as the findings of Zhao et al. [40,41,43]. Taking $\Delta = 0$ as an example, the peak shear strengths are 3.80 MPa, 3.92 MPa and 4.24 MPa for joint roughnesses J1, J2, and J3. However, due to the existence of the filling layer, the joint surface specimen changes from the original "rock-rock" surface contact to "rock-filling layer" surface contact, and the strength of the weak filling layer is obviously lower than that of the rock-like strength, and the "rock-filling layer" bumps are more prone to failure when subjected to the same force. The strength of the weak filling layer is obviously lower than the strength of the rock-like layer, and when the same force is applied, the "rock-filling layer" bulge is more likely to be broken, and the proportion of the resistance provided by a single bulge in the shear capacity of the joint surface decreases, which weakens the influence of joint roughness on the integrity of the specimen.

3.3. Normal Displacement–Shear Displacement Curves

Figure 8 shows the normal displacement–shear displacement relationship curves corresponding to different joint roughness coefficients (*JRC*) for normal stress σ_n = 4 MPa. Figure 9 shows the normal displacement–shear displacement relationship curves corresponding to different normal stresses for J2 conditions. Figure 10 shows the shear dilatancy-shear contraction deformation of the specimen with filling degree $\Delta = 1.0$ during the whole process of shearing under the conditions of normal stress σ_n = 4 MPa and J2, where the dashed line represents the original height of the specimen and δ is the value of the normal displacement.

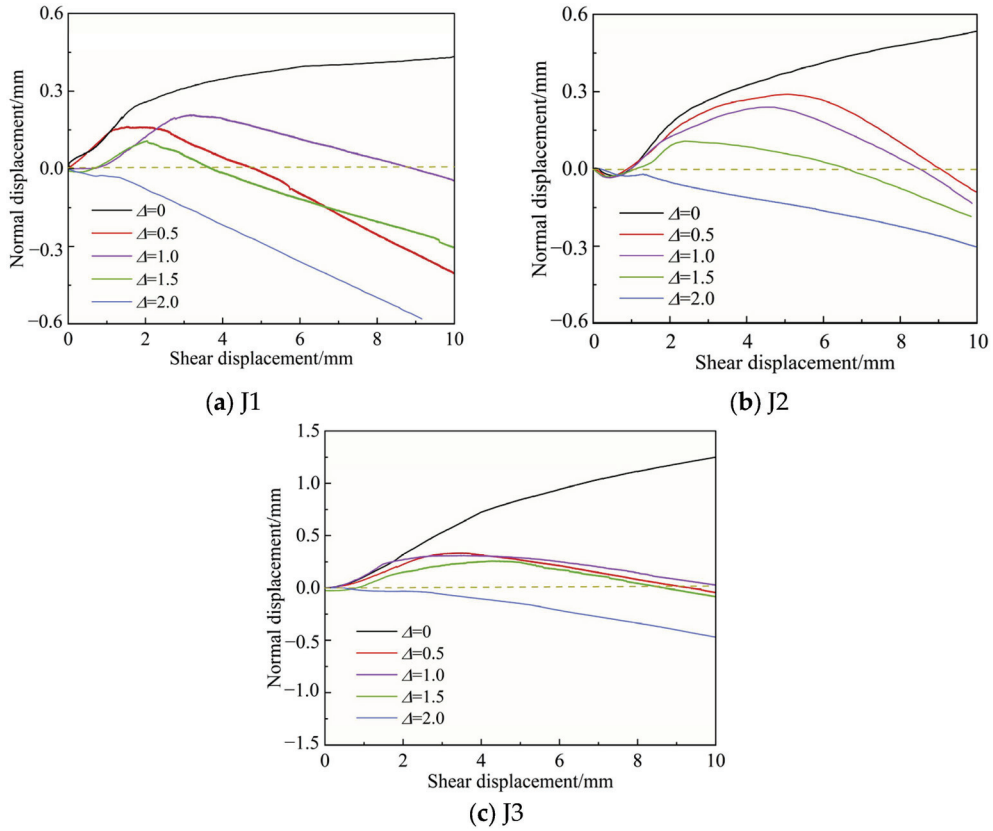

Figure 8. Normal displacement–shear displacement curves with different *JRC*s.

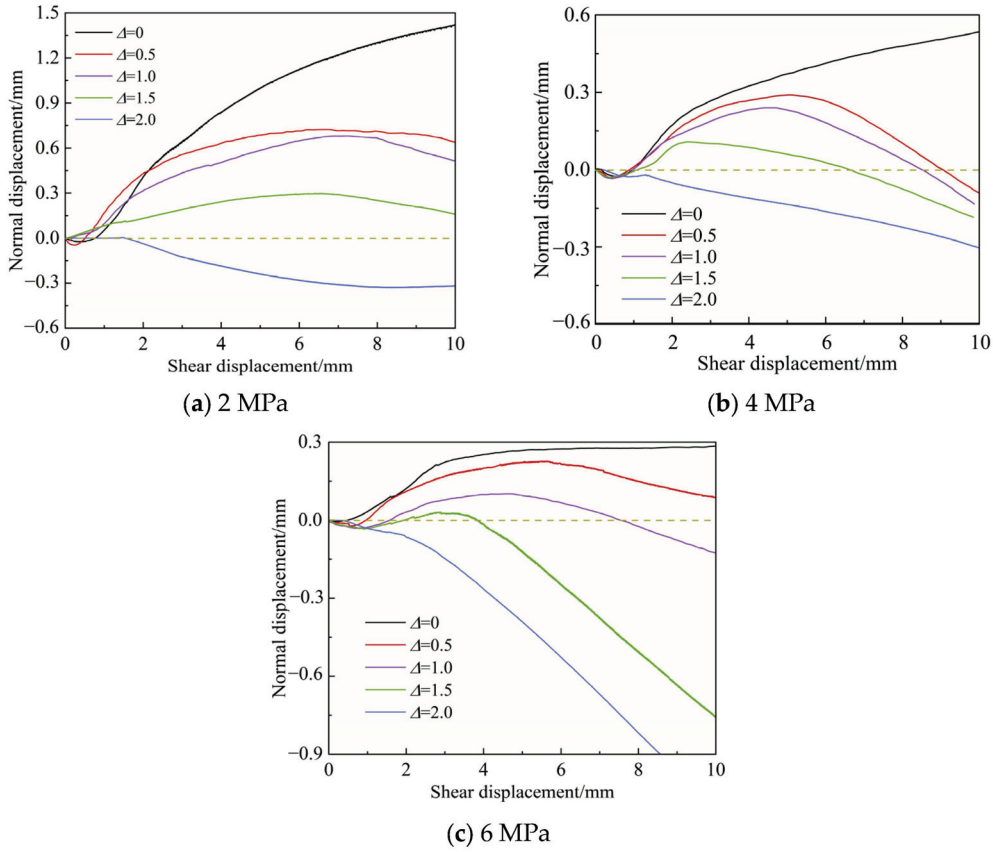

Figure 9. Normal displacement–shear displacement curves under different normal stresses.

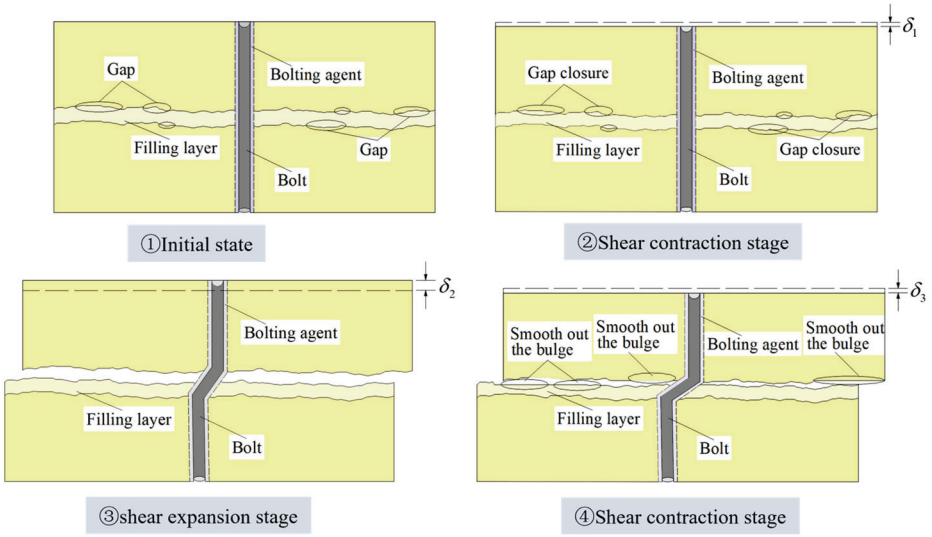

Figure 10. Schematic diagram of shear dilatancy-shear shrinkage for Δ = 1.0 bolted filled joint specimen.

As can be seen from Figure 8, according to the different filling degrees, the change rule of normal displacement with shear displacement can be roughly classified into three kinds. When Δ = 0, the specimen first shear shrinkage deformation and then shear dilatancy deformation. The specimen is subjected to normal stress in the early stage of shear, and the gaps between joint surfaces are closed by compression, after which, with the increase in shear displacement, the climbing behavior of the joint surface bulge occurs, and although there is a shear failure of the joint bulge in the process, the whole is still manifested as shear dilatancy deformation. With the decrease in *JRC*, the degree of shear dilatancy gradually decreases. When Δ = 0.5, 1.0, and 1.5, the specimen is first shear shrinkage deformed, then shear dilatancy deformed and finally shear shrinkage deformed. The presence of the filling layer has an effect on the change in normal displacement compared to Δ = 0. As shown in Figure 10, after the filling joints were compacted after a short period of shear shrinkage deformation at the early stage of shear, the filling layer and the joint surfaces on both sides experienced climbing behavior along the bulge, which was manifested as shear dilatancy deformation; as the shear displacement continued to increase, the filling layer was crushed due to the bulge under the action of compression and shear with its low strength, and the specimen was subjected to shear shrinkage deformation. In particular, depending on the climbing behavior and the specific gravity of the bulge crushing, there are differences in the time for which the shear shrinkage and shear dilatancy deformations are maintained. When Δ = 2.0, the specimen has been kept in shear shrinkage deformation. Due to the greater thickness and lower strength of the filling layer, failure or fragmentation of the filling layer began to occur soon after the start of the shear experiment, the climbing behavior was not obvious, and the specimen underwent shear shrinkage deformation.

As shown in Figure 9, with the increase of σ_n, the degree of shear dilatancy deformation increases and shear shrinkage deformation slows down. Taking Δ = 0 as an example, the maximum normal displacements are 1.42 mm, 0.53 mm, and 0.28 mm at 2 MPa, 4 MPa, and 6 MPa. This is because the increase in normal stress aggravates the failure of joint bulge, the "climbing effect" becomes smooth, and the shear dilatancy is limited, at the same time, the increase in normal stress will lead to the more serious failure of filling layer, which provides space for the specimen to undergo shear deformation [44,45].

3.4. Characterization of Failure of Filled Joints

In order to better understand the bolted filled joint shear mechanical properties, the bolted filled joint failure characteristics were macroscopically analyzed [46]. Taking the joint surface J2 at σ_n = 4 MPa as an example, its specimen failure is shown in Figure 11.

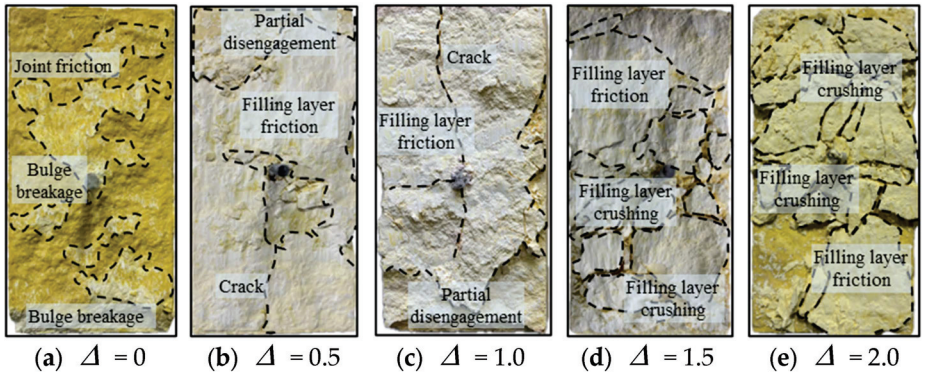

Figure 11. Figure of failure of specimens of bolted filled joints.

It is known from Figure 11 that when Δ = 0, the specimen is in "joint-joint" surface contact, and the joint surface undergoes friction and bulge gnawing by the shear action. When Δ = 0.5 and Δ = 1.0, due to the presence of weak filler, the specimen is "joint-filling layer" surface contact, but due to the small thickness of the filling layer, there will be a small area of "joint-joint" surface contact in the shear process. Therefore, the specimen mainly suffers from the friction of the filling medium and the whole detachment of part of the filling medium, accompanied by the friction and gnawing failure of fewer joint bulges. When Δ = 1.5 and Δ = 2.0, the thickness of the weak filling is larger, the contribution of the joints to the shear capacity is limited, the filling layer and the bolt mainly bear the shear effect of the specimen, under the joint action of the normal stress and the shear stress, the filling layer is more likely to be a failure than the upper and lower blocks and the fragmentation is more obvious.

3.5. Characterization of Failure of BFRP Bolt

The failure characteristics of the BFRP bolt under normal stress of 4 MPa with different filling degrees are shown in Figure 12; A and B both indicate the turning point where the bolt undergoes deformation, θ denotes the bending angle of the bolt, and H and S denote the vertical and horizontal components of the bending and deformation part of the bolt. In this paper, we focus on analyzing the effect of the filling degree and the laws governing the effects of normal stress and roughness on bolted joint roughness have been revealed [47,48] and will not be repeated here.

From Figures 12 and 13, it can be seen that the BFRP bolts showed a slight "Z" bending deformation during the shear process, and with the increase in the filling degree, the deformation and failure area and bending degree of the bolts were enlarged. This is due to the low strength of the filling layer, the part of the layer in contact with the bolt is easily crushed by the extrusion pressure during the shear process and forms an extrusion crushing zone. Therefore, it is difficult for the filling layer to exert shear force on the bolt; it can be considered that the contact point between the upper and lower nodal surfaces and the bolt is the point of action of shear stress, as shown in Figure 14. The normal force on the BFRP bolt F_p' is the bonding constraint force exerted by the bolting agent, which is expressed as the bolt is subjected to the tension force exerted by the upper block specimen upward along the surface of the bolt and the tension force exerted by the lower block downward along the surface of the bolt. The bolt is subjected to the shear force F_s' in the horizontal direction

in the region of the bolted filled joints, and F_n denotes the force exerted on the shear box in the normal direction. Therefore, most of the turning points of the bolt deformation exist at the junction of the upper and lower blocks and the filling layer, and with the increase in the filling degree, the distance between points A and B increases, and the range of the bolt deformation expand.

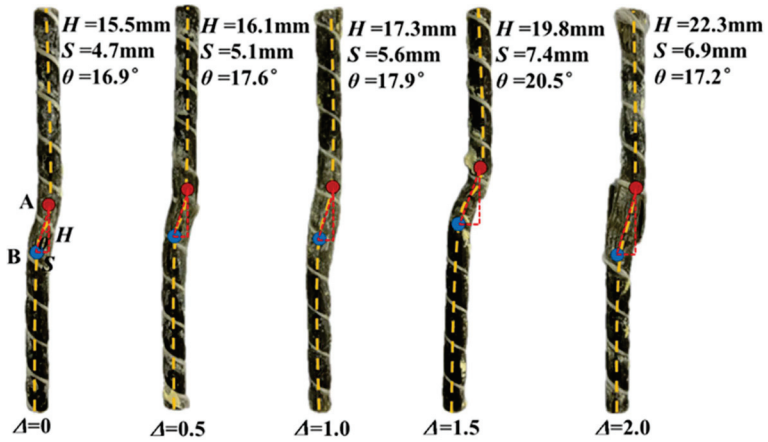

Figure 12. Deformation failure figure of BFRP bolt: A and B both indicate the turning point where the bolt undergoes deformation.

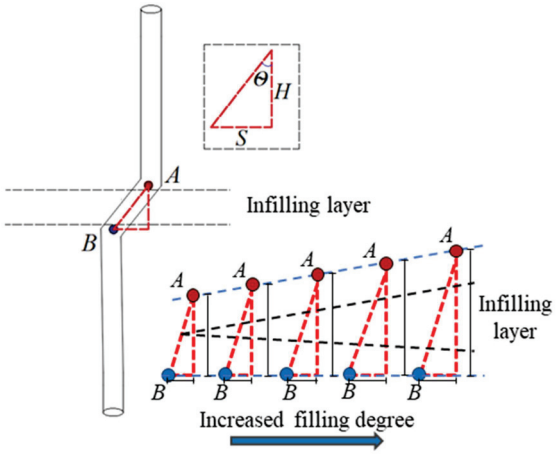

Figure 13. Schematic diagram of the geometric relationship between shear deformation of the bolt.

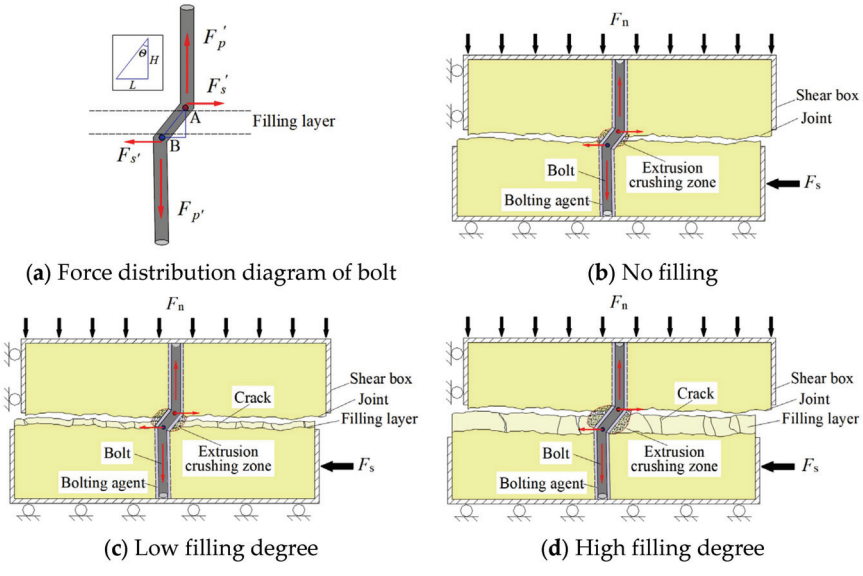

(**a**) Force distribution diagram of bolt

(**b**) No filling

(**c**) Low filling degree

(**d**) High filling degree

Figure 14. Schematic diagram of the failure of the bolt under force.

BFRP bolts are virtually free from shear throughout the pre-peak elastic stage. After entering the post-peak plasticity stage, the shear force on the bolt increases rapidly, and the basalt fiber absorbs a lot of energy and is elongated, with the increase in the stretching length of the basalt fiber, a small portion of the fiber appears to be worn out, broken phenomenon, but overall, it continues to play a role; this achievement has the effect of "letting change". In the residual strength stage, the shear displacement is larger, and the bolt is more exposed to the tensile load caused by the misalignment of the filled joints in the shear residual stage, while the BFRP bolt is more resistant to tensile ability and therefore shows a greater advantage in the residual stage. The BFRP bolt has a low modulus of elasticity and shows high elastic deformation capacity when subjected to force. During the shear process of filling joints, the BFRP bolt undergoes significant deformation when subjected to large tensile and shear forces, but it is not easy to fracture, which ensures that the BFRP bolt continues to play a shear-resistant role. However, it can be seen in Figure 12 that the horizontal deformation of the BFRP bolt, *S*, ranges between 4.7 mm and 6.9 mm, which is less than the set maximum shear displacement of 10 mm. This is due to a certain degree of deformation recovery of the BFRP bolt after the release of pressure and unconfinement of the rock-like material.

4. Acoustic Emission Characterization

4.1. Characteristics of AE Energy Changes

The AE energy is closely related to the specimen failure and can be used to characterize the specimen failure [49,50]. The shear stress–shear displacement curves and energy change curves under different filling degrees, normal stress and *JRC* conditions are listed, respectively, and the specimen failure law is described after comparative analysis.

In the pre-peak elastic phase, due to the elastic deformation of the specimen, the bolted filled joint specimen is basically undamaged, the AE signal is calmer, and the AE energy is smaller. In the post-peak plastic phase, the bolted filled joints reached the yield strength and began to undergo plastic failure, which was manifested by the friction failure of the filled joint surfaces, the fracture of the basalt fibers of the bolts, and the extrusion failure of the bolts against the filled joints, which resulted in a significant enhancement of the AE signals, and the AE energy increased rapidly to the peak. Afterwards, due to the gradual reduction in the number of projections and the gradual formation of the crush zone, the AE energy shows a general decreasing trend. In the residual strength stage, the interface of bolted filled joints is smoother, the deformation of the BFRP bolt is basically stable, the plastic failure is relatively less, the AE energy is lower, and the cumulative AE energy curve is smoother.

The AE energies show different patterns as influenced by the soft fill. When $\Delta = 0$, i.e., the specimen has no weak filling layer, the failure is dominated by brittleness with less energy release, while $\Delta \neq 0$, i.e., when there is a filling layer, due to the lower strength of the filling layer, it is prone to plastic deformation and rupture, and the failure mode of the filled joint specimen is gradually transformed into plastic failure with more significant energy release. At the same time, with the increase in filling degree, the volume of the filling layer increases, and the range and intensity of energy release in the shear process also increases. From Figure 15a, the maximum values of AE energy are 122, 142, and 216 ($\times 10^3$ mV·ms), and the cumulative values of AE energy are 70, 87, and 141 ($\times 10^5$ mV·ms) when $\Delta = 0$, 1.0, 2.0.

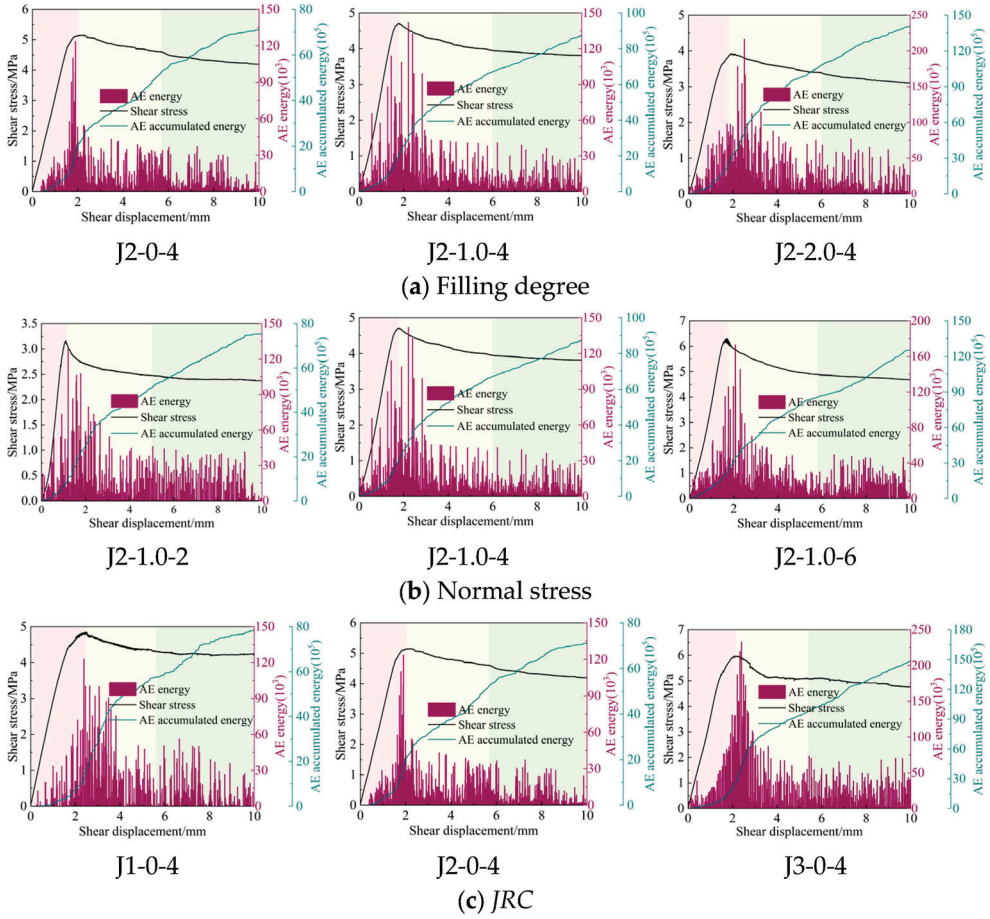

Figure 15. Characteristics of AE energy changes in bolted filled joint specimens.

The normal stress also has an effect on the AE energy values, with both the AE energy and the cumulative energy increasing as the normal stress becomes larger. From Figure 15b, the maximum values of AE energy are 128, 142, and 173 ($\times 10^3$ mV·ms), and the cumulative AE energy values are 75, 87, and 125 ($\times 10^5$ mV·ms) for normal stresses equal to 2, 4, and 6 MPa. This is due to the fact that the normal stresses can enhance the degree of engagement of the filled joints, the more severe failure occurs in the specimen under shear, and the AE energy released increases. In addition, the increase in *JRC* leads to more severe joint surface bulge failure and the release of instantaneous AE energy from bulge fracture increases.

4.2. AE Event Distribution Characteristics

The spatiotemporal distribution characteristics of AE signals in bolted filled joint specimens reflect the failure morphology of the specimens. Statistics on the distribution of AE signals and analysis of the connection between the distribution characteristics of AE signals and the failure of the specimens are conducive to analyzing the failure mechanism of the bolts and improving the bolting performance of the bolting system.

Figure 16 lists the characteristic figures of AE spatial distribution for different shear stages of the J2-2-4 bolted filled joint specimen, where each AE signal represents a failure event. From the figure, it can be seen that most of the AE events at small shear displacements tend to occur at the back end along the shear direction, and the AE events generated at this stage are caused by the closure of primary fractures and microcrack extension within the rock mass, which is the same as the study of Dong [51]. With the increase in shear displacement, the filling joint crack sprouting and expansion gradually increased and moved forward, and the AE events were uniformly distributed along the shear direction

on the filling joint surface, and, exceptionally, the AE signals around the bolts were more intensive, which was caused by the formation of fracture zones in the rock mass around the extrusion of the bolts, as shown in Figure 16b. The AE signals increased after that, but the number was not large. It can also be seen from the figure that AE events occurred mostly at shear displacements of 2~6 mm (200~600 s), while there were fewer AE events at 0~2 mm (0~200 s) and 6~10 mm (600~1000 s).

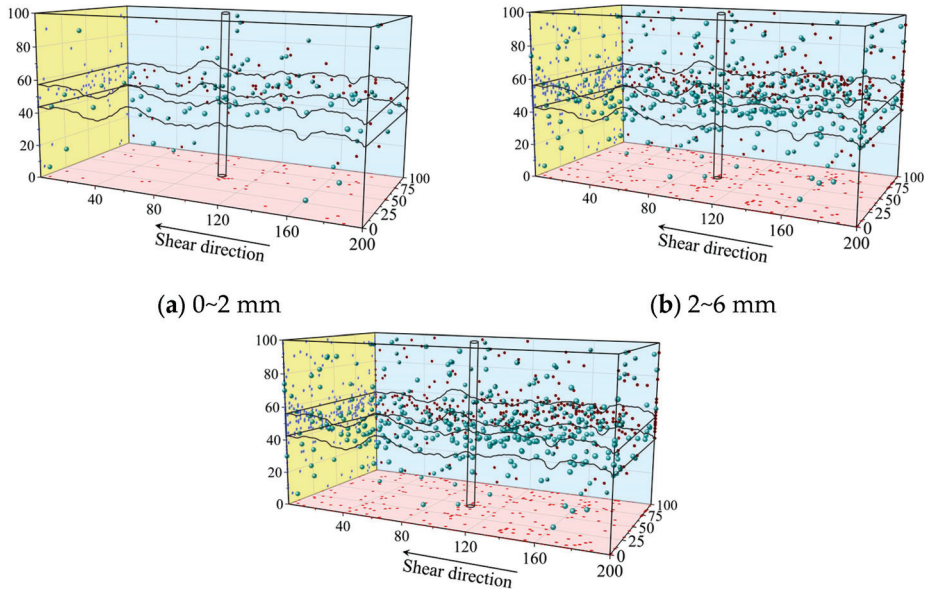

(**a**) 0~2 mm (**b**) 2~6 mm

(**c**) 6~10 mm

Figure 16. Characteristic figure of the spatial distribution of AE in the specimens of bolted filled joints: The green ball represents the AE signal; the red, blue and purple balls represent the projections of the AE signal in the three directions.

As can be seen from the side projection, the AE signals are concentrated in the filling layer and near the joint surface, and there are fewer AE signals in the upper and lower blocks. In connection with the previous analysis, the filling joints are more prone to failure as a weak structure of the intact specimen as compared with the upper and lower rock specimens, and there is also a small amount of microcracks sprouting and expanding inside the upper and lower blocks.

The AE events of BFRP bolted filled joint specimens bolted with five filling degrees at J2 and σ_n = 4 MPa were counted according to the occurrence time, and the results are shown in Figure 17, in which Stage I (0~200 s), Stage II (200~600 s), and Stage III (600~1000 s) correspond to pre-peak elasticity, post-peak plasticity, and residual strength stages, respectively, in Section 3.1 stage. As can be seen from the figure, the proportion of AE events in Stage I increases with the increase of Δ. This is because the AE events in this stage are generated by the closure of primary cracks and the expansion of microcracks within the rock, and the number of cracks sprouting in the filling layer is higher than that in the upper and lower blocks under the same conditions. It can also be seen from the figure that, regardless of the filling degree, the AE events generated by the damage of the bolted filled joint specimens were mainly concentrated in Stage II, which accounted for about the same proportion as the sum of the proportions in Stages I and III, which were 59%, 54%, 56%, 57%, and 57%, respectively. According to the previous analysis, when Δ is larger, the filling layer is heavily fragmented and the crush zone is larger, and this damage occurs mostly in Stage II, so the proportion of acoustic emission events in Stage II increases with increasing Δ. Some AE events are generated by the slip of the filled joints in Stage III,

where the influence of the filling degree is not significant, so the percentage of AE in Stage III mainly depends on the first two stages.

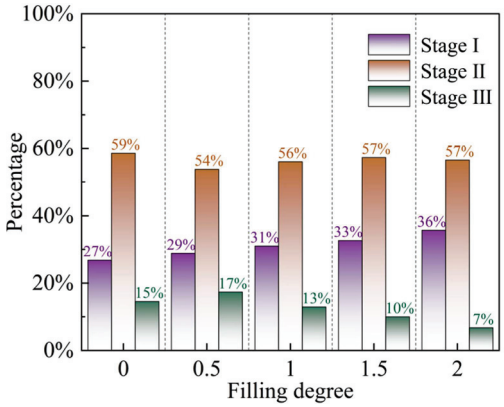

Figure 17. Characteristic figure of AE time distribution of bolted filled joint specimens.

Based on the above analysis, it can be seen that there is a good correspondence between the AE evolution characteristics and the shear failure process of the bolted filled joint specimen, which reveals the failure evolution process, the failure mechanism, and the change rule of the mechanical behavior of the rocks or joint surfaces in the shear experiment of the bolted filled joints. The AE energy value and the cumulative energy value of the AE quantify the degree of failure and failure of the specimen in the process of shear. The AE spatial distribution characteristics can intuitively reflect the spatial distribution and expansion path of cracks at each stage, and the AE time distribution characteristics verify the stage of specimen failure.

4.3. Discussion

This study confirms that BFRP bolts can effectively inhibit the shear slip of filled joints by virtue of their high tensile strength and controlled deformation characteristics (vertical deformation of 15.5–22.3 mm and horizontal deformation of 4.7–6.9 mm). Its progressive fiber fracture mechanism is superior to the brittle failure of traditional steel bolts, and it is especially suitable for the reinforcement of jointed rock bodies that require coordinated deformation. As underground construction continues to expand to the deep, the engineering challenges posed by the "three highs and one disturbance" (high geostress, high geothermal temperature, high karst water, and strong construction disturbance) are becoming more and more prominent, and future research should focus on optimization of high-stress working conditions and long-term performance.

5. Conclusions

In this paper, the effects of the degree of filling, joint roughness and normal stress on the shear mechanical properties and shear failure mode of intact specimens were investigated by carrying out the straight shear experiment of BFRP bolts bolted filled joint roughness and the shear failure properties of BFRP bolts were analyzed. Meanwhile, the AE energy evolution characteristics and AE distribution characteristics in the process of shear were systematically analyzed by combining them with the acoustic emission (AE) monitoring technology. The main conclusions are as follows:

1. Peak shear strength decreases with increasing filling degree, while normal stress, joint roughness and peak shear strength all show a positive correlation, which is due to the fact that they can directly or indirectly increase the engaging force of the filled joints.

2. The normal deformation of bolted filled joints is closely related to the filling degree, with the increase in filling degree, there are three kinds of evolution laws: first shear shrinkage and then shear dilatancy, first shear shrinkage and then shear dilatancy and then shear shrinkage, and shear shrinkage, and *JRC* and normal stress affect the degree of change in the specimen shear dilatancy-shear shrinkage.
3. The failure characteristics of the specimen are affected by the filling layer: the nodular bulge friction and gnawing failure when there is no filling, the filling layer friction and detachment with a small amount of nodular bulge gnawing failure when the filling degree is low, and the filling layer crumbles seriously when the filling degree is high.
4. BFRP bolts mainly play a shear capacity in the post-peak plastic stage, some fibers break in the process of shear, achieving the effect of "letting change", and still have the ability to resist tensile and shear deformation in the later stage. With the increase in filling degree, the distance between A and B deformation critical points increases, and the deformation range of the bolt expands.
5. The acoustic emission energy evolution is closely related to the failure of the specimen. The pre-peak elasticity stage of the filled joint specimen basically does not cause damage, and the acoustic emission signal is relatively calm; the plasticity failure occurs mostly in the post-peak plasticity stage, where the acoustic emission energy surges and appears at its maximum, and then returns to be calm in the residual stage. The AE events are mainly concentrated in Stage II, the proportion of which is about the sum of the proportion of Stage I and Stage III, and this proportion increases with the increase in the filling degree.

Author Contributions: Methodology, Writing—review and editing, Funding acquisition: H.L.; Writing—original draft, Validation: Q.S.; Methodology, Writing—review and editing, Funding acquisition: C.W.; Supervision: Y.J.; Methodology: S.Z.; Investigation: J.L. and K.L. All authors have read and agreed to the published version of the manuscript.

Funding: This study is funded by the National Natural Science Foundation of China (No. 52209141) and the Shandong Provincial Natural Science Foundation (No. ZR2024ME065). This support is gratefully acknowledged.

Institutional Review Board Statement: Not applicable.

Informed Consent Statement: Not applicable.

Data Availability Statement: The original contributions presented in this study are included in the article. Further inquiries can be directed to the corresponding author.

Conflicts of Interest: Authors Hengjie Luan, Qingzhai Shi, Changsheng Wang, Yujing Jiang, Jianrong Liu and Kun Liu were employed by the Inner Mongolia Shanghaimiao Mining Co., Ltd. The remaining author declare that the research was conducted in the absence of any commercial or financial relationships that could be construed as a potential conflict of interest.

References

1. Yu, W.J.; Wu, G.S.; Liu, H.; Wang, P.; An, B.; Liu, Z.; Zhong, H.; Liu, F. Deformation characteristics and stability control of soft coal-rock mining roadway in thin coal seam. *J. China Coal Soc.* **2018**, *43*, 2668–2678.
2. Huang, Q.X.; Zhao, M.Y.; Zhang, Q.F.; Song, S.; Meng, K. Mechanisms of outward dislocation sliding of roadway sides and its support in a thick coal seam with a soft mudstone interlayer. *Rock Soil Mech.* **2016**, *37*, 2353–2358.
3. Atapour, H.; Moosavi, M. The influence of shearing velocity on shear behavior of artificial joints. *Rock Mech. Rock Eng.* **2014**, *47*, 1745–1761. [CrossRef]
4. Peng, Y.X.; Yu, L.; Qian, J.; Li, W.; Zhang, T.; Zhou, L. Dynamic tensile behavior and crack propagation in coral aggregate seawater shotcrete: Experimental investigation and numerical simulation. *Cem. Concr. Compos.* **2025**, *159*, 106010. [CrossRef]

5. Li, Z.Q.; Nie, L.; Xue, Y.; Li, W.; Fan, K. Model Testing on the Processes, Characteristics, and Mechanism of Water Inrush Induced by Karst Caves Ahead and Alongside a Tunnel. *Rock. Mech. Rock. Eng.* **2025**, *58*, 5363–5380. [CrossRef]
6. Zheng, L.B.; Liu, K.W. Shear behavior of single-joint bolted sandstone subjected to dry–wet cycles: Experimental and analytical approaches. *J. Rock Mech. Geotech. Eng.* **2024**, *16*, 4216–4228. [CrossRef]
7. Liu, J.R.; Luan, H.J.; Jiang, Y.J.; Shang, H.; Wang, M.; Wang, C.; Zhang, S. Effect of normal boundary conditions on the shear mechanics and acoustic emission characteristics of anchored rock joints. *J. Min. Sci. Technol.* **2025**, *10*, 173–183.
8. Xu, W.B.; Chen, W. The triaxial compressive mechanical properties and failure characteristics of backfill-rock combined bodies with different interface angles. *J. Min. Sci. Technol.* **2023**, *8*, 633–641.
9. Liu, H.L.; Yang, G.Y.; Guo, Y.J.; Zhang, Q.; Sun, Z. Experimental study on the shear deformation characteristics and mechanical properties of bolted joints. *Int. J. Geomech.* **2023**, *23*, 4022265. [CrossRef]
10. Cui, G.J.; Zhang, C.Q.; Chen, J.L.; Yang, F.J.; Zhou, H.; Lu, J.J. Effect of bolt inclination angle on shear behavior of bolted joints under CNL and CNS conditions. *J. Cent. South Univ.* **2020**, *27*, 937–950. [CrossRef]
11. Wang, X.; Lou, J.; Li, J.; Gao, F.; Yuan, G. Influence of rockbolt pretension on bolting behaviors by gravel bolting tests. *J. Rock Mech. Geotech. Eng.* 2025, in press. [CrossRef]
12. Wang, G.; Zhang, Y.Z.; Jiang, Y.J.; Liu, P.; Guo, Y.; Liu, J.; Ma, M.; Wang, K.; Wang, S. Shear behaviour and acoustic emission characteristics of bolted rock joints with different roughnesses. *Rock Mech. Rock Eng.* **2018**, *51*, 1885–1906. [CrossRef]
13. Wu, X.Z.; Jiang, Y.J.; Wang, G.; Gong, B. Performance of a new yielding rock bolt under pull and shear loading conditions. *Rock Mech. Rock Eng.* **2019**, *52*, 3401–3412. [CrossRef]
14. Zhang, Y.C.; Jiang, Y.J.; Wang, Z.; Yin, Q.; Chen, M. Anchorage effect of bolt on en-echelon fractures: A comparison between energy-absorbing bolt and conventional rigid bolt. *Eng. Fail. Anal.* **2022**, *137*, 106256. [CrossRef]
15. Jiang, Y.J.; Zhang, S.H.; Luan, H.J.; Wang, C. Experimental study on shear characteristics of bolted rock joints under constant normal stiffness boundary conditions. *Chin. J. Rock Mech. Eng.* **2021**, *40*, 663–675.
16. Zuo, H.F.; Jiang, Y.J.; Li, C.P.; Liu, G.; Zhang, S.; Guan, Y.; Luan, H.; Liu, J.; Li, X. Numerical simulation of anchor angle effect of bolts based on modified model of Pile element. *J. Shandong Univ. Sci. Technol. (Nat. Sci.)* **2023**, *42*, 30–39.
17. Sun, B.J.; Liu, Q.W.; Li, W.T.; Yang, X.Z.; Yang, B.; Li, T.C. Numerical implementation of rock bolts with yield and fracture behaviour under tensile-shear load. *Eng. Fail. Anal.* **2022**, *139*, 106462. [CrossRef]
18. Liu, Q.S.; Lei, G.F.; Peng, X.X.; Wei, L. Study on shear mechanical properties of sandstone, marble and granite after anchoring. *Chin. J. Rock Mech. Eng.* **2018**, *37* (Suppl. S2), 4007–4015.
19. Tao, Z.G.; Xie, D.; Sui, Q.R.; Sun, J.; He, M. Study on active support method and control effect of NPR anchor cables for large deformation of tunnel surrounding rock under complex geological conditions. *Chin. J. Rock Mech. Eng.* **2024**, *43*, 276–286.
20. Wang, W.; Pan, Y.S.; Xiao, Y.H. Synergistic resin anchoring technology of rebar bolts in coal mine roadways. *Int. J. Rock Mech. Min. Sci.* **2022**, *151*, 105034. [CrossRef]
21. Li, G.F.; Wang, J.H.; Liu, J.R.; Luan, H.; Zhang, S.; Wang, C.; Wang, D. Study on shear properties and failure characteristics of bolted joint of roadway surrounding rock. *J. Shandong Univ. Sci. Technol. (Nat. Sci.)* **2022**, *41*, 47–55.
22. Luan, H.J.; Cao, Y.W.; Jiang, Y.J.; Guan, Y.; Li, C.; Sun, J.; Liu, J. Implementation of tension-shear coupling failure mode of rock bolts in FLAC3D and its application. *J. Min. Strat. Control Eng.* **2022**, *4*, 63029.
23. Liu, H.S.; Luan, H.J.; Qiao, J.L.; Li, G.; Zhang, S. Failure mechanism and strengthening support technology of gangue-containing coal roadway sidewall. *J. Min. Strat. Control Eng.* **2022**, *4*, 33031.
24. He, M.C.; Ren, S.L.; Guo, L.J.; Lin, W.; Zhang, T.; Tao, Z. Experimental study on influence of host rock strength on shear performance of Micro-NPR steel bolted rock joints. *Int. J. Rock Mech. Min. Sci.* **2022**, *159*, 105236. [CrossRef]
25. Wu, X.Z.; Jiang, Y.J.; Gong, B.; Deng, T.; Guan, Z. Behaviour of rock joint reinforced by energy-absorbing rock bolt under cyclic shear loading condition. *Int. J. Rock Mech. Min. Sci.* **2018**, *110*, 88–96. [CrossRef]
26. Han, G.S.; Chen, Z.J.; Li, B.; Zhou, Y.; Ding, S.; Zhong, Z. Experimental study on shear characteristics of energy-absorbing bolt anchored jointed rock mass under constant normal stiffness condition. *Chin. J. Rock Mech. Eng.* **2024**, *43*, 999–1012.
27. Fan, X.C.; Xu, T.; Zhou, Z.R.; Zhou, X. Experimental study on basic mechanical properties of BFRP bars. *IOP Conf. Ser. Mater. Sci. Eng.* **2017**, *250*, 12014. [CrossRef]
28. Protchenko, K.; Zayoud, F.; Urbanski, M.; Szmigiera, E. Tensile and shear testing of basalt fiber reinforced polymer (BFRP) and hybrid basalt/carbon fiber reinforced polymer (HFRP) bars. *Materials* **2020**, *13*, 5839. [CrossRef] [PubMed]
29. Duo, Y.Y.; Liu, X.G.; Liu, Y.; Tafsirojjaman, T.; Sabbrojjaman, M. Environmental impact on the durability of FRP reinforcing bars. *J. Build. Eng.* **2021**, *43*, 102909. [CrossRef]
30. Cao, X.F.; Zhao, W.; Xie, Q.; Yang, G. Experimental study on mechanical properties of basalt fiber reinforced plastic rebar. *Highw. Eng.* **2016**, *41*, 215–217.
31. Zhang, S.B.; Wang, C.S.; Wang, G.; Wu, X.; Zheng, X.; He, P.; Xu, F. Experimental study on the shear behaviors of bolted rock joints reinforced with BFRP bars. *Chin. J. Rock Mech. Eng.* **2022**, *41*, 712–724.

32. Zhang, S.B.; Wang, C.S.; Wang, G.; Zheng, X.; Guan, H.; Liu, T.; Xu, F. Experimental and numerical study on shear behaviors of rock joints reinforced by SFCBs and BFRP bars. *Rock Mech. Rock Eng.* **2022**, *56*, 1717–1737. [CrossRef]
33. Xie, J.Z.; Wang, X.; Ding, L.N.; Peng, Z.; Liu, X.; Mao, W.; Wu, Z. Shear behavior of BFRP anchor-jointed rock mass considering inclination angle and pre-tension. *Constr. Build. Mater.* **2024**, *447*, 138157. [CrossRef]
34. Wang, H.P.; Song, Y.; Zhou, J.H.; Mao, J.; Zhang, W. Research on the mechanical model of anchorage resistance in deeply filled jointed rock masses. *Eng. Fail. Anal.* **2024**, *163*, 108565. [CrossRef]
35. Wei, H.; Wu, H.G.; Wu, D.Y.; Tang, L.; Pai, L.F.; Guan, W. Stress response characteristics of BFRP anchors on loess mudstone slope under rainfall conditions. *J. Mt. Sci.* **2023**, *20*, 1469–1482. [CrossRef]
36. Du, Z.G.; Li, N.; Ding, W.X.; Tao, Y.; Wu, X.; Guo, J.; You, P.; Wang, C.; Archbold, P.; Mullarney, B. Development of the Large–Tonnage Pressure–Type Prestressed Anchor Cable with BFRP for Geotechnical Engineering and Its Mechanical Properties. *Geofluids* **2022**, *4*, 7467842. [CrossRef]
37. Culshaw, M.G.; Ulusay, R. The ISRM suggested methods for rock characterization, testing and monitoring: 2007–2014. *Bull. Eng. Geol. Environ.* **2015**, *74*, 1499–1500. [CrossRef]
38. Song, Y.; Wang, H.P.; Zhang, W.D.; Zhao, L.; Zhou, J.; Mao, J. Shear characteristics of anchored filling jointed rock mass under constant normal stiffness. *Rock Soil Mech.* **2024**, *45*, 2695–2706.
39. Ladanyi, B.; Archambault, G. *Shear Strength and Deformability of Filled Indented Joints*; Associazione Geotechnica Italiana: Rome, Italy, 1977; pp. 317–326.
40. Zhao, Y.L.; Zhang, L.Y.; Wang, W.J.; Liu, Q.; Tang, L.L.; Chen, G. Experimental study on shear behavior and a revised shear strength model for infilled rock joints. *Int. J. Geomech.* **2020**, *20*, 4020141. [CrossRef]
41. Simangunsong, G. Effect of normal stress on direct shear test. In Proceedings of the International Symposium on Earth Science and Technology, Fukuoka, Japan, 25–26 November 2021.
42. Wu, X.Z.; Zheng, H.F.; Jiang, Y.J.; Guan, Z.; Miao, Y. Experimental and numerical simulation research of shear characteristics of infilled rock joints reinforced by rock bolt. *J. Eng. Geol.* **2024**, *32*, 1814–1824.
43. Wu, X.Z.; Jiang, Y.J.; Li, B. Influence of joint roughness on the shear behaviour of fully encapsulated rock bolt. *Rock Mech. Rock Eng.* **2018**, *51*, 953–959. [CrossRef]
44. Li, W.; Zhang, Q.S.; Wang, X.C.; Yu, L.Y.; Li, Z.Q. Synergistic effect of particle size, carboxymethyl starch and Na_2CO_3 on rheological and filtration property of bentonite-based material. *Case Stud. Constr. Mater.* **2024**, *21*, e03537. [CrossRef]
45. Li, W.; Yu, L.Y.; Tan, Y.Z.; Wu, L.R.; Qian, J.Y. Mechanical properties and impact behavior of frozen clay: Insights from static mechanical tests, fly-plate tests, and split-Hopkinson pressure bar analysis. In *Physics of Fluids*; AIP Publishing: Melville, NY, USA, 2024; Volume 36, p. 57138.
46. Li, W.; Yu, L.; Zhang, T. Quantitative analysis of grain size effect on tensile mechanical behavior of granite based on multi-level force chain networks. *Comp. Part. Mech.* **2024**, *11*, 2245–2266. [CrossRef]
47. Song, Y.; Fan, B.; Wang, H.P. Research on shear mechanics model of anchored-jointed rock mass considering normal stress and rock strength. *Chin. J. Rock Mech. Eng.* **2023**, *42*, 1325–1335.
48. Wang, L.Q.; Zhu, L.F.; Zheng, L.B.; Fan, B.; Sun, Z.; Chen, H. Shear test of bolted joint rock masses considering joint roughness. *China J. Highw. Transp.* **2021**, *34*, 38–47.
49. Wang, C.S.; Jiang, Y.J.; Wang, G.; Luan, H.; Zhang, Y.; Zhang, S. Experimental investigation on the shear behavior of the bolt-grout interface under CNL and CNS conditions considering realistic bolt profiles. *Geomech. Geophys. Geo-Energy Geo-Resour.* **2022**, *8*, 111. [CrossRef]
50. Zhu, P.; Wang, Z.; Wu, W.B.; Yao, Z.; Wang, T.; Li, X.; Chen, L. Research on acoustic emission characteristics and failure mechanism of granite treated by repeated cooling. *J. Shandong Univ. Sci. Technol. (Nat. Sci.)* **2024**, *43*, 1–9.
51. Dong, H.Y. Experimental Study on Mechanical Shear Properties of Irregular Rock Fractures. Master's Thesis, Henan University of Science and Technology, Luoyang, China, 2017.

Disclaimer/Publisher's Note: The statements, opinions and data contained in all publications are solely those of the individual author(s) and contributor(s) and not of MDPI and/or the editor(s). MDPI and/or the editor(s) disclaim responsibility for any injury to people or property resulting from any ideas, methods, instructions or products referred to in the content.

materials

MDPI

Article

Meso-Scale Breakage Characteristics of Recycling Construction and Demolition Waste Subgrade Material Under Compaction Effort

Lu Han [1], Weiliang Gao [1], Yaping Tao [1] and Lulu Liu [2,*]

[1] School of Transportation Engineering, Huanghe Jiaotong University, Jiaozuo 454000, China
[2] School of Mechanics and Civil Engineering, China University of Mining & Technology, Xuzhou 221116, China
* Correspondence: liululucumt@cumt.edu.cn

Abstract: The application of construction and demolition waste (CDW) as roadbed filler faces challenges due to the variable mechanical properties caused by fragile recycled brick aggregates. This study elucidates the breakage mechanism of CDW fillers under compaction effort through a combination of standardized laboratory compaction tests and discrete element method (DEM) simulations. Furthermore, the breakage evolution patterns of mixed fills comprising recycled concrete and brick aggregates at various mixing ratios were revealed. A DEM model was developed to characterize recycled concrete and brick aggregates, adopting polygonal clumps for particles >4.75 mm and spherical clumps for finer fractions. The results indicate that particle breakage progresses through three distinct stages: linear fragment stage (0–200 kJ/m^3, 50% of total breakage), deceleration growth stage (200–1000 kJ/m^3, 38% of total breakage), and residual crushing stage (1000–2684.9 kJ/m^3, 12% of total breakage). Recycled concrete aggregates form a skeleton restraining deep cracks, while brick aggregates enhance stability through energy dissipation and void filling. However, exceeding 30% brick content impedes skeleton development. Critically, a 30% brick content optimizes performance, achieving peak dry density with 25% lower compression deformation than concrete-only fillers, while limiting breakage index rise. These results provide a science-based strategy to optimize CDW roadbed design, improving recycling efficiency and supporting sustainable infrastructure.

Keywords: construction waste recycled filler; particle breakage; discrete element simulation; meso-mechanics

1. Introduction

Urban reconstruction and infrastructure development have generated a substantial amount of construction and demolition waste (CDW). In China, the recycling rate of CDW remains below 20%. Improper disposal methods, such as storage and landfilling, exacerbate environmental pressures [1,2]. Utilizing CDW as a building regeneration material is one of the most effective means for large-scale utilization. However, due to the relatively low strength of CDW recycled materials, their application in civil construction projects has been limited [3,4]. Consequently, at this stage, the primary applications of CDW are as roadbed fillers [5,6], asphalt concrete [7], and roller-compacted concrete [8]. Among these, roadbed fillers have the least stringent requirements [9–11], allowing CDW to be used directly without additional processing. Therefore, CDW is more extensively employed as a roadbed filler [12–14].

The mechanical properties of CDW recycled materials, primarily concrete and bricks, differ significantly from those of natural fillers. These materials exhibit water absorption rates as high as 12% to 20% [15,16], which can lead to technical issues such as inadequate compaction of the roadbed and fluctuating California Bearing Ratio (CBR) values when used as a roadbed filler. Previous studies have focused on macroscopic tests, including compaction and shear properties [17,18], ratio optimization [19], elastic modulus characteristics [20], CBR [21], freeze-thaw cycling performance [22], water resistance [23], and long-term deformation behavior under laboratory conditions [24]. In practical applications, some case studies have summarized the long-term settlement characteristics and internal temperature and humidity changes in CDW-filled roadbeds based on field monitoring methods [25,26]. The results of these studies indicate that using recycled CDW materials as roadbed filler has disadvantages such as unstable compaction properties and significant influence from temperature and humidity variations, which hinder large-scale application. However, from an economic and environmental perspective, utilizing CDW recycled materials as roadbed filler reduces road construction costs while addressing the issue of CDW stockpiling [27].

The key factor contributing to the instability of the mechanical properties of CDW roadbed filler is the breakage characteristics of particles. This material is prone to secondary crushing under dynamic loading, leading to dynamic changes in gradation [28]. However, the regulatory mechanism by which microstructural characteristics and service behavior of CDW recycled materials influence their macroscopic mechanical properties remains unclear. Huang et al. [29] combined repeated loading triaxial tests with discrete element analysis to reveal the force chain transfer process between particles at a meso-scale and established a long-term settlement prediction model. Nevertheless, the discrete element analysis did not account for the breakable characteristics of the particles. Ding et al. [30] proposed a crushing assessment system for CDW aggregates based on fractal dimension and relative crushing rate, using vibratory compaction test (VCT) and compaction test (CT) molding methods. Their results showed that the fractal dimension increases with input energy, and larger initial particle sizes exhibit more pronounced fractal characteristics. The permanent deformation of the specimen is exponentially correlated with the crushing rate. At a single particle size, vertical strain is dominated by particle rearrangement at low energies (below 2 kJ), while crushing becomes dominant at medium to high energies (2–6 kJ). The strain of recycled brick aggregate exhibits 40% higher sensitivity to particle size compared to concrete [31]. The strong discrete nature of particle morphology exacerbates the formation of anisotropic structures. Straight shear tests confirmed that the normal vectors of contact surfaces of irregularly shaped particles show an obvious non-uniform distribution [32]. Some scholars have focused on the breakage of CDW fillers using DEM simulation methods [33,34]. Oskooei et al. [35] established a DEM model to analyze the breakage behavior and fracture energy of recycled brick aggregates. The tensile strength of recycled brick aggregates depends on the shape and size of the particles. Wang et al. [36] proposed a novel DEM method to reveal the breakage mechanisms of mixture recycled mortar, recycled brick and natural gravel. The recycled brick aggregates showed an easier trend to break compared with natural gravel and recycled mortar. These findings from the meso-scale provide new insights into the reconfiguration mechanisms of the force chain network during the crushing process. However, further research is required to fully understand the crushing behavior of CDW mixed fillers under compaction, particularly in conditions involving differential strength among recycled aggregate particles.

The CDW aggregates have been widely utilized in roadbed filler, but their crushing performance is significantly influenced by the mixing ratio and grading during the force-crushing process. Currently, the combination of experimental methods and discrete element

simulations has emerged as the predominant approach for investigating the properties of geotechnical granular materials [37–39]. Therefore, based on previous publications, the crushing mechanisms of CDW mixed fillers under compaction remain poorly quantified, particularly how differential strength between concrete and brick aggregates regulates force chain redistribution and breakage stages. Existing DEM models fail to capture the hybrid effects of particle shape, size, and strength heterogeneity on compaction-induced breakage patterns. To address these gaps, in this study, the particle crushing characteristics of CDW mixed roadbed fillers are investigated through three principal advancements grounded in meso-scale analysis. First, dynamic compaction loading is explicitly simulated to replicate field construction conditions, with particle breakage mechanisms being analyzed under cyclic energy inputs—a departure from conventional static models. Second, hybrid concrete-brick systems are systematically evaluated, where the influence of mixing ratios on breakage index is quantitatively established for multi-component CDW aggregates, addressing prior oversights in heterogeneous mixture behavior. Third, fine particle breakage is modeled through a multi-scale DEM framework, wherein both coarse fractions and fines are integrated, overcoming limitations of earlier studies restricted to coarse-grained simulations. Firstly, indoor compaction tests were conducted on different proportions of CDW mixed filler to analyze the changes in fractal dimension under varying mixing ratios. Then, using the random polyhedron model, a clump discrete element model was constructed, accounting for differences in the crushing characteristics of various particle components. This model was used to analyze the variation rules of internal porosity, particle count, and other parameters during compaction. Consequently, this approach reveals the force chain transfer and particle size effects during the compaction and crushing of CDW materials from a meso-scale viewpoint.

2. Materials and Methods

2.1. Raw Materials

The CDW raw materials tested in this study were collected from Xuzhou, China. The main components included waste concrete and waste brick. The collected waste concrete and waste bricks were crushed into different particle sizes, respectively. A standard sieve was employed to screen the crushed concrete and brick particles. Following the screening process, the particles were categorized into seven size ranges: 31.5 mm to 19 mm, 19 mm to 9.5 mm, 9.5 mm to 4.75 mm, 4.75 mm to 2.36 mm, 2.36 mm to 0.6 mm, 0.6 mm to 0.075 mm, and less than 0.075 mm. Based on the particle size distribution curve presented in Figure 1, the concrete and brick fragments were processed into standard graded recycled aggregates, respectively. Table 1 provides the density and water absorption characteristics of the graded waste concrete and brick recycled aggregates.

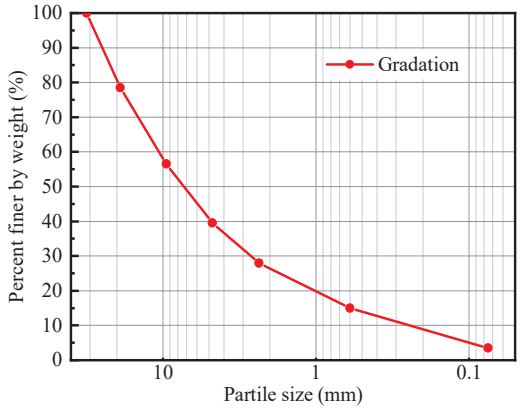

Figure 1. Grading curve of waste concrete and brick recycled aggregates.

Table 1. Basic physical properties of raw materials.

Raw Materials	Apparent Density (g/cm^3)	Packing Density (g/cm^3)	Water Absorption Rate (%)
Waste concrete recycled aggregate	1.32	2.32	6.9
Waste brick recycled aggregate	0.81	1.74	23.1

2.2. Compaction Test

The maximum dry density and optimum moisture content of CDW fillers under different mixture proportions were determined by compaction test, respectively, referenced from the Test Standards of soils in Highway Engineering (JTG 3430–2020) [40]. The mixing ratios for each group of CDW fillers were listed in Table 2. The volumetric and weight ratios were converted according to the packing density of recycled concrete aggregates and recycled brick aggregates, respectively, before the tests. An electric compaction device was utilized to compact the CDW mixtures in a heavy-duty compaction drum (150 mm diameter × 120 mm height). The tests were conducted following the Chinese standard Test Standards of Soils in Highway Engineering (JTG 3430–2020) to determine the optimal moisture content and maximum dry density. Preliminary tests were first performed to estimate the approximate optimal moisture content range for each mixture ratio. Subsequently, five compaction tests were conducted for each mixture, with the moisture content incrementally increased by 1% in each test. Each layer was struck 98 times, with the hammering points evenly distributed across the soil surface, ensuring that the compacted material did not exceed the top of the drum by more than 6 mm. The compaction effort applied was 2684.9 kJ/m^3.

Table 2. Mixing ratio of CDW filler (weight %).

Group Number	Waste Concrete Recycled Aggregate	Waste Brick Recycled Aggregate
G1	100	0
G2	90	10
G3	80	20
G4	70	30
G5	60	40
G6	50	50
G7	0	100

2.3. Sieve Test After Compaction Test

After the compaction test, the specimens were placed in a drying oven and dried to a constant weight at 105 °C. The dried specimens were subsequently broken into a loose condition using a wooden hammer and sieved through a vibrating screen to obtain particle size distributions across seven grades, including 31.5 mm to 19 mm, 19 mm to 9.5 mm, 9.5 mm to 4.75 mm, 4.75 mm to 2.36 mm, 2.36 mm to 0.6 mm, 0.6 mm to 0.075 mm, and less than 0.075 mm. These distributions were used to analyze the changes in particle size of CDW fillers before and after compaction under different mixing ratios.

2.4. Discrete Element Method Simulation of Compaction Test

2.4.1. Numerical Model

In this study, PFC^{3D} software was utilized to simulate the compaction process of CDW mixed filler. Since the base particle units in PFC^{3D} are unbreakable rigid particles, it is not feasible to directly simulate the compaction process while considering particle crushing conditions. Currently, two primary methods are employed for simulating particle crushing: direct compression of large particles and the bonded particle model (BPM) [41]. In this

study, the BPM method was adopted to simulate CDW particles. The linear parallel bond model not only transmits the tensile and tangential forces but also the bending moment. The BPM model bundles several or dozens of particles together rather than modeling them individually. When the bonds between these basic particle units break, the particles are considered to have fractured.

Previous studies have categorized particles with sizes larger than 4.75 mm as coarse aggregates and those smaller than 4.75 mm as fine aggregates [30]. From the perspective of particle crushing, fine aggregates exhibit a lower crushing rate compared to coarse aggregates [42,43]. In discrete element method (DEM) simulations, an excessive amount of fine aggregate significantly increases the number of particles, thereby reducing computational efficiency. However, fine aggregates constitute a significant proportion of the mixture and play a crucial role in filling voids within the mix. To balance computational speed and accuracy, especially given this study's focus on the particle crushing process, particles smaller than 0.6 mm were excluded from the simulation, with their proportion redistributed into the 0.6 mm to 4.75 mm size range. In the DEM model, particles are classified into two categories: recycled concrete particles and recycled brick particles. Both types are modeled using clump particles with random polyhedral shapes. To simplify the model, particles with sizes smaller than 4.75 mm were simulated using spherical clump particles rather than random polyhedra. This approach reduced computational demand while still effectively simulating the crushing behavior of fine aggregates. The gradation composition was identical for both materials: 21.5% of the particles fell within the 31.5 mm to 19 mm size range, 22% within the 19 mm to 9.5 mm range, 17% within the 9.5 mm to 4.75 mm range, and 39.5% within the 4.75 mm to 0.6 mm range.

Firstly, a cylindrical wall with a height of 17 mm and a diameter of 15.2 mm was built. Clump particles of specific sizes and numbers were then generated between the walls and arranged in three layers from bottom to top according to the specified particle size distribution. The positions and sizes of the large particle units were recorded using the FISH. In their original positions, the large particle units were regenerated from basic particle units to form the original large particle size, and the newly generated particle units were updated with the appropriate parameter values. Finally, the self-balancing procedure was executed to ensure that the discrete element model reached a self-balanced state. The established three-dimensional discrete element model is shown in Figure 2.

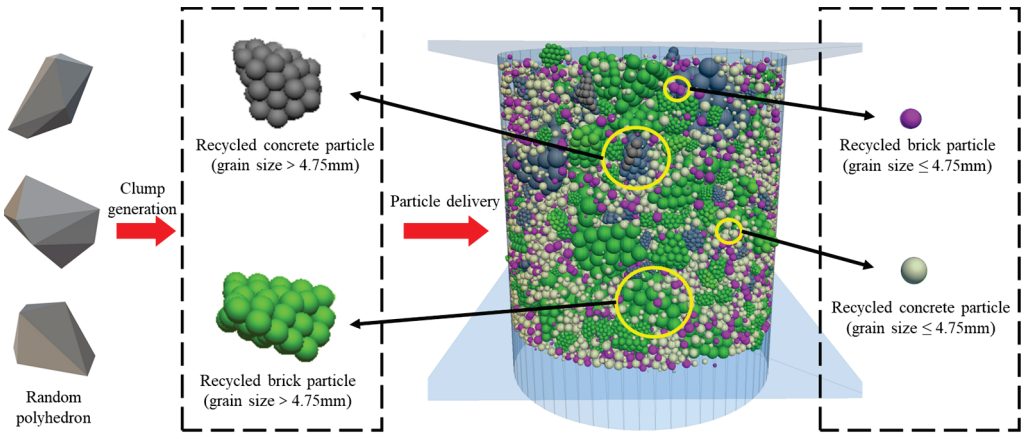

Figure 2. The modeling process of the DEM model.

2.4.2. Contact Models and Parameter Calibration

In the DEM model, contact properties were assigned to recycled concrete particles and recycled brick particles, respectively. For both materials, the parallel bond contact model (PB) was selected, allowing for disconnection between base particle units. However,

the fine-scale parameters of the particle contact model cannot be set directly and require calibration based on test results. For recycled concrete particles, the test result of group G1 was used for calibration. Initially, preliminary fine-scale parameters were set according to previous research [30]. Parameter analysis was conducted in the DEM model using equidistant variations to assess the impact of each parameter on the crushing rate. The particle crushing rate was then calculated based on changes in the fractal dimension of recycled concrete particles before and after the compaction test. The calculated crushing rate served as the target value, and the model was calibrated using a trial-and-error approach to obtain the fine-scale parameters of the recycled concrete particle model. Similarly, the test result of group G7 was used to calibrate the fine-scale parameters of the recycled brick particle model. The calibrated fine-scale parameters for both models are summarized in Table 3.

Table 3. Parameters of DEM model.

Samples	Effective Modulus (MPa)	Cohesion (MPa)	Tensile Strength (MPa)	Friction Angle (°)
Recycled waste brick particles	100	0.4	0.3	23
Recycled waste concrete particles	200	10	8	25

2.4.3. Load Application Method and Data Monitoring

The compaction effort is applied to the specimen using a compaction hammer in the compaction test. In this study, a block was constructed to simulate the compaction hammer and apply the compaction effort to the CDW mixed filler model. To simplify the calculations, the compaction effort was applied uniformly to the upper surface of the model specimen after all particles were positioned. The cumulative number of compaction was 98, and the total compaction effort was 2684.9 kJ/m^3.

The compressive deformation of the specimen under compaction, the particle fragmentation rate, and the development of inter-particle fissures need to be monitored. Recycled concrete particles and recycled brick particles were generated by the basic particles through bonds to form large particles. During compaction, these bonds break, causing the basic particle units to develop cracks and gradually detach from the larger units, leading to fragmentation. Therefore, monitoring the number of bond changes during compaction can reflect the degree of particle fragmentation. Additionally, tracking the evolution of cleavage development between the basic particle units is crucial for understanding the fine-scale mechanisms of granular crushing.

3. Results and Analysis

3.1. Impact of Mixing Ratio on Optimum Moisture Content and Maximum Dry Density of CDW Fillers

The optimum moisture content and maximum dry density of CDW filler with different mixture ratios obtained from the compaction tests were demonstrated in Figure 3. As shown in Figure 3, the optimum moisture content generally increased with the proportion of recycled brick particles. This trend can be attributed to the significantly higher water absorption capacity of recycled brick particles compared to recycled concrete particles. The maximum dry density initially increases and then decreases as the proportion of brick particles rises, reaching a peak value of 1.93 g/cm^3 at an optimal mixing ratio (G3 group). This variation in maximum dry density is closely related to the structural characteristics of the CDW mixed filler. Specifically, the higher strength of recycled concrete particles relative to recycled brick particles means that the latter are more susceptible to crushing

during compaction. Crushed brick particles can fill the voids between concrete particles, promoting the formation of a dense skeleton structure. However, when the proportion of recycled brick particles becomes excessive, the increased moisture content enhances the wetting effect on these particles, leading to easier fragmentation. In this case, the reduced quantity of recycled concrete particles cannot adequately support the formation of a robust skeleton structure, thereby diminishing the overall densification of the CDW mixed filler and resulting in a lower dry density. Recycled brick aggregates exhibit high water absorption (exceeding 20%), while recycled concrete aggregates have significantly lower absorption (typically below 10%). Consequently, increasing the proportion of brick aggregates in the mixture elevates the system's overall water demand, thereby shifting the optimal moisture content to higher values.

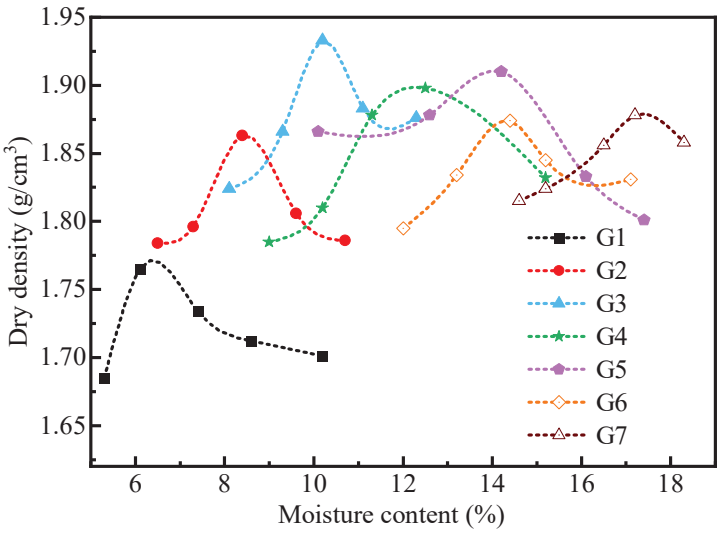

Figure 3. Moisture content–dry density curve of CDW filler with different mixture ratios.

3.2. Variation in Fractal Dimension and Particle Breakage Index of CDW Fillers Before and After Compaction Test

During the compaction process, some of the particles in the CDW filler were crushed by the compaction effort, resulting in a reduction in particle size and a change in the overall particle size distribution when the crushing rate exceeded a certain threshold. Figure 4 illustrates the changes in particle size distribution of CDW filler before and after compaction under different mixing ratio conditions. The grading curve of recycled brick aggregates exhibited a more pronounced upward trend compared to that of recycled concrete aggregates, indicating greater fragility. Specifically, particles larger than 4.75 mm showed the most significant changes in distribution. Conversely, the gradation curve of recycled concrete aggregates exhibited a smaller overall rise, indicating their higher resistance to fragmentation. Both recycled materials experienced the largest percentage mass loss in the 19 mm to 31.5 mm particle size range, at −7.5% for recycled concrete particles and −17.5% for recycled brick particles. However, the two recycle aggregates exhibited different characteristics in terms of mass gain across various grain size ranges. Recycled brick particles showed the highest mass gain in the 4.75 mm to 9 mm range with a 20% increase, whereas recycled concrete particles had their maximum mass gain in the 0.075 mm range with a 7.5% increase. Recycled concrete particles showed higher particle strength than recycled brick particles and were less likely to undergo overall fragmentation under compaction effort, resulting in increased breakage index and a higher content of fine particles. Recycled brick particles had lower particle strength and easier to overall fragmentation, particularly for larger particles. Larger brick particles tend to fragment

more easily, leading to an increase in the number of medium-sized particles [25,33]. For the mixed CDW fillers, their particle size curves after compaction are similar, except for the particle size range of 2.36 mm to 9 mm. Compared with the recycled concrete particle filler, the addition of recycled brick particles increases the degree of change in the particle size distribution curve. In the 9.5–19 mm and 4.75–9.5 mm particle size ranges, the percentage of mass change for each group generally increased. For particles within these two size ranges, initial mass loss can be attributed to the fragmentation of larger particles. The combined effects of mass loss and mass gain within these ranges result in a relatively small net change in the percentage of mass change.

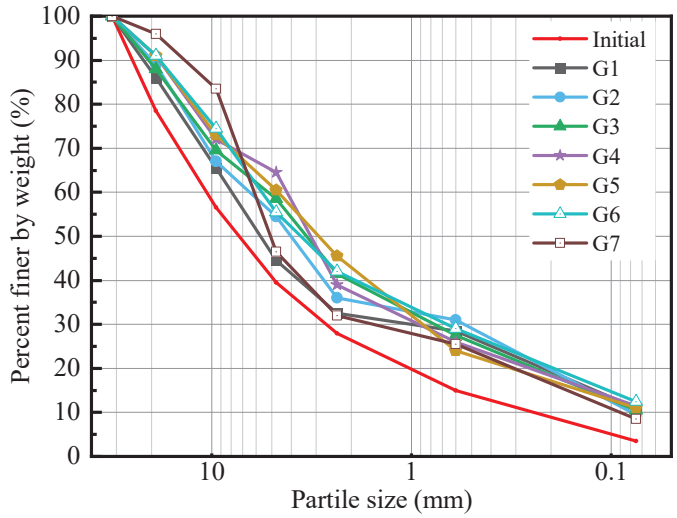

(**a**)

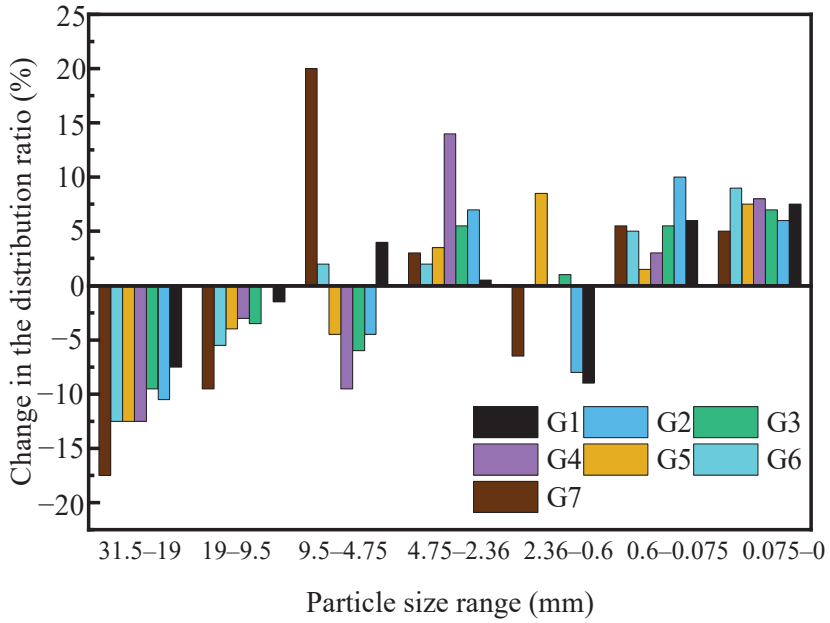

(**b**)

Figure 4. Changes in particle size distribution before and after compaction, (**a**) grading curve of CDW filler under different mixing ratio conditions, (**b**) change in the distribution ratio of different particle size ranges.

To better understand the particle breakage characteristics of CDW mixed fillers, the relative breakage index calculation method (Equation (1)) proposed by Hardin was employed to estimate the overall fragment behavior of CDW fillers under different mixing ratio conditions [44,45].

$$B_r = \frac{B_t}{B_p} \tag{1}$$

where B_r represents the relative particle breakage index; B_t represents the area between 0.075 mm and 31.5 mm on the gradation curve before the compaction test; B_p represents the area between the initial particle size distribution curve and the post-test particle size distribution curve.

The results of the relative particle breakage index are shown in Figure 5. According to the estimation results, the relative particle breakage index of recycled concrete particles under compaction was approximately 24%, while that of recycled brick particles reached approximately 70%. However, the relative particle breakage index of the mixture of CDW fillers exhibited a non-linear increase with the rise in brick particle content.

The G5 group exhibited a peak crushing rate of approximately 55%, whereas the G6 group (approximately 53%) was slightly lower. This phenomenon may be attributed to two potential reasons. For the first reason, larger recycled brick particles are fragmented and filled into the void spaces formed by the extrusion of recycled concrete particles, thereby protecting the low-strength particles from further breakage within the high-strength skeleton formed by the concrete particles. For another potential reason, the method used to estimate the relative particle breakage index showed limitations when applied to mixed aggregates with significant differences in particle strength, leading to calculating errors in the results. Therefore, to further analyze the meso-scale breakage characteristics of mixture CDW fillers, this study employed the relative particle breakage indices of recycled concrete particles and recycled brick particles to calibrate the DEM model for these two types of particles.

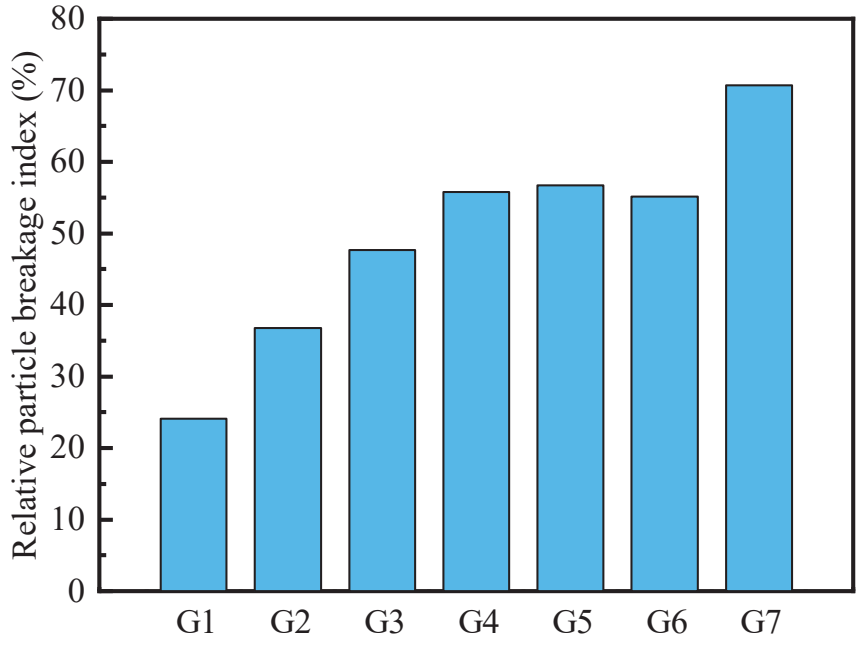

Figure 5. Particle breakage index of CDW filler under different mixing ratio conditions.

3.3. Meso-Scale Analysis of Compression Deformation During Compaction

During the compaction process, particles within the sample gradually transition from a dispersed distribution to a state of mutual extrusion, with the void spaces between

particle units progressively decreasing. The contact forces between particle units also increase, causing the edges of the particles to extrude and begin fragmenting. Based on the established DEM model for mixture CDW fillers, the vertical displacement of the block units during compaction was extracted to calculate the compression deformation of the CDW filler model as compaction effort increased during the simulation process (see Figure 6).

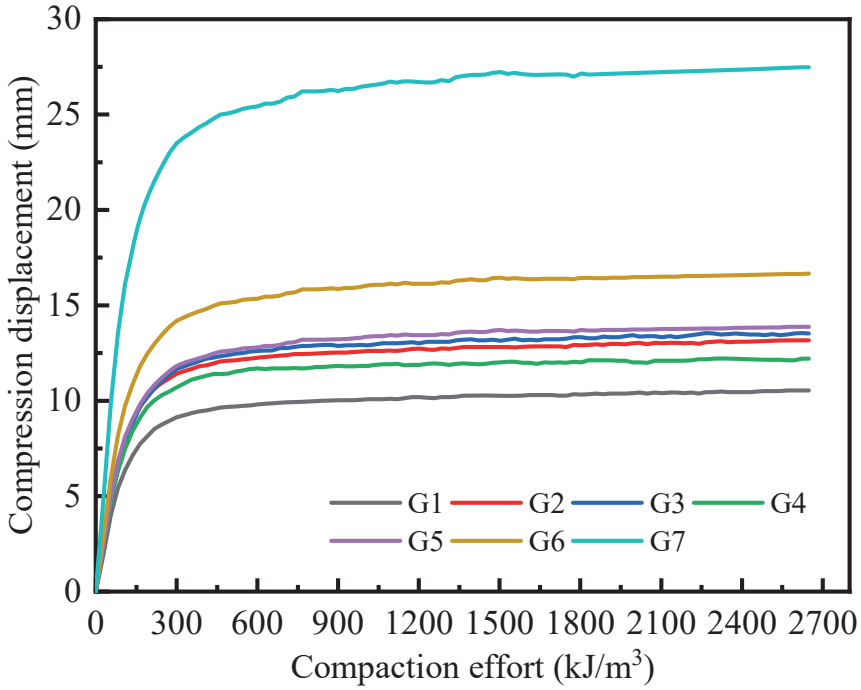

Figure 6. Compression displacement curves of CDW filler during compaction under different mixing ratio conditions.

As shown in Figure 6, the compressive deformation of each group of specimens exhibited a trend of gradually decreasing increments as the compaction work increased. Previous DEM simulations have shown that the compressive deformation of the mixture system increases approximately linearly with increasing load [45]. However, in this study, the DEM simulation results revealed that the compaction deformation of CDW filler under the influence of compaction work could be divided into three distinct stages. In the first stage, the vertical deformation of CDW fillers increased linearly with the increase in compaction work. This stage typically occurs below 200 kJ/m^3 and can be attributed to particle rearrangement accompanied by preliminary extrusion-induced crushing. In the second stage, the vertical deformation rate of the specimens began to decrease, and the curve displayed an obvious inflection point, which generally occurred within the range of 200–500 kJ/m^3. During this stage, recycled concrete particles started forming a stabilizing force chain structure, significantly reducing the specimen's compressibility potential. In the third stage, the vertical deformation of the specimens tended to stabilize but still exhibited a slight upward trend with increasing compaction energy. This stage usually occurred at compaction efforts exceeding 500 kJ/m^3, where the source of compression deformation was primarily attributed to particle fragmentation. Under equal compaction work conditions, recycled brick filler demonstrated the largest compression deformation, with cumulative compression deformation reaching 27 mm—approximately three times that of recycled concrete aggregate (G1 group). Additionally, the inflection point of the compression deformation curve for recycled concrete aggregate appeared earlier than that for recycled brick aggregate. When recycled concrete particles were progressively replaced by recycled

brick particles, the compression deformation of the mixture CDW filler increased. Notably, the sample in the G4 group exhibited the lowest compression deformation compared to other mixing ratios, despite having a 30% brick content. Conversely, mixture CDW fillers with 10%, 20%, and 40% recycled brick content showed similar compression deformation characteristics. However, when the content of recycled brick particles in the mixture CDW filler exceeded 40%, the compression deformation increased rapidly. This indicates that a stable skeletal structure did not form with a minor content of recycled concrete particles. The stabilization of the skeletal structure occurs only after significant compression deformation, which results in increased fragmentation of recycled brick particles.

Figure 7 illustrates the characteristics of the internal contact force chains in each group of samples after compaction. During the compaction process, the transmission of contact forces within the model occurred through point-to-point interactions. The transmission paths were influenced by particle size distribution and porosity, leading to non-uniformity in the force chain networks. After compaction, the bonding keys of the contact force chains on the surface of each sample group were disrupted. However, in groups with higher proportions of recycled concrete particles (G1, G2, G3, and G4), a number of intact contact force chains remain visible. As the proportion of recycled concrete particles decreases in the mixed CDW filler, the number of stable force chains diminishes. When the content of recycled brick particles exceeds 40% (G5, G6, and G7), larger internal contact force chains nearly vanish. This indicates that an excessive proportion of recycled brick particles inhibits the formation of contact force chains typical of recycled concrete particles and exacerbates the fracture of bond bonds in the contact force chains of recycled brick particles, thereby increasing the compressive deformation of the samples. On the other hand, the particle contact force chain in the compacted sample can be categorized into two types: compression and tension. For the recycled brick aggregates (G7 group), the tensile contact force chains were nearly imperceptible, whereas they were generally observable in samples containing recycled concrete aggregates. The formation of a tensile contact force chain can be attributed to the splitting effect exerted by recycled concrete aggregates on recycled brick aggregates. Although the skeletal structure formed by recycled concrete particles enhances stability, the particles contributing to this skeletal structure are typically the higher-strength portions of recycled concrete particles. For some recycled concrete particles and recycled brick particles located between these skeletal structures, a non-uniform extrusion effect arises, inducing a tensile state in the contact force chains of certain particles.

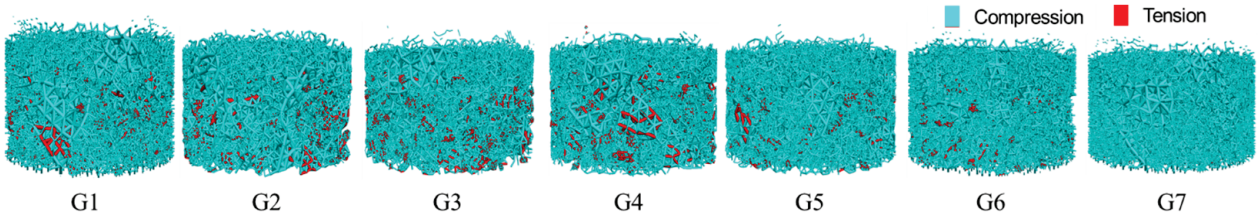

Figure 7. Contact force chains of compacted CDW fillers under different mixing ratio conditions.

3.4. Meso-Scale Analysis of Particle Breakage Characteristics

Figure 8 illustrates the spatial distribution characteristics of fractures in each group of samples after compaction. The fragmentation of recycled concrete aggregates (G1 group) exhibited significant aggregation characteristics, with most fractures appearing in the upper half of the sample (approximately 2/5 of the sample height). As depth increased, the fragmentation effect caused by compaction effort on recycled concrete aggregates became increasingly limited. Concrete particles at the bottom maintained body integrity. Influenced by the skeletal structure, stress was highly concentrated along the force chain network

at the particle contact ends. The fracture distribution characteristics revealed that tooth edge contacts were observed to fragment first, leading to an increase in the content of fine particles below 4.75 mm in the compacted sample. The fracture propagation direction was generally consistent with the force chain path, thereby demonstrating directional breakage characteristics under the constraint of the skeletal structure. The recycled brick aggregates (G7 group) showed a completely different breakage mode, mainly body fragmentation. The internal defects of the recycled brick aggregates caused local stress concentration, which led to the initiation of fractures at the edges of the pores and their rapid inward expansion. According to the distribution characteristics of fractures, the breakage of a single aggregate generally produced two to five smaller particles. Under the action of compaction effort, the recycled brick aggregates were uniformly fragmented from top to bottom; however, the surface recycled brick aggregates failed to form a stable skeleton structure. In the mixed system, the breakage characteristics of the particles changed, with fragmentation occurring more frequently at the contact surface between recycled concrete and recycled brick aggregates. The recycled concrete aggregates squeezed the recycled brick aggregates, forming a stress concentration zone. Under the same compaction effort, the number of internal fractures in recycled brick aggregates was approximately three times that of recycled concrete aggregates. However, as the proportion of recycled brick aggregates in mixed CDW fillers increased, the number of internal fractures exhibited a non-linear growth trend. When the content of recycled brick aggregates exceeded 30%, the growth rate accelerated. The fragmentation of recycled brick aggregates consumed compaction energy, while their preferential breakage helped protect the concrete skeleton. A reasonable mixing ratio reduced the breakage index in key areas (G4 group) and promoted the formation of a dense skeleton structure.

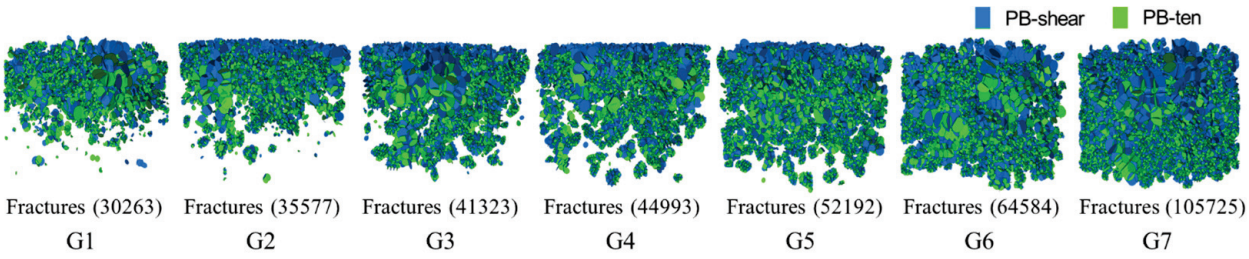

Figure 8. Fracture distribution characteristics of CDW filler under different mixing ratio conditions.

Figure 9 demonstrates the variation pattern of particle breakage rate during compaction effort application. The breakage index curve exhibited a three-stage development characteristic that mirrored the compression deformation behavior. In the primary stage, the breakage index increased linearly. Wang et al. [36] demonstrated that brick content directly governs the breakage rate of mixed systems, with rates ranging between 45–65% when brick proportions exceed 50%. Our results align closely with this observation. The proportion of recycled brick aggregates in the mixed CDW filler affected the interval of the linear growth stage [46]. Each 10% increment in recycled brick aggregate content delayed the linear growth tendency threshold by approximately 8 kJ/m^3. For the mixed system, the average linear growth stage occurred within the range of 0 to 200 kJ/m^3. The breakage index during the linear growth stage accounted for approximately 50% of the total breakage index after compaction. The secondary stage featured curvilinear deceleration, indicating that the growth rate of the breakage index progressively slowed down. This stage contributed 38% to cumulative fragmentation. For the mixed system, the average slow growth stage occurred within the range of 200 to 1000 kJ/m^3. The tertiary stage manifested brick-dependent pseudo-linearity: systems with higher brick content displayed enhanced residual fragmentation potential. For the mixed system, the average linear slow growth

stage occurred between 1000 and 2684.9 kJ/m^3. The maximum crushing rate during the tertiary stage reached approximately 12% of the total crushing rate after compaction.

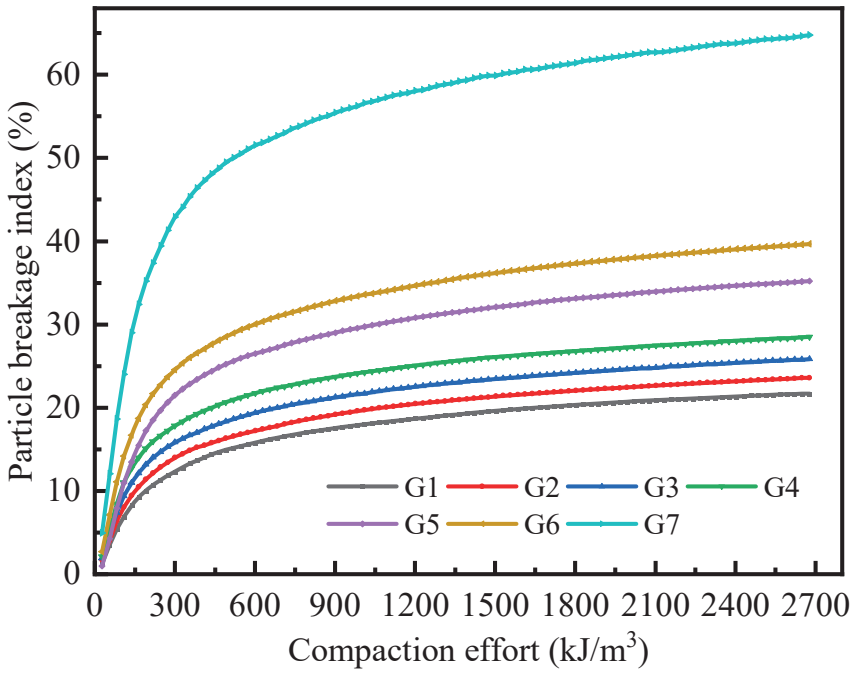

Figure 9. Particle breakage index curves of CDW filler during compaction under different mixing ratio conditions.

The correlation between the amount of compression deformation during compaction and the particle breakage index for each group of specimens is presented in Figure 10. Based on the fitted results in Figure 10, the compressive deformation of the samples during compaction exhibits an approximately exponential relationship with the particle breakage index. These fitted curves exhibited a distinct two-stage characteristic. In the first stage, which was linear, the particle breakage index increased steadily with increasing compression deformation. However, as the content of recycled brick aggregates increased, a larger compression deformation was required. This stage corresponds to the uniform fragmentation of surface particles and the redistribution of particle distribution. Under the application of compaction effort, the voids between particles were compressed, leading to energy absorption and breakage of surface particles. Meanwhile, the vibration facilitated the gradual filling of voids between coarse aggregates by fine particles, thereby forming a dense structure. The second stage was characterized by exponential growth dynamics, where the particle breakage index escalated sharply with increasing compression deformation, despite the relatively limited deformation magnitude observed. Specifically, for recycled concrete particles (G1 group), the deformation reached only approximately 3 mm, while the breakage index increased by 15%. Notably, the inclusion of recycled brick particles significantly extended the range of compression deformation in this stage and amplified the breakage index increase, particularly when the recycled brick aggregate content exceeded 30%. This stage marked the progressive formation of a force chain network, facilitating the transfer of energy to deeper particles and indicating a transition from void compression and surface crushing to internal particle fracturing. Upon the establishment of the force chain network, deeper particles began compressing against one another, generating localized stress concentrations. In systems containing recycled brick particles, part of the compaction energy was dissipated through brick particle crushing, which contributed to the stabilization of the force chain network.

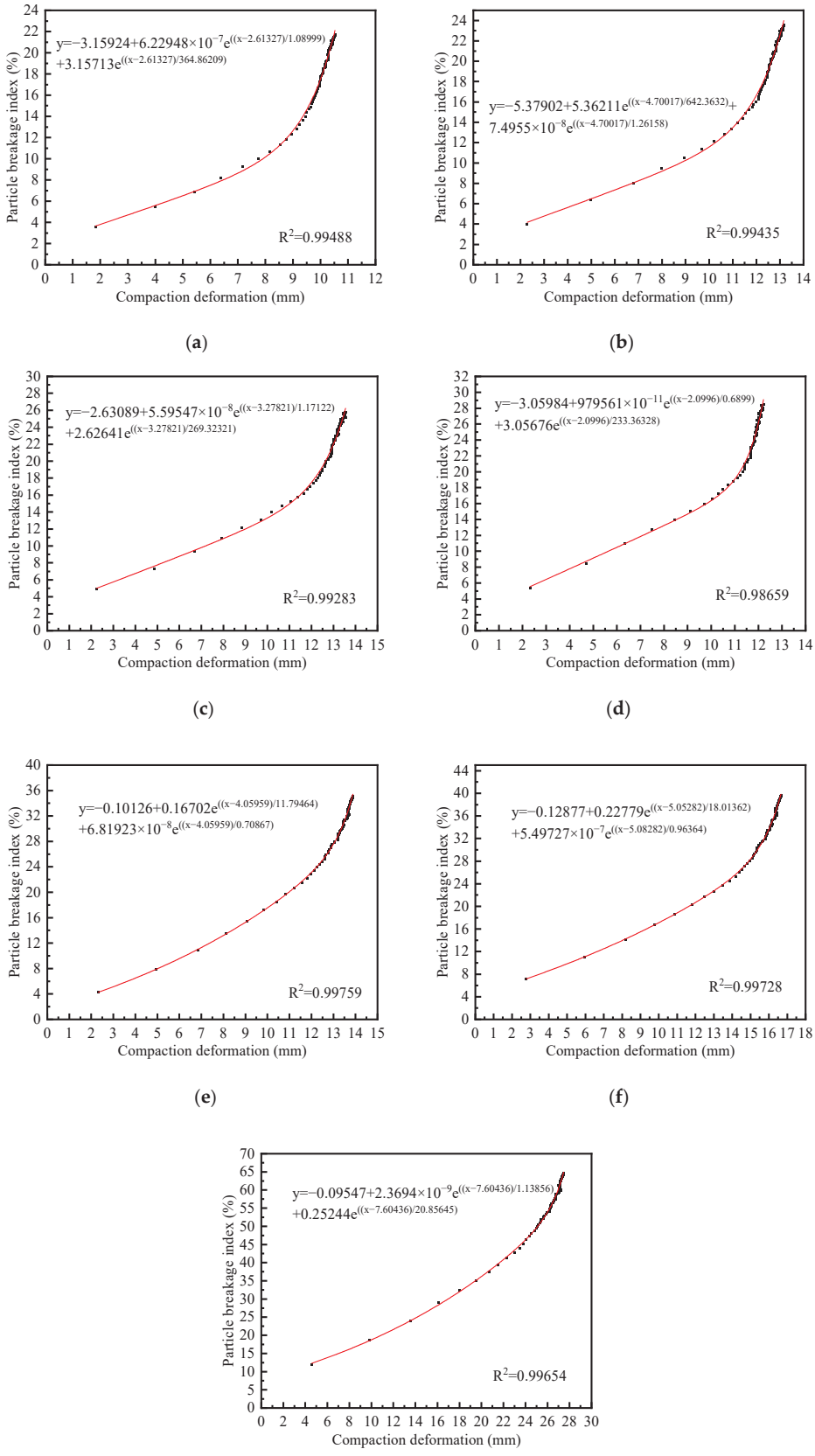

Figure 10. Correlation between compaction deformation and particle breakage index: (**a**) G1 group; (**b**) G2 group; (**c**) G3 group; (**d**) G4 group; (**e**) G5 group; (**f**) G6 group; (**g**) G7 group.

4. Conclusions

The instability of mechanical properties in CDW roadbed filler is predominantly governed by particle breakage under compaction. Through standardized laboratory tests and DEM simulations, this study elucidates the crushing mechanisms of mixed CDW fillers comprising recycled concrete and brick aggregates. The primary findings are as follows:

(1) A discrete element model was developed to characterize breakable particles: polygonal clumps simulated irregularly shaped fragments (>4.75 mm), while spherical clumps represented finer fractions (<4.75 mm). This model successfully captured the interplay between particle shape, size-dependent breakability, and force chain evolution during compaction, providing a mesoscale perspective on the reconfiguration of CDW skeletal structures.

(2) The optimal mixture ratio of 70% recycled concrete and 30% recycled brick aggregates emerged as a critical balance between mechanical performance and structural stability. Recycled concrete aggregates formed a load-bearing skeleton that restricted deep crack propagation but limited compaction density under dynamic loading. In contrast, brick aggregates enhanced densification through energy dissipation during fragmentation and subsequent void filling by crushed fines. However, exceeding 30% brick content disrupted the concrete skeleton, leading to unstable gradation. Experimental and numerical results demonstrated that the 7:3 mixture achieved peak dry density, reduced compression deformation by 25% compared to concrete-only filler, and controlled the breakage index rise within 25%, highlighting its engineering viability.

(3) Particle breakage evolution under compaction was classified into three distinct stages. The linear fragmentation stage (0–200 kJ/m^3) accounted for 50% of total breakage, dominated by rapid brick particle crushing. In the decelerated growth stage (200–1000 kJ/m^3), breakage slowed to 38% as the concrete skeleton resisted further fragmentation. Finally, the residual crushing stage (>1000 kJ/m^3) contributed only 12% breakage, reflecting a stabilized particle arrangement. These findings quantitatively link compaction energy thresholds to breakage mechanisms, offering actionable insights for optimizing CDW roadbed design.

This study primarily focused on the laboratory-scale compaction behavior of CDW mixtures under controlled conditions. While the DEM model captures key breakage mechanisms, its validation relies on simplified particle shapes and homogeneous material properties, potentially underestimating real-world heterogeneity. Additionally, the CDW aggregates were sourced from a single regional waste stream; variations in brick/concrete composition across demolition sites may influence crushing patterns. Future research should prioritize field validation of the optimal 7:3 mix ratio in actual roadbeds to assess long-term performance under traffic loads and environmental fluctuations, and systematic evaluation of CDW sourced from diverse origins to establish universal design guidelines.

Author Contributions: L.H.: Conceptualization, Methodology, Investigation, Formal analysis, Writing—Original Draft. W.G.: Conceptualization, Methodology, Investigation, Data curation, Writing—Review and Editing. Y.T.: Investigation, Formal analysis. L.L.: Reviewing, Resources, Visualization. All authors have read and agreed to the published version of the manuscript.

Funding: (1) Transportation Engineering (Henan Provincial Key Discipline), Huanghe Jiaotong University. (2) Henan Provincial Key Research Project in Higher Education Institutions: Heat-Mass Transfer Evolution in Subgrade under Traffic Loading & Polymer Grouting Toughness Improvement. (3) "Basic Principles of Concrete Structures" First-class Course at Huanghe Jiaotong University (NO. HHJTXY-2022ylkc41).

Institutional Review Board Statement: Not applicable.

Informed Consent Statement: Not applicable.

Data Availability Statement: The datasets supporting the findings of this study are currently in a confidential phase due to intellectual property protection considerations. Key processed parameters, including particle breakage rates, aggregate gradations, and compaction energy inputs, are available in Tables 1–3 and Figures 1–10 of this article. Researchers demonstrating academic needs may contact the corresponding author to request access to specific datasets under non-disclosure agreements.

Conflicts of Interest: The authors declare that they have no known competing financial interests or personal relationships that could have appeared to influence the work reported in this paper.

References

1. Behera, M.; Bhattacharyya, S.K.; Minocha, A.K.; Deoliya, R.; Maiti, S. Recycled aggregate from C&D waste & its use in concrete—A breakthrough towards sustainability in construction sector: A review. *Constr. Build. Mater.* **2014**, *68*, 501–516.
2. Gkyrtis, K.; Pomoni, M. An Overview of the Recyclability of Alternative Materials for Building Surface Courses at Pavement Structures. *Buildings* **2024**, *14*, 1571. [CrossRef]
3. Tabsh, S.W.; Abdelfatah, A.S. Influence of recycled concrete aggregates on strength properties of concrete. *Constr. Build. Mater.* **2009**, *23*, 1163–1167. [CrossRef]
4. Arulrajah, A.; Piratheepan, J.; Disfani, M.M.; Bo, M.W. Geotechnical and Geoenvironmental Properties of Recycled Construction and Demolition Materials in Pavement Subbase Applications. *J. Mater. Civ. Eng.* **2013**, *25*, 1077–1088. [CrossRef]
5. Xue, Y.X.; Arulrajah, A.; Narsilio, G.A.; Horpibulsuk, S.; Chu, J. Washed recycled sand derived from construction and demolition wastes as engineering fill materials. *Constr. Build. Mater.* **2022**, *358*, 129433. [CrossRef]
6. Rondinella, F.; Oreto, C.; Abbondati, F.; Baldo, N. Laboratory Investigation and Machine Learning Modeling of Road Pavement Asphalt Mixtures Prepared with Construction and Demolition Waste and RAP. *Sustainability* **2023**, *15*, 16337. [CrossRef]
7. Lopez-Uceda, A.; Agrela, F.; Cabrera, M.; Ayuso, J.; López, M. Mechanical performance of roller compacted concrete with recycled concrete aggregates. *Road Mater. Pavement Des.* **2018**, *19*, 36–55. [CrossRef]
8. Contrafatto, L.; Cosenza, R.; Barbagallo, R.; Ognibene, S. Use of Recycled Aggregates in Road Sub-base Construction and Concrete Manufacturing. *Ann. Geophys.* **2018**, *61*, S1. [CrossRef]
9. Li, Z.; Lv, S.X.; Liu, L.L.; Guo, J.; Liu, T. Compressive Deformation Characteristics of Sintered Loess after Being Saturated with Water. *Int. J. Geomech.* **2024**, *24*, 04024177. [CrossRef]
10. Li, Z.; Ma, J.; Liu, X.Y.; Liu, L.L.; Cai, G.J.; Peng, L.X.; Xiong, H.B. Exploring the temperature, humidity, and deformation characteristics of gravel replacement foundations in seasonally frozen zones: A model testing study. *Bull. Eng. Geol. Environ.* **2025**, *84*, 141. [CrossRef]
11. Liu, X.Y.; Surya, S.C.C.; Cai, G.J.; Liu, L.L.; Liu, S.Y.; Anand, J.P.; Zhang, W.W. Development and validation of a method to predict the soil thermal conductivity using thermal piezocone penetration testing (T-CPTU). *Can. Geotech. J.* **2022**, *59*, 510–525. [CrossRef]
12. Zhang, J.H.; Gu, F.; Zhang, Y.Q. Use of building-related construction and demolition wastes in highway embankment: Laboratory and field evaluations. *J. Clean. Prod.* **2019**, *230*, 1051–1060. [CrossRef]
13. Vieira, C.S.; Pereira, P.M. Use of recycled construction and demolition materials in geotechnical applications: A review. *Resour. Conserv. Recycl.* **2015**, *103*, 192–204. [CrossRef]
14. Katz, A. Properties of concrete made with recycled aggregate from partially hydrated old concrete. *Cem. Concr. Res.* **2003**, *33*, 703–711. [CrossRef]
15. Poon, C.S.; Shui, Z.H.; Lam, L. Effect of microstructure of ITZ on compressive strength of concrete prepared with recycled aggregates. *Constr. Build. Mater.* **2004**, *18*, 461–468. [CrossRef]
16. Shi, C.L.; Wang, Y.; Wu, C.L.; Song, W.Z. Study on the Mechanical Properties and Design Parameters of Floor Slabs Waste Subgrade Filler. *Adv. Mater. Sci. Eng.* **2022**, *2022*, 4913825. [CrossRef]
17. Melbouci, B. Compaction and shearing behaviour study of recycled aggregates. *Constr. Build. Mater.* **2009**, *23*, 2723–2730. [CrossRef]
18. Park, T. Application of construction and building debris as base and subbase materials in rigid pavement. *J. Transp. Eng.* **2003**, *129*, 558–563. [CrossRef]
19. Barbudo, A.; Agrela, F.; Ayuso, J.; Jiménez, J.R.; Poon, C.S. Statistical analysis of recycled aggregates derived from different sources for sub-base applications. *Constr. Build. Mater.* **2012**, *28*, 129–138. [CrossRef]
20. Nataatmadja, A.; Tan, Y. Resilient response of recycled concrete road aggregates. *J. Transp. Eng.* **2001**, *127*, 450–453. [CrossRef]
21. Zhang, J.H.; Ding, L.; Li, F.; Peng, J.H. Recycled aggregates from construction and demolition wastes as alternative filling materials for highway subgrades in China. *J. Clean. Prod.* **2020**, *255*, 120223. [CrossRef]
22. Li, Z.; Liu, L.L.; Yan, S.H.; Zhang, M.K.; Xia, J.J.; Xie, Y.L. Effect of freeze-thaw cycles on mechanical and porosity properties of recycled construction waste mixtures. *Constr. Build. Mater.* **2019**, *210*, 347–363. [CrossRef]

23. Liu, L.L.; Li, Z.; Cai, G.J.; Liu, X.Y.; Yan, S.H. Humidity field characteristics in road embankment constructed with recycled construction wastes. *J. Clean. Prod.* **2020**, *259*, 120977. [CrossRef]
24. Li, Z.; Yan, S.H.; Liu, L.L.; Dai, B.S.; Dong, W.J. Long-Term Deformation Analysis of Recycled Construction Waste Subgrade Filler. *Adv. Civ. Eng.* **2019**, *2019*, 5891759. [CrossRef]
25. Liu, L.L.; Li, Z.; Cai, G.J.; Geng, X.Y.; Dai, B.S. Performance and prediction of long-term settlement in road embankments constructed with recycled construction and demolition waste. *Acta Geotech.* **2022**, *17*, 4069–4093. [CrossRef]
26. Zhang, J.H.; Zhang, A.S.; Huang, C.; Yu, H.Y.; Zhou, C. Characterising the resilient behaviour of pavement subgrade with construction and demolition waste under freeze-thaw cycles. *J. Clean. Prod.* **2021**, *300*, 126702. [CrossRef]
27. Huang, B.J.; Wang, X.Y.; Kua, H.W.; Geng, Y.; Bleischwitz, R.; Ren, J.Z. Construction and demolition waste management in China through the 3R principle. *Resour. Conserv. Recycl.* **2018**, *129*, 36–44. [CrossRef]
28. Li, Z.; Liu, L.L.; Yan, S.H.; Zhang, M.K.; Xie, Y.L. Properties of microscopic particle morphology and particle contact of renewable construction waste mixtures. *Constr. Build. Mater.* **2019**, *207*, 190–205. [CrossRef]
29. Huang, C.; Zhang, J.H.; Zhang, A.S.; Li, J.; Wang, X.Y. Permanent deformation and prediction model of construction and demolition waste under repeated loading. *J. Cent. South Univ.* **2022**, *29*, 1363–1375. [CrossRef]
30. Ding, L.; Zhang, J.H.; Zhou, C.; Han, S.P.; Du, Q.H. Particle breakage investigation of construction waste recycled aggregates in subgrade application scenario. *Powder Technol.* **2022**, *404*, 117448. [CrossRef]
31. Zhang, J.H.; Liu, K.; Peng, J.H.; Yang, H. Under the Single Particle Size of Subgrade Filling Construction and Demolition Waste Breakage Characteristics. *J. Beijing Univ. Technol.* 2024, *online*.
32. Liang, L.J.; Tong, J.S.; Xu, C.J.; Fan, X.Z. Review on shear strength of construction waste reclamation subgrade fillers. *J. Civ. Environ. Eng.* 2024, *online*.
33. Cil, M.B.; Alshibli, K.A. 3D assessment of fracture of sand particles using discrete elementmethod. *Geotech. Lett.* **2012**, *2*, 161–166. [CrossRef]
34. Yu, Y.; Zheng, Y.; Zhao, X.Y. Mesoscale modeling of recycled aggregate concrete under uniaxial compression and tension using discrete element method. *Constr. Build. Mater.* **2021**, *268*, 121116. [CrossRef]
35. Oskooei, P.R.; Mohammadinia, A.; Arulrajah, A.; Horpibulsuk, S. DEM modeling and experimental analysis of the breakage behavior of recycled crushed brick particles. *Transp. Geotech.* **2021**, *30*, 100586. [CrossRef]
36. Wang, X.M.; Xiao, Y.J.; Li, W.Q.; Chen, Y.L.; Meng, F.W. Assessing particle crushing mechanism and optimizing design for recycled aggregates in road bases via a novel particle crushing DEM method. *Constr. Build. Mater.* **2024**, *438*, 137046. [CrossRef]
37. Peng, Y.X.; Yu, L.Y.; Qian, J.Y.; Li, W.; Zhang, T.; Zhou, L.J. Dynamic tensile behavior and crack propagation in coral aggregate seawater shotcrete: Experimental investigation and numerical simulation. *Cement. Concrete. Comp.* **2025**, *159*, 06010. [CrossRef]
38. Li, Z.Q.; Nie, L.; Xue, Y.; Li, W.; Fan, K. Model Testing on the Processes, Characteristics, and Mechanism of Water Inrush Induced by Karst Caves Ahead and Alongside a Tunnel. *Rock. Mech. Rock. Eng.* **2025**, *58*, 5363–5380. [CrossRef]
39. Li, W.; Yu, L.; Zhang, T. Quantitative analysis of grain size effect on tensile mechanical behavior of granite based on multi-level force chain networks. *Comp. Part. Mech.* **2024**, *11*, 2245–2266. [CrossRef]
40. *Chinese Standard JTG 3430–2020*; Test Standards of Soils in Highway Engineering. Ministry of Transport: Beijing, China, 2020.
41. Tan, P.; Xiao, Y.J.; Wang, M.; Yang, T.; Zhang, C.C.; Li, W.Q. Insights into particle breakage induced macroscopic and microscopic behavior of railway ballast via DEM. *Comput. Geotech.* **2025**, *182*, 107135. [CrossRef]
42. Zhang, J.H.; Li, J.; Yao, Y.S.; Zheng, J.L.; Gu, F. Geometric anisotropy modeling and shear behavior evaluation of graded crushed rocks. *Constr. Build. Mater.* **2018**, *183*, 346–355. [CrossRef]
43. Einav, I. Breakage mechanics—Part II: Modelling granular materials. *J. Mech. Phys. Solids* **2007**, *55*, 1298–1320. [CrossRef]
44. Hardin, B.O. Crushing of soil particles. *J. Geotech. Eng.-ASCE* **1985**, *111*, 1177–1192. [CrossRef]
45. Liu, H.B.; Zeng, K.F.; Zou, Y. Particle breakage of calcareous sand and its correlation with input energy. *Int. J. Geomech.* **2020**, *20*, 04019151. [CrossRef]
46. Zhang, H.L.; Tang, Y.; Meng, T.; Zhan, L.T. Evaluating the crushing characteristics of recycled construction and demolition waste for use in road bases. *Transp. Geotech.* **2021**, *28*, 100543. [CrossRef]

Disclaimer/Publisher's Note: The statements, opinions and data contained in all publications are solely those of the individual author(s) and contributor(s) and not of MDPI and/or the editor(s). MDPI and/or the editor(s) disclaim responsibility for any injury to people or property resulting from any ideas, methods, instructions or products referred to in the content.

materials

MDPI

Article

Study on Similar Materials for Weakly Cemented Medium and Indoor Excavation Test

Shanchao Hu [1], Lei Yang [1], Shihao Guo [1,*], Chenxi Zhang [2], Dawang Yin [1], Jinhao Dou [1] and Yafei Cheng [1]

[1] College of Energy and Mining Engineering, Shandong University of Science and Technology, Qingdao 266590, China; skd994527@sdust.edu.cn (S.H.); 15564801327@163.com (L.Y.); m15285817719@163.com (D.Y.); djh15092318906@163.com (J.D.); chengyafei911@163.com (Y.C.)
[2] College of Water Resource & Hydropower, Sichuan University, Chengdu 610065, China; cpu18135835371@163.com
* Correspondence: 202481010003@sdust.edu.cn

Abstract: The escalating disasters caused by the movement of shallow buried strata in China's western mining areas are increasingly threatening operational safety. A critical issue in ensuring secure mining practices in these areas is the creep failure of weakly cemented soft rock under low-stress conditions. The unique particle contact mechanisms in weakly cemented mudstone, combined with the persistence of the cemented materials and the particulate matter they form, lead to mechanical responses that differ significantly from those of typical soft rocks during loading. Building on an existing multivariate linear regression equation for new similar materials, this study developed qualified weakly cemented medium similar materials, offering appropriate materials for long-term creep tests of weakly cemented formations. This was accomplished by employing orthogonal proportioning tests. The principal findings of our investigation are as follows: The new, similar material exhibits low strength and prominent creep characteristics, accurately simulating weakly cemented materials in western mining areas. The concentration of rosin–alcohol solution has a measurable impact on key parameters, such as σ_c, E, and γ in the weakly cemented similar material specimens. Furthermore, the creep characteristics of the specimens diminish progressively with an increase in the proportion of iron powder (I) and barite powder (B). The material was applied to a similar indoor model test simulating the weakly cemented material surrounding the auxiliary haulage roadway in Panel 20314 of the Gaojialiang Coal Mine, with speckle analysis employed for detailed examination. The experimental findings suggest that both the conventional mechanical properties and long-term creep characteristics of the material align with the required specifications, offering robust support for achieving optimal outcomes in the similar model test.

Keywords: weakly cemented medium; creep; similar material; model test

1. Introduction

In recent years, the focus of China's coal mining has progressively shifted toward the coal-rich western regions. However, the soft rock strata found in these western mining areas differ significantly from those in the central and eastern regions of China. These rocks are characterized by macro-scale physical and mechanical properties, such as weak cementation, low strength, and susceptibility to water-induced slaking. Furthermore, they undergo creep deformation under relatively low stress levels, categorizing them as a special type of soft rock [1–5]. Such weakly cemented soft rock severely compromises the self-stability of roadway-surrounding rock in western mining areas, resulting in considerable long-term

deformation and damage. This substantially impedes the safe and efficient development of coal resources in this region [6,7]. Consequently, a comprehensive understanding of the long-term creep behavior and failure mechanisms of weakly cemented soft rock, especially under shallow burial and low-stress environments, becomes of paramount engineering significance and profound scientific value for ensuring safe extraction in these areas.

Given the challenges associated with obtaining weakly cemented soft rock cores, including their inherent poor integrity and the vulnerability of their physical and mechanical properties to disturbance and deterioration, physical model testing, particularly excavation model testing using specially formulated similar materials, has emerged as an indispensable and effective methodology for investigating their deformation and failure characteristics [8–12].

A considerable body of research on soft rock and similar materials has been conducted by numerous scholars. Stück, H et al. [13] studied the physical properties of sandstone as a component in similar materials. Holtzman, R [14] investigated the micro-mechanical properties of weakly cemented rock, laying the groundwork for the composition of weakly cemented similar materials. Xu Ren et al. [15] developed an innovative soft rock material, utilizing fine iron powder, barite powder, and quartz sand as aggregates, with gypsum as a binder, and redispersible polymer powder as a modifier to simulate the stability issues of soft rock induced by excavation. Sun et al. [12] formulated coal measure rock-like materials based on materials like river sand, heavy calcium carbonate, cement, and gypsum, exploring the sensitivity of various factors. Qian Yongmei et al. [16] conducted tests on the mechanical properties of a new epoxy resin concrete, identifying specific mix ratios that significantly enhanced material performance while also refining the theoretical understanding of its tensile failure mechanism and structural design. Cui et al. [17] utilized the discrete element method to determine the optimal coarse-to-fine aggregate ratio for similar materials simulating weak surrounding rock. Li Yuanhai et al. [18], addressing the limitations of traditional physical model observations, proposed a method for preparing transparent rock masses, developing a transparent similar material suited for simulating soft rocks. Yang Xu et al. [19] determined appropriate, similar materials and mix ratios for soft rock by studying factors like the softening coefficient, tensile strength, and cohesion. Zhang Yanli et al. [20] conducted orthogonal experiments using river sand, coal powder, gypsum, and calcium carbonate as raw materials, determining key factors influencing the physical and mechanical properties of coal-like materials. Lin Haifei et al. [21], in developing "solid–gas" coupling-like materials, incorporated hydraulic oil as a regulator. They observed its favorable viscosity and observed that an increase in hydraulic oil content significantly reduced the material strength while elevating Poisson's ratio, providing valuable guidance for the subsequent development of low-strength soft rock materials.

Regarding the creep characteristics of soft rock-like materials, Ma Zhenguo [22] selected styrene–butadiene latex as a binder to successfully formulate a soft rock-like material that could effectively simulate soft rock creep failure patterns. Wang Hanpeng et al. [23] used aggregates consisting of fine iron powder, barite powder, quartz sand, and quicklime to formulate an iron crystal sand cemented-like material, where the specimens exhibited good simulation of the instantaneous mechanical properties of medium- to low-strength rocks. Chu et al. [24–26], building upon previous research findings, developed a novel similar material for simulating soft rock creep. This material not only simulates the instantaneous elastoplastic properties of soft rock but also effectively mimics its creep characteristics. Furthermore, they employed a multiple linear regression method to determine the relationship between key factors and the mixture ratio of the similar material. This approach overcame the limitations of the trial-and-error method, which is often cumbersome and prone to randomness when determining the optimal mixture ratio. Consequently, the

experimentally derived mixture ratios were significantly more accurate, and the process became significantly more efficient. Their advancements provided a robust foundation for the present study.

However, the research on materials similar to weakly cemented soft rock—characterized by substantial deformations, low strength, and significant creep behavior under low stress—remains insufficient. To better characterize the creep properties of weakly cemented soft rock and overcome the challenges of coring and preserving such cores, this paper first determines the target mix ratio based on existing multiple linear regression equations for soft rock creep and similar materials [25]. Secondly, the influence of various components on the conventional mechanical parameters and creep characteristics of specimens is investigated through orthogonal tests (three factors, three levels) and proportional tests to determine a suitable mix ratio for weakly cemented soft rock. Building on this, using the auxiliary haulage roadway of the 20314 working face in the Gaojialiang Coal Mine as a case study, a two-dimensional plane model test is conducted employing the identified weakly cemented soft rock-like material. The digital speckle correlation method (DSCM) is utilized for analysis to study the creep failure mechanism of weakly cemented surrounding rock roadways induced by shallow burial and low stress, thereby providing both material assurance and a theoretical foundation for subsequent research on weakly cemented soft rock.

2. Research Background

2.1. Project Overview

The primary coal seams mined at the Gaojialiang Coal Mine include the 2-2 upper, 2-2 middle, 3-1, 4-2 middle, 5-1, and 6-2 middle seams. These coal seams are characterized by stable stratigraphic positions and simple structures (Figure 1).

System	Series	Rodman-shaped	Thickness/m	Lithological description
Quaternary system	Holocene series		0~6.45	Surface soil: yellow, the upper part is aeolian sand, the lower part is loose soil layer, containing gravel.
Tertiary system	Pliocene series		25.4~54.13	Sandy conglomerate, coarse-grained sandstone, sandy mudstone and siltstone.
Cretaceous system	Lower cretaceous series			
Jurassic system	Middle jurassic Series		89.4~125.93	Containing fine-grained sandstone, sandy mudstone and mudstone
	Lower-Middle jurassic series		9~24.85	Contains coarse and fine sandstone, sandy mudstone
			0.5~1.8	Coal : black, striped structure
			6.65~11.9	Sandy mudstone containing coarse and fine sandstone and sandy mudstone
			2.46~4.19	Coal: black, striped structure
			24.25~30.62	Containing mudstone, fine-grained sandstone and sandy mudstone.

Figure 1. Geological comprehensive histogram of the Gaojialiang Coal Mine.

The 20314 working face mines the 2-2 middle coal seam, located in the 203 panel. The ground elevation at the working face ranges from 1445.8 m to 1499.0 m, while the elevation of the coal seam floor varies between 1281.4 m and 1297.9 m. The working face spans a strike length of 300.5 m and a dip length of 1459.2 m, with recoverable reserves amounting to 2.423 million tons. The coal seam thickness ranges from 3.20 m to 4.70 m, averaging 4.06 m, with a dip angle of 0–5°. The design employs full-seam mining in a single pass.

The 20314 adequately mechanized working face is arranged along the strike of the coal seam, while the working face roadways are oriented along the dip direction of the 2-2 middle coal seam.

As depicted in Figure 1, the immediate roof and floor of the coal seam consist of weakly cemented sandy mudstone. Due to the short diagenetic time, low cementation degree, loose rock mass structure, and well-developed fractures in the surrounding rock, the strength of the roof and floor strata is lower than that of the coal seam itself.

2.2. Deformation and Failure Characteristics of Roadway

The haulage roadway of 20314 fully mechanized mining face exhibits various forms of structural distress, including floor fractures, roof beam bending, stepped roof subsidence, severe floor heave, and failure of the support system (as revealed in Figure 2). These substantial roadway deformations impede its normal functionality.

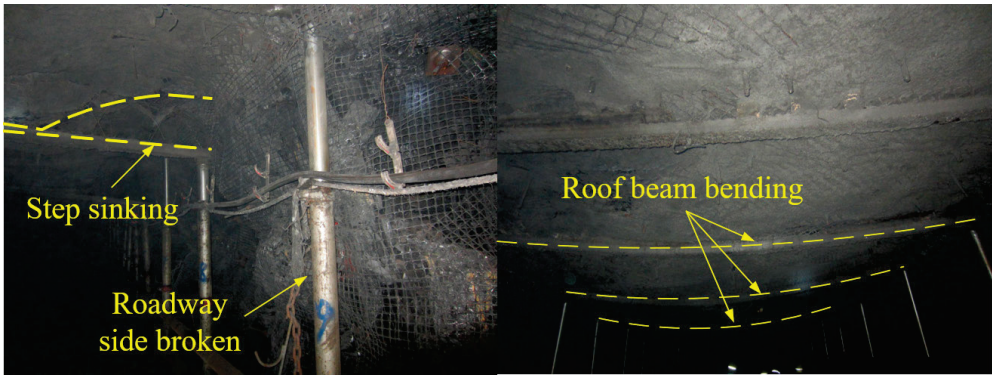

Figure 2. On-site failure characteristics.

This is predominantly attributable to the properties of the shallow, buried, weakly cemented strata, which exhibit a low diagenetic degree, poor cementation, and creep behavior under low stress levels, compounded by the influence of the overlying goaf, which results in significant mining disturbance effects. Subsequent to the completion of mining in the upper working face, the residual coal pillars above generate concentrated stress on the haulage roadway, thereby inducing creep deformation and subsequent failure of the weakly cemented medium in the roadway roof.

3. Development of Weakly Cemented Similar Materials

3.1. Similarity Criteria and Model for Weakly Cemented Materials

Given the intrinsic challenges associated with studying the deformation and failure conditions of weakly cemented strata roadways in situ, coupled with the difficulties in coring and preserving weakly cemented medium samples from western regions, the method of similar material simulation has been employed to investigate the creep deformation and failure characteristics of weakly cemented mediums. To accurately simulate these characteristics, it is imperative to determine an appropriate model similarity scale and to develop similar materials that sufficiently replicate the creep properties of weakly cemented medium.

When considering the creep effects of weakly cemented medium, both conventional physical–mechanical parameters and time-dependent creep mechanical parameters must be considered. The conventional physical–mechanical parameters include the geometric dimension L, unit weight γ, stress σ, strain ε, elastic modulus E, Poisson's ratio μ, cohesion C, internal friction angle φ, and uniaxial compressive strength σ_c. In accordance with similarity theory, the ratio of physical quantities with the same dimension between the prototype material (P) and the similar model (M) is referred to as the similarity scale, denoted by C_X (where X represents each parameter).

By considering the equilibrium equations, geometric equations, physical equations, stress boundary conditions, and displacement boundary conditions of the prototype material and the similar model, the following similarity associations for the similar model test can be derived [27]:

$$\begin{cases} C_\sigma = C_\gamma C_L \\ C_\delta = C_\varepsilon C_L \\ C_\sigma = C_\varepsilon C_E \\ C_\varepsilon = C_f = C_\varphi = C_\mu = 1 \\ C_\sigma = C_E = C_c = C_{\sigma_c} \end{cases} \tag{1}$$

The meaning of each symbol is provided in Nomenclature. The creep mechanical parameters of the weakly cemented medium are determined by its creep constitutive correlation. Both the Nishihara model (as revealed in Figure 3) and the Burgers model are widely recognized theoretical models used to describe the viscoelastic–plastic behavior of soft medium, and both are utilized to simulate the rheological characteristics of soft medium. Nevertheless, Tao et al. [28] put forth a standpoint that the Nishihara model is more suitable than the Burgers model for describing the creep properties of soft medium. Consequently, the parameters of the Nishihara model are adopted as the creep similarity parameters between the weakly cemented similar material and the prototype material. Given the experimental operability, the corresponding creep parameters are determined through uniaxial creep compression tests.

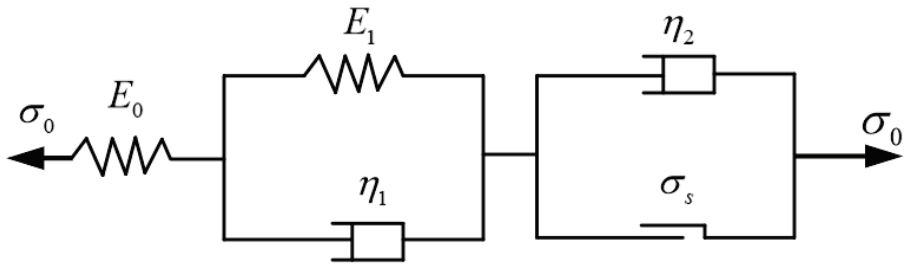

Figure 3. Ishihara rheological model.

The one-dimensional Nishihara creep equation is

$$\varepsilon(t) = \begin{cases} \frac{\sigma_0}{E_0} + \frac{\sigma_0}{E_1}[1 - exp(-\frac{E_1}{\eta_1}t)], \sigma_0 < \sigma_s \\ \frac{\sigma_0}{E_0} + \frac{\sigma_0}{E_1}[1 - exp(-\frac{E_1}{\eta_1}t)] + \frac{(\sigma_0 - \sigma_s)}{\eta_2}t, \sigma_0 > \sigma_s \end{cases} \tag{2}$$

The creep rate of the Nishihara model is

$$\dot{\varepsilon}(t) = \begin{cases} \frac{\sigma_0}{\eta_1} e^{-\frac{E_1}{\eta_1}}, \sigma_0 < \sigma_s \\ \frac{\sigma_0}{\eta_1} e^{-\frac{E_1}{\eta_1}} + \frac{\sigma_0 - \sigma_s}{\eta_2}, \sigma_0 > \sigma_s \end{cases} \tag{3}$$

where: ε refers to the strain; σ_0 symbolizes the creep stress; E_0 represents the instantaneous elastic modulus; E_1 denotes the viscoelastic modulus; η_1 and η_2 represent the viscosity coefficients; σ_s symbolizes the long-term strength; $\dot{\varepsilon}$ denotes the strain rate.

Scholars have [29] highlighted that creep-induced deformation and failure are time-dependent (correlated with time t), which means that the conventional time similarity association $C_t = \sqrt{C_L}$ cannot be applied. Assuming the similarity ratios of viscosity coefficients η_1 and η_2 as C_η, and the strain rate similarity ratio as $C_{\dot{\varepsilon}}$, it can be deduced from Equation (1) that the similarity ratios of creep stress σ_0, viscoelastic moduli E_1 and E_2 should be C_σ, while the strain ε similarity ratio $C_\varepsilon = 1$. For this reason, the parameters for the prototype materials and the similar materials should satisfy the following connections [24]:

$$\begin{cases} \sigma_{0,p} = C_\sigma \sigma_{0,m}, t_p = C_t t_m \\ E_{0,p} = C_\sigma E_{0,m}, E_{1,p} = C_\sigma E_{1,m}, E_{2,p} = C_\sigma E_{2,m} \\ \eta_{1,p} = C_\eta \eta_{1,m}, \eta_{2,p} = C_\eta \eta_{2,m} \\ \varepsilon_p = \varepsilon_m, \dot{\varepsilon}_p = C_{\dot{\varepsilon}} \dot{\varepsilon}_m \end{cases} \tag{4}$$

In the equation, subscripts "p" and "m" represent the prototype materials and similar material, respectively. The one-dimensional creep equation for both the prototype materials and similar materials is calculated as. follows:

$$\varepsilon_t = \begin{cases} \frac{\sigma_0}{E_0} + \frac{\sigma_0}{E_1}[1 - exp(-\frac{E_1}{\eta_1}t)], \sigma_0 < \sigma_s \\ \frac{\sigma_0}{E_0} + \frac{\sigma_0}{E_1}[1 - exp(-\frac{E_1}{\eta_1}t)] + \frac{\sigma_0 - \sigma_s}{\eta_2}t, \sigma_0 > \sigma_s \end{cases} \tag{5}$$

Substituting Equation (4) into Equation (5), and simplifying, yields

$$\varepsilon_p(t_p) = \begin{cases} \frac{C_\sigma \sigma_{0,m}}{C_\sigma E_{0,m}} + \frac{C_\sigma \sigma_{0,m}}{C_\sigma E_{1,m}}[1 - exp(-\frac{C_\sigma E_{1,m}}{C_\eta \eta_{1,m}} C_t t_m)], \sigma_{0,m} < \sigma_{s,m} \\ \frac{C_\sigma \sigma_{0,m}}{C_\sigma E_{0,m}} + \frac{C_\sigma \sigma_{0,m}}{C_\sigma E_{1,m}}[1 - exp(-\frac{C_\sigma E_{1,m}}{C_\eta \eta_{1,m}} C_t t_m)] + \frac{C_\sigma (\sigma_{0,m} - \sigma_{s,m})}{C_\eta \eta_{2,m}} C_t t_m, \sigma_{0,m} > \sigma_{s,m} \end{cases} \tag{6}$$

From the above, it follows that $C_\varepsilon = 1$, meaning that for any time t, the strain of the prototype materials equals that of the similar material, i.e., $\varepsilon_p(t_p) = \varepsilon_m(t_m)$. Therefore, the similarity ratios C_η, C_σ, and C_t can be derived as

$$C_\eta = C_t C_\sigma \tag{7}$$

By substituting Equation (4) into (3) and considering Equation (5), we obtain

$$C_{\dot{\varepsilon}} = 1/C_t \tag{8}$$

On that account, when C_σ is constant, larger C_t values lead to greater $C_{\eta 1}$ and $C_{\eta 2}$ values. This indicates that the viscosity coefficients of the similar material decrease while its creep rate increases. Rooted in this principle, materials with higher creep rates must be selected to simulate the long-term creep effects of weakly cemented medium within a short timeframe.

3.2. Material Selection and Similarity Ratio Determination

Chu et al. developed a similar material that effectively simulates the rheology of soft rock using iron ore powder, heavy stone powder and quartz sand as aggregate, with rosin alcohol solution as the cementing agent and hydraulic oil as the adhesive [24–26]. Therefore, the similar materials for this test utilized quartz sand, iron ore powder (300 mesh) and barite powder as aggregates. For the binder, a rosin–alcohol solution was selected, with

99% pure industrial alcohol used as the solvent to dissolve the rosin. Subsequent to alcohol volatilization, the rosin formed cementation force. Grade 6 industrial hydraulic oil was chosen as the viscous agent.

Grounded in parameters of weakly cemented medium and the connection between various factors and mix proportion of similar materials, this paper selected the unit weight γ, elastic modulus E, internal friction angle φ, and viscosity coefficient η_1 as the main control parameters of similar materials [25]. Let the rosin concentration n be X_1, the mass ratio of barite powder to iron powder (*IB/IBS*) be X_2, the mass ratio of iron powder to the sum of barite and iron powder (*I/IB*) be X_3, and the hydraulic oil content ω be X_4. Through multiple linear regression analysis, the material mix proportion can be determined. The regression equation is as follows [25]:

$$\left.\begin{aligned} \gamma &= -2.64X_1 + 5.6X_2 + 4.4X_3 + 3X_4 + 20.7 \\ E &= 1175.5X_1 + 142.9X_2 + 103.2X_3 - 5269.3X_4 + 84.8 \\ \varphi &= -8.6X_1 - 20.6X_2 + 0.63X_3 - 58X_4 + 56.2 \\ \eta_1 &= 874.7X_1 - 80.8X_2 + 98.5X_3 - 3851.3X_4 + 171.4 \end{aligned}\right\} \quad (9)$$

Formula (9) is inversely solved to obtain the material ratio expression:

$$\left.\begin{aligned} X_1 &= -0.026\gamma - 0.0026E - 0.0411\varphi + 0.0041\eta_1 + 2.357 \\ X_2 &= 0.021\gamma + 0.0031E - 0.0049\varphi - 0.0042\eta_1 + 0.293 \\ X_3 &= 0.1868\gamma - 0.005E - 0.012\varphi + 0.0071\eta_1 - 3.99 \\ X_4 &= -0.0016\gamma - 0.0008E - 0.0095\varphi + 0.0009\eta_1 + 0.472 \end{aligned}\right\} \quad (10)$$

4. Test Scheme and Process

4.1. Orthogonal Test Design

In the orthogonal test design, the mass of the rosin–alcohol solution was fixed at 6% of the total aggregate mass. The test primarily focused on three key control factors: first, the ratio of iron powder mass to the total mass of barite powder and iron powder; second, the ratio of the total mass of barite powder plus iron powder to the aggregate mass; and third, the concentration of the rosin–alcohol solution. For these factors, three dissimilar levels were established for the experimental research.

Notably, the level ranges for aggregates and binders were determined with reference to Chu, Zhang et al. [24,30]. The hydraulic oil content (ω) was determined based on its influence on similar materials, and the results obtained from multiple linear regression equation calculations. The final experimental design is presented in Table 1, while the mix proportion scheme is outlined in Table 2. Let the rosin concentration be n, the mass ratio of barite powder to iron powder be (*IB/IBS*), the mass ratio of iron powder to the sum of barite and iron powder be (*I/IB*), and the hydraulic oil content be ω.

Table 1. Orthogonal test levels of similar materials.

Level	*n*/%	*IB/IBS*	*I/IB*	*ω*/%
1	7.5	0.6	0.05	3.5
2	12.5	0.7	0.2	3.5
3	17.5	0.8	0.35	3.5

Table 2. Proportioning scheme of similar materials.

Proportion Number	*n*/%	*IB*/*IBS*	*I*/*IB*	*ω*/%
1	7.5	0.6	0.05	3.5
2	7.5	0.7	0.20	3.5
3	7.5	0.8	0.35	3.5
4	12.5	0.6	0.20	3.5
5	12.5	0.7	0.35	3.5
6	12.5	0.8	0.05	3.5
7	17.5	0.6	0.35	3.5
8	17.5	0.7	0.05	3.5
9	17.5	0.8	0.20	3.5

4.2. Sample Preparation and Testing Process

4.2.1. Sample Preparation and Testing Procedure

In accordance with the ratio outlined in Table 2, standard specimens with a diameter of 50 mm and a height of 100 mm were made in strict compliance with the recommended standards of the International Society of Rock Mechanics (ISRM). The specific test steps are as follows:

(1) Material preparation: Raw materials were prepared in line with the proportions specified in Table 2.

(2) Mold preparation: Pre-compression is essentially ascribable to the special characteristics of the materials adopted in this test and the relatively low strength of the prepared samples. Conventional soil sample molds would have resulted in demolding difficulties, rendering pre-compression unfeasible. Consequently, specially designed structured molds were employed, as depicted in Figure 4a.

(3) Quartz sand, barite powder, iron powder, hydraulic oil, and rosin–alcohol solution were individually weighted. Afterward, the measured aggregates were combined in a container for mixing. After thorough mixing, the rosin–alcohol solution was added sequentially. Once the solution had been fully absorbed, hydraulic oil was incorporated, and the mixing process continued. After completion, the mixture was set aside for later use, and the mold walls were lubricated with silicone oil, as displayed in Figure 4b.

(4) The mixed material was loaded into the newly designed mold cavity, and manual compaction was carried out. The compacted material volume was controlled to approximately 120% of that of the specimen.

(5) Pressing: The mold plunger was installed, and pressure was applied using an electro-hydraulic press, allowing the formation of standard specimens for rock mechanics testing.

(6) Demolding: The mold plunger was installed, and pressure was applied using an electro-hydraulic press, facilitating the formation of standard rock mechanics test specimens.

(7) As indicated by *Z* in Table 2, a total of 9 test groups were conducted. Each group consisted of 4 specimens: 3 specimens for uniaxial compression tests and 1 specimen for uniaxial creep tests.

(8) The specimens were numbered and cured under room-temperature and dry conditions for 10 days, allowing the alcohol to fully evaporate. The cured specimens are illustrated in Figure 4c.

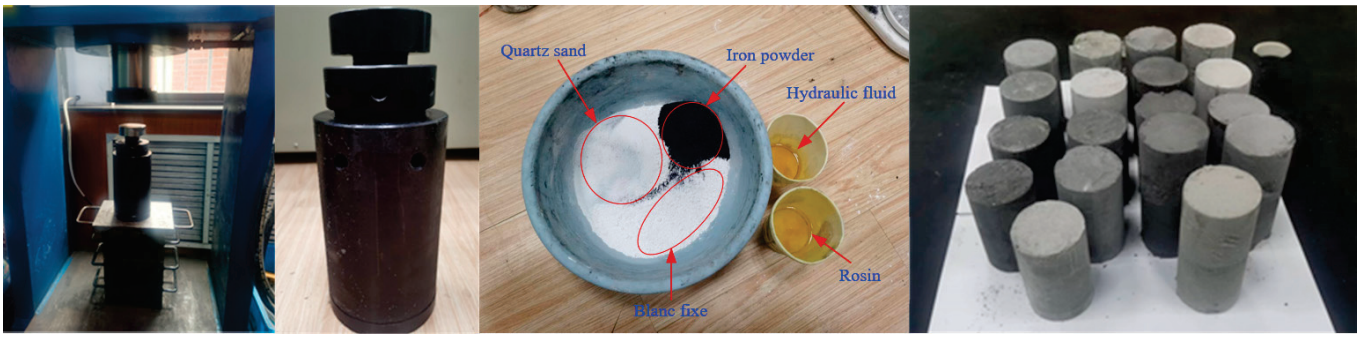

(**a**) (**b**) (**c**)

Figure 4. Mold and preparation process. (**a**) Special structured mold. (**b**) Similar material display diagram before mixing. (**c**) Formed specimens.

Basic physical and mechanical tests were conducted to investigate the cured specimens. The physical tests included density and dimension measurements, where the density and dimensions of the specimens were assessed to obtain the average density γ for each mix ratio. The mechanical tests comprised uniaxial compression tests and uniaxial creep tests, which were performed using the RLJW-2000 mechanical test system (Produced in Qingdao, China). The uniaxial compression test was used to measure the Poisson's ratio μ, elastic modulus E, and uniaxial compressive strength σ_c of the specimens, while the uniaxial creep test captured the creep deformation characteristics of the specimens. The testing system is demonstrated in Figure 5.

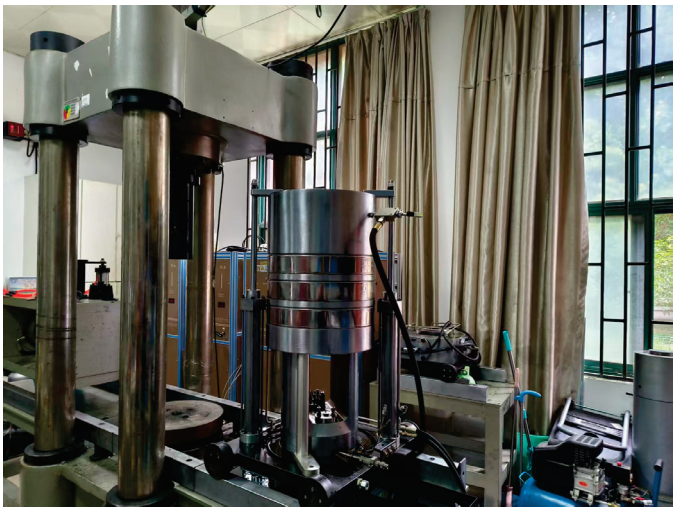

Figure 5. Basic mechanical test system.

The steps for the uniaxial compression test were as follows:

(1) The prepared similar material specimen was positioned at the center of the pressure head of the testing machine, and a circumferential extensometer and axial strain gauge was attached to it.
(2) Loading began at a displacement-controlled rate of 0.05 mm/s until specimen failure occurred.

The steps for the uniaxial creep test were as follows:

(1) The prepared similar material specimen was placed at the center of the testing machine's pressure head, and an axial strain gauge was attached to it.
(2) Loading began at a stress-controlled rate of 0.001 MPa/s until the specimen failed.

4.2.2. Physical Test Results and Analysis

(a) Conventional Physical Test Results and Analysis

As revealed in Table 3 and Figure 6, the conventional physical and mechanical parameters for each mix ratio were obtained from the uniaxial compression tests. A comprehensive analysis of the data from each mix ratio revealed the following: For this weakly cemented medium simulant material, the bulk density (γ) of the mix ratios 1 to 9 ranged from 24.32 to 26.91 kN/m^3, the elastic modulus (E) ranged from 79.4 to 241.05 MPa, the uniaxial compressive strength ranged from 0.30 to 0.77 MPa, and the Poisson's ratio ranged from 0.21 to 0.27. The variation in bulk density for this simulant material was relatively modest, aligning closely with the typical bulk density range observed in soft rocks.

Table 3. Results of conventional physical and mechanical parameters.

Proportion Number	Volumetric Weight γ/(kN·m^{-3})	Elastic Modulus E/MPa	Compressive Strength σ_c/MPa	Poisson Ratio μ
1	24.32	79.4	0.30	0.27
2	25.25	109.2	0.42	0.26
3	26.91	138.97	0.48	0.25
4	24.17	153.69	0.51	0.23
5	25.64	183.46	0.61	0.23
6	24.98	166.79	0.59	0.24
7	25.24	227.95	0.71	0.21
8	24.33	211.28	0.69	0.22
9	25.57	241.05	0.77	0.22

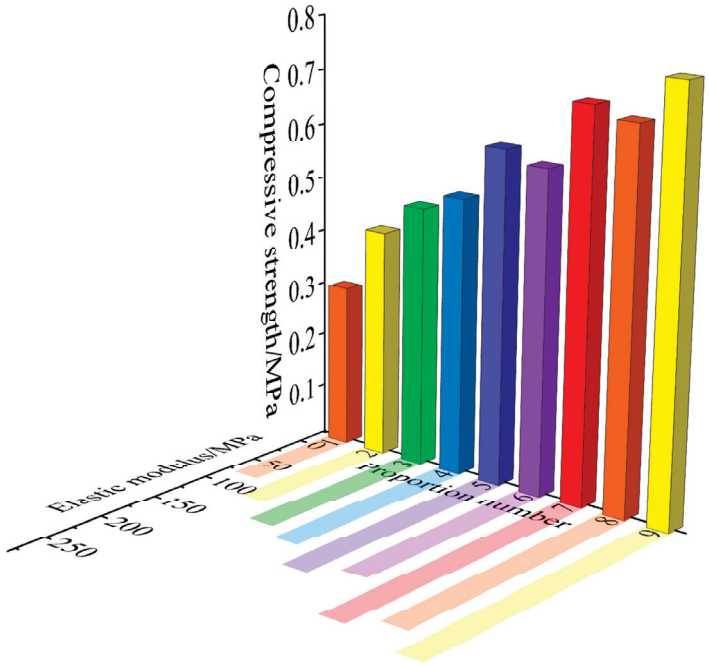

Figure 6. Variation in elastic modulus and compressive strength.

Figure 7 depicts the rupture pattern of certain test specimens. As illustrated, the specimens exhibited vertical tensile failure. Under loading, transverse tensile stresses were induced, accompanied by a noticeable Poisson's effect. Crack propagation in the specimens progressed gradually along the axial direction, eventually culminating in structural failure. This process was accompanied by the formation of minor secondary cracks adjacent to the primary penetrating cracks.

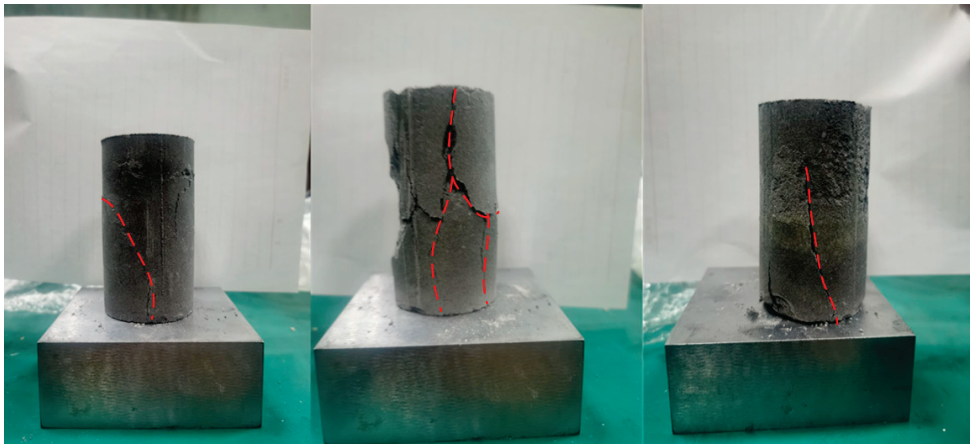

Figure 7. Macroscopic failure state of specimen under uniaxial compression test.

In accordance with the standard [31], the uniaxial compressive strength of engineering soft medium typically falls below 15 MPa. Rooted in Equation (1) and the previously determined ranges for the density similarity ratio and geometric similarity ratio in similar material simulation tests [25], it can be inferred that the stress similarity ratio C_σ should typically exceed 15. Consequently, the uniaxial compressive strength of weakly cemented similar materials should generally be below 1 MPa.

The data presented in Table 3 and Figure 6 confirm that the weakly cemented similar materials prepared in this study satisfactorily conform to the required strength range and other mechanical parameter requirements.

The results of the uniaxial compression tests on similar materials are depicted in Figure 8. As the concentration of rosin alcohol increased, the overall compressive strength of the specimens gradually rose, illustrating that the rosin–alcohol solution had a notable impact on enhancing the compressive strength of the specimens. This finding aligns with the conclusions drawn by Dong et al. [32], thereby validating the reliability of the similar material tests.

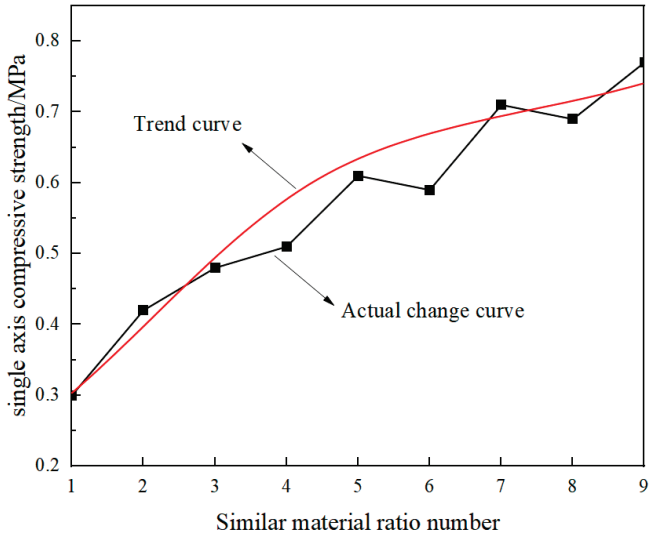

Figure 8. The variation law of uniaxial compressive strength of specimens with diverse ratios.

(b) Results and Analysis of Uniaxial Creep Tests

Table 4 presents the mechanical parameters of weakly cemented soft materials. Based on the previously determined similarity scale, the mechanical parameters of the similar materials were calculated for the target specimens, with the specific results shown in

Table 5. A comprehensive comparison demonstrates that the proportions of Mix No. 4 and Mix No. 5 basically satisfy the strength and other parameter requirements for the weakly cemented similar materials necessary for this study. As a consequence, uniaxial creep tests were conducted on specimens prepared with the proportions of Mix No. 4 and Mix No. 5.

Table 4. Mechanical parameters of weakly cemented materials.

Materials	Volumetric Weight γ/(kN·m^{-3})	Elastic Modulus *E*/GPa	Single-Axis Compressive Strength σ_c/MPa	Poisson Ratio μ
Weekly cemented mudstone	23.4	1.96	10.01	0.29
Weakly cemented sandy mudstone	24.1	13.7	11.59	0.20

Table 5. Mechanical parameters of similar material samples.

Materials	Volumetric Weight γ/(kN·m^{-3})	Elastic Modulus *E*/GPa	Single-Axis Compressive Strength σ_c/MPa	Poisson Ratio μ
Mudstone-like material	25.4	0.098	0.5	0.29
Sandy mudstone-like material	26.1	0.685	0.58	0.20

As demonstrated in Figure 9, the creep test curves of specimens with varying material ratios exhibited distinct characteristics. The axial strains of specimens with ratios No. 4 and No. 5 show a marked increase during the initial stage, followed by a gradual deceleration in the strain rate over time. This phenomenon illustrates that both specimens enter the decay creep stage at this point. After the strain rates stabilize at 0.23% and 0.22%, separately, the rate of strain growth strikingly slows down, eventually transitioning into a steady and uniform increase. This demonstrates that the weakly cemented similar material specimens, prepared according to ratio schemes No. 4 and No. 5, demonstrate favorable creep characteristics, with their creep curves closely resembling the shape of real creep curves, meeting the experimental requirements. Simultaneously, as the proportion of iron powder (I) and barite powder (B) increases, the creep characteristics of the specimens gradually diminish.

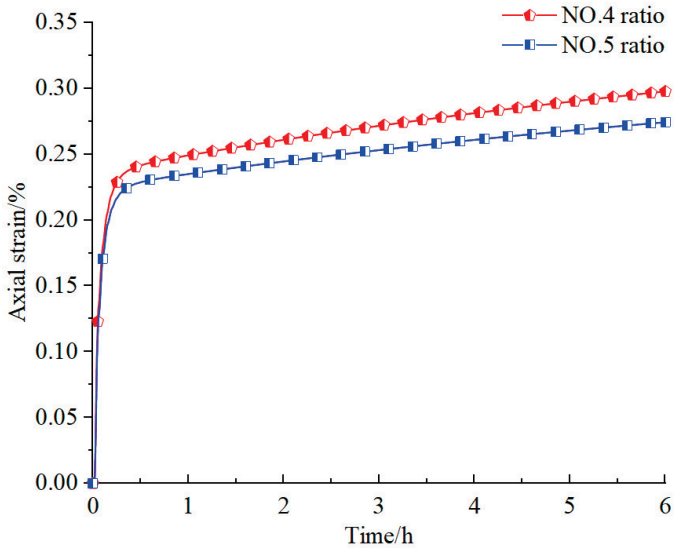

Figure 9. Creep test curves of similar material specimens with dissimilar proportions.

5. Model Test

5.1. Model Design

Drawing from the auxiliary transportation roadway of the 20314 working face at the Gaojialiang Coal Mine, Ordos City, Inner Mongolia Autonomous Region, a plane model test was conducted to investigate the creep failure mechanism of weakly cemented stratum medium roadways induced by shallow burial and low stress. Given that roadway excavation induces stress redistribution, and the stress essentially reverts to its original state beyond five times the chamber radius, an influence range of eight times the chamber radius was chosen to streamline calculations and reduce errors.

The auxiliary transportation roadway of the 21304 working face has a width of 5 m and a height of 3.5 m, which led to the determination of an influence range of 40 m × 28 m. The model test platform employed in this experiment has dimensions of 2.0 m × 0.22 m × 1.8 m (as revealed in Figure 10).

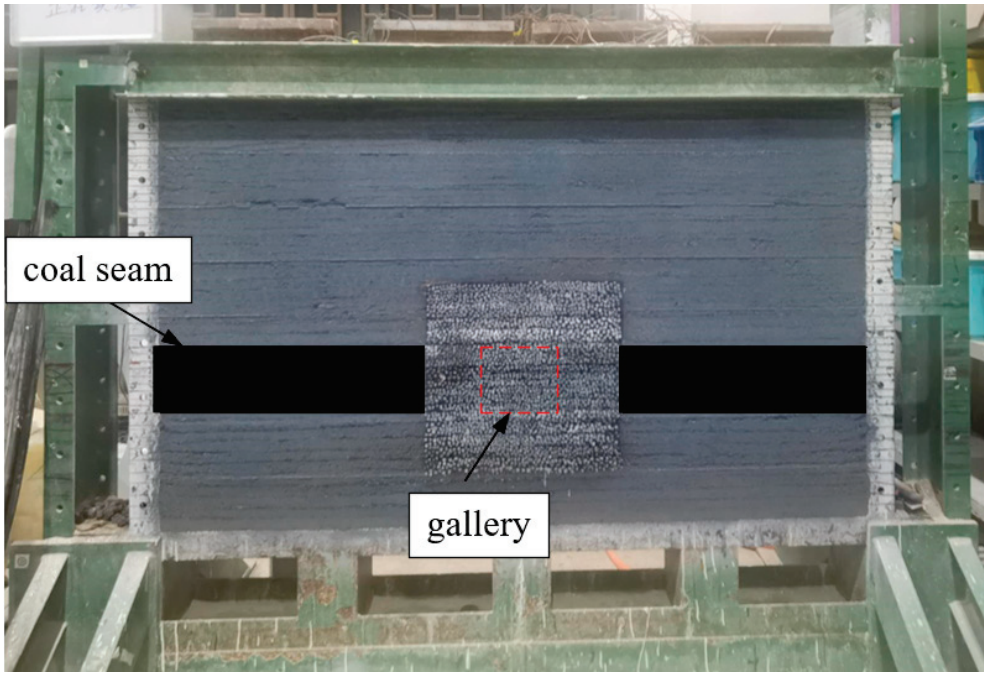

Figure 10. Simulator stand.

In this model test, the fundamental similarity ratios of the materials were as follows:

$$\left.\begin{aligned} C_L = \frac{\delta_P}{\delta_m} = \frac{40\text{m}}{2\text{m}} = 20 \\ C_\sigma = C_\gamma C_L = 20 \times 0.83 \approx 17 \\ C_t = 4 \\ C_\eta = C_t C_\sigma = 4 \times 17 = 68 \end{aligned}\right\} \tag{11}$$

In the equation, C_L denotes the geometric similarity ratio of the model, C_t symbolizes the time similarity ratio, and C_η refers to the viscosity coefficient similarity ratio. The formation model proportionately selected schemes No. 4, No. 5, and No. 6 to simulate weakly cemented mudstone, weakly cemented sandy mudstone, and coal (the coal seam refers to Xu [33]), as presented in Table 6.

Table 6. Stratum model ratio.

Materials	Rosin–Alcohol Concentration *m*/%	$\frac{IB}{IBS}$	$\frac{I}{IB}$	Hydraulic Oil Content *w*/%
Weakly cemented mudstone	12.5	0.6	0.20	3.5
Weakly cemented sandy mudstone	12.5	0.7	0.35	3.5
Coal	12.5	0.8	0.05	3.5

5.2. Test Process and Monitoring

This experiment was conducted on a two-dimensional test platform, serving as the model stand, with fixed boundaries on the front, back, left, right, and lower sides. To minimize boundary effects, the surface was smoothed prior to laying the strata. Throughout the testing process, the strata similarity materials were prepared in accordance with the ratios in Table 6, and the strata were subsequently applied in layers. Mica powder was uniformly distributed between each layer to act as a weak interlayer, ensuring consistency and stratum homogeneity. After the model was completed and dried, an equivalent concentrated load of 0.132 MPa was applied to the top of the model to simulate the concentrated stress exerted by the residual coal pillars above. Simultaneously, the excavation of the 2-2 middle coal seam roadway commenced, accompanied by continuous monitoring.

As shown in Figures 11 and 12, the comprehensive monitoring of the entire model encompassed stress monitoring, roadway deformation, and macroscopic failure monitoring.



(**a**) (**b**)

Figure 11. Monitoring system. (**a**) DH3818Y static strain test system. (**b**) Speckle monitoring.

The stress monitoring system utilized the DH3818Y static strain gauge (Produced in Qingdao, China), which operated on the principle of static stress testing to track stress variations via bridge-type stress sensors embedded in the model. A total of 10 measurement points were strategically positioned in the roof and sidewalls of the roadway.

As illustrated in Figure 11b, the digital speckle testing system comprised a high-definition camera, supplementary lighting, speckle spray paint, and speckle analysis software(Ncorr v1.2.2). Black primer and white speckle dots were sprayed around the roadway, with the camera set to automatically capture images every 5 min. Following roadway excavation, the weakly cemented soft medium underwent deformation under stress, causing displacement of the speckle dots on the roadway surface. The captured images were subsequently uploaded to the analysis software, enabling the determination of the deformation characteristics and macroscopic fracture behavior of the roadway.

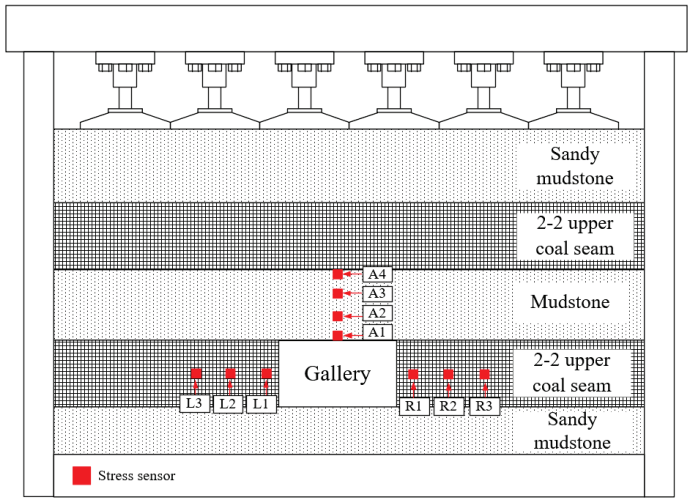

Figure 12. Stress sensor measuring point arrangement.

5.3. Analysis of Physical Model Test Results

(1) Evolution Law of Weakly Cemented Soft Medium

Figure 13 illustrates the stress evolution curves of the measurement points over time. During the initial stage, the model experienced a rapid stress release, causing a redistribution of stress that resulted in significant fluctuations in the stress curves of the roof and both sidewalls. Overall, the stress at the measurement points in the roadway gradually increased over time, with the stress diminishing as the distance from the roadway increased.

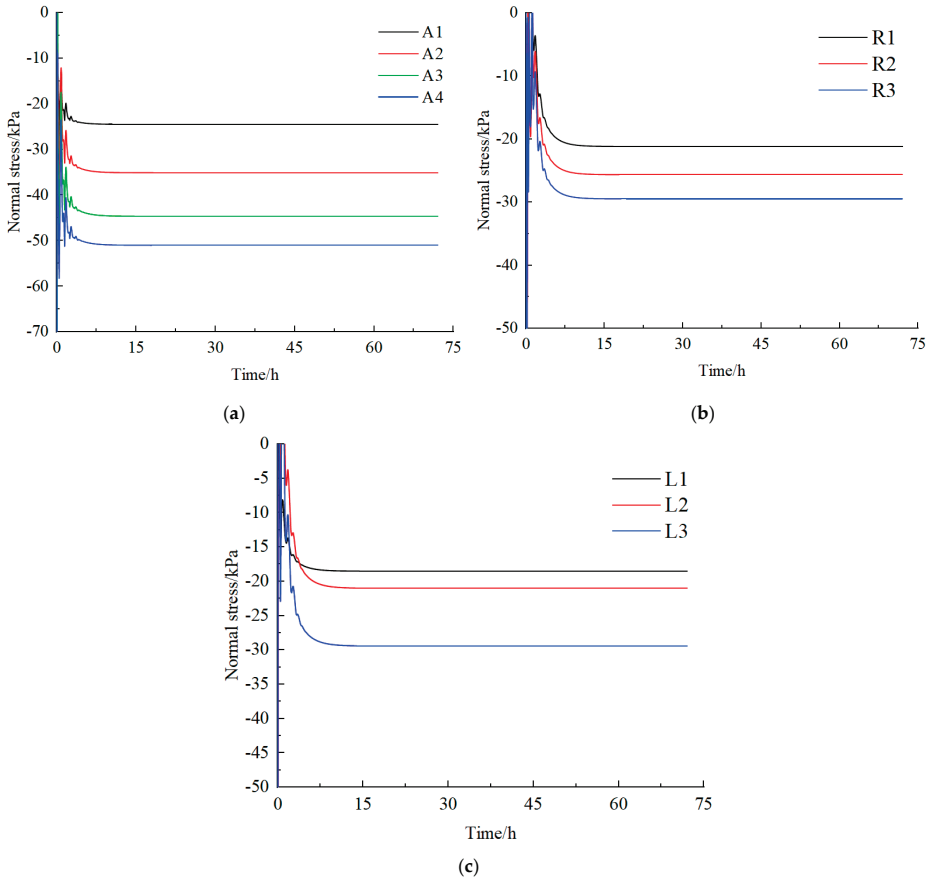

Figure 13. Vertical stress–time curve of measuring point. (**a**) Roof station. (**b**) Measuring points on left side of roadway. (**c**) Measuring points on the right side of roadway.

The stress in the roof of the model was more pronounced than that in the two sides. This phenomenon can be attributed to the concentration of load above the roof of the roadway. After 10 h of excavation, the trend of stress increase began to decelerate and eventually stabilized. At this point, the stress value of the roof ranged between −24.49 and −50.99 kPa, while the stress value of the sides ranged between −18.5 and 29.46 kPa. The ratio of side stress to roof stress was between 0.36 and 0.83, demonstrating that stress was mainly concentrated in the roof area. By comparing the stress conditions of the roof and side measurement points over time, it is evident that the roadway deformation exhibited significant creep characteristics.

(2) Surface Deformation and Failure Patterns of Weakly Cemented Soft Medium

In accordance with the experimental design, the roadway was excavated, and the digital speckle method was employed to accurately capture the deformation of the roadway sides and roof. The experimental results are depicted in Figures 14–16.

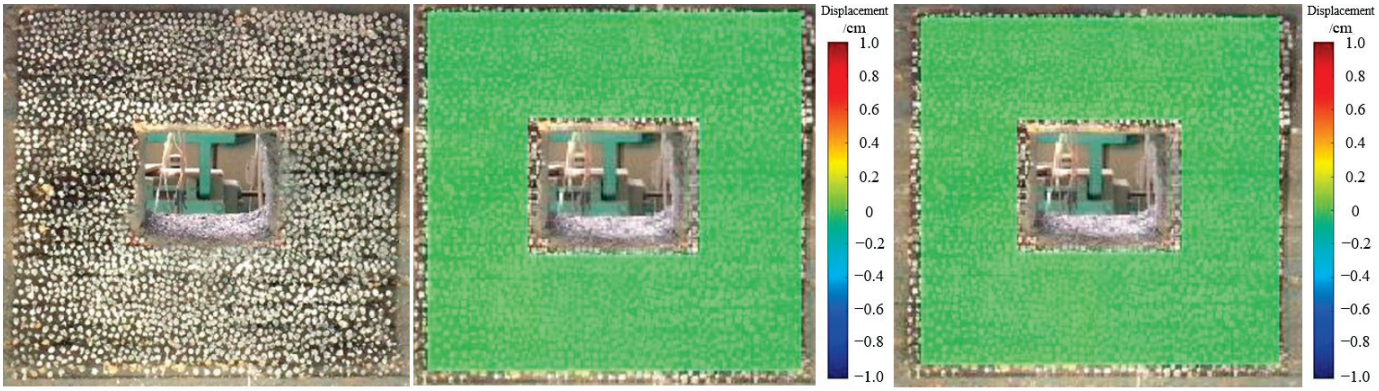

Figure 14. Deformation and failure of roadway after initial excavation. (**a**) Characteristics of roadway failure. (**b**) Horizontal displacement situation. (**c**) Vertical displacement situation.

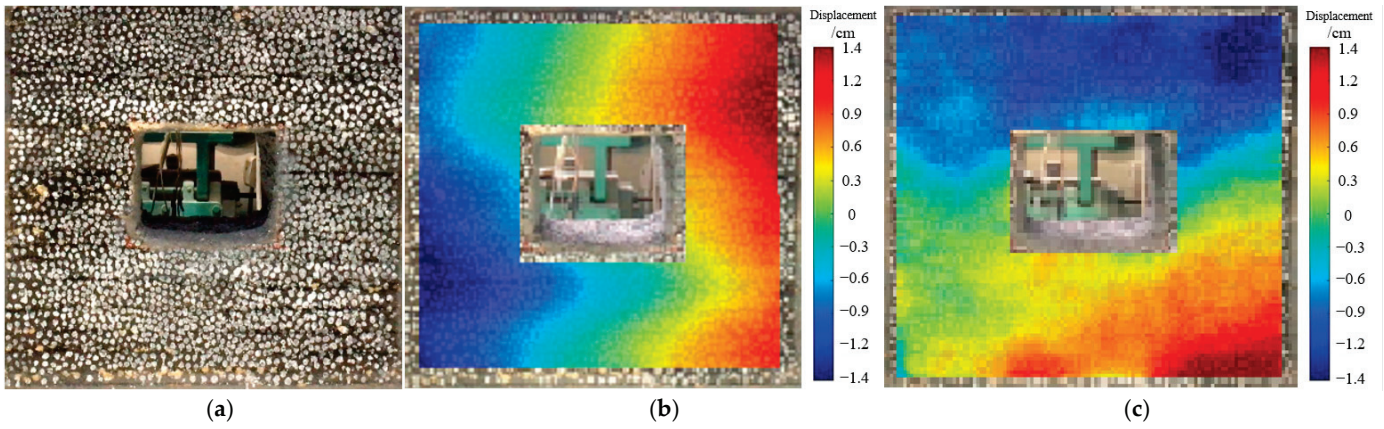

Figure 15. Deformation and failure of roadway after excavation for 1 day. (**a**) Characteristics of roadway failure. (**b**) Horizontal displacement situation. (**c**) Vertical displacement situation.

As shown in Figure 14, during the initial excavation, the stress above the roadway was rapidly released, resulting in deformation. Nonetheless, the overall stability of the roadway was maintained. As shown in Figure 17, The displacement of the roof and sidewalls was relatively small, with the maximum roof subsidence approximately 2 mm and the maximum sidewall convergence about 1 mm, both exhibiting a symmetrical distribution.

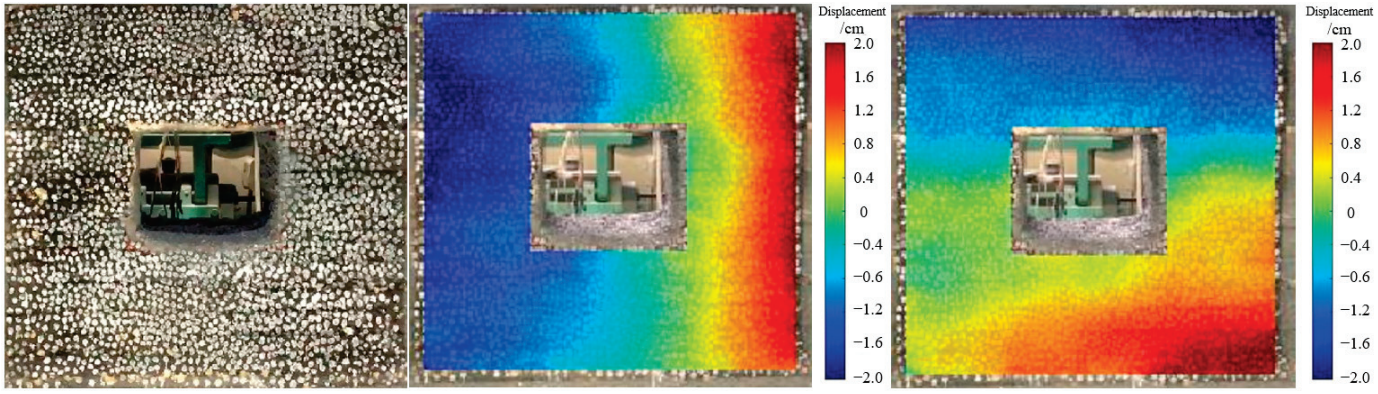

Figure 16. Deformation and failure of roadway after excavation for 3 days. (**a**) Characteristics of roadway failure. (**b**) Horizontal displacement situation. (**c**) Vertical displacement situation.

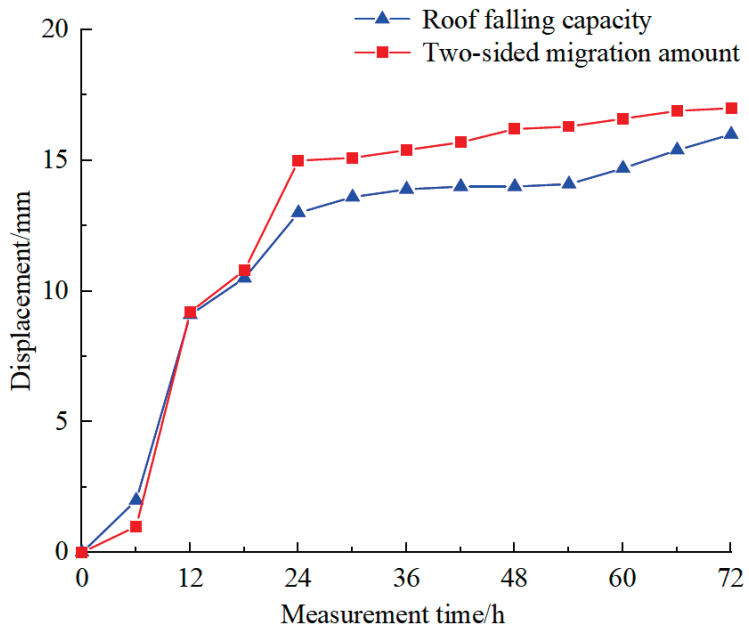

Figure 17. Variation law of surface displacement of roadway.

As revealed in Figure 15, one day after excavation, the vertical deformation of the roadway was predominantly characterized by roof subsidence, which reached approximately 13 mm. The deformation pattern of the sidewalls shifted from a symmetrical to an asymmetrical distribution, with the left sidewall exhibiting greater deformation than the right sidewall.

As depicted in Figure 16, the movement of the roadway roof and floor continued to show roof subsidence, with a maximum subsidence of 16 mm. The deformation of the side walls was principally concentrated near the center, with a maximum convergence of 17 mm.

As depicted in Figure 17, following the excavation of the roadway, creep deformation progressively occurred under concentrated loads. During the initial excavation stage, creep deformation was induced by concentrated loads. Ascribable to the relatively high overall strength, the deformation of the roof and sidewalls remained minimal at this stage, with the sidewall deformation showing a symmetrical distribution. Subsequently, the roadway began to exhibit clear creep characteristics under the action of concentrated loads. Throughout this phase, the rate of deformation accelerated, with the convergence of the sidewalls and subsidence of the roof increasing strikingly. Nonetheless, as the excavation

time progressed, the stress of the roadway gradually stabilized, and the deformation transitioned from a sharp increase to a steady state. At this stage, the convergence of the sidewalls exceeded the subsidence of the roof, and the sidewall deformation shifted from a symmetrical to an asymmetrical distribution.

6. Conclusions

This study, building upon the existing multivariate linear regression equation for the new soft medium, not only determined the target specimen proportion range but also identified the elastoplastic and creep characteristics of the novel material through orthogonal proportion tests. Additionally, a two-dimensional model test was conducted to evaluate the stability of the auxiliary transportation roadway in the 20314 working face of the Gaojialiang Coal Mine, considering long-term stratum load as the background. The test revealed the deformation and stress variation patterns in weakly cemented formation medium roadways. The main research findings are as follows:

(1) A similar material to simulate weakly cemented soft rock was successfully developed. The similar materials exhibited low strength and pronounced creep properties, making them particularly suitable for simulating weakly cemented medium in western mining areas. This methodology offers a brand new material selection option for conducting model tests on weakly cemented formation medium in these regions.

(2) The results from the orthogonal tests reveal that the concentration of rosin–alcohol solution significantly influenced critical parameters, such as the σ_c, E, and γ of the weakly cemented similar material specimens. Creep tests on specimens 4 and 5 demonstrated that as the proportion of iron powder (I) and barite powder (B) increased, the creep characteristics of the specimens progressively weakened.

(3) When this similar material was employed in the similarity model test to evaluate the surrounding rock stability of the auxiliary transportation roadway in Panel 20314 of the Gaojialiang Coal Mine under long-term stratum load, the test results indicate that approximately 10 h after excavation, the stress measured at the roof and sidewall monitoring points gradually slowed and eventually stabilized. As the excavation continued, the surrounding rock deformation transitioned from a sharp increase to gradual stabilization, shifting from a symmetrical to an asymmetrical distribution. This indicates that under the combined influence of concentrated load and creep load, the surrounding rock of the roadway underwent creep deformation. Both the conventional mechanical properties and long-term creep characteristics of this material satisfied the test requirements, effectively simulating the long-term creep behavior of weakly cemented soft rock in shallow buried strata. This provided reliable material support for achieving favorable test results.

Author Contributions: Conceptualization, S.H.; writing—original draft, S.H. and L.Y.; supervision, L.Y.; funding acquisition, S.H.; writing—review and editing, L.Y., S.G. and C.Z.; data curation, S.G., D.Y. and J.D.; formal analysis, C.Z. and Y.C. All authors have read and agreed to the published version of the manuscript.

Funding: The research described in this paper was financially supported by the National Natural Science Foundation of China (No. 52274087) and the Natural Science Foundation of Shandong Province (ZR2023ME189).

Institutional Review Board Statement: Not applicable.

Informed Consent Statement: Not applicable.

Data Availability Statement: The original contributions presented in the study are included in the article, further inquiries can be directed to the corresponding author.

Conflicts of Interest: The authors declare no conflicts of interest.

Nomenclature

Symbols	Implication
P	Prototype materials
M	Similar materials
L	Geometric dimension
γ	Unit weight
σ	Stress
ε	Strain
E	Elastic modulus
μ	Poisson's ratio
C	Cohesion
φ	Internal friction angle
σ_c	Uniaxial compressive strength
C_σ	Stress similarity ratio
C_γ	Unit weight similarity ratio
C_L	Geometric similarity ratio
C_δ	Displacement similarity ratio
C_ε	Strain similarity ratio
C_E	Elastic modulus similarity ratio
C_f	Friction coefficient similarity ratio
C_μ	Poisson's ratio similarity ratio
C_{σ_c}	Similarity ratio of uniaxial compressive strength
C_c	Cohesion similarity ratio
C_t	Time similarity ratio
C_η	Viscosity coefficient similarity ratio
σ_0	Creep stress
E_0	Elastic modulus of spring elements
E_1	Elastic modulus of elastomer in Kelvin body
η_1, η_2	Viscosity coefficients
σ_s	Long-term strength
$\dot{\varepsilon}$	Strain rate

References

1. Hu, S.; Zhang, C.; Ru, W.; Han, J.; Guo, S.; Zhou, X.; Yang, L. Creep properties and energy evolution characteristics of weakly cemented rock under step loading. *Int. J. Rock Mech. Min. Sci.* **2023**, *170*, 105428. [CrossRef]
2. Ru, W.K. Creep Damage and Engineering Application of Weakly Cemented Soft Rock Based on Energy Analysis. Ph.D. Thesis, Shandong University of Science and Technology, Qingdao, China, 2021.
3. Zhang, Y.; Zhang, W.; Wang, K.; Xie, K.; Song, K.; Wang, Y. Hydromechanical Properties and Engineering Applications of Weakly Cemented Soft Rock in Jurassic Strata. *ACS Omega* **2023**, *8*, 16373–16383. [CrossRef]
4. Cui, S.Y. Study on Hydro-dynamic Field and Media Characteristics of Weakly-Cemented Jurassic Aquifer in Dananhu Area. Ph.D. Thesis, China University of Mining and Technology, Xuzhou, China, 2017.
5. Yang, Y.; Li, W.; Wang, Q.; Chen, W.; Zhou, K. Experimental Study on Mechanical Behavior and Permeability Evolution of Weakly Cemented Sandstone under Unloading Conditions. *Bull. Eng. Geol. Environ.* **2024**, *83*, 115. [CrossRef]
6. Xu, R.; Zhao, Y.; Dou, B.; Hou, R.; Li, Z.; Dong, J. Experimental Investigation of the Effect of Strain Rate on the Cracking Behaviour and Acoustic Emission Characteristics of Red Sandstone Containing Orthogonal Cross Flaws under Quasistatic Uniaxial Compression. *Eng. Fail. Anal.* **2025**, *170*, 109323. [CrossRef]
7. Xu, R.; Gao, L.; Jin, Y.; Wang, Y.; Li, Z.; Hu, S. Influence of Strain Measurement Methods on Crack Initiation and Crack Damage Thresholds of Shale. *Geomech. Geophys. Geo-Energy Geo-Resour.* **2025**, *11*, 34. [CrossRef]
8. Ma, C.; Yuan, Y.; Zha, J.; Li, H.; Xu, Y. Determine Method of Effective Experimental Period of Similar Material Model for Improving the Simulation Results. *Energy Sources Part A* **2024**, *46*, 16165–16174. [CrossRef]
9. Zhou, B.; Shan, Y.; Yao, S. Deformation Monitoring of Similar Material Model Based on Point Cloud Feature Extraction. *J. Eng.* **2019**, *20*, 6790–6794. [CrossRef]

10. Hu, G.; Song, W.; Yu, X.; Lin, M.; Tie, Y.; He, B. Study on the Ratio and Model Test of Similar Materials of Heavily Weathered Granite. *Materials* **2024**, *17*, 5324. [CrossRef]
11. Su, H.; Liu, S.; Hu, B.; Nan, B.; Zhang, X.; Han, X.; Zhang, X. Experimental Study on Proportion Optimization of Rock-like Materials Based on Genetic Algorithm Inversion. *Materials* **2024**, *17*, 4940. [CrossRef]
12. Sun, L.; Wang, W.-X.; Xu, J.-S. Study on Proportioning Scheme of Coal System Rocky Similar Material Based on Orthogonal Test. *Materials* **2023**, *16*, 7113. [CrossRef]
13. Stück, H.; Koch, R.; Siegesmund, S. Petrographical and petrophysical properties of sandstones: Statistical analysis as an approach to predict material behaviour and construction suitability. *Environ. Earth Sci.* **2013**, *69*, 1299–1332. [CrossRef]
14. Holtzman, R. Micromechanical Model of Weakly-Cemented Sediments. *Int. J. Numer. Anal. Meth. Geomech.* **2012**, *36*, 944–958. [CrossRef]
15. Ren, X.; Zhang, Z.; Xiang, M.; Xu, G.; Cao, W. An Experimental Study on the Preparation of Soft Rock Similar Materials Using Redispersible Latex Powder as a Modifier. *Molecules* **2022**, *27*, 7404. [CrossRef]
16. Qian, Y.; Li, Z.; Jin, Y.; Wang, R. Experimental Study on Axial Tension Members of New Epoxy Resin Concrete. *Build. Struct.* **2020**, *50*, 124–127. [CrossRef]
17. Cui, L.; Sheng, Q.; Miao, C.; Luo, S. Mechanical Properties of Similar Materials Simulating Weak Surrounding Rocks with Different Ratios of Fine-to-Coarse Aggregate. *Appl. Sci.* **2025**, *15*, 3540. [CrossRef]
18. Li, Y.H.; Lin, Z.B. Innovative Experimental Method Based on Development of Transparent Rock Mass Materials for Physical Tests. *Chin. J. Geotech. Eng.* **2015**, *37*, 2030–2039. [CrossRef]
19. Xu, Y.; Su, D.-L.; Zhou, B.; Liu, Z.; Zhou, C.-Y. Experiment Study on Similarity Ratio of Similar Material for Model Test on Red-Bed Soft. *Rock. Rock Soil Mech.* **2016**, *37*, 2231–2237. [CrossRef]
20. Zhang, Y. Research on Orthogonal Experiment of Ratio of Similar Material for Coal. *Coal Technol.* **2018**, *37*, 72–74. [CrossRef]
21. Lin, H.F.; Zhai, Y.L.; Li, S.G.; Li, L.; Bai, Y. Research on Mechanics and Permeability Characteristics of Similar Material of Solid-Gas Coupling Based on Orthogonal Design. *J. China Coal Soc.* **2016**, *41*, 672–679. [CrossRef]
22. Ma, Z.G. *Study of Simulating Creep Properties of Soft Rock with Latex Cement*; Qingdao University of Science and Technology: Qingdao, China, 2014.
23. Wang, H.P.; Li, S.C.; Zhang, Q.Y.; Li, Y.; Guo, X.H. Development of a New Geomechanical Similar Material. *Chin. J. Rock Mech. Eng.* **2006**, *25*, 1842–1847.
24. Chu, Z.F. Study on Interaction between Tunnel Support and Surrounding Rock in Soft Rheology Rock. Ph.D. Thesis, Beijing Jiaotong University, Beijing, China, 2018.
25. Chu, Z.F.; Liu, B.G.; Sun, J.L.; Shen, J.; Song, Y.; Li, T. Research on Rheological Similar Material of Soft Rock Based on Burgers Model. *Chin. J. Rock Mech. Eng.* **2018**, *37*, 1185–1198. [CrossRef]
26. Chu, Z.-F.; Liu, B.-G.; Ren, D.-R.; Song, Y.; Ma, Q. Development of Rheology Similar Material of Soft Rock and Its Application in Model Test. *Rock Soil Mech.* **2019**, *40*, 2172–2182. [CrossRef]
27. Du, B.; Liu, B.G. *Similarity Simulation and Its Application in Shield Construction of Coal Mine Inclined Shafts*; Tsinghua University Press: Beijing, China, 2016.
28. Tao, B.; Wu, F.-Q.; Guo, G.-M.; Zhou, R.-G. Flexibility of Visco-Elastoplastic Model to Rheological Characteristics of Rock and Solution of Rheological Parameter. *Chin. J. Rock Mech. Eng.* **2005**, *24*, 3165–3171.
29. Fan, P.X.; Wang, M.Y.; Xing, H.Z.; Jiang, K.F.; Li, Z.Z. Time-Dependent Problems of Deformation and Failure in Geo-Mechanical Model Tests. *Chin. J. Rock Mech. Eng.* **2014**, *33*, 1843–1851. [CrossRef]
30. Zhang, Q.Y.; Li, S.C.; Guo, X.H.; Li, Y.; Wang, H.P. Research and Development of New Typed Cementitious Geotechnical Similar Material for Iron Crystal Sand and Its Application. *Rock Soil Mech.* **2008**, *29*, 2126–2130. [CrossRef]
31. *GB 50021-2001*; Code for Investigation of Geotechnical Engineering. China Architecture & Building Press: Beijing, China, 2009.
32. Dong, J.Y.; Yang, J.H.; Yang, G.X.; Wu, F.Q.; Liu, H.S. Research on Similar Material Proportioning Test of Model Test Based on Orthogonal Design. *J. China Coal Soc.* **2012**, *37*, 44–49. [CrossRef]
33. Xu, Q. Study on Stress Transfer Law and Reasonable Size of Section Pillar in Multi-Seam Mining. Ph.D. Thesis, Shandong University of Science and Technology, Qingdao, China, 2019.

Disclaimer/Publisher's Note: The statements, opinions and data contained in all publications are solely those of the individual author(s) and contributor(s) and not of MDPI and/or the editor(s). MDPI and/or the editor(s) disclaim responsibility for any injury to people or property resulting from any ideas, methods, instructions or products referred to in the content.

materials

MDPI

Article

Experimental Study on the Preparation of Paste Filling Materials from Coal-Based Solid Wastes

Chaowen Hu [1,2,*], Xiaojie Yang [3,*], Feng Zhang [2], Bo Pan [1], Ruifeng Huang [4], Bing Hu [1], Yongyuan Li [1], Lei Zhang [1], Bingshan Wang [1], Jianxun Gao [1], Huifeng Wang [1] and Yun Yu [5]

[1] Huaneng Coal Technology Research Co., Ltd., Beijing 100070, China; 18518556655@163.com (B.P.); 13810603612@163.com (B.H.); 15203308090@163.com (Y.L.); 13165479123@163.com (L.Z.); 18612568551@163.com (B.W.); 13001100105@163.com (J.G.); 18681930371@163.com (H.W.)
[2] China Coal Technology and Engineering Group, Chongqing Research Institute, Chongqing 400037, China; zfhxq1030@163.com
[3] State Key Laboratory for Tunnel Engineering, China University of Mining and Technology, Beijing 100083, China
[4] School of Emergency Technology and Management, North China Institute of Science and Technology, Beijing 101601, China; hrfcumt@163.com
[5] Huaneng Coal Co., Ltd., Beijing 100070, China; 13001152093@163.com
* Correspondence: chaowen_hu@163.com (C.H.); yxjcumt@163.com (X.Y.)

Abstract: To reduce the cost of coal mine filling materials, a novel composite cementitious material was developed by utilizing coal-based solid waste materials, including fly ash, desulfurized gypsum, and carbide slag, along with cement and water as raw materials. Initially, a comprehensive analysis of the physical and chemical properties of each raw material was conducted. Subsequently, proportioning tests were systematically carried out using the single-variable method. During these tests, multiple crucial performance indicators were measured. Specifically, the fluidity and bleeding rate of the slurry were evaluated to assess its workability, while the compressive strength and chemically bound water content of the hardened sample were tested to determine its mechanical properties and hydration degree. Through in-depth analysis of the test results, the optimal formulation of the composite cementitious material was determined. In the basic group, the mass ratio of fly ash to desulfurized gypsum was set at 70:30. In the additional group, the carbide slag addition amount accounted for 20% of the total mass, the cement addition amount was 15%, and the water–cement ratio was fixed at 0.65. Under these optimal proportioning conditions, the composite cementitious material exhibited excellent performance: its fluidity ranged from 180 to 220 mm, the bleeding rate within 6 h was less than 5%, and the 28-day compressive strength reached 17.69 MPa. The newly developed composite cementitious material features good fluidity and high strength of the hardened sample, fully meeting the requirements for mine filling materials.

Keywords: mining under structures; coal-based solid waste; composite cementitious backfill materials; land subsidence

1. Introduction

China is abundant in coal resources. However, continuous mining has led to the increasing prominence of the issue of coal mining under buildings, railways, and water bodies. Statistics indicate that the reserves of coal affected by these pressures in China exceed 14 billion tons, accounting for 63.5% of the country's recoverable coal reserves [1–3]. Consequently, the scientific and safe extraction of these overburdened coal resources has

become a focal point in the coal mining industry. Currently, backfill mining, a method that controls strata movement by filling goafs with backfill materials, has proven to be an effective solution for the issue of coal mining under buildings, railways, and water bodies [4–6]. After years of development, backfill mining technology has matured, and backfill materials have evolved into three major categories: inert backfill materials, cemented backfill materials, and new functional backfill materials. Inert backfill materials encompass gangue, river sand, loess, etc. Cemented backfill materials include paste backfill materials, industrial waste residue cemented materials, and others. New functional backfill materials consist of high-water quick-setting backfill materials, fire-prevention and fire-fighting backfill materials, polymer materials, and subsidence-reducing backfill materials [7–10]. In recent years, extensive research on the characteristics of backfill materials has been conducted by scholars both domestically and internationally. Academician Xie Heping's team has introduced a novel concept and technical framework for carbon-negative backfill mining. They have established a structural design for carbon-negative, highly porous backfill materials composed of a mixture of CO_2, gangue, and rapid-setting cementing agents. By improving and designing a closed carbon-sequestering stirring reactor, wet-stirring carbon-sequestration tests were conducted to investigate the carbon-sequestration performance of coal gangue solid waste. The correlation between carbon-sequestration performance and factors such as stirring speed and reaction temperature was analyzed, providing theoretical support for the design and application of carbon-negative backfill materials and promoting the implementation of the "double carbon" goal in the coal industry [11]. To address the air leakage problem around gas drainage boreholes, a relevant research team has developed a novel sealing material for dynamic filling and plugging of fractures. This study tested and compared the material's rheological properties, permeability, and stability. The experimental results demonstrated that the new material exhibits superior performance [12]. Based on the characteristics of hydration heat and volume resistivity, this study thoroughly investigates the hydration kinetics process and microstructural formation mechanism of fresh fly-ash cemented backfill materials. Using multiple testing methods, key nodes in the material hydration process are identified, and the evolution law of the microstructure is analyzed. This research is of great significance for reasonably regulating the performance of backfill materials [13]. Yin Bo et al. [14] focused on fly-ash cemented backfill materials and studied the enhancement of their strength and deformation properties through electrochemical treatment. The paper elaborated on the experimental procedures, analyzed the microstructural changes in the treated materials, and revealed the internal mechanisms underlying the performance enhancement. This work provides a new approach for optimizing the properties of backfill materials.

Although many scholars have developed various backfill materials with excellent mechanical properties, reducing the cost of backfill materials remains a key concern in the coal mining industry. This research aimed to reduce the cement consumption in traditional cemented backfill materials and break through the technical bottleneck of high backfilling costs. Meanwhile, by following the path of solid waste resource utilization, this study achieved the collaborative underground disposal of industrial wastes such as fly ash, desulfurized gypsum, and calcium carbide sludge, forming a green backfill technology system of "treating waste with waste and turning waste into treasure." This system provides theoretical foundations and technical support for the safe and efficient mining of coal resources and ecological environmental protection in coal mines. A novel composite cementitious backfill material was developed, primarily using industrial solid wastes such as fly ash, desulfurized gypsum, and carbide sludge. Single-variable method was employed to complete the proportioning tests of the composite cementitious material, and the fluidity and water bleeding rate of the slurry, as well as the compressive strength

and chemically bound water content of the solidified body, were tested. XRD and SEM techniques were utilized to analyze the crystal phases of hydration products and the micro-morphology of the composite cementitious material, enabling an in-depth investigation of its hydration process and mechanism.

2. Materials and Methods

The raw materials used in this study include fly ash, desulfurized gypsum, calcium carbide slag, and cement. Fly ash is a fine powder collected from the flue gases of coal-fired power plants and is the main solid waste discharged from coal-fired power plants, with major components including SiO_2, Al_2O_3, and Fe_2O_3. Desulfurized gypsum is an industrial by-product generated during the flue gas desulfurization process in coal-fired power plants or steel mills, with the main component being $CaSO_4$ $2H_2O$. The fly ash and desulfurized gypsum used in the experiments were sourced from a local coal-fired power plant. Calcium carbide slag is an industrial waste residue from the production of acetylene by the hydrolysis of calcium carbide (CaC_2), with the main component being calcium hydroxide ($Ca(OH)_2$). The calcium carbide slag used in the experiments was sourced from a local PVC plant. The cement used in the experiments was ordinary Portland cement produced by a local cement factory, with major chemical components including Al_2O_3, SiO_2, and CaO.

To ensure that the mechanical properties of the composite cemented backfill material meet the on-site engineering requirements, it is necessary to determine the optimal mix proportion of the composite cemented backfill material through tests such as slurry fluidity, water separation rate, compressive strength of the hardened sample, and chemically bound water content. The performance of the composite cemented backfill material is analyzed via crystalline phase and micro-morphology tests of the hydration products.

Due to the similar state between the slurry of fly ash composite cementitious material and cement mortar, the fluidity of the slurry can be measured by referring to the *Test Method for Fluidity of Cement Mortar* (GB/T 2419-2005) [15]. The bleeding rate of the slurry should be determined according to the *Technical Specification for Application of Cementitious Grouting Materials* (GB/T 50448-2015) [16]. The compressive strength of the solidified body shall be tested in accordance with the *Test Method for Strength of Cement Mortar (ISO Method)* (GB/T 17671-2021) [17]. The chemically bound water content of the solidified body shall be measured as specified in the *Methods of Chemical Analysis of Cement* (GB/T 176-2017) [18].

2.1. Experimental Investigation into the Mix Proportion Optimization of Composite Cemented Backfill Materials

2.1.1. Slurry Fluidity

To facilitate pipeline transportation and ensure efficient backfilling, the composite cementitious material must exhibit optimal fluidity, with its flowability maintained within the range of 180–240 mm. Given that the slurry of fly-ash composite cementitious material closely resembles cement mortar in consistency, a cement mortar flowability tester is suitable for measuring its flowability [19,20]. Flowability is quantified as the average diameter of the cement mortar spread on a flow table. A larger average diameter indicates higher flowability and, consequently, better fluidity [21,22].

2.1.2. Slurry Water Separation Rate

The water separation rate of the slurry is a critical performance index that reflects its stability. A lower water separation rate indicates better stability. Generally, a slurry is defined as stable if its 6-h water separation rate is less than 5% [23,24]. The 6 h water separation rate is commonly used as an indicator to evaluate the stability of slurries. The test method for determining the water separation rate is as follows [25,26]: A 500 mL

graduated cylinder is filled with approximately 400 mL of the slurry, and the initial slurry volume is recorded as V_1. After standing undisturbed for 6 h, the volume of separated water above the slurry is measured and recorded as V_2. The water separation rate α is calculated as the ratio of V_2 to V_1.

2.1.3. Compressive Strength of the Hardened Sample

Uniaxial compressive strength tests were performed on the hardened sample [27,28]. Specimens were cast using three-joint mortar molds with dimensions of 70.7 × 70.7 × 70.7 mm. After demolding, the specimens were cured in a standard cement constant temperature and humidity chamber. Compressive strengths were measured at ages of 3, 7, and 28 days. For each test group, three specimens were tested, and the average value of their compressive strengths was regarded as the test result of the group, accurate to 0.01 MPa. In case the compressive strength reading of an individual specimen deviated significantly (±20%) from the others, it was excluded, and the average value was recalculated based on the remaining specimens. The loading rate applied during the compression tests was set at 2.4 kN/s, in accordance with the relevant testing standards, to ensure consistent and comparable results.

2.1.4. Chemically Bound Water Content in the Hardened Sample

In this study, the hydration degree of the composite cementitious material is characterized by its chemically bound water content, which is determined using the ignition loss method [29,30]. The specific procedures are as follows: Initially, the sample is ground into a fine powder with an average particle size of 80 μm to terminate the hydration process, typically by soaking in absolute ethanol. This particle size control ensures consistent reaction kinetics and uniform termination of the hydration process. Next, 3 g of the ethanol-treated powder is placed in a pre-weighed crucible. The crucible is then dried at 105 °C until a constant weight is achieved. The sample is removed, cooled to room temperature, and weighed as m_{105}. Subsequently, the sample is transferred to a muffle furnace, heated from room temperature to 950 °C, and held at this temperature for 20 min. After cooling in a desiccator to room temperature, the sample is weighed again as m_{950}. The chemically bound water content is calculated using the following formula [31,32]:

$$w = \frac{m_{105} - m_{950}}{m_{105}} \times 100\% - (1 - \alpha - \beta)L_1 - (1 - \alpha)L_2 - \beta L_3 \quad (1)$$

where: W—Chemically bound water content, (%); m_{105}—Mass of the sample after drying at 105 °C and cooling to room temperature, (g); m_{950}—Mass of the sample after drying at 950 °C and cooling to room temperature, (g); L_1, L_2, L_3—Ignition loss of cementitious materials, (%); α,β—Proportions of cementitious materials α and β in the total amount of cementitious materials, (%).

2.2. Performance Evaluation of Composite Cemented Backfill Materials

The crystalline phase composition and structure of hydration products are key factors that determine the performance of mine backfill materials. The micro-morphology of these hydration products directly influences the engineering properties of composite cemented backfill materials, including mechanical strength, durability, permeability, and stability. Therefore, following the determination of the mix proportion of the composite cemented backfill material, its performance is evaluated by analyzing the crystalline phase and micro-morphology of its hydration products [33].

2.2.1. Crystalline Phases of Hydration Products

In this study, X-ray diffraction (XRD) tests are employed to analyze critical parameters such as the crystalline state and changes in the crystal structure of hydration products in cementitious materials [34,35]. The specific procedures are as follows: Prior to testing, the sample is vacuum-dried to eliminate moisture interference. The sample is then ground into a fine powder with a particle size distribution of D90 < 20 μm (verified by laser diffraction analysis), and 3 g of the powder is weighed to prepare a 10 mm × 10 mm thin slice. The powder is compacted under 10 MPa to minimize preferred orientation effects, following the protocol of ASTM C1365-18. The X-ray source is a rotating anode with a vibration amplitude controlled below 0.125 mm. The light spot focuses from 0.04°, with a focusing range of 0.25 mm × 15 mm. The copper tube provides a maximum voltage of 45 kV and a maximum rated current of 40 mA. The scanning equipment consists of a 2θ rotating goniometer driven by a motor, positioned vertically with a maximum speed of 1600°/min. The slit system includes a Soller slit (15 mm), a divergence slit (0.12 mm), a receiving slit (7.5 mm), and an anti-scatter slit (0.2 mm). The sample measurement angle ranges from 4° to 70°. The test results are analyzed and processed using JADE 6.5 software.

2.2.2. Micro-Morphology of Hydration Products

The micro-morphology of hydration products directly influences the engineering properties of composite cementitious backfill materials, including mechanical strength, durability, permeability, and stability [36,37]. In this study, a GAIA3-type dual-beam field emission scanning electron microscope (FESEM, TESCAN Orsay Holding, a.s., Brno, Czech Republic) equipped with an X-ray diffractometer (D8 ADVANCE, Bruker Corporation, Billerica, MA, USA) was used to examine the micro-morphology of hydration products at curing ages of 3, 7, and 28 days. The EDS analysis was performed under the following conditions: an accelerating voltage of 15 kV, a working distance of 10 mm, an acquisition time of 100 s, and a beam current of 1.2 nA. Prior to testing, samples were pretreated as follows: 1 g of each sample was crushed (rather than ground, to preserve the crystal structure) and immersed in absolute ethanol to terminate the hydration reaction and to disperse the sample. A droplet of the dispersed sample was then placed onto the conductive adhesive using a dropper. After the ethanol evaporated, the conductive adhesive strips with attached samples were subjected to gold sputtering using an ion sputtering instrument. Prepared samples were stored in a sealed container to prevent contamination.

2.2.3. Field Test

The overburden surface of the #3 coal seam in Xinyuan Coal Mine is occupied by Chenjiagou Village. The requirement for the holistic relocation of Chenjiagou Village to facilitate the mining of the #3 coal seam has significantly increased the operational costs associated with coal resource extraction. To address this challenge, this study explores the development of composite cementitious backfill materials derived from coal-based solid waste. The research aims to ensure that surface subsidence remains within the permissible limits set by industry standards, while simultaneously reducing backfilling costs to enable safe and economically viable exploitation of coal resources in the #3 coal seam.

Three short-wall working faces (3211, 3212, and 3213) in the #3 coal seam were selected as test sites. Each working face has a dip length of 65 m and a strike length ranging from 340 to 390 m. The layout of these test working faces is depicted in Figure 1.

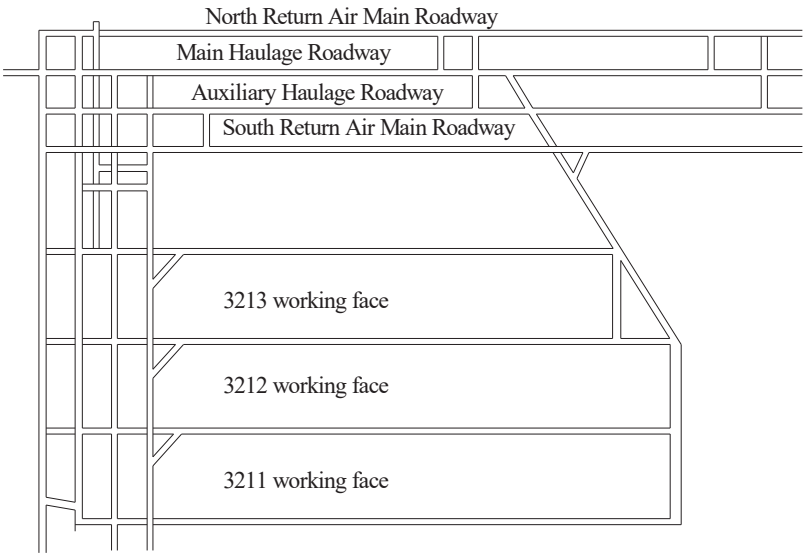

Figure 1. The layout of these test working faces.

3. Results and Discussion

3.1. Mix Proportion Optimization of Composite Cementitious Backfill Materials

3.1.1. The Ratio of Fly Ash to Desulfurized Gypsum

The dosage of carbide slag was set at 15%, cement at 10%, and the water-to-cement ratio at 0.65. Five experimental groups were designed with varying ratios of fly ash to desulfurized gypsum: 50:50, 60:40, 70:30, 80:20, and 90:10. The test proportions for the influence of fly ash to desulfurized gypsum ratio on slurry properties are shown in Table 1.

Table 1. Mixing proportions of fly ash and desulfurization gypsum.

No.	Fly Ash: Desulfurization Gypsum	Content of Calcium Carbide Slag (%)	Cement Dosage (%)	Water–Cement Ratio
Figure 1	50:50	15	10	0.65
Figure 2	60:40	15	10	0.65
Figure 3	70:30	15	10	0.65
Figure 4	80:20	15	10	0.65
Figure 5	90:10	15	10	0.65

(1) Slurry Fluidity

The fluidity of the slurry significantly affects the pipeline transportation and filling effectiveness of backfill materials. Figure 2 illustrates the slurry fluidity under various experimental conditions.

As illustrated in Figure 2, as the proportion of fly ash increases from 50% to 90% (from Figure 1 to Figure 5), the proportion of desulfurized gypsum correspondingly decreases from 50% to 10%, and the fluidity of the slurry continuously improves. This increase in fluidity is attributed to the spherical shape and dense, smooth surface of fly ash particles, which function as a "ball bearing" within the composite slurry, enhancing its flowability. The test results indicate that the fluidity of the slurry in Figures 1 and 2 is relatively low, failing to meet the pipeline transportation requirements for backfill materials. In contrast, the fluidity of the slurry in Figures 3–5 exceeds 180 mm, which is sufficient to satisfy the on-site pipeline transportation needs.

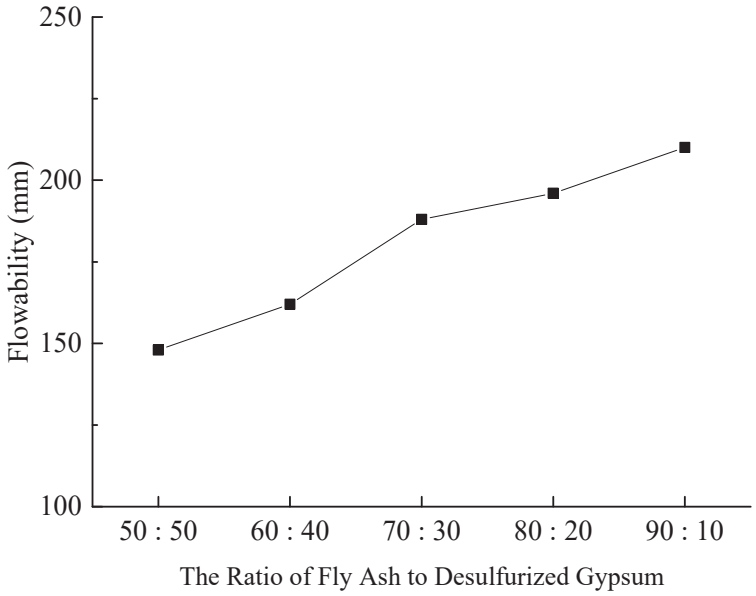

Figure 2. Effect of fly ash and desulfurized gypsum ratios on slurry fluidity.

(2) Slurry Water Separation Rate

The water separation rate of the slurry is a key indicator for assessing the stability and performance of backfill materials. Figure 3 illustrates the water separation rates of the slurry under various experimental conditions.

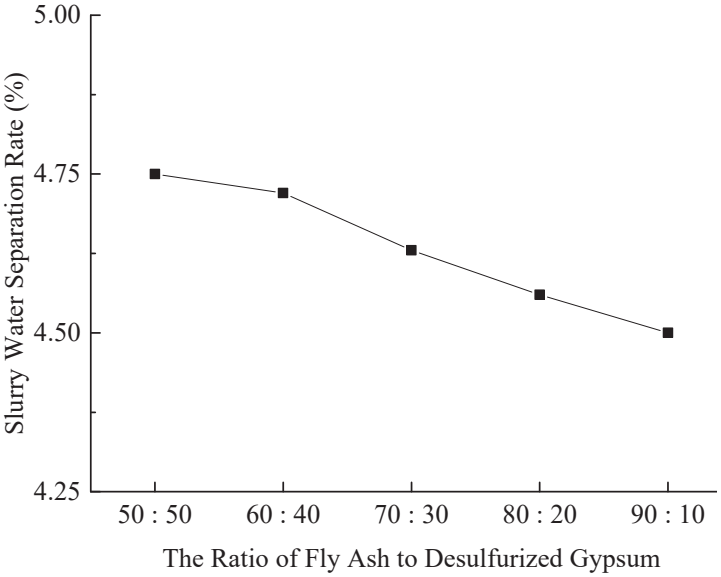

Figure 3. Effect of fly ash-to-desulfurized gypsum ratio on slurry water separation rate.

As illustrated in Figure 3, the water separation rates of the slurry under all five experimental Figures are below 5%, thus satisfying the on-site performance requirements for backfill materials.

(3) Compressive Strength of Hardened Sample

The compressive strength of the hardened sample, a critical mechanical property for mine filling materials, directly determines its effectiveness in supporting overlying strata. Figure 4 illustrates the compressive strengths of the hardened sample under different experimental conditions.

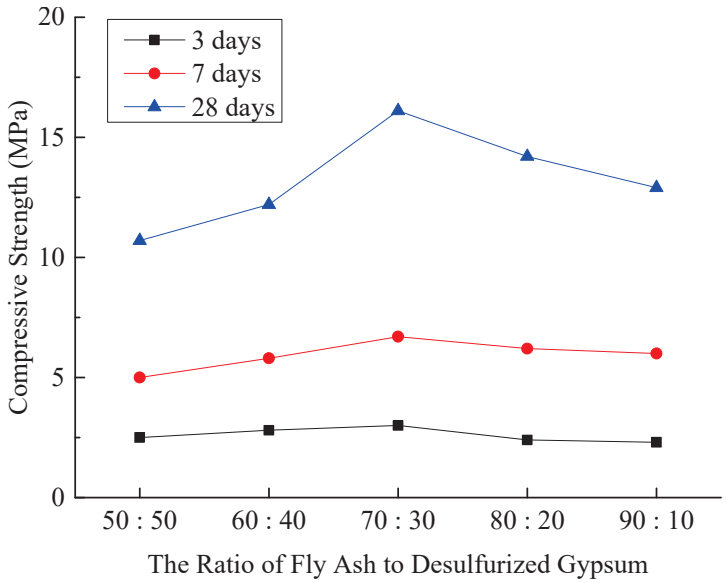

Figure 4. Effect of fly ash-to-desulfurized gypsum ratio on compressive strength of hardened sample.

As depicted in Figure 4, the compressive strength of the hardened sample increases progressively with increasing curing age. Under different experimental conditions, the compressive strength initially rises and then declines as the proportion of fly ash increases. At a curing age of 3 days, the compressive strength curve exhibits minimal variation. At 7 days, the variation in the compressive strength curve becomes more pronounced, and at 28 days, a distinct inflection is observed. When the ratio of fly ash to desulfurized gypsum shifts from 50:50 to 70:30, the compressive strength reaches its maximum. However, as the ratio increases further to 90:10, the compressive strength gradually decreases. This indicates that, initially, desulfurized gypsum primarily functions as a physical filler with minimal impact on strength. As the curing age progresses, desulfurized gypsum activates the reactivity of fly ash, thereby enhancing the strength of the system.

(4) Chemically Bound Water Content in Hardened Sample

The chemically bound water content in the hardened sample acts as a "bridge parameter" linking the microstructures and macroscopic properties of mine filling materials. Its primary function is to balance the requirements for strength, durability, cost, and environmental protection by modulating the degree of the hydration reaction. Figure 5 illustrates the chemically bound water content in the hardened sample under various experimental conditions.

As illustrated in Figure 5, at curing ages of 3 and 7 days, the chemically bound water content in hardened sample of composite cementitious filling materials under different experimental conditions exhibited minimal variation, with Figure 3 showing a slightly higher content than other figures. However, at 28 days, the chemically bound water content in the hardened sample of Figure 3 was significantly higher than that of other Figures. The test results indicate that the reaction rate of the basic fly ash-desulfurized gypsum system is slow, resulting in fewer initial hydration products, and their ratio has minimal impact on the degree of hydration. At 28 days, the pozzolanic effect of fly ash is fully activated, with higher fly ash content leading to more generated hydration products. Desulfurized gypsum plays a role in activating fly ash at later stages. When the fly ash content is high, the proportion of desulfurized gypsum decreases, weakening its activation effect on fly ash and preventing the full utilization of fly ash's pozzolanic activity, thereby reducing the degree of hydration. Therefore, the chemically bound water content in Figures 4 and 5 gradually decreases.

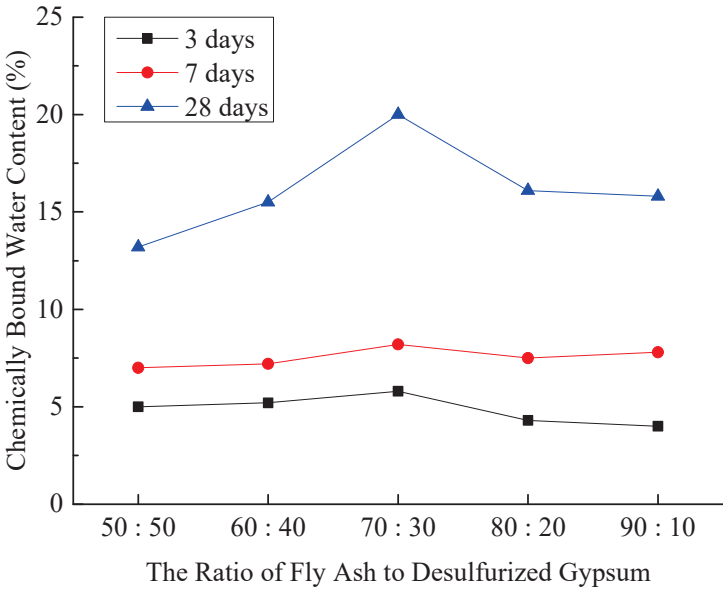

Figure 5. Effect of fly ash-to-desulfurized gypsum ratio on chemically bound water content in hardened sample.

Taking into account the slurry fluidity, water separation rate, and the compressive strength and chemically bound water content of the hardened sample, the optimal ratio of fly ash to desulfurized gypsum was determined to be 70:30.

3.1.2. Addition of Calcium Carbide Sludge

Based on the findings in Section 3.1.1, the optimal ratio of fly ash to desulfurized gypsum was determined to be 70:30. In this section, the cement dosage is set at 10%, and the water-to-cement ratio is maintained at 0.65. Three experimental sets are designed with varying additional amounts of calcium carbide sludge: 10% in Figure 1, 15% in Figure 2, and 20% in Figure 3. The effect of calcium carbide slag addition amount on slurry performance is shown in Table 2 for the test mix proportions.

Table 2. Test mix proportions of calcium carbide slag dosage.

No.	Fly Ash: Desulfurization Gypsum	Content of Calcium Carbide Slag (%)	Cement Dosage (%)	Water–Cement Ratio
Figure 1	70:30	10	10	0.65
Figure 2	70:30	15	10	0.65
Figure 3	70:30	20	10	0.65

(1) Slurry Fluidity

Figure 6 illustrates the slurry fluidity under various experimental conditions.

As illustrated in Figure 6, the fluidity of the slurry increases progressively with the addition of calcium carbide sludge, exhibiting an approximate increase of 30%. Notably, when the calcium carbide sludge content is set at 20%, the slurry achieves optimal fluidity, reaching 193 mm. This level of fluidity is highly suitable for pipeline transportation.

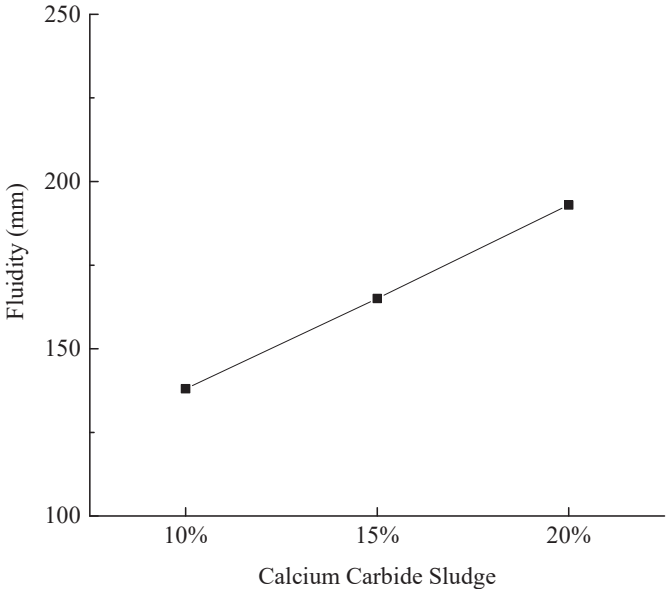

Figure 6. Effect of calcium carbide sludge content on slurry fluidity.

(2) Slurry Water Separation Rate

Figure 7 illustrates the water separation rates of the slurry under various experimental conditions.

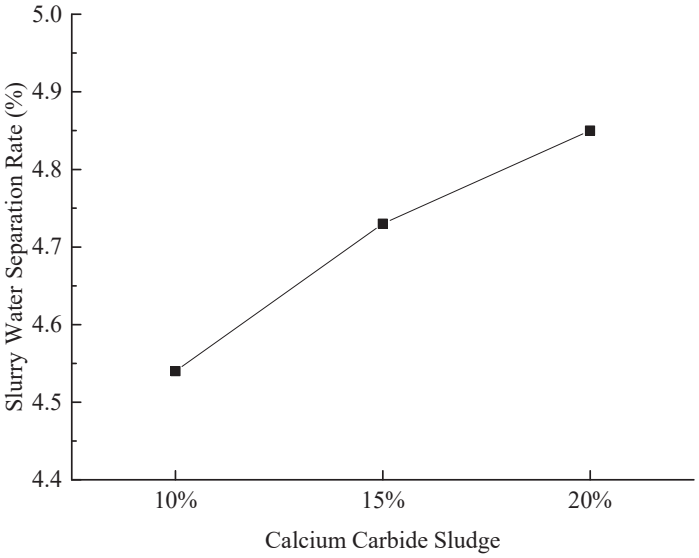

Figure 7. Effect of calcium carbide sludge content on slurry water separation rate.

As illustrated in Figure 7, the water separation rate of the slurry gradually increases with the addition of calcium carbide sludge, although the increase remains relatively modest. Notably, the water separation rate consistently remains below 5%, indicating no significant adverse impact on the slurry's stability. Experimental results reveal that the incorporation of calcium carbide sludge enhances the slurry's fluidity. The OH^- ions facilitate the formation of gels by reacting with the aluminum oxide and silicon dioxide in the fly ash. Simultaneously, an electrophoretic effect occurs, causing partial precipitation in the system and consequently increasing the water separation rate.

(3) Compressive Strength of Hardened Sample

Figure 8 illustrates the compressive strengths of the hardened sample under different experimental conditions.

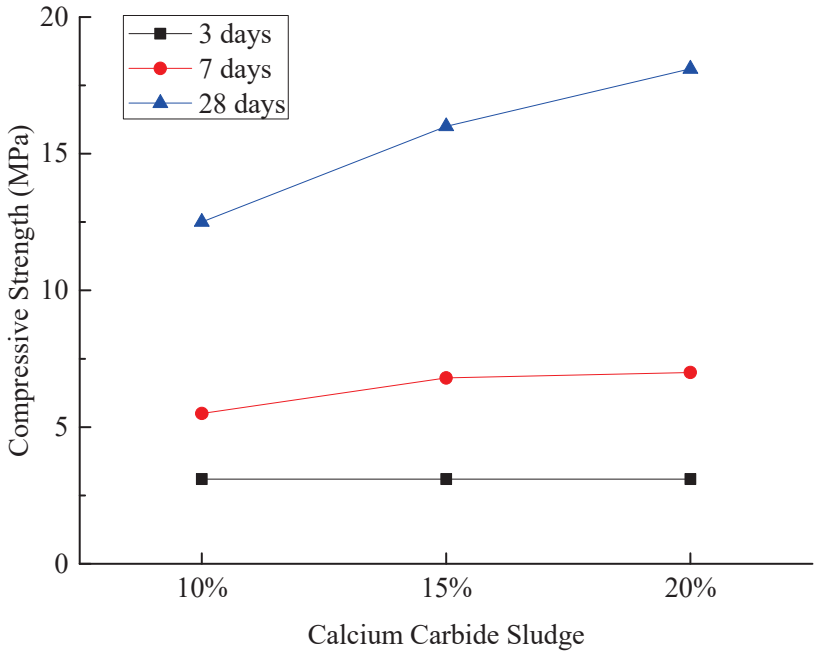

Figure 8. Effect of calcium carbide sludge content on compressive strength of hardened sample.

As illustrated in Figure 8, the compressive strength of the hardened sample at the 3-day curing age remains nearly unchanged with increasing calcium carbide sludge content. At the 7-day curing age, the strength exhibits a slight increase, albeit with a moderate growth margin. Notably, at the 28-day curing age, the compressive strength shows a significant enhancement. These findings suggest that the development of compressive strength in the cementitious material system is a slow-growth process, and a higher calcium carbide sludge content facilitates the gradual increase in the system's compressive strength.

Mechanistic analysis reveals that the incorporation of calcium carbide sludge enhances the internal structure of the cementitious system. Specifically, $Ca(OH)_2$ rapidly increases the alkalinity of the system, providing a highly alkaline environment that activates fly ash. The hydrated $Ca(OH)_2$ diffuses to the periphery of the fly ash glassy spheres, effectively disrupting their structure and releasing active Al_2O_3 and SiO_2. In this alkaline environment, Ca^{2+} reacts with Al-O and Si-O bonds to form calcium silicate hydrate (C-S-H) and calcium aluminate hydrate (C-A-H) gels. These gels densify the microstructure of the hardened sample, thereby enhancing their compressive strength [38,39].

(4) Chemically Bound Water Content in Hardened Sample

Figure 9 illustrates the chemically bound water content in the hardened sample under various experimental conditions.

As illustrated in Figure 9, the chemically bound water content in the hardened sample shows minimal growth with increasing calcium carbide sludge content and remains relatively low at curing ages of 3 and 7 days. In contrast, a significant increase is observed at a curing age of 28 days. This indicates that during the early hydration stages, the dissolution of Al-O and Si-O bonds in fly ash occurs slowly under alkaline conditions, leading to a low degree of hydration and minimal chemically bound water. Consequently, the effect of calcium carbide sludge is not pronounced. However, at 28 days, test groups with higher calcium carbide sludge content exhibit enhanced activation of fly ash, resulting in a greater degree of hydration, more hydration products, and a higher chemically bound water content [40,41].

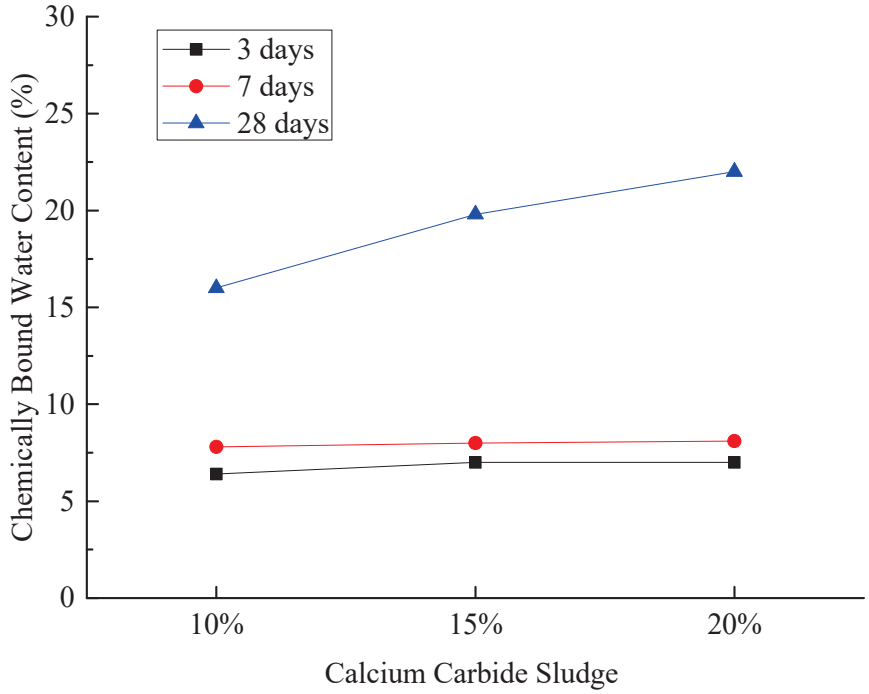

Figure 9. Effect of calcium carbide sludge content on chemically bound water content in hardened sample.

3.1.3. Cement Content

Based on the aforementioned research results, the optimal ratio of fly ash to desulfurized gypsum is determined to be 70:30, and the optimal content of calcium carbide sludge is established at 20%. On this basis, this section sets the water-to-cement ratio at 0.65 and designs three experimental groups with cement contents of 5%, 10%, and 15%, respectively. The test mix proportions for the effect of cement dosage on slurry performance are shown in Table 3.

Table 3. Test mix proportions of cement dosage.

No.	Fly Ash: Desulfurization Gypsum	Content of Calcium Carbide Slag (%)	Cement Dosage (%)	Water–Cement Ratio
Figure 1	70:30	20	5	0.65
Figure 2	70:30	20	10	0.65
Figure 3	70:30	20	15	0.65

(1) Slurry Fluidity

Figure 10 illustrates the slurry fluidity under various experimental conditions.

As illustrated in Figure 10, the slurry fluidity decreases with increasing cement content. This decrease is attributed to the higher water demand associated with increased cement content, which results in a relative reduction in free water within the system, thereby diminishing the slurry's fluidity.

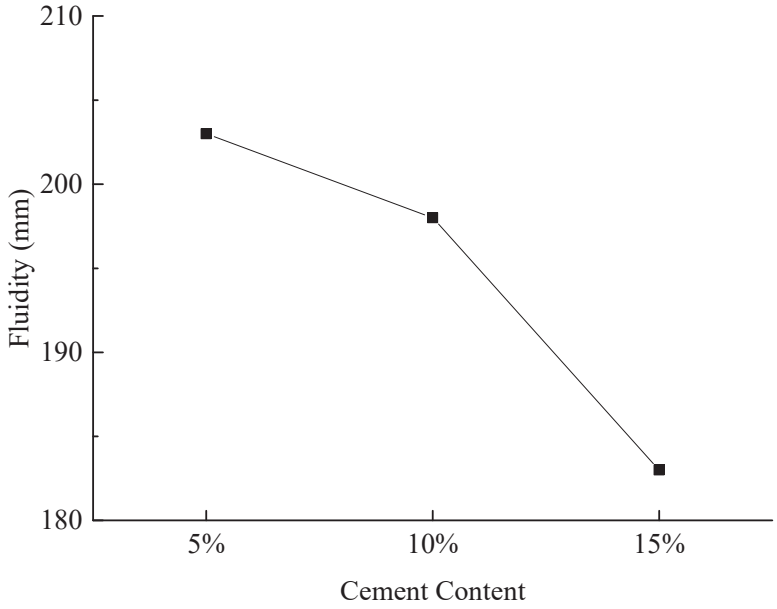

Figure 10. Effect of cement content on slurry fluidity.

(2) Slurry Water Separation Rate

Figure 11 illustrates the water separation rates of the slurry under various experimental conditions.

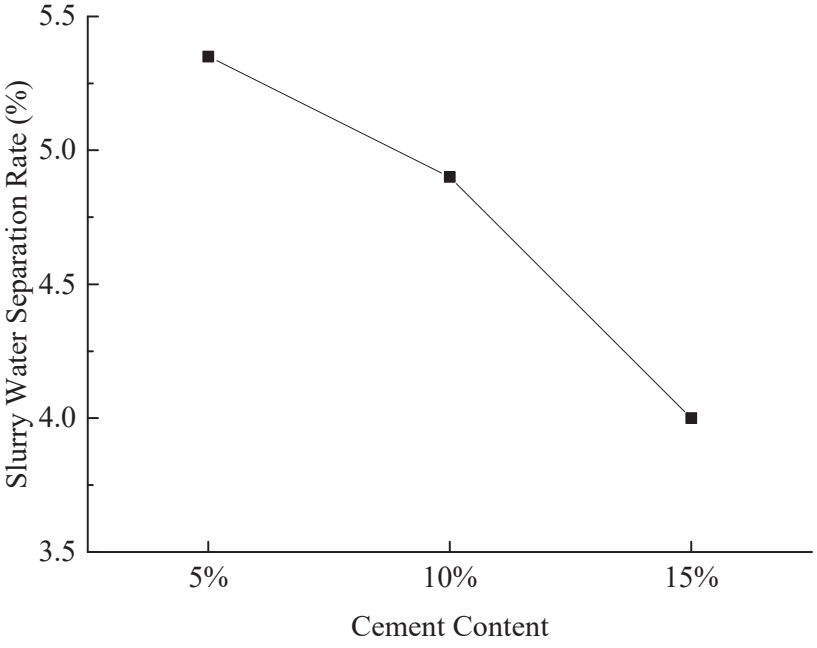

Figure 11. Effect of cement content on slurry water separation rate.

As illustrated in Figure 11, the water separation rate of the slurry decreases with increasing cement content. This decrease is attributed to the rapid hydration of cement, which solidifies fly ash and desulfurized gypsum together, thereby enhancing the stability of the system.

(3) Compressive Strength of Hardened Sample

Figure 12 illustrates the compressive strengths of the hardened sample under different experimental conditions.

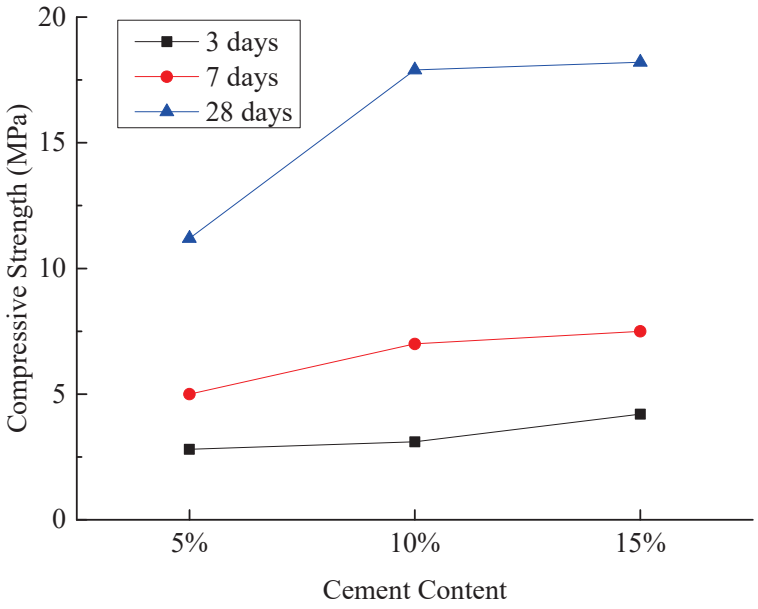

Figure 12. Effect of cement content on compressive strength of hardened sample.

As illustrated in Figure 12, increasing the cement content from 5% to 10% results in an increase in the compressive strength of the hardened sample at all curing ages, with a particularly significant increase observed at 28 days. Further increasing the cement content from 10% to 15% continues to enhance the compressive strength, although the rate of increase slows at 28 days. When the cement content is set at 10%, the compressive strength of the hardened sample reaches 17.69 MPa, meeting the on-site construction requirements. The test results indicate that as the cement content increases, the strength of the cementitious materials gradually rises. When the cement content exceeds 10%, the late-stage compressive strength of the composite cementitious materials continues to increase, albeit at a decreasing rate. This suggests that an appropriate cement content fully activates the active minerals in the composite cementitious materials through alkaline activators. The early compressive strength of the composite cementitious materials is primarily contributed by the active minerals in cement clinker, which exhibit high cementitious activity and rapid hydration reactions, forming hydration products in the initial mixing stage. The late-stage compressive strength is mainly contributed by the active minerals in fly ash and the unreacted active minerals in clinker. The alkaline environment formed by the reaction of cement clinker and the addition of alkaline activators provides the necessary alkalinity for the active components in fly ash, enabling these components to hydrate slowly in the later stages and significantly contribute to the late strength [42,43].

(4) Chemically Bound Water Content in Hardened Sample

Figure 13 illustrates the chemically bound water content in the hardened sample under various experimental conditions.

As illustrated in Figure 13, the chemically bound water content in the hardened sample increases with curing age under different experimental conditions. When the cement content increases from 5% to 10%, the chemically bound water content at the 28-day curing age shows a significant increase. However, when the cement content increases from 10% to 15%, the increase in chemically bound water content at 28 days is less pronounced. The test results indicate that the early hydration reaction of ordinary Portland cement and fly ash is relatively slow. As the curing age increases, cement hydration generates more $Ca(OH)_2$, creating a more favorable alkaline environment for the activation of fly ash and desulfurized gypsum, leading to the formation of additional hydration products. At

28 days, the cement contents of 10% and 15% provide more C_2S and C_3S, which accelerate the growth of chemically bound water in the test groups. As curing continues, the late-stage hydration of C_2S progresses, causing the chemically bound water content in both test groups to converge and increase gradually [44,45].

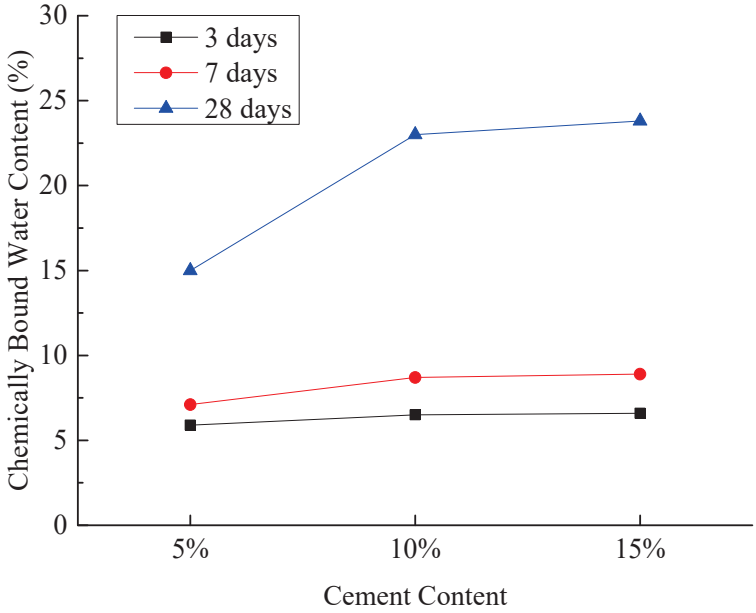

Figure 13. Effect of cement content on chemically bound water content in hardened sample.

3.1.4. Water–Cement Ratio

Based on the previous research results, the optimal ratio of fly ash to desulfurized gypsum was determined to be 70:30, with the optimal addition amounts of calcium carbide sludge and cement set at 20% and 10%, respectively. On this basis, three experimental sets were designed in this section, with water-to-cement ratios of 0.55, 0.65, and 0.75. It should be noted that the mixing water used for composite cementitious backfill materials shall be purified and desalinated water. The test mix proportions for investigating the effect of water–cement ratio on slurry performance are shown in Table 4.

Table 4. Test mix proportions for water–cement ratio experiments.

No.	Fly Ash: Desulfurization Gypsum	Content of Calcium Carbide Slag (%)	Cement Dosage (%)	Water–Cement Ratio
Figure 1	70:30	20	10	0.55
Figure 2	70:30	20	10	0.65
Figure 3	70:30	20	10	0.75

(1) Slurry Fluidity

Figure 14 illustrates the slurry fluidity under various experimental conditions.

As illustrated in Figure 14, the slurry fluidity increases significantly and continuously with the water-to-cement ratio rising from 0.55 to 0.75. At a water-to-cement ratio of 0.55, the slurry flow value is 140 mm, which is insufficient for pipeline transportation. In contrast, at water-to-cement ratios of 0.65 and 0.75, the slurry flow values exceed 180 mm, satisfying the requirements for on-site pipeline transportation.

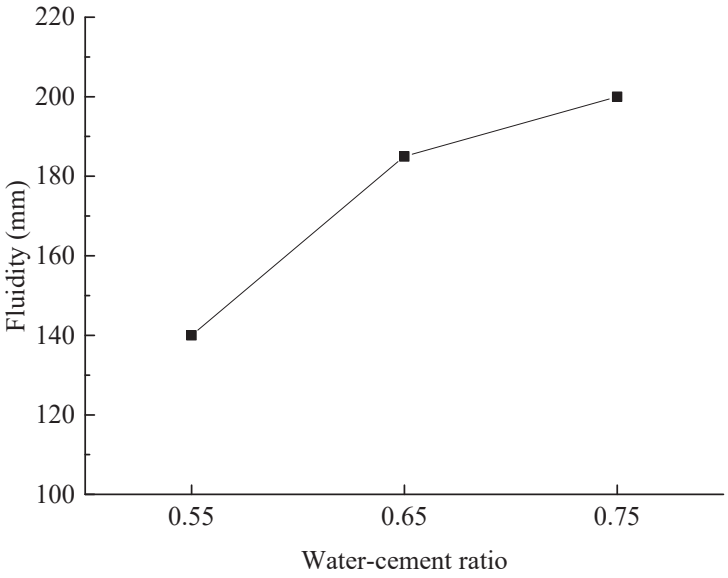

Figure 14. Effect of water-to-cement ratio on slurry fluidity.

(2) Slurry Water Separation Rate

Figure 15 illustrates the water separation rates of the slurry under various experimental conditions.

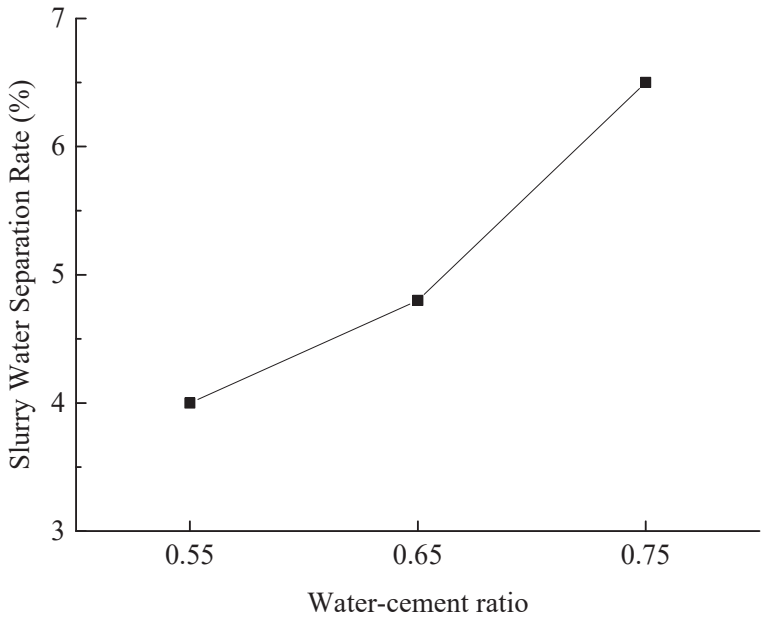

Figure 15. Effect of water-to-cement ratio on slurry water separation rate.

As illustrated in Figure 15, the water separation rate of the slurry increases progressively with the water-to-cement ratio. At water-to-cement ratios of 0.55 and 0.65, the water separation rates are both below 5%, indicating satisfactory slurry stability. However, at a water-to-cement ratio of 0.75, the water separation rate rises to 6.43%, suggesting diminished slurry stability.

Taking into account both the fluidity and water separation rate of the slurry, the optimal water-to-cement ratio is determined to be 0.65.

3.2. Microstructural Characteristics and Hydration Mechanism of Composite Cementitious Backfill Materials

Based on the mix proportion parameters established in the preceding section, the base group has a fly ash-to-desulfurized gypsum ratio of 70:30. In the additive group, the calcium carbide sludge content is 20%, the cement content is 15%, and the water-to-cement ratio is set at 0.65. The hydration process and reaction mechanism of the cementitious materials were analyzed microscopically using X-ray diffraction (XRD) and scanning electron microscopy (SEM) techniques.

3.2.1. XRD Analysis of Composite Cementitious Backfill Materials

Figure 16 illustrates the XRD patterns of composite cementitious backfill materials at curing ages of 3, 7, and 28 days.

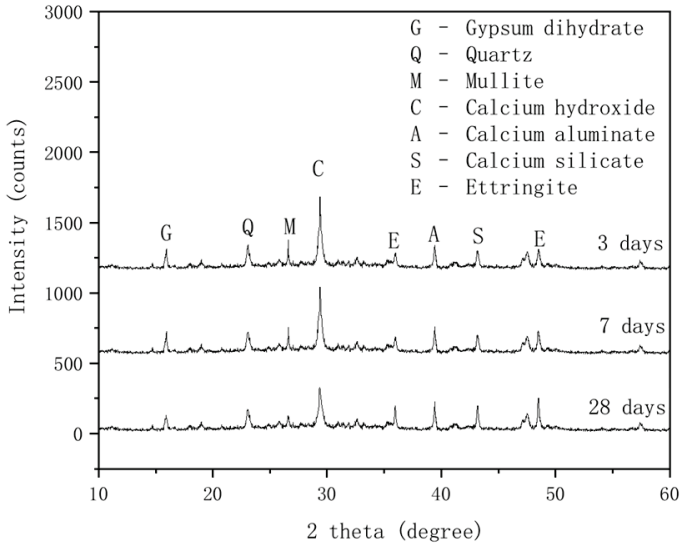

Figure 16. XRD patterns of hydration products in cementitious materials.

As illustrated in Figure 16, at a curing age of 3 days, the hydration reaction begins to take place. The diffraction peaks of $Ca(OH)_2$, mullite, and quartz in the composite cementitious backfill materials are relatively distinct, with minor peaks of ettringite, calcium silicate, and calcium aluminate also present. Ettringite plays a primary role in the early strength of the backfill material. The $Ca(OH)_2$ diffraction peak remains prominent at all ages, but as the curing age extends to 7 days, $Ca(OH)_2$ is consumed by hydration reactions, leading to a decrease in peak intensity. The peaks of mullite and quartz also decrease, as Al_2O_3 and SiO_2 in fly ash react with $Ca(OH)_2$ (a cement hydration product) to form C-A-H and C-S-H gels. When the curing age increases to 28 days, the $Ca(OH)_2$ diffraction peak continues to decline. The pozzolanic effect of fly ash is further activated, and the hydration reaction consumes substantial $Ca(OH)_2$, generating more C-A-H and C-S-H gels, which enhance the compressive strength of the backfill material.

With increasing curing age, the diffraction peak of gypsum (calcium sulfate dihydrate) begins to decrease: the decline is minimal at 7 days but becomes pronounced at 28 days. In the later stages, the activity of fly ash is secondarily activated by desulfurized gypsum, leading to significant consumption of desulfurized gypsum. At 28 days, the peaks of calcium silicate and ettringite increase significantly. Part of the calcium aluminate reacts with gypsum to form ettringite crystals, consuming calcium aluminate and $Ca(OH)_2$ while increasing the content of hydration products, particularly ettringite crystals. The hydration products are primarily composed of C-S-H gel and ettringite, which contribute to the strength of the fly ash composite cementitious materials [46–48].

3.2.2. SEM Analysis of Composite Cementitious Backfill Materials

Figure 17 illustrates the SEM results of composite cementitious backfill materials.

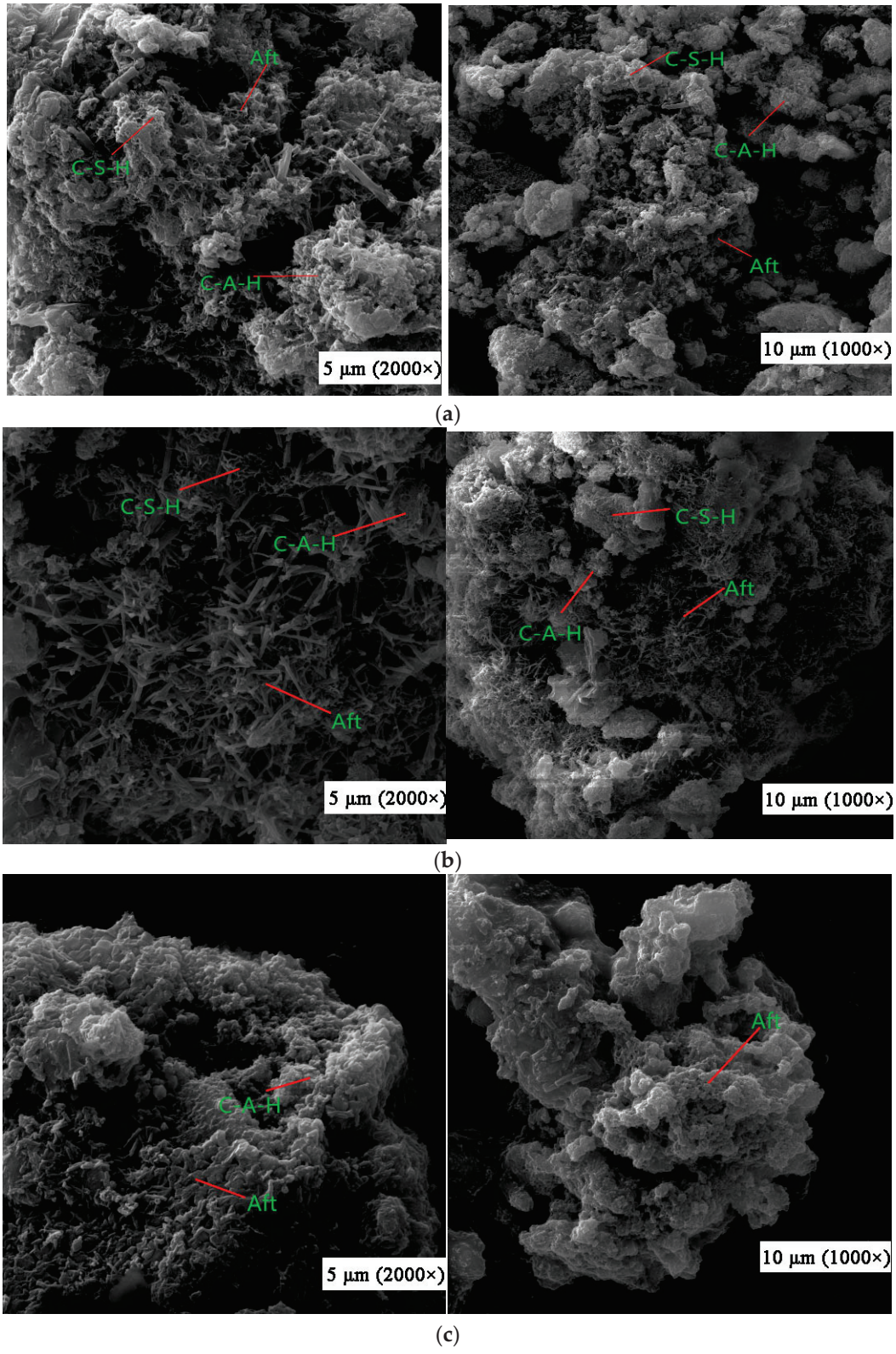

Figure 17. SEM images of hydration products in composite cementitious filling materials at (**a**) 3 days of hydration; (**b**) 7 days of hydration; (**c**) 28 days of hydration.

From Figure 17a, it is evident that the composite cementitious backfill materials exhibit surface erosion at a hydration age of 3 days. At this stage, the vitreous structure of fly ash is disrupted, leading to the gradual cleavage of Si-O and Al-O bonds on the fly ash surface. The presence of white flocculent substances indicates that the reactive components of fly ash have initiated reactions. Specifically, $Ca(OH)_2$ reacts with SiO_2 in fly ash to form C-S-H gel (calcium silicate hydrate), while $Ca(OH)_2$ reacts with Al_2O_3 to generate C-A-H gel (calcium aluminate hydrate). The interlaced acicular substances observed are ettringite (Aft, calcium sulfoaluminate hydrate) formed by the reaction of Al_2O_3 with SO_4^{2-} and $Ca(OH)_2$, which significantly contributes to the early strength development of the composite cementitious backfill materials [49,50].

As the hydration process progresses and under the dual activation effect of $Ca(OH)_2$ and desulfurized gypsum, Figure 17b shows that at 7 days of hydration, the surface erosion of the composite cementitious backfill materials becomes more pronounced. The white flocculent substances increase, and hydration products accumulate. A continuous network structure gradually forms on the surface of fly ash particles, where alumina and silica in the fly ash vitreous body are increasingly dissolved and participate in hydration reactions. Many individual erosion points on the particle surface merge into continuous areas, and more granular hydration products appear on the surface of the cementitious materials. The acicular ettringite crystals grow longer, denser, and interlace more intensively. Under the alkaline conditions provided by the hydration of carbide slag and cement, the vitreous structure of fly ash gradually disintegrates. Driven by desulfurized gypsum, the pozzolanic activity of fly ash is continuously activated, leading to an increasing number of hydration reactions.

At 28 days of hydration, Figure 17c shows that the vitreous structure of fly ash is almost entirely eroded, and its surface is completely covered by hydration products. The morphological characteristics of fly ash become indistinct. In the cementitious materials, acicular ettringite crystals interlock to form an integral structure with fewer voids and a denser texture, enhancing the compactness and strength of the backfill materials. Meanwhile, hexagonal plate-like crystals of desulfurized gypsum can be seen precipitating and interpenetrating the cementitious material system, further increasing the strength of the system.

The EDS spectra of the hydration products of composite cementitious backfill materials are illustrated in Figure 18.

As illustrated in Figure 18a, at a hydration age of 3 days, the peaks of Al and Si are relatively low, indicating that the activity of fly ash has not yet been fully activated. The Al-Si bonds in fly ash are tightly bonded, while the peak of Ca is relatively high. The initial reaction is slow, with OH^- ions from $Ca(OH)_2$ playing a dominant role in accelerating the breakage of Al-Si bonds in fly ash. At 7 days of hydration (Figure 18b), the Ca peak gradually decreases, suggesting the formation of more calcium silicate and calcium aluminate gels. As shown in Figure 18c, by 28 days of hydration, the hydration reaction is essentially complete, with ettringite crystals being the primary reaction product. The peaks of Al and Si increase significantly, as the system consumes Ca^{2+} to generate a large amount of ettringite.

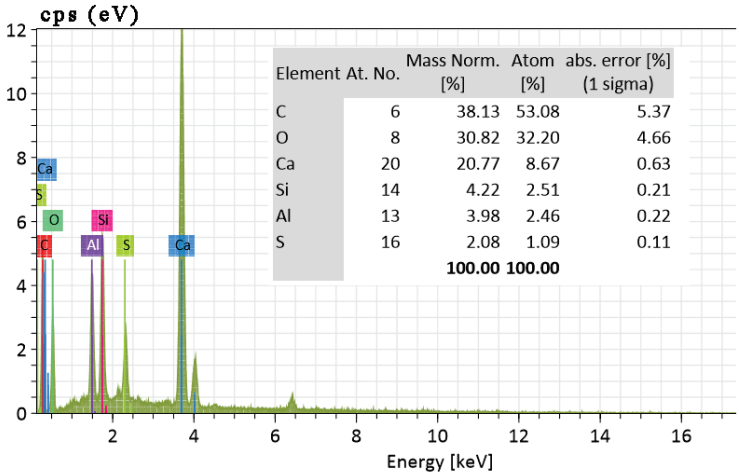

(**a**)

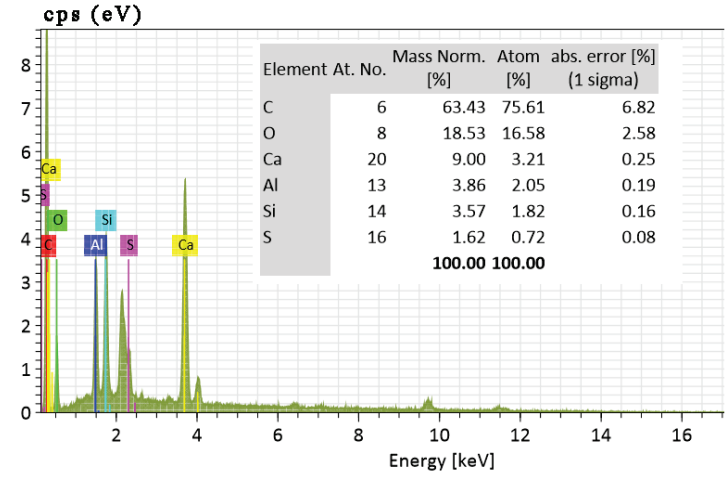

(**b**)

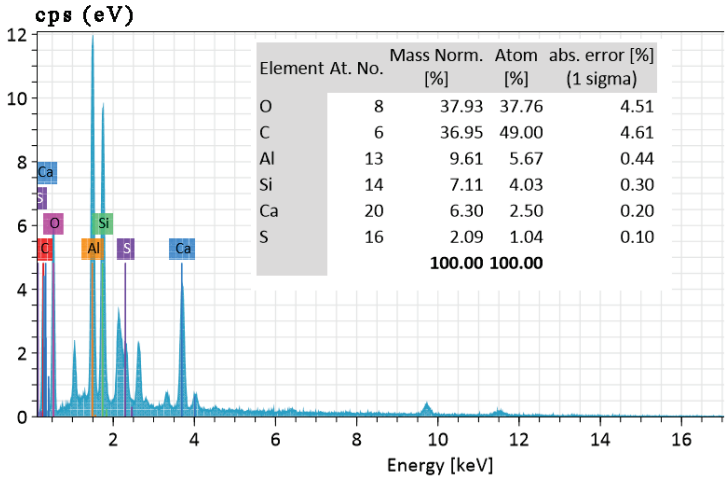

(**c**)

Figure 18. EDS spectra of hydration products in composite cementitious backfill materials at (**a**) 3 days of hydration; (**b**) 7 days of hydration; (**c**) 28 days of hydration.

3.3. Hydration Mechanism Analysis

The crystalline phases and micro-morphologies of composite cementitious backfill materials at different curing ages were systematically analyzed using XRD (X-ray Diffraction)

and SEM (Scanning Electron Microscopy) techniques to investigate the hydration process of the fly ash-desulfurized gypsum-calcium carbide sludge–cement composite system.

During the hydration of cement, a significant amount of $Ca(OH)_2$ colloidal particles are generated. Similarly, calcium carbide sludge forms substantial $Ca(OH)_2$ colloidal particles upon contact with water. When fly ash is mixed with water, a water film forms on its surface. Upon contact with $Ca(OH)_2$, Ca^{2+} and OH^- ions penetrate the water film on the fly ash surface, forming an alkaline film containing OH^- and Ca^{2+}. Once the alkaline film is established, the fly ash surface begins to corrode, leading to the partial rupture of Si-O and Al-O bonds on the fly ash particle surface and initiating the pozzolanic reaction, as follows [51,52]:

$$SiO_2 + mCa(OH)_2 + nH_2O = mCaO{\cdot}SiO_2{\cdot}nH_2O \quad (2)$$

$$Al_2O_3 + mCa(OH)_2 + nH_2O = mCaO{\cdot}Al_2O_3{\cdot}nH_2O \quad (3)$$

$$mCaO \bullet Al_2O_3 \bullet nH_2O + CaSO_4 \bullet 2H_2O = mCaO \bullet Al_2O_3 \bullet CaSO_4 \bullet (n+2)H_2O \quad (4)$$

As the system experiences a progressive increase in both free water and chemically bound water, the concentration of OH^- ions within the alkaline microenvironment at the fly ash surface correspondingly rises. Concurrently, these ions infiltrate the interior through interstices among surface hydrates, instigating corrosion of the fly ash vitreous phase and promoting the deepening of the pozzolanic reaction. With the increase in $[OH^-]$ and $[Ca^{2+}]$ molarities in the cementitious matrix, the hydration kinetics of fly ash accelerates in a stepwise manner. Initially, trace amounts of ettringite are formed, while cement hydration contributes calcium silicate hydrate (C-S-H) gel, which supports early strength development. However, as deduced from the early-age compressive strength data presented in Chapter 4, the cementitious grouting material exhibits suboptimal early strength. This is attributed to the strong electrostatic adsorption of Ca^{2+} and OH^- by colloidal nuclei within the $Ca(OH)_2$ particle matrix, which imposes a thermodynamic constraint on ion availability—particularly for Ca^{2+}—in the alkaline interfacial solution. The hydration products, primarily existing as $CaO{\cdot}SiO_2{\cdot}nH_2O$ (C-S-H) and $CaO{\cdot}Al_2O_3{\cdot}nH_2O$ (C-A-H) gels (see reactions in Equations (2) and (3)), further exacerbate ion sequestration through their inherent sorption capacity. Given that C-S-H and C-A-H constitute the fundamental strength-contributing phases in fly ash-based systems, the retarded hydration kinetics result in diminished early-age mechanical performance. As curing progresses, the accumulating C-A-H phase engages in a secondary reaction with dihydrate gypsum to form ettringite ($CaO{\cdot}Al_2O_3{\cdot}3CaSO_4{\cdot}(n + 2)H_2O$), as delineated in Equation (4), driving progressive strength gain through the formation of a denser crystalline network [53,54].

Based on the foregoing analysis, the hydration reaction of the fly ash-desulfurized gypsum-calcium carbide sludge–cement composite system is fundamentally characterized as a synergistic process that integrates cement clinker hydration and the pozzolanic activation of fly ash by desulfurized gypsum and calcium carbide sludge. This process can be delineated into three distinct stages [55,56]:

Stage I: Activation of Silicon–Aluminum Bonds in Fly Ash

Cement clinker hydration releases calcium hydroxide, while calcium carbide sludge introduces additional $Ca(OH)_2$, creating a highly alkaline microenvironment (pH > 12.5) rich in OH^- ions. These OH^- ions initiate nucleophilic attacks on the Si-O and Al-O bonds of fly ash vitreous particles, facilitating the dissolution of reactive SiO_2 and Al_2O_3 species.

The dissolved SiO_2 reacts with $Ca(OH)_2$ to form calcium silicate hydrate (C-S-H) gel, while Al_2O_3 generates calcium aluminate hydrate (C-A-H) gel. Concurrently, C-A-H gel reacts with sulfate ions (SO_4^{2-}) from desulfurized gypsum and excess $Ca(OH)_2$ to precipitate ettringite ($3CaO{\cdot}Al_2O_3{\cdot}3CaSO_4{\cdot}32H_2O$). These hydration products—C-S-H, C-A-H, and ettringite—deposit on particle surfaces to form a dense encapsulation layer, as confirmed by in situ SEM observations [57].

Stage II: Progressive Hydration and Structural Erosion

The continuous erosion of the fly ash vitreous network occurs as Ca^{2+}, OH^-, and SO_4^{2-} ions diffuse through the porous encapsulation layer. The needle-like morphology of ettringite crystals enhances structural porosity, thereby accelerating ion transport and promoting deeper dissolution of aluminosilicate phases. This stage is kinetically governed by multiple factors, including the Al/Si ratio of the vitreous phase, reaction temperature (activation energy: 55–65 kJ/mol), and fly ash reactivity. Isothermal calorimetry reveals a secondary exothermic peak at approximately 14 days, attributed to the accelerated pozzolanic reaction. XRD analysis confirms the gradual consumption of amorphous phases and the formation of a heterogeneous hydration product matrix [58].

Stage III: Crystalline Growth and Strength Development

The sustained structural degradation of fly ash particles expands the reactive interface, enabling alkaline solutions to penetrate deeper into particle cores. Continuous hydration generates an increasingly dense microstructure characterized by interlocking C-S-H/C-A-H gels and ettringite crystals. Mercury intrusion porosimetry demonstrates a reduction in median pore diameter from 120 nm at 3 days to 45 nm at 28 days, correlating with the development of mechanical strength. Compressive strength data follow a quadratic growth model, reflecting the progressive densification of the hydration product network. Thermogravimetric analysis (TGA) confirms a 25% increase in chemically bound water content over the same period, further validating the hydration progression [59].

3.4. Field Test

After the working face is mined, a retaining wall composed of "I-beams + metal mesh + air duct cloth" is constructed at the end of the working face. The prepared composite cemented backfill material is then filled into the goaf through pipelines. The No. 3 coal seam has an average buried depth of 550 m and an average thickness of 2.5 m. According to the relevant regulations of the Coal Mine Surveying Code, when the mining depth exceeds 300 m, the working point spacing of the surface movement observation station should be 20–25 m. In this study, based on the topographic conditions of the surface corresponding to the three test working faces (3211, 3212, and 3213), the point spacing is set to 25 m. Specifically, a monitoring curve is arranged in the middle of each working face along the strike direction, labeled as S1, S2, and S3, respectively. Additionally, a monitoring curve is arranged along the dip direction, labeled as D. The S1 survey line comprises 27 measuring points, the S2 survey line comprises 26 measuring points, the S3 survey line comprises 25 measuring points, and the D survey line comprises 18 measuring points. The corresponding range of the working face surface and the layout of the surface measuring points are depicted in Figure 19.

Figure 20 illustrates the surface movement and deformation monitoring data.

As illustrated in Figure 20, the maximum surface subsidence along the S1 survey line is 9 mm, along the S2 survey line is 11 mm, along the S3 survey line is 9 mm, and along the D survey line is 12 mm. The field monitoring data indicate that the surface movement and deformation are minimal, falling within the Grade I range specified in the Regulations for Coal Mining Under Buildings, Railways, and Water Bodies (hereinafter referred to as

the "Three Under" Mining Regulations). This level of movement meets the protection requirements for surface buildings and structures.

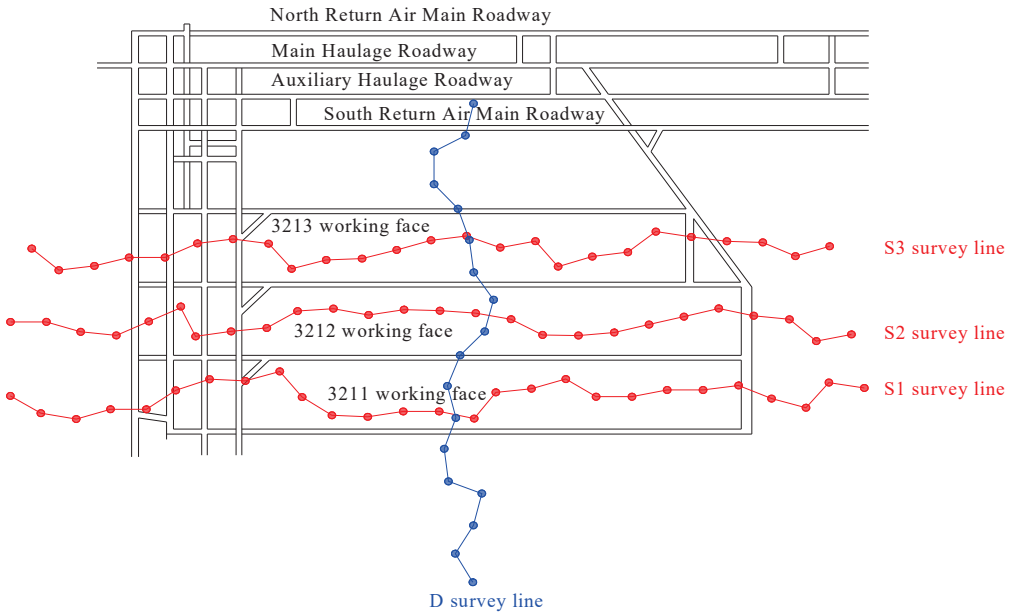

Figure 19. Layout of surface monitoring points.

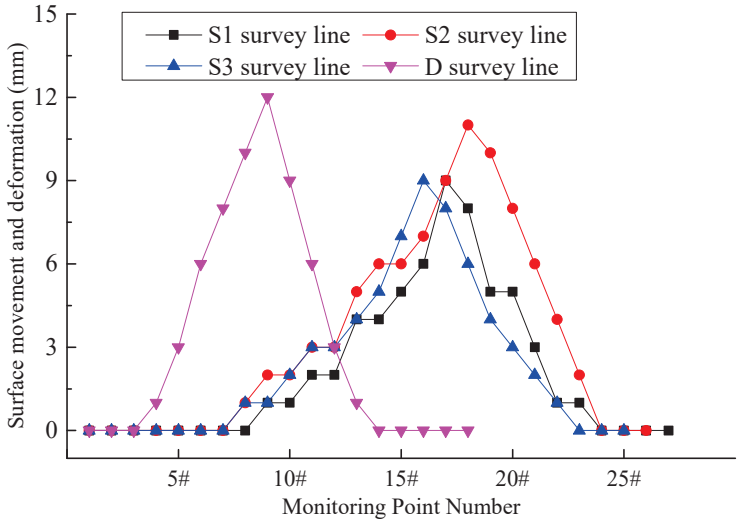

Figure 20. Surface movement and deformation monitoring curves.

4. Conclusions

This study utilizes coal-based solid waste materials, including fly ash, desulfurized gypsum, and carbide sludge, as the foundation and incorporates cement, water, and other raw materials to develop a novel composite cementitious backfill material. Field tests were conducted at Xinyuan Coal Mine, yielding the following principal conclusions:

(1) The hydration process of cementitious backfill materials is characterized by the synergistic interaction among fly ash, desulfurized gypsum, and carbide sludge. The calcium hydroxide in carbide sludge rapidly elevates the alkalinity of the system, facilitating the depolymerization of the glassy structure in fly ash. This significantly enhances the early pozzolanic activity of fly ash and accelerates the formation of C-S-H gels. The addition of cement provides early strength support to the material

system. The ettringite and C-S-H gels generated during cement hydration form the strength framework. Desulfurized gypsum, on the other hand, continuously undergoes secondary reactions with the hydration products of fly ash in the later stages. Through the continuous crystallization and growth of ettringite, it ensures the steady increase in material strength.

(2) The optimal mix proportion of cementitious backfill materials was determined through single-variable method tests as follows: The mass ratio of fly ash to desulfurized gypsum is 70:30, the carbide sludge content is 20%, the cement content is 15%, and the water–binder ratio is 0.65. Under this proportion, the fluidity of the composite cementitious backfill materials ranges from 180 to 220 mm, the water bleeding rate within 6 h is less than 5%, and the 28-day compressive strength reaches 17.69 MPa. In addition, XRD and SEM analyses indicate that the hydration products of the system under this mix proportion have high crystallinity and a dense pore structure, providing a guarantee for long-term stability.

(3) The results of on-site industrial tests indicate that after the goafs are filled with the new composite cementitious backfill materials, the maximum surface subsidence is only 12 mm, which is far lower than the Grade I settlement standard ($\leq$30 mm) specified in the Regulations for Mining Under Buildings, Railways and Water Bodies, fully meeting the protection requirements for surface buildings and structures. As the raw materials mainly consist of coal-based solid waste materials such as fly ash, desulfurized gypsum, and carbide sludge, the filling cost is effectively reduced, achieving the unity of environmental and economic benefits. Subsequent research could focus on the long-term durability assessment of the materials under complex geological conditions (such as high-confined water and highly corrosive strata). In the future, tests on chloride salt erosion, sulfate erosion, and freeze–thaw cycles could be carried out. Meanwhile, exploring nanomaterial modification techniques to further enhance the mechanical properties and impermeability of the materials, expanding their application potential in deep mining fields.

(4) It should be noted that the experimental results presented in this study are based on a limited number of samples due to constraints in material availability. While the findings provide valuable insights into the performance of the developed backfill material, further validation with a larger sample size is recommended to ensure statistical reliability and support industrial-scale decision-making. This study can be considered a preliminary investigation, and future work should focus on expanding the dataset to enhance the robustness of the conclusions.

Author Contributions: Conceptualization, C.H.; methodology, X.Y.; software, C.H. and F.Z.; validation, R.H., F.Z. and J.G.; formal analysis, C.H. and B.P.; investigation, B.H., R.H. and Y.Y.; resources, C.H., B.H. and Y.L.; data curation, L.Z. and Y.L.; writing—original draft preparation, C.H.; writing—review and editing, C.H. and X.Y.; visualization, B.W., L.Z. and H.W.; supervision, H.W. and B.W.; project administration, J.G. and Y.Y.; funding acquisition, B.P. All authors have read and agreed to the published version of the manuscript.

Funding: This research was funded by "the National Natural Science Foundation of China, grant number 42377195", "the National Natural Science Foundation of China-Railway Fundamental Research Joint Fund Project, grant number U2468219", "the Fundamental Research Funds for the Central Universities, grant number 3142023015", "A Science and Technology Support Project in Langfang City, grant number 2023011025", and "the Science and Technology Project of Huaneng Coal Technology Research Co., Ltd., grant number HNCTR25-03".

Institutional Review Board Statement: Not applicable.

Informed Consent Statement: Not applicable.

Data Availability Statement: The original contributions presented in this study are included in the article. Further inquiries can be directed to the corresponding authors.

Acknowledgments: We are grateful to the anonymous reviewers for their constructive reviews of the manuscript, and to the editors for carefully revising the manuscript.

Conflicts of Interest: Chaowen Hu, Bo Pan, Bing Hu, Yongyuan Li, Lei Zhang, Bingshan Wang, Jianxun Gao and Huifeng Wang are employed by the Huaneng Coal Technology Research Co., Ltd. Yun Yu is employed by the Huaneng Coal Co., Ltd. The remaining authors declare that the research was conducted in the absence of any commercial or financial relationships that could be construed as a potential conflict of interest.

References

1. Ma, Q.; Zhang, Y.D.; Zheng, Y.; Li, Z.X.; Song, G.Y.; Hu, L. Overlying Strata Movement and Mine-Pressure Weakening Law of High-Efficiency Longwall Paste Backfilling of Thick Coal. *Sustainability* **2022**, *14*, 15356. [CrossRef]
2. Wang, H.S.; Tian, J.H.; Li, L.; Chen, D.F.; Yuan, Y.X.; Li, B. Research on the Development Height Prediction Model of Water-Conduction Fracture Zones under Conditions of Extremely Thin Coal Seam Mining. *Water* **2024**, *16*, 2273. [CrossRef]
3. Zhou, N.; Xu, J.F.; Zhang, J.X.; Yan, H.; Zhu, C.L.; Li, M. An Experimental Study of the Permeability of Sand-based Cemented Backfill Under the Influence of Multi-factor Interaction. *Environ. Earth. Sci.* **2022**, *81*, 1–16. [CrossRef]
4. Hu, C.W.; Li, Q.; Wang, Y.L.; Chang, K.; Li, Y.Y.; Wang, Y.Q.; Liu, H. Key Technology Research on the Rapid-Molding In-Closed Retaining-Wall in Filling Mining. *Shock. Vib.* **2022**, *2022*, 1–14. [CrossRef]
5. Feng, J.W.; Zhang, Z.Y.; Guan, W.M.; Wang, W.; Xu, X.Y.; Song, Y.Z.; Liu, H.; Su, H.; Zhao, B.; Hou, D.Z. Review of the Backfill Materials in Chinese Underground Coal Mining. *Minerals* **2023**, *13*, 473. [CrossRef]
6. Emad, M.Z. Numerical Modelling Approach for Mine Backfill. *Sadhana-Acad. P. Eng. S.* **2017**, *42*, 1595–1604.
7. Li, M.; Peng, Y.F.; Ding, L.W.; Zhang, J.X.; Ma, D.; Huang, P. Analysis of Surface Deformation Induced by Backfill Mining Considering the Compression Behavior of Gangue Backfill Materials. *Appl. Sci.* **2023**, *13*, 160. [CrossRef]
8. Ngo, I.; Ma, L.Q.; Zhai, J.T.; Wang, Y.Y.; Wei, T.X. Durability of CO_2-fly ash-based Backfill Materials in Cation Water Deterioration. *Int. J. Mining Reclam. Environ.* **2023**, *37*, 544–567.
9. Kim, Y.S.; Kim, J.; Cho, D.S. Implementation of Optimized Backfill Materials for Underground Electric Power Cables. *J. Porous. Media* **2014**, *17*, 831–840.
10. Zhao, Z.Y.; Ma, L.Q.; Ngo, I.; Yu, K.P.; Xu, Y.J.; Zhai, J.T.; Gao, Q.Q.; Peng, C.K.; Wang, D.L.; Alarifi, S.S. Experimental Investigation on Hydrophobic Alteration of Mining Solid Waste Backfill Material. *Minerals* **2024**, *14*, 580. [CrossRef]
11. Zhang, J.X.; Li, B.Y.; Xie, Y.C.; Li, C.B.; Zhou, N.; Guo, Y.M.; Li, Z.J.; Xie, H.P. Carbon Negative Backfill Mining in Coal Mines for Carbon Neutralization: Chemical Carbon Fixation Performances with Mineralized Gangue. *Int. J. Rock. Mech. Min.* **2025**, *186*, 106016. [CrossRef]
12. Lou, Z.; Wang, K.; Yao, H.W.; Zhao, W.; Qin, H.J.; Wu, Z.Q.; Wei, G.Y. A Novel Dynamic Filling Material for Plugging Fractures Around Underground Gas Extraction Boreholes: Experimental and Engineering Performances. *Energy* **2025**, *314*, 134202. [CrossRef]
13. Yin, B.; Kang, T.H.; Kang, J.T.; Chen, Y.J.; Wu, L.L.; Du, M.Z. Investigation of the Hydration Kinetics and Microstructure Formation Mechanism of Fresh Fly Ash Cemented Filling Materials Based on Hydration Heat and Volume Resistivity Characteristics. *Appl. Clay. Sci.* **2018**, *166*, 146–158.
14. Yin, B.; Kang, T.H.; Kang, J.T.; Chen, Y.J. Experimental and Mechanistic Research on Enhancing the Strength and Deformation Characteristics of Fly-Ash-Cemented Filling Materials Modified by Electrochemical Treatment. *Energy Fuels* **2018**, *32*, 3614–3626.
15. *GB/T 2419-2005*; Test Method for Fluidity of Cement Mortar. Standardization Administration of the People's Republic of China: Beijing, China, 2005.
16. *GB/T 50448-2015*; Technical Specification for Application of Cementitious Grouting Materials. Ministry of Housing and Urban-Rural Development of the People's Republic of China: Beijing, China, 2015.
17. *GB/T 17671-2021*; Test Method for Strength of Cement Mortar (ISO Method). Standardization Administration of the People's Republic of China: Beijing, China, 2021.
18. *GB/T 176-2017*; Methods of Chemical Analysis of Cement. Standardization Administration of the People's Republic of China: Beijing, China, 2017.
19. Murakami, Y.; Miwa, K.; Kito, M.; Honda, T.; Kanetake, N.; Tada, S. Fluidity Evaluation of the AC4CH (A356) Aluminum Alloy Semi-Solid Slurry Made by Mechanical Vibration Method. *Mater. Trans.* **2016**, *57*, 168–173.
20. Mori, T.; Kitagawa, R. Experimental Study on the Time Change in Fluidity and Particle Dispersion State of Alumina Slurries with and without Sintering Aid. *Ceram. Int.* **2017**, *43*, 13422–13429.

21. Ouyang, G.S.; Wang, J.S.; Wang, R.; Chen, L.P.; Bu, B. Rheokinetics and Fluidity Modification of Alkali Activated Ultrafine Metakaolin Based Geopolymers. *Constr. Build. Mater.* **2021**, *269*, 121268. [CrossRef]
22. Murakami, Y.; Miwa, K.; Kito, M.; Honda, T.; Kanetake, N.; Tada, S. Effects of Injection Conditions in the Semi-Solid Injection Process on the Fluidity of JIS AC4CH Aluminum Alloy. *Mater. Trans.* **2013**, *54*, 1788–1794.
23. Khodagholi, M.A.; Hemmati, M.R.; Pour, A.N. Efficient Filtration System for Paraffin-catalyst Slurry Separation. *Chem. Ind. Chem. Eng. Q* **2013**, *19*, 295–301.
24. Li, W.; Yu, L.Y.; Tan, Y.Z.; Wu, L.R.; Qian, J.Y. Mechanical Properties and Impact Behavior of Frozen Clay: Insights from Static Mechanical Tests, Fly-plate tests, and Split-Hopkinson Pressure Bar Analysis. *Phys. Fluids* **2024**, *36*, 057138. [CrossRef]
25. Amin, N.; Tahir, M.S.; Saleem, M.; Khan, Z.; Aslam, M.; Bazmi, A.A.; Ghatui, M.; Sagir, M. Rheological Improvement in Performance of Low-rank coal-water Slurries Using Novel Cost-effective Additives. *Asia-Pac. J. Chem. Eng.* **2020**, *15*, e2400. [CrossRef]
26. Ghadirian, M.; Afacan, A.; Hayes, R.E.; Mmbaga, J.P.; Mahmood, T.; Xu, Z.H.; Masliyah, J. A Study of the Hydrocyclone for the Separation of Light and Heavy Particles in Aqueous Slurry. *Can. J. Chem. Eng.* **2015**, *93*, 1667–1677.
27. Bahramyan, M.; Mousavian, R.T.; Brabazon, D. Determination of Atomic-scale Structure and Compressive Behavior of Solidified AlCxCoFeCuNi High Entropy Alloys. *Int. J. Mech. Sci.* **2020**, *171*, 105389. [CrossRef]
28. Li, W.; Yu, L.Y.; Zhang, T.; Su, H.J.; Mi, X.Z.; Fan, D.D.; Jin, B. Quantitative Analysis of Grain Size Effect on Tensile Mechanical Behavior of Granite Based on Multi-level Force Chain Networks. *Comput. Part. Mech.* **2024**, *11*, 2245–2266.
29. Strangfeld, C.; Klewe, T. Comparison of the Calcium Carbide Method and Darr Drying to Quantify the Amount of Chemically Bound Water in Early Age Concrete. *Materials* **2022**, *15*, 8422. [CrossRef]
30. Peng, Y.X.; Yu, L.Y.; Qian, J.Y.; Li, W.; Zhang, T.; Zhou, L.J. Dynamic Tensile Behavior and Crack Propagation in Coral Aggregate Seawater Shotcrete: Experimental Investigation and Numerical Simulation. *Cem. Concr. Comp.* **2025**, *159*, 106010. [CrossRef]
31. Kim, S. Chemically Bound Water in Brown Coal and Impact of Ambient Oxidation on its Characteristics. *Fuel* **2017**, *214*, 293–299.
32. Cho, E.; Kim, J.; Park, C.W.; Lee, K.W.; Lee, T.S. Chemically Bound Prussian Blue in Sodium Alginate Hydrogel for Enhanced Removal of Cs Ions. *J. Hazard. Mater.* **2018**, *360*, 243–249.
33. Tariq, A.; Yanful, E.K. A Review of Binders Used in Cemented Paste Tailings for Underground and Surface Disposal Practices. *J. Environ. Manag.* **2013**, *131*, 138–149.
34. Park, B.; Choi, Y.C. Effect of Healing Products on the Self-healing Performance of Cementitious Materials with Crystalline Admixtures. *Constr. Build. Mater.* **2021**, *270*, 121389. [CrossRef]
35. Harutyunyan, V.S. XRD and Combined SEM-EDS Analysis of Long-term Hydration Products of Ye'elimite. *Mater. Chem. Phys.* **2021**, *276*, 125373. [CrossRef]
36. Dembovska, L.; Bajare, D.; Ducman, V.; Korat, L.; Bumanis, G. The use of different by-products in the production of lightweight alkali activated building materials. *Constr. Build. Mater.* **2017**, *135*, 315–322.
37. Li, Z.Q.; Nie, L.C.; Xue, Y.G.; Li, W.; Fan, K.R. Model Testing on the Processes, Characteristics, and Mechanism of Water Inrush Induced by Karst Caves Ahead and Alongside a Tunnel. *Rock. Mech. Rock. Eng.* **2025**, *58*, 5363–5380.
38. Wang, S.C.; Wang, F.; Che, J.L.; Ma, L.H. Study on the Performance and Mechanism of Cement Solidified Desulfurization Manganese Residue. *Materials* **2023**, *16*, 16114184. [CrossRef]
39. Kozai, N.; Sato, J.; Osugi, T.; Shimoyama, I.; Sekine, Y.; Sakamoto, F.; Ohnuki, T. Sewage Sludge Ash Contaminated with Radiocesium: Solidification with Alkaline-reacted Metakaolinite (Geopolymer) and Portland Cement. *J. Hazard. Mater.* **2021**, *416*, 125965. [CrossRef]
40. Li, D.F.; Tian, B.; Niu, K.M.; Li, L.H.; Quan, L.; Zhu, X.W. Effects of Ambient Humidity on Water Migration and Hydrate Change in Early-Age Hardened Cement Paste. *Materials* **2023**, *15*, 8803. [CrossRef]
41. Jin, M.; Ma, Y.F.; Li, W.W.; Huang, J.L.; Zeng, H.Y.; Lu, C.; Zhang, J.; Liu, J.P. Degradation of C-S-H(I) at Different Decalcification Degrees. *J. Mater. Sci.* **2022**, *57*, 19260–19279.
42. Lim, Z.H.; Lee, F.W.; Mo, K.H.; Lim, J.H.; Yew, M.K.; Kwong, K.Z. Compressive Strength Forecasting of Air-Entrained Rubberized Concrete during the Hardening Process Utilizing Elastic Wave Method. *Crystals* **2020**, *10*, 912. [CrossRef]
43. Tanaka, S.; Sakai, Y. Study on the Correlation Between the Compressive Strength of Hardened Cement Paste and the Physical Properties of Drilling Powder. *Constr. Build. Mater.* **2021**, *269*, 121815. [CrossRef]
44. Uzunoglu, M.M.; Özgan, E.; Kap, T. The Investigation into the Effect of Hydrostatic Pressure on the Engineering Properties of Hardened Concrete. *J. Asian Archit. Build.* **2018**, *17*, 565–571.
45. Guo, S.C.; Dai, Q.L.; Sun, X.; Sun, Y.; Liu, Z. Ultrasonic Techniques for Air Void Size Distribution and Property Evaluation in Both Early-Age and Hardened Concrete Samples. *Appl. Sci.* **2017**, *7*, 290. [CrossRef]
46. Zhao, W.H.; Ji, C.Y.; Sun, Q.; Gu, Q. Preparation and Microstructure of Alkali-Activated Rice Husk Ash-Granulated Blast Furnace Slag Tailing Composite Cemented Paste Backfill. *Materials* **2022**, *15*, 4397. [CrossRef]
47. Liu, W.H.; Zhou, Z.Y.; Li, H.; Zhang, T.S.; Mai, Q.L.; Li, C.H. Research on the performance of low carbon mine filling cementing material based on red mud: A comprehensive review. *Case Stud. Constr. Mat.* **2025**, *22*, e04375. [CrossRef]

48. Liu, L.; Lyu, Y.Z.; Zhou, J.; Zhao, Y.Y.; Sun, W.J. Effect and Mechanism of the Salt-alkali Composite for the Improvement of the Early Mechanical Properties of High-content Fly Ash-based Filling Materials. *Constr. Build. Mater.* **2025**, *464*, 140138. [CrossRef]
49. Koohestani, B.; Koubaa, A.; Belem, T.; Bussière, B.; Bouzahzah, H. Experimental Investigation of Mechanical and microstructural properties of cemented paste backfill containing maple-wood filler. *Constr. Build. Mater.* **2016**, *121*, 222–228.
50. Wu, M.G.; Wang, C.; Zuo, Y.J.; Yang, S.; Zhang, J.Z.; Luo, Y. Study on Strength Prediction and Strength Change of Phosphogypsum-based Composite Cementitious Backfill Based on BP Neural Network. *Mater. Today Commun.* **2024**, *41*, 110331. [CrossRef]
51. Bullard, J.W.; Jennings, H.M.; Livingston, R.A.; Nonat, A.; Scherer, G.W.; Schweitzer, J.S.; Scrivener, K.L.; Thomas, J.J. Mechanisms of Cement Hydration. *Cem. Concr. Res.* **2011**, *41*, 1208–1223.
52. López-Lilao, A.; Gómez-Tena, M.P.; Mallol, G.; Monfort, E. Clay Hydration Mechanisms and their Effect on Dustiness. *Appl. Clay Sci.* **2017**, *14*, 157–164.
53. Scrivener, K.; Ouzia, A.; Juilland, P.; Mohamed, A.K. Advances in Understanding Cement Hydration Mechanisms. *Cem. Concr. Res.* **2019**, *124*, 105823. [CrossRef]
54. Forgács, A.; Papp, V.; Paul, G.; Marchese, L.; Len, A.; Dudás, Z.; Fábián, I.; Gurikov, P.; Kalmár, J. Mechanism of Hydration and Hydration Induced Structural Changes of Calcium Alginate Aerogel. *ACS Appl. Mater. Interfaces* **2021**, *13*, 2997–3010.
55. Hemalatha, T.; Arthi, K.; Mapa, M. Effect of Calcium Formate on Hydration Mechanism of Cement Fly Ash Blends. *Aci. Mater. J.* **2019**, *116*, 51–59.
56. Kawabata, H.; Tachikawa, H. Dissociation Mechanism of a C60-Li+ Complex by Microscopic Hydration: Density Functional Theory Study. *Jpn J. Appl. Phys.* **2022**, *61*, 071004. [CrossRef]
57. Dorn, T.; Hirsch, T.; Stephan, D. Working Mechanism of Calcium Nitrate as an Accelerator for Portland Cement Hydration. *J. Am. Ceram. Soc.* **2023**, *106*, 752–766.
58. Pinarci, I.; Kocak, Y. Hydration Mechanisms and Mechanical Properties of Pumice Substituted Cementitious Binder. *Constr. Build. Mater.* **2022**, *335*, 127528. [CrossRef]
59. Kocak, Y.; Pinarci, I. Effects of Hydration Mechanism on Mechanical Properties of Diatomite-cement Composites. *Eur. J. Environ. Civ. Eng.* **2023**, *27*, 3707–3721.

Disclaimer/Publisher's Note: The statements, opinions and data contained in all publications are solely those of the individual author(s) and contributor(s) and not of MDPI and/or the editor(s). MDPI and/or the editor(s) disclaim responsibility for any injury to people or property resulting from any ideas, methods, instructions or products referred to in the content.

materials

MDPI

Article

Experimental Study and Application of TPO Waterproofing Membrane Lapping Process Parameters

Keyong Wang [1], Zhenhua Zang [1], Jie Li [1], Zhenyue Shi [1,2,*], Mingcai Liu [3], Zhipeng Li [3], Qingbiao Wang [4], Yandong Shang [1], Chenglin Tian [1], Zifan Jia [1] and Hui Wang [1]

[1] School of Resources, Shandong University of Science and Technology, Tai'an 271000, China; skd996607@sdust.edu.cn (K.W.); 202383300028@sdust.edu.cn (Z.Z.); 202283300056@sdust.edu.cn (J.L.); cornor@163.com (Y.S.); skdtcl@126.com (C.T.); 202483300045@sdust.edu.cn (Z.J.); 202383300027@sdust.edu.cn (H.W.)
[2] Laboratory of Rock Burst Prevention Technology and Equipment, Shandong Energy Group Co., Ltd., Jinan 250200, China
[3] China Railway Construction Investment (Shandong) Dongyang Expressway Co., Ltd., Liaocheng 252299, China
[4] Jinan Campus, Shandong Jianzhu University, Jinan 250101, China; skd990748@sdust.edu.cn
* Correspondence: skd992844@sdust.edu.cn

Abstract: Taking the TPO waterproofing membrane as an example, this paper studies the influence of temperature, speed and welding pressure on the welding quality of a TPO waterproofing membrane lap area through a peel test and a water impermeability test, determines the optimal construction process, and observes and compares the permeable path through laser confocal microscope. Finally, it is applied to the actual effect test in the project. The results show that the welding pressure test tool for the lap area of the waterproofing membrane is designed to meet the welding work test requirements of various lap areas of the waterproofing membrane. The peel strength increases first and then decreases with the increase in welding temperature, and the optimal construction temperature is 400 °C. The optimal construction speed is 4 m/min; at 400 °C welding temperature, the peel strength increases first and then decreases slightly with the increase in welding pressure. The optimal construction pressure is 14.97 N; under the condition of 0.2 MPa, 30 min to 0.6 MPa, 120 min, the water impermeability test of the overlapping area was qualified. In this paper, the optimal construction technology of a TPO waterproofing membrane is determined, which provides guidance for its application and promotion in engineering.

Keywords: TPO waterproofing membrane; construction technology; peel strength; permeable path; impermeability test

1. Introduction

Underground engineering waterproofing is an important process of engineering construction, and its construction quality is directly related to the safe operation of underground engineering in the future. A waterproofing membrane is one of the main means of waterproofing in underground engineering. Different types of membranes determine different construction techniques. At present, commonly used waterproofing membranes include modified asphalt waterproofing membranes, ethylene propylene diene monomer (EPDM) rubber waterproofing membranes, polyvinyl chloride (PVC) waterproofing membranes, etc., but there are many problems such as poor stability, complex processes, easy aging and high pollution [1–3].

The thermoplastic polyolefin (TPO) waterproofing membrane, as a new type of polymer waterproofing material, has been widely used in engineering in recent years due to its good aging resistance, excellent tensile strength, and environmental friendliness [1]. The waterproof performance of TPO waterproofing membrane depends largely on the welding quality of its lap joint, so a good welding process is the key to ensuring its engineering performance. However, at present, there is still a lack of systematic and standardized construction technology guidance for the hot-melt welding of TPO waterproofing membranes. In practical projects, problems such as missing welding, virtual welding, and over-welding often occur, which seriously affect the safety of structural waterproofing.

Previous studies have focused on the influence of a single welding parameter (such as temperature, speed or pressure) on the welding quality [4–6]. However, there is still a lack of systematic research on the coupling mechanism of the lap performance of TPO coils under the combination of multiple welding process parameters (such as temperature, speed and pressure). In this study, through the peel strength test and water permeability analysis, combined with laser confocal microscopy, the performance variation law of the TPO waterproofing membrane lap area under different temperature and speed combinations was revealed, aiming to provide theoretical basis and experimental basis for the formulation of standardized construction technology of the TPO waterproofing membrane, which has important engineering application value and practical significance.

In the construction technology of waterproofing membranes, the predecessors have carried out the following research: Michal et al. studied the influence of welding speed, welding temperature, welding time and other factors on the welding quality of waterproofing membranes through experiments and determined the most suitable combination of factors [7]. Zhang proposed a new leakage location online monitoring system, which integrates the detection core on the traditional waterproofing membrane to realize the function of leakage location monitoring [8]. Jiang studied the influence of a new polymer waterproofing membrane on the mechanical properties of tunnel lining structure [9]. Lee determined the applicability and contact conditions of waterproofing membranes under various conditions through numerical analysis [10]. Miyauchi proposed a method to determine the location of fasteners in waterproofing membranes [11]. Hailesilassie studied the influence of displacement rate and temperature of three different types of modified asphalt membranes on the bonding fracture energy by peeling test [12]. Tsukagoshi studied the carbon dioxide permeability of waterproofing membranes and carried out numerical simulation [13]. In the test method, according to the static mechanical test, Hopkinson impact test, and fly plate test used by Li W, the following test method is determined [14]: In terms of research and analysis, the force chain network analysis method is adopted [15]. Peng et al. carried out nanoindentation tests to evaluate the micromechanical properties of CASS and used the Split Hopkinson Pressure Bar (SHPB) device to study its dynamic mechanical behavior [16]. Li et al. studied the influence of karst caves in front of and along the tunnel on the stability of the surrounding rock by using the self-developed three-dimensional fluid–solid coupling model test system [17]. The changes in stress and seepage pressure of rock mass during tunnel excavation are analyzed. The synergistic effect of bentonite particle size and content, carboxymethyl starch (CMS) and Na_2CO_3 content on the properties of bentonite slurry was studied by rheological measurement and filtration test. The rheological behavior, parameters and the filtration loss of bentonite slurry with different factors were obtained. The range analysis was used to evaluate the influence of various factors on the slurry performance, and the best bentonite-based slurry ratio was proposed [18].

The number and content of the above research on the construction technology of the lap area of waterproofing membranes are relatively small, and the research mainly

focuses on the waterproofing material and impermeability of waterproofing membranes. He et al. studied the effects of OMMT on the physical properties, chemical structure and microstructure of films before and after thermal aging, and they predicted the service life of SMB films based on the Arrhenius model [19]. Wang et al. focused on the coupling aging characteristics of SBS-modified asphalt waterproofing membranes, aiming to reveal its influence mechanism on material properties under high temperature and a freeze–thaw environment [20]. However, for the waterproofing membrane, the impermeability of the waterproofing membrane plays an extremely important role. There are few studies on the construction technology of the overlapping parts of the TPO membrane and the quality effect after construction. Only Garber used statistical methods to analyze the factors that promote and hinder the defects of the lap welding of the membrane during the production of cold-rolled strip steel in the bell-type furnace annealing [21]. Yang introduced in detail the connection problems, defects and countermeasures of synthetic polymer pre-laid waterproofing membranes in construction, which provided reference for the construction application and quality acceptance of synthetic polymer pre-laid waterproofing membranes [22]. Liu et al. constructed an effective deformation calculation model for the lap area of polyethylene polypropylene waterproofing membranes, considering the combined effects of lap size, process and environmental oxidation erosion [23]. In particular, the research on the construction temperature, speed and pressure parameters at the overlap of TPO waterproofing membrane still needs to be improved [24,25].

In the current engineering practice, the lap construction quality of TPO waterproofing membranes is directly related to the performance stability of the overall waterproofing system. In view of the influence of key parameters such as temperature, speed and pressure on the lap quality during the construction process, this paper systematically studies the optimal process parameters of TPO waterproofing membrane lap construction and verifies them through peel tests, the observation of permeable paths, and impermeability tests. The research results provide effective technical support for optimizing the lapping process of TPO waterproofing membranes, and they have important engineering application value for improving the construction quality of membranes and ensuring the durability of this project.

2. Materials and Methods

In this study, the optimal welding temperature, speed and compression tests were carried out, and, combined with the penetration dyeing, permeable path detection and impermeability test of the lap area, the effects of different construction technologies on the impermeability of the lap area of waterproofing membranes were systematically evaluated. The aim is to determine the optimal construction technological parameters and provide technical support for subsequent related projects. Firstly, the optimal welding temperature and speed parameters of the lap area of the waterproofing membrane were determined by welding temperature and speed tests. Subsequently, based on the above two sets of optimal parameters, the welding pressure test was carried out to determine the optimal welding pressure. Secondly, according to the determined optimal construction technology, the impermeability of the lap area of the waterproofing membrane was tested under water immersion and thermal aging conditions to verify its waterproofing effect. Finally, the optimal construction process was derived based on the test results. The technical roadmap is shown in Figure 1.

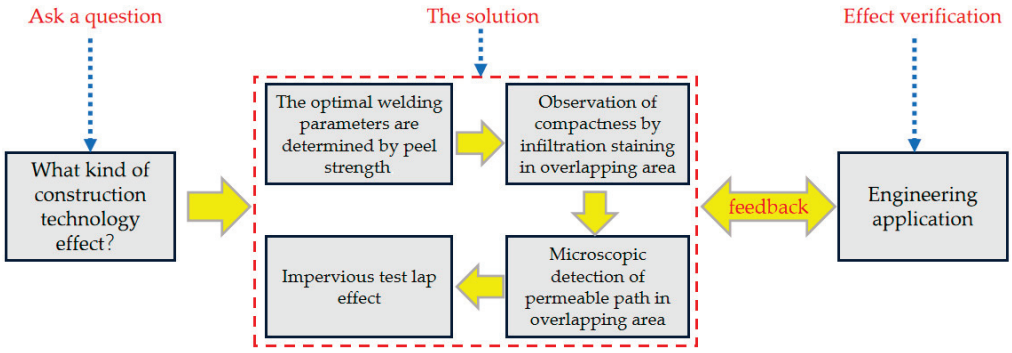

Figure 1. Technology roadmap.

2.1. Sample Specimen Preparation

2.1.1. Sample-Making Equipment and Improvement

The preparation of TPO waterproofing membrane sample adopts the method of heating metal wedge with heating rod. By fully contacting the metal wedge with the polymer membrane, the surface of the membrane was melted and pressed, so as to promote the fusion of the overlapping surface of two adjacent membranes. Subsequently, under the action of the pressure roller, the welding surface was gradually compacted.

In order to determine the optimal welding process parameters, a test device was designed and built as shown in Figure 2. The device is composed of a climbing welding machine, an angle display, a limit device and a limit nail. Among them, the climbing welding machine equipment was provided by Wenzhou Mingqi Welding Equipment Co., Ltd., Wenzhou, China. Angle display, limit device and limit nail are produced by Delixi Electric Co., Ltd., Leqing City, Zhejiang Province, China. The temperature adjustment range is 150 °C–600 °C, and the welding speed range is 0.5 m/min–5 m/min; the digital angler was fixed to the pressure wrench for real-time monitoring of the welding angle. The pressure display was installed on the side wall of the welding machine to measure the welding pressure, as shown in Figure 2.

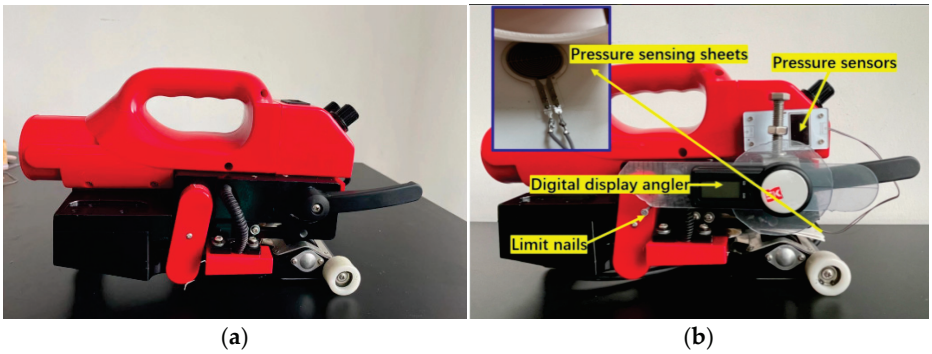

(**a**) (**b**)

Figure 2. Sample-making equipment diagram: (**a**) Before the improvement of sample-making equipment. (**b**) After the improvement of sample-making equipment.

During the test, the pressure sensor was placed between the upper and lower waterproofing membranes, and the pressure was accurately controlled by adjusting the rotation angle of the pressure wrench. The wrench angle when the pressure sensor first displays the pressure value was taken as the initial angle (set to 0°), and then the angle–pressure relationship curve is drawn (Figure 3).

In order to more accurately evaluate the relationship between the angle and pressure of the climbing welding equipment, the experimental data were fitted by an exponential function. The error range of each fitting parameter is shown in Figure 3. Specifically, the

initial pressure term y_0, the fitting coefficient A_1 and the angle response coefficient t_1 are 1.491 ± 0.02702, −1.50329 ± 0.02497 and 19.87883 ± 0.94422, respectively.

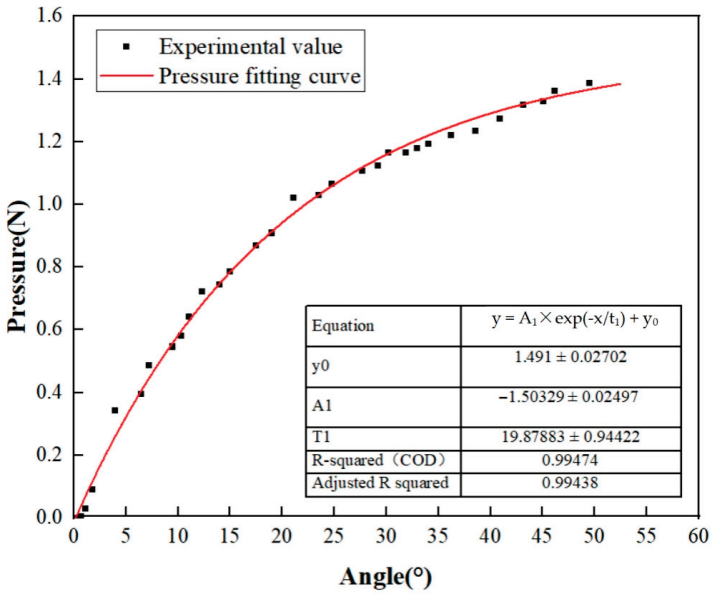

Figure 3. Fitting curve of the angle–pressure relationship for the climbing welding equipment.

In addition to providing the fitting coefficients, this study also conducted a residual analysis, as shown in Figure 4. The residual standard deviation (SD) between the experimental and fitted values was calculated to quantify the fitting error, yielding a residual SD of 0.03752 N, with a maximum absolute residual error of 0.0685 N. The small residual errors indicate high fitting accuracy.

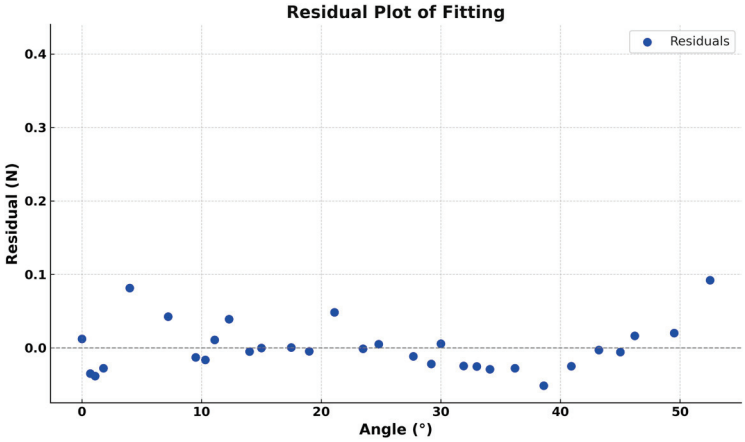

Figure 4. The fitting function residual diagram of the relationship between angle and pressure.

To reflect data uncertainty more clearly, error bars representing the standard deviation of repeated measurements were added to the graph. Each experimental data point was measured at least three times, and the error bars correspond to the calculated standard deviations. The error analysis followed the principles of the Guide to the Expression of Uncertainty in Measurement (GUM), incorporating both Type A (statistical) and Type B (instrumental) uncertainties.

The coefficient of determination R^2 is 0.99474, and the adjusted R^2 is 0.99438, confirming the reliability of the fitting model.

2.1.2. Specimen Preparation

The test material used in this study is TPO-15H1 thermoplastic polyolefin waterproofing membrane (thickness 1.5 mm) produced by China Jiangsu Suzhou Karen Building Materials Co., Ltd. (Suzhou, China). The initial size of the waterproofing membrane is 150 mm × 2000 mm. According to the requirements of different test parameters, two waterproofing membranes were welded by the improved welding machine. After welding, two strip samples of 16 mm welding band and 12 mm detection seam were formed, as shown in Figure 5.

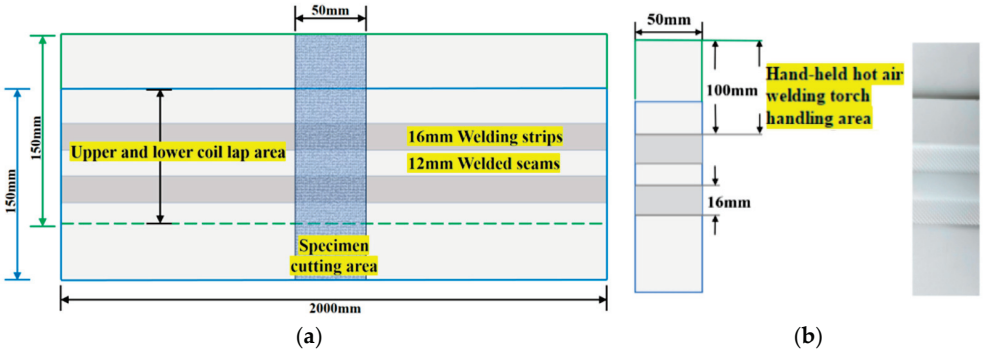

Figure 5. TPO waterproofing membrane welding specimen: (**a**) waterproofing membrane samples; (**b**) waterproofing membrane cutting test piece.

A rectangular specimen with a width of 50 mm was cut in the middle of each sample to ensure that the edge of the specimen reached 100 mm. The short side was welded by a hand-held hot air welding gun to meet the predetermined length requirements [26].

1. The optimal welding temperature and speed test sample preparation

When the welding temperature is 200 °C and the welding speed is 0.5 m/min, the heat accumulation in the welding area of the waterproofing membrane is insufficient, and the effective melting state cannot be achieved. Therefore, the minimum welding temperature is set to 300 °C, and the minimum welding speed is set to 1 m/min.

Under the condition of welding temperature of 600 °C and welding speed of 6 m/min, the surface of the waterproofing membrane was unevenly heated, and the bonding effect was poor due to the fast running speed of the equipment. And the welding temperature exceeds 600 °C, which is not conducive to on-site construction operation. Based on the above factors, the maximum welding temperature was set to 600 °C, and the maximum welding speed was set to 5 m/min. The preparation of the samples is detailed in Table 1.

Table 1. Sample 1 preparation and test type table.

Sample Number	Welding Temperature (°C)	Welding Speed (m/min)	Quantity
Sample 1–300	300	1	5
		2	5
		3	5
		4	5
		5	5
Sample 1–400	400	1	5
		2	5
		3	5
		4	5
		5	5

Table 1. *Cont.*

Sample Number	Welding Temperature (°C)	Welding Speed (m/min)	Quantity
Sample 1–500	500	1	5
		2	5
		3	5
		4	5
		5	5
Sample 1–600	600	1	5
		2	5
		3	5
		4	5
		5	5

2. Sample preparation of optimal welding pressure test

Based on the above test results, five types of waterproofing membrane lap specimens were prepared under the conditions of the determined optimal welding temperature and speed. By adjusting the rotation angle of the pressure handle to 10°, 20°, 30°, 40° and 50°, the welding pressure was controlled, respectively. The relationship curve between the rotation angle and the pressure is shown in Figure 3, and the preparation of the sample is detailed in Table 2.

Table 2. Specimen 2 preparation and test type table.

Sample Number	Pressure Handle Rotation Angle (°)	Corresponding Welding Pressure (N)	Quantity
2-1	10°	7.47	5
2-2	20°	11.62	5
2-3	30°	13.81	5
2-4	40°	14.97	5
2-5	50°	15.57	5

3. Impermeability test sample preparation

According to the above test results, the optimal construction process of the lap area of the waterproofing membrane should meet the optimal welding temperature, speed and pressure parameters at the same time. The lap samples prepared under these process conditions were first aged in the thermal aging test chamber according to the established procedure, and then the impermeability test was carried out on the lap area after aging. The specific preparation and aging conditions of the samples are detailed in Table 3.

Table 3. Specimen 3 preparation and test type table.

Sample Number	Test Name	Test Environment and Conditions	Quantity
3-1	No treatment	Air, 23 °C, 7 d	5
3-2	Soaking treatment	Water, 23 °C, 7 d	5
3-3	Thermal aging treatment	Aging apparatus, 80 °C, 7 d	5

2.2. Test Scheme and Equipment

2.2.1. Peel Test

The peel test adopts the WDW-05 microcomputer control universal testing machine, the instrument is produced in Jinan Wenteng Test Instrument Co., Ltd., Jinan, China. The maximum test force is 5000 N, and the accuracy of the force value is better than ±0.5% of the indicated value (see Figure 6b). Five rectangular specimens with a width of 50 mm perpendicular to the lap edge were cut from the middle of each lap specimen. The specimen was fastened to the fixture of the tensile testing machine to ensure that the longitudinal axis of the specimen coincides with the axis of the testing machine and the fixture. The distance between the fixtures is (100 ± 5) mm, and there is no preload. The test was carried out at a constant tensile speed of (100 ± 10) mm/min until the specimen was separated, and the failure modes of the lap area were recorded and analyzed, as shown in Figure 7.

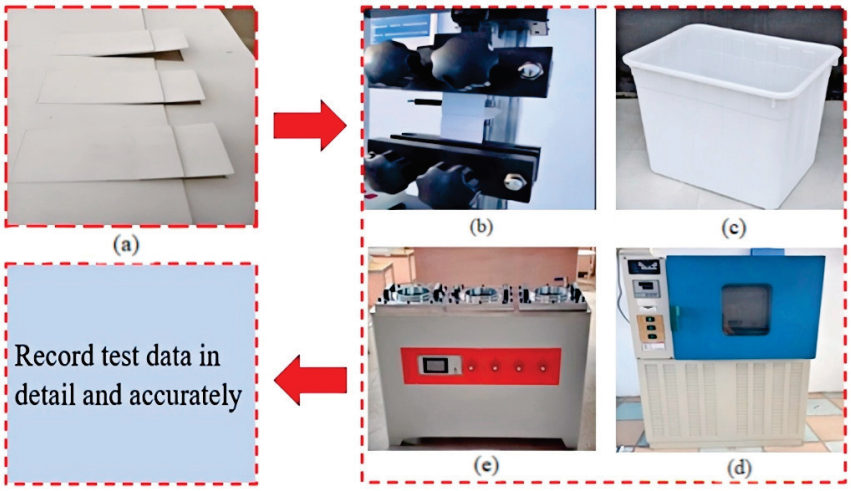

Figure 6. Test equipment diagram: (**a**) Specimen preparation uses TPO-15H1 thermoplastic polyolefin waterproofing membrane produced by China's Jiangsu Province Suzhou Karen Building Materials Co., Ltd., Suzhou, China (**b**) Peeling test used WDW-05 microcomputer control universal testing machine produced by Jinan Wenteng Test Instrument Co., Ltd., Jinan, China. (**c**) The immersion test was carried out in an ordinary plastic box. (**d**) The thermal aging test adopts the high temperature aging test chamber produced by Rongjida Instrument Technology Co., Ltd., Minhang District, Shanghai City, China. (**e**) Impermeability test using China's Shanghai Minhang District Rongjida Instrument Technology Co., Ltd., Shanghai, China, produced DFTS-1 waterproof membrane lap area impermeability instrument.

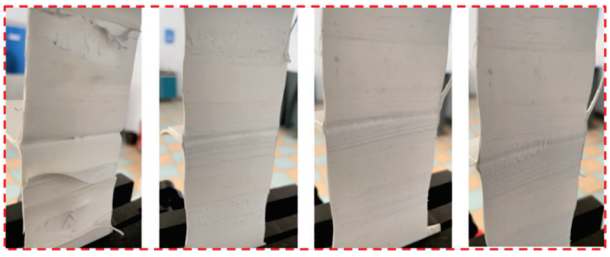

Figure 7. Partial peel test effect diagram.

The regions of [0–1/4) and (3/4–1] were removed, and the values at 10 equipartition points were retained as the average peeling strength. The average peel strength of 5 specimens in each group was taken as the final result, unit N/50 mm [27], as shown in Figure 8.

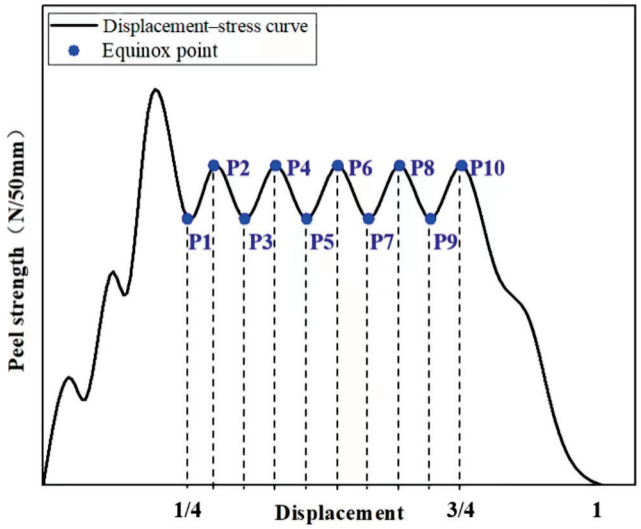

Figure 8. A schematic diagram for calculating the average peel strength.

2.2.2. Impermeability Test

According to the general specification for waterproofing of building and municipal engineering GB55030-2022 [27], the impermeability test was carried out by using DFTS-1 waterproof membrane lap area impermeable instrument, as shown in Figure 6e. Under the condition of 0.2 Mpa, 30 min, impermeability is qualified. There are two conditions:

1. Soaking treatment

The waterproofing membrane samples after welding and edge sealing were immersed in water at 23 °C, the water surface was 20 mm higher than the sample, and the samples were continuously immersed for 7 days. After removing, the surface moisture was sucked dry to ensure that there was no water stain on the surface of the sample. The test piece was cut with the middle of the lap as the center line, and then the impermeability test was carried out according to the specification requirements, as shown in Figure 6c.

2. Thermal aging treatment

The welded waterproofing membrane samples were placed in the aging box of model 401B (Jiangdu Jingang Machinery Factory, Nantong, China), and the condition was set at 80 °C for 7 days. After the aging, the impermeability of the sample lap was tested according to the requirements of the specification, as shown in Figure 6d.

3. Results and Discussion

According to the design scheme of the experimental group in Table 1, the peel strength test and impermeability test were carried out on the samples of the lap area of TPO waterproofing membrane. Through systematic processing and analysis of the collected test data, the performance differences in each experimental group under different test conditions are clarified. The specific test results and their analysis will be described in detail below.

3.1. Analysis of Peel Strength Test Results

3.1.1. Variable Temperature and Variable Speed Peeling Test

Through the peel test of TPO waterproofing membrane specimens under different temperature and speed conditions, the displacement–stress data are obtained. Because the sample production equipment adopts double welding strips, and the peeling strength of the two welding strips is the same, only the test data of one of the welding strips are recorded

during the test. The peeling test results of TPO waterproofing membrane specimens under various temperature and speed conditions are shown in Figure 9.

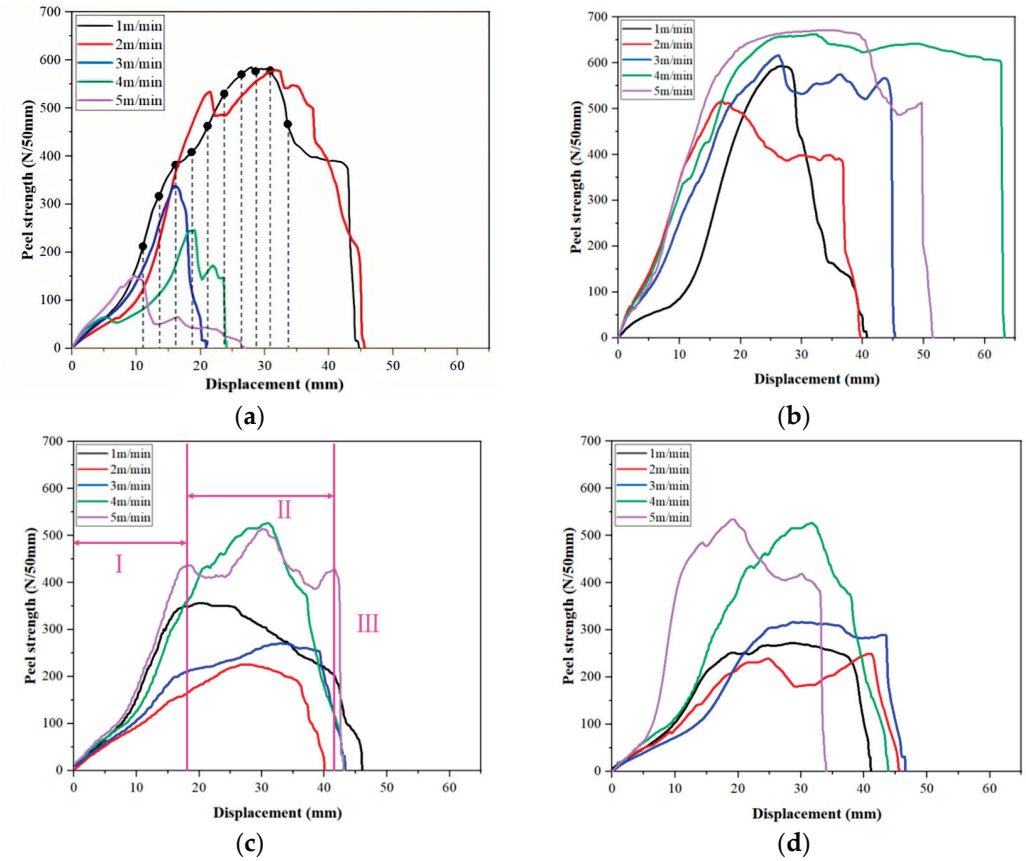

Figure 9. Displacement–stress curves at different temperatures and different speeds: (**a**) Peeling strength at different speeds at 300 °C. (**b**) Peeling strength at different speeds at 400 °C. (**c**) Peeling strength at different speeds at 500 °C, Region I is the initial stage of TPO waterproofing membrane failure. Region II is the stable stripping stage of TPO waterproofing membrane failure. Region III is the failure stage of TPO waterproofing membrane failure. (**d**) Peeling strength at different speeds at 600 °C.

Taking the stripping curve at 500 °C and 5 m/min in Figure 9c as an example, the stripping process of the waterproofing membrane can be divided into three typical stages:

Region I (initial stage): This stage is the establishment process of the initial adhesion force, and the peel strength gradually increases with the displacement, indicating that the stress concentration occurs in the bonding layer during the loading process and gradually increases.

Region II (stable stripping stage): This stage presents a longer platform area, showing that the waterproofing membrane has better ductility and adhesion under these temperature and speed conditions. The existence of the platform area indicates that the waterproof membrane has undergone sufficient plastic deformation during the stretching process, which effectively avoids the brittle fracture phenomenon.

Region III (failure stage): As the displacement further increases, the peel strength decreases rapidly, indicating that the adhesive layer fails or completely peels off under continuous stretching.

Under the condition of 300 °C, the average peeling strength was 450.45 N/50 mm and 449.92 N/50 mm when the bonding speed was 1 m/min and 2 m/min, respectively. With the increase in bonding speed, the peeling strength is significantly improved, the peak position is obviously advanced, and the displacement is reduced. The higher bonding speed

makes the peel strength curve show a steep trend, indicating that the waterproofing membrane has not yet completely softened, resulting in damage under a smaller displacement, which is manifested as the peak value of peel strength appearing in advance, reflecting the poor adhesion at this temperature.

Under the condition of 400 °C, when the bonding speed is 4 m/min and 5 m/min, the peeling strength is higher, and the average peeling strength is 628.08 N/50 mm and 607.13 N/50 mm, respectively. In the speed range of 1–2 m/min, the peeling strength reaches the peak, showing significant plastic deformation characteristics, and the peeling strength is up to more than 600 N/50 mm. Especially at the speed of 4–5 m/min, the peeling strength is further improved with the increase in speed. However, when the bonding speed reaches 5 m/min, the overall peeling strength decreases slightly due to the accelerated peeling process.

Under the condition of 500 °C, the average peeling strength at the bonding speed of 4 m/min and 5 m/min is 369.68 N/50 mm and 409.53 N/50 mm, respectively. Due to the slow bonding speed, the internal molecular group of the material is quickly broken, resulting in a low peak value of the peel strength; with the increase in bonding speed, the effect of high temperature on the material molecular group in a short time is relatively small, so the peeling strength shows an upward trend. However, the ductility of the material at this temperature is reduced, which can easily lead to early failure.

Under the condition of 600 °C, the average peeling strength at the bonding speed of 4 m/min and 5 m/min is 378.44 N/50 mm and 432.45 N/50 mm, respectively. At this temperature, the peel strength of the waterproofing membrane is similar to that at 500 °C, but the ductility of the material is slightly improved.

In summary, the peel strength at 400 °C is significantly higher than that at other temperature conditions, showing good adhesion and ductility.

From Figure 10, it can be seen that, at 300 °C, the peeling strength decreases with the increase in welding speed. This is because, at a constant temperature, the faster the welding speed of the equipment, the lower the heat energy absorbed by the waterproofing membrane in unit time. When the heat energy is lower than the melting point of the membrane, the number of macromolecular chains that creep and diffuse between the welding surfaces is less, and the interface layer of cooling fusion is thinner, so the strength is low, and the peeling performance is poor.

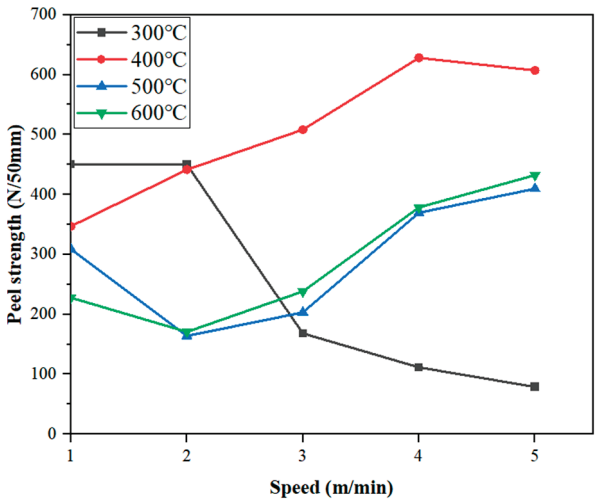

Figure 10. The velocity and peel strength diagram at each temperature.

Under the condition of 400 °C, with the increase in the speed of the climbing welder, the average peeling strength reaches the peak at 4 m/min and then decreases slightly.

This phenomenon can be attributed to the gradual diffusion of polymer molecules under external force after the contact surface of the TPO waterproofing membrane absorbs heat energy under high temperature conditions. With the increase in heat input or the extension of heating time, when the interface of the waterproofing membrane reaches the melt viscous flow state, not only do the mutual diffusion and penetration between the polymer melts occur, but also the macromolecular chains intertwine and diffuse across the interface melt layer to form a new molecular chain entanglement network, thus significantly improving the thermal welding peel strength. Subsequently, as the temperature gradually decreases, when the interface temperature is lower than the viscous flow temperature, the movement of macromolecular chains is limited, rearrangement, orientation and crystallization occur, and finally a dense melt interface layer with a certain thickness and strength is formed.

At 500 °C, with the increase in the speed of the welding machine, the average peel strength showed a continuous upward trend. However, when the welding speed is 1 m/min, the average peel strength of the waterproofing membrane decreases to 309.08 N/50 mm, which is the lowest value under this temperature condition. The reason is that, at a lower welding speed, the heat energy absorbed by the waterproofing membrane in unit time is too high, which leads to the fracture of the polymer molecular chain or the precipitation of small molecules, and the overflow layer is formed at the welding gap, thus weakening the adhesion strength at the lap area.

Under the condition of 600 °C welding, the change trend of peel strength with welding speed is similar to that at 500 °C. It is noteworthy that, at 600 °C, the peel strength exceeds that observed at 500 °C. This may be due to enhanced polymer flow and chain diffusion under extremely high heat input, promoting stronger bonding. Alternatively, it may be influenced by local temperature distribution or pressure inconsistencies. Further investigation is required to confirm whether this is a systematic effect or a measurement deviation.

By each speed at different temperatures of TPO waterproofing membrane specimens, a peeling test was conducted to obtain its peel strength data. The peel test results of TPO waterproofing membrane specimens at different welding speeds and different temperatures are shown in Figure 11.

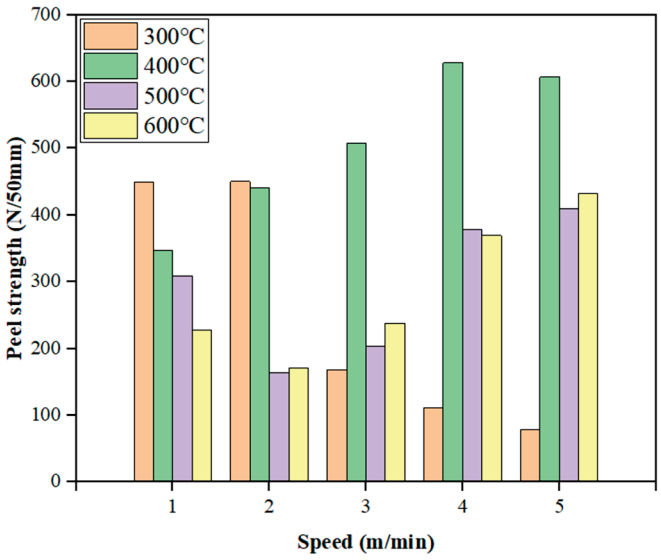

Figure 11. Temperature and peel strength diagram at each speed.

It can be seen from Figure 11 that, when the welding speed is 1 m/min, the waterproofing membrane with a welding temperature of 300 °C exhibits the highest average peel strength of 449.92 N/50 mm. Under the condition of the same speed, with the increase

in welding temperature, the average peeling strength of the waterproofing membrane decreases in a stepwise manner. The reason is that, as the welding temperature increases, the heat energy absorbed by the welded surface of the waterproofing membrane increases, resulting in the fracture of the polymer molecular chain or the precipitation of small molecules, thereby reducing the peel strength.

Under the condition of a welding speed of 3 m/min, the highest value of average peeling strength appears in the waterproof membrane with a welding temperature of 400 °C, reaching 508.25 N/50 mm, showing obvious cliff-type improvement. This is mainly because the TPO waterproofing membrane, as a semi-crystalline polymer, must absorb heat energy higher than its melting point to form a molten layer that can undergo the peristaltic diffusion of macromolecular chains. If the heat energy is insufficient, an effective molten layer cannot be formed; on the contrary, if the heat energy is too high to exceed the cracking energy of the molecular chain, it will cause the molecular chain to break, and the complete melting layer cannot be formed. Therefore, the welding temperature plays a decisive role in the formation of the fusion layer at the welding interface, which in turn affects the quality and peel strength of the lap weld of the waterproofing membrane. The optimal welding temperature should ensure that the heat energy transferred to the waterproofing membrane is between its melting temperature and molecular chain-breaking temperature.

In addition, this law also shows a similar change trend under other welding speed conditions.

3.1.2. Variable Pressure Stripping Test Under Better Conditions

Two groups of speeds with higher average peel strength in each group were selected at different temperatures to test the effect of different pressures on the peel strength. The results are shown in Figure 12.

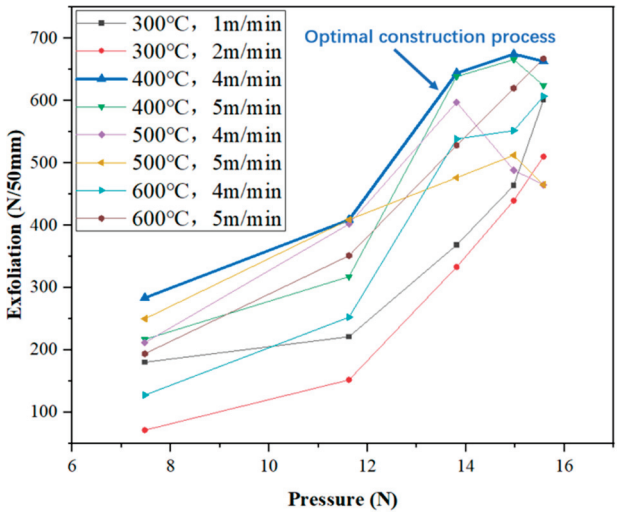

Figure 12. Different pressure-peel strength diagrams under better temperature and speed conditions.

It can be seen from Figure 12 that, when the welding temperature is 300 °C and the welding speed is 1 m/min and 2 m/min, the peel strength increases with the increase in welding pressure, but the peel strength when the welding speed is 1 m/min is always higher than that when the welding speed is 2 m/min.

When the welding temperature is 400 °C and the welding speed is 4 m/min, with the increase in welding pressure, the peeling strength continues to increase to the highest value and then decreases. The highest peeling strength is 674.92 N/50 mm, corresponding to the X-axis welding pressure of 14.97 N. The peeling process of TPO waterproofing membrane first passes through the elastic stage. After being pulled to the peak bearing capacity, the load is almost unchanged, the displacement increases, and it finally suddenly breaks after

a period of platform period. Under the condition of a welding speed of 5 m/min, it also has a similar change rule, and the highest peeling strength is 666.06 N/50 mm.

When the welding temperature is 500 °C and the welding temperature is 4 m/min, with the increase in welding pressure, the maximum value of peeling strength is 597.49 N/50 mm when the welding pressure is 13.81 N. When the welding temperature is 5 m/min, the welding pressure reaches the maximum peeling strength of 512.53 N/50 mm at 14.97 N. The overall curve fluctuates greatly. In the early stage, the peeling force is small, and the peeling force rises rapidly. In the later stage, it gradually decreases until the two specimens are separated. The main reason for this result is that the temperature of the hot wedge welding method is difficult to control during construction. If the temperature is too high, the large molecular chain will decompose. If the temperature is too low, the surface of the waterproofing membrane will not melt completely, which is easy to cause hollowing and poor bonding, resulting in low peel strength.

When the welding temperature is 600 °C, whether the welding speed is 4 m/min or 5 m/min, the peel strength always increases with the increase in welding pressure and reaches the highest value when the welding pressure is 15.57 N.

3.2. Permeable Path Detection and Result Analysis

3.2.1. Macroscopic Detection

The permeable dyeing observation of the lap area of the waterproofing membrane was carried out, and the nano-dyeing agent was dripped into the lap area of the waterproofing membrane to make it penetrate the lap area. The purpose is to evaluate the water permeability of the waterproofing membrane and the sealing effect of the lap area through the penetration test.

According to Figure 9, the welding speed with the highest peel strength was selected as the test sample of penetration path detection at each temperature; that is, the waterproof membrane lapped at 300 °C, 1 m/min (300 °C, 1 m/min indicates a welding temperature of 300 °C, a welding speed of 1 m/min); 400 °C, 4 m/min; 500 °C, 5 m/min; 600 °C, 5 m/min, and the welding pressure is 14.97 N permeable path detection, as shown in Figure 13.

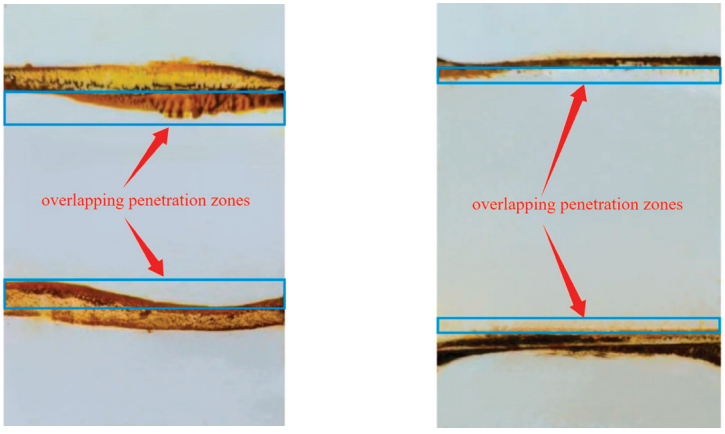

(**a**) (**b**)

Figure 13. *Cont.*

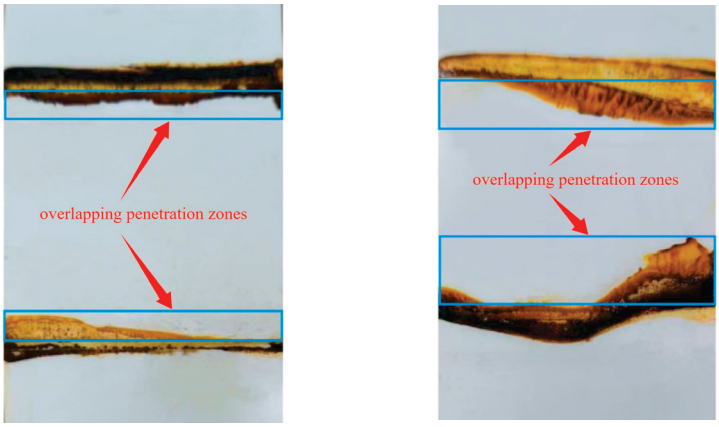

Figure 13. Permeability of lap area of waterproofing membrane: (**a**) 300 °C, 1 m/min; (**b**) 400 °C, 4 m/min; (**c**) 500 °C, 5 m/min; (**d**) 600 °C, 5 m/min.

The larger the dyeing area of the lap penetration zone is, the worse the lap compactness of the waterproofing membrane is. The evaluation of the penetration range and sealing performance under each parameter group is shown in Table 4:

Table 4. Permeability summary and comparison.

Process Parameters	Permeability Regions	Sealing Performance Evaluation
300 °C, 1 m/min	Larger	Poor
400 °C, 4 m/min	Minimal	Good
500 °C, 5 m/min	Smaller	Better
600 °C, 5 m/min	Maximum	Very poor

From the observation of the penetration results, especially at the edges of both sides, there is a significant dyeing diffusion phenomenon, in which the temperature is too high and the dyeing area is irregular and shows obvious bending, indicating that the penetration phenomenon of the lap area is the most serious.

3.2.2. Microscopic Detection

The lap area sample (size: 50 mm × 16 mm × 1.5 mm) of the stripped waterproofing membrane is characterized by laser confocal microscopy (Japan Olympus OLS4100 produced in China Henan Zhengzhou e Test Co., Ltd., Zhengzhou, China) at the relatively weak water permeability of the lap edge, as shown in Figure 14.

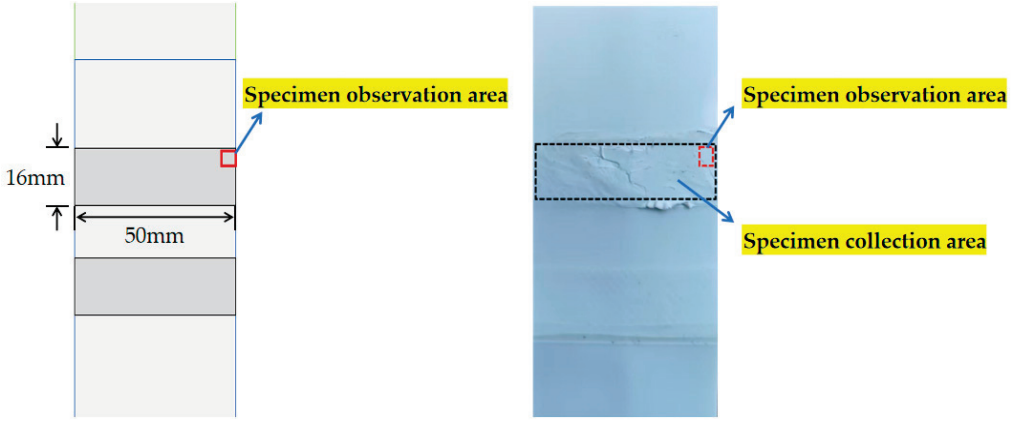

Figure 14. Microscopic detection of sample location.

The purpose of this study is to reveal the microscopic permeable path of the waterproofing membrane and to provide a basis for the standardization of welding construction technology, so as to prolong the service life of waterproofing membranes. Figure 15 shows the three-dimensional morphology of the sample. The blue area corresponds to a lower relative height, indicating that the overlap density is insufficient, and the water forms a permeable path along the low-lying part. The X, Y and Z triaxial units in the figure are all μm, and the magnification is 200 μm.

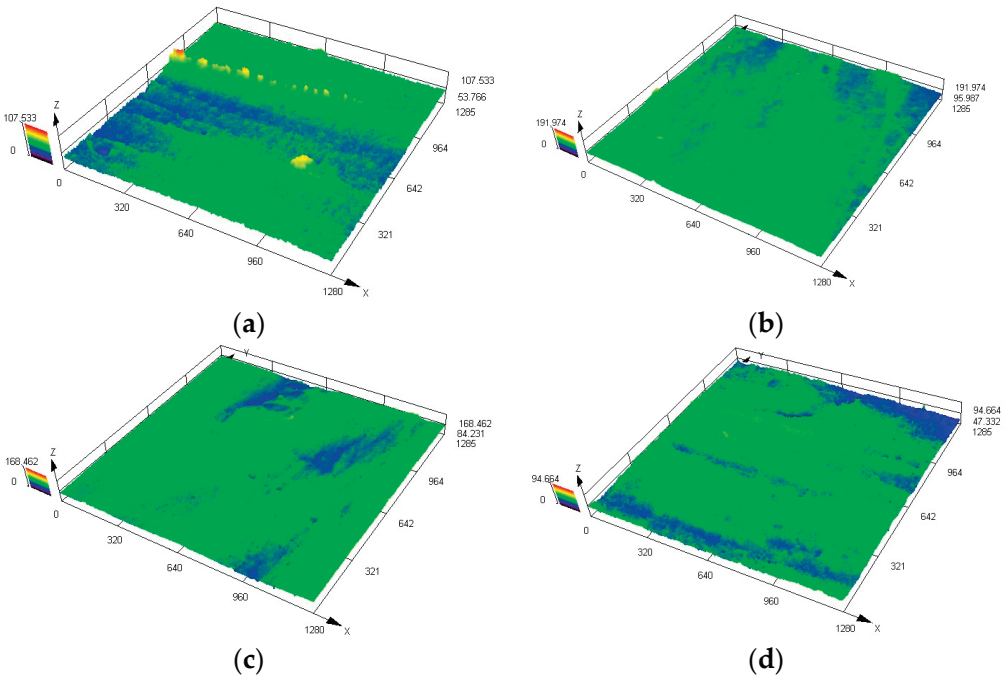

Figure 15. Three-dimensional topography of lap area of waterproofing membrane: (**a**) 300 °C, 1 m/min; (**b**) 400 °C, 4 m/min; (**c**) 500 °C, 5 m/min; (**d**) 600 °C, 5 m/min.

It can be seen from the three-dimensional topography of Figure 15 that the surface morphology of the lap interface is significantly different under different welding temperature and speed combinations. The maximum height and morphological characteristics of the Z-axis under each parameter group are shown in the following Table 5:

Table 5. Summary and comparison of three-dimensional morphology characteristics.

Process Parameters	Maximum Height of Z-Axis (μm)	Surface Undulation Characteristics	Assessment of Permeable Path in Lap Area
300 °C, 1 m/min	107.53	Large ups and downs, local protrusions and depressions coexist	Multiple, there is obvious direct current penetration path.
400 °C, 4 m/min	191.97	The morphology is uniform, less concave and convex	Very little, the interface is closely integrated.
500 °C, 5 m/min	168.46	The flatness is high, but the local fluctuation is large	Fewer, the compactness is good, but there is a short flow path.
600 °C, 5 m/min	94.66	Fluctuations, uneven distribution	Moderate, there are local voids to form a flow around, and the path is long.

3.2.3. Analysis of Results

In the construction of a TPO waterproofing membrane lap area, the area with large penetration is concentrated on the edge of the waterproofing membrane, which is obviously closely related to the process parameters such as welding temperature, welding speed and welding pressure. Therefore, in order to improve the sealing and waterproofing performance of the waterproofing membrane, especially the sealing effect in the edge part, the optimized construction process must be strictly followed.

Through the comparison of Figure 15, it can be found that, with the appropriate increase in welding temperature and speed, the surface depression area of the lap area gradually decreases, and the blue low-lying area obviously shrinks, indicating that the number of permeable paths gradually decreases. Especially under the condition of 400 °C and 4 m/min, the lap area shows a relatively smooth three-dimensional morphology, the blue area is the least, and the overall height difference in the interface is small, indicating that the weld area under this process combination has good compactness and optimal welding quality. In contrast, the interface formed at 300 °C and 1 m/min has obvious ups and downs. This is due to insufficient welding heat input, resulting in insufficient melting of the material, forming a large number of unmelted areas and voids, which in turn causes more tiny water paths and reduces the sealing performance of the waterproofing membrane. Furthermore, under the condition of 600 °C and 5 m/min, although the permeable path is less and the Z-axis height fluctuation is the smallest, the excessive heat input may lead to material over-melting or thermal damage, so that the waterproofing membrane forms a longer flow path, which in turn affects the microstructure stability and long-term reliability of the waterproofing membrane.

The analysis results of the morphology characteristics show that, when the welding temperature is 400 °C and the welding speed is 4 m/min, the morphology of the lap area of the waterproofing membrane is the most ideal, the dyeing area is the smallest, the permeable path is the least, and the interface compactness is the highest, which can be used as the recommended welding parameters. In order to ensure the welding quality and avoid thermal stress concentration or insufficient heat input caused by too high or too low temperatures, it is recommended to avoid the use of a 'high temperature + low speed' or 'low temperature + high speed' combination process; otherwise, it will be difficult to guarantee the welding quality and waterproof performance of the lap area.

Based on the test results of the experimental group, the following optimal welding parameters are recommended:

Welding temperature: 400 °C, to ensure that the waterproof membrane fully melted and to improve the sealing performance; welding speed: 4 m/min, to avoid a too-fast welding speed, leading to uneven weld or a waterproof membrane not fully fused.

3.3. Analysis of Test Results of Impermeability Test

The waterproof membrane lap area based on the optimal construction technology was tested for impermeability after immersion treatment and thermal aging treatment. The test results are shown in Table 6. The results show that the overlapping area shows good impermeability under the standard requirements (0.2 MPa, 30 min) and higher requirements (0.6 MPa, 120 min), which fully verifies the effective improvement of the waterproof performance of the overlapping area of the waterproofing membrane by optimizing the construction process.

Table 6. Test results of impermeability of overlapping area of waterproofing membrane.

Construction Technology of Lapping Area	Test Conditions and Results					
Welding temperature 400 °C Welding speed 4 m/min Welding pressure 14.9 N	No treatment 0.2 Mpa 30 min Qualified	No treatment 0.6 Mpa 120 min Qualified	Soaking treatment 0.2 Mpa 30 min Qualified	Soaking treatment 0.6 Mpa 120 min Qualified	Thermal aging treatment 0.2 Mpa 30 min Qualified	Thermal aging treatment 0.6 Mpa 120 min Qualified

3.4. Engineering Application

3.4.1. Project Profile

The project is located in Lingshanwan Road, Huangdao District, Qingdao City, Shandong Province, from Dazhushan Middle Road in the west to Dongyue East Road in the east. The utility tunnel plays an important role in urban construction. The pipelines of water, electricity, gas and heating are summarized in the utility tunnel structure, which solves the problem of complex pipelines in urban infrastructure construction. However, the underground environment of the utility tunnel is complex, especially near the coast, and the groundwater level is high, which seriously threatens the long-term safe operation of the utility tunnel.

Therefore, the waterproof engineering of the pipe gallery is an important step in its construction, and it must be constructed with high quality. In view of the requirements of the utility tunnel project for the impermeability of waterproof materials, the TPO waterproofing membrane was finally adopted after comprehensive consideration of the test results and design requirements. As shown in Figure 16, the hot wedge welding process with a welding temperature of 400 °C, welding speed of 4 m/min and welding pressure of 14.97 N was used for the construction of the overlapping area.

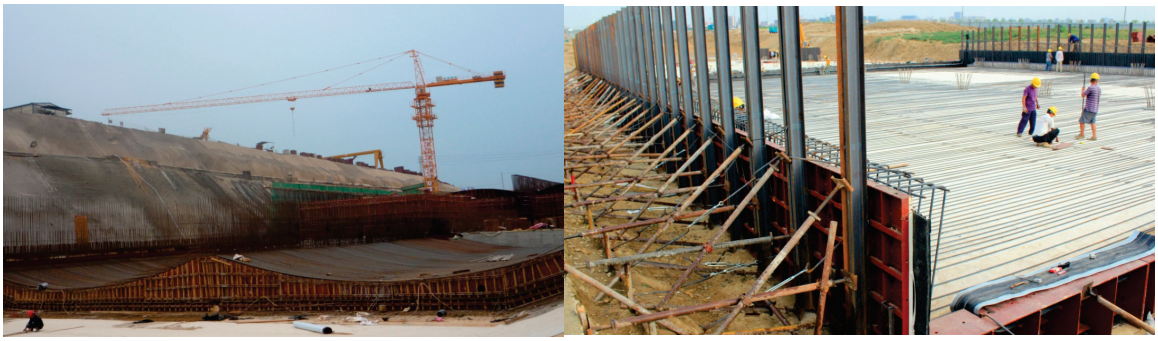

(**a**) (**b**)

Figure 16. Construction site drawing: (**a**) Construction stage. (**b**) Completion stage.

3.4.2. Effect Inspection

The results obtained by the test are applied to the pipe gallery project, and both the construction efficiency and the construction quality of the workers have been greatly improved. The waterproof coil sampling test is carried out after the completion of the project construction. The test results are shown in Table 7, and they meet the requirements.

Table 7. Test results of waterproofing membrane in construction site.

Construction Technology of Lapping Area	Peeling Test Results	Test Conditions and Results of Impermeability Test	
Welding temperature 400 °C Welding speed 4 m/min Welding pressure 14.9 N	671.37 N/50 mm	Test conditions: Soaking treatment 0.2 Mpa, 30 min Qualified	Test conditions: thermal aging treatment 0.2 Mpa, 30 min Qualified

3.4.3. Effect Contrast

In this section, the bonding properties of different waterproofing membranes were compared [28–30], and the specific results are shown in Table 8. The test included two indicators: peel strength and impermeability (no treatment). Obviously, the peel strength of the TPO waterproofing membrane welded under the optimal construction process is significantly higher than that of other waterproofing membranes.

Table 8. Comparison of effects of different waterproofing membranes.

Type	Peel Strength	Impermeability (No Treatment)
TPO waterproofing membrane	671.37 N/50 mm	0.6 MPa, 120 min
SBS oil-soaked waterproofing membrane	180 N/50 mm	0.2 MPa, 30 min
Coating + SBS waterproofing membrane	90 N/50 mm	0.4 MPa, 30 min
POEA-PET	118 N/50 mm	0.3 MPa, 120 min

4. Conclusions

The main conclusions obtained by testing the mechanical properties of the overlapping area of the TPO waterproofing membrane are as follows:

(1) The experimental results show that there is an obvious nonlinear relationship between the peel strength of the waterproofing membrane and the welding temperature: with the temperature from low to high, the peel strength increases first and then decreases, indicating that there is an optimal welding temperature. The results show that the best welding temperature is 400 °C. At this time, the welding quality of the waterproofing membrane is the best, and the peel strength reaches its peak. Under different temperature conditions, the sensitivity of peel strength to welding speed is also different: at 300 °C, the peel strength continues to decrease with the increase in speed; at 400 °C, the peeling strength first increases with the increase in speed to the peak and then decreases. At 500 °C and 600 °C, it shows a complex mode of decreasing first and then rising. Considering the welding quality and construction efficiency, it is recommended to use 400 °C and 4 m/min as the best welding parameters to fully guarantee the mechanical properties and waterproof performance of the welded lap. Considering the welding quality and construction efficiency, it is recommended to use 400 °C and 4 m/min as the best welding parameters to fully guarantee the mechanical properties and waterproof performance of the lap area.

(2) In this paper, the influence of welding pressure on the peel strength of the waterproofing membrane was studied, and the regulation effect of welding temperature was analyzed. The results show that the peel strength increases with the increase in welding pressure at 300 °C and 600 °C. At 400 °C and 500 °C, the peel strength increased first and then decreased slightly. The comprehensive analysis shows that the optimal construction pressure is 14.97 N, and the optimal peel strength can be obtained under this pressure, which provides an effective reference for optimizing the welding process of waterproofing membranes.

(3) The experimental results of penetration path detection show that the edge of the lap area is the area with the largest penetration. It is found that the combination of a 'high temperature + low speed' or 'low temperature + high speed' welding process can easily lead to penetration problems, which further emphasizes the importance of the strict implementation of welding standards in the actual construction process. Especially at the edge of the lap zone, the welding process control should be strengthened to effectively reduce the penetration risk, prolong the service life of the waterproofing membrane and improve its waterproofing performance.

(4) After the impermeability test, it is verified that there is no leakage in the welding lap of the waterproofing membrane under the working conditions of 0.2 MPa, 30 min to 0.6 MPa and 120 min. All the indexes meet the relevant qualification standards, indicating that the lap process can effectively guarantee the waterproofing performance and has good engineering application value.

(5) In this paper, a special pressure test tool for the welding performance test of the lap area of a waterproofing membrane is designed. The tool can be effectively applied to the welding performance test of various common waterproofing membrane materials including high-density polyethylene (HDPE), polyvinyl chloride (PVC) and ethylene propylene diene monomer (EPDM). By providing accurate welding pressure data, the test tool can provide a scientific basis and technical support for optimizing welding parameters, improving the welding quality and waterproofing performance of waterproofing membranes.

It can be directly applied to roofing, basement, tunnel and other projects involving TPO waterproofing membranes and guide the construction side to select the optimal welding temperature (400 °C), welding speed (4 m/min) and pressure (14.97 N) to ensure that the lap area has good anti-stripping and impervious performance. The research results can provide data support for the construction specifications and technical guidelines of TPO waterproofing membranes and other polymer waterproofing membranes, as well as help to promote the standardization and standardization of construction in the industry. The peeling strength test, impermeability test method and microscopic path observation method proposed in this paper can be used as one of the quality inspection methods of waterproof engineering, which can be used for on-site sampling and quality supervision. The designed welding pressure test tool and parameter response mechanism can be applied to the development of construction equipment to improve the adaptability and automation of equipment. In the future, multi-factor coupling numerical simulation and the optimization of temperature, velocity, pressure and interface quality can be carried out based on experimental data to improve the prediction ability of theoretical models.

Author Contributions: Conceptualization, K.W. and Q.W.; Methodology, Z.S.; Software, Z.Z., J.L. and C.T.; Validation, M.L., Z.L., Z.Z. and H.W.; Formal analysis, Z.Z. and J.L.; Investigation, Z.Z. and Z.J.; Resources, M.L. and Z.L.; Data curation, K.W.; Writing—original draft, Z.Z.; Writing—review & editing, Z.Z.; Visualization, Z.Z.; Supervision, Z.S. and Y.S.; Project administration, K.W.; Funding acquisition, K.W. All authors have read and agreed to the published version of the manuscript.

Funding: This research received no external funding.

Institutional Review Board Statement: Not applicable.

Informed Consent Statement: Not applicable.

Data Availability Statement: The original contributions presented in this study are included in this article. Further inquiries can be directed to the corresponding author.

Conflicts of Interest: Author Zhenyue Shi is employed by the Laboratory of Rock Burst Prevention Technology and Equipment of Shandong Energy Group Co., Ltd., Mingcai Liu and Zhipeng Li are employed by the China Railway Construction Investment (Shandong) Dongyang Expressway Co., Ltd. The remaining authors declare that the research was conducted in the absence of any commercial or financial relationships that could be construed as a potential conflict of interest.

Abbreviations

EPDM	Ethylene propylene diene monomer
PVC	Polyvinyl chloride
TPO	Thermoplastic polyolefin
SHPB	Split Hopkinson pressure bar
CMS	Carboxymethyl starch
OMMT	Organo-montmorillonite
SBS	Styrene–Butadiene–Styrene
SD	Standard deviation
POEA-PET	Palm oil-based polyurethane composite waterproofing membrane

References

1. Jourabchi, S.; Ostad Movahed, S. The effect of microwave irradiation on the molecular diffusion of the ethyl acetate (EA) into the blend of styrene-butadiene rubber (SBR)/ethylene-propylene-diene monomer rubber (EPDM). *Prog. Rubber Plast. Recycl. Technol.* **2025**, *41*, 201–217. [CrossRef]
2. He, Y.H.; Cao, Z.L.; Ge, Y.Y.; Liu, Z.Y.; Li, J.T.; Yu, J.Y. Effect of Heat Aging on Properties and Structure of SBS Modified Bitumen Waterproof Membrane. *Mater. Sci. Forum* **2021**, *1035*, 951–957. [CrossRef]
3. Tan, J.; Zhang, C.; Sun, G.; Ma, X.; Du, H. An Investigation of the Effects of Thermo-Oxidative Aging and the Freeze–Thaw Cycle on the Performance of Polyester-Based, Self-Adhesive Asphalt Waterproofing Membranes. *Appl. Sci.* **2024**, *14*, 8237. [CrossRef]
4. Ding, H.; Hai, M.; Ge, Y. Research on the Durability of Thermoplastic Polyolefin Waterproof Rolls Based on Thermal Oxygen Aging. *New Chem. Mater.* **2025**, *53*, 247–252.
5. Park, W.G.; Choi, S.Y.; Park, J.S.; Kim, D.B.; He, X.Y.; Oh, S.K. Analysis on the Effects of External Temperature and Welding Speed on the Safety of EVA Waterproofing Sheet Joints by Hot Air Welding. *Materials* **2020**, *13*, 5586. [CrossRef]
6. Waldvogel, M.; Zurbriggen, R.; Berger, A.; Herwegh, M. Influences of temperature and opening rate of substrate cracks on the mechanical behaviour, crack–bridging ability and deformation mechanisms of one–component, cementitious, flexible waterproofing membranes. *Cem. Concr. Res.* **2020**, *136*, 106140. [CrossRef]
7. Bucko, M.M.; Hloch, S.; Valicek, J.; Tozan, H.; Javadi, Y.; Ghosh, A. Influence of welding physical conditions on waterproofing membrane weld quality. *Tech. Gazett* **2012**, *19*, 683–687.
8. Zhang, B. Research on Leakage Localization Online Monitoring System Based on Intelligent Perception Waterproof Membrane. Master's Dissertation, Zhengzhou University, Zhengzhou, China, April 2022.
9. Jiang, Y.; He, B.; Zhao, J.; Pei, H.; Liu, J.; Wang, H. Influence of novel polymer waterproofing membrane on mechanical properties of tunnel lining structure. *Constr. Build. Mater.* **2022**, *360*, 129579. [CrossRef]
10. Lee, K.; Kim, D.; Chang, S.-H.; Choi, S.-W.; Park, B.; Lee, C. Numerical approach to assessing the contact characteristics of a polymer-based waterproof membrane. *Tunn. Undergr. Space Technol.* **2018**, *79*, 242–249. [CrossRef]
11. Miyauchi, H.; Katou, N.; Tanaka, K. Force transfer mechanism on fastener section of mechanically anchored waterproofing membrane roofs under wind pressure during typhoons. *J. Wind. Eng. Amp. Ind. Aerodyn.* **2011**, *99*, 1174–1183. [CrossRef]
12. Hailesilassie, B.W.; Hean, S.; Partl, M.N. Testing of blister propagation and peeling of orthotropic bituminous waterproofing membranes. *Mater. Struct.* **2015**, *48*, 1095–1108. [CrossRef]
13. Tsukagoshi, M.; Miyauchi, H.; Tanaka, K. Protective performance of polyurethane waterproofing membrane against carbonation in cracked areas of mortar substrate. *Constr. Build. Mater.* **2012**, *36*, 895–905. [CrossRef]
14. Li, W.; Yu, L.; Tan, Y.; Wu, L.; Qian, J. Mechanical properties and impact behavior of frozen clay: Insights from static mechanical tests, fly-plate tests, and split-Hopkinson pressure bar analysis. *Phys. Fluids* **2024**, *36*, 057138. [CrossRef]
15. Li, W.; Yu, L.; Zhang, T. Quantitative analysis of grain size effect on tensile mechanical behavior of granite based on multi-level force chain networks. *Comp. Part. Mech.* **2024**, *11*, 2245–2266. [CrossRef]
16. Peng, Y.; Yu, L.; Qian, J.; Li, W.; Zhang, T.; Zhou, L. Dynamic tensile behavior and crack propagation in coral aggregate seawater shotcrete: Experimental investigation and numerical simulation. *Cement. Concrete. Comp.* **2025**, *159*, 106010. [CrossRef]
17. Li, Z.Q.; Nie, L.; Xue, Y.; Li, W.; Fan, K. Model Testing on the Processes, Characteristics, and Mechanism of Water Inrush Induced by Karst Caves Ahead and Alongside a Tunnel. *Rock. Mech. Rock. Eng.* **2025**, *58*, 5363–5380. [CrossRef]
18. Li, W.; Zhang, Q.; Wang, X.; Yu, L.; Li, Z. Synergistic effect of particle size, carboxymethyl starch and Na2CO3 on rheological and filtration property of bentonite-based material. *Case. Stud. Constr. Mater.* **2024**, *31*, e03537. [CrossRef]
19. He, Y.; Zhang, T.; Mao, S.; Zeng, S.; Wu, L.; Yu, J. Investigation of Antiaging Performance and Service Life of OMMT/SBS Modified Bitumen Waterproof Membranes. *J. Mater. Civ. Eng.* **2024**, *36*, 04024025. [CrossRef]

20. Wang, J.; Li, X.; Sun, G.; Ma, X.; Du, H. Experimental Investigation on the Performance of SBS-Modified Asphalt Waterproofing Membrane by Thermo-Oxidative Aging and Freeze-Thaw Cycle. *Polymers* **2024**, *16*, 2593. [CrossRef]
21. Garber, E.A.; Diligenskii, E.V.; Antonov, P.V.; Shalaevskii, D.L.; Dyatlov, I.A. Application of statistical methods to reveal and remove the causes of welding of coil laps upon annealing of cold-rolled steel strips. *Russ. Metall. (Met.)* **2017**, *2017*, 771–774. [CrossRef]
22. Yang, C.; Peng, F.; Cui, Y.; Wang, Y. Analysis of common problems in overlapping edges of synthetic polymer pre laid waterproofing membranes. *China Build. Waterproofing* **2025**, *45*, 45–48+52.
23. Liu, X.; Wang, H.; Li, J.; Kong, C.; Ren, S.; Liu, C. The Effect of Corrosion Aging on the Tensile Properties of Polyethylene Polypropylene Roll Overlapping Zone. *J. Xi'an Univ. Technol.* **2021**, *37*, 136–142.
24. Sun, C.; Liu, D.; Liu, J. Processing technology and characteristics of TPO waterproofing membrane. *Plast. Technol.* **2015**, *43*, 61–64.
25. Han, Z.; Tian, F.; Duan, W.; Zhang, L. The influence of welding process on the welding performance of TPO waterproofing membrane. *New Build. Mater.* **2015**, *42*, 40–42.
26. *GB27789-2011*; Thermoplastic Polyolefin TPO Waterproofing Membrane. China National Standardization Administration Committee: Beijing, China, 2011.
27. *GB55030-2022*; General Specification for Waterproofing of Building and Municipal Engineerin; Announcement No. 147. Ministry of Housing and Urban-Rural Development of the People's Republic of China: Beijing, China, 2022.
28. Han, P.; Luo, W.; Li, C.; Zhong, H.; Chang, H.; Li, K.; Zhang, S. Product design and T-joint lap performance of a twin-based elastomer modified asphalt waterproofing membrane. *China Build. Waterproofing* **2024**, *8*, 9–12+25.
29. Zhang, M.; Fan, S.; Bai, N. Research on the improvement of peel strength of elastomer modified asphalt waterproofing membrane. *China Build. Waterproofing* **2025**, *5*, 1–4.
30. Zeng, Y.; Huang, Z.; Lin, W.; Chen, Y.; Qiu, R.; Liu, W. Preparation and properties of PET fiber / palm oil-based polyurethane composite waterproofing membrane. *Biomass Chem. Eng.* **2025**, *59*, 1–7.

Disclaimer/Publisher's Note: The statements, opinions and data contained in all publications are solely those of the individual author(s) and contributor(s) and not of MDPI and/or the editor(s). MDPI and/or the editor(s) disclaim responsibility for any injury to people or property resulting from any ideas, methods, instructions or products referred to in the content.

materials

MDPI

Article

Development of Fault Similar Material for Model Test of Fault Water Inrush Disaster

Zhipeng Li [1], Deming Wang [1,*], Kai Wang [2], Qingsong Zhang [3], Lianzhen Zhang [4], Yang Gao [5] and Yongqi Dai [1]

[1] School of Transportation and Civil Engineering, Shandong Jiaotong University, Jinan 250357, China; lizhipeng@sdjtu.edu.cn (Z.L.); daiyongqisdjtxy@163.com (Y.D.)
[2] Shandong High-Speed High-Tech Investment Co., Ltd., Jinan 250102, China; wakai9958@163.com
[3] Research Center of Geotechnical and Structural Engineering, Shandong University, Jinan 250100, China; zhangqingsong@sdu.edu.cn
[4] College of Pipeline and Civil Engineering, China University of Petroleum, Qingdao 266580, China; zhanglianzhen@upc.edu.cn
[5] Key Laboratory of Structural Health Monitoring and Control, Shijiazhuang Tiedao University, Shijiazhuang 050043, China; gaoyang_sjz@163.com
* Correspondence: wangdeming@sdjtu.edu.cn

Abstract: The applicability of similar materials is a key factor affecting the results of geomechanical model tests. In order to investigate the multi-physical field evolution mechanism of surrounding rocks during water inrush disasters in tunnels crossing fault zones, based on the similarity theory of geomechanical model tests, the physical–mechanical parameters of a prototype rock's mass were first analyzed for similarity, and the target values of similar materials were determined. Secondly, using sand as coarse aggregate, talcum powder as fine aggregate, gypsum and clay as binders, and Vaseline as a regulator, a fault-simulating material suitable for model tests was developed through extensive laboratory experiments. Finally, with material deformation characteristics and strength failure characteristics as key control indicators, parameters such as uniaxial compressive strength, permeability coefficient, unit weight, and elastic modulus are synergistically regulated to determine the influence of different component ratios on material properties. The experimental results show that the uniaxial compressive strength and permeability coefficient of similar materials are mainly controlled by gypsum and Vaseline. Cohesion is mainly controlled by clay and Vaseline. The application of this similar material in the model test of the tunnel fault water inrush disaster successfully reproduced the disaster evolution process of fault water inrush, meeting the requirements of the model test for similar materials of faults. Furthermore, it provides valuable guidance for the selection of similar materials and the optimization of mix proportions for fault disaster model tests involving similar characteristics.

Keywords: model test; fault water inrush; similar material; mix ratio; physical–mechanical parameters

1. Introduction

Fault-zone rock masses are characterized by developed fractures, loose and fragmented structures, and high-pressure water-rich conditions. Tunnels crossing faults are extremely prone to inducing water inrush disasters [1–3], which endanger the safety of construction personnel, cause construction delays, and threaten the ecological environment of the tunnel site and the long-term operation safety of the tunnel. Studying the variation

laws of each physical field in the surrounding rock during the occurrence of water inrush disasters is of great significance for guiding tunnel design, construction, and risk avoidance.

Currently, the research methods for tunnel water inrush mainly include theoretical calculations [4–6], numerical simulations [7–9], and model tests [1,10–13]. However, the complex formation mechanism and occurrence conditions of faults make the evolution process of water inrush disasters extremely complex, with significant coupling effects of physical field parameters. It is difficult to conduct a comprehensive analysis and research relying solely on theoretical and numerical calculations. As a critical research method, geomechanical model testing accurately reproduces the entire evolution process of tunnel water inrush disasters, with easily controllable test conditions and variables, which play a critical role in addressing underground engineering disaster mechanisms. Reasonable and reliable similar materials have an important impact on the results of model tests. Fault rock masses have characteristics such as high porosity, high softening coefficients, and easy disintegration when exposed to water. The selection and proportioning of material components are key factors in fault similarity simulation.

Dai et al. [14] used talcum powder, gypsum, and liquid paraffin as raw materials, optimizing the ratio through orthogonal tests to successfully simulate the permeability characteristics of tunnel rock masses. Ko et al. [15] used Portland cement and gypsum as binders, combined with mica powder filling, to construct similar materials that can characterize the crack propagation behavior of rocks. Zan et al. [16] used a granular mixture of similar materials composed of quartz sand, barite powder, and gypsum, adjusting the hydraulic properties of the similar materials through silicone oil, liquid paraffin, industrial glycerin, and petrolatum gel, which were successfully applied to a seepage model test of tunnel excavations in Xi'an Metro Line 9. Shemenda et al. [17] used paraffin, mud, and other materials as cementing materials, and river sand and gypsum were used as aggregates to make similar rock materials. Zhang et al. [18] derived the similarity criteria for permeability coefficient, seepage velocity, flow velocity, and seepage pressure under high ground stress and high groundwater conditions based on the similarity theory of hydraulic coupling, and they developed similar materials using iron ore concentrate powder, barite powder, and quartz sand as aggregates, white cement as a cementing agent, and silicone oil to regulate the hydraulic properties of the materials. The above scholars' inorganic cementing materials, with Portland cement and gypsum as the core, have the characteristics of low cost and high temperature resistance, but they are relatively brittle and have insufficient long-term stability.

Xu et al. [19] developed similar materials composed of quartz sand, barite powder, silicone oil, Vaseline, and paraffin, adjusting the ratio through orthogonal tests to configure the surrounding similar rock materials that can meet the requirements of uniaxial compressive strength, elastic modulus, gravity, and bondability. These scholars introduced organic components such as nano-clay and silicone oil, significantly improving the toughness of materials. Liu et al. [20] developed a new type of fluid–solid-coupling similar material, which was mixed with river sand, calcium carbonate, talcum powder, white cement, Vaseline, and anti-wear hydraulic oil, verifying its feasibility through physical simulation tests in coal mine surface water inrush events. Guo et al. [21] developed similar fault materials using mountain sand, gravel, and red clay as raw materials based on the fluid–solid coupling similarity theory and carried out a large number of matching tests, revealing the evolution process of water inrush in deeply buried tunnels. Wu et al. [22] developed fluid–solid coupling similar materials (SCVO) using sand, barite powder, and talcum powder as aggregates; cement and Vaseline as cementing agents; and silicone oil as a regulator, and they successfully applied them to a geomechanical model test of the Qingdao Jiaozhou Bay Submarine Tunnel.

It can be seen from the above that although certain progress has been made in the development of fault similar materials, there is still the problem of poor similar material simulation. At present, very few similar materials can simultaneously meet the physical, mechanical, and hydrogeological properties of faults, and targeted regulation cannot be performed on the characteristic parameters of different simulation objects. Based on the above research results and similarity theory, this paper uses sand, talcum powder, gypsum, Vaseline, and clay as the main components to develop a fault similar material that meets physical, mechanical, and hydrogeological properties through mix ratio tests, and we successfully applied it in a model test of a tunnel fault water inrush disaster.

2. Methods and Specimen Preparation

2.1. Similarity Principle

When designing similar model tests, the similar conditions should be determined according to the similarity of the research object: that is, the geometric dimensions, loads, boundary conditions, material density, strength, deformation characteristics, and hydrogeological characteristics of the prototype and the model follow the similarity principle [23]. The similarity scale (C) refers to the ratio of physical quantities with the same dimension between the prototype (P) and the model (M). Based on dimensional analysis and the basic equations of elastic mechanics, combined with the fluid–solid coupling theory, the following similarity relationships are derived.

(1) According to dimensional analysis, the similarity scales of physical quantities with the same dimension are equal, and the similarity scale with a dimension of one is equal to 1; we then have the following:

$$C_\mu = C_\varepsilon = C_\varphi = 1, \tag{1}$$

$$C_\sigma = C_{\sigma_c} = C_{\sigma_t} = C_E = C_c, \tag{2}$$

(2) The similarity relationship derived from the equilibrium equation is as follows: Prototype equilibrium equation:

$$\left(\sigma_{ji,j}\right)_p + \left(f_i\right)_p = 0, \tag{3}$$

Model equilibrium equation:

$$\left(\sigma_{ji,j}\right)_m + \left(f_i\right)_m = 0, \tag{4}$$

According to the definition of similarity scales, substituting the similarity scales of stress, geometry, and volume force $C_\sigma, C_L, C_f = C_\gamma$ into Equation (3) gives

$$\frac{C_\sigma}{C_L}\left(\sigma_{ji,j}\right)_m + C_\gamma\left(f_i\right)_m = 0, \tag{5}$$

Comparing Equations (4) and (5) gives

$$\frac{C_L C_\gamma}{C_\sigma} = 1, \tag{6}$$

(3) In addition, according to the geometric equation, physical equation, stress boundary condition, and displacement boundary condition, the following similarity relationships can be derived:

$$\frac{C_\delta}{C_\varepsilon C_E} = 1, \tag{7}$$

(4) Based on the mathematical model of fluid–solid coupling in homogeneous and continuous media, the similarity theory of fluid–solid couplings is derived, and the corresponding similarity relationships are obtained as follows:

$$C_K = \frac{\sqrt{C_L}}{C_\gamma}, \tag{8}$$

In Equations (1)–(8), we have the following: γ is the unit weight; L is the geometric dimension; δ is the displacement; E is the elastic modulus; σ is the stress; σ_t is the tensile strength; σ_c is the compressive strength; ε is the strain; c is cohesion; φ is the internal friction angle; μ is Poisson's ratio; K is the permeability coefficient. For similarity scales, C_μ is the Poisson ratio similarity scale; C_ε is the strain similarity scale; C_φ is the friction angle similarity scale; C_σ is the stress similarity scale; C_{σ_c} is the compressive strength similarity scale; C_{σ_t} is the tensile strength similarity scale; C_E is the elastic modulus similarity scale; C_c is the cohesion similarity scale; C_L is the geometric similarity scale; C_γ is the unit weight similarity scale; C_K is the permeability coefficient similarity scale.

2.2. Determination of Similar Material Parameters

In order to accurately simulate the mechanical behavior and engineering response of a faulted rock body in an actual project, materials similar to the actual faulted rock body in terms of mechanical properties are developed. In this study, the Zhongjiashan Tunnel Project of the Quannan Expressway in China is used as the background. Based on the geological investigation report of the project and the core samples taken from the site, it is clarified that the lithology of the fault-filling medium is mainly muddy, fully weathered shale, which contains fault clay and fault breccia, and it is characterized by a loose structure with alternating soft and hard layers; plasticity is exhibited when the water content is high, and cracking is observed when water loss occurs. The parameters of this prototype faulted rock mass are shown in Table 1.

Table 1. Physical–mechanical parameters of faulted protoliths and targeted similar materials.

Material Type	Density ρ/(g/cm^3)	Compressive Strength σ_c/MPa	Elastic Modulus E/GPa	Permeability Coefficient K/(cm/s)	Cohesion c/kPa	Internal Friction Angle φ/(°)
Fault undisturbed rock mass	1.94~2.05	8.0~12.0	1.0~1.2	2.46×10^{-4}~5.76×10^{-4}	118.53~159.78	33~41
Targeted Similar Materials	1.94~2.05	0.13~0.2	0.017~0.02	3.16×10^{-5}~7.44×10^{-5}	1.98~2.66	33~41

To simulate the characteristics of the fault rock body and related engineering problems, the similarity ratio is determined based on the similarity principle, which is based on the requirement of realism of the model test. Here, $C_L = 60$, $C_\gamma = 1$, $C_\sigma = 60$, $C_E = 60$, $C_K = \sqrt{60}$, $C_c = 60$, and $C_\varphi = 1$, and the calculations are obtained to simulate the similar material of each target parameter, as shown in Table 1.

2.3. Material Preparation

The prototype fault rock mass in this test contains fault clay and fault breccia, which are characterized by a loose structure with alternating soft and hard layers, and plastic behavior is observed when the water content is high, with cracking occurring upon water loss. In this study, gypsum and clay were used as binders; Vaseline as a regulator; and sand and talcum powder as aggregates, and an appropriate amount of mixing water was

used to develop a new type of fault similar material. The material components are shown in Figure 1.



Figure 1. Fault similar material composition.

To meet the requirements of the physical, mechanical, and hydrogeological properties of similar materials, the particle size of sand is <2 mm, and the particle size distribution diagram of the sand is shown in Figure 2, the gypsum used is building gypsum with a fineness of 600 meshes, the clay selected is silica–aluminate clay, and the fineness of talcum powder is 1250 meshes, with the main component being $Mg_3Si_4O_{10}(OH)_2$, which is a kind of water-containing magnesium silicate mineral that accounts for more than 90% of the talc.

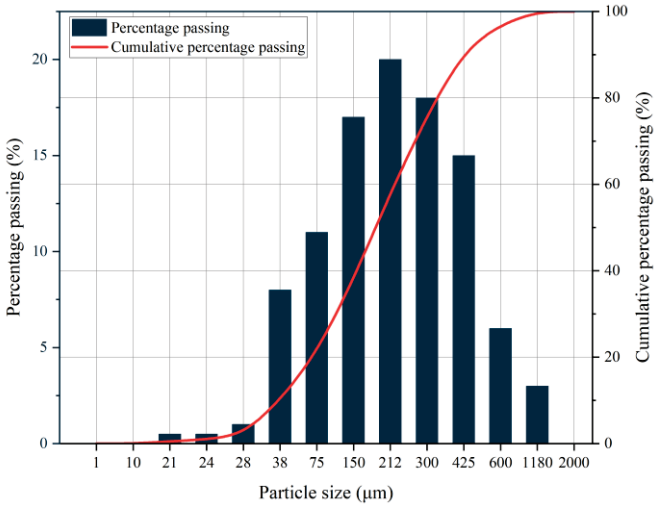

Figure 2. Sieving curves for sand.

Specimens of the similar material were prepared using molds with dimensions of ϕ50 mm × 100 mm. The coarse and fine aggregates, binders, and regulators were accurately weighed according to mass. The coarse and fine materials and clay were mixed and stirred evenly, water was added, followed by Vaseline, and the mixture was thoroughly stirred. The mixture was then placed into the mold and compacted in multiple layers to ensure uniformity in both the upper and lower parts of the specimen. After demolding, the specimens were cured at room temperature. The specimens of the similar material are shown in Figure 3.



Figure 3. Similar material specimen.

2.4. Test Methods

The performance test of similar materials includes a test [24] of the basic mechanical parameters and hydrogeological parameters of the materials. The test of basic mechanical parameters includes the test of uniaxial compressive strength σ_c, elastic modulus E, cohesion c, and internal friction angle φ. The test of hydrogeological parameters includes the disintegration and permeability coefficient K of the materials. These parameters are tested as shown in Figure 4. To test the performance of different ratios of similar materials and obtain the influence of each factor on the material parameters, three specimens were made for each parameter of each ratio.

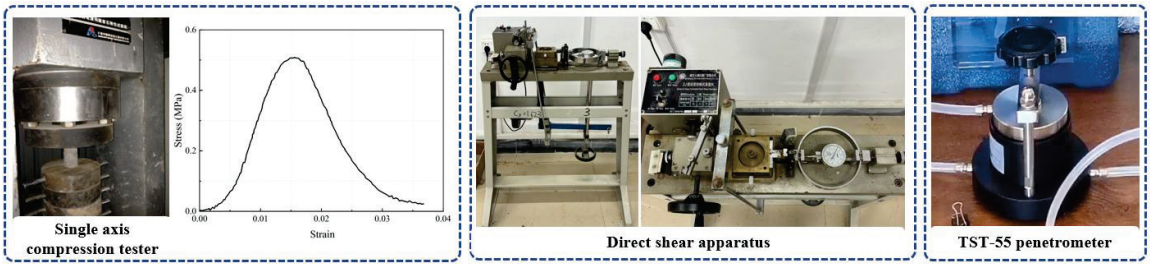

(a) Uniaxial compressive strength test (b) Cohesion and angle of internal friction test (c) Penetration test

Figure 4. Schematic diagram of the test method.

(1) Determination of Uniaxial Compressive Strength and Elastic Modulus of the Materials

For standard specimens with dimensions of ϕ50 mm × 100 mm, a microcomputer-controlled electro-hydraulic servo testing machine was used to perform uniaxial compression tests, as shown in Figure 4, to determine the stress–strain curve of the material specimens during the compression process, as shown in Figure 4. The slope of the elastic stage of the curve is the elastic modulus.

(2) Determination of Material Cohesion and Internal Friction Angle

The internal friction angle and cohesion of the fault similar material were determined using a strain-controlled direct shear instrument (Naijiuweiyen Technology Co., Beijing, China). First, the similar material was pressed into direct shear specimens with dimensions of ϕ61.8 mm × 20 mm using a special mold. After demolding, the specimens were placed in a constant-temperature and constant-humidity box for standard curing (temperature = 20 ± 2 °C; relative humidity ≥ 95%) [25] for 7 days, and natural air drying took place for 3 days. Subsequently, the cured specimens were placed in the shear box of the direct shear instrument, with permeable stones above and below the specimens. After the specimens were properly installed, loading was performed. Four specimens were used for each experiment, and direct shear tests were conducted under vertical pressures of 100, 200, 300, and 400 kPa at a shear rate of 0.8 mm/min. The specimens were sheared to failure

within 4–5 min, and the maximum readings on the dial gauge were recorded under each level of vertical load. The shear strength of the material was calculated using the following formula:

$$\tau = \sigma \tan \varphi + c, \tag{9}$$

In the formula, τ is shear stress, and σ is normal stress.

The c and φ values of the fault similar material specimens with typical mix ratios are shown in Table 2.

Table 2. Values of c and φ of fault similar materials' representative specimens.

Test Number	Material Ratio (S:T:C:G:W:V)	Cohesion c (kPa)	Angle of Internal Friction φ (°)
1	1:0.05:0.04:0.16:0.12:0.09	2.208	32
2	1:0.05:0.04:0.30:0.12:0.09	2.672	37
3	1:0.05:0.04:0.25:0.12:0.09	2.262	35
4	1:0.05:0.01:0.25:0.12:0.09	2.036	40
5	1:0.05:0.05:0.25:0.12:0.09	1.943	36

Note: S:T:C:G:W:V represents sand, talcum powder, clay, gypsum, water, and Vaseline, respectively.

(3) Material Hydro-Physical Property Testing

① Water Disintegration Test

The fault-filling medium, when exposed to water, experiences partial dilution, softening, or dissolution of its cementing agents, leading to a reduction in cohesion and an increase in looseness. As the water–rock interaction continues, this process ultimately causes the weakening and disintegration of the fault-filling material, resulting in water surges. To simulate this characteristic of fault similar materials, specimens of fault similar materials are cured at room temperature for 7 days before undergoing a water disintegration test. The disintegration times of specimens with typical mix ratios are shown in Table 3.

Table 3. Disintegration time of fault similar material specimens with typical mix ratios.

Test Number	Material Ratio (S:T:C:G:W:V)	Disintegration Time (s)
1	1:0.24:0.05:0.25:0.15:0.12	185
2	1:0.24:0.05:0.32:0.15:0.12	215
3	1:0.24:0.02:0.25:0.15:0.12	330

② Permeability Coefficient K Test

Permeability, as another important indicator of the hydro-physical properties of similar materials, can be characterized by the permeability coefficient. The higher the permeability coefficient, the stronger the permeability. Considering that the permeability coefficient of geotechnical materials is generally small, typically in the range of 10^{-7}–10^{-3}, and that various interference factors make it difficult to ensure high measurement accuracy, a TST-55 permeability meter (NAIJIUWEIYEN TECHNOLOGY CO., Beijing, China) was used in this study to measure the K value through the variable-head method. The test setup is shown in Figure 4. The calculation formula is as follows:

$$K = 2.3 \frac{aL}{At} \lg \frac{h_1}{h_2}, \tag{10}$$

where

a is the cross-sectional area of the variable-head pipe (in this test $a = 1.075$ cm^2);

L is the length of the permeable path (in this test, $L = 4.0$ m);

h_1 is the initial water head height;
h_2 is the final water head height;
A is the cross-sectional area of the specimen;
t is the time interval.

Permeability tests were conducted on the fault similar materials, and the permeability coefficients of specimens with typical mix ratios are shown in Table 4.

Table 4. Permeability coefficients of fault similar material specimens with typical mix ratios.

Test Number	Material Ratio (S:T:G:C:V:W)	Permeability Coefficient K (cm/s)
1	1:0.24:0.05:0.25:0.15:0.12	8.4×10^{-5}
2	1:0.24:0.05:0.32:0.15:0.12	5.2×10^{-5}
3	1:0.24:0.05:0.25:0.15:0.12	4.5×10^{-5}

3. Analysis of Factors Affecting the Properties of Similar Materials

Through numerous mix ratio experiments, the influence of various components on the uniaxial compressive strength, cohesion, elastic modulus, and permeability coefficient, among other characteristic parameters of similar materials, has been investigated.

3.1. Analysis of Factors Affecting Uniaxial Compressive Strength

Among the components of similar materials, the binding capacity of the binder for coarse and fine aggregates directly reflects the strength of the material. The uniaxial compressive strength, as a key indicator of material strength, is influenced by the content of various components in the binder. Adjusting the gypsum and Vaseline content in fault similar materials significantly affects the uniaxial compressive strength of the material.

As shown in Figure 5a, when the content of other components in the fault similar material remains constant, increasing the gypsum content leads to a corresponding increase in material strength. However, when the gypsum content exceeds 13%, strength begins to slightly decrease. Figure 5b illustrates that when the Vaseline content is less than 4%, the material strength increases with an increase in Vaseline content. However, when the Vaseline content exceeds 4%, the material strength decreases significantly. This is because at lower Vaseline contents, it acts as a partial binder, but as the content increases, Vaseline disrupts the bonding force between aggregates, leading to a reduction in material strength.

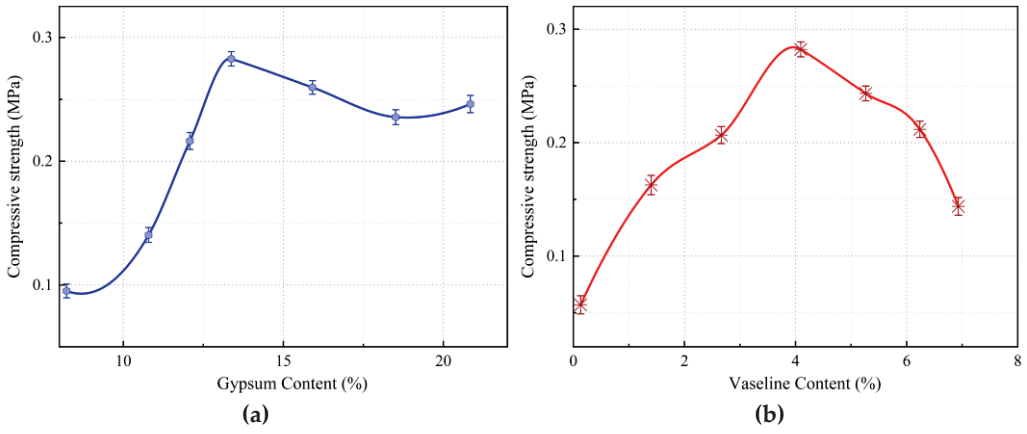

Figure 5. (**a**) The variation curve of compressive strength with gypsum content. (**b**) The variation curve of compressive strength with Vaseline content. Influence curves of gypsum and Vaseline contents on compressive strength of fault similar material.

3.2. Analysis of Factors Affecting Permeability Coefficient

Permeability, as a key indicator of the hydro-physical properties of similar materials, is influenced by the material's porosity and binder content. Varying the gypsum and Vaseline content in the material can significantly alter the permeability coefficient of the similar material.

Both gypsum and Vaseline content have a substantial impact on the permeability coefficient of fault similar materials. As shown in Figure 6a, when the gypsum content is below 4%, the permeability coefficient remains relatively stable. Although gypsum, as a binder, has some bonding effect on fine aggregates, its weak water-disintegration properties prevent a significant reduction in the permeability coefficient. When the gypsum content exceeds 4%, its cementing effect becomes more pronounced, resulting in a sharp decrease in the permeability coefficient. Figure 6b shows that the permeability coefficient decreases continuously with increasing Vaseline content and stabilizes at a value of 3.1×10^{-5} cm/s. This stabilization occurs because Vaseline, as a hydrophobic oil-based modifier, effectively fills the voids between coarse aggregates and blocks the percolation pathways when it reaches a certain content. Additionally, it can withstand some water pressure, leading to a final stable permeability coefficient.

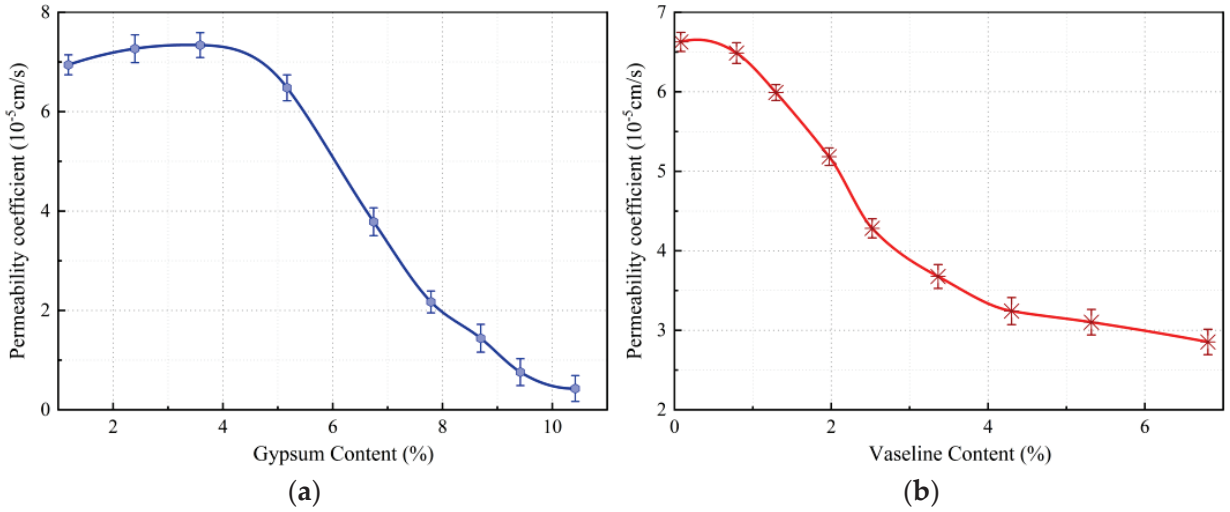

Figure 6. (**a**) The variation curve of the permeability coefficient with respect to gypsum content. (**b**) The variation curve of the permeability coefficient with respect to Vaseline content. Influence curves of gypsum and Vaseline contents on the permeability coefficient of fault similar materials.

3.3. Analysis of Factors Affecting Elastic Modulus

The elastic modulus of fault similar materials can be adjusted by varying the gypsum and Vaseline content, as shown in Figure 7.

The elastic modulus of fault similar materials can be regulated by adjusting the gypsum and Vaseline content. As shown in Figure 7, the elastic modulus of fault similar materials increases approximately linearly with gypsum content and exhibits a negative correlation with Vaseline content. As depicted in Figure 7a, when the content of other components remains constant, increasing the gypsum content significantly improves the elastic modulus of the material. In contrast, Figure 7b shows that as the Vaseline content increases, the elastic modulus of the material continuously decreases.

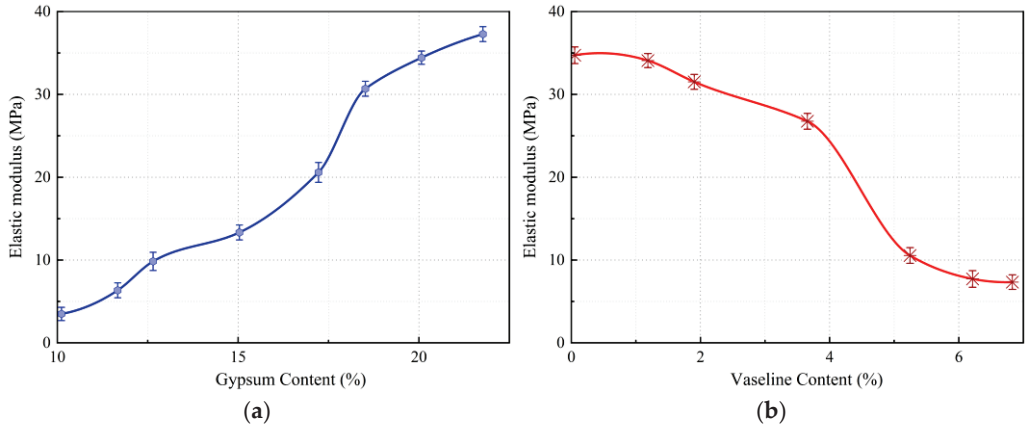

Figure 7. (**a**) The variation curve of elastic modulus with an increase in gypsum content. (**b**) The variation curve of elastic modulus with an increase in Vaseline content. Influence curves of gypsum and Vaseline contents on the elastic modulus of fault similar material.

3.4. Analysis of Influencing Factors of Cohesion

The grading of aggregates and the binder content significantly affect the cohesion of similar materials. By varying Vaseline and clay contents, the cohesion of the material can be adjusted within a certain range, as shown in Figure 8.

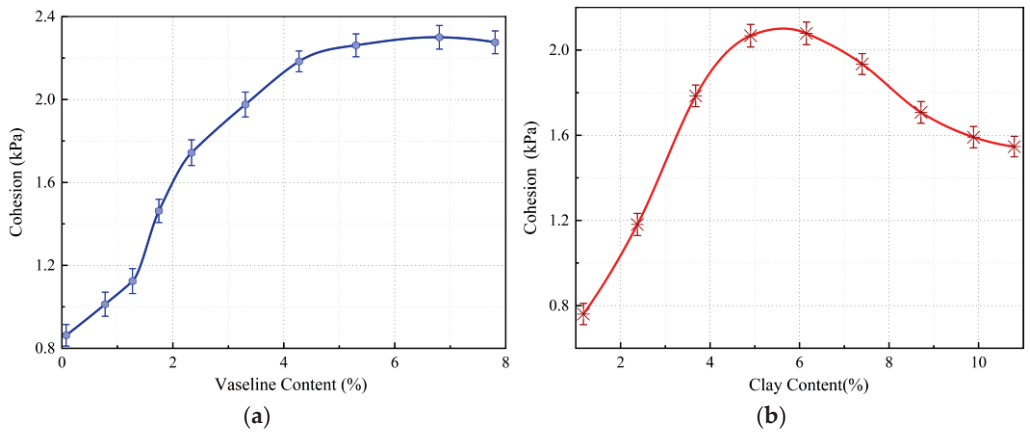

Figure 8. (**a**) The variation curve of cohesion with an increase in Vaseline content. (**b**) The variation curve of cohesion with an increase in clay content. Influence curves of Vaseline and clay contents on the cohesion of fault similar material.

Figure 8a illustrates the effect of Vaseline content on the cohesion of fault similar materials. Vaseline acts as an adjusting agent in fault materials, and when its content is below 4%, cohesion increases with increasing Vaseline content. However, when the Vaseline content exceeds 4%, the effect on cohesion becomes minimal, and it remains almost unchanged. Figure 8b shows the effect of clay content on the cohesion of fault materials. When the clay content is below 6%, the cohesion of the material increases as the clay content increases. However, when the clay content exceeds 6%, the cohesion begins to decrease, eventually stabilizing around 1.6 kPa.

Based on the above experimental analysis of the influence of similar material components and characteristic parameters, the regulatory mechanism of each component on the mechanical and permeability properties of the material can be clarified. For this reason, this study is based on the response relationships between the obtained components and parameters, which were obtained through the systematic proportioning test, and finally,

the similar materials' ratios were optimized in line with the target requirements shown in Table 5 below.

Table 5. Fault similar materials' mix ratios.

A:B	S:G	W:G	T:C	W:V
3.51:1	6.22:1	0.82:1	2.3:1	3.52:1

4. Application of the Tunnel Water Inrush Model Test

4.1. Test Overview

The total length of the Zhongjiashan Tunnel of Quannan Expressway in Jiangxi Province is about 5000 m, which is a deeply buried tunnel with a maximum burial depth of 450 m. There are several secondary faults, such as the major fault F2 and F3~F5 in the tunnel site area, among which F2 is the main fault, with a strike of N30° E, inclination of SE, a dip of 65°, and a width of 15–20 m. F3 and F5 are located at the southeast side of F2 at a distance of 50 m and 120 m, respectively.

The fault zone is rich in recharge water sources. Complex construction conditions are present, and water inrush disasters occur frequently. Construction at the F2 fault resulted in a number of large-scale water inrush disasters. In the F2 fault zone, the accumulation of broken gray-black carbonaceous sand shale is observed as a result of tectonic activities and the impact of the water inrush effect. The sediments show loose, broken characteristics and are accompanied by mud migration. The F2 fault section is shown in Figure 9.

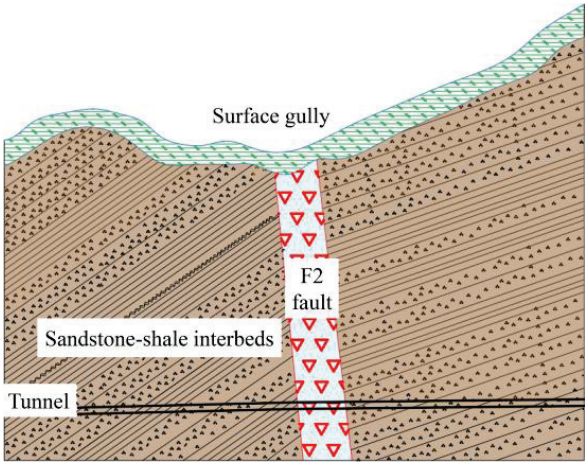

Figure 9. F2 fault profile.

The model test is based on the physical and mechanical parameters of the real fault rock samples of the project. The similarity ratio of the model test is selected as 1:60, and the target parameters of the fault similar material are calculated using the similarity criterion to determine the target parameters of the fault similar material. The evolution mechanism of the tunnel fault surge flooding is investigated. In order to verify the reasonableness of the developed material. The physical and mechanical parameters of the similar materials under the optimized ratios after the test are shown in Table 6, and by comparing the physical and mechanical parameters and hydrological parameters to those of the similar materials of the target expected faults, the results show that the materials can better simulate the key mechanical behaviors of the faulted rock body.

Table 6. Comparison of physical and mechanical parameters of materials.

Medium	Density ρ/(g/cm^3)	Compressive Strength σ_c/MPa	Elastic Modulus E/GPa	Permeability Coefficient K/(cm/s)	Cohesion c/kPa	Internal Friction Angle φ/(°)
Test proportioning materials	1.98	0.18	0.02	3.87×10^{-5}	2	38

The prototype dimensions of the test are length × width × height = 96 m × 60 m × 180 m. Based on the scale ratio, the model dimensions are length × width × height = 1.6 m × 1.0 m × 3 m. The test system consists of four parts: the model frame, the geostress loading system, the water pressure loading system, and the information-monitoring system. The experimental model system is shown in Figure 10.

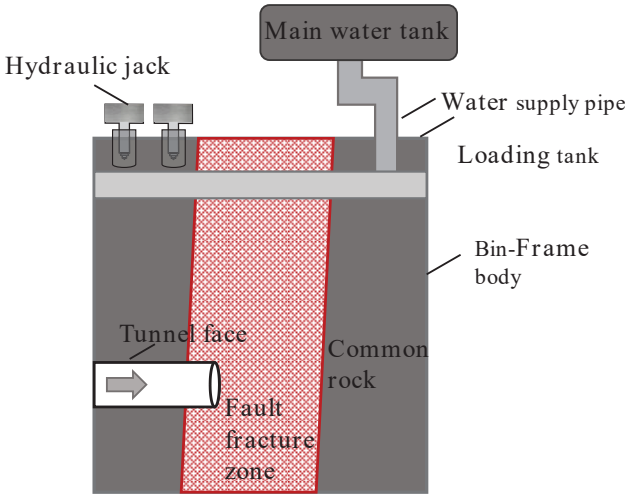

Figure 10. Model test system.

The materials were prepared according to the specific mix ratios for fault similar materials, with the installation of components and material filling carried out simultaneously. Three monitoring sections were set within the fault: Section I, Section II, and Section III. Sections I and II were located within the fault zone, while Section III was positioned at the junction of the fault and the surrounding rock. Key areas, such as the tunnel crown, arch shoulders, waist, and invert, were equipped with sensors at each monitoring section. The specific layout of the monitoring sections and key sensor positions is shown in Figure 11.

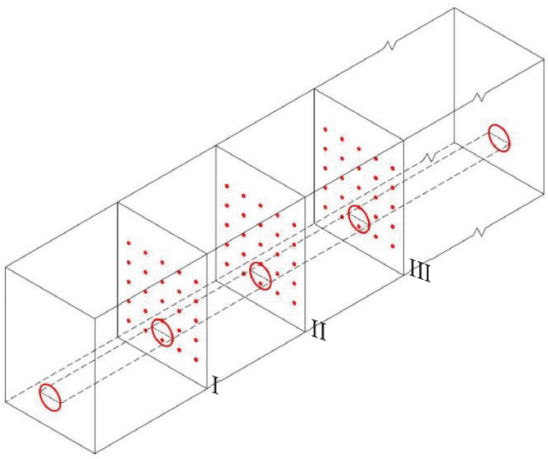

Figure 11. Layout of monitoring points.

4.2. Test Process and Results

Based on the determined material mix ratios, the individual raw material components were precisely weighed and mixed until uniform. The materials were then placed in layers using a partitioning method and compacted layer by layer, with compaction density being controlled to ensure uniformity. After completing the model's filling, water was injected for 7 days to achieve saturation, and then, the tunnel simulation excavation was conducted until a water inrush disaster occurred. The excavation was performed using a stepping method, with a 2 cm advance per cycle and an 8 cm step length. After each excavation cycle, real-time monitoring of various information, including surrounding rock stress, displacement, and seepage pressure, was conducted. Once the data stabilized, the next excavation cycle could begin.

4.2.1. Variation Law of Gushed Materials

After exposing the fault, outflow data were collected approximately every 15 s. From Figure 12, the following observations can be made:

(1) Early Monitoring Stage: As seepage pressure increases, the weakened geotechnical body is carried out by groundwater, causing the surrounding rock porosity to gradually increase. The outflow mass shows an upward trend. Approximately 10 min after the start of monitoring, the outflow stabilizes. This is believed to be related to the stabilization of seepage pressure. When water inrush occurs, the outflow reaches its peak, indicating that a higher hydraulic gradient results in a more significant water inrush effect.

(2) Pre-Water Inrush Stage: Before the water inrush disaster occurs, starting from the 145th data collection point in Figure 12, the outflow mass decreases significantly. At this point, the structural integrity of the surrounding rock is damaged, and the geotechnical body is compacted. As a result, the pore volume of the material decreases, and the migration of soil particles is obstructed, leading to a reduction in outflow.

(3) Water Inrush Stage: As groundwater continues to penetrate and soften the surrounding rock, accompanied by a decrease in seepage pressure, the tunnel face begins to fail. A large volume of groundwater and solid matter flows into the tunnel, causing the outflow to suddenly increase, resulting in a water inrush disaster. After the disaster occurs, the outflow rate rapidly decreases and stabilizes. At this point, the changes in outflow are closely related to the water-disintegration characteristics of the fractured fault-zone rock and the magnitude of the seepage pressure.

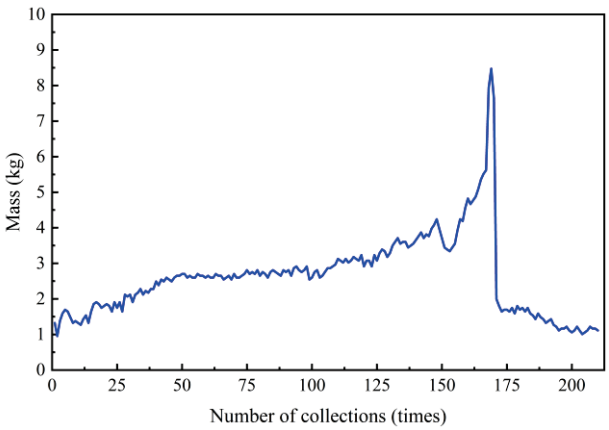

Figure 12. Outflow variation.

4.2.2. Displacement–Time Variation

To observe the impact of excavation disturbance on tunnel water inrush, a displacement meter was placed at Section III, where the fault intersects the normal surrounding rock. The position of this meter corresponds to monitoring point 5# in Sections I and II.

From Figure 13, it can be seen that prior to the occurrence of the disaster, all monitoring points show a slow increase in displacement. When the water inrush disaster occurs, there is a sudden surge in displacement at Sections I and II, while the displacement at the corresponding monitoring point in Section III remains relatively stable. Figure 13 indicates that, whether during normal surrounding rock excavation or after exposing the fault, the displacement amplitude of the fault-zone material is always greater than that of the normal surrounding rock. Moreover, the closer the monitoring point is to the fault-zone and tunnel excavation profile, the greater the displacement and settlement values. After the water inrush event concludes, the surrounding rock reaches a relatively stable state again.

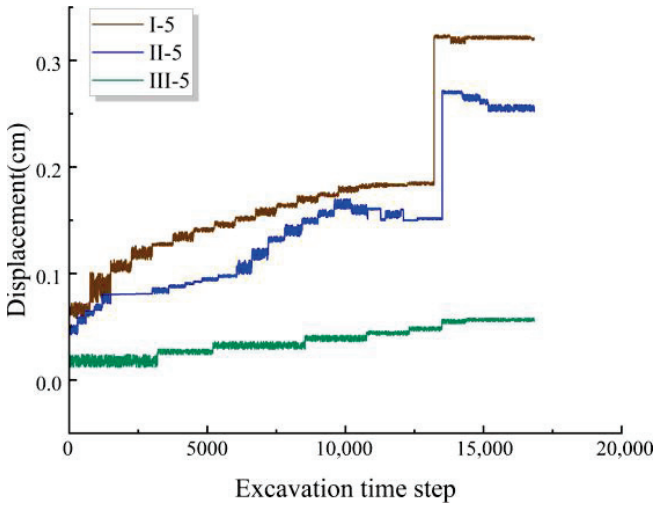

Figure 13. Horizontal displacement–time variation curve.

4.3. Comparative Analysis of the Engineering Data

The following section presents a comparative analysis of the water inrush process, displacement data, and other relevant results from the Zhongjiashan Tunnel with respect to those from the model experiment.

4.3.1. Water Inrush Process

When the tunnel excavation reached the F2 fault zone, the excavation disturbance altered the groundwater seepage field. The process of tunnel water inrush is shown in Figure 14: In the left hole, K91 + 338, water seepage occurred on the right side of the tunnel vault (Figure 14a), and loose collapse occurred with a small gush of water (Figure 14b). This water discharge point became the breakthrough, with fault soil particles continuously carried out by the water's flow (Figure 14c). Eventually, an irregular, circular water inrush hole with a diameter of approximately 1 m formed. Under high hydraulic head, a large volume of muddy water was ejected (Figure 14d), triggering a water inrush disaster. As the mud-filled rock mass and groundwater from the fault zone continued to flow out, the amount of muddy water gradually decreased to a natural outflow state. This process aligns well with the results from the model experiment.



Figure 14. Water inrush process.

4.3.2. Displacement Change

Figure 15 shows the displacement variation near the fault zone at the tunnel crown, both for the normal surrounding rock segment and the fault-zone rock after excavation through the F2 fault zone. It is evident that, at the same time, the displacement growth rate of the fault zone's surrounding rock is faster than that of the normal surrounding rock. During the water inrush disaster, the displacement in the fault zone experienced a sharp increase, whereas the displacement at the crown of the normal surrounding rock was relatively unaffected by the disaster, only showing a slight increase during the water inrush event.

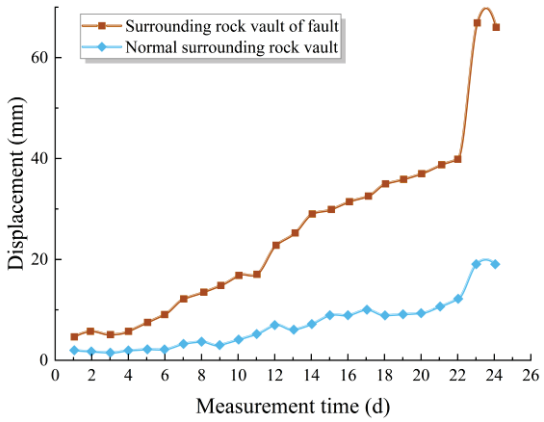

Figure 15. Actual displacement change curve of surrounding rock.

By comparing the model's experimental results with the actual engineering water inrush process and related data, it is clear that the fault similar materials developed in this study can effectively simulate the fault water inrush process. The trends observed in the monitoring data are consistent with the physical laws governing multi-physical field changes. The experimental phenomena align closely with the actual engineering disaster process, confirming that the material meets the requirements of our experiment.

5. Conclusions

(1) A suitable similar material for fault water inrush model experiments was developed by optimizing the mix ratios. The material was composed of sand as the coarse aggregate; talc powder as the fine aggregate; gypsum and clay as binders; and Vaseline as an

adjusting agent. This material effectively satisfies the simulation requirements for both the physical–mechanical properties and hydro-physical characteristics of faults.

(2) The uniaxial compressive strength and permeability coefficient of the similar material are primarily controlled by the content of gypsum and Vaseline. Increasing gypsum contents enhances strength, but excessive amounts reduce permeability. When Vaseline contents are less than 4%, strength is increased, but an excess of Vaseline disrupts the bonding structure. Cohesion is mainly influenced by the content of clay and Vaseline. When clay contents are below 6%, cohesion increases with the amount of clay, but it decreases when the content exceeds 6%. Vaseline significantly enhances cohesion when present in low concentrations.

(3) The similar material was applied in a three-dimensional model experiment simulating tunnel fault water inrush disasters. The experiment successfully reproduced the disaster evolution process of fault water inrush, and the monitoring data from the experiment showed good consistency with actual engineering disaster phenomena. This demonstrates that the similar material's physical–mechanical properties and hydro-physical characteristics are well-suited for simulating fault water inrush processes and provides a reliable foundation for studying the response mechanisms of various physical fields during the fault water inrush event.

(4) There are still limitations in the development of similar materials and the simulation of tunnel fault surge flooding. The optimization of the ratio of similar materials is based on a specific fault prototype, and its adaptability to different surrounding rock conditions or complex hydrogeological environments still needs to be further verified. In the future, we can combine multidisciplinary methods to improve the material's constitutive model and expand the conditions of multi-field coupling tests to reveal the disaster mechanism of fault water inrush in a more comprehensive way.

Author Contributions: Conceptualization, Z.L. and D.W.; data curation, D.W.; formal analysis, Z.L. and Q.Z.; funding acquisition, Z.L. and D.W.; investigation, K.W., L.Z., and Y.G.; methodology, Q.Z. and D.W.; project administration, K.W.; software, L.Z.; supervision, Y.G.; validation, Y.D.; writing—original draft, Z.L.; writing—review and editing, D.W. All authors have read and agreed to the published version of the manuscript.

Funding: This paper was completed under the support of the National Key R&D Program of China (2024YFB2606100) and the National Natural Science Foundation of China (No. 52171267).

Institutional Review Board Statement: Not applicable.

Informed Consent Statement: Not applicable.

Data Availability Statement: The original contributions presented in this study are included in the article. Further inquiries can be directed to the corresponding author.

Conflicts of Interest: Author Kai Wang was employed by the company Shandong High-Speed High-Tech Investment Co., Ltd. The remaining authors declare that the research was conducted in the absence of any commercial or financial relationships that could be construed as a potential conflict of interest.

References

1. Zhang, Q.; Jiang, Q.; Zhang, X.; Wang, D. Model test on development characteristics and displacement variation of water and mud inrush on tunnel in fault fracture zone. *Nat. Hazards* **2019**, *99*, 467–492. [CrossRef]
2. Shi, S.; Xie, X.; Bu, L.; Li, L.; Zhou, Z. Hazard-based evaluation model of water inrush disaster sources in karst tunnels and its engineering application. *Environ. Earth Sci.* **2018**, *77*, 141. [CrossRef]
3. Dai, C.; Long, Y.; Lv, Y.; Hou, W.; Sui, H. Water inrush mechanism and safety control in drilling and blasting construction of subsea tunnel. *J. Coast. Res.* **2019**, *94*, 218–222. [CrossRef]

4. Song, T.; Zeng, J.; Ma, J.; Ma, C.; Li, T.; Xia, T.; Aloisio, A. Water inrush risk assessment based on AHP and advance forecast approach, A case study in the Micangshan tunnel. *Adv. Civ. Eng.* **2021**, *2021*, 9750447. [CrossRef]
5. Wang, M.; Yang, W.; Zhou, Z.; Yang, J.; Yang, F.; Sheng, S. Experimental study on fractal characteristics of fault filling medium in the tunnel and relationship between fractal dimension and permeability coefficient. *Geomech. Geophys. Geo-Energy Geo-Resour.* **2022**, *8*, 6. [CrossRef]
6. Wang, X.; Zhang, L.; Zhang, Q.; Liu, R.; Huang, C. A stepwise calculation method for grouting penetration in rough rock fracture based on fracture segment division. *Tunn. Undergr. Space Technol.* **2025**, *166*, 106944. [CrossRef]
7. Xin, G.; Wang, B.; Zheng, H.; Zeng, L.; Yang, X. Study on Water Inrush Characteristics of Hard Rock Tunnel Crossing Heterogeneous Faults. *Appl. Sci.* **2024**, *14*, 2536. [CrossRef]
8. Li, X.; Xue, Y.; Zhang, Z. Progressive evolution model of fault water inrush caused by underground excavation based on multiphysical fields. *Geofluids* **2023**, *2023*, 8870126. [CrossRef]
9. Zhou, Z.; Li, L.; Shi, S.; Liu, C.; Gao, C.; Tu, W.; Wang, M. Study on tunnel water inrush mechanism and simulation of seepage failure process. *Rock Soil Mech.* **2020**, *41*, 3621–3631. [CrossRef]
10. Zhong, Z.-L.; Shen, Z.; Qiao, H.-Y.; Li, Y.-P.; Zhu, K.-X. Study on mechanism of water and mud inrush in deep-buried large-section tunnel crossing water-rich fault fracture zone. *Rock Mech. Rock Eng.* **2025**, *58*, 1147–1164. [CrossRef]
11. Li, Y.; Weng, X.; Wang, R.; Zhang, L.; Zhang, L. Experimental study on mechanism of water and mud inrush in tunnel crossing fault fracture zone. *J. Highw. Transp. Res. Dev.* **2020**, *37*, 89–99.
12. Zhang, Q.; Chen, W.; Yuan, J.; Liu, Q.; Rong, C. Experimental study on evolution characteristics of water and mud inrush in fault fractured zones. *Rock Soil Mech.* **2020**, *41*, 1911–1922. [CrossRef]
13. Wang, Y.; Chen, F.; Sui, W.; Meng, F.; Geng, F. Large-scale model test for studying the water inrush during tunnel excavation in fault. *Bull. Eng. Geol. Environ.* **2022**, *81*, 238. [CrossRef]
14. Dai, S.H.; Wang, H.R.; Han, R.J.; Wang, Z.W. Properties of similar materials used in fluid-solid coupling model test. *Rock Soil Mech.* **2020**, *S2*, 1–8.
15. Ko, T.Y.; Lee, S.S. Characteristics of crack growth in rock-like materials under monotonic and cyclic loading conditions. *Appl. Sci.* **2020**, *10*, 719. [CrossRef]
16. Zan, W.; Lai, J.; Zhang, W.; Yang, Q.; Qin, Y.; Su, X. Experimental and applied research on similar materials to granular mixtures for solid-liquid coupling model test of an underwater tunnel. *Constr. Build. Mater.* **2024**, *416*, 135170. [CrossRef]
17. Shemenda, A.I. Horizontal lithosphere compression and subduction: Constraints provided by physical modeling. *J. Geophys. Res. Solid Earth* **1992**, *97*, 11097–11116. [CrossRef]
18. Zhang, Z.; Zhang, Q.; Xiang, W.; Yin, X.; Xue, T.; Lin, H.; Lei, C.; Xin, G. Development and application of new-style hydro-mechanical coupling similar materials in complex environment. *J. Cent. South Univ. (Sci. Technol.)* **2021**, *52*, 4168–4180.
19. Xu, Z.; Luo, Y.; Chen, J.; Su, Z.; Zhu, T.; Yuan, J. Mechanical properties and reasonable proportioning of similar materials in physical model test of tunnel lining cracking. *Constr. Build. Mater.* **2021**, *300*, 123960. [CrossRef]
20. Liu, S.; Liu, W. Experimental development process of a new fluid–solid coupling similar-material based on the orthogonal test. *Processes* **2018**, *6*, 211. [CrossRef]
21. Guo, Y.; Yang, Y.; Kong, Z.; He, J.; Wu, H. Development of Similar Materials for Liquid-Solid Coupling and Its Application in Water Outburst and Mud Outburst Model Test of Deep Tunnel. *Geofluids* **2022**, *2022*, 8784398. [CrossRef]
22. Wu, W.; Guo, J.; Liu, X.; Zhu, Z.; Wang, E. Experimental study on similar materials for fluid-solid coupling for model test of water inrush in karst tunnel. *Geotech. Geol. Eng.* **2023**, *41*, 4119–4135. [CrossRef]
23. Ning, Z.; Li, J.; Wang, H.; Li, Z.; Zhuang, D.; Xu, W.; Zambrano-Narvaez, G.; Zhan, L.; Chen, Y. Application of physical model test in underground engineering: A review of methods and technologies. *Transp. Geotech.* **2025**, *52*, 101594. [CrossRef]
24. Gibson, R.E. The analytical method in soil mechanics. *Geotechnique* **1974**, *24*, 115–140. [CrossRef]
25. Ren, X.; Xu, G.; Chen, Z.; Ran, S.; Zhang, J. Development of similar materials for fluid-solid coupling model testing and application in damage constitutive models. *Sci. Rep.* **2024**, *14*, 14786. [CrossRef]

Disclaimer/Publisher's Note: The statements, opinions and data contained in all publications are solely those of the individual author(s) and contributor(s) and not of MDPI and/or the editor(s). MDPI and/or the editor(s) disclaim responsibility for any injury to people or property resulting from any ideas, methods, instructions or products referred to in the content.

materials

MDPI

Article

Experimental Study on the Filtration of Seawater Bentonite Slurry Under the Cutting Influence of Shield Cutterhead

Deming Wang [1], Zhipeng Li [1,*], Qingsong Zhang [2], Lianzhen Zhang [3], Yang Gao [4], Hongzhen Dong [1], Yirui Li [1], Yueyue Wu [1] and Yongqi Dai [1]

[1] School of Transportation and Civil Engineering, Shandong Jiaotong University, Jinan 250357, China; wangdeming@sdjtu.edu.cn (D.W.); donghongzhen630@outlook.com (H.D.); lyr23107019@stu.sdjtu.edu.cn (Y.L.); 204157@sdjtu.edu.cn (Y.W.); daiyongqisdjtxy@163.com (Y.D.)
[2] School of Civil Engineering, Shandong University, Jinan 250100, China; zhangqingsong@sdu.edu.cn
[3] College of Pipeline and Civil Engineering, China University of Petroleum, Qingdao 266580, China; zhanglianzhen@upc.edu.cn
[4] School of Safety Engineering and Emergency Management, Shijiazhuang Tiedao University, Shijiazhuang 050043, China; gaoyang_sjz@163.com
* Correspondence: lizhipeng@sdjtu.edu.cn

Abstract: Slurry shields maintain excavation face stability by forming a sealing filter cake through pressurized slurry filtration, though cutterhead rotation inevitably compromises this integrity. This study investigates seawater-based slurry filtration behavior under cutterhead disturbance using model testing, utilizing the effective support force conversion rate to quantify the filter cake formation efficiency. Quantitative analysis evaluated key slurry constituents—bentonite, carboxymethyl cellulose (CMC), and fine sand (content/particle size)—and operational parameters including cutterhead rotation speed, advance rate, and slurry pressure. Results demonstrate enhanced conversion rate and stability with increased bentonite, CMC, and fine sand content; reduced fine sand particle size; elevated slurry pressure; and decreased cutterhead speed/advance rate. Nonlinear relationships exist between bentonite content and fine sand particle size, on the one hand, and the mean conversion rate and its fluctuation range, on the other. Stratum permeability and slurry pressure exhibit nonlinear effects on fluctuation range but linear relationships with mean value, indicating marginal impacts on support force magnitude and operational stability. Sensitivity analysis confirms bentonite as the dominant influencing factor, followed by cutterhead speed and CMC.

Keywords: slurry shield tunneling; bentonite slurry materials; cutterhead cutting; effective support force conversion rate; influencing factors

1. Introduction

Slurry shields rely on a pressurized slurry to form a filter cake at the excavation face, balancing water and soil pressures. This technique allows tunneling through strata with poor self-stability, high groundwater pressure, and high permeability. It is now widely used in constructing tunnels across rivers and seas. Water-rich rock fracture is a typical poor geology condition often encountered in tunnel and underground construction engineering [1]. During subsea tunnel construction, the bentonite slurry used in slurry shield tunneling can lose rheological properties due to seawater contamination, which negatively affects the stability of the excavation face [2], especially when the shield crosses subsea fault zones [3]. Therefore, studying the filtration process of slurry in fractured and highly permeable strata, along with the mechanism of filter cake formation during seawater

intrusion, is crucial to maintaining the stability of the excavation face in difficult geological conditions, such as subsea faults and fractured zones.

Most studies on the filtration mechanism of slurry at the excavation face are conducted using one-dimensional slurry filtration devices. These devices are usually cylindrical, with stratum materials placed inside. Under air pressure, the slurry forms a filter cake on the surface of the stratum material, and the filtrate is discharged from the other end of the device. Many researchers have used such devices to conduct extensive studies on the filtration behavior of slurry under static cutterhead conditions, examining factors such as slurry materials and stratum conditions. These studies have shown that slurry density, viscosity, clay content, and particle size in the slurry significantly influence the quality of the filter cake [4–8].

During slurry balance shield tunneling, the filter cake at the excavation face undergoes a repeated cycle of "destruction–formation–destruction". Experiments based on one-dimensional slurry filtration devices cannot accurately reflect the working conditions of slurry during tunneling. Some researchers have modified these devices by adding cutting tools and power systems to study how the filter cake forms under dynamic conditions. Results showed that the slurry filtration rate during cutterhead rotation was much higher than during static conditions. The slurry filtration loss was found to be directly proportional to the cutterhead rotation speed and inversely proportional to the slurry pressure, while the excess pore water pressure in the soil was inversely proportional to the distance from the excavation face [9–11]. Compared to slurry filtration tests, shield tunneling model tests offer a more complete simulation of the excavation process. Some researchers have used these models to study how tunneling affects surface settlement, soil stress, and failure modes at the excavation face [12–18].

Some studies have developed theoretical models for filter cake formation that take into account the cutting action of the cutterhead. These models examine the effects of cutterhead rotation speed and slurry pressure on the thickness, elastic modulus, formation time, and effective stress of the filter cake. The models indicate that cutterhead excavation periodically disrupts the pressure transmission mechanism, and different combinations of cutterhead rotation speed and penetration depth can lead to variations in slurry pressure transmission [19–24]. These studies are of great significance for setting tunneling parameters, such as cutterhead rotation speed, slurry pressure, and advance speed, as well as for maintaining the stability of the excavation face during slurry shield tunneling.

Bai Yang [9] primarily investigated the mechanisms of slurry infiltration and filter cake formation at the excavation face of slurry shields, as well as the stability of the excavation face under "cutter–soil" interaction. This study revealed how the cutting effects of shield cutterheads and tools influence filter cake characteristics, formation mechanisms, and excavation face stability. Mao Jiahua [25] employed theoretical analysis, laboratory tests, and numerical simulations to study the patterns and mechanisms of slurry infiltration and filter cake formation in sandy strata, exploring the slurry support mechanism at the excavation face under cutterhead and tool action. However, these studies primarily focused on the impact of factors like cutterhead opening ratio, cutter arrangement, and cutterhead rotational speed on filter cake formation and excavation face stability, with limited attention to the influence of slurry properties. Furthermore, no existing research has quantitatively analyzed the effects of bentonite, additives, slurry pressure, cutterhead rotational speed, and other factors on excavation face support effectiveness under cutter cutting conditions. In contrast, studies represented by Su Qin et al. [26] investigated slurry infiltration in sandy and similar strata. These studies typically utilized slurries prepared with fresh water, neglecting the effects of ions in groundwater (such as flocculation and sedimentation) on

bentonite under subsea conditions, and did not consider the influence of cutter cutting on filter cake formation.

Based on a slurry shield tunneling model testing device, this study investigates the filtration behavior of seawater-based slurry at the excavation face under the cutting action of the cutterhead. By analyzing the changes in pore water pressure in the stratum during slurry filtration, the effects of slurry materials—such as bentonite, sodium carboxymethyl cellulose, and fine sand—along with cutterhead rotation speed, advance speed, slurry pressure, and stratum conditions on slurry filtration are studied. The role of these factors in maintaining the stability of the excavation face is also analyzed.

2. Experimental Apparatus and Procedures

To investigate the filtration characteristics of seawater-based slurry under cutterhead disturbance during cutter excavation, a slurry permeation test apparatus was developed. This apparatus enables permeation tests under both cutter excavation and static cutter conditions, with preliminary experiments under non-excavating conditions having been previously conducted [27]. The experimental apparatus (Figure 1) constitutes a modified one-dimensional slurry filtration and cake formation system, comprising a slurry filtration column, cutting mechanism, data acquisition system, and pressure supply unit. This configuration simulates excavation face slurry filtration processes under cutterhead cutting action. During testing, cutterhead rotation speed and advance rate are dynamically controlled through torque and thrust adjustment, while real-time monitoring captures slurry pressure, stratum pore water pressure, and drive shaft torque.

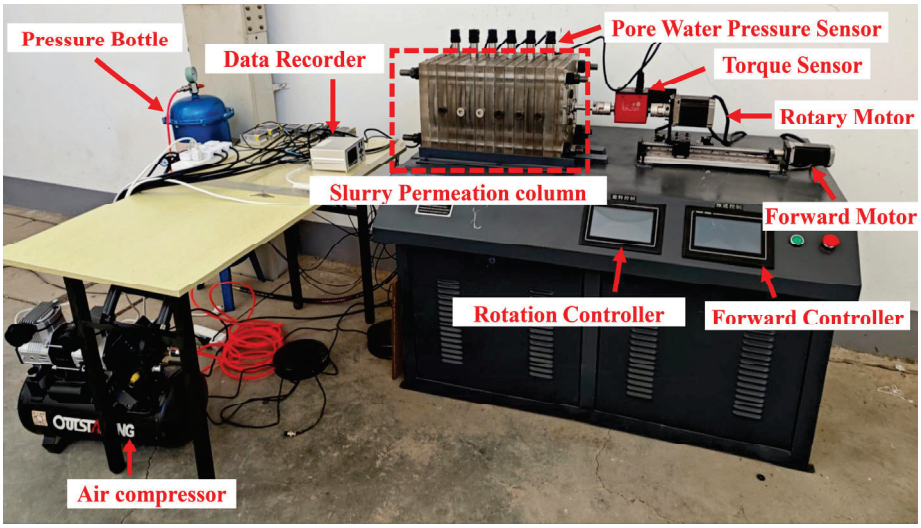

Figure 1. Slurry shield tunneling model testing device [27].

The filtration column, which is filled with formation materials, is the main component for conducting the filtration test. It is assembled using PMMA plates with different diameters, creating internal cavities, as shown in Figure 2. The alternating installation of two types of PMMA plates forms a zigzag-shaped internal space within the filtration column. This design prevents the compression of the stratum under pressure and avoids slurry filtration through gaps between the stratum and the container wall [28]. Type A PMMA plates have interfaces on the side walls for sensor connections, while unused interfaces are sealed with bolts.

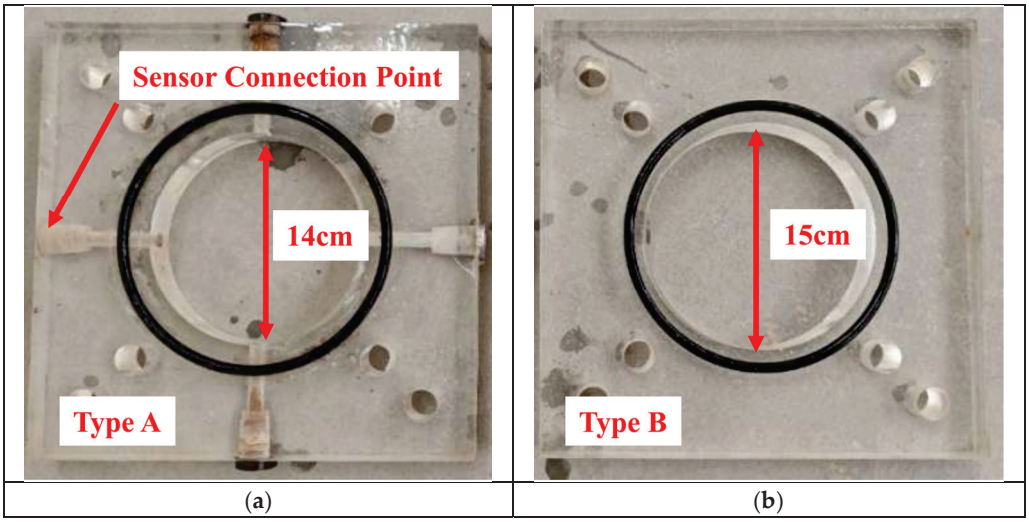

Figure 2. Two types of PMMA plates [27]: (**a**) type A acrylic board with sensor interface (**b**) type B acrylic board.

The cutterhead is connected to the top cover of the filtration column. It is welded to the drive shaft, which is connected to the top cover through a rotating seal. This sealing mechanism allows the drive shaft to rotate and extend while maintaining the seal of the top cover. The other side of the drive shaft is connected to the power system via coupling.

Generally, scraper cutters are employed to excavate stiff, compacted soils, while disk cutters are used for rock fragmentation [29]. In sandy strata, slurry shield tunneling predominantly utilizes scraper cutters; therefore, scraper cutters were selected for the cutting tools in this experimental setup [10]. The cutterhead features a symmetrical four-arm design, with three cutters mounted on each arm and a central scraper blade installed at its center. The cutterhead configuration and installation methodology are illustrated in Figure 3.

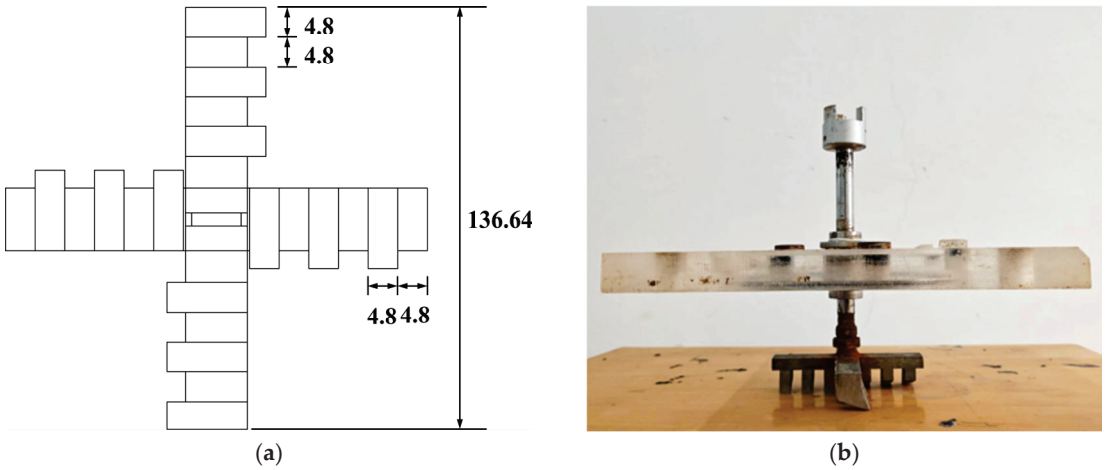

Figure 3. Schematic diagram of the cutterhead: (**a**) Cutterhead dimensions (mm) and (**b**) cutterhead and top cover plate.

The cutting system consists of a thrust motor, a transmission mechanism, and a rotary motor. The transmission mechanism converts the rotational motion of the thrust motor into horizontal movement, allowing the rotary motor to drive the cutterhead to cut the excavation face. The data acquisition system is used to collect data such as pore water pressure, torque, and the weight of slurry filtrate during the experiment. The pressure supply system consists of an air compressor, a pressure regulator, and a pressure tank, which provide power for the slurry filtration process.

A schematic diagram of the experimental setup is shown in Figure 4. The device uses compressed air to drive the slurry filtration process. The slurry is placed in a pressurized steel tank and is pushed by compressed air at a fixed pressure through a pipeline into the filtration column. The slurry is filtered by the sand layer material inside the filtration column, and the filtrate is collected in a container. During slurry filtration, the cutterhead cuts the surface of the sand layer, driven by two motors. Pore water pressure sensors mounted on the side wall of the filtration column record the changes in slurry pressure and pore water pressure in the stratum throughout the experiment.

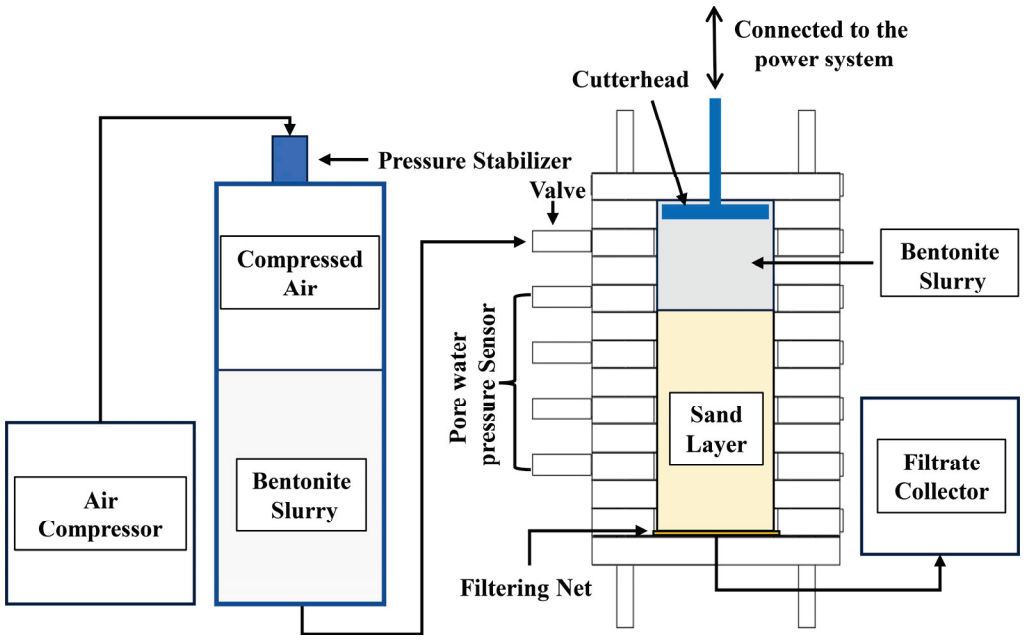

Figure 4. Schematic diagram of the experimental setup [27].

Due to the cutting action of shield cutter tools, a complete filter cake cannot form at the excavation face. This allows continuous slurry infiltration into the surrounding stratum, which leads to an increase in excess pore water pressure within the formation. The generation of pore water pressure reduces the effective stress acting on the soil mass [30–32].

To better illustrate the variation in effective support pressure acting on the excavation face during slurry infiltration, ω is defined as the Effective Support Pressure Conversion Rate (Equation (1)). This parameter characterizes the ability of the filter cake to transform slurry pressure into effective stress [33]. A higher Effective Support Pressure Conversion Rate corresponds to greater effective stress acting on the filter cake particles and consequently enhances excavation face stability. Therefore, analysis of the variation in this parameter enables the assessment of filter cake formation status at the excavation face during cutterhead cutting [19,34].

$$\omega = \frac{P_s - P_h - P_e}{P_s - P_e} \tag{1}$$

In this equation, P_S is slurry pressure (MPa), P_h is hydrostatic pressure at the measurement point (MPa), and P_e is excess pore water pressure at the measurement point (MPa).

When conducting slurry filtration tests with cutterhead cutting, a filtration test without cutterhead cutting is first performed to allow a stable filter cake to form at the excavation face. This step is taken to prevent the surface of the sand layer inside the filtration column from collapsing when the column is mounted horizontally on the test bench. Afterward, the valve is closed, the filtration column is mounted horizontally on the test bench, and the

cutterhead drive shaft is connected to the power system. The cutterhead rotation speed and advance speed are set by the controller, and the test begins.

3. Experimental Materials and Test Design

3.1. Slurry Preparation

The materials used to prepare the slurry are shown in Figure 5, including sodium-based bentonite, CMC (Sodium Carboxymethyl Cellulose), fine sand (particle size less than 1 mm), freshwater, and artificial seawater.



(**a**) (**b**) (**c**)

Figure 5. Slurry materials: (**a**) CMC; (**b**) bentonite; and (**c**) fine sand.

Artificial seawater was prepared according to the ASTM D1141-98 [35] standard, with trace components such as potassium bromide, strontium chloride, and sodium fluoride omitted due to their very low concentrations. The proportions of the components in the artificial seawater are shown in Table 1.

Table 1. Composition of seawater for testing.

Components	NaCl	$MgCl_2$	Na_2SO_4	$CaCl_2$	KCl	$NaHCO_3$
Content (g/L)	24.53	5.20	4.09	1.16	0.69	0.20
Proportion (%)	68.4	14.5	11.4	3.2	2.0	0.6

When preparing the slurry, CMC is mixed evenly into the bentonite. The mixture is then gradually added to the mixing water and stirred in a mixer for 20 min. Fine sand is added and stirred for an additional 10 min. After mixing, the slurry is placed in a sealed container and allowed to stand for 24 h. Before conducting the slurry filtration test, the slurry is stirred again for 30 min.

3.2. Sand Layer Material

Three types of stratum materials were used in the experiment, consisting of quartz sand with particle sizes of 1–2 mm, 1–4 mm, and 4–8 mm (Figure 6). These materials can effectively simulate the characteristics of fault fracture zones and weathered troughs, which are highly fractured, have poor integrity, and exhibit strong permeability [35].



(**a**) (**b**) (**c**)

Figure 6. Sand layer materials: (**a**) 1–2 mm quartz sand; (**b**) 2–4 mm quartz sand; and (**c**) 4–8 mm quartz sand.

The permeability coefficients of the three materials, tested using the constant head method, are shown in Table 2.

Table 2. Strata material parameters.

Stratum Particle Size (mm)	Permeability Coefficient (cm/s)
1~2	2.49×10^{-2}
2~4	4.19×10^{-2}
4~8	9.51×10^{-2}

3.3. Test Design

To simulate filter cake formation under cutterhead excavation conditions during subsea shield tunneling, a series of slurries was prepared by adjusting the content of bentonite, carboxymethyl cellulose (CMC), and fine sand, along with the particle size distribution of the fine sand. The slurry formulations were designed based on construction experience in highly permeable strata, including those encountered in the Foshan–Dongguan Intercity Railway's Shiziyang Tunnel [36] and the Suai Passage project in Shantou traversing medium-coarse sand layers and highly weathered conglomeratic sandstone [37]. Under seawater salinity exposure, bentonite in the slurry undergoes flocculation and sedimentation, causing significant deterioration of key properties such as colloidal stability and viscosity. This performance degradation correlates directly with the proportion of seawater in the mixing water. When seawater constitutes 0–30% of the total mixing water, slurry properties deteriorate rapidly with increasing seawater content. When seawater content exceeds 30%, significant segregation is observed in sodium bentonite slurry, with further seawater increases exerting minimal additional impact on slurry performance [35–39]. To investigate seawater's effect on slurry permeability, all test slurries were prepared with mixing water containing 30% artificial seawater. Concurrently, to examine bentonite's role in slurry stability, additional formulations were tested, with bentonite-to-water mass ratios of 0.3, 0.35, 0.4, 0.45, and 0.6.

The experiments were conducted in strata with a particle size of 1–2 mm, a slurry pressure of 0.3 MPa, an advance speed of 10 mm/min, and a cutterhead rotation speed of 4 r/min.

Using slurry formula No. 4 from Table 3, 11 sets of experiments were conducted under different slurry pressures, cutterhead rotation speeds, advance speeds, and stratum

conditions. The test arrangement is shown in Table 4. The slurry pressure, cutterhead rotation speed, and advance rate employed in the tests were determined based on operational parameters from shield tunneling at the Jintang Subsea Tunnel [40,41] and experimental configurations established in shield excavation model tests conducted by Zhang Henghui [40].

Table 3. Slurry material experimental arrangement.

Test ID	Freshwater (g)	Seawater (g)	Bentonite (g)	Fine Sand (g)	CMC (g)	Fine Sand 0–0.5 mm (g)	Fine Sand 0.5–1 mm (g)
1	700	300	300	250	10	0	0
2	700	300	350	250	10	0	0
3	700	300	400	250	10	0	0
4	700	300	450	250	10	0	0
5	700	300	600	250	10	0	0
6	700	300	450	250	6	0	0
7	700	300	450	250	7	0	0
8	700	300	450	200	10	0	0
9	700	300	450	100	10	0	0
10	700	300	450	0	10	250	0
11	700	300	450	0	10	150	100
12	700	300	450	0	10	100	150
13	700	300	450	0	10	0	250

Table 4. Shield tunneling parameter experimental arrangement.

Test ID	Strata Particle Size (mm)	Slurry Pressure (MPa)	Cutterhead Rotation Speed (r/min)	Advance Speed (mm/min)
1	1–2	0.3	2	10
2	1–2	0.3	3	10
3	1–2	0.3	4	10
4	1–2	0.3	4	10
5	1–2	0.3	4	30
6	1–2	0.1	4	10
7	1–2	0.2	4	10
8	1–2	0.3	4	10
9	1–2	0.3	4	10
10	2–4	0.3	4	10
11	4–8	0.3	4	10

4. Test Results

The pore water pressure data collected during the slurry filtration process under cutterhead cutting were organized, and the effective support force conversion rate was calculated using Equation (1). The relationship between experimental time, stratum pore water pressure, and effective support force conversion rate was obtained under various conditions. Sections 4.1–4.8 will discuss the effects of each influencing factor on stratum pore water pressure and effective support force conversion rate.

4.1. Bentonite Content

Five sets of slurries were prepared with varying amounts of bentonite for testing. The corresponding results appear in Figure 7. The results indicate significant differences in the pore water pressure curves and effective support force conversion rate curves when the bentonite content is greater than or less than 400 g. The amount of 400 g of bentonite serves as a boundary, dividing the curves into two categories. When the bentonite content exceeds 400 g, the effective support force conversion rate shows minimal fluctuations over

time. Conversely, when the bentonite content is less than 400 g, the effective support force conversion rate experiences substantial fluctuations immediately after the test begins, with the level of fluctuation gradually decreasing and stabilizing as the test progresses. This phenomenon was also observed in the study by Bai Yang [42].

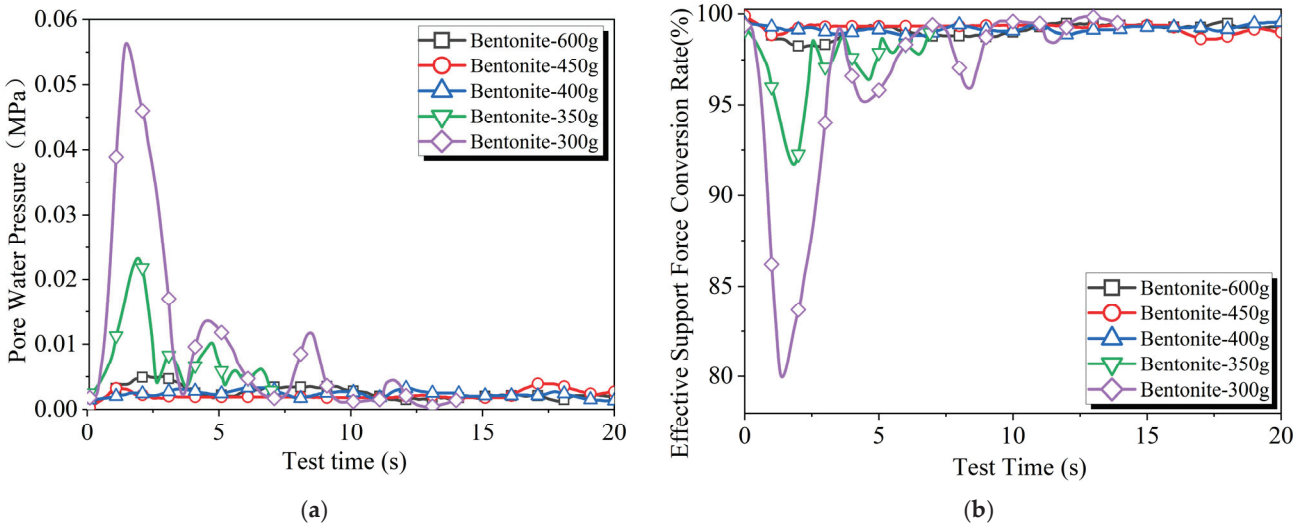

Figure 7. Experimental results of slurry infiltration with different amounts of bentonite: (**a**) pore water pressure and (**b**) effective support force conversion rate.

The reason for the two categories of effective support force conversion rate curves when varying the bentonite content is that a permeable zone forms behind the excavation face. Following the start of the experiment, under the cutting action of the tools, solid particles from the slurry accumulate within the stratum as they permeate through the excavation face, altering the stratum's permeability. With a lower bentonite content, the range of the permeable zone formed is larger. Due to the slow advance speed of the cutterhead, the cutting action cannot rapidly disrupt the stratum that has been blocked by bentonite particles, leading to a slower rate of slurry permeation into the stratum. However, when the bentonite content is greater than 400 g, after the filter cake is damaged by the cutterhead, the slurry can quickly form a new filter cake at the excavation face, with particles in the slurry accumulating close to the excavation face, resulting in minimal changes to the stratum's permeability.

4.2. CMC Content

As shown in Figure 8, the increase in CMC content leads to a decrease in pore water pressure and an increase in the effective support force conversion rate, while also reducing the fluctuations of both parameters. When CMC is increased from 6 g to 7 g, the fluctuations in the pore water pressure and effective support force conversion rate curves decrease. Furthermore, when the CMC content reaches 10 g, the effective support force conversion rate significantly improves, indicating that CMC has a greater impact on the stability of the effective support force conversion rate.

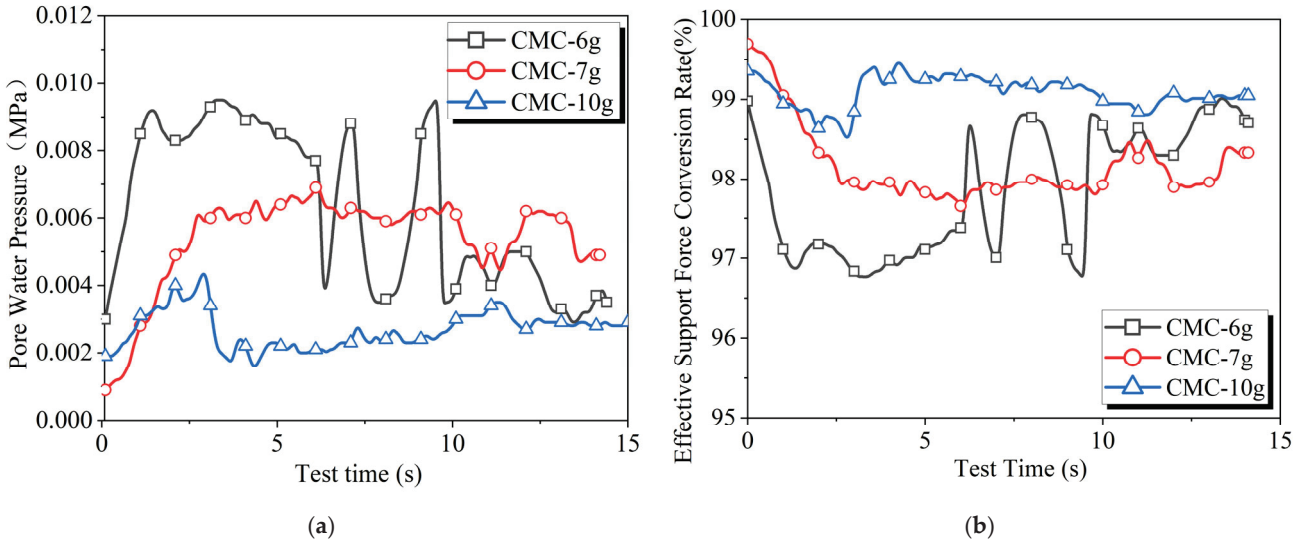

Figure 8. Experimental results of slurry infiltration with different amounts of CMC: (**a**) pore water pressure and (**b**) effective support force conversion rate.

4.3. Fine Sand Content

The results of the slurry filtration tests under different fine sand content conditions are shown in Figure 9. As the fine sand content increases from 100 g to 200 g, the effective support force conversion rate curve shifts upward, but the level of fluctuations does not significantly decrease. When the fine sand content is further increased to 250 g, the effective support force conversion rate curve continues to rise, and the fluctuations in the curve significantly decrease.

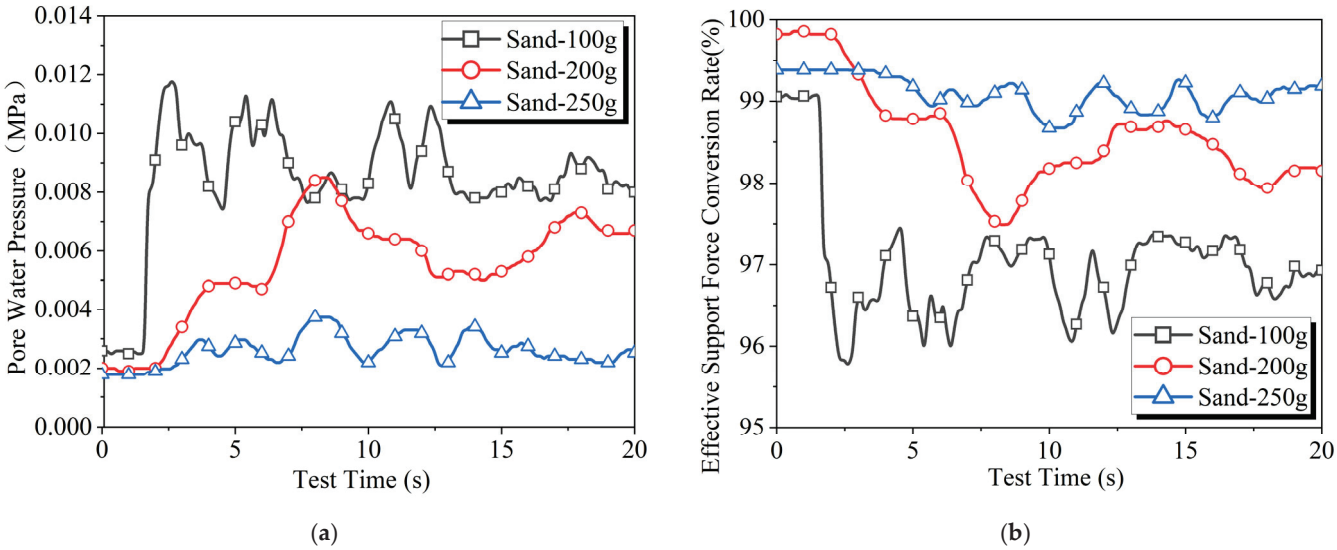

Figure 9. Experimental results of slurry infiltration with different amounts of fine sand: (**a**) pore water pressure and (**b**) effective support force conversion rate.

Comparing the test results of slurries with different fine sand contents and varying CMC contents reveals that the two components have different effects on the average level and fluctuation degree of the effective support force conversion rate during slurry filtration. CMC and fine sand represent different aspects of slurry performance, with CMC affecting the rheological properties of the slurry and fine sand influencing particle gradation. This indicates that the rheological properties of the slurry have a significant impact on the

stability of the support force at the excavation face, while the particle gradation of the slurry has a greater effect on the magnitude of the support force.

4.4. Fine Sand Particle Size

The results of the slurry filtration tests under different fine sand particle size conditions are shown in Figure 10. When the fine sand consists entirely of particles with a size of 0.5–1 mm, the effective support force conversion rate fluctuates significantly. However, this phenomenon is markedly improved by adding small particles of size 0–0.5 mm to the fine sand. As the proportion of smaller particles continues to increase, the effective support force conversion rate increases while the degree of fluctuation decreases. This differs from the results obtained in non-cutting conditions.

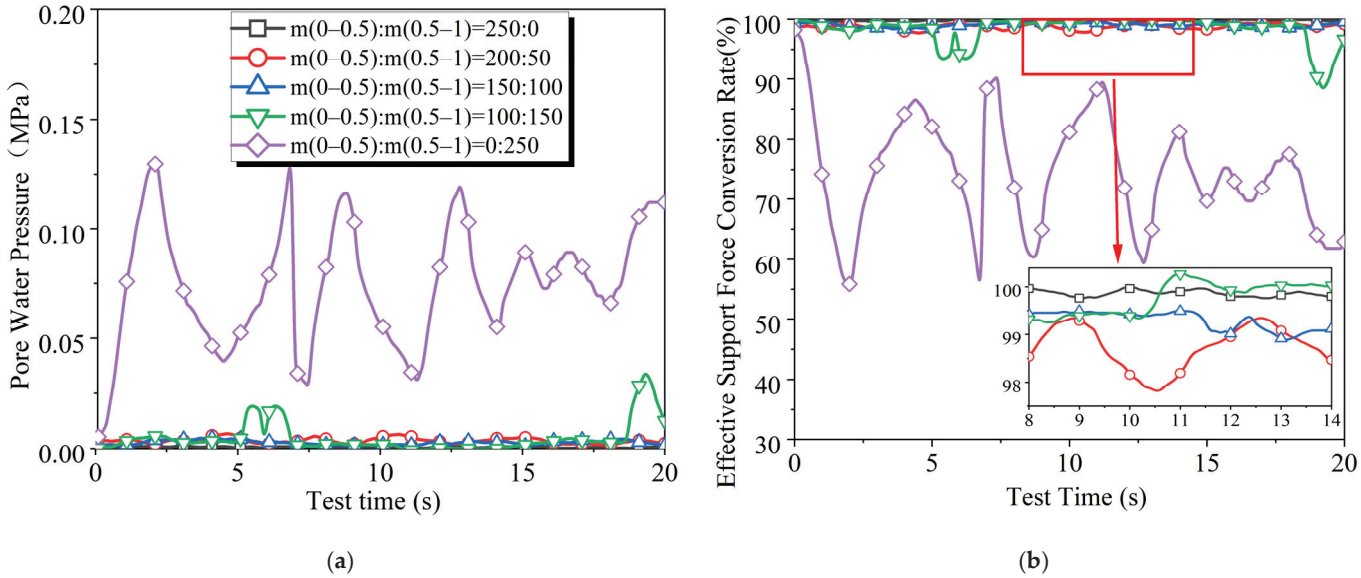

Figure 10. Experimental results of slurry infiltration with different amounts of fine sand size: (**a**) pore water pressure and (**b**) effective support force conversion rate.

The results of non-cutting slurry filtration tests conducted under the same conditions indicate that the optimal ratio for minimizing the pore water pressure generated during the formation of the filter cake is m(0–0.5):(0.5–1) = 2:3 [27]. The reason for this may be that the cutterhead's destruction of the filter cake allows more fine particles to remain within the stratum behind the excavation face, leading to improved sealing of the stratum's pores by the finer slurry.

4.5. Cutterhead Rotation Speed

Figure 11 shows the test results obtained under varying cutterhead rotation speeds. The increase in cutterhead rotation speed accelerates the destruction of the filter cake, allowing more slurry to permeate through the excavation face. This leads to an increase in stratum pore water pressure and a decrease in the effective support force conversion rate. A significant change in stratum pore water pressure and effective support force conversion rate is observed when the cutterhead rotation speed increases from 3 r/min to 4 r/min. This notable change point has also been observed in the studies by Bai Yang [9] and Mao Jiahua [25], although at different positions, specifically 23 r/min and 1–2 r/min, respectively. The position of this change point may depend on factors such as slurry performance, stratum permeability, cutterhead characteristics, and slurry pressure.

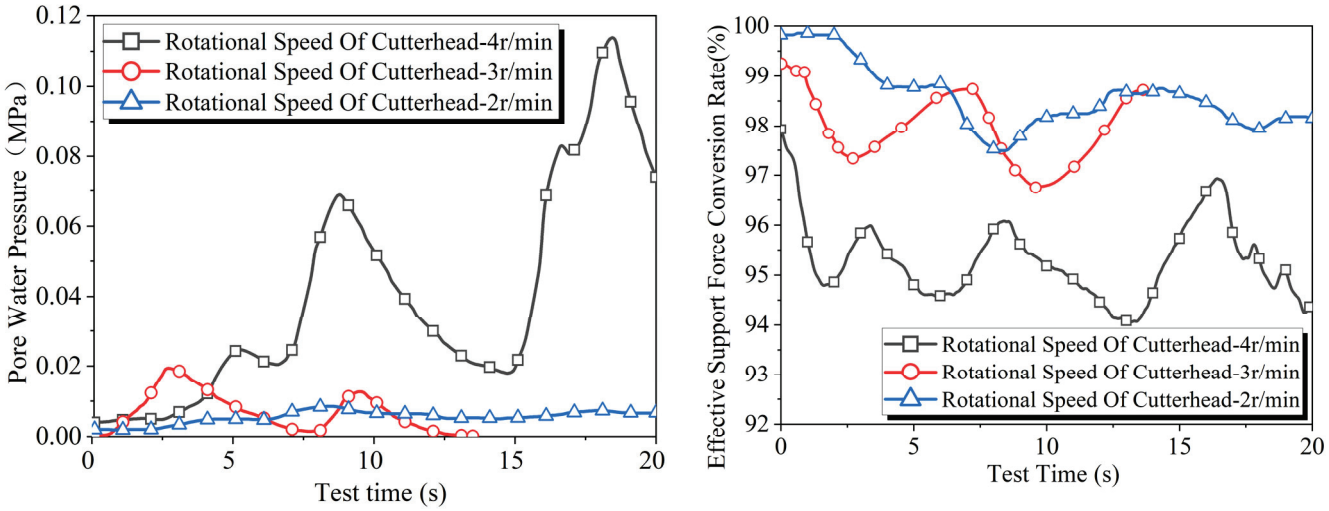

Figure 11. Results of slurry filtration experiments at different cutterhead rotation speeds: (**a**) pore water pressure and (**b**) effective support force conversion rate.

4.6. Advanced Speed

Test results at different advance speed are shown in Figure 12. The increase in advance speed significantly enhances the fluctuations in the effective support force conversion rate curve, while having minimal impact on the average value of the curve. This is because the increased advance speed of the shield allows the cutter to cut deeper, which exacerbates the damage to the permeable zone behind the excavation face. This weakens the slurry particles' ability to block the stratum, necessitating more slurry to permeate behind the excavation face to rebuild the permeable zone, thereby increasing the fluctuations in the effective support force conversion rate. Higher slurry pressure helps form a denser filter cake and accelerates the filter cake formation process [26,27]. However, it also enlarges the range of pore water pressure effects caused by slurry infiltration into the stratum [43], which increases the disturbance experienced by the stratum.

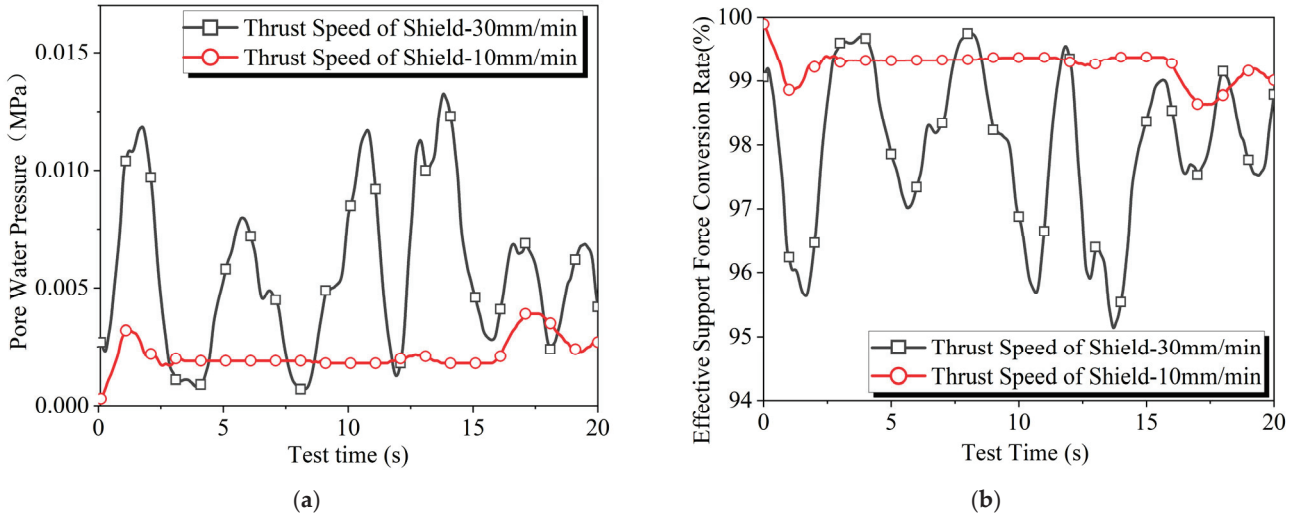

Figure 12. Results of slurry filtration experiments at different advance speed: (**a**) pore water pressure and (**b**) effective support force conversion rate.

4.7. Slurry Pressure

In Figure 13a, the pore water pressure curves during the slurry filtration process under different pressures intersect with each other. In contrast, in Figure 13b, the effective support force conversion rate curve at a pressure of 0.1 MPa does not intersect with the other curves. This indicates that increasing the slurry pressure does not significantly raise the stratum pore water pressure; rather, it increases the ratio of effective stress exerted on the filter cake to the slurry pressure. This suggests that the impact of slurry pressure on the actual support force experienced by the excavation face is twofold: increasing the slurry pressure can raise both the upper limit of effective support force and its conversion ratio. It also indicates that, compared to pore water pressure, the effective support force conversion rate is a clearer indicator of the actual supporting effect of the slurry pressure on the excavation face.

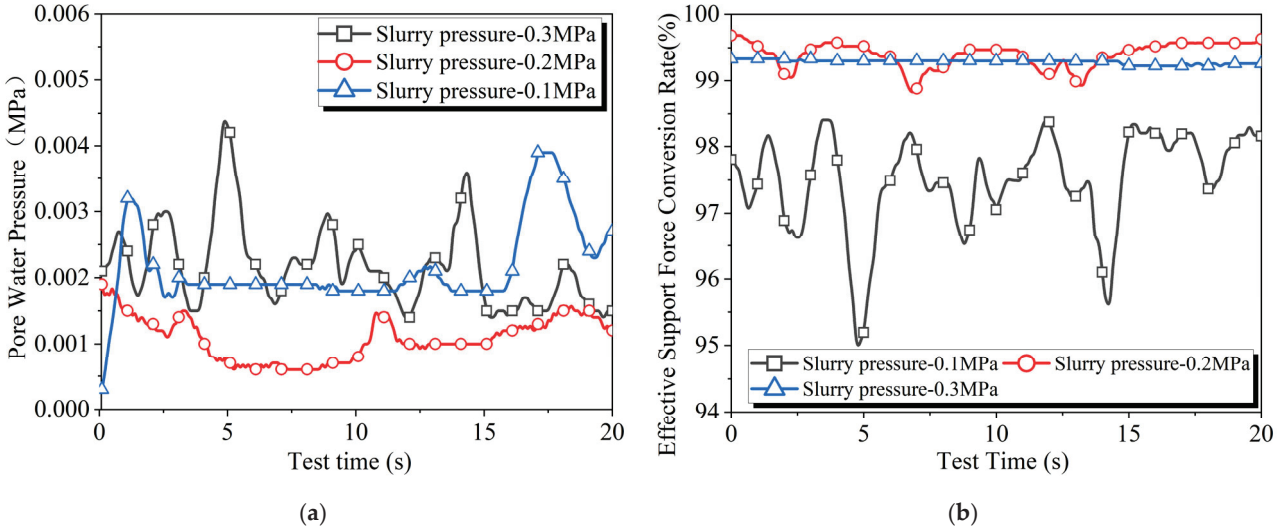

Figure 13. Results of slurry filtration experiments at different slurry pressure: (**a**) pore water pressure and (**b**) effective support force conversion rate.

4.8. Stratum Permeability

As shown in Figure 14, as the stratum particle size increases, the stratum pore water pressure rises while the effective support force conversion rate decreases, and the level of fluctuations also increases.

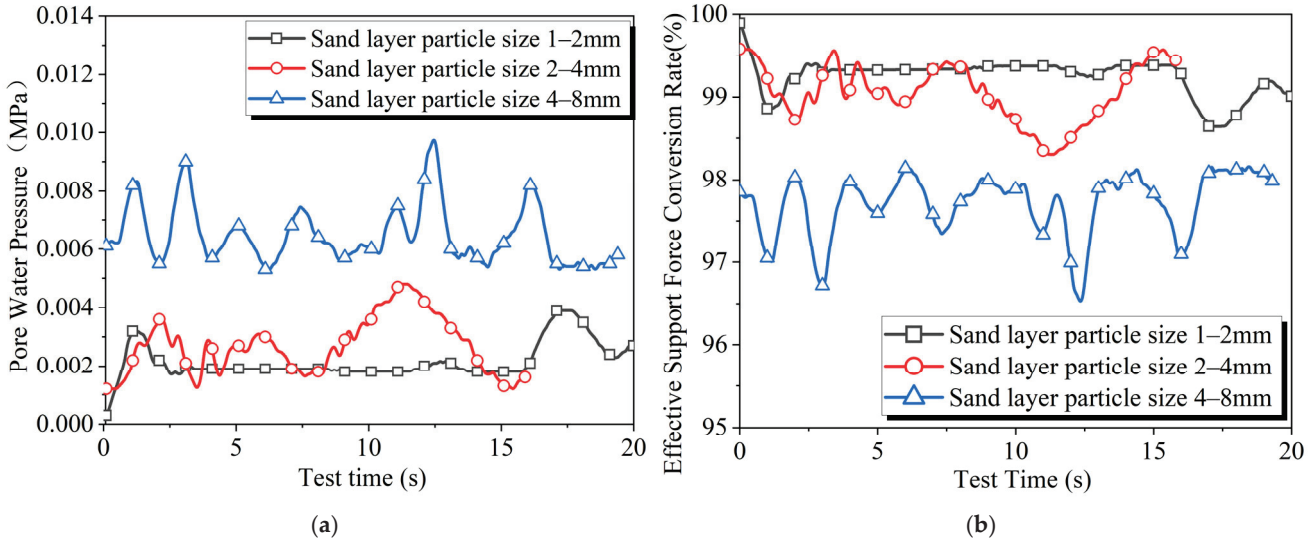

Figure 14. Results of slurry filtration experiments at different stratum permeability: (**a**) pore water pressure and (**b**) effective support force conversion rate.

Further analysis was conducted using the average value and range of the effective support force conversion rate curve from Figure 14b. These parameters indicate the magnitude and fluctuation degree of the support force at the excavation face, with the results shown in Figure 15. It can be observed that the average effective support force conversion rate has a linear relationship with the stratum permeability coefficient, while the range shows a nonlinear relationship. When the stratum permeability coefficient increases from 0.0419 cm/s to 0.0915 cm/s (corresponding to an increase in stratum particle size from 2–4 mm to 4–8 mm), there is a sudden increase in the range. This indicates that the increase in stratum permeability exacerbates the fluctuations in the effective support force conversion rate. It also explains the phenomenon of sudden and intense fluctuations in the pressure of the slurry chamber when the shield unexpectedly advances into a highly permeable stratum.

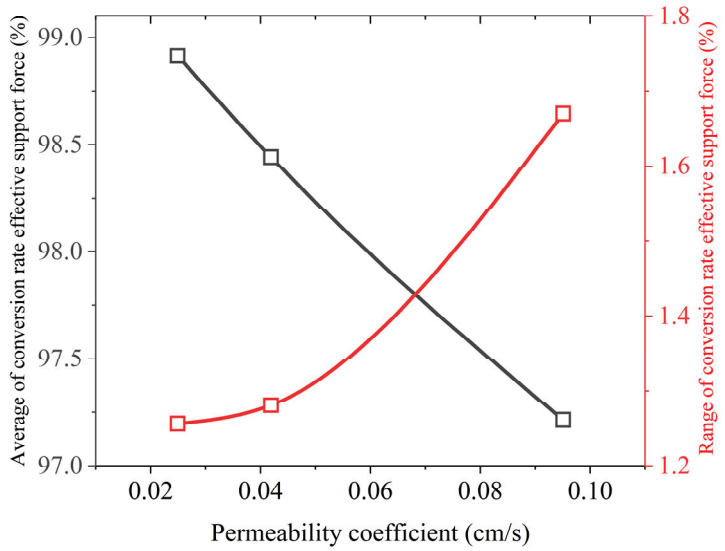

Figure 15. Relationship between the average, range, and stratum permeability coefficient.

5. Discussion

In this chapter, the quantitative relationships between factors such as bentonite and CMC on slurry permeability are studied. By analyzing the effective support force conversion rate curves, the average value and range are used to represent the magnitude and stability of the slurry's supporting capacity at the excavation face.

5.1. Effects of Different Factors on Effective Support Force Conversion Rate

5.1.1. Influence of Slurry Materials on Effective Support Force Conversion Rate

The average and range of the effective support force conversion rate during the slurry filtration process are used as indicators to characterize the slurry's supporting capacity and stability at the excavation face. These two metrics reflect the magnitude and fluctuation degree of the effective support force conversion rate, providing a comprehensive description of the characteristics of the effective support force conversion rate curve. The relationships between various factors and the aforementioned indicators are plotted as curves and fitted accordingly. The fine sand particle size is expressed as a mass of 0–0.5 mm particle size. Appendix A presents the raw data (average and range) of the effective support force conversion rate, along with corresponding fitting equations and R^2 values quantifying relationships between influencing factors and both the mean values and range of this parameter.

The influence of slurry composition on the effective support force conversion rate is presented in Figure 16. A nonlinear relationship is observed between bentonite content

and fine sand gradation with respect to both the mean and range of the conversion rate, whereas CMC content and fine sand quantity exhibit well-defined linear correlations with these metrics. The susceptibility of bentonite slurry to seawater-induced flocculation stems from cation infiltration: When seawater enters the slurry, abundant cations neutralize the negative surface charges of clay particles. This electrolyte intrusion compresses the diffuse double layer of clay colloids, diminishing interparticle repulsion forces. Consequently, the slurry system transitions from fine dispersion to coarse dispersion, forming flocculated structures that manifest macroscopically as rapid sedimentation and water separation [44].

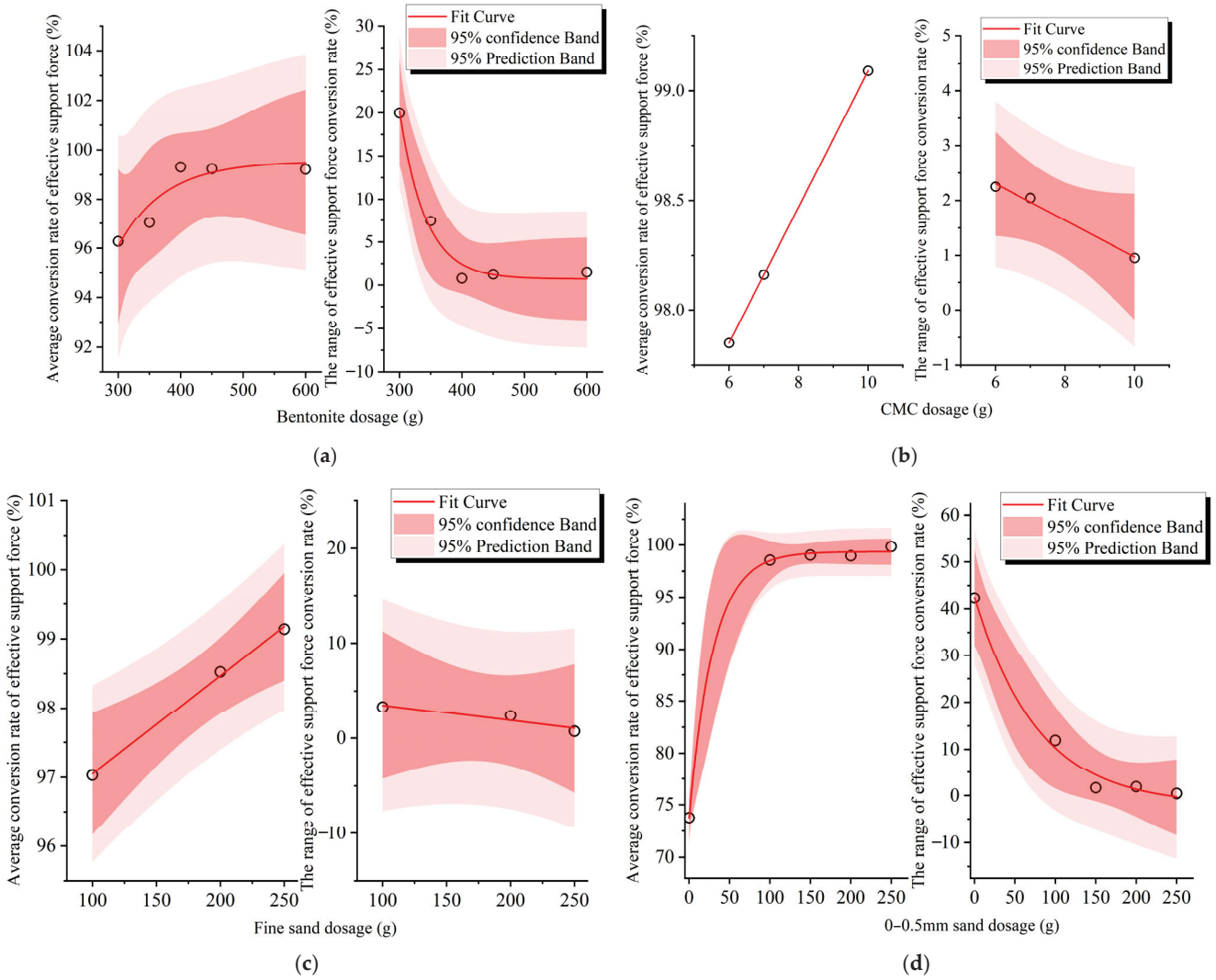

Figure 16. Influence of slurry materials on effective support force conversion rate: (**a**) bentonite content; (**b**) CMC content; (**c**) fine sand content; and (**d**) fine sand size.

SEM analysis of filter cakes confirms that seawater-exposed specimens develop more compact soil particle aggregates with enhanced intra-aggregate porosity and improved connectivity compared to seawater-free counterparts [44,45]. CMC counteracts these effects through hydrogen bonding with bentonite particles. Its molecular chains establish network structures that increase slurry viscosity, imparting cohesive density to flocculated structures. This mechanism preserves bentonite swelling capacity and maintains favorable rheological properties in seawater-contaminated slurries [2]. Fine sand primarily alters the particle size distribution of the slurry with minimal impact on its viscosity. As evident from Figure 16c, the quantity of fine sand exhibits well-defined linear correlations with both the mean value and range of the conversion rate. Collectively, these phenomena explain the nonlinear

relationship between bentonite content and the mean/range of the effective support force conversion rate: bentonite differentially impacts slurry viscosity and particle size gradation, with increasing concentrations producing distinct effects on these parameters.

The nonlinear relationship between fine sand particle size and the indicators may be attributed to the fact that when the fine sand particle size is significantly different from the particle size that determines whether the slurry can form a filter cake at the excavation face [32], the impact of fine sand particle size on the effective support force conversion rate is substantial; conversely, if the particle sizes are similar, the effect is diminished.

5.1.2. Effects of Tunneling Parameters and Stratum Permeability on Effective Support Force Conversion Rate

The effects of tunneling parameters and stratum permeability on the effective support force conversion rate are illustrated in Figure 17. With the exception of the nonlinear relationship between slurry pressure and both the average value and range, all other relationships are linear. This indicates that enhancing the slurry's supporting performance at the excavation face by increasing slurry pressure is most pronounced when the slurry pressure is relatively low.

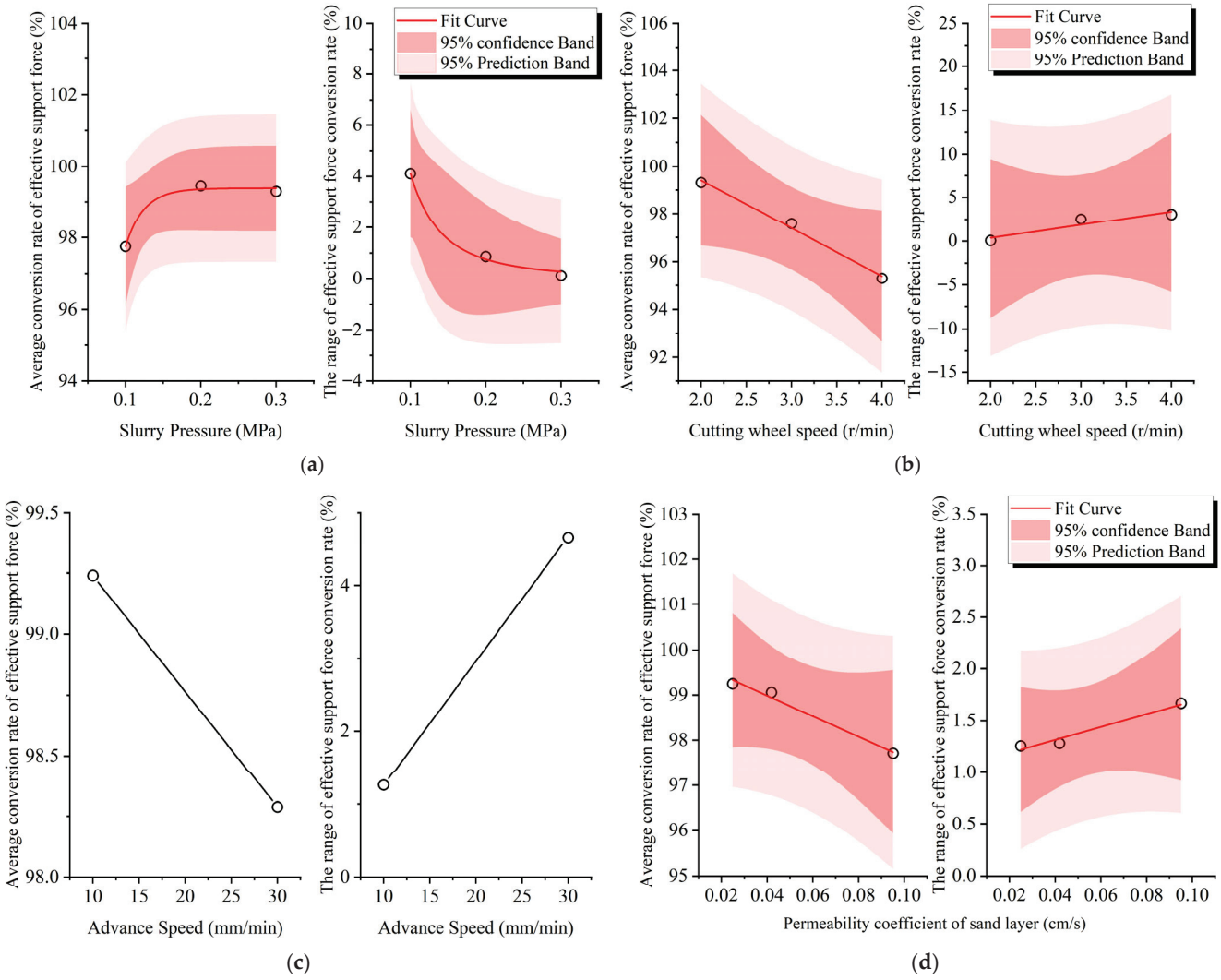

Figure 17. Effects of tunneling parameters and stratum permeability on effective support force conversion rate: (**a**) slurry pressure; (**b**) cutterhead rotation speed; (**c**) advance speed; and (**d**) stratum permeability coefficient.

5.2. Sensitivity Analysis of the Average Value and Range of Effective Support Force Conversion Rate

The data obtained in Section 5.1 were analyzed to determine the ratio of the average rate of change in the effective support force conversion rate (both the average value and range) to the average rate of change in each factor. This ratio serves as a parameter for assessing the relative importance of each factor. The calculation method is detailed in reference [27].

The relative importance parameters of each factor were ranked, with the results shown in Figure 18. The ranking based on the relative importance of each factor to the average value of the effective support force conversion rate, from highest to lowest, is as follows: bentonite, cutterhead rotation speed, CMC, fine sand particle size, fine sand content, slurry pressure, and advance speed. For the relative importance to the range, the ranking from highest to lowest is bentonite, CMC, cutterhead rotation speed, fine sand particle size, slurry pressure, fine sand content, and advance speed.

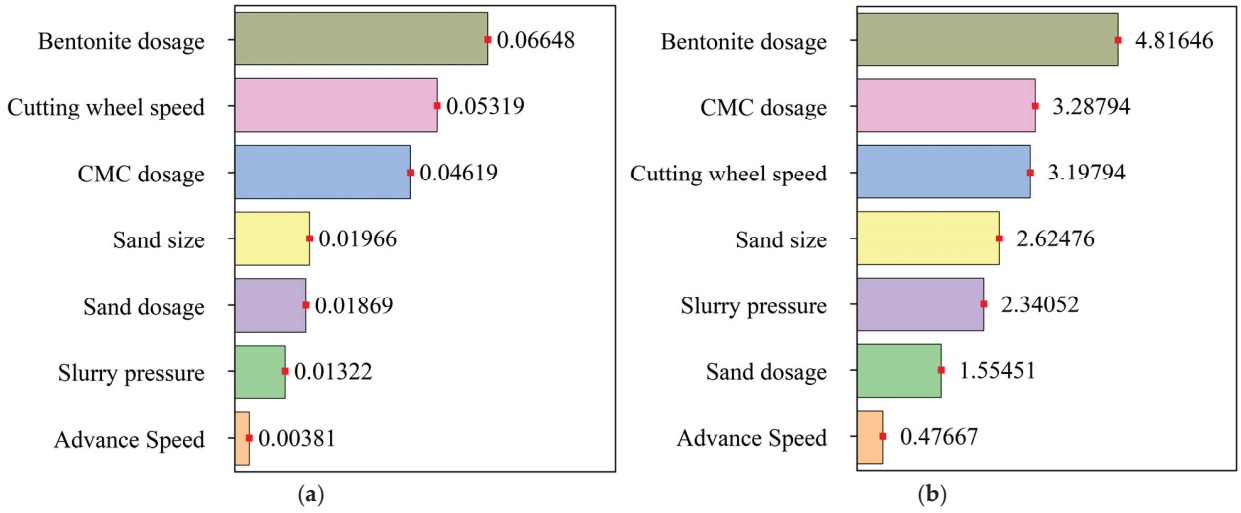

Figure 18. Results of sensitivity analysis on slurry supporting performance: (**a**) average value and (**b**) range.

By comparing the values of the relative importance parameters for each factor, it can be observed that the impact of the factors on the range of the effective support force conversion rate is greater than their impact on the average value. The support force at the excavation face is more susceptible to fluctuations [46]. The amounts of bentonite and CMC are the two material factors that have the greatest influence on both indicators, with bentonite having a more significant effect on the effective support force conversion rate than CMC, a finding that is supported by the research of Ye et al. [47]. The cutterhead rotation speed is the most influential tunneling parameter; compared to the penetration depth of the cutter, the cutter speed has a more pronounced effect on the conversion rate of slurry support pressure at the tunnel face [48]. The heightened sensitivity of the effective support force conversion rate to bentonite content compared to CMC is primarily driven by bentonite's dual functionality: it simultaneously modifies both particle size distribution and viscosity in the slurry system. Elevating bentonite content increases particulate density within the slurry, thus enhancing pore-plugging capacity in geological formations and promoting filter cake development. Increased slurry viscosity substantially reduces seepage velocity, facilitating bentonite particle retention within excavation face pores. Higher viscosity slurry further enables transportation of finer particulates, inducing particle bridging phenomena along seepage pathways that effectively enhance formation pore sealing [34]. In engineering applications, when introducing viscosity-enhancing additives like CMC, concurrently

incorporating clay or silt to optimize particle size distribution synergistically enhances additive efficacy.

6. Conclusions

This study investigates the filtration characteristics of bentonite slurry under the cutting influence of the shield cutterhead in high-permeability strata within a subsea environment using a model testing device. The effects of slurry materials, including bentonite, CMC, and fine sand, as well as tunneling parameters such as slurry pressure, advance speed, and cutterhead rotation speed, on the effective support force conversion rate at the excavation face during the slurry filtration process were examined. The results indicate that.

(1) Under cutterhead cutting conditions, the pore water pressure rises immediately after the start of the experiment and fluctuates as the test progresses, while the effective support force conversion rate drops immediately after the experiment begins and fluctuates within a certain range, unable to reach 100%.

(2) Adding bentonite, CMC, and fine sand to the slurry, reducing the particle size of fine sand, increasing slurry pressure, and decreasing cutterhead rotation speed and advance speed help improve the effective support force conversion rate and enhance its stability.

(3) The effective support force conversion rate's average value and range are used to characterize the support effect and stability of the slurry at the excavation face during cutterhead cutting, and the influence of various factors on both metrics was studied. The relationships between the average value and range of the effective support force conversion rate with bentonite content and fine sand particle size are nonlinear. The stratum permeability coefficient and slurry pressure exhibit a nonlinear relationship with the range and a linear relationship with the average value, indicating marginal effects of these factors on the average value and range.

(4) A sensitivity analysis of the average value and range of the effective support force conversion rate was conducted, with the ranking of the effects on the average value of effective support force conversion rate from greatest to least being bentonite, cutterhead rotation speed, CMC, fine sand particle size, fine sand content, slurry pressure, and advance speed. For the range of the effective support force conversion rate, the ranking from greatest to least is bentonite, CMC, cutterhead rotation speed, fine sand particle size, slurry pressure, fine sand content, and advance speed.

(5) Based on the experimental results of this study, the following slurry formulation and tunneling parameter adjustments are proposed for slurry shield tunneling in submarine formations characterized by high salinity and high permeability: the bentonite-to-water ratio should exceed 40%, the carboxymethyl cellulose (CMC) dosage should be greater than 10 g per liter of water, and the fine sand should have an optimal particle size ratio of 0–0.5 mm to 0.5–1 mm = 2:3. The speed of the cutterhead should not exceed 3 r/min, and the forward speed should be kept below 10 mm/min. These conclusions, derived from laboratory-scale tests, require further verification through engineering applications.

Author Contributions: Conceptualization, Z.L. and D.W.; methodology, Z.L.; software, L.Z.; validation, Z.L., L.Z. and D.W.; formal analysis, Q.Z.; investigation, Z.L. and D.W.; resources, L.Z. and D.W.; data curation, Y.W.; writing—original draft preparation, H.D., Z.L. and D.W.; writing—review and editing, H.D., Y.L., Y.D. and D.W.; visualization, L.Z.; supervision, Q.Z. and Y.G.; project administration, L.Z. and D.W.; funding acquisition, Z.L. and D.W. All authors have read and agreed to the published version of the manuscript.

Funding: This paper was completed with the support of the National Key R&D Program of China (2024YFB2606100) and the National Natural Science Foundation of China (No.52171267).

Data Availability Statement: The original contributions presented in this study are included in the article. Further inquiries can be directed to the corresponding author.

Conflicts of Interest: The authors declare no conflicts of interest.

Appendix A

Table A1 presents the raw data of the effective support force conversion rate (average and range). Tables A2 and A3 summarize the corresponding fitting equations and R^2 values quantifying relationships between influencing factors and both the mean values and range of this conversion rate.

Table A1. The raw data of the effective support force conversion rate.

Influence Factor	Parameter Value	Average Conversion Rate of Effective Support force	The Range of Effective Support Force Conversion Rate
Bentonite dosage (g)	300	96.271	19.982
	350	97.036	7.437
	400	99.31	0.779
	450	99.239	1.256
	600	99.217	1.49
CMC dosage (g)	6	97.85	2.248
	7	98.16	2.042
	10	99.09	0.953
Fine sand dosage (g)	250	99.138	0.715
	200	98.526	2.369
	100	97.031	3.317
0–0.5 mm sand dosage(g)	250	99.831	42.343
	200	98.953	1.871
	150	99.02	1.634
	100	98.548	11.909
	0	73.747	42.343
Slurry Pressure (MPa)	0.3	99.449	4.098
	0.2	99.449	0.858
	0.1	97.751	4.098
Cutting wheel speed (r/min)	4	99.308	3.016
	3	97.59	2.488
	2	99.308	0.037
Advance Speed (mm/min)	30	99.239	4.666
	30	98.287	4.666
	10	99.239	1.256
Permeability coefficient of sand layer (cm/s)	0.0249	99.239	1.256
	0.0419	99.053	1.281
	0.0951	97.707	1.67

Table A2. Regression equations between various influencing factors and the average effective support force conversion rate.

Influence Factor	Regression Equations	R^2
Bentonite dosage	$y = 99.54344 - 197.90599 \times e^{-0.01349x}$	0.86621
CMC dosage	$y = 95.98947 + 0.31009x$	1
Fine sand dosage	$y = 95.63295 + 0.01417x$	0.99776
0–0.5 mm sand dosage	$y = 99.35535 - 25.60777 \times e^{-0.03379x}$	0.99921
Slurry pressure	$y = 99.38171(1 - e^{-41.1159x})$	0.99021
Cutting wheel speed	$y = 103.41607 - 2.00622x$	0.99317

Table A2. *Cont.*

Influence Factor	Regression Equations	R^2
Advance speed	/	/
Permeability coefficient of sand layer	$y = 99.88905 - 22.6573x$	0.98497

Table A3. Regression equations between various influencing factors and the range of effective support force conversion rate.

Influence Factor	Regression Equations	R^2
Bentonite dosage	$y = 0.69618 + 27812.96802 \times e^{-0.02422x}$	0.98417
CMC dosage	$y = 4.2991 - 0.33283x$	0.99122
Fine sand dosage	$y = 5.10834 - 0.01622x$	0.88529
0–0.5 mm sand dosage	$y = -2.09823 + 44.5591 \times e^{-0.01282x}$	0.99108
Slurry pressure	$y = 0.01503 \times x^{-2.4364}$	0.9957
Cutting wheel speed	$y = -2.62063 + 1.48919x$	0.87798
Advance speed	/	/
Permeability coefficient of sand layer	$y = 1.06592 + 6.23537x$	0.96758

References

1. Wang, X.; Zhang, L.; Zhang, Q.; Liu, R.; Huang, C. A stepwise calculation method for grouting penetration in rough rock fracture based on fracture segment division. *Tunn. Undergr. Space Technol.* **2025**, *166*, 106944. [CrossRef]
2. Wang, Z.; Ding, W.; Zhu, Z.; Liu, R.; Wang, C.; Yu, W.; Wang, Z. Experimental study on rheological behaviors of Na-bentonite slurries under seawater intrusion. *Constr. Build. Mater.* **2022**, *357*, 129369. [CrossRef]
3. Holzhaeuser, J.; Hunt, S.W.; Mayer, C. Global experience with soft ground and weak rock tunneling under very high groundwater heads. In Proceedings of the North American Tunneling 2006: North American Tunneling 2006 Conference, Chicago, IL, USA, 10–15 June 2006; Babendererde Engineers Lle: Kent, WA, USA, 2006.
4. Han, X.R.; Zhu, W.; Liu, Q.W. Influence of slurry property on filter cake quality on working face of slurry shield. *Rock Soil Mech.* **2008**, *29*, 288–292.
5. Min, F.-L.; Zhu, W.; Han, X.-R.; Zhong, X.-C. The Effect of Clay Content on Filter-Cake Formation in Highly Permeable Gravel. In Proceedings of the Geoshanghai International Conference, Shanghai, China, 3–5 June 2010. [CrossRef]
6. Min, F.; Zhu, W.; Han, X. Filter cake formation for slurry shield tunneling in highly permeable sand. *Tunn. Undergr. Space Technol. Inc. Trenchless Technol. Res.* **2013**, *38*, 423–430. [CrossRef]
7. Wu, D.; Zhou, S.; Wen, X. Laboratory test and application of filter cake formation in sand during slurry shield construction. *Chin. J. Rock Mech. Eng.* **2015**, *34*, 3460–3467.
8. Xu, T.; Bezuijen, A. Bentonite slurry infiltration into sand, filter cake formation under various conditions. *Géotechnique* **2019**, *69*, 1095–1106. [CrossRef]
9. Bai, Y. Study on Slurry Penetration and Stability of Slurry Shield Tunnel Face Based on Interaction of "Cutter-Soil". Ph.D. Thesis, China University of Mining and Technology, Beijing, China, 2022.
10. Mao, J.; Yuan, D.; Chen, J.; Yang, P.; Liu, S. Study on the Characteristics of Slurry Support Efficiency on Excavation Face Induced by Shield Cutterhead Cutting in Sand Stratum. *KSCE J. Civ. Eng.* **2024**, *28*, 2982–2996. [CrossRef]

11. Zdenek, Z.; Britta, S.; Markus, T. Investigations on transient support pressure transfer at the tunnel face during slurry shield drive part 1: Case A—Tool cutting depth exceeds shallow slurry penetration depth. *Tunn. Undergr. Space Technol. Inc. Trenchless Technol. Res.* **2021**, *118*, 104168.
12. Nomoto, T.; Imamura, S.; Hagiwara, T.; Kusakabe, O.; Fujii, N. Shield Tunnel Construction in Centrifuge. *J. Geotech. Geoenvironmental Eng.* **1999**, *125*, 289–300. [CrossRef]
13. Liu, X.; Xiong, F.; Zhou, X.; Liu, D.; Chen, Q.; Zhang, J.; Han, Y.; Xu, B.; Deng, Z.; He, C. Physical model test on the influence of the cutterhead opening ratio on slurry shield tunnelling in a cobble layer. *Tunn. Undergr. Space Technol.* **2022**, *120*, 104264. [CrossRef]
14. Yang, J.; Liu, C.; Chen, Q.; Xie, X. Performance of overlapped shield tunneling through an integrated physical model tests, numerical simulations and real-time field monitoring. *Undergr. Space* **2017**, *2*, 45–59. [CrossRef]
15. Hu, X.; He, C.; Walton, G.; Fang, Y.; Dai, G. Laboratory Model Test of EPB Shield Tunneling in a Cobble-Rich Soil. *J. Geotech. Geoenvironmental Eng.* **2020**, *146*, 04020112. [CrossRef]
16. Ma, S.; Duan, Z.; Huang, Z.; Liu, Y.; Shao, Y. Study on the stability of shield tunnel face in clay and clay-gravel stratum through large-scale physical model tests with transparent soil. *Tunn. Undergr. Space Technol.* **2022**, *119*, 104199. [CrossRef]
17. Hu, X.; Fang, Y.; Walton, G.; He, C. Laboratory model test of slurry shield tunnelling in saturated sandy soil. *Géotechnique* **2023**, *73*, 885–906. [CrossRef]
18. Shen, X.; Yuan, D.; Jin, D.; Chen, X.; Luo, W.; Peng, Y.; Duan, K. Model test on cutterhead-soil interaction during shield tunneling and its theoretical model. *Undergr. Space* **2025**, *20*, 46–68. [CrossRef]
19. Mao, J.; Yuan, D.; Jin, D.; Liu, S. Influence of Cutting Tools on Filter Cake Formation during Slurry Shield Tunnelling. *KSCE J. Civ. Eng.* **2021**, *25*, 2261–2274. [CrossRef]
20. Kong, X.; Bai, Y.; Xu, D. The Elastic Modulus of Slurry Membrane in Excavation Face for Slurry Shield. *Chin. J. Undergr. Space Eng.* **2012**, *8*, 307–310.
21. Xisheng, Y. Cake Filtration and Face Stability of Slurry Shield Tunnel. Ph.D. Thesis, Zhejiang University, Zhejiang, China, 2017.
22. Jin, D.; Yuan, D. Face stability analysis of the slurry-type shield tunneling considering the dynamic filter cake. *Rock Soil Mech.* **2022**, *43*, 2952–2962.
23. Wang, Q.; Xia, Y.; Huang, S.; Yang, M.; Zhang, L.; Sheng, J.; Xiao, H. Numerical Investigation of the Impact of Tunneling Parameters on the Mud Discharge Performance of Atmospheric Cutterhead. *Ksce J. Civ. Eng.* **2024**, *28*, 5895–5908. [CrossRef]
24. Zizka, Z.; Schoesser, B.; Thewes, M.; Schanz, T. Slurry Shield Tunneling: New Methodology for Simplified Prediction of Increased Pore Pressures Resulting from Slurry Infiltration at the Tunnel Face Under Cyclic Excavation Processes. *Int. J. Civ. Eng.* **2019**, *17*, 113–130. [CrossRef]
25. Mao, J.H. Research on Laws of Dynamic Filter Cake Formation and Face Stability During Slurry Shield Tunnelling in Sand Stratum. Ph.D. Thesis, Beijing Jiaotong University, Beijing, China, 2021.
26. Qin, S.; Cheng, Y.; Zhou, W.-H. State-of-the-art review on pressure infiltration behavior of bentonite slurry into saturated sand for TBM tunneling. *Smart Constr. Sustain. Cities* **2023**, *1*, 14. [CrossRef]
27. Dong, H.; Wang, D.; Li, Z.; Zhang, Q.; Li, Y.; Zhang, J.; Zhang, L.; Zhang, L. Experimental Study on Infiltration of Seawater Bentonite Slurry. *Buildings* **2024**, *14*, 2609. [CrossRef]
28. Lin, Y.; Fang, Y.; He, C.; Wang, W. Experimental study on degree of match between slurry and ground based on particle retention rate. *Tunn. Undergr. Space Technol.* **2021**, *116*, 104105. [CrossRef]
29. Chen, K.; Hong, K.; Jiao, S. *Shield Construction Technology*; People's Communications Publishing House: Beijing, China, 2016; pp. 3–20.
30. Broere, W. Influence of excess pore pressures on the stability of the tunnel face. In *Geotechnical Aspects of Underground Construction in Soft Ground*; International Society for Soil Mechanics and Geotechnical Engineering (ISSMGE): London, UK, 2002; pp. 179–184.
31. Broere, W.; Van Tol, A.F. Influence of infiltration and groundwater flow on tunnel face stability. *Geotech. Asp. Undergr. Constr. Soft Ground* **2000**, *1*, 339–344.
32. Broere, W. Tunnel Face Stability and New CPT Applications. Ph.D. Thesis, Delft University of Techonology, Delft, The Netherlands, 2001.
33. Wei, D.W.; Zhu, W.; Min, F.L. Experimental study of forming time of filter cake and conversion rate of slurry pressure in slurry shield in sand stratum. *Rock Soil Mech.* **2014**, *35*, 423–428.
34. Chen, Y.; Cai, Y.; Ye, W.; Cui, Y.; Chen, B. Progresses in researches on adsorption and migration properties of bentonite colloids and their co-migration with nuclide in repository. *Chin. J. Geotech. Eng.* **2021**, *43*, 2149–2158.
35. Ding, H. Seepage Law and Prediction of Water Inflow in Surrounding Rock of Weathering Trough in Xiamen Subsea Tunnel. Master's Thesis, Southwest JiaotongUniversity, Chengdu, China, 2019.
36. Zhang, H.; Shan, X. Quantitative Measurement Research on Slurry Blending and Pulping Engineering of Slurry Balance Shield. *Railw. Eng. Technol. Econ.* **2022**, *37*, 39–43.
37. Ding, X. Research on Key Construetion Technology of Slurry Shield Crossing Shiziyang Fault Fracture Zone. *Eng. Technol. Res.* **2023**, *8*, 50–53. [CrossRef]

38. Yin, Z.; Zhang, Q.; Zhang, X.; Li, X.; Zheng, D. Effect of seawater on bentonite slurry and its infiltration behavior into saturated sand for tunnelling. *Bull. Eng. Geol. Environ.* **2024**, *83*, 178. [CrossRef]
39. Yang, Y.; Yuan, D.; Jin, D.; Yi, Y. Development and experiment study on seawater-based slurry for subsea tunnels in slurry shield tunneling. *Constr. Build. Mater.* **2024**, *451*, 138646. [CrossRef]
40. Yang, F. Research on the Parameter Law and Optimization of Shield Tunneling in Hard Rock Composite Strata in Sea Area. *Railw. Constr. Technol.* 2024; 163–167+194.
41. Huang, Q. Research on Interaction with Soil of TBM Cutting-Wheel Tools and Their Type Selection Design in Gravel Stratum. Ph.D. Thesis, Beijing Jiaotong University, Beijing, China, 2010.
42. Bai, Y.; Jiang, B.; Yang, L.; Liu, Y.; Zheng, H.; Li, Y. Experimental Study on the Characteristics and Formation Mechanism of Dynamic Filter Cake for Slurry Shield Tunneling. *Minerals* **2022**, *12*, 331. [CrossRef]
43. Yang, Y.; Jin, D.; Yuan, D.; Yao, Z. Spatial distribution of excess pore water pressure and slurry infiltration zone in slurry shield tunneling. *Tunn. Undergr. Space Technol.* **2024**, *153*, 105965. [CrossRef]
44. Min, F.; Du, J.; Zhang, N.; Chen, X.; Lv, H.; Liu, L.; Yu, C. Experimental study on property change of slurry and filter cake of slurry shield under seawater intrusion. *Tunn. Undergr. Space Technol.* **2019**, *88*, 290–299. [CrossRef]
45. Qin, S.; Zhou, W.H.; Xu, T. Effects of seawater on the infiltration behavior of bentonite slurry into sand. *Constr. Build. Mater.* **2023**, *371*, 130759. [CrossRef]
46. Wei, G.; Zhu, Y.; Yin, X. Research progress of slurry penetration test and filter cake forming law of slurry shield. *Low Temp. Archit. Technol.* **2021**, *43*, 76–81+87.
47. Ye, W.; Fu, L.; Zhou, S. Influence of Shield Slurry Property on Filter Cake Quality in Sand Stratum. In *Advances in Transportation Geotechnics IV, Proceedings of the 4th International Conference on Transportation Geotechnics, Chicago, IL, USA, 23–26 May 2021*; Springer International Publishing: Cham, Switzerland, 2022.
48. Liu, K.; Yang, R.; Wang, S.; Zhao, W.; Qi, P. Slurry Support Mechanism for Shield Tunneling Considering Slurry Infiltration and Cutter-Disk Cutting Effect. *Int. J. Geomech.* **2024**, *24*, 04024223. [CrossRef]

Disclaimer/Publisher's Note: The statements, opinions and data contained in all publications are solely those of the individual author(s) and contributor(s) and not of MDPI and/or the editor(s). MDPI and/or the editor(s) disclaim responsibility for any injury to people or property resulting from any ideas, methods, instructions or products referred to in the content.

materials

MDPI

Article

Research on Optimizing the Steel Fiber/CSH Interface Performance Based on Ca/Si Ratio

Yalin Luan [1,2], Yongmei Wu [1], Runan Wang [2], Dongbo Cai [1], Lianzhen Zhang [2,*] and Pengxiang Luan [3]

[1] The Seventh Engineering Co., Ltd. of CCCC First Highway Engineering Co., Ltd., Zhengzhou 451452, China; luanyalin@upc.edu.cn (Y.L.); 19854212857@163.com (Y.W.); 15583130944@163.com (D.C.)
[2] College of Pipeline and Civil Engineering, China University of Petroleum (East China), Qingdao 266580, China; 19862857721@163.com
[3] Wuxi National Hi-Tech Development District SCI-TECH Innovation Promotion Center, Wuxi 214142, China; luanpx@foxmail.com
* Correspondence: zhanglianzhen@upc.edu.cn; Tel.: +86-18265328519

Abstract: Steel fiber reinforced concrete in marine environments often suffers from stress corrosion coupling. Under mechanical loading, the formation of penetrating cracks in the matrix increases susceptibility to seawater penetration and interfacial degradation. Using molecular dynamics simulations, this study investigated the effects of calcium-to-silicon (Ca/Si) ratios on the interfacial bonding and transport properties of a γ-FeOOH/CSH system. The results show that higher Ca/Si ratios strengthen ionic bonding between CSH and γ-FeOOH, thereby improving interfacial adhesion. Additionally, increased Ca/Si ratios significantly slow the transport of water molecules and ions (Na^+, Cl^-, SO_4^{2-}) within γ-FeOOH/CSH nanopores. It was observed that Cl^- and SO_4^{2-} exhibited pronounced filtration effects at Ca/Si = 2.0. These findings suggest that optimizing the Ca/Si ratio in concrete can simultaneously enhance interfacial strength and reduce permeability. This provides an effective strategy for improving the marine erosion resistance of steel fiber reinforced concrete structures.

Keywords: steel fiber reinforced concrete; calcium-to-silicon ratio; γ–FeOOH/CSH nanopore; molecular dynamics simulations

1. Introduction

As an essential building material, concrete plays a crucial role in marine engineering construction. The durability of concrete structures is a critical factor in determining the service life of port infrastructure [1–3]. The incorporation of steel fibers into concrete enhances its mechanical properties and durability, making steel fiber reinforced concrete widely used in marine environments [4–7]. However, micro-gaps at the steel fiber/cement matrix interface create a mechanically weak zone that promotes fiber debonding and crack bridging, enhancing toughness [8,9]. When seawater penetrates the interface, chloride ions (Cl^-) play a critical role by depassivating steel fibers and inducing corrosion. However, coexisting ions such as Na^+ and SO_4^{2-} may further exacerbate degradation through synergistic effects; Na^+ increases ionic conductivity, while SO_4^{2-} reacts with cement hydrates, collectively reducing interfacial adhesion and impermeability [10–12]. This degradation leads to a progressive decline in the macroscopic performance of concrete, ultimately compromising the long-term safety of marine concrete structures [13–17]. While experimental methods are limited by scale constraints, molecular dynamics (MD) simulations can bridge the gap between macroscopic experiments and microscopic mechanisms, providing critical insights for improving concrete durability at the fundamental level [18,19].

Current research has focused on modification of concrete interfacial properties to address its inherent weaknesses. Some studies have explored material composition adjustments: Hou et al. [20] investigated the interaction of water molecules with calcium silicate hydrate (CSH) gels at varying calcium-to-silicon (Ca/Si) ratios. The results indicate that low-Ca/Si CSH has a denser structure, which results in larger water contact angles due to hindered penetration into silicate chains. Thus, higher Ca/Si ratios improve wettability. Wu et al. [21] conducted uniaxial tensile tests on four CSH gel models with Ca/Si ratios (1.24, 1.41, 1.64 and 1.80), revealing that increased Ca/Si reduced the Young's modulus and peak stress of CSH, weakening tensile performance. Zhou et al. [22] combined experiments and simulations to demonstrate that higher Ca/Si ratios break long silicate chains into shorter fragments, creating more non-bridging oxygen sites that promote water and Ca^{2+} accumulation, thereby enhancing chloride adsorption.

Other studies have employed interfacial adhesives to improve performance. Yang Qingrui et al. [23] showed that graphene nanosheets can form a "idge" the epoxy/CSH interface, enhancing the interfacial bonding performance through Ca_{CSH}–O_{GO}–H_{epoxy}, O_{CSH}–H_{GO}–O_{epoxy} (N_{epoxy}), and H_{CSH}–O_{GO}–H_{epoxy} bonds. Guo et al. [24] found that graphene oxide slit size affects CSH formation; larger slits facilitate Si and Ca^{2+} adsorption and promote polymerization, while smaller slits cause structural inhomogeneity. Yang et al. [25] pointed out that the addition of 3–(aminopropyl) triethoxysilane (3–APTES) could change the fracture process of CSH, increase the atomic density, and enhance its tensile toughness and adsorption capacity for water molecules.

The studies mentioned above provide two strategies for optimizing the steel fiber/CSH interface. On one hand, the molecular structure of CSH can be changed by adjusting the material ratio, such as constructing CSH models with different Ca/Si. On the other hand, molecular bond connections can be strengthened by incorporating interface enhancers such as graphene oxides and 3–APTES. However, existing work primarily focuses on the mechanical, wetting, and transport properties of CSH matrix, with insufficient attention to steel fiber/CSH interfacial adhesion and ion transport. Furthermore, there is a lack of comprehensive simulations on steel fiber concrete with varying compositions.

To address these gaps, this study employed MD simulations to investigate the steel fiber/CSH interface in a NaCl + Na_2SO_4 composite solution environment. Four CSH crystal models with Ca/Si ratios of 1.3, 1.5, 1.7, and 2.0 were constructed to form γ–FeOOH/CSH interfacial bonding–transport systems. The interfacial adhesion was evaluated through interaction energy analysis and water/ion binding mechanisms, while transport properties were assessed via ion penetration depth and local bonding effects. Finally, suggestions for optimizing the performance of steel fiber/CSH interface are proposed from the perspective of Ca/Si ratio selection. The research aims to determine how different Ca/Si ratios affect the interfacial bonding strength and ion transport behavior in the γ–FeOOH/CSH system, providing insights for optimizing concrete formulations to enhance corrosion resistance in marine environments.

2. Materials and Methods

2.1. Model Construction

Tobermorite 11 Å crystal served as the initial structure for modeling CSH with varying Ca/Si ratios. To achieve different ratios, the Q_n species distribution in the silicate chains was adjusted based on NMR data [26], and electrically neutral SiO_2 groups were removed to shorten the silicate chains [27]. Increasing the Ca/Si ratio introduced more micropores between the truncated chains. Water adsorption was then simulated using Grand Canonical Monte Carlo (GCMC) at 300 K with a chemical potential of 0 eV, employing the CSH–FF force field [28].

The system reached saturation after 100 million simulation steps. Each CSH model was sliced along the (0 0 1) interlayer direction, and surface water was removed to minimize interference. Surface Ca^{2+} and hydroxyl groups were adjusted to maintain charge balance, with consistent Ca^{2+} content across models to preserve the target Ca/Si ratios. lower Ca/Si ratios resulted in longer silicate chains and higher Q^2_b abundance (where Q represents Si–O tetrahedron, 2 indicates the number of other Q units to which it is bonded increases, b represents the bridging Si). The Q species distribution for each model is summarized in Table 1 [20].

Table 1. Q species percentage distribution [20].

	Q^0 (%)	Q^1 (%)	Q^2 (%)
Ca/Si = 1.3	0	43.24	56.76
Ca/Si = 1.5	0	56.25	43.75
Ca/Si = 1.7	1.22	80.49	18.29
Ca/Si = 2.0	8.45	78.87	12.68

The steel fiber/CSH interface models with different Ca/Si ratios were constructed using three primary components. Firstly, four distinct tobermorite crystal structures with Ca/Si ratios of 1.3, 1.5, 1.7, and 2.0 were established, as shown in Figure 1a. These CSH structures were modified to represent realistic hydration products through the selective removal of H_2O molecules and random elimination of bridging Si–O tetrahedra within the silicate chains [28,29]. Secondly, the steel fiber component was modeled using γ–FeOOH, which represents the primary constituent of the passive film formed on steel surfaces under the strong alkaline conditions [30] created by calcium hydroxide in cement hydration products [31]. This approach accounts for long-term environmental effects on steel fiber surfaces [32,33], as illustrated in Figure 1b. Thirdly, an aqueous solution environment was created using a NaCl + Na_2SO_4 mixture with a density of 1.04 g/cm^3, to simulate realistic marine conditions [34].

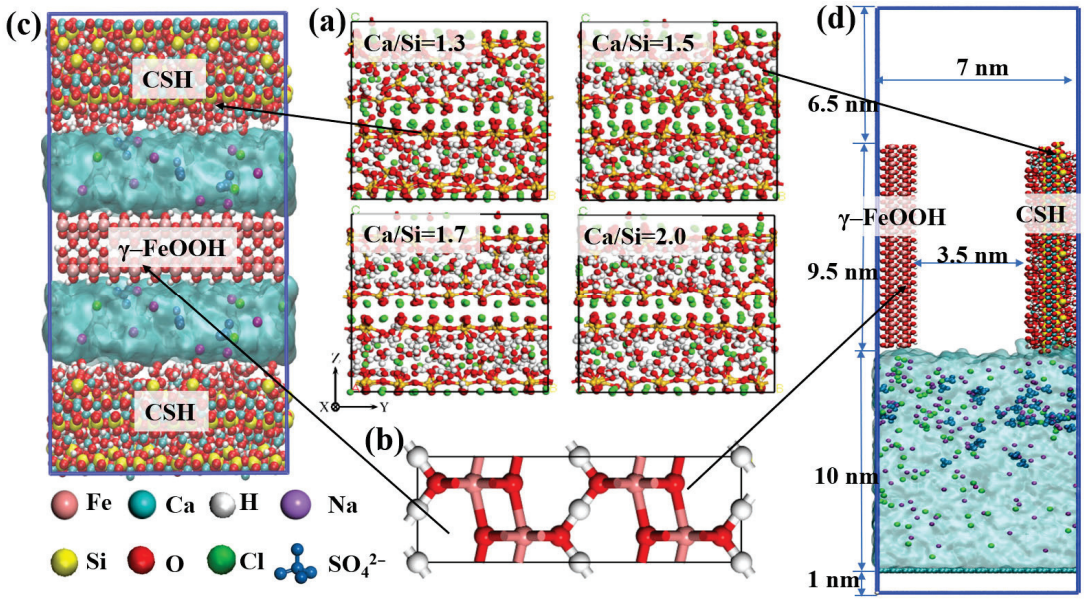

Figure 1. (**a**) Different Ca/Si CSH models, (**b**) γ–FeOOH, (**c**) γ–FeOOH/CSH interface bonding model and the blue square represents the boundary of the box (**d**) γ–FeOOH/CSH interface transport model.

The four CSH structures and γ–FeOOH structure were expanded along their crystallographic axes to form CSH/γ–FeOOH/CSH sandwich configurations. A 12.5 Å vacuum

layer was maintained between the γ–FeOOH and CSH surfaces [35], which was subsequently filled with the NaCl + Na_2SO_4 composite solution to establish the interfacial bonding model in Figure 1c. In the transport model, the expanded sizes of CSH and γ–FeOOH structures with four Ca/Si ratios were 22.6 Å × 95 Å × 20 Å and 22.6 Å × 95 Å × 15 Å, respectively [36]. CSH and γ–FeOOH structures were positioned on either side of a central 3.5 nm–wide channel, with the erosive solution placed at the channel outlet in Figure 1d.

2.2. Force Field and Molecular Dynamics Procedure

Molecular dynamics (MD) simulations were performed using the Large–scale Atomic Molecular Massively Parallel Simulator (LAMMPS) [37,38] free software package, with visualization of the processes realized by Visual Molecular Dynamics (VMD). The ClayFF force field [39] was used due to its general applicability for simulating various cement hydration products, interfaces between minerals and solutions, anion and cation adsorption on hydroxide surfaces, and the interatomic potentials between solution species and the calcium silicate skeleton.

The bonding simulation process was conducted as follows: a 300 ps NPT ensemble for all atoms was established for energy minimization. Then, a 1000 ps NVT ensemble simulation was applied to achieve complete system equilibration. The transmission simulation involved three stages, as follows. First, both CSH and γ–FeOOH walls were set as rigid bodies, i.e., in a "frozen" state [40], and an invisible wall was placed between the channel entrance and the solution to prevent water molecules and ions from escaping. Second, the solution was simulated for 200 ps in the NVT ensemble to achieve equilibrium [41]. Third, the "frozen" walls were released, and the invisible wall at the pore channel entrance was removed. A 2000 ps simulation was performed in the NVT ensemble, allowing water and ions to freely enter the pore. Periodic boundary conditions were applied in all simulations to eliminate size effects, and the temperature was maintained at 300 K using a Nosé–Hoover thermostat. Additionally, atomic coordinates were calculated every 0.1 ps, and the resulting atomic trajectories were used for structural and dynamic analysis.

3. Results and Discussion

3.1. Interaction Energy of γ–FeOOH/CSH Interface

Interaction energy refers to the energy generated between molecules or atoms due to the interaction of various force fields (such as van der Waals forces, Coulomb forces, hydrogen bonds, etc.), and it is an important physical quantity that describes the strength of the interaction between molecules. To investigate interfacial adhesion properties of γ–FeOOH/CSH systems with varying Ca/Si ratios of 1.3, 1.5, 1.7, and 2.0, the unit area interaction energies between different components were calculated, using the following equation. The computational results are presented and analyzed below.

$$E_{1/2} = \frac{E_{total} - (E_1 + E_2)}{A_{1/2}} \quad (1)$$

where $E_{1/2}$ denotes the interaction energy per unit area between components 1 and 2; E_{total} is the total energy of the system containing both components; E_1 and E_2 are the individual energies of components 1 and 2, respectively, and $A_{1/2}$ represents the cross-sectional area between components 1 and 2. The calculated interaction energies are shown in Figure 2.

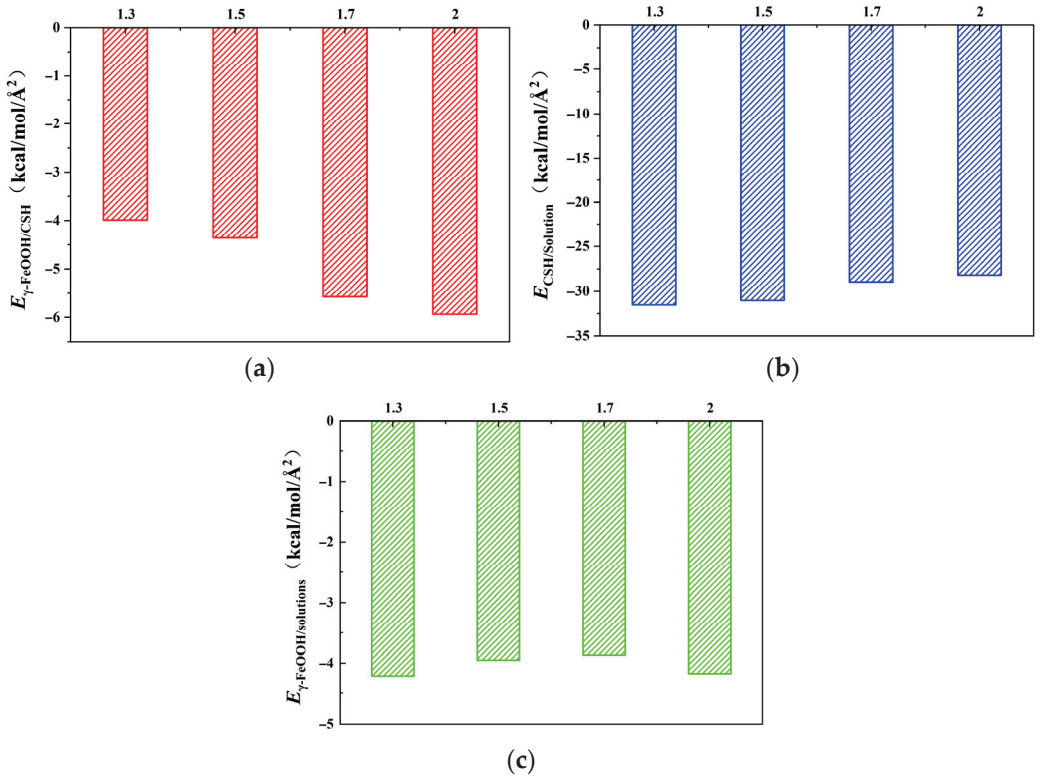

Figure 2. Interaction energy per unit contact area between different components. (**a**) γ–FeOOH and CSH; (**b**) CSH and solutions; (**c**) γ–FeOOH and solutions.

With the change of Ca/Si ratios, the interaction energies between each pair of components (γ–FeOOH/CSH, CSH/NaCl + Na_2SO_4 composite solution, and γ–FeOOH/solution) all exhibited a certain variation pattern. $E_{\gamma\text{–FeOOH/CSH}}$ exhibited a gradual increase with increasing Ca/Si ratioe. When Ca/Si = 1.3, $E_{\gamma\text{–FeOOH/CSH}}$ reached its minimum value of −3.987 kcal/mol·Å^2. The negative value indicates mutual attraction between the two components. $E_{\gamma\text{–FeOOH/CSH}}$ increased by 9.22%, 39.8%, and 48.7%, respectively, with increasing Ca/Si ratios. When Ca/Si = 2.0, $E_{\gamma\text{–FeOOH/CSH}}$ reached a maximum of $E_{\text{CSH/solutions}}$ = −5.937 kcal/mol/Å^2. Conversely, $E_{\text{CSH/solutions}}$ showed an opposite trend, with the maximum value of $E_{\text{CSH/solutions}}$ = −31.537 kcal/mol·Å^2 observed at Ca/Si = 1.3. As the Ca/Si ratio increased, $E_{\text{CSH/solutions}}$ decreased by 1.56%, 8.15%, and 10.63%, respectively. $E_{\gamma\text{–FeOOH/solutions}}$ remained relatively stable across different Ca/Si ratios, with values of −4.211, −3.952, −3.867, and −4.174 kcal/mol·Å^2, indicating that structural variations in CSH had negligible effects on the interaction between γ–FeOOH and the corrosive solution.

The results above suggest that lower Ca/Si ratios in CSH promote stronger interactions with the NaCl + Na_2SO_4 composite solution, leading to increased adsorption of solution molecules on the CSH surface. This adsorption forms a solution barrier that hinders direct bonding between CSH and γ–FeOOH, consequently weakening their interfacial interaction [42,43]. In contrast, higher Ca/Si ratios facilitate stronger direct bonding between CSH and γ–FeOOH by reducing solution adsorption effects.

From the perspective of energy, the stronger attraction between CSH and γ–FeOOH in Figure 2a promotes direct bonding at higher Ca/Si ratios, creating a denser interfacial zone that physically obstructs the penetration of water and ions. The energy barrier for solution molecules to disrupt this bonded interface is elevated, thereby reducing transport. In Figure 2b, fewer solution molecules are adsorbed at higher Ca/Si ratios, diminishing the formation of a solution "barrier layer" near the interface. Consequently, the competitive

effect of solution adsorption on CSH–γ–FeOOH bonding is suppressed, further favoring the direct CSH–γ–FeOOH interface. In Figure 2c, the near-constant $E_{\gamma\text{–FeOOH/solutions}}$ values across Ca/Si ratios confirm that changes in transport properties are primarily governed by CSH's structural evolution rather than γ–FeOOH's affinity for the solution.

3.2. The Influence of Water Molecules on the Interfacial Adhesion Performance

The observed significant differences in interaction energy at γ–FeOOH/CSH interfaces with varying Ca/Si ratios under the same solution environment conditions warrant further mechanistic investigation. To elucidate the role of Ca/Si ratio in interfacial adhesion, CSH structures with different Ca/Si ratios were systematically analyzed through calculating the radial distribution function (RDF), coordination number (CN), and the number of hydrogen bond of Ca^{2+} ions and hydroxyl groups (O_h and H_o) in the exposed area of the CSH surface with water molecules in solution, and analyzing the bonding interactions of each component.

Firstly, the RDF and CN of Ca^{2+} ions on the surface of CSH among the oxygen atoms (O_{Water}) in water molecules, the hydroxyl oxygen atoms in CSH, and oxygen atoms (O_h and O_s) in silicon chains were calculated, respectively. The bonding differences of Ca^{2+} ions in the free regions of CSH structure surface under different Ca/Si ratios were characterized. The RDF curves between Ca_{CSH} and O_{water} under four different Ca/Si ratios revealed distinct bonding patterns, as shown in Figure 3a. A primary peak appeared at 2.45 Å in RDF curve, indicating that free Ca^{2+} ions on the CSH surface had a strong attraction effect on water molecules in the solution [44]. RDF peak intensities of Ca_{CSH}–O_{water} decreased gradually from 8.688, 7.903, 6.288 to 5.315 as the Ca/Si ratio increased from 1.3, 1.5, 1.7 to 2.0. It denoted that the adsorption of Ca^{2+} ions on water molecules was weakened at higher Ca/Si ratios, consistent with the variation trend of $E_{CSH/solutions}$ mentioned in Section 3.1. In addition, a secondary peak appeared at 4.55–4.95 Å near the primary peak of RDF curve, which demonstrates preserved long-range spatial correlations between Ca^{2+} ions and O_{water} regardless of Ca/Si ratio variations.

To quantitatively characterize the Ca_{CSH}–O_{water} ionic bonding under varying Ca/Si ratios, the corresponding coordination numbers (CN) based on the RDF results were calculated (Figure 3b). The temporal evolution of CN values reveals the following distinct phases. When t = 0~800 ps, the CN value of Ca_{CSH}–O_{water} ion pairs exhibited a monotonic increase, indicating hydration of surface Ca^{2+} ions progressively occurred. During the simulation process, the free Ca^{2+} ions on the surface of CSH gradually absorbed water molecules and form Ca_{CSH}–O_{water} ionic bonds with water. When t > 800 ps, the increase rate of the Ca_{CSH}–O_{water} CN value slowed down, reflecting the equilibrium state of the combination of CSH and water molecules in the solution. The four types of CSH with different Ca/Si ratios were compared. With the increase in the Ca/Si ratio, the CN value of Ca_{CSH}–O_{water} gradually decreased, indicating that the surface free Ca^{2+} ions of the CSH structure with a high Ca/Si ratio had a weaker attraction to water, and the most pronounced reduction occurred when Ca/Si exceeded 1.5.

Although the variation trend of Ca_{CSH}–O_{water} exhibits a certain regularity, analysis of the original structural models of CSH with different Ca/Si ratios reveals that the higher Ca/Si ratios correspond to more hydroxyl groups in the structure. Therefore, in addition to bonding with oxygen atoms in the solution, the interaction between free Ca^{2+} ions on CSH surface and hydroxyl oxygen atoms (O_h) within CSH warrants investigation. The RDF curve of Ca_{CSH}–O_h was calculated; results are presented in Figure 3c. The primary peak for CSH appeared at 2.35 Å with different Ca/Si ratios and was more pronounced than the corresponding RDF peak of Ca_{CSH}–O_{water}. This indicates that Ca^{2+} ions preferentially form Ca_{CSH}–O_h ionic bonds with O_h atoms rather than Ca_{CSH}–O_{water} bonds with water

molecules. The CN values of Ca_{CSH}–O_h are shown in Figure 3d. CSH with a higher Ca/Si ratio formed more Ca_{CSH}–O_h ion pairs. During the simulation, as water molecules accumulated towards the CSH surface, the number of Ca_{CSH}–O_h ion pairs decreased slightly. When the Ca/Si ratio was the same, the CN values of Ca_{CSH}–O_h consistently exceeded those of Ca_{CSH}–O_{water}, indicating that Ca^{2+} ions were predominantly coordinated by O_h rather than O_{water}. This preference suggests stronger interactions between Ca^{2+} ions and hydroxyl groups compared to water molecules in the CSH system.

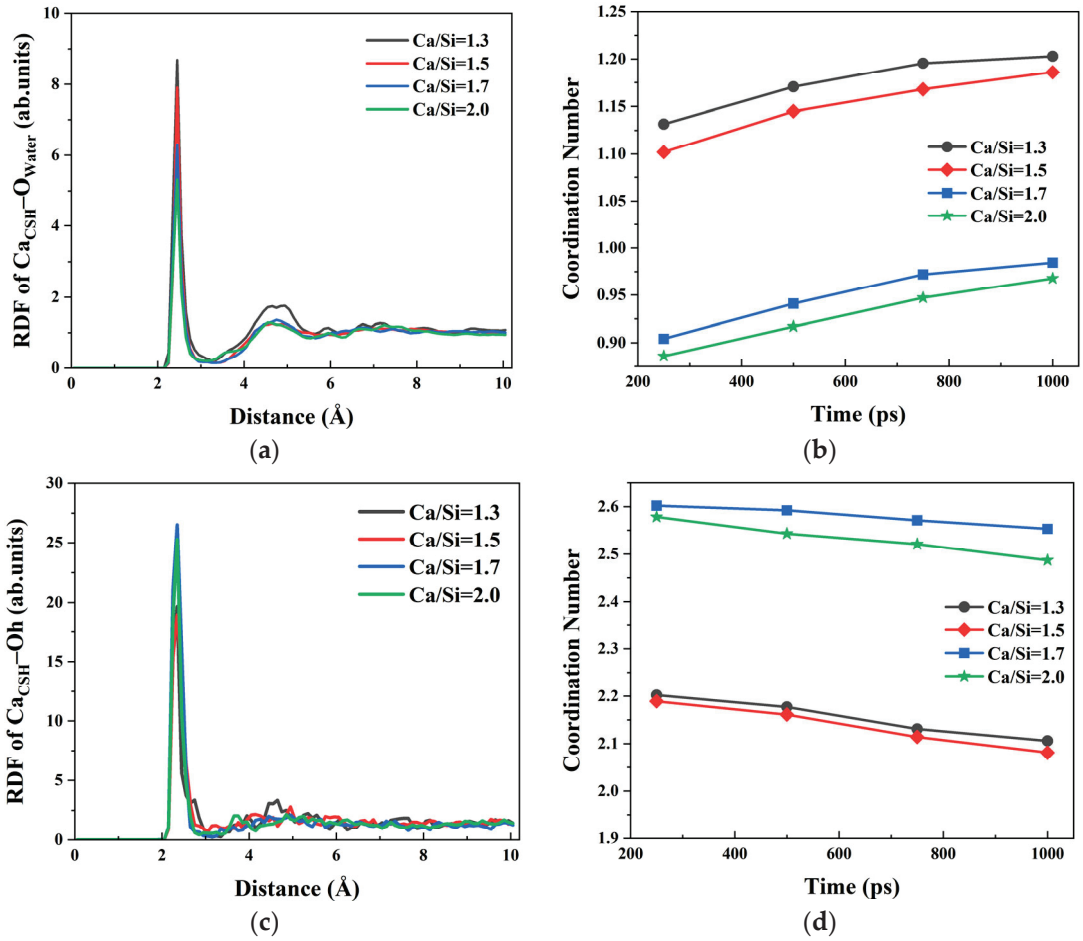

Figure 3. The RDF and CN between Ca^{2+} ions on the CSH surface and O atoms. (**a**) RDF of Ca_{CSH}–O_{water}; (**b**) CN of Ca_{CSH}–O_{water}; (**c**) RDF of Ca_{CSH}–O_h; (**d**) CN of Ca_{CSH}–O_h.

Furthermore, as the Ca/Si ratio of CSH decreased, the number of silicon oxygen tetrahedra in the structure increased, enhancing the likelihood of Ca^{2+} ions bonding with bridging oxygen atoms (O_s) in the tetrahedra, thereby impeding the formation of Ca_{CSH}–O_{water} ion pairs. The RDF curves of Ca_{CSH}–O_s shown in Figure 4a exhibit a consistent peak at 2.35 Å across all Ca/Si ratios, indicating a stable bonding distance between Ca^{2+} and O_s atoms. Notably, lower Ca/Si ratios yield higher RDF peak intensities, denoting that Ca^{2+} preferentially coordinates with O_s in CSH structures with more silicon oxygen tetrahedra. The CN numbers of the Ca_{CSH}–O_s analysis at different simulation time points in Figure 4b reveal a parallel trend between Ca_{CSH}–O_s and Ca_{CSH}–O_h, suggesting that the accumulation of water molecules on the CSH surface not only competes with O_h but also partially occupies the coordination sites of Ca_{CSH}–O_s ion pairs.

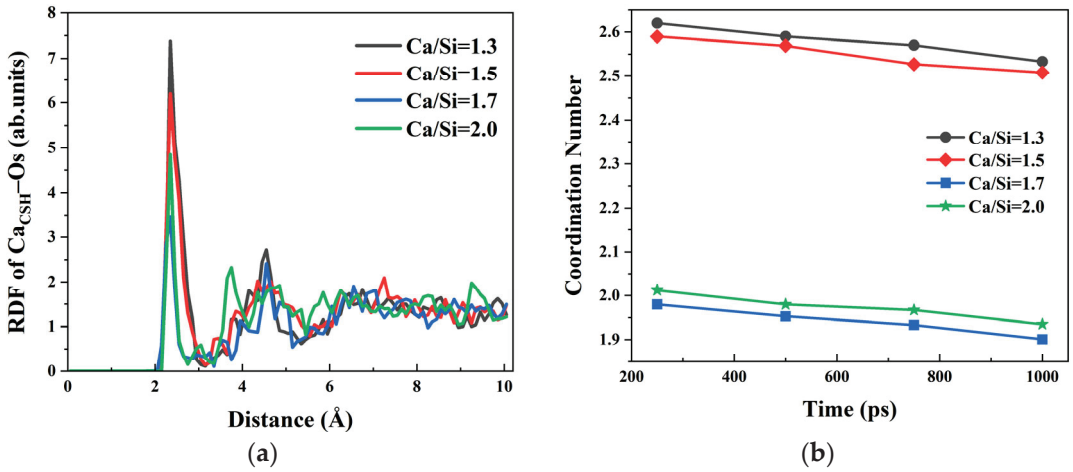

Figure 4. The RDF and CN between Ca^{2+} ions on the CSH surface and O_s: (**a**) RDF of Ca_{CSH}–O_s; (**b**) CN of Ca_{CSH}–O_s.

Based on the results mentioned above, the relative strength of ionic bonding between Ca^{2+} ions and the three oxygen species follows the order: Ca_{CSH}–O_h > Ca_{CSH}–O_s > Ca_{CSH}–O_{water}. However, the variation trends of RDF peak intensities with Ca/Si ratio exhibit inconsistencies between Ca_{CSH}–O_s and Ca_{CSH}–O_h systems. Specifically, in the Ca_{CSH}–O_h RDF profile, the peak intensity for Ca/Si = 2.0 is lower than that for Ca/Si = 1.7, while in the Ca_{CSH}–O_s system, the peak intensity is 4.851 at Ca/Si = 2.0, which significantly exceeds the intensify of 3.466 at Ca/Si = 1.7. This apparent discrepancy primarily stems from distinct spatial configurations and distributions of silicon oxygen tetrahedra on CSH surfaces with different Ca/Si ratios. In the Ca/Si = 2.0 CSH structure, the silicon chain network adopts a more dispersed arrangement, which facilitates more migration of free Ca^{2+} ions into the structural interlayers, particularly into the first layer. Furthermore, Ca^{2+} ions in the first layer demonstrate preferential coordination with O_s atoms, while Ca^{2+} ions in the second layer exhibit stronger affinity for O_h groups.

By analyzing the bonding interactions between Ca^{2+} ions in the free zone of CSH surface and oxygen atoms in other components, it was found that the crystal structure of CSH with varying Ca/Si ratios influenced the distribution of Ca^{2+} ions. As a result, it subsequently altered the hydration behavior of free Ca^{2+} ions on the CSH surface and ultimately led to differences in the adhesion performance between CSH and γ–FeOOH.

The results demonstrate that free Ca^{2+} ions on the surface of CSH with high Ca/Si ratio form fewer bonds with water molecules in the solution. Ca^{2+} ions preferentially interact with the free hydroxyl groups on the surface of CSH to form Ca_{CSH}–O_h bonds. During the simulation progress, the free Ca_{CSH}–O_h bonds exhibited higher mobility toward the surface of γ–FeOOH and formed O_h–Ca_{CSH}–$O_{\gamma\text{–FeOOH}}$ with it, thereby effectively reducing the inhibitory effect of water molecules on the interfacial interaction between CSH and γ–FeOOH.

In addition to the free Ca^{2+} ions, the exposed hydroxyl groups (H_{CSH} and O_{CSH}) on the CSH surface with different Ca/Si ratios also formed chemical bonds with other components, thereby influencing the interfacial interaction between CSH and γ–FeOOH. The RDF curves between surface hydroxyl groups of CSH with different Ca/Si ratios and water molecules in the solution are shown in Figure 5. As illustrated in Figure 5a, the first peak of of H_{CSH}–O_{water} in RDF appeared at 1.95 Å, followed by a second peak at 3.15 Å. Meanwhile, Figure 5b shows that O_{CSH}–H_{water} in RDF had its first peak at 1.65 Å and a second peak at 3.05 Å. The positions of the first peaks of both H_{CSH}–O_{water} and O_{CSH}–H_{water}, the most probable distance between the two atoms, are shorter than the

typical hydrogen bond length (2.45 Å), indicating that CSH can act as both a hydrogen bond donor and acceptor with water molecules in solutions of varying Ca/Si ratios.

Comparing CSH with different Ca/Si ratios, the peak intensities of H_{CSH}–O_{water} and O_{CSH}–H_{water} in RDF curves gradually increase with the decrease in Ca/Si ratio, suggesting stronger hydrogen bonding interactions between CSH with low–Ca/Si ratios and water molecules. For example, in O_{CSH}–H_{water} RDF curves, as the Ca/Si ratio increases from 1.3, 1.5, 1.7 to 2.0, the peak values decrease from 1.187, 1.075, 0.781 to 0.641, respectively. This trend demonstrates that a lower Ca/Si ratio enhances the hydrogen bond strength between CSH and water molecules.

Since the H_{CSH} and O_{CSH} groups on CSH surface preferentially form hydrogen bonds with O_{water} and H_{water} (H_{CSH}–O_{water} and O_{CSH}–H_{water}), the coordination sites that could originally bind to hydroxyl groups on the γ–FeOOH surface are occupied by water molecules. Consequently, the number and strength of hydrogen bonds (H_{CSH}–$O_{γ–FeOOH}$ and O_{CSH}–$H_{γ–FeOOH}$) formed between CSH and γ–FeOOH are significantly reduced.

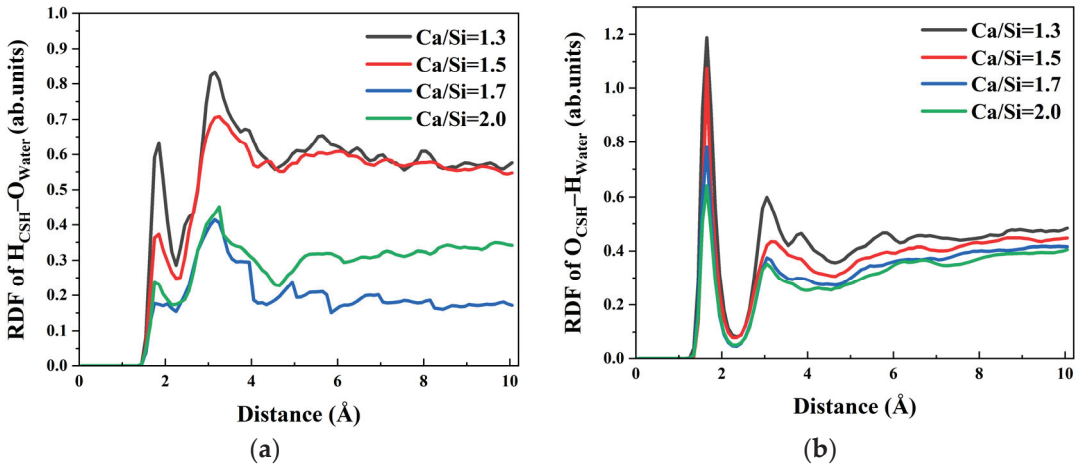

Figure 5. The RDF of H_{CSH}–O_{water} andO_{CSH}–H_{water}: (**a**) RDF of H_{CSH}–O_{water}; (**b**) RDF of O_{CSH}–H_{water}.

In summary, CSH with varying Ca/Si ratios forms Ca_{CSH}–O_{water} ionic bonds and hydrogen bonds (H_{CSH}–O_{water} and O_{CSH}–H_{water}) with water molecules in solution. These bonding interactions occupy the coordination sites on the CSH surface, thereby weakening the interfacial interaction between γ–FeOOH and CSH. The comparative analysis of the RDF peak values for Ca_{CSH}–O_{water}, H_{CSH}–O_{water}, and O_{CSH}–H_{water} under different Ca/Si ratios reveals an increasing trend in peak intensity with decreasing Ca/Si ratio. This phenomenon indicates that CSH with lower Ca/Si ratios exhibits stronger binding with water molecules, which more effectively inhibits the interfacial interaction between γ–FeOOH and CSH. Consequently, this competitive bonding mechanism ultimately leads to the deterioration of bonding performance at the γ–FeOOH/CSH interface.

3.3. The Influence of Erosive Ions on the Interfacial Adhesion Performance

In the molecular dynamics simulation of γ–FeOOH/CSH interfacial bonding under varying Ca/Si ratios, NaCl + Na_2SO_4 composite solution was employed to simulate the external corrosive environment. Beyond examining the interaction between water molecules and CSH with four distinct Ca/Si ratios, the effects of Na^+, Cl^-, and SO_4^{2-} ions on interfacial bonding performance were systematically investigated. This section elucidates the degradation mechanisms induced by each ionic from a microscopic perspective.

Notably, Na^+ ions tend to accumulate on the CSH surface, promoting water molecule ingress into the CSH matrix. However, the adsorption characteristics under varying CSH

crystal structures induced by different Ca/Si ratios require further exploration. Through the RDF results of Na–O_{water} at γ–FeOOH/CSH interfaces with different Ca/Si ratios, as shown in Figure 6a, the influence of Na^+ ions on the interaction of γ–FeOOH/CSH interface with different Ca/Si ratios was evaluated. The RDF profiles exhibit a pronounced peak at 2.35 Å across all four Ca/Si ratios, indicating persistent strong Na^+–water interactions regardless of CSH composition. This peak corresponds to a well-defined hydration shell where water molecules coordinate Na^+ ions at this characteristic distance. Moreover, the peak intensity demonstrates an inverse relationship with Ca/Si ratio, revealing that higher Ca/Si ratios in CSH attenuate the secondary hydration effects of Na^+ ions in solution.

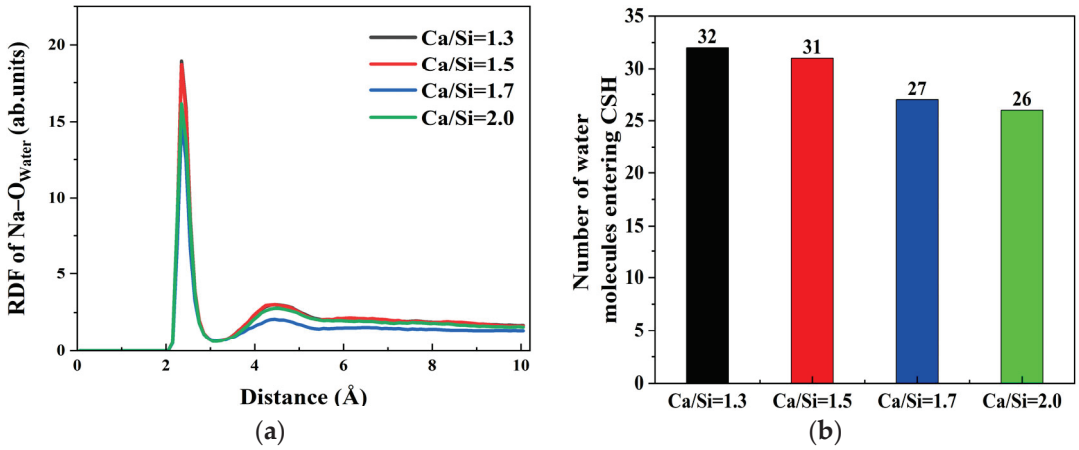

Figure 6. The attraction mechanism of Na^+ ions to water molecules: (**a**) RDF of Na–O_{water}; (**b**) number of water molecules entering CSH.

This trend is further corroborated by Figure 6b, demonstrating an inverse correlation between Ca/Si ratio and water molecule penetration into the CSH surface. Quantitative analysis reveals that at Ca/Si = 2.0, approximately 26 water molecules access the CSH surface, while this number increases to 32 when Ca/Si decreases to 1.3. The findings prove that Ca/Si ratio modulates the hydration capability of Na^+ ions. Higher Ca/Si ratios attenuate the hydration strength of surface Na^+ ions, consequently reducing the possibility of water molecules bonding with CSH. The phenomenon promotes the migration of free Ca^{2+} ions and hydroxyl groups (O_h and H_o) from CSH to γ–FeOOH surfaces for interfacial bonding. Ultimately, CSH with elevated Ca/Si ratios exhibits weaker solution interactions but stronger interfacial bonding with γ–FeOOH.

In addition to Na^+ ions, the interfacial behavior of Cl^- and SO_4^{2-} anions at varying Ca/Si ratios warrants systematic investigation. Owing to electrostatic attraction, Cl^- ions form Ca_{CSH}–Cl ionic bonds with Ca^{2+} ions in the free zone of CSH surface. To elucidate the effect of Ca/Si ratios on these interactions, RDF curves of Ca_{CSH}–Cl were calculated across four Ca/Si ratios in Figure 7. The results reveal significant Ca/Si–dependent variations in bond characteristics. When Ca/Si = 1.3, 1.5, and 1.7, the peak position of RDF gradually increases from 2.95 Å, 3.45 Å to 4.95 Å. When Ca/Si = 2.0, no distinct peak appears. The peak position represents the distance of interaction between Ca^{2+} ions on the CSH surface and Cl^- ions in the solution. Therefore, when Ca/Si = 1.3, Cl^- ions aggregate at a distance of 2.95 Å around Ca^{2+} ions. As the Ca/Si ratio increases, Cl^- ions gradually aggregate at farther positions on the CSH surface until there is no significant aggregation. Peak intensity attenuates with increasing Ca/Si ratio, indicating that the bonding quantity and strength of the two ions gradually weaken. It can be concluded that lower Ca/Si ratios promote Cl^- coordinate to surface Ca^{2+} ions, while higher ratios progressively weaken this interaction.

Consequently, CSH surfaces with high Ca/Si ratio exhibit reduced Cl^- binding probability, liberating more Ca^{2+} ions for γ–FeOOH interfacial bonding.

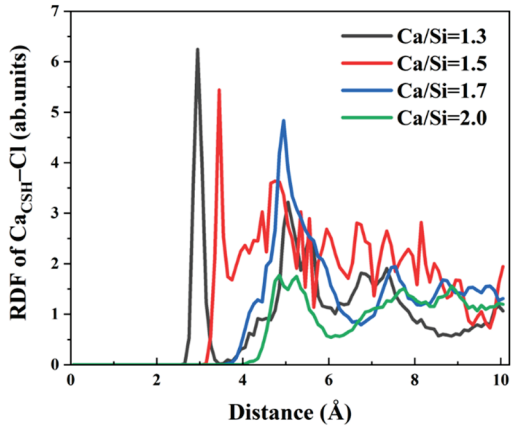

Figure 7. RDF of Ca_{CSH}–Cl.

The chemical bonding mechanisms differ between Cl^- and SO_4^{2-} ions. Each SO_4^{2-} anion possesses four oxygen atoms, providing four potential coordination sites for hydrogen bond formation with CSH. To elucidate the influence of varying Ca/Si ratios on the hydrogen bonds formation between SO_4^{2-} and CSH, RDFs between O_{SO4} and H_{CSH} were analyzed, as presented in Figure 8. The key observations include the following points. Firstly, all Ca/Si ratios exhibit a distinct H_{CSH}–O_{SO4} RDF peak at 1.85 Å, well within the typical hydrogen bonding distance threshold of 2.45 Å, confirming strong hydrogen bonding interactions. Secondly, comparative analysis reveals significantly higher peak intensities at lower Ca/Si ratios (1.3 and 1.5) compared to higher ratios (1.7 and 2.0), demonstrating that high Ca/Si ratios suppress H_{CSH}–O_{SO4} hydrogen bond formation. It is hard for hydrogen atoms on a CSH surface with a high Ca/Si ratio to bind to SO_4^{2-} ions in solution and form hydrogen bonds. Thirdly, the suppression effect above liberates more H_{CSH} sites for interfacial bonding with γ–FeOOH, facilitating the formation of stronger H_{CSH}–$O_{γ–FeOOH}$ hydrogen bonds that enhance overall CSH/γ–FeOOH interaction energy.

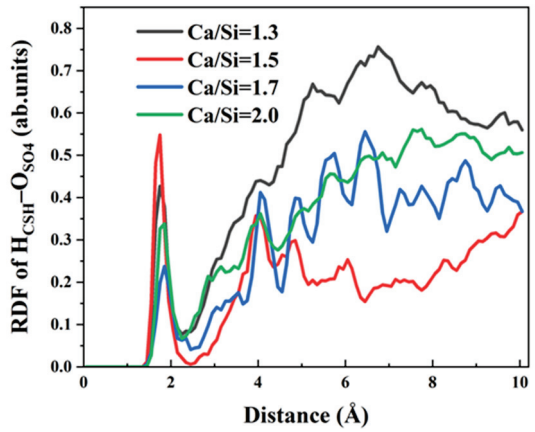

Figure 8. RDF of H_{CSH}–O_{SO4}.

3.4. Transport Behaviour of Solutions in Pores with Varying Ca/Si Ratios

While the interfacial bonding behavior between CSH and γ–FeOOH elucidates the structural characteristics, the ion transport within the nanopore further reflects its dynamic functional performance. Figure 9 presents capillary transport snapshots of NaCl + Na_2SO_4 solution in CSH/γ–FeOOH nanopores with varying Ca/Si ratios of 1.3, 1.5, 1.7, and 2.0 when the simulation time t = 2000 ps [45]. From the aspect of the water transport dynamics,

it is observed that complete surface coverage by water molecules occurs across all Ca/Si ratios, which indicates that strong hydrophilic attraction from CSH substrates with varying Ca/Si ratios drives water molecules' migration. However, the specific impact of CSH with varying Ca/Si ratios on the transport velocity of water molecules still requires further investigation. Compared with water molecules, the movement velocity of Na^+, Cl^-, and SO_4^{2-} ions is much slower. This indicates that ion transport is partially dependent on water molecular driving force to move forward. Differences in ion invasion depths are also apparent. When CSH Ca/Si ratio = 1.3, 1.5, and 1.7, they occupy about 75% of the entire pore length. When CSH Ca/Si ratio increases to 2.0, the ion invasion depth decreases to about 70% of the entire pore. In terms of the interfacial distribution, ions showed pronounced ion accumulation preference for CSH over γ–FeOOH interfaces. Particularly, SO_4^{2-} exhibits significant clustering behavior, forming multiple large ion clusters and adsorbing on the CSH surface. The phenomena above indicate that the transport mechanism not only involves the diffusion of the solution itself, but is also affected by the matrix interface interaction, and the interaction with CSH is stronger than that with γ–FeOOH.

The preceding analysis demonstrates that variations in CSH crystal structure induced by different Ca/Si ratios influence the transport behavior of NaCl + Na_2SO_4 composite solution within the nanopores. To quantitatively characterize the transport differences, the temporal evolution of penetration depths for water molecules and ions (Na^+, Cl^-, and SO_4^{2-}) along the pore surfaces was systematically recorded. Considering the invariant structure of γ–FeOOH substrates and their negligible ion adsorption capacity, the capillary transport behavior was quantified by analyzing ion penetration profiles along CSH surfaces with varying Ca/Si ratios.

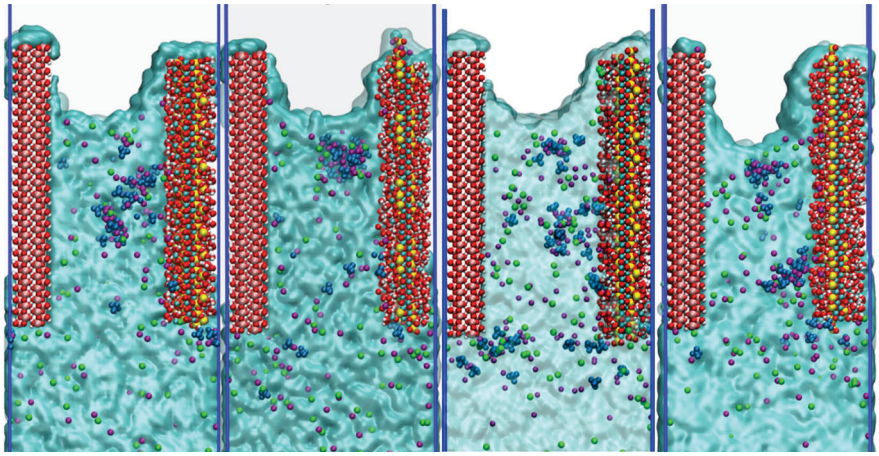

Figure 9. Snapshot of transport of solution in pores with different Ca/Si at 2000 ps.

The penetration depth profiles of water molecules on CSH surfaces with different Ca/Si ratios is presented in Figure 10a. Complete surface coverage was achieved by t = 100 ps in all cases. It was observed that the higher the Ca/Si ratio, the smaller the penetration depth of water molecules on the CSH surface. When t = 75 ps, the measured penetration depths were 84 Å, 82 Å, 78 Å, and 75 Å for CSH Ca/Si ratios of 1.3, 1.5, 1.7, and 2.0, respectively. The decrease in the penetration depth with the increase in the Ca/Si ratio indicates that in systems with a high Ca/Si ratio, the interaction at the water–CSH interface weakens, resulting in the slow transport of water molecules.

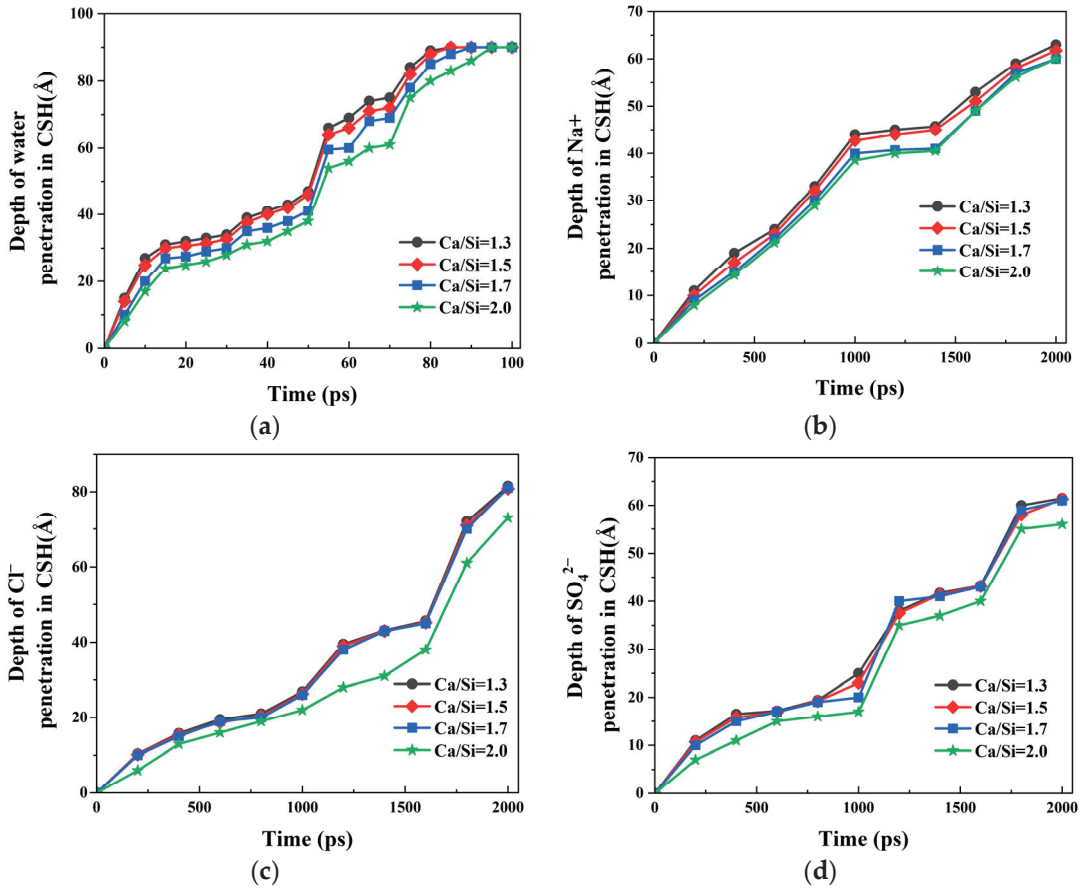

Figure 10. Depth of invasion along the surface of CSH: (**a**) water; (**b**) Na^+; (**c**) Cl^-; (**d**) SO_4^{2-}.

Figure 10b–d illustrate the penetration depths of Na^+, Cl^-, and SO_4^{2-} ions on CSH surfaces with varying Ca/Si ratios. It can be concluded that all ions exhibit significantly shallower penetration than water molecules at all timepoints, confirming preserved transport asynchronicity regardless of Ca/Si ratio variations. The ion penetration depths on the CSH surface keep decreasing as Ca/Si ratios increases. Compared with Na^+ ions, Cl^- and SO_4^{2-} show greater Ca/Si ratio dependence, particularly when Ca/Si = 2.0 where divergence was most significant. Quantitative analysis of the data at t = 1600 ps reveals that when t = 1600 ps, the penetration depth of Na^+ ions on CSH interface with Ca/Si = 1.3 was measured to be 53 Å. When the Ca/Si ratio increased to 2.0, the penetration depth decreased by 7.54%. Under identical conditions, Cl^- ions exhibited a more substantial reduction in penetration depth by 16.66%. These results demonstrate that increasing the Ca/Si ratio of CSH induces selective ion filtration, with enhanced filtration efficiency observed for Cl^- and SO_4^{2-} ions compared to Na^+ ions at Ca/Si = 2.0. The differential filtration effects suggest that the interfacial interactions are strongly influenced by both ionic charge and hydration characteristics [46,47].

The results presented in Figure 10c demonstrate that the penetration rate of Cl^- ions is significantly reduced in CSH nanochannels with higher Ca/Si ratios, indicating an accumulation and prolonged retention of chloride ions within the nanopore. This observation is in good agreement with the experimental findings reported by Zhou et al. [22]. Through systematic experimental investigations, Zhou examined the transport and adsorption behaviors of water molecules, Ca^{2+} ions, and Cl^- ions in CSH nanochannels with varying Ca/Si ratios. Their immersion tests clearly showed that CSH specimens with higher Ca/Si ratios exhibit enhanced chloride ion adsorption capacity.

The NaCl + Na_2SO_4 composite solution exhibited significantly different transport behaviors in the γ–FeOOH/CSH nanopores with four different Ca/Si ratios. This correlation suggests that structural modifications in CSH directly influence both the quantity and strength of interfacial bonds formed with water molecules and ions. The results showed that systems with higher Ca/Si ratios demonstrated significantly reduced transport rates for both aqueous and ionic components. Although these observations clearly establish the Ca/Si ratio as a critical regulator of transport phenomena, the precise molecular-scale bonding mechanisms responsible for the blocking effect require further investigation.

3.5. Differences in Bonding Between Solutions and CSH with Different Ca/Si

In order to elucidate the influence mechanism of CSH with different Ca/Si ratios on solution transport behaviour, the RDFs between Ca^{2+} ions and hydroxyl groups (O_h and H_o) in the exposed regions of CSH surface and the surrounding solution were assessed. Initial investigation focused on water–CSH interactions across different Ca/Si ratios. The RDF curves of O_{water}–Ca_{CSH} under four different Ca/Si ratios were shown in Figure 11a, revealing a characteristic first peak at 2.45 Å. The peak position confirms strong chemical bonding between O_{water} and Ca^{2+} ions on CSH surfaces with varying Ca/Si. This bonding is also one of the primary driving forces for promoting the forward transport of water molecules within γ–FeOOH/CSH pores.

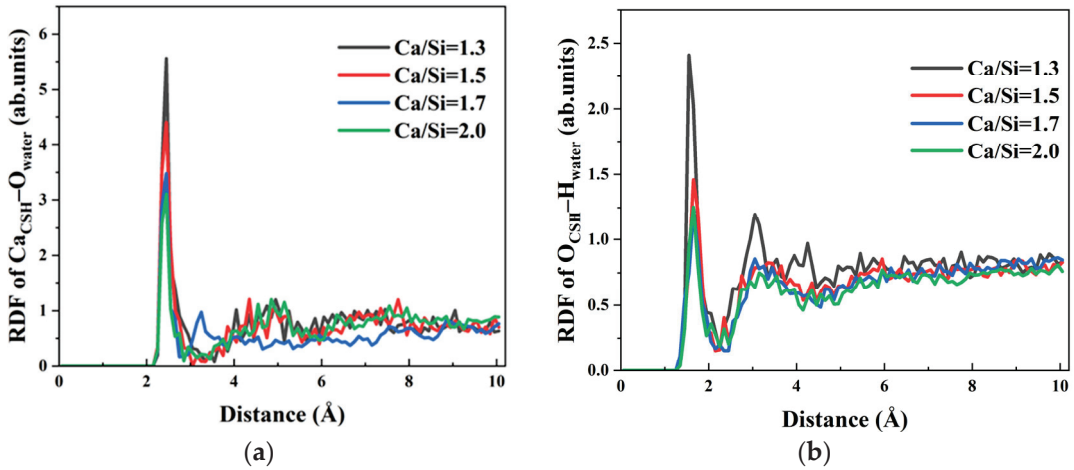

Figure 11. RDF curve of Ca_{CSH}–O_{water} and O_{CSH}–H_{water}: (**a**) RDF of Ca_{CSH}–O_{water}; (**b**) RDF of O_{CSH}–H_{water}.

The peak intensity showed a progressive decrease from 5.558, 4.401, 3.478 to 3.10 as the Ca/Si ratio increased from 1.3 to 2.0. This indicates that the CSH structure with higher Ca/Si ratio attenuated both the quantity and strength of chemical bonds between Ca^{2+} ions on the surface and water molecules, consequently weakening the water–CSH interfacial attraction. The observed RDF variations originate fundamentally from structural differences in the initial CSH models. Specifically, CSH with higher Ca/Si ratios contains more hydroxyl groups within its molecular structure. The hydroxyl oxygen atoms (O_h) in CSH preferentially occupy coordination sites of Ca^{2+} ions, forming stable Ca_{CSH}–O_h ion pairs. When water molecules in the solution approach the CSH surface, the number of free Ca^{2+} ions that can bond with O_{water} on the surface is reduced, thereby decreasing Ca_{CSH}–O_{water} interactions.

Hydroxyl groups on CSH surfaces additionally participate in hydrogen bonding with water molecules, constituting another significant driving force for aqueous transport. The RDF curves of O_{CSH}–H_{water} under varying Ca/Si ratios were calculated, as shown in Figure 11b. The first peak positions of the curves are distributed in the range of

1.55 Å~1.65 Å, which is shorter than the characteristic hydrogen bond distance of 2.45 Å. This indicates that CSH forms hydrogen bonds with water molecules in solution under all Ca/Si ratios. The Ca/Si ratio of CSH increases with the gradual RDF peak reduction in O_{CSH}–H_{water}, indicating a progressive weakening of hydrogen bond strength with increasing Ca/Si ratio. Particularly, when Ca/Si = 1.3, it exhibits much higher hydrogen bonding capacity compared to high Ca/Si ratio structure. Specifically speaking, peak intensity attenuates by 39.87%, 48.15%, and 49.73% with Ca/Si ratio increases from 1.3, 1.5, 1.7 to 2.0, respectively.

The analysis demonstrates that CSH with varying Ca/Si ratios facilitates water molecule transport through formation of Ca_{CSH}–O_{water} and O_{CSH}–H_{water} bonds, enabling complete substrate surface coverage by water. However, increasing Ca/Si ratio modifies the CSH crystal structure, leading to the strength weakening of Ca_{CSH}–O_{water} and O_{CSH}–H_{water} bonds formed on surface free regions. This attenuation reduces the driving force for water molecule transport, ultimately resulting in decreased penetration depths observed for high Ca/Si ratio CSH surfaces at equivalent timepoints.

Ion transport within the capillary system derives partially from the driving effect of water molecules. RDF analysis of Na–O_{water}, Cl–O_{water}, and S–O_{water} interactions in Figure 12 reveals that the first peaks appear at 2.35 Å, 3.15 Å, and 3.65 Å, respectively, confirming strong hydration effects for all ions across different Ca/Si ratios, while Na–O_{water} and Cl–O_{water} interactions show minimal Ca/Si ratio dependence, S–O_{water} bonding exhibits significant sensitivity. Specifically, the hydration of SO_4^{2-} remains consistent when Ca/Si ratios = 1.3, 1.5, and 1.7, but shows marked weakening at Ca/Si = 2.0 as evidenced by reduced RDF peak intensity. The decreased S–O_{water} interaction directly correlates with the observed block of SO_4^{2-} transport in systems with high Ca/Si ratio.

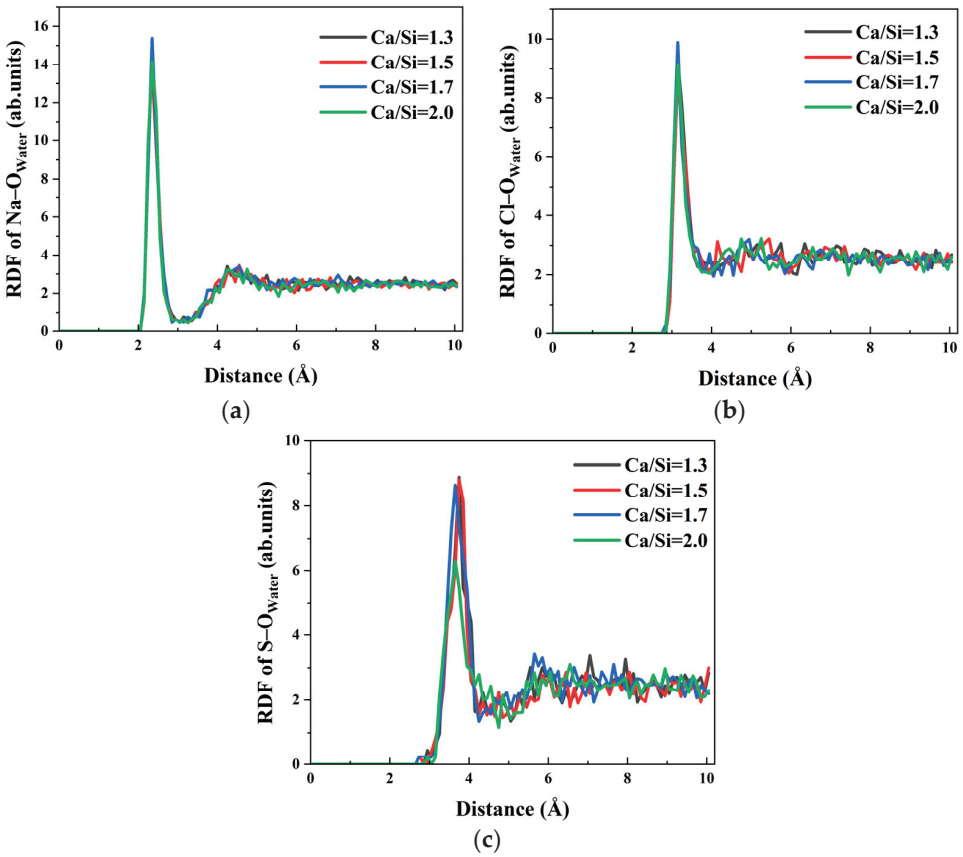

Figure 12. RDF of water molecules and ions in solution: (**a**) RDF of Na–O_{water}; (**b**) RDF of Cl–O_{water}. (**c**) RDF of S–O_{water}.

In addition to the water–ion bonding cooperation that facilitates ions transport through the pores, ion adsorption by the matrix on both interfaces of the pores promotes the continuous transport of ions. Given the invariant γ–FeOOH crystal structure with all Ca/Si ratio models and Na^+, Cl^-, and SO_4^{2-} ions, ions tend to accumulate on CSH surfaces. As demonstrated in Section 3.4, the difference in ion adsorption primarily stems from variations in CSH–ion bonding characteristics.

RDF analysis of Na–O_{CSH}, Cl–O_{CSH}, and S–O_{CSH} interactions in Figure 13 reveals continuous attenuation of peak intensities with increasing Ca/Si ratios. This trend indicates progressively weaker bonding between various ions in the solution and the available surface sites (free hydroxyl groups and Ca^{2+} ions) on CSH with high Ca/Si ratio. Notably, while the first peak in Na–O_{CSH} RDF remains constant at 2.25 Å at all Ca/Si ratios, both Cl–O_{CSH} and S–O_{CSH} exhibit significant Ca/Si–dependent peak shifts. Specifically, when Ca/Si ratios = 1.3, 1.5 and 1.7, the first peaks of Cl–O_{CSH} and S–O_{CSH} appear at 0.85 Å and 3.05 Å, respectively. When Ca/Si ratio = 2.0, the peak positions shift outward to 2.45 Å and 3.65 Å. The substantial increase in equilibrium bonding distances, coupled with reduced peak intensities, confirms weakened Cl–O_{CSH} and S–O_{CSH} interactions at high Ca/Si ratios. The phenomenon correlates with the penetration depth results in Figure 10, explaining the enhanced filtration effect of Cl^- and SO_4^{2-} ions observed at Ca/Si = 2.0 through weakened interfacial bondings.

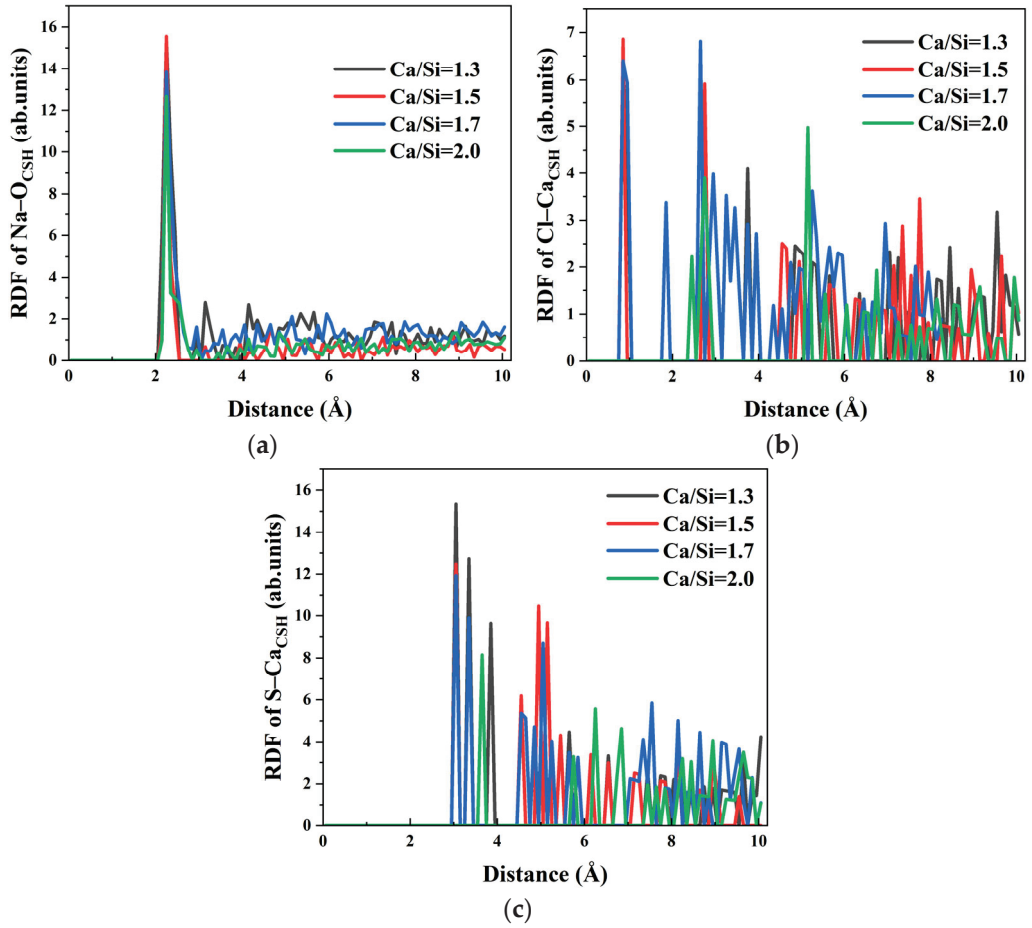

Figure 13. RDF between ions and CSH: (**a**) RDF of Na–O_{CSH}; (**b**) RDF of Cl–Ca_{CSH}; (**c**) RDF of S–Ca_{CSH}.

4. Conclusions

This study employed molecular dynamics simulations to investigate the adhesion and transport characteristics of γ–FeOOH/CSH interfaces formed by combining four distinct

CSH crystal models (Ca/Si = 1.3, 1.5, 1.7, and 2.0) with γ–FeOOH in a NaCl + Na_2SO_4 composite solution environment. The following conclusions can be drawn from the calculation and analysis of interaction energy, RDFs, coordination numbers, hydrogen bonding, and penetration depths:

1. The change in Ca/Si ratio had a significant impact on the interaction energy between CSH and γ–FeOOH, as well as between CSH and solution. As the Ca/Si ratio increased from 1.3 to 2.0, the CSH/γ–FeOOH interaction energy increased by 48.7%, while CSH/solution interaction energy decreased by 10.63%. Optimal interfacial bonding between CSH and γ–FeOOH occurred at Ca/Si = 2.0;
2. The bonding between water in solution and CSH with high Ca/Si ratios is attenuated, leading to the reduced coordination site occupancy by water. The formation possibility of hydrogen bonds such as Ca_{CSH}–O_{water}, H_{CSH}–O_{water}, and O_{CSH}–H_{water} bonds is decreased, thereby enhancing CSH preferential bonding with γ–FeOOH to form Ca_{CSH}–$O_{\gamma-FeOOH}$, H_{CSH}–$O_{\gamma-FeOOH}$, and O_{CSH}–$H_{\gamma-FeOOH}$ hydrogen bonds. As a result, the interaction between γ–FeOOH and CSH is elevated;
3. CSH with high Ca/Si ratios modifies ionic effects in the following ways. Inhibiting the secondary hydration of Na^+ ions on water molecules reduces Na–O_{water} bond strength and weakens the influence of water molecule degradation on the interfacial adhesion performance. Reducing the interfacial bonding performance of Cl^- and SO_4^{2-} ions has an affect on the free Ca^{2+} ions and hydrogen atoms on the CSH surface. The decreased bonding effects of Ca_{CSH}–Cl and H_{CSH}–O_{SO4} bonds weakens interfacial bonding performance.
4. The transport characteristics in γ–FeOOH/CSH nanopores with high Ca/Si ratio include the overall retardation of water and ion transport rates and significant variations in penetration depths. Compared with Na^+ ions, the filtration selectivity on Cl^- ions and SO_4^{2-} ions is enhanced when the Ca/Si ratio of CSH increases to 2.0;
5. The higher the Ca/Si ratio of CSH, the lower the strength and quantity of Ca_{CSH}–O_{water} and O_{CSH}–H_{water} bonds, which weakens the adsorption of water molecules by the matrix and slows down the invasion rate of water molecules. The decreasing transport rate of Na^+ and Cl^- ions in γ–FeOOH/CSH nanopores with high Ca/Si ratio results from the weakened interaction between Na–O_{CSH} and Cl–Ca_{CSH}. The decreasing transport rate of SO_4^{2-} ions is influenced by both S–Ca_{CSH} ion pairs and S–O_{water} bonds. The interaction between Cl–Ca_{CSH}, S–Ca_{CSH}, and S–O_{water} ion pairs is weakened the most when Ca/Si = 2.0.

The findings of this study suggest that increasing the Ca/Si ratio of cementitious materials can enhance their resistance to marine erosion. For instance, in concrete preparation, using high-calcium Portland cement or low-silica quartz sand can improve the durability of marine structures by strengthening the interfacial bonding between CSH and γ–FeOOH and reducing the penetration of corrosive ions. While this work primarily focuses on the mechanical, wetting, and transport properties of the CSH matrix, further investigations should address the interfacial adhesion and ion transport behavior between steel fibers and CSH. Additionally, comprehensive simulations are needed to explore the performance of concrete reinforced with steel fibers of varying compositions under aggressive environments.

Author Contributions: Conceptualization, Y.L. and L.Z.; methodology, Y.W. and D.C.; software, R.W.; formal analysis, Y.L. and P.L.; data curation, R.W.; writing—original draft preparation, Y.L. and R.W.; writing—review and editing, P.L. and L.Z.; visualization, Y.W. All authors have read and agreed to the published version of the manuscript.

Funding: This research was funded by the National Key Research and Development Project (2022YFB2603000), the National Natural Science Foundation of China (52179120, 52171267, 51909270 and 51909147), and the Fundamental Research Funds for the Central Universities (23CX07013A and 25CX07007A).

Institutional Review Board Statement: Not applicable.

Informed Consent Statement: Not applicable.

Data Availability Statement: The original contributions presented in this study are included in the article. Further inquiries can be directed to the corresponding author.

Acknowledgments: The authors thank the editors and two anonymous reviewers for their careful work and thoughtful suggestions.

Conflicts of Interest: Authors Yalin Luan, Yongmei Wu and Dongbo Cai are employed by The Seventh Engineering Co., Ltd. of CCCC First Highway Engineering Co., Ltd. Author Pengxiang Luan is employed by Wuxi National Hi-Tech Development District SCI-TECH Innovation Promotion Center. The remaining authors declare that the research was conducted in the absence of any commercial or financial relationships that could be construed as a potential conflict of interest.

References

1. Tang, S.W.; Yao, Y.; Andrade, C.; Li, Z.J. Recent durability studies on concrete structure. *Cem. Concr. Res.* **2015**, *78*, 143–154. [CrossRef]
2. Li, Z.Q.; Nie, L.; Xue, Y.; Li, W.; Fan, K. Model Testing on the Processes, Characteristics, and Mechanism of Water Inrush Induced by Karst Caves Ahead and Alongside a Tunnel. *Rock Mech. Rock Eng.* **2025**, *58*, 5363–5380. [CrossRef]
3. Golewski, G.L. A novel specific requirements for materials used in reinforced concrete composites subjected to dynamic loads. *Compos. Struct.* **2019**, *223*, 110939. [CrossRef]
4. Li, W.; Zhang, Q.; Wang, X.; Yu, L.; Li, Z. Synergistic effect of particle size, carboxymethyl starch and Na_2CO_3 on rheological and filtration property of bentonite-based material. *Case Stud. Constr. Mater.* **2024**, *21*, e03537. [CrossRef]
5. Gholamhoseini, A.; Khanlou, A.; MacRae, G.; Scott, A.; Hicks, S.; Leon, R. An experimental study on strength and serviceability of reinforced and steel fibre reinforced concrete (SFRC) continuous composite slabs. *Eng. Struct.* **2016**, *114*, 171–180. [CrossRef]
6. Lu, X.; Hsu, C.T.T. Behavior of high strength concrete with and without steel fiber reinforcement in triaxial compression. *Cem. Concr. Res.* **2015**, *36*, 1679–1685. [CrossRef]
7. Sevil, T.; Baran, M.; Bilir, T.; Canbay, E. Use of steel fiber reinforced mortar for seismic strengthening. *Constr. Build. Mater.* **2011**, *25*, 892–899. [CrossRef]
8. Zhang, P.; Wang, C.; Gao, Z.; Wang, F. A review on fracture properties of steel fiber reinforced concrete. *J. Build. Eng.* **2023**, *67*, 105975. [CrossRef]
9. Zhang, W.; Kang, S.; Lin, B.; Huang, Y. Mixed-mode debonding in CFRP-to-steel fiber–reinforced concrete joints. *J. Compos. Constr.* **2024**, *28*, 04023069. [CrossRef]
10. Li, W.; Yu, L.; Zhang, T.; Su, H.; Mi, X.; Fan, D.; Jin, B. Quantitative analysis of grain size effect on tensile mechanical behavior of granite based on multi-level force chain networks. *Comput. Part. Mech.* **2024**, *11*, 2245–2266. [CrossRef]
11. Du, F.; Jin, Z.; She, W.; Xiong, C.; Feng, G.; Fan, J. Chloride ions migration and induced reinforcement corrosion in concrete with cracks: A comparative study of current acceleration and natural marine exposure. *Constr. Build. Mater.* **2020**, *263*, 120099. [CrossRef]
12. Xiang, D.; Liu, S.; Li, Y.; Liu, Y. Improvement of flexural and cyclic performance of bridge deck slabs by utilizing steel fiber reinforced concrete (SFRC). *Constr. Build. Mater.* **2022**, *329*, 127184. [CrossRef]
13. Anas, M.; Khan, M.; Bilal, H.; Jadoon, S.; Khan, M.N. Fiber reinforced concrete: A review. *Eng. Proc.* **2022**, *22*, 3.
14. Mohod, M.V. Performance of steel fiber reinforced concrete. *Int. J. Eng. Sci.* **2012**, *1*, 1–4.
15. Li, W.; Yu, L.; Tan, Y.; Wu, L.; Qian, J. Mechanical properties and impact behavior of frozen clay: Insights from static mechanical tests, fly-plate tests, and split-Hopkinson pressure bar analysis. *Phys. Fluids* **2024**, *36*, 5. [CrossRef]
16. Granju, J.L.; Balouch, S.U. Corrosion of steel fibre reinforced concrete from the cracks. *Cem. Concr. Res.* **2005**, *35*, 572–577. [CrossRef]
17. Gong, C.; Ding, W.; Mosalam, K.M.; Günay, S.; Soga, K. Comparison of the structural behavior of reinforced concrete and steel fiber reinforced concrete tunnel segmental joints. *Tunn. Undergr. Space Technol.* **2017**, *68*, 38–57. [CrossRef]
18. Barbhuiya, S.; Das, B.B. Molecular dynamics simulation in concrete research: A systematic review of techniques, models and future directions. *J. Build. Eng.* **2023**, *76*, 107267. [CrossRef]

19. Attom, M.F.; Vandanapu, R.; Khan, Z.; Yamin, M.; Astillo, P.V.; Eltayeb, A.; Khalil, A. Prediction of internal erosion parameters of clay soils using initial physical properties. *Water* **2024**, *16*, 232. [CrossRef]
20. Hou, D.; Zheng, H.; Wang, P.; Wan, X.; Wang, M.; Wang, H. Molecular insight in the wetting behavior of nanoscale water droplet on CSH surface: Effects of Ca/Si ratio. *Appl. Surf. Sci.* **2022**, *587*, 152811. [CrossRef]
21. Wu, H.; Pan, J.; Wang, J. Molecular dynamics simulation study on dynamic mechanical properties of CSH with diverse Ca/Si ratios. *Mater. Today Commun.* **2022**, *31*, 103755. [CrossRef]
22. Zhou, Y.; Hou, D.; Jiang, J.; Liu, L.; She, W.; Yu, J. Experimental and molecular dynamics studies on the transport and adsorption of chloride ions in the nano-pores of calcium silicate phase: The influence of calcium to silicate ratios. *Microporous Mesoporous Mater.* **2018**, *255*, 23–35. [CrossRef]
23. Hou, D.; Yang, Q.; Wang, P.; Jin, Z.; Wang, M.; Zhang, Y.; Wang, X. Unraveling disadhesion mechanism of epoxy/CSH interface under aggressive conditions. *Cem. Concr. Res.* **2021**, *146*, 106489. [CrossRef]
24. Guo, K.; Miao, H.; Liu, L.; Zhou, J.; Liu, M. Effect of graphene oxide on chloride penetration resistance of recycled concrete. *Nanotechnol. Rev.* **2019**, *8*, 681–689. [CrossRef]
25. Yang, F.; Cui, Y.; She, A.; Hai, R.; Zhu, Z. Molecular dynamics simulation of silane inserted CSH nanostructure. *Materials* **2023**, *17*, 149. [CrossRef]
26. Chen, J.J.; Thomas, J.J.; Taylor, H.F.; Jennings, H.M. Solubility and structure of calcium silicate hydrate. *Cem. Concr. Res.* **2004**, *34*, 1499–1519. [CrossRef]
27. Dolado, J.S.; Griebel, M.; Hamaekers, J. A molecular dynamic study of cementitious calcium silicate hydrate (C-S-H) gels. *J. Am. Ceram. Soc.* **2007**, *90*, 3938–3942. [CrossRef]
28. Pellenq, R.J.M.; Kushima, A.; Shahsavari, R.; Van Vliet, K.J.; Buehler, M.J.; Yip, S.; Ulm, F.J. A realistic molecular model of cement hydrates. *Proc. Natl. Acad. Sci. USA* **2009**, *106*, 16102–16107. [CrossRef]
29. Hou, D.; Ma, H.; Zhu, Y.; Li, Z. Calcium silicate hydrate from dry to saturated state: Structure, dynamics and mechanical properties. *Acta Mater.* **2014**, *67*, 81–94. [CrossRef]
30. Hou, D.; Xu, X.; Ge, Y.; Wang, P.; Chen, J.; Zhang, J. Molecular structure, dynamics and adsorption behavior of water molecules and ions on [0 1 0] surface of γ-FeOOH: A molecular dynamics approach. *Constr. Build. Mater.* **2019**, *224*, 785–795. [CrossRef]
31. Guo, Q.; Li, X.; Song, Y.; Liu, J. Effect of rust inhibitor on the composition of steel passive film in carbonized concrete. *Case Stud. Constr. Mater.* **2022**, *16*, e00892. [CrossRef]
32. Xu, Y.; Fang, J.; Shen, J.; Chen, W.; Jin, R.; Mao, J.; Jin, W. Molecular dynamics simulation of reinforcing steel corrosion when subjected to both chloride attack and mechanical loading. *Mater. Sci.* **2020**, *26*, 261–268. [CrossRef]
33. Li, M.; Wu, S.; Wang, P.; Zhang, J.; Dong, B.; Ma, M.; Wang, M. Molecular progress of the corrosion of passivated Iron: The effects of structural strain. *Constr. Build. Mater.* **2022**, *360*, 129537. [CrossRef]
34. Hou, D.; Li, T.; Wang, P. Molecular dynamics study on the structure and dynamics of NaCl solution transport in the nanometer channel of CASH gel. *ACS Sustain. Chem. Eng.* **2018**, *6*, 9498–9509. [CrossRef]
35. Zhang, L.; Wang, R.; Luan, Y.; Wang, H.; Tong, H. Molecular dynamics study on bonding behaviors of γ–FeOOH/CSH interface under aggressive conditions. *Appl. Surf. Sci.* **2025**, *680*, 161342. [CrossRef]
36. Hou, D.; Jia, Y.; Yu, J.; Wang, P.; Liu, Q. Transport properties of sulfate and chloride ions confined between calcium silicate hydrate surfaces: A molecular dynamics study. *J. Phys. Chem. C* **2018**, *122*, 28021–28032. [CrossRef]
37. Thompson, A.P.; Aktulga, H.M.; Berger, R.; Bolintineanu, D.S.; Brown, W.M.; Crozier, P.S.; Plimpton, S.J. LAMMPS—A flexible simulation tool for particle-based materials modeling at the atomic, meso, and continuum scales. *Comput. Phys. Commun.* **2022**, *271*, 108171. [CrossRef]
38. Humbert, M.T.; Zhang, Y.; Maginn, E.J. PyLAT: Python LAMMPS analysis tools. *J. Chem. Inf. Model.* **2019**, *59*, 1301–1305. [CrossRef]
39. Pouvreau, M.; Greathouse, J.A.; Cygan, R.T.; Kalinichev, A.G. Structure of hydrated kaolinite edge surfaces: DFT results andfurther development of the ClayFF classical force field with metal–O–H angle bending terms. *J. Phys. Chem. C* **2019**, *123*, 11628–11638. [CrossRef]
40. Yang, J.; Jia, Y.; Hou, D.; Wang, P.; Jin, Z.; Shang, H.; Zhao, T. Na and Cl immobilization by size controlled calcium silicate hydrate nanometer pores. *Constr. Build. Mater.* **2019**, *202*, 622–635. [CrossRef]
41. Zehtab, B.; Tarighat, A. Molecular dynamics simulation to assess the effect of temperature on diffusion coefficients of different ions and water molecules in CSH. *Mech. Time-Depend. Mat.* **2018**, *22*, 483–497. [CrossRef]
42. Liu, G.; Zhang, Y.; Ni, Z.; Huang, R. Corrosion behavior of steel submitted to chloride and sulphate ions in simulated concrete pore solution. *Constr. Build. Mater.* **2016**, *115*, 1–5. [CrossRef]
43. Shaheen, F.; Pradhan, B. Influence of sulfate ion and associated cation type on steel reinforcement corrosion in concrete powder aqueous solution in the presence of chloride ions. *Cem. Concr. Res.* **2017**, *91*, 73–86. [CrossRef]
44. Yaphary, Y.L.; Lau, D.; Sanchez, F.; Poon, C.S. Effects of sodium/calcium cation exchange on the mechanical properties of calcium silicate hydrate (CSH). *Constr. Build. Mater.* **2020**, *243*, 118283. [CrossRef]

45. Suwito, A.; Cai, X.C.; Xi, Y. Parallel finite element methods for coupled chloride penetration and moisture diffusion in concrete. *Int. J. Numer. Anal. Mod.* **2006**, *3*, 481–503.
46. Miao, R.; Wang, L.; Zhu, M.; Deng, D.; Li, S.; Wang, J.; Lv, Y. Effect of hydration forces on protein fouling of ultrafiltration membranes: The role of protein charge, hydrated ion species, and membrane hydrophilicity. *Environ. Sci. Technol.* **2017**, *51*, 167–174. [CrossRef] [PubMed]
47. Binazadeh, M.; Xu, M.; Zolfaghari, A.; Dehghanpour, H. Effect of electrostatic interactions on water uptake of gas shales: The interplay of solution ionic strength and electrostatic double layer. *Energy Fuels* **2016**, *30*, 992–1001. [CrossRef]

Disclaimer/Publisher's Note: The statements, opinions and data contained in all publications are solely those of the individual author(s) and contributor(s) and not of MDPI and/or the editor(s). MDPI and/or the editor(s) disclaim responsibility for any injury to people or property resulting from any ideas, methods, instructions or products referred to in the content.

materials

MDPI

Article

Material Behavior and Computational Validation of Deep CO_2 Closed-Loop Geothermal Systems in Carbonate Reservoirs

Xinghui Wu [1,2], Peng Li [2,*], Meifeng Cai [2], Tingting Jiang [1], Bolin Mu [1], Wanlei Su [1], Min Wang [2,3] and Chunxiao Li [1]

[1] School of City and Architecture Engineering, Zaozhuang University, Zaozhuang 277160, China
[2] Beijing Key Laboratory of Urban Underground Space Engineering, University of Science and Technology Beijing, Beijing 100083, China
[3] School of Resources Environment and Safety Engineering, University of South China, Hengyang 421001, China
* Correspondence: pengli@ustb.edu.cn

Abstract: Closed-loop geothermal systems (CLGSs) avoid groundwater production and offer stable deep heat supply, but their long-term performance hinges on reliable coupling between the wellbore, the near-well interface and the surrounding formation. Using the D22 well in the Xiongan New Area (deep carbonate reservoir), we built a three-domain thermo-hydraulic framework that updates CO_2 properties with temperature and pressure and explicitly accounts for wellbore-formation thermal resistance. Two geometries (U-tube and single-well coaxial) and two working fluids (CO_2 and water) were compared and optimized under field constraints. With the coaxial configuration, CO_2 delivers an average thermal power of 186.3 kW, exceeding that of water by 44.9%, while the fraction of wellbore heat loss drops by 3–5%. Under field-matched conditions, the predicted outlet temperature (76.8 °C) agrees with the measured value (77.2 °C) within 0.52%, confirming the value of field calibration for parameter transferability. Long-term simulations indicate that after 30 years of continuous operation the outlet temperature decline remains <8 °C for CO_2, outperforming water and implying better reservoir utilization and supply stability. Sensitivity and Pareto analyses identify a practical operating window, i.e., flow velocity of 0.9–1.1 m s^{-1} and depth of 3000–3500 m, favoring the single-well coaxial + CO_2 scheme. These results show how field-calibrated modeling narrows uncertainty and yields implementable guidance on geometry, operating conditions, and wellbore insulation strategy. This study provides quantitative evidence that CO_2-CLGSs in deep carbonate formations can simultaneously increase thermal output and limit long-term decline, supporting near-term engineering deployment.

Keywords: finite element analysis; material behavior; computational validation; CO_2 closed-loop system; multi-objective optimization

1. Introduction

Geothermal energy, characterized by stability, high efficiency, and low carbon emissions, is increasingly recognized as a vital component of the global energy transition. Medium-to-deep geothermal resources, with higher energy density than shallow systems, are particularly suited to district heating and industrial applications [1–3]. However, conventional hydrothermal exploitation relies on groundwater withdrawal, often causing reservoir depletion, thermal imbalance, and land subsidence, which significantly limit sustainability [4].

Closed-loop geothermal systems (CLGSs), also referred to as "heat extraction without water withdrawal," have been proposed to overcome these challenges. By circulating a working fluid through sealed borehole heat exchangers, CLGSs eliminates direct groundwater use and reduces environmental risks. Existing research has primarily focused on shallow geothermal heat pump applications, while medium-to-deep systems remain less explored [5]. Among potential working fluids, CO_2 has drawn increasing attention due to its unique thermophysical characteristics: low viscosity, high specific heat capacity, and nonlinear enhancement of heat transfer near the critical point. Early pioneering studies highlighted the promise of CO_2-based enhanced geothermal systems (EGSs) for combined heat recovery and carbon sequestration. Subsequent work extended these concepts to numerical simulations and laboratory studies, but most efforts remained limited to shallow reservoirs or simplified conditions [6–8].

For deep carbonate reservoirs, particularly under high-temperature and site-specific geological constraints, several gaps that remain are as follows: (i) the coupled behavior of nonlinear CO_2 properties, wellbore heat transfer, and reservoir conduction is not fully understood; (ii) long-term operational sustainability of CO_2-based CLGSs lacks systematic evaluation; and (iii) the co-benefits of heat extraction and CO_2 sequestration have not been quantitatively assessed [9–13].

The Xiongan New Area in northern China, designated as a national demonstration zone for green development, provides a representative case for addressing these questions [14,15]. The D22 well intersects multiple deep carbonate formations and has undergone acid stimulation and reservoir characterization, supplying a reliable dataset for high-fidelity modeling. Based on this context, the objectives of this study are threefold: (i) to establish a THMC-coupled modeling framework that accounts for dynamic CO_2 properties, wellbore thermal resistance, and reservoir constraints; (ii) to compare the performance of CO_2 and water as working fluids in both U-shaped and coaxial single-well CLGSs; and (iii) to assess long-term operational sustainability and quantify the CO_2 sequestration potential [16,17]. Most previous studies simplified CO_2 thermophysical behavior or neglected the interface resistance between wellbore and formation. This study overcomes these limitations through a field-calibrated, three-domain coupled model with dynamic CO_2 properties and optimization framework validated against the D22 well.

To clearly articulate the advancements of this work, Table 1 provides a systematic comparison between the key features of conventional CO_2-CLGS models and the approach developed in this study. The principal innovations of this study include: Development of a three-domain coupled model integrating dynamic CO_2 thermophysical properties, wellbore thermal resistance, and reservoir conduction, which is seldom addressed in existing CLGS studies; Implementation of a Pareto-based multi-objective optimization framework to identify optimal operating conditions, balancing thermal efficiency and pressure drop; Long-term performance evaluation and field validation using data from a deep carbonate reservoir, providing quantitative insights into system sustainability and CO_2 utilization potential, as shown in Figure 1. By integrating numerical modeling with validation against field data from the D22 well, this study advances the theoretical understanding of CO_2-based CLGSs in carbonate formations and provides practical insights for optimizing system design. The results not only enhance the scientific foundation for geothermal exploitation but also highlight the dual role of CO_2 in energy recovery and greenhouse gas mitigation, offering guidance for sustainable deployment of geothermal technologies in China and beyond.

Table 1. Comparative analysis of CO_2-CLGS modeling approaches.

Modeling Aspect	Conventional Models	This Study	Improvement
CO_2 Properties	Ideal gas or constant properties	Dynamic T-P functions from NIST REFPROP	Captures near-critical enhancement
Thermal Coupling	Mainly rock–fluid (2-domain)	Rock–interface–fluid (3-domain)	Reduces wellbore heat loss error by ~8%
Validation	Limited to laboratory scale	Field data (D22 well) with multi-parameter match	Temperature error < 0.52%, pressure error < 4.9%
Optimization	Single-parameter sensitivity	Pareto multi-objective optimization	Identifies optimal operating window
Long-term Prediction	Typically <10 years	30-year projection with uncertainty bounds	Provides reliable sustainability assessment

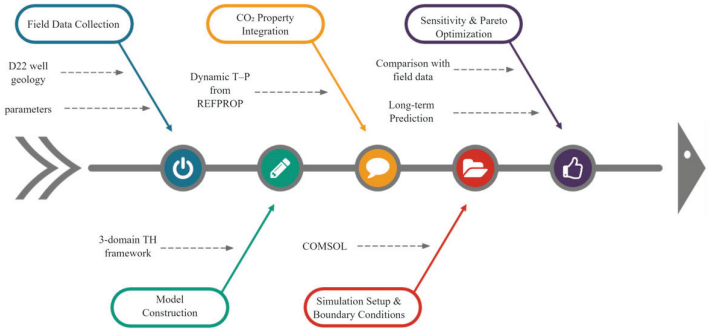

Figure 1. Flowchart summarizing the methodological framework for CO_2-based closed-loop geothermal system analysis.

2. Geologic Setting and Field Background

The Xiongan New Area is situated in the central section of the North China Geothermal Belt and is characterized by a sedimentary basin tectonic framework with well-developed medium-to-deep carbonate geothermal reservoirs. The study area, located near Santai Town in Anxin County, lies at the core of the Dongrongcheng Uplift—one of the principal zones for medium- to high-temperature geothermal resources in northern China [18,19]. The regional geothermal gradient typically exceeds 3.8 °C per 100 m, offering favorable geological conditions for the implementation of closed-loop geothermal heating systems and providing a robust thermal energy base for sustainable exploitation [20].

This study centers on the D22 well, which reaches a total depth of 3517 m and intersects several medium- to high-temperature geothermal reservoirs, including those within the Wumishan and Gaozhuang Formations. The primary thermal reservoir zone lies between depths of 980–1842 m. The Wumishan Formation predominantly comprises medium-to-thick and massive dolomite layers, with minor intercalations of diorite and siliceous conglomerate. These formations exhibit high thermal conductivity and strong heat storage capacity. Stratigraphically, the well displays a clearly defined structure: the upper section consists of mudstone-sandstone sequences from the Neogene Minghuazhen Formation, while the underlying section comprises typical Middle Proterozoic carbonate reservoirs known for their thermal stability. The dolomite layers are notably brittle and possess low tensile strength, making them highly suitable for acid stimulation.

Following deep acid stimulation at the D22 well, the unit water yield increased markedly—from 0.024 $m^3/h/m$ to 0.449 $m^3/h/m$—representing nearly a 20-fold improvement. Simultaneously, the bottom-hole temperature rose to 70 °C, significantly enhancing the well's heat supply capacity. Numerical simulations predict that the high-conductivity channels created by acid stimulation will maintain robust thermal stability, with reservoir temperatures decreasing by less than 4 °C over a 100-year continuous operation period.

These conditions satisfy the thermal and structural requirements for the deployment of a closed-loop heat exchange system within the reservoir.

3. Methodology and Modeling

3.1. System Description

This study investigates deep geothermal development in the D22 well area of the Xiongan New Area by employing a CLGS for subsurface heat recovery. Two representative system configurations are considered: a U-shaped well and a coaxial single-well structure (Figure 2). The U-shaped well features a relatively simple geometry and is better suited for shallow, low-permeability reservoirs. In contrast, the coaxial single-well configuration is optimized for deep geothermal environments, offering greater heat exchange capacity and reduced maintenance demands [21–23]. In both systems, heat is extracted from the geothermal reservoir through a subsurface pipeline network and transferred to the working fluid, which circulates back to the surface where the thermal energy is released.

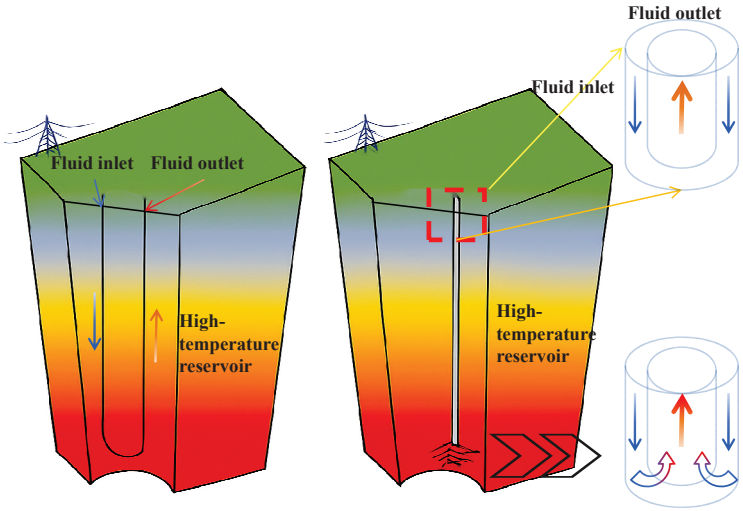

Figure 2. Schematic diagram of U-shaped and coaxial single-well CLGS configurations.

Building upon the classical thermo-hydraulic coupling control equations, this study introduces several key innovations: structural domain partitioning, dynamic regulation of CO_2 thermophysical property functions, wellbore thermal resistance boundary modeling, and an instantaneous heat transfer efficiency function. These enhancements collectively enable high-fidelity simulation of the actual thermal response behavior in CLGSs and provide a robust theoretical foundation for the engineering optimization of high-temperature geothermal energy systems.

3.2. Governing Equations and Closure

In the thermal-fluid simulation of closed-loop geothermal heating systems, the energy conservation equation serves as the theoretical foundation for describing the interactions among the wellbore, working fluid, and surrounding reservoir domains [24]. Unlike conventional simplified one-dimensional steady-state heat transfer models, this study employs a multi-zone coupled modeling approach to establish a more physically comprehensive and scalable set of multi-physics governing equations.

3.2.1. Three-Domain Decomposition

From a structural standpoint, the model is divided into three distinct subdomains: (1) the geothermal reservoir rock mass, (2) the wellbore heat exchange boundary zone, and

(3) the closed-loop fluid circulation channel. These subdomains are governed by the Fourier heat conduction equation, an interfacial thermal resistance model, and coupled flow–heat transfer control equations, respectively. This domain-partitioning strategy overcomes the limitations inherent in traditional "lumped parameter" or "whole-equivalent" models, allowing for a more accurate representation of heat transfer pathways in deep, closed-well geothermal systems.

Within the closed system, the geothermal reservoir acts as the primary heat source, where temperature evolution is governed solely by conductive heat transfer mechanisms [25,26]. The Fourier heat conduction equation is used to characterize the isotropic thermal diffusion behavior of the rock matrix. The governing equation for this subdomain is expressed as Equations (1) and (2):

$$\frac{\partial T_r}{\partial t} = \alpha_r \nabla^2 T_r \tag{1}$$

where T_r is the rock temperature (°C); α_r is the rock diffusion coefficient (m^2/s).

$$\alpha_r = \frac{k_r}{\rho_r C_{p,r}} \tag{2}$$

where k_r is the thermal conductivity (W/m·K); ρ_r is the density (kg/m^3); $C_{p,r}$ is the specific heat capacity (J/kg·K).

Introducing a thermal resistance term at the interface between the wellbore wall and the surrounding rock is critical for accurately modeling heat loss and the decline in wellbore thermal efficiency. This term represents the equivalent thermal resistance of insulation materials and multilayered pipe wall structures. Equation (3) defines the interfacial thermal resistance boundary flux model, which couples the temperature fields of the adjacent subdomains through heat flux continuity across the interface.

$$q_n = \frac{T_f - T_r}{R_{\mathrm{inter}face}} \tag{3}$$

where q_n is the component of the heat flux vector in the normal direction of the interface (W/m^2); T_f is the temperature of the wellbore workings (°C); T_r is the temperature of the formation rock (°C); and $R_{interface}$ is the interface thermal resistance ($K \cdot m^2/W$), which indicates the thermal resistivity of the well wall structure.

The interfacial thermal resistance $R_{interface}$ is set to 0.05 $K \cdot m^2 \cdot W^{-1}$ based on typical values for insulated wellbores in geothermal applications [27,28]. A sensitivity analysis was conducted by varying $R_{interface}$ by ±30%, which resulted in less than 2% change in outlet temperature, confirming the robustness of the model to this parameter.

Within the wellbore, the working fluid flows through the piping system and exchanges heat with the pipe wall via both convective and conductive mechanisms. The coupled energy conservation equations (Equation (4)) accurately capture the spatial evolution of temperature and velocity fields within the closed-loop system, with particular emphasis on the transient thermal response behavior of low-viscosity working fluids such as CO_2 as shown in Equation (4).

$$\rho_f c_{p,f} \left(\frac{\partial T_f}{\partial t} + v \cdot \nabla T_f \right) = \nabla \cdot (k_f \nabla T_f) + S \tag{4}$$

where ρ_f is the density of the working fluid (kg/m^3); $C_{p,f}$ is the specific heat capacity of the working fluid (J/kg·K); T_f is the temperature of the working fluid (°C); v is the velocity vector of the working fluid (m/s); μ is the viscosity of the working fluid; g is the

gravitational acceleration; and k_f is the thermal conductivity of the fluid (W/m·K); S is the source term (W/m^3) within the fluid domain, representing the internal heat source or sink.

3.2.2. Temperature- and Pressure-Dependent Fluid Properties

To simulate carbon dioxide (CO_2) as the working fluid, this study establishes a set of dynamic thermophysical property functions dependent on both thermal and pressure conditions. These functions characterize key properties—density, specific heat capacity, thermal conductivity, and viscosity—as functions of state variables. The model effectively captures the enhanced heat transfer phenomena exhibited by CO_2 near its critical point, representing a key innovation that differentiates it from conventional water-based working fluid models. The thermophysical properties (density, specific heat, viscosity, and thermal conductivity) of CO_2 are implemented using a look-up table derived from the NIST REFPROP database (version 10.0). The table interpolates properties in real-time based on local temperature and pressure, ensuring accurate representation of near-critical behavior (7.3–8.0 MPa, 30–40 °C). Validation against experimental data in the critical region shows a maximum deviation of 3.2% for thermal conductivity.

In addition, a transient heat recovery efficiency function, denoted as $\eta(t)$ and defined in Equation (5), is introduced to characterize the system's thermal output response under fluctuating operating conditions during unsteady-state operation. This expression provides a valuable basis for real-time performance monitoring and dynamic regulation of thermal energy systems, and it holds promise for future engineering applications and system scalability.

For a working fluid (either water or CO_2) circulating in a closed-loop system and influenced by both axial temperature gradients and flow velocity within the wellbore, the coupled convection-conduction control Equations (5) and (6) is employed to accurately describe its temperature evolution behavior [29].

$$\eta(t) = \frac{mC_{p,r}[T_{out}(t) - T_{in}(t)]}{A_s q(t)} \tag{5}$$

$$\rho_f C_{p,r} \frac{\partial T_f}{\partial t} + v \cdot \rho_f C_{p,r} \nabla T_f = \nabla \left(k_f \cdot \nabla T_f \right) \tag{6}$$

where m is the mass flow rate of the work mass (kg/s), and A_s is the heat transfer interface area (m^2).

3.2.3. Boundary and Initial Conditions

To accurately simulate the thermo-hydraulic behavior under the three-domain coupled framework, this study establishes a hierarchical boundary condition system grounded in zonal responses, material properties, and theoretical enhancements.

The lateral boundaries are positioned 50 m from the wellbore center—determined through sensitivity analysis showing <0.5% temperature change beyond 40 m distance, thus eliminating boundary effects. The bottom boundary maintains a constant temperature of 135 °C at 3500 m depth based on the local geothermal gradient. Initial conditions assume hydrostatic pressure distribution and temperature following Equation (7) with surface temperature of 20 °C and gradient of 3.8 °C/100 m.

$$T_r = T_{surface} + G \cdot Z \tag{7}$$

where T_{surface} is the ground temperature (T_{surface} = 20 °C); G is the geothermal gradient (G = 3.8 °C/100 m); and Z is depth (m).

The horizontal boundaries of the simulation domain are thermally insulated and positioned far enough from the wellbore to negate any external heat exchange. The bottom boundary is modeled as a constant-temperature surface, representing the continuous geothermal heat supply from deeper formations. A pressure-outlet boundary condition is applied at the outflow end to simulate ambient pressure conditions [30].

The thermophysical properties, i.e., density, specific heat capacity, viscosity, and thermal conductivity, of the water or CO_2 working fluid are defined as functions of both temperature (T) and pressure (P), and are governed by the following relationship, as shown in Equation (8):

$$\phi_f = f(T, P) \tag{8}$$

where ϕ represents physical property parameters such as density, specific heat capacity, viscosity, and thermal conductivity.

In simulations involving supercritical CO_2, abrupt variations in thermophysical properties are observed within the critical region-specifically between 30 and 40 °C and 7.3 and 8.0 MPa. This zone exhibits heightened sensitivity in terms of system stability and heat transfer efficiency. To account for these effects, the model dynamically updates fluid properties in real time using either a precompiled look-up table or fitted thermophysical functions.

3.2.4. CO_2 Inventory in Closed-Loop Systems

In a closed-loop system, CO_2 is recirculated and not permanently sequestered. The mass of CO_2 retained in the subsurface loop can be estimated by Equation (9), representing the system's working fluid inventory rather than sequestration potential.

$$M_{CO_2} = \rho_{CO_2}(P, T) \cdot V_{loop} \tag{9}$$

where M_{CO2} is the total mass of CO_2 stored; $\rho_{CO2}(P,T)$ is the density of CO_2 as a function of pressure and temperature; and V_{loop} is the effective fluid volume within the closed-loop system. For the D22 well system with V_{loop} = 28.5 m^3, the CO_2 inventory ranges from 12.8 to 18.6 tons depending on operational conditions (P = 7–10 MPa, T = 40–80 °C). While the CO_2 is recirculated rather than permanently sequestered in this closed-loop configuration, the system enables significant emissions avoidance. When displacing conventional natural gas heating, this represents annual emissions reduction of 28–35 tons CO_2-equivalent, accumulating to 840–1050 tons over the 30-year system lifetime. This dual benefit of enhanced heat extraction and emissions reduction strengthens the environmental rationale for CO_2-CLGS deployment.

When integrated over the system's operational lifetime, the cumulative sequestration can be compared to the equivalent avoided emissions from fossil fuel-based heating systems, thereby quantifying the dual benefits of energy extraction and greenhouse gas mitigation.

3.3. Simulation Setup

To enable high-fidelity simulation of heat transfer in a deep-borehole closed-loop geothermal system, we use COMSOL Multiphysics 6.1. A 2-D axisymmetric geometry is created that captures the longitudinal section of a typical U-tube closed-loop well. The model couples three distinct domains—borehole, reservoir rock, and circulating working fluid—whose thermo-physical properties are assigned from site-specific geologic logs and well-test data.

Computational limitations include mesh sensitivity and time-step effects. Comprehensive mesh independence tests confirm that solutions stabilize with element counts > 45,000, resulting in <1.2% variation in key output parameters. Time steps below 60 s ensure nu-

merical stability for transient simulations. The current 2D axisymmetric model requires approximately 6–8 h for a complete 30-year simulation on a 32-core workstation. This computational demand suggests the potential utility of reduced-order models for rapid optimization or extensive uncertainty quantification studies in future work.

3.3.1. Mesh Discretization and Validation

An unstructured triangular mesh is employed for spatial discretization in the numerical model. To ensure the accuracy of heat flux calculations, a local mesh refinement strategy is applied in regions with steep thermal gradients, particularly near the wellbore wall, where the minimum element size is controlled within 0.05 m. Figure 3 presents the mesh configuration of a typical single-well model, clearly showing significant mesh refinement in the wellbore region to accurately resolve thermal boundary layer variations.

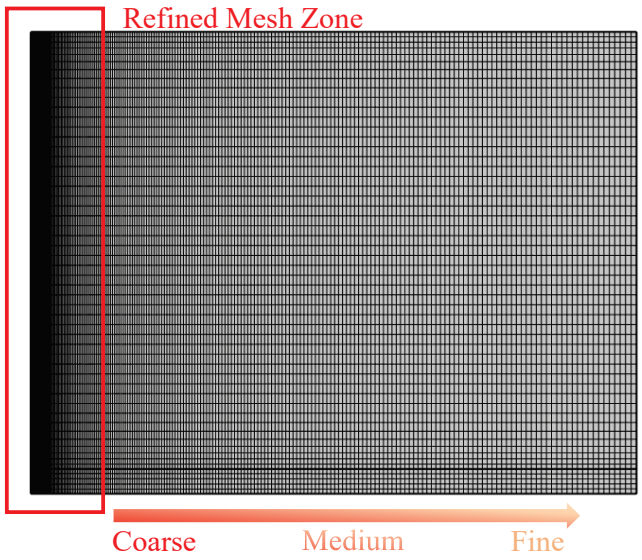

Figure 3. Grid partitioning diagram of the well model.

Grid independence is assessed by evaluating simulation results across three mesh densities—coarse, medium, and fine. Key output variables, including outlet temperature and thermal recovery rate, are compared across these configurations. Results indicate that once the total number of mesh elements exceeds 4.5×10^4, the variation in outlet temperature falls below 1.2%, confirming that the medium-density mesh provides an effective balance between computational accuracy and efficiency.

3.3.2. Design of Operating Variables

To comprehensively evaluate the thermal performance of the closed-loop geothermal system, multiple simulation scenarios were designed based on variations in system configuration and key operating parameters. These scenarios aim to systematically analyze the effects of the following core factors:

(1) A comparative analysis was performed to evaluate the heat transfer performance of water (H_2O) and carbon dioxide (CO_2) as working fluids. Given the significant sensitivity of CO_2 thermophysical properties to changes in temperature and pressure, a combination of look-up tables and real-time updating models was employed to dynamically retrieve values for specific heat capacity, density, thermal conductivity, and viscosity. In contrast, water was modeled as a fluid with constant physical properties, serving as a benchmark under conventional heat transfer conditions.

(2) To assess the impact of fluid velocity on system performance, the circulating flow rate was set to five discrete values: 0.2 m/s, 0.4 m/s, 0.8 m/s, 1.0 m/s, and 1.2 m/s.

Corresponding changes in outlet temperature, heat recovery rate, and pressure drop were evaluated under each flow condition.

(3) Based on the structural and lithological profile of the D22 well in the Xiongan New Area, simulated well depths were set at 1000 m, 1500 m, 2000 m, 2500 m, and 3000 m. The geothermal reservoir temperature at each depth was estimated using a regional geothermal gradient of 3.8 °C per 100 m. These values were used to analyze variations in heat exchange capacity and wellbore heat loss behavior under different burial depths.

4. Results and Analysis

4.1. Thermal Response Analysis

4.1.1. Temporal Variation in Outlet Temperature

To assess the dynamic heat transfer response of different working fluids in a deep closed-loop geothermal system, this study numerically simulates the outlet temperature variation during the initial 120 min of circulation at a well depth of 3000 m.

The simulation conditions are uniformly initialized with an inlet temperature of 20 °C and a wellbore temperature of 105 °C, matching the ambient formation temperature. The circulation velocity is fixed at 1.0 m/s. Two working fluids are considered in the simulation: water (H_2O) and carbon dioxide (CO_2).

As shown in Figure 4, the CO_2 system demonstrates a markedly faster temperature rise compared to the water system during the initial start-up phase. Within the first 20 min of operation, the outlet temperature of the CO_2 system increases rapidly from 20 °C to approximately 70.3 °C, whereas the water system reaches only around 66.1 °C. This corresponds to an approximately 30% higher temperature rise rate for CO_2.

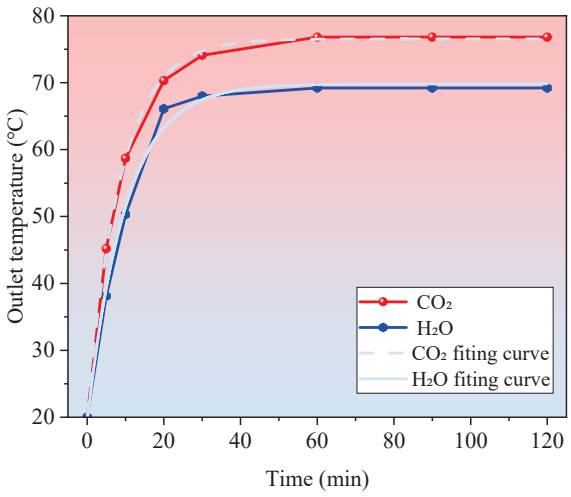

Figure 4. Transient outlet temperature response over 120 min for CO_2 and H_2O at 3000 m depth and 1.0 m/s flow velocity. CO_2 exhibits faster thermal stabilization and higher steady-state temperature.

This superior performance is primarily attributed to the enhanced thermophysical properties of CO_2 near its critical point, including high thermal conductivity, low viscosity, and pronounced density fluctuations, which collectively facilitate rapid heat absorption from the geothermal reservoir.

During the subsequent steady-state phase, the outlet temperature of the CO_2 system stabilizes at 76.8 °C, while that of the water system levels off at 69.2 °C. Exponential curve fitting of the temperature-time profiles indicates that the thermal response behaviors of

the two systems conform to the following relationships governing equations are given in Equations (10) and (11):

$$T_{H_2O}(t) = 62.33 + 5.77 \cdot e^{-0.049t} \quad (10)$$

$$T_{CO_2}(t) = 65.60 + 10.20 \cdot e^{-0.031t} \quad (11)$$

The mathematical expressions reveal that the CO_2 system not only achieves a higher steady-state outlet temperature but also exhibits a smoother thermal ramp-up process. This behavior indicates superior thermal stability and a stronger buffering capacity in response to operational fluctuations during long-term operation. Such characteristics are of particular importance for the continuous energy supply capability of deep CLGSs, especially in high-demand applications such as industrial parks and district heating networks.

4.1.2. Thermal Power Comparison Analysis

To further assess the thermal performance of CLGSs, this study simulates the average heat exchange power for two configurations—U-shaped and coaxial single-well structures—under identical geothermal conditions: a well depth of 3000 m and a circulation velocity of 1.0 m/s. Simulations were conducted for both water (H_2O) and carbon dioxide (CO_2) as working fluids.

As shown in Table 2, CO_2 enhances the thermal output relative to water by 15.7% in the U-shaped configuration and by 44.9% in the single-well configuration. The CO–single-well system reaches the highest output of 186.3 kW, approximately 1.45 times the water-based value of 128.5 kW.

Table 2. Comparison of average thermal power output under different well types and working fluids.

System Structure	Working Fluid	Average Thermal Power (kW)
U-shaped	H_2O	132.0
U-shaped	CO_2	152.8
coaxial single-well	H_2O	128.5
coaxial single-well	CO_2	186.3

These results indicate that CO_2 not only exhibits superior heat transfer efficiency in closed-loop systems but also capitalizes on its advantages more effectively in the single-well configuration due to lower structural thermal resistance. Structural comparisons further show that while the U-shaped well benefits from a longer flow path and greater heat exchange surface area, it also experiences greater thermal losses along the extended circulation route. In contrast, the single-well system improves thermal collection efficiency through centralized injection–production and annular heat exchange along the wellbore —an approach particularly effective when paired with CO_2 due to its favorable thermophysical properties.

In conclusion, the single-well closed-loop configuration combined with CO_2 as the working fluid should be prioritized in practical applications, especially for deep carbonate geothermal reservoirs in North China. This combination offers enhanced heat capture and more efficient thermal energy delivery.

4.2. Wellbore Heat Loss and Efficiency

Wellbore heat loss represents a critical and often non-negligible component of energy dissipation in the design of deep CLGSs. Owing to the extended vertical transport path of the working fluid, significant thermal energy can be conducted through the wellbore

walls into the surrounding formation—particularly under conditions of poor insulation, low flow velocity, or during the initial phase of system operation.

To quantitatively assess this loss, the heat loss ratio is defined as the ratio of wellbore heat loss power to the total heat absorption power from the reservoir. This metric serves as an indicator of the impact of wellbore losses on overall system efficiency. In this study, a wellbore heat loss response model was developed to evaluate thermal losses under varying flow rates and structural configurations. The results are presented in Figure 5.

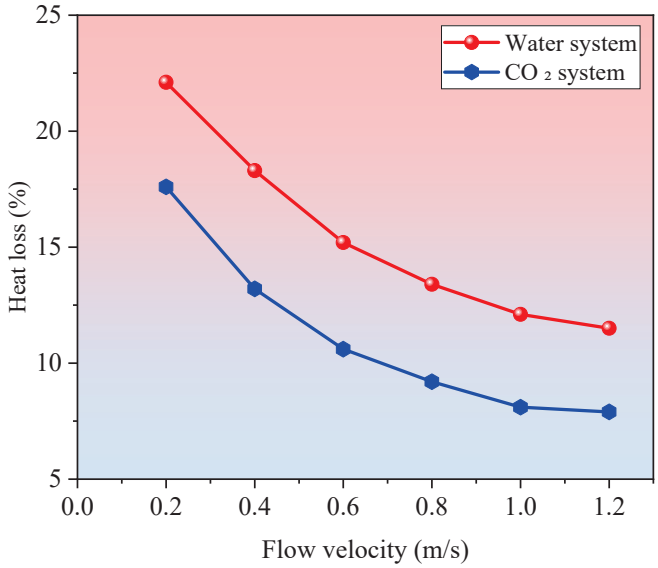

Figure 5. Comparison of wellbore heat loss ratio versus flow velocity for H_2O and CO_2 systems. CO_2 shows 3–5% lower losses across all conditions.

As shown in Figure 5, the proportion of heat loss through the wellbore relative to the total heat extracted by the system decreases significantly with increasing flow velocity, highlighting the strong influence of circulation rate on heat transfer efficiency. Under low flow velocity conditions (0.2 m/s), the wellbore heat loss accounts for 22.1% of total heat input in the water-based system and 17.6% in the CO_2-based system. This elevated loss is primarily due to the low heat flux density and extended residence time of the working fluid within the wellbore, which increases conductive heat dissipation to the surrounding rock.

As the flow rate increases to 1.0 m/s, the heat loss ratio drops markedly—to 12.1% for water and 8.1% for CO_2. This reduction is attributed to the greater heat transport per unit volume of fluid and the shortened transit time through the wellbore, which limits conductive losses. Notably, CO_2 consistently exhibits lower heat loss than water at all flow rates, due to its lower viscosity and enhanced convective heat transfer capability, with the differential ranging from 3% to 5%.

In addition to thermal loss, pressure drop is a key metric for evaluating operational efficiency. At a flow rate of 1.0 m/s, simulation results show that the total pressure drop is 0.86 MPa for the CO_2 system, slightly higher than the 0.72 MPa observed in the water system. However, CO_2 delivers a significantly higher thermal power output per unit pressure drop—216.5 kW/MPa versus 178.5 kW/MPa for water—indicating superior overall energy efficiency in CO_2-based CLGSs.

4.3. Sensitivity Analysis

To gain deeper insight into the influence of key operational parameters on the thermal performance of a deep closed-loop geothermal system, a multi-factor sensitivity analysis was conducted. Flow velocity, well depth, and pressure drop were selected as the core

variables. The simulation results are systematically presented in Figures 6–8. Additionally, a Pareto-based multi-objective optimization analysis was performed to identify the optimal range of operating conditions that balance thermal efficiency and system performance.

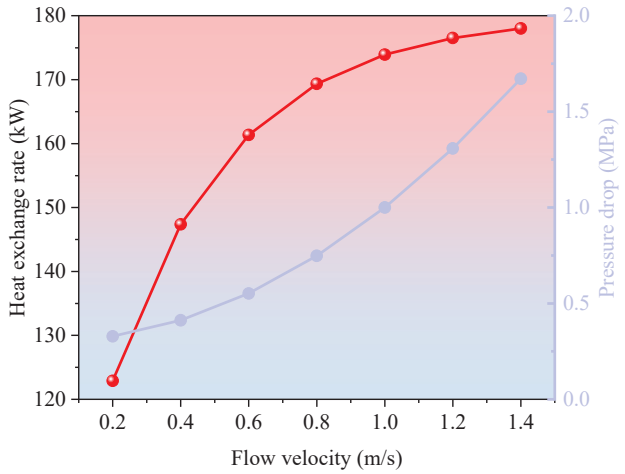

Figure 6. Effect of flow velocity on heat transfer rate and pressure drop.

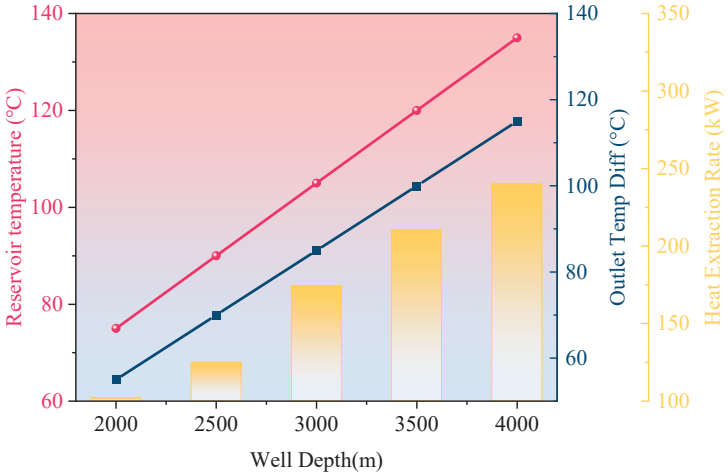

Figure 7. Effect of well depth on system performance.

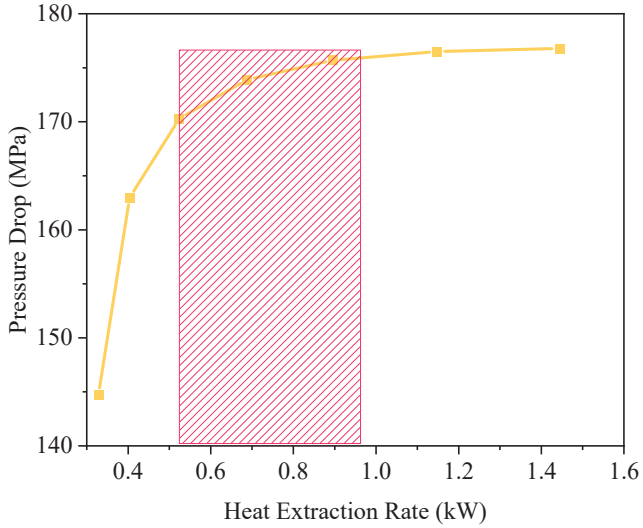

Figure 8. Pareto front of heat transfer rate versus pressure drop for single-well CO_2 system. Optimal operating zone lies between 0.65 and 0.95 MPa and 165 and 175 kW.

As shown in Figure 6, the system's heat transfer rate increases sharply as the circulation flow velocity rises from 0.2 m/s to 1.4 m/s, growing from 96.4 kW to 174.2 kW and exhibiting a clear logarithmic trend. In the lower velocity range, the enhanced flow significantly improves the working fluid's heat-carrying capacity, thereby increasing the heat flux through the heat exchange section per unit time and improving the overall thermal recovery rate.

However, beyond a flow velocity of 1.0 m/s, the rate of increase in heat transfer begins to taper, suggesting that the system is approaching a saturation point where further velocity increases yield diminishing returns in thermal performance. Simultaneously, the pressure drop within the wellbore shows a pronounced upward trend with increasing flow velocity, rising from 0.33 MPa to 1.67 MPa. This pressure rise becomes exponential in the high-velocity regime (>1.2 m/s), substantially increasing the energy demand of the circulation pump and the system's operational pressure burden. Therefore, from both thermal efficiency and economic perspectives, an optimal flow velocity range of 0.9–1.1 m/s is recommended to balance heat transfer enhancement with acceptable pressure losses.

Figure 7 explores the variation in geothermal response with increasing well depth for the single-well coaxial system using CO_2 as the working fluid at a flow velocity of 1.0 m/s. As the well depth increases from 2000 m to 4000 m, formation temperatures are estimated using a linear geothermal gradient of 3.8 °C/100 m, with a surface temperature baseline of 20 °C. Under this gradient, the formation temperature increases from 75 °C to 135 °C, while the outlet temperature differential expands from 55 °C to 105 °C. Correspondingly, the heat exchange rate improves from 102 kW to 153 kW—representing a 50% increase.

These results indicate that well depth is a primary geometric factor governing the recoverable thermal energy under constant geothermal gradient conditions. However, deeper wells are associated with exponentially increasing costs and construction risks—particularly in carbonate rock formations or faulted zones, where challenges such as wellbore stability and casing thermal expansion are more likely to occur. Therefore, a well depth range of 3000–3500 m is recommended, offering an optimal trade-off between thermal performance gains and engineering safety.

Based on the preceding simulation results, a Pareto front was constructed to evaluate the trade-off between heat transfer rate and pressure drop, thereby identifying optimal operating solutions within a multi-objective optimization framework. Uncertainty analysis was conducted using Monte Carlo simulations with 1000 iterations, considering parameter variations: geothermal gradient (±0.5 °C/100 m), thermal conductivity (±15%), and flow rate (±5%). Figure 8 presents the non-dominated solution set representing various operating conditions for the closed-loop geothermal system. The lower-left region of the Pareto curve denotes high-efficiency configurations, where the pressure drop ranges from 0.65 to 0.95 MPa and the corresponding heat transfer rate lies between 160 and 175 kW—defining the recommended operational envelope. The analysis reveals that solution combinations within the 0.65–0.95 MPa pressure drop and 165–175 kW heat transfer rate ranges constitute a non-inferior solution set, achieving optimal synergy between thermal performance and energy consumption. These optimal configurations are primarily associated with flow velocities near 1.0 m/s, reinforcing the nonlinear dominant role of flow velocity in governing system efficiency. These findings provide valuable guidance for the development of system control strategies, particularly in dynamic operational scenarios such as remote-controlled intelligent geothermal stations and variable-frequency pump regulation.

In summary, the heat transfer rate of deep CLGSs is significantly influenced by the coupled effects of multiple operating parameters. Effective system design and optimization must account for the combined impact of geothermal well depth, working fluid velocity,

and operating pressure drop. Based on the sensitivity analyses and Pareto optimization results presented in this study, it is recommended that future geothermal system deployments incorporate multi-objective constraint models during the engineering design phase. Such an approach will support the efficient, safe, and sustainable utilization of geothermal resources.

4.4. Comparison with Field Data (D22 Well)

To validate the transient behavior of the model, the simulated start-up response (0–120 min) was compared with field measurements from the D22 well (Figure 9). The root-mean-square error (RMSE) between simulated and measured outlet temperatures during this period is 1.8 °C, indicating good agreement in dynamic response. In order to validate the applicability and predictive capability of the numerical model in deep closed geothermal systems, this study selected the D22 well in the Xiongan New Area for field engineering comparison. The D22 well is a deep carbonate rock thermal reservoir system with a drilling depth of 3080 m and a formation temperature of 104.7 °C. Following acid stimulation enhancement, effective fracture channels were formed and a closed-loop circulation mode using CO_2 was employed for on-site heating tests. Comparing the model's predictions with the measured data, including outlet temperature, heating power and heating area, allows us to further evaluate its accuracy and adaptability.

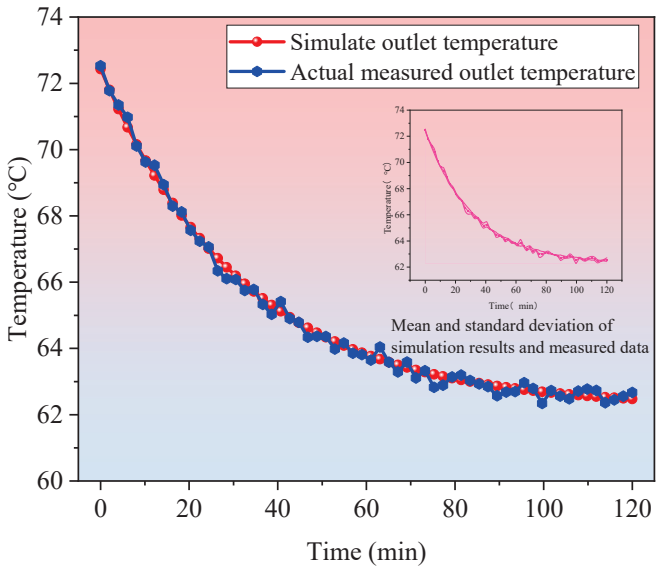

Figure 9. Comparison of outlet temperatures at the D22 well (simulation vs. actual measurement).

The simulation conditions were set to match the actual operating conditions at the site, with an inlet temperature of 20 °C, a flow velocity of 1.0 m/s and CO_2 as the circulating working fluid. The results in Figure 8 show that the predicted outlet temperature in the simulation is 76.8 °C, while the actual outlet temperature measured using an infrared thermometer is 77.2 °C under stable operating conditions, with a deviation of just 0.52%. In terms of heat transfer power, the model calculated a value of 186.3 kW, corresponding to a heating area of approximately 6035 m^2 (based on a heat load standard of 65 W/m^2). The measured heating area after heat conversion at the D22 well was 6062 m^2, with an error of less than 0.5%. Additionally, no groundwater extraction was observed during the D22 well's entire operational cycle, validating the model's boundary condition for a 'closed-loop system without water extraction'. These results demonstrate that the numerical model effectively reflects the primary characteristics of deep closed-loop systems in terms of heat transfer, flow field distribution and heat load conversion, and has high predictive reliability.

The validation extends beyond temperature predictions to include pressure drop and CO_2 density variations. The simulated pressure drop of 0.86 MPa aligns with field measurements (0.82 ± 0.05 MPa), representing a 4.9% relative error. CO_2 density profiles along the wellbore show maximum deviation of 4.3% from theoretical values, primarily in the near-critical region. Long-term stability assessment using 180-day operational data demonstrates thermal power consistency within ±5% variation, confirming the model's reliability for extended performance prediction.

Although the overall simulation results are highly consistent with the measured data, there are still some minor discrepancies. The sources of error primarily include the following aspects: Firstly, the heterogeneity of the thermal reservoir is a key factor. The model uses equivalent homogeneous thermal conductivity and permeability parameters, whereas the rock type actually encountered in the D22 well is primarily fractured limestone with significant variations in pore development in localized areas. This results in non-uniform heat conduction pathways, which may exert a minor influence on the exit temperature. Secondly, the formation contains natural structural fracture systems that have not been explicitly modeled. Seismic and logging data indicate that the D22 well area contains multiple tensile fractures which, after acid stimulation, formed high-thermal-conductivity channels that potentially redistributed the local CO_2 flow field and enhanced heat exchange effects near the wellbore. However, the model only approximates these effects using volume source terms, which may underestimate local heating rates.

Additionally, the wellbore's thermal insulation performance parameters were set using empirical values. However, the actual thermal insulation layer may have construction-related deviations, such as joints or moisture absorption, leading to slightly higher heat loss than theoretical values. Finally, the model boundary conditions were set to a stable, linear geothermal gradient of 30 °C/km. However, the geothermal field in the Xiongan New Area may be subject to complex influences, such as fracture heat flux and regional tectonic thermal disturbances. This could result in actual temperature fields that are slightly higher than theoretical estimates.

In summary, while there are some errors, the prediction errors of the numerical model for key indicators such as outlet temperature, heat exchange power and heating area are all controlled within ±3%. This indicates that the model has good engineering applicability and thermal response prediction capabilities. To enhance the modeling accuracy of heterogeneous thermal reservoirs and improve the model's broad applicability under complex reservoir conditions, it is recommended that future studies incorporate microseismic fracture monitoring, dynamic temperature-sensitive imaging logging, and core thermal conductivity experiments.

5. Discussion

5.1. Mechanism Illustration of CO_2 Heat Transfer Enhancement

Heat extraction in closed-loop wells emerges from a three-domain coupling among wellbore, near-well interface, and formation. Near-critical CO_2 exhibits lower viscosity and higher c_p, which pushes the dimensionless groups upward and reduces the fraction of wellbore heat loss at a comparable pressure drop.

$$R_e = \rho_\mu \cdot D_h/\mu, P_r = \mu C_p/k, N_\mu = f(R_e, P_r) \tag{12}$$

Under field-matched conditions, the single-well coaxial geometry with CO_2 achieves 186.3 kW average thermal power (+44.9% vs. water) with 3–5% lower wellbore heat-loss fraction.

The overall heat-transfer coefficient:

$$U^{-1} = h_{inner} + R_{\text{int}} + \delta_{ins}/k_{ins} + h_{outer}^{-1} \tag{13}$$

The analysis reveals that the superior heat transfer performance of CO_2 is partly attributed to its high inner convective heat transfer coefficient (h_{inner}), which effectively weakens the constraint imposed by the interfacial thermal resistance (R_{int}). This synergy between the working fluid and the wellbore design, when complemented with adequate insulation, significantly mitigates wellbore thermal losses and thereby retards the rate of outlet temperature decline during long-term operation.

Our results corroborate Randolph and Saar's [10] fundamental finding of CO_2's superior heat extraction capability but provide quantitative enhancement specifically for carbonate reservoirs (44.9% improvement over water vs. their reported 30–50% range for sandstone formations). Compared to Chen et al. [31] coaxial system model, our incorporation of dynamic CO_2 properties and interface thermal resistance yields more realistic wellbore heat loss predictions (3–5% reduction vs. their estimated 2–4%). The identified optimal flow velocity range of 0.9–1.1 m/s aligns with theoretical predictions but provides crucial field-validated constraints for engineering design in carbonate settings.

5.2. Long-Term Operational Performance

Extending field-calibrated parameters, the CO_2 system keeps the 30-year outlet temperature decline < 8 °C, while water drops by ≈12 °C.

The evolution is captured by the following stretched-exponential form:

$$T_{out}(t) = T_\infty + (T_0 - T_\infty)\exp\left[-(t/\tau)^\beta\right] \quad (14)$$

where CO_2 features a larger τ and smaller ultimate decline than water, indicating better reservoir utilization and steadier supply.

Around 0.9–1.1 m·s^{-1}, CO_2 shows slower early-time decay and a higher late-time plateau. Departing from this band raises pump power without proportional loss-reduction benefits, aligning with the Pareto trade-offs identified earlier.

From Figure 10, the 30-year outlet temperature decline is smaller for CO_2 than for water. Both trajectories decelerate with time; the effective half-life is 8.73 yr for CO_2 and 6.52 yr for water. Information-criterion differences strongly favor a stretched-exponential over a simple exponential model. Integrated over 0–30 yr, CO_2 yields 2168.58 °C·yr versus 2066.94 °C·yr for water. The resulting uncertainty bounds are shown in Figure 10, with the 95% confidence interval for CO_2 outlet temperature after 30 years being 68.2–69.9 °C. Sensitivity analysis reveals that thermal conductivity contributes 62% to the total uncertainty, highlighting the importance of accurate reservoir characterization.

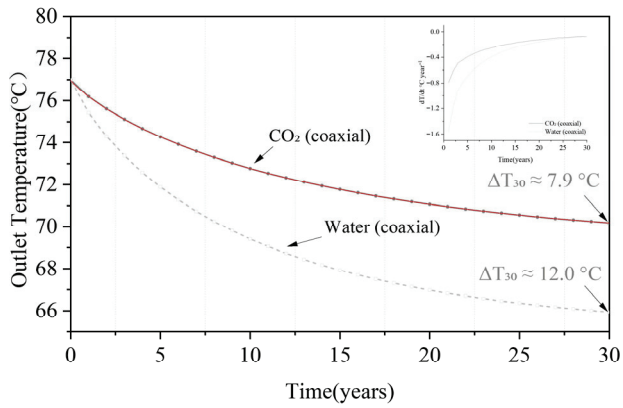

Figure 10. Long-term outlet-temperature evolution for CO_2 and water over 30 years.

While the model demonstrates strong agreement with field data, several limitations should be acknowledged. The assumption of reservoir homogeneity overlooks the influence

of fractures and localized porosity variations, which may lead to underestimation of local heat exchange rates. Furthermore, the long-term projections are based on a constant geothermal gradient and do not account for potential changes in regional heat flow. Future work should incorporate fracture network modeling and transient geothermal field data to improve predictive accuracy under heterogeneous conditions.

The carbonate reservoirs in the Xiongan area exhibit significant heterogeneity, particularly in the fractured Wumishan Formation. While our homogeneous model provides reasonable first-order predictions, localized fracture networks may create preferential flow paths. Post-acidization analysis indicates fracture density variations of 2–8 fractures per meter, which could lead to local temperature deviations of ± 3 °C from our predictions. Sensitivity analysis shows that $\pm 20\%$ variation in formation thermal conductivity results in $\pm 3.2\%$ change in outlet temperature. Future models should incorporate discrete fracture networks to better capture these heterogeneous effects.

6. Conclusions

This study developed a high-resolution, three-domain coupled model for closed-loop geothermal heat extraction in deep carbonate formations, using the D22 well in the Xiongan New Area as a representative case. Key innovations include the incorporation of dynamic thermophysical CO_2 properties, interface thermal resistance modeling, and multi-objective performance optimization. The following major conclusions are drawn:

(1) The proposed rock–interface–fluid coupling model, integrated with pressure- and temperature-sensitive CO_2 property functions, accurately predicts thermal responses in closed systems. Field validation against the D22 well demonstrates a deviation of less than 0.52% in outlet temperature and 0.5% in heating area, indicating strong predictive capacity.

(2) Compared to water, CO_2 exhibits superior heat transfer performance in deep geothermal environments due to enhanced thermal conductivity and low viscosity near its critical point. In single-well coaxial configurations, CO_2 yields 44.9% higher thermal power output and 3–5% lower wellbore heat losses, making it a more efficient and sustainable choice for deep heat extraction.

(3) Parametric sensitivity analysis and Pareto front optimization reveal that a flow rate of 0.9–1.1 m/s and a depth of 3000–3500 m offer the best trade-off between heat transfer efficiency and pressure drop. These results provide practical guidance for optimizing system design and reducing operating costs in similar geologic settings.

Based on the findings and limitations identified in this study, future research will focus on the following: (a) multi-well interaction effects and thermal interference management strategies; (b) techno-economic analysis incorporating drilling costs and operational expenses; (c) scaling logistics for district heating applications, including integration with seasonal thermal storage; (d) coupled geomechanical–thermal modeling to assess long-term reservoir integrity under thermal cycling; and (e) field demonstration of the identified optimal operating conditions in geologically similar carbonate reservoirs. These directions will further improve model robustness and applicability to a broader range of geothermal development scenarios.

Author Contributions: Software, X.W., T.J., B.M., W.S. and C.L.; Investigation, P.L. and M.W.; Data curation, T.J., B.M., W.S. and C.L.; Writing—original draft, X.W.; Writing—review & editing, X.W. and P.L.; Visualization, M.W.; Supervision, M.C.; Funding acquisition, P.L. All authors have read and agreed to the published version of the manuscript.

Funding: This work was financially supported by the Science and Technology Innovation Program of Xiongan New Area (No. 2023XAGG0061), the National Natural Science Foundation of China

(Nos. 52204084 and 52474091), and the National Key Research and Development Program of China (Nos. 2022YFC2905600 and 2022YFC3004601).

Data Availability Statement: The original contributions presented in this study are included in the article. Further inquiries can be directed to the corresponding author.

Acknowledgments: The authors are grateful to the field engineering team of the D22 well in the Xiongan New Area for providing essential data and technical support.

Conflicts of Interest: The authors declare no conflicts of interest.

Nomenclature

T_{r}	Rock temperature (°C)
α_r	Thermal diffusivity ($m^2 \cdot s^{-1}$)
$R_{\mathrm{interface}}$	Interfacial thermal resistance ($K \cdot m^2 \cdot W^{-1}$)
ρ_f	Fluid density ($kg \cdot m^{-3}$)
$c_{\mathrm{p,f}}$	Specific heat capacity ($J \cdot kg^{-1} \cdot K^{-1}$)
CLGS	Closed-loop geothermal system
TH	Thermo-hydraulic
EGS	Enhanced geothermal system

References

1. Huo, C.; Lin, Y.; Li, G.; Zhang, J.; Pan, H.; Zhao, Y.; Wang, D. Research progress on geothermal resource exploration technologies in China under carbon neutrality background. *Sci. Technol. Eng.* **2023**, *23*, 4917–4927.
2. Xia, Q.; Guo, S.; Ma, J.; Meng, B.; Cai, W.; Kong, Y. Review of geothermal energy utilization technologies. *Taiyangneng* **2024**, *7*, 109–117.
3. Zhao, C.; Shang, H.; Jin, D.; Wang, H.; Xu, S.; Wang, X.; Zhang, W. Numerical simulation analysis of coaxial heat exchange capacity in deep vertical wells. *Meitan Dizhi Yu Kantan* **2020**, *48*, 174–181.
4. Feng, B.; Liu, X.; Zhang, G.; Shangguan, S.; Hu, Z.; Yuan, Y.; Feng, G. Numerical simulation of sustainable development potential for single-well closed-loop geothermal systems. *Nat. Gas Ind.* **2020**, *40*, 146–155.
5. Wang, Z.; Hu, B.; Zhang, J.; Li, Z. Simulation of pump head for circulating power equipment in large-volume single-well heat exchange systems in layered thermal reservoirs. *Zhongguo Kuangye* **2022**, *31*, 164–171.
6. Liu, W.; Dong, Y.; Zhang, X.; Wang, T. Development potential and environmental benefits analysis of medium-deep borehole heat exchanger heating systems in northwestern provincial capitals. *Xibei Dizhi* **2023**, *56*, 186–195.
7. Chen, C.; Li, J.; Wang, Z.; Gu, S.; Li, S. Distribution characteristics and development strategies of geothermal resources in northern Songliao Basin. *Petrol. Geol. Oilfield Dev. Daqing* **2024**, *43*, 215–222.
8. Bi, S.; Wan, Z.; Zhang, H.; Wang, M.; Wang, J.; Liu, Z.; Wang, C. Development and utilization of geothermal resources in Tangkou Coal Mine. *Meitan Kexue Jishu* **2018**, *46*, 208–214.
9. Pruess, K. Enhanced geothermal systems (EGS) using CO_2 as working fluid—A novel approach for generating renewable energy with simultaneous sequestration of carbon. *Geothermics* **2006**, *35*, 351–367. [CrossRef]
10. Randolph, J.B.; Saar, M.O. Combining geothermal energy capture with geologic carbon dioxide sequestration. *Geophys. Res. Lett.* **2011**, *38*. [CrossRef]
11. Cai, X.; Liu, Z.; Xu, K.; Li, B.; Yang, M. Numerical simulation on converting abandoned wells into double-well open-loop geothermal system. *Appl. Therm. Eng.* **2024**, *248*, 123324. [CrossRef]
12. Aryanfar, Y.; Wu, W. Performance assessment of a transcritical CO_2 cycle integrated with a double flash geothermal system and reverse osmosis desalination. *Desalination* **2025**, *613*, 119107. [CrossRef]
13. Aydın, H.; Camcı, U.; Akın, S. An experimental investigation of hydraulic fracturing mechanisms in menderes metamorphic rocks: Prospects for enhanced geothermal systems. *Geothermics* **2025**, *130*, 103328. [CrossRef]
14. Chen, H.; Shi, Y.; Liu, C.; Zhao, Z.; Yue, Y.; Li, M. Performance comparison of different well configurations for medium-deep coaxial closed-loop geothermal systems. *Appl. Therm. Eng.* **2025**, *271*, 126393. [CrossRef]
15. Wu, X.; Cai, M.; Wu, X.; Li, P.; Zhang, S.; Sun, J. Experimental study on nonlinear failure criterion of HDR under cyclic water-induced thermal shock. *Bull. Eng. Geol. Environ.* **2025**, *84*, 255. [CrossRef]
16. Liu, Z.; Xu, K.; Zhang, Q.; Yang, M. Numerical simulation on the heat recovery law of exploiting geothermal energy from a closed-loop geothermal system converted from an abandoned five-spot well pattern. *ACS Omega* **2022**, *7*, 41723–41731. [CrossRef]

17. Wang, G.; Zhou, F.; Jia, H.; Wang, L.; Klitzsch, N.; Feng, G.; Yan, C.; Ma, H.; Liu, S.; Yin, Q.; et al. Heat extraction performance of multi-level, multi-branch, closed loop coaxial horizontal borehole heat exchanger geothermal system. *Appl. Therm. Eng.* **2025**, *269*, 126045. [CrossRef]
18. Wu, X.; Li, P.; Miao, S.; Cai, M.; Liu, Y.; Wang, M.; Xiong, W. Multi-field Coupling Mechanism and Optimization of Heat Transfer in Deep Carbonate Geothermal Reservoirs Based on Acid Fracturing Modification. *Case Stud. Therm. Eng.* **2025**, *73*, 106591. [CrossRef]
19. Wang, Y.; Wang, Y.; Jiang, G.; Hu, J.; Shi, Y.; Wang, S.; Hu, S. A Method for Determining Target Areas of Hot Dry Rock Resources: A Case Study in Continental China. *Energies* **2024**, *17*, 2435. [CrossRef]
20. Liu, Z.; Wu, M.; Zhou, H.; Chen, L.; Wang, X. Performance evaluation of enhanced geothermal systems with intermittent thermal extraction for sustainable energy production. *J. Clean. Prod.* **2024**, *434*, 139954. [CrossRef]
21. Xu, Z.; Zhao, H.; Fan, L.; Jia, Q.; Zhang, T.; Zhang, X.; Han, D.; Tan, Y.; Liu, J. A literature review of using supercritical CO2 for geothermal energy extraction: Potential, methods, challenges, and perspectives. *Renew. Energy Focus* **2024**, *51*, 100637. [CrossRef]
22. Cui, Y.; Zhu, C.; Qiu, N.; Tang, B.; Guo, S.; Lu, Z. The heat source origin of geothermal resources in Xiong'an new area, north China, in view of the influence of igneous rocks. *Front. Earth Sci.* **2022**, *10*, 818129. [CrossRef]
23. Zhang, H.; Wang, G.; Zhang, W.; Ma, F.; Zhu, X.; Yue, G.; Yu, M. Characteristics of the Rongcheng Bulge geothermal field and the evolution of geothermal fluids, Xiong'an New Area, China. *Water* **2022**, *14*, 2468. [CrossRef]
24. Wang, G.; Ma, H.; Liu, S.; Yang, D.; Xu, X.; Fu, M.; Jia, H. Thermal power extraction from a deep, closed-loop, multi-level, multi-branch, U-shaped borehole heat exchanger geothermal system. *Renew. Energy* **2022**, *198*, 894–906. [CrossRef]
25. Liu, Z.; Yang, W.; Xu, K.; Zhang, Q.; Yan, L.; Li, B.; Cai, X.; Yang, M. Research progress of technologies and numerical simulations in exploiting geothermal energy from abandoned wells: A review. *Geoenergy Sci. Eng.* **2023**, *224*, 211624. [CrossRef]
26. Zhong, C.; Xu, T.; Yuan, Y.; Feng, B.; Yu, H. The feasibility of clean power generation from a novel dual-vertical-well enhanced geothermal system (EGS): A case study in the Gonghe Basin, China. *J. Clean. Prod.* **2022**, *344*, 131109. [CrossRef]
27. Zheng, Z.; Ma, Z.; Qi, J.; Su, G.; Lu, G.; Pei, S.; Jiang, Q. Multi-directional disturbance effect of shear mechanical behaviors and fracturing mechanisms of rockmass intermittent structural plane under true triaxial shear test. *Int. J. Min. Sci. Technol.* **2025**, *35*, 933–960. [CrossRef]
28. Zheng, Z.; Li, R.; Pan, P.; Wang, W. Excavation disturbance response of deep-buried tunnel with novel dynamic anisotropic mechanical model and failure degree index. *Tunn. Undergr. Space Technol.* **2025**, *158*, 106429. [CrossRef]
29. Davoodi, S.; Al-Shargabi, M.; Wood, D.A.; Slivkin, S.; Shishaev, G.; Rukavishnikov, V.S. Geothermal energy recovery from abandoned petroleum wells: A review of the challenges and opportunities. *Sustain. Energy Technol. Assess.* **2024**, *68*, 103870. [CrossRef]
30. Song, X.; Xu, F.; Ji, J.; Shi, Y. Evaluation of the heat extraction performance of an abandoned well pattern in multilayer commingled production oil reservoirs. *Nat. Gas Ind. B* **2022**, *9*, 578–587. [CrossRef]
31. Chen, C.; Xu, P. Cellular functions of cGAS-STING signaling. *Trends Cell Biol.* **2023**, *33*, 630–648. [CrossRef]

Disclaimer/Publisher's Note: The statements, opinions and data contained in all publications are solely those of the individual author(s) and contributor(s) and not of MDPI and/or the editor(s). MDPI and/or the editor(s) disclaim responsibility for any injury to people or property resulting from any ideas, methods, instructions or products referred to in the content.

materials

MDPI

Article

Research on Mechanical Properties of Nano-Modified Foam Concrete Improved by Micro-inCorporated Carbon Nanotubes

Shukun Zhang [1], Peng Jiang [1,*], Haohao Wang [1], Dianzhi Feng [2] and Hao Wang [3]

[1] School of City and Architecture Engineering, Zaozhuang University, Zaozhuang 277160, China; 4254423@163.com (S.Z.)
[2] School of Civil Engineering, Liaoning Technical University, Fuxin 123000, China
[3] College of Pipeline and Civil Engineering, China University of Petroleum (East China), Qingdao 266580, China; 18663670776@163.com
* Correspondence: pengjiang@uzz.edu.cn

Abstract

Foamed concrete is a lightweight, environmentally friendly civil engineering material with excellent absorption capacity. It has been widely applied in engineering fields such as building thermal insulation and pore filling of underground buried pipelines. But the mechanical properties of existing foamed concrete cannot meet the engineering requirements for support, pressure relief and filling of weak surrounding rock. The mechanical properties of foamed concrete were improved with CNTs to prepare CNT foamed concrete (CNTFC) pressure-relieving filling materials. The effects of five factors (the fly ash (FA) incorporation rate, aggregate–cement ratio, water–binder ratio, CNT incorporation rate and foam volume fraction) on the density and 2:1 cylinder strength (the ratio of uniaxial compressive strength to apparent density), splitting tensile (the ratio of splitting tensile strength to apparent density) and specific strength of the CNTFC were analyzed. By combining stress–strain and scanning electron microscopy analyses, the mechanism of improvement of the mechanical strength of CNTFC due to CNTs was clarified. The results show that the foam volume fraction, water–binder ratio and aggregate–cement ratio are the top three factors affecting its strength, followed by the CNT incorporation rate and FA incorporation rate. Among the five influencing factors, only the incorporation of CNTs increases the 2:1 cylinder strength, splitting tensile strength and specific strength. When the doping rate is 0.05%, this ratio specifically refers to the mass of CNTs accounting for 0.05% of the mass of the total cementitious materials of cement and fly ash. At this doping dosage, compared with the condition without CNTs (0% doping dosage), the uniaxial compressive strength increased from 6.23 MPa to 7.18 MPa (with an increase rate of 15.3%). The splitting tensile strength increased from 0.958 MPa to 1.02 MPa (with an increase rate of 6.5%). The density only slightly increased from 0.98 g/cm^3 to 1.0 g/cm^3 (with an increase rate of 2.0%), achieving the balance of "high strength-low density". CNTs and cement hydrates are interwoven into a network structure, and the mechanical properties of the CNTFC are effectively improved by the excellent nanoscopic tensile properties. Excessive doping of CNTs takes 0.05% as the threshold. Exceeding this doping dosage (such as 0.10% and 0.15%) leads to a decrease in its strength and ductility due to CNT agglomeration and deterioration of pore structure. And 0.05% is the ratio of the mass of CNTs to the total cementitious materials of cement and fly ash. At this doping dosage, CNTs are uniformly dispersed and can balance the strength and density of CNTFC. The optimum proportion of CNTs is 0.05%.

Keywords: CNTs; foamed concrete; proportion; mechanical properties of pressure relief filling; support of weak surrounding rock

1. Introduction

There have been some papers studying the characteristics of foamed concrete with low density, good post-peak ductility and strong sealing and absorbing deformation [1–3], and it has many applications in building insulation, underground pipeline filling and so on [4,5]. Currently, the industry usually classifies low-density foamed concrete according to apparent density [6]. Ultra-light foamed concrete has high porosity and low thermal conductivity [7] and is mainly used for building thermal insulation layers and lightweight partition walls. Low-density foamed concrete has light weight and certain bearing capacity and is suitable for filling non-load-bearing structures and plugging pipeline pores [8]. Medium-low-density foamed concrete has a better balance between strength and density and can be used for light load-bearing filling or pretreatment of surrounding rock support. The introduction of fly ash and air bubbles greatly reduces the consumption of cement in the process of foamed concrete preparation and also solves the problems of coal ash storage and environmental pollution. By improving the mechanical properties of foamed concrete, the pressure-relief material suitable for supporting soft surrounding rock is improved [9].

At present, researchers have made many achievements in improving the physical and mechanical properties of foamed concrete. For example, previous studies have shown that the incorporation of glazed hollow beads enhances the compressive strength of foamed concrete [10]. Some studies prepared ultra-light foamed concrete with a density of less than 150 kg/m^3 by the foaming method [11]. Other studies used stone powder as aggregate to replace foamed concrete mixed with river sand to reduce material costs [12]. Additionally, the influence of porosity on the performance of foamed concrete was studied by using the discrete element method [13]. The corrosion resistance of foamed concrete was improved by adding silica fume (SF) [14]. By mixing kenaf fiber [15], the concrete toughness of foamed concrete was improved, and by mixing in carbon nanotubes (CNTs), the flexural strength and compressive strength of autoclaved foamed concrete were increased [16]. Some researchers showed that as a new material [17], foamed concrete has not been widely studied in terms of proportion optimization [18], and the improvement of the performance of foamed concrete is in the exploratory stage. Research on improving the physical and mechanical properties of foamed concrete by nanofiber is even more rare [7]. In this paper, by adding CNTs, the nanoscale and tensile strength properties of foamed concrete are improved, and the mechanical properties of foamed concrete are effectively improved [19,20]. A CNT foamed concrete (CNTFC) filling medium suitable for unloading surrounding rock is prepared. The mechanical and microscopic characteristics of CNTFC with different proportions are analyzed by the orthogonal test method. The optimal proportioning of CNTFC is determined by comprehensive analysis according to the actual control requirements of surrounding rock deformation [21–24].

2. Experimental Design and Specimen Preparation of CNT Foamed Concrete (CNTFC) as Pressure-Relief Filling Material

2.1. Constituents

The cement was Fuxin Yingshan ordinary Portland cement PO42.5 according to national standards GB/T12960 [25] the supplemental fly ash (FA) was produced by Fuxin Power Plant, with a density of 2.12 g/cm^3, a fineness of 10.8% and a quality grade of I. This curve was plotted using the laser particle size analysis method. "Differential volume" refers

https://doi.org/10.3390/ma19010184

to the volume during particle size analysis. The percentage of the volume of fly ash particles within a specific particle size range (such as 0.1~1 μm, 1~10 μm, 10~100 μm, etc.) accounts for the total volume of all fly ash particles. It reflects the particle size characteristics of fly ash: "dominated by fine particles, concentrated gradation, and few coarse particles". The grading curve is shown in Figure 1. The aggregate was a natural river sand with a particle size less than 2.36 mm after screening, and its apparent density was 2.23 g/cm^3. The liquid was produced by Zhengzhou Pengyi Chemical Products Co., Ltd. (Zhengzhou, China). ZT-F50 type cement has a foaming volume of 60 mL/g, an active substance content of 30% and a decomposition temperature of 5 °C. The surface tension at 25 °C is 28–32 mN/m, and it can effectively reduce the surface energy of aqueous solution and promote the formation of uniform bubbles. The surfactant composition is dominated by anionic surfactant (sodium dodecylbenzene sulfonate, mass fraction 15–20%) and blended with nonionic surfactant (fatty alcohol polyoxyethylene ether, mass fraction 5–8%). The synergistic effect of the two can improve foam stability. The CNTs were produced by Shenzhen Turing Evolution Technology Co., Ltd. (Shenzhen, China). The CNTs are multi-walled carbon nanotubes (MWCNTs), treated by mixed acid ultrasonic oxidation. Their surface is grafted with carboxyl (–COOH) and hydroxyl (–OH) groups. The total content of functional groups is 2.5–3.0%, and it can improve interface compatibility with cement paste and reduce agglomeration. The residual catalyst is Fe and Ni metal particles, with a mass fraction $\leq$0.5%. The parameters of the CNTs are shown in Table 1. The chemical compositions of materials are shown in Table 2.

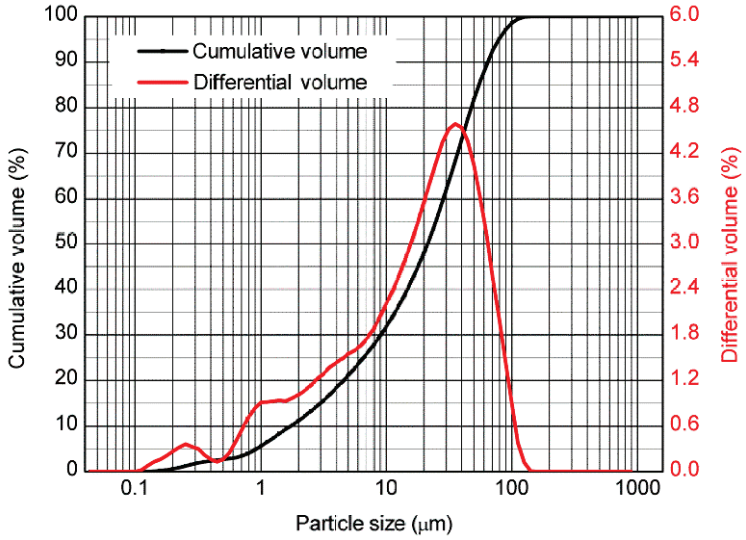

Figure 1. Particle size curve of FA [26].

Table 1. Material parameters of CNTs [23].

Material Type	Morphology	Purity (%)	Grey (%)	Diameter (nm)	Tube Length (μm)	Specific Surface Area cm^2/g	Bulk Density (g/cm^3)
MWCNTs	fluffy black powder	>97	<2.5	3–15	15–30	250–270	0.06–0.09

https://doi.org/10.3390/ma19010184

Table 2. Chemical compositions of materials (mass fraction %) [26].

Chemical Compositions	Fly Ash	Cement
SiO_2	53.75	22.56
Al_2O_3	29.37	4.64
CaO	3.68	61.28
Fe_2O_3	5.64	2.35
MnO	1.08	2.04
Na_2O	–	0.60
K_2O	0.68	0.75
SO_3	1.29	2.83
LOSS	3.58	2.01

2.2. Test Specimen Preparation

The effect of CNT dispersion on the mechanical properties of foamed concrete is very important, and CNT dispersion mainly comprises physical dispersion and chemical dispersion [27]. The study used ultrasonic dispersion plus physical stirring to disperse CNTs. First, the CNTs were wetted in a closed plastic container, and then the CNTs were mechanically stirred and ultrasonically dispersed for 30 min to prepare a CNT dispersion. The slurry mixture was prepared by thoroughly mixing cement, FA, natural sand and water according to the selected ratio [26]. The foaming agent and water were placed in a deep plastic bucket at a ratio of 1:40 and mechanically stirred with a stirrer rotating at 1500 r/min to prepare a uniform and stable foam. The prepared CNT dispersion was mixed into the slurry mixture, stirred for 10 min, mixed with foam for approximately 4 min, and allowed to stand for 2 to 3 min. Then, the foamed concrete sample was poured. The cast specimens were cylindrical, with a diameter of 5 cm and a height of 10 cm. After standing for 48 h in 20 °C with the test model covered with wet cloth, each specimen was demolded, placed in a curing box for standard curing for 28 days, removed to air dry for 3 h, and then subjected to mechanical tests. The strength test was performed according to the relevant specifications [28].

2.3. Test Scheme

Based on the material performance requirements of roadway support and pressure relief, an orthogonal test was designed to measure the CNTFC specimens with different FA incorporation rates, aggregate–cement ratios, water–binder ratios, CNT incorporation rates and foam volume fractions. The uniaxial compression strength, splitting tensile strength and density data are used to analyze the influence of various factors on the performance of CNTFC and initially determine the proportioning scheme applicable to the surrounding rock support and roadway pressure relief. The device for the characterization test is an in situ transmission electron microscope. The device used for the characterization test is a JSM-7500F scanning electron microscope (SEM), which is available at Liaoning Technical University (Fuxin, Liaoning Province, China). The manufacturer of this SEM is JEOL Ltd., a well-known equipment supplier in the field of electron microscopy, and its headquarters is situated in Tokyo, Japan. The image quality is clear. To save costs, no metal plating was conducted before the SEM analysis. To analyze the internal structure and pore characteristics of the corresponding CNTFC specimens, we used SEM technology with medium voltage (5–10 kV) and medium WD (8–12 mm), which laid the foundation for the subsequent determination of the optimal mixing ratio. The specific test specimen preparation and testing process are shown in Figure 2.

https://doi.org/10.3390/ma19010184

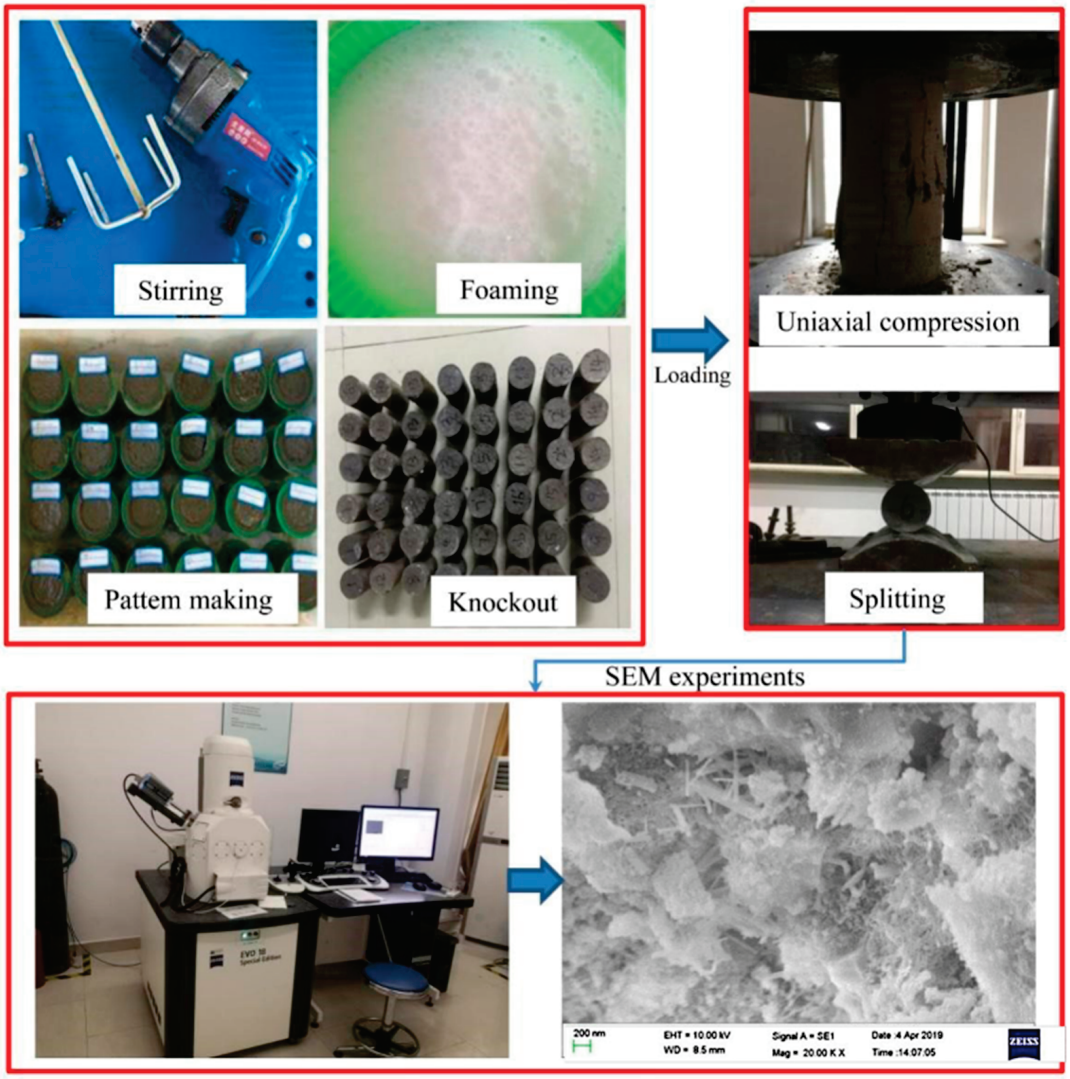

Figure 2. Specimen preparation and testing process.

Some studies indicate that it is unable to provide a surrounding rock support strength close to 1 MPa [29,30]. Considering the stress concentration that arises in the high-strength support structure, researchers showed that the required strength for the performance of the surrounding rock support pressure-relief material is between 1~10 MPa [31,32]. Compared with traditional concrete, foamed concrete has the characteristics of large deformation, light weight and low cost, and the excellent plasticity of foamed concrete can be used as a large deformation absorption material [33–35]. CNTs are high-strength and high-toughness materials with tensile strength of 50–200 GPa and elastic modulus of about 1 TPa. In recent years, some scholars have proposed to improve foamed concrete by using CNTs [17]. According to the literature and the preliminary research results of this research group, natural sand is used as the aggregate, FA and cement are used as the cementing materials and CNT fibers are micro-doped to prepare CNTFC filling and pressure-relief material. A 5-factor, 4-level orthogonal test was designed. The specific ratio scheme is shown in Table 3.

https://doi.org/10.3390/ma19010184

Table 3. Horizontal table of orthogonal factors [35].

Factors / Level	A FA Incorporation Rate/%	B Aggregate–Cement Ratio/%	C Water–Binder Ratio/%	D CNT Incorporation Rate/%	E Foam Volume Fraction/%
1	40	0	45	0	50
2	60	5	50	0.05	80
3	80	10	55	0.10	120
4	100	15	60	0.15	150

Note: The foam content is the volume fraction, and the others are mass fractions.

The FA incorporation rate is the mass ratio of the FA to that of the cement. The aggregate–cement ratio is the mass ratio of the natural sand to that of the cementitious material. The water–binder ratio is the mass ratio of the water to that of the cementitious material. The CNT incorporation rate is the mass of the CNTs to that of the glue. The amount of foam is the ratio of the volume of the foam to the volume of the mixture.

The tests were carried out at the Structural Laboratory of the School of Civil Engineering, Liaoning Technical University. The loading test instrument employed in this study is a WDW-300KN electronic universal testing machine, which is produced by Jinan Times Tester Co., Ltd. (Jinan, Shandong Province, China). The test was carried out using this equipment housed at Liaoning Technical University (Fuxin, Liaoning Province, China). The loading rate was controlled to 0.05 MPa/s during the splitting tensile strength tests, and the loading rate during the 2:1 cylinder strength tests was controlled to 1 mm/min. The device for characterization tests is an in situ transmission electron microscope. A commissioned third party, namely "Testing Dog" (a professional testing service platform in China), performed the microstructure testing. The SEM device used for the test was model SUPRA55, which is manufactured by Carl Zeiss AG (Oberkochen, Germany). This equipment has a resolution of 1.0 nm and a magnification range of 12~900,000×.

3. Analysis on Influence Rules and Mechanisms of CNTs on Mechanical Properties of CNTFC

3.1. Strength and Density Test Results

The 2:1 cylinder strength, splitting tensile strength and density test results of the CNTFC filling and pressure-relieving material after curing for 28 days are shown in Table 4. Each result is accurate to the third decimal place.

Table 4. Orthogonal test table and mechanical test results.

Category / Number	A	B	C	D	E	2:1 Cylinder Strength /MPa	Splitting Tensile Strength/MPa	Density/ g/cm^3
#1	1	1	1	1	1	12.853	1.921	1.370
#2	1	2	2	2	2	5.427	0.892	0.920
#3	1	3	3	3	3	6.579	0.574	1.010
#4	1	4	4	4	4	7.862	0.705	1.030
#5	2	1	2	3	4	3.880	0.441	0.760
#6	2	2	1	4	3	18.381	1.210	1.350
#7	2	3	4	1	2	4.344	0.405	0.710
#8	2	4	3	2	1	12.095	1.997	1.380
#9	3	1	3	4	2	3.311	0.593	1.020
#10	3	2	4	3	1	14.054	1.871	1.010
#11	3	3	1	2	4	8.835	0.786	0.980
#12	3	4	2	1	3	5.127	0.804	0.930

https://doi.org/10.3390/ma19010184

Table 4. *Cont.*

Number \ Category	A	B	C	D	E	2:1 Cylinder Strength /MPa	Splitting Tensile Strength/MPa	Density/ g/cm^3
#13	4	1	4	2	3	2.382	0.390	0.690
#14	4	2	3	1	4	2.605	0.724	0.900
#15	4	3	2	4	1	11.663	0.909	1.250
#16	4	4	1	3	2	6.094	1.122	1.020

3.2. Visual Analysis

The specimens were divided into two large groups, and 16 proportioned specimens were prepared for each large group; three specimens with the same ratio were processed for parallel testing. A total of 96 specimens was prepared. The 2:1 cylinder strength and splitting tensile strength tests with five factors and four levels were carried out to obtain the corresponding stress–strain data; additionally, the specimen density was measured.

Table 4 shows that the #6 specimen has the highest 2:1 cylinder strength, and the combination ratio is $A_2B_2C_1D_4E_3$. The corresponding FA incorporation rate is 60%, aggregate–cement ratio is 5%, water–binder ratio is 45%, CNT incorporation rate is 0.15% and foam volume fraction is 120%; the corresponding splitting tensile strength ranks fourth in the 16-group test, and the corresponding density ranks third in the 16-group trial. The #8 specimen has the highest splitting tensile strength and density, and the combination ratio is $A_2B_4C_3D_2E_1$, corresponding to an FA incorporation rate of 60%, an aggregate–cement ratio of 15%, a water–binder ratio of 55% and a CNT incorporation rate of 0.05%. The corresponding foam volume score is 50%. The 2:1 cylinder strength of the #8 specimen ranks fourth in the 16 groups of tests. Specimens #5, #13 and #14 have the lowest densities, and specimen #5 is directly eliminated due to not only its low strength index but also its low FA incorporation rate, high CNT incorporation rate and poor economy and applicability. Although the FA incorporation rates of specimens #13 and #14 are high and their CNT ratios are low, their mechanical strength indexes are low, and it is difficult to meet the pressure-relief requirements of the surrounding rock support. These combinations are also directly excluded.

3.3. Orthogonal Test Range Analysis

The extreme difference between the 2:1 cylinder strength and splitting tensile strength shown in Table 5 suggests that the foam volume fraction, the water–binder ratio and the aggregate–cement ratio affect the strength of the test specimens the most, while the CNT incorporation rate and FA incorporation rates have a secondary effect. This result is because the foam volume fraction and the water–binder ratio determine the porosity of a test specimen. The lower the porosity of a test specimen, the higher the density and the more favorable the corresponding strength parameter, significantly affecting the 2:1 cylinder strength and splitting tensile strength. And the higher strength parameters of specimens correspond with higher 2:1 cylinder strength and splitting tensile strength. Table 4 also proves this point. Porosity is a core intermediate factor linking CNTFC's mix parameters to its final properties, exerting three key effects. For strength, it correlates negatively—when the foam volume fraction (key for porosity control) rises from 50% to 150%, 2:1 cylinder strength drops by 54.2% and splitting tensile strength by 60.4%, and excessive porosity disrupts CNT-hydrate networks, further weakening strength. For density, it also correlates negatively (air in pores is far less dense than a solid matrix like cement/fly ash)—the foam volume fraction 50%→150% cuts density by 26.74%, while the water–binder ratio 45%→60% reduces it by 27.12%. For ductility/toughness, moderate porosity boosts ductility via deformation space, but excess causes brittle failure; only when

https://doi.org/10.3390/ma19010184

porosity matches 0.05% CNT incorporation (CNTs fill small pores and inhibit cracks) can CNTFC balance strength, density and ductility. The subsequent specific strength analysis shows this in detail. At present, it is difficult to further improve the mechanical properties and economy of foamed concrete by adjusting factors such as the foam volume fraction, water–binder ratio and aggregate–cement ratio. The incorporation of FA can adjust the gradation of the mixture and replace part of the cement to achieve economic efficiency. However, due to its low activity, increasing the dosage will reduce the strength of the CNTFC. Therefore, the incorporation of CNTs is required to improve the micro-scale characteristics of foamed concrete, which further improves the mechanical properties of foamed concrete.

Table 5. Orthogonal test range.

Types	*A* Fly Ash Incorporation Rate (%)	*B* Bone Glue Ratio (%)	*C* Water–Cement ratio (%)	*D* CNT Doping Rate (%)	*E* Foam Volume Fraction (%)
2:1 Cylinder strength	3.989	4.507	5.394	4.074	7.872
Splitting tensile strength	0.235	0.513	0.501	0.165	1.010
Density	1.175	1.225	3.275	2.200	3.275

3.4. Influence Analysis of the Strength and Density of CNT Foamed Concrete

3.4.1. Analysis of Compressive Strength

According to the orthogonal test method, we calculated the average value of the 2:1 cylinder strength of CNT foamed concrete (CNTFC) at 28 days under each level of each influencing factor from the visual analysis table (Table 4) and also drew a column chart (Figure 3). When the fly ash (FA) incorporation rate increases from 40% to 60%, the 2:1 cylinder strength of CNTFC rises from 8.180 MPa to 9.675 MPa, with an increase rate of 18.28%; when it increases from 60% to 80%, the strength drops to 7.832 MPa, with a decrease rate of 18.5%; when it increases from 80% to 100%, the strength drops to 5.686 MPa, with a decrease rate of 27.40%. The reason for these changes is the "morphological effect" of the glass beads in the lesser amount of FA. It promotes the deflocculation effect during the initial cement hydration. Additionally, the microbeads and small particles can gather in dense clusters outside the foam pores. The other pores, together with the cement gel, form a dense bubble wall that increases the strength of the CNTFC. The FA incorporation rate is further improved. Because its activity is lower than the cement activity, using FA in place of an equal amount of cement reduces the amount of cement required, delays the hydration degree of the whole system, and leads to a decrease in the 2:1 cylinder strength of the CNTFC. When the aggregate–cement ratio ranges from 0 to 15%, the 2:1 cylinder strength of the CNTFC first increases and then decreases. The corresponding strengths are 5.607 MPa, 10.117 MPa, 7.855 MPa and 7.795 MPa. When the aggregate–cement ratio is 5%, the 2:1 cylinder strength of the CNTFC is the highest. When the incorporation rate of natural sand (used as aggregate) is low, the sand is surrounded by FA, cement and air bubbles. At this time, the strength of the CNTFC mainly depends on the strength of the FA and cement slurry, so the strength is low. As the aggregate–cement ratio increases, cement and FA encapsulate the sand aggregate. They form a bearing matrix around the bubbles. Thus, the CNTFC achieves higher compressive strength. When the sand ratio is high, the hydrated products from FA and cement are less likely to surround the aggregate particles, and inclusions are difficult to carry within the air bubbles, resulting in a decrease in the strength of the CNTFC.

https://doi.org/10.3390/ma19010184

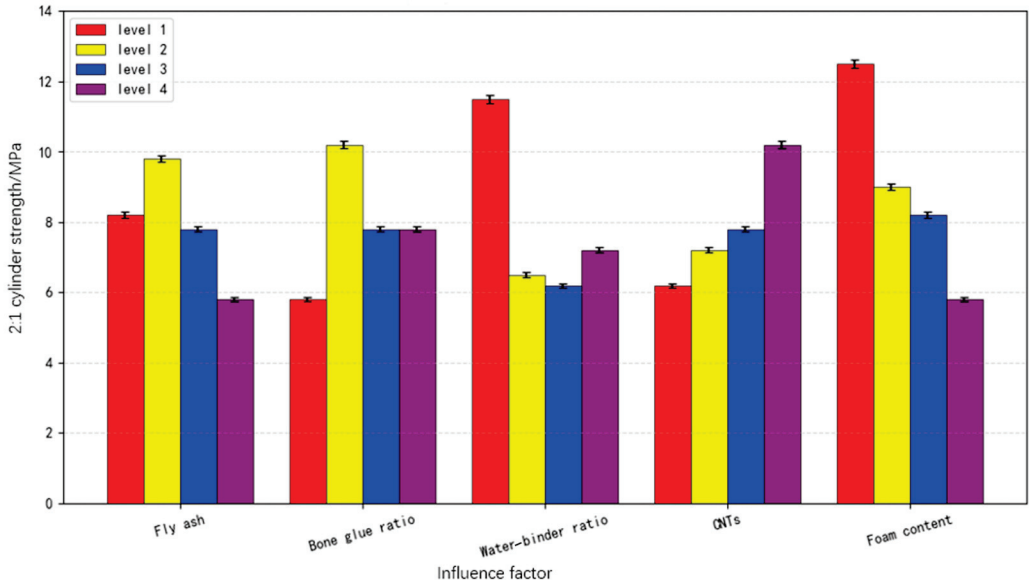

Figure 3. Variation in CNTFC 2:1 cylinder strength under the influence of various factors.

When the water–binder ratio is 45%, the 2:1 cylinder strength of the CNTFC is the highest, being 11.541 MPa. When the water–binder ratio is increased from 45% to 50%, the 2:1 cylinder strength of the CNTFC drops sharply by 43.47%. When the water–binder ratio is between 50% and 60%, the strength regularity of the CNTFC is not obvious. Low-water cement has a higher strength than CNTFC, high-water cement has a lower strength than CNTFC and the effect is consistent with that of ordinary concrete. When the water–binder ratio exceeds 50%, the influence on CNTFC is not obvious, and the strength is at a low level, which may be related to the CNTFC solidification and curing.

When the CNTs increased from 0 to 0.15%, the 2:1 cylinder strength of the CNTFCs showed a stepwise increase, and the corresponding strengths were 6.232 MPa, 7.185 MPa, 7.652 MPa and 10.304 MPa, with growth rates of 15.29%, 6.50% and 34.66%, respectively. CNTs, by virtue of their excellent tensile properties, are intertwined with the cement, FA and hydrates and enclose the aggregate more densely, improving the foamed concrete characteristics and thus effectively improving the strength of the foamed concrete. Foam incorporation is the most significant factor affecting the strength of CNTFC. As the foam incorporation increases from 50% to 150%, the 2:1 cylinder strength of CNTFC decreases: 12.666 MPa, 9.794 MPa, 8.117 MPa and 5.796 MPa, corresponding to decreases of 22.67%, 17.12% and 28.59%, respectively. The introduction of bubbles increases the void space, reduces the load-carrying capacity of the cement and aggregate and greatly reduces the strength of the CNTFC.

Based on the density test results in the paper (Table 4, Figure 4) and combined with the classic correlation formula between porosity and density of foamed concrete [13,17],

$$P = 1 - \frac{\rho}{\rho_0} \quad (1)$$

where P is the total porosity (%), ϱ (g/cm^3) is the measured density of CNTFC (Table 4), and ϱ_0 (g/cm^3) is the solid-phase density of the matrix (based on the chemical composition of cement and fly ash in Table 2). The calculated value of ϱ_0 is 2.28 g/cm^3. Thus, the actual porosity is estimated. Taking the groups with a foam volume fraction of 50%, a foam volume fraction of 150%, a water–binder ratio of 45% and a water–binder ratio of 60% separately, we calculate their average densities to be 1.253 g/cm^3, 0.918 g/cm^3, 1.180 g/cm^3 and 0.860 g/cm^3, respectively. According to the formula, the porosity of the group with a foam volume fraction of 50% is 45.04%. The porosity of the group with a foam volume

https://doi.org/10.3390/ma19010184

fraction of 150% is 60.09%; the porosity of the group with a water–binder ratio of 45% is 48.25%. The porosity of the group with a water–binder ratio of 60% is 62.28%. The results are highly consistent with the conclusion that "foam volume fraction and water–binder ratio are the primary factors affecting strength". This verifies the causal relationship that "porosity regulates strength as an intermediary variable".

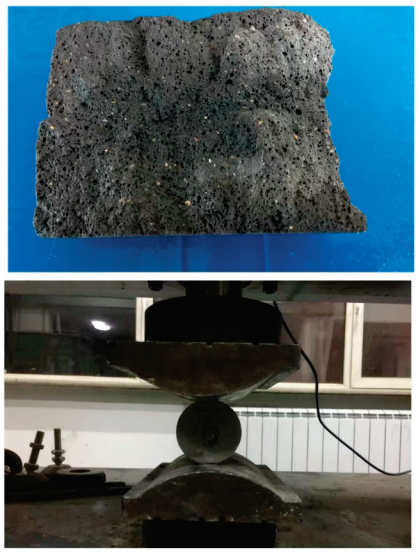

Figure 4. Splitting test diagram.

3.4.2. Splitting Tensile Strength Analysis

According to the orthogonal test method, the average value of the 28-day splitting tensile strength index at each level of each factor is obtained from the visual analysis table, and a columnar section was drawn, as shown in Figure 5. When the FA incorporation rate is 40%, 60% and 80%, the CNTFC splitting tensile strength is 1.023 MPa, 1.013 MPa and 1.014 MPa, respectively, and the relationship between these two parameters is not obvious. When the FA incorporation rate is increased from 80% to 100%, the CNTFC splitting tensile strength is reduced to 0.786 MPa. When the FA incorporation rate is less than 80%, it has no obvious effect on the tensile properties of the cement. When the FA incorporation rate reaches 100%, the splitting tensile strength of the CNTFC is similar to the 2:1 cylinder strength, a decrease of 22.49% from the latter result. This trend is similar to that of the 2:1 cylinder strength. The activity of FA is lower than the activity of cement. The replacement of cement by the same amount of FA reduces the amount of cement, delays the hydration degree of the whole system, and thus causes the CNTFC splitting tensile strength to decrease. When the aggregate–cement ratio ranges from 0 to 15%, it is 0.836 MPa, 1.174 MPa, 0.669 MPa and 1.157 MPa, respectively. The trend of the variation in the CNTFC splitting tensile strength shows disordered fluctuation, indicating that the sand aggregate contributes only slightly to the tensile strength of the matrix. The formula for specific fracture energy (Gf) [34] is

$$G_f = \frac{w}{A} = \frac{\int_0^{\varepsilon} \sigma(\varepsilon)\varepsilon}{A} V \quad (2)$$

where $\int_0^{\varepsilon} \sigma(\varepsilon)\varepsilon$ is the area under the stress–strain curve (J/m^3), V is the sample volume (m^3) and A is the fracture area (m^2). According to the formula, the specific fracture energy of Sample #8 (with a CNT content of 0.05% and a sand–binder ratio of 15%) is calculated to be 128 J/m^2, and the splitting tensile strength is 1.997 MPa. Sample #12 (without CNTs, with a sand–binder ratio of 15%) has a specific fracture energy of 86 J/m^2 and a splitting tensile

https://doi.org/10.3390/ma19010184

strength of 0.804 MPa. Sample #11 (with a CNT content of 0.05% and a sand–binder ratio of 10%) has a specific fracture energy of 115 J/m^2 and a splitting tensile strength of 0.786 MPa. Results show that when the sand–binder ratio increases from 5% to 15%, the specific fracture energy only increases by 8.2%. It verifies the conclusion that "sand has little contribution to splitting tensile strength". Combined with SEM images (Figures 4, 6 and 7), we deduce the macroscopic fracture mode: Groups without CNTs/low CNT content: fracture occurs along the aggregate–matrix interface, which is brittle fracture, with a flat fracture surface. Group with a CNT content of 0.05%: CNTs interweave with hydration products to form a network structure; fracture needs to overcome the bonding force of CNT bridging, which shows ductile fracture, with a serrated fracture surface. High CNT content group (such as Sample #6, 0.15%): CNT agglomeration causes local stress concentration; fracture propagates along the edges of agglomerates, and toughness decreases. This is consistent with the result that "the growth rate of splitting tensile strength decreases".

When the water–binder ratio is 45%, the CNTFC splitting tensile strength is the highest, at 1.260 MPa. When the water–binder ratio is increased from 45% to 50%, the splitting tensile strength of the CNTFC increased by 40.43%. When the water–binder ratio is between 45% and 60%, the regularity of the CNTFC splitting tensile strength is not obvious. The effect of the water–binder ratio on the splitting tensile strength is similar to that on the 2:1 cylinder strength, indicating that a 45% water–binder ratio has the best effect on FA and cement hydration. When the amount of CNTs is increased from 0 to 0.15%, the splitting tensile strength of the CNTFC generally increases, and the corresponding strengths are 0.964 MPa, 1.016 MPa, 1.002 MPa and 1.053 MPa, respectively. The growth rate is not high, showing that the increase in the macroscopic tensile properties of CNTs in foamed concrete is not significant.

The foam incorporation is the most significant factor affecting the CNTFC splitting tensile strength. As the foam incorporation increases from 50% to 80%, the CNTFC splitting tensile strength decreases by 55.04%, from 1.675 MPa to 0.753 MPa. As the foam incorporation increases from 80% to 150%, the CNTFC splitting tensile strength decreases, from 0.753 MPa to 0.745 MPa to 0.664 MPa, and the splitting tensile strength decreases by 1.06% and 10.87%, respectively. The introduction of bubbles increases the void space in the CNTFC and reduces the bearing capacity of the cement and aggregate. In particular, the splitting tensile strength of CNTFC is greatly reduced when the foam incorporation is increased from 50% to 80%.

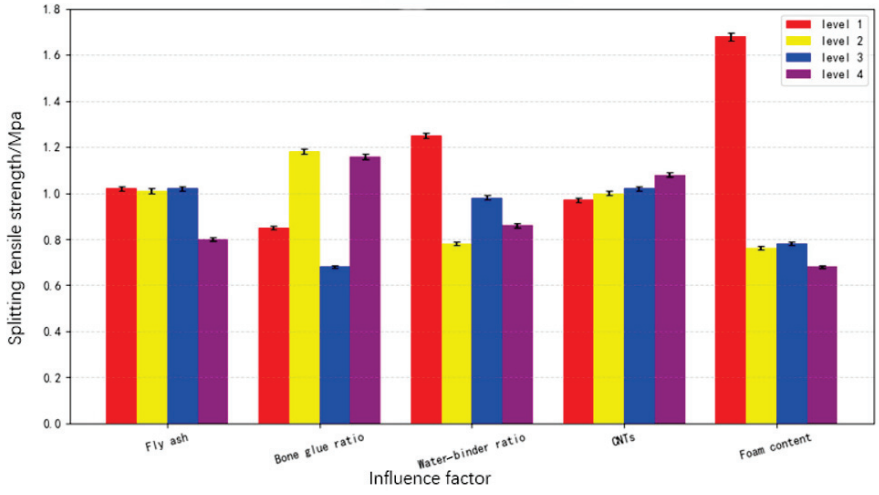

Figure 5. Variation in CNTFC splitting tensile strength under the influence of various factors.

https://doi.org/10.3390/ma19010184

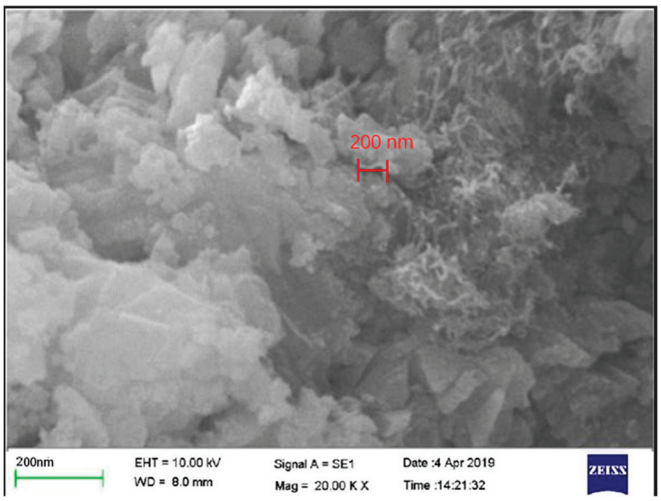

(**a**) #6

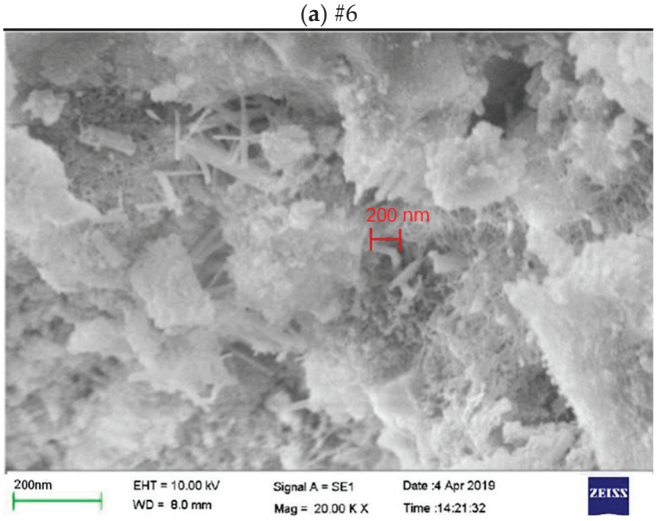

(**b**) #8

Figure 6. SEM of CNTFC specimens (200 nm).

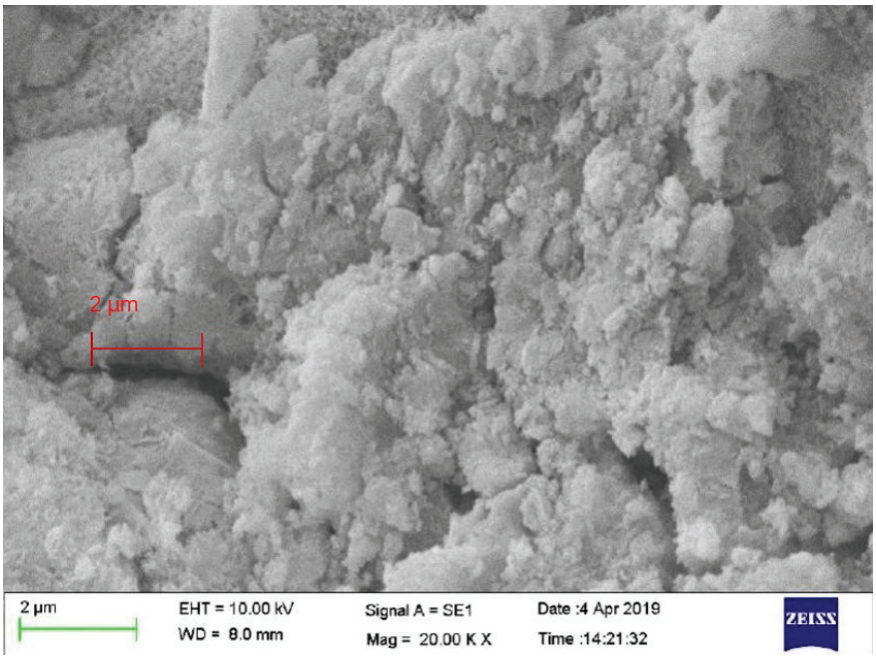

Figure 7. SEM of CNTFC specimen (2 µm #13).

https://doi.org/10.3390/ma19010184

3.4.3. Density Analysis

According to the orthogonal test method, the average value of the 28-day density index at each level of each factor is obtained from the visual analysis table. To facilitate trend analysis, a function is used to fit the trend of the discrete points, as shown in Figure 8. When the FA incorporation rate increases from 40% to 100%, the apparent density of the CNTFC decreases by 10.90% from 1.083 g/cm^3 to 0.965 g/cm^3. The overall decline is relatively small. The density of FA is slightly lower than the density of cement. As the replacement rate increases, the overall strength of the specimen decreases, but the magnitude of the decrease is not considerable. As the water–binder ratio and foam production increase, the density also decreases at a higher rate of decrease. When the water–binder ratio increases from 45% to 60%, the density decreases by 27.12% from 1.180 g/cm^3 to 0.860 g/cm^3. When the foam volume fraction increases from 50% to 150%, the density decreases by 26.74% from 1.253 g/cm^3 to 0.918 g/cm^3. The water and gas densities are much lower than the density of the mixture, and the increases in the water–binder ratio and the amount of foam greatly reduce the density of the specimen. When the aggregate–cement ratio increases from 0 to 15%, the density increases by 13.54% from 0.960 g/cm^3 to 1.090 g/cm^3. When the incorporation of CNTs is increased from 0 to 0.15%, the density increases by 18.92% from 0.978 g/cm^3 to 1.163 g/cm^3. The incorporation of aggregate cement, compared to that of CNTs, increased the density of the specimen, but the increase was relatively small because when preparing CNTFCs, it is necessary to add natural sand (as an aggregate) and CNTs to improve the CNTFC characteristics and prepare lightweight concrete with a certain strength. Therefore, the amount of sand and CNTs with a higher density is controlled, and the density of the CNTFC is not substantially increased.

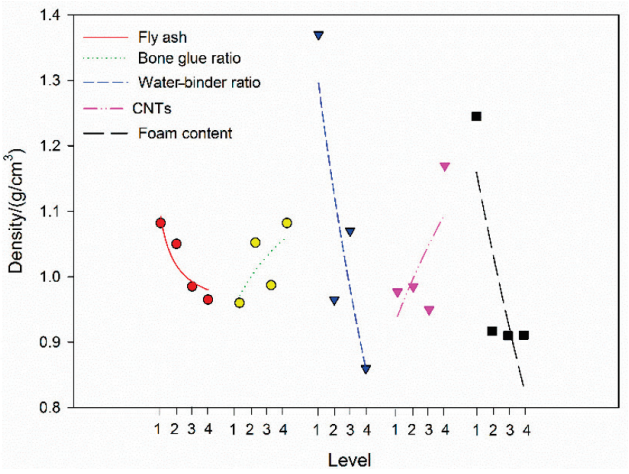

Figure 8. CNTFC density changes under the influence of various factors.

Symbols and lines in the figure correspond to different influencing factors of CNTFC density: solid line for fly ash incorporation rate, circle + dot line for aggregate–cement ratio, short dash line for water–binder ratio, triangle + dash-dot line for CNT incorporation rate and long dash line for foam volume fraction.

3.4.4. Specific Strength Analysis

Low density and high strength are ideal roadway surrounding rock support pressure-relief material characteristics. The specific strength is an important index used to measure the performance of filling materials [35], and there are few studies on the specific strength of foamed concrete materials. The specific strength curve is plotted by calculating the ratio of 2:1 cylinder strength, tensile splitting strength and apparent density for each ratio, as shown in Figure 9. C/D is the compressive specific strength (the ratio of uniaxial

https://doi.org/10.3390/ma19010184

compressive strength to apparent density). S/D is the splitting tensile specific strength (the ratio of splitting tensile strength to apparent density). For CNTFC, the specific strength is approximately the same as the splitting tensile strength because these strengths are both a function of a basic fixed coefficient [18], and the trends of the curves formed by considering the same density ratio are similar. The average compressive strength of the prepared CNTFC is 8.472 N·m/g, and the average splitting tensile strength is 0.903 N·m/g. The cylinder strength of the #6 specimen reaches 15.194 N·m/g, which is 27.32% higher than the optimum specific strength of 11.960 N·m/g recorded [35], and the corresponding ratio combination is $A_2B_2C_1D_4E_3$; the specific strength of the 2:1 cylinder strength of the #4 specimen is 3.616 N·m/g, and the corresponding mix proportion is $A_1B_4C_4D_4E_4$; the tensile strength of the #10 specimen reaches 1.850 N·m/g, and the tensile strength of the #7 specimen is 0.547 N·m/g. The corresponding mix proportions are $A_3B_2C_4D_3E_1$ and $A_2B_3C_4D_1E_2$.

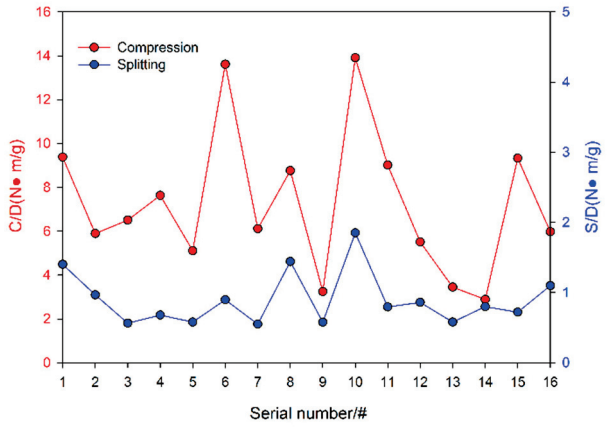

Figure 9. Different ratios of CNTFC specific strength.

Since the 2:1 cylinder strength has an intrinsic relationship with the splitting tensile strength, only the CNTFC compressive strength at each level of each influencing factor is analyzed. According to the orthogonal test method, the average value of the 28-day 2:1 cylinder strength and density ratio index at each level of each factor is obtained from the visual analysis table, and the function is used to fit the trend of the discrete points for the trend analysis, as shown in Figure 10. When the FA incorporation rate increases from 40% to 100%, the CNTFC compressive specific strength curve trend first increases and then decreases, and 60% is the optimal incorporation rate. As the FA incorporation rate is increased from 40% to 60%, the CNTFC strength increases, and the FA is used to replace the cement to reduce the density of the mixture; when the FA incorporation rate increases from 60% to 80%, the strength and density of CNTFC decrease, and the strength decreases more. When the aggregate–cement ratio increases from 0 to 15%, the strength trend first increases and then decreases. When the aggregate–cement ratio is 5%, the 2:1 cylinder strength of the CNTFC is the highest; excessive added aggregate causes a decrease in the strength of the CNTFC and a considerable increase in density, so the specific strength curve decreases.

When the water–binder ratio is increased from 45% to 55%, the strength and density of CNTFC decrease, but the decrease is not large, so there is no obvious regularity in the specific strength trend; when the water–binder ratio is increased from 55% to 60%, the CNTFC density is more reduced with respect to the strength, resulting in a sharp increase in the specific strength curve. When the CNT doping amount is increased from 0 to 0.15%, the CNTFC specific strength curve tends to increase sharply because the micro-doped CNTs have little effect on the CNTFC density but can greatly increase the 2:1 cylinder strength.

https://doi.org/10.3390/ma19010184

The specific strength curve under the influence of the increase in foam incorporation exhibits a steep drop. For the specific strength, the introduction of bubbles causes the 2:1 cylinder strength of the CNTFC to further decrease. To obtain low-density, high-strength CNTFC materials, in addition to controlling the conventional FA incorporation rate, aggregate–cement ratio and water–binder ratio, it is necessary to incorporate materials that can have a small effect on density but greatly increase the strength of concrete. CNTs can satisfy this requirement.

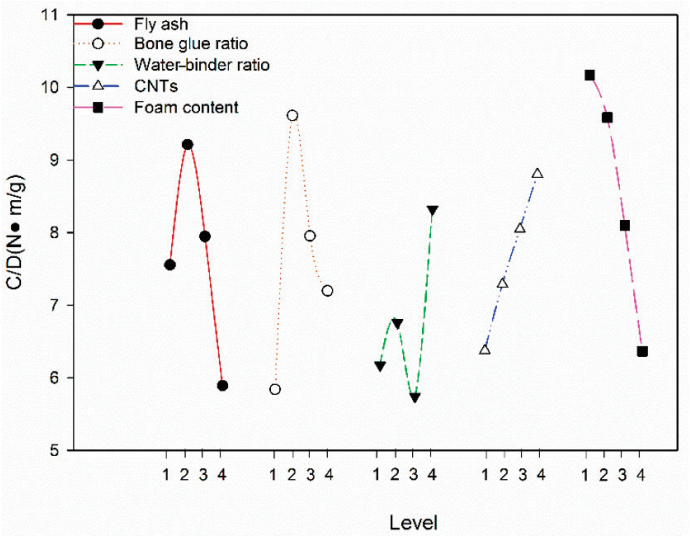

Figure 10. The average value of the strength-to-density ratio index of a cylinder under different factors 3.5. Influence of CNT Content on CNTFC Performance.

3.5. Influence of CNT Content on CNTFC Performance

The above analysis shows that among the five factors of the FA incorporation rate, aggregate-cement ratio, water-binder ratio, CNT incorporation rate and foamed volume fraction, the incorporation of FA and foamed can reduce the cost of concrete but also reduce its overall mechanical properties. The increase in water-binder ratio decreases the overall strength, and a suitable aggregate-cement ratio can effectively increase the CNTFC specific strength. Only the incorporation of CNTs increases the 2:1 cylinder strength, splitting tensile strength and specific strength of the CNTFC, and a suitable incorporation amount allows the CNTFC to maintain a lower density level while maintaining a higher strength. Based on this, a hypothesis is proposed that in the CNT foamed concrete (CNTFC) surrounding rock pressure relief filling material, micro-dosage carbon nanotubes (CNTs) (dosage range of 0–0.15%) can intertwine with cement and fly ash hydration products to form nanoscale bridging and spatial network structures, it can effectively inhibit the initiation and propagation of cracks. Within this dosage range, as the CNTs dosage increases, the material density increases moderately (with an increase rate $\leq$16.2%), and its uniaxial compressive strength, splitting tensile strength and specific strength increase simultaneously. When the CNTs dosage is 0.05%, the above mechanical indicators are comprehensively optimal. If the CNTs dosage exceeds 0.05%, CNTs tend to agglomerate, which will expand the medium transition zone and weaken the bridging and nucleation effects, ultimately leading to a decrease in the material's strength and ductility instead. It is concluded that CNTs improve the microscopic characteristics and nanoscale tensile properties of the mixture and effectively inhibit the initiation and expansion of fractures. Therefore, to study the mechanism of the overall improvement in the mechanical performance of CNTFC, the CNTFC ultimate strain improvement and micro-scale properties are further studied [36].

https://doi.org/10.3390/ma19010184

3.5.1. Analysis of the Effect of the Ultimate Strain on Improvement

According to the ultimate strain value corresponding to the stress–strain curve of each specimen in the orthogonal test method, the average value of the ultimate 28-day strain index of each factor of the CNT incorporation rate is obtained, and the influence of CNTs on the ultimate strain of CNTFC is analyzed, as shown in Figure 11.

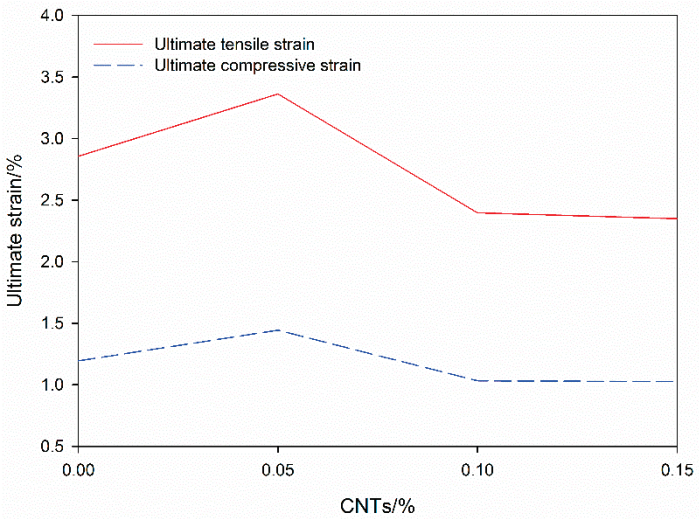

Figure 11. CNTFC ultimate strain under the influence of different CNT incorporation rates.

The ultimate strains of the CNTFCs under tensile and compressive pressures first increased and then decreased, and the trends were basically the same; however, the change after the ultimate strain exceeded 0.1 was not obvious. When the incorporation rate of CNTs increases from 0 to 0.05%, the ultimate compressive strain increases by 17.62%, and the ultimate tensile strain increases by 20.91%. When the incorporation rate of CNTs increases from 0.05% to 0.10%, the ultimate compressive strain is reduced by 28.7%, and the ultimate tensile strain is reduced by 28.50%. From 0.10% to 0.15%, the ultimate compressive strain continues to decrease by 1.966%, and the ultimate tensile strain decreases by 0.691%, which is a small decrease. CNT network integrity replaces conductivity data, based on the correlation of "CNT content-specific strength" (Figure 10). The 0.05% CNT group: the specific strength is 8.9 N·m/g, which is 1.44 times that of the group without CNTs (6.2 N·m/g), indicating that the CNT network is intact without agglomeration; 0.10% CNT group: the specific strength is 7.8 N·m/g, decreasing by 12.4%, corresponding to slight agglomeration; 0.15% CNT group: the specific strength is 7.2 N·m/g, decreasing by 19.1%, corresponding to severe agglomeration. This is consistent with the law that "conductivity decreases as the degree of CNT agglomeration increases" [17], and it can replace conductivity data to characterize CNT network integrity. CNTs improve the mechanical properties of a specimen by virtue of their excellent tensile properties at the nanoscale, effectively suppressing the initiation and expansion of cracks; therefore, CNTs have a significant effect on the improvement of the ultimate strain. When the incorporation of CNTs is 0.05%, the ultimate strain lifting effect is the most obvious. Continuing to increase the blending amount will reduce the ultimate strain. Excessive CNT agglomeration increases the dielectric transition region and reduces the overall tensile properties of CNTFCs. After the incorporation of CNTs exceeds 1.04%, a small decrease is still exhibited, indicating that the agglomeration transition zone has formed a weak region of CNTFC, which is reflected in the tensile strength of the fiber interlaced group. A continuous increase in the amount of CNTs incorporated does not change the mechanical properties of the fiber agglomeration zone, which is not necessary from a cost perspective.

https://doi.org/10.3390/ma19010184

3.5.2. Microanalysis

The SEM test was carried out on the #6 specimen with the highest 2:1 cylinder strength and the #8 specimen with the highest split tensile strength in the orthogonal test, as shown in Figure 6. During curing, the concrete has many pores. Hydrated products and CNTs crisscross to form a network that runs through its pores, enhancing pore structure connectivity. Although the pores are abundant, the intertwined complex network structure connects the cement with the aggregate and effectively increases the strength of the CNTFC at a lower density level. Due to the introduction of a large number of bubbles, the pore structure between the particles further develops, and a distinct throughgoing crack is formed in the resultant stress field. As shown in Figure 6, in the #6 specimen and the #8 specimen, a large amount of acicular, layered and flake hydrates are observed at a 200 nm scale. CNT fibers are clearly seen interspersed between cement bodies, forming bridges. Intertwined CNT fibers interweave with hydrates into a spatial network structure, filling voids. CNT incorporation complicates the propagation path of CNTFC nanoscale cracks. This makes the material absorb more external energy during crack expansion, and it improves the macroscopic mechanical properties of CNTFC. It also effectively enhances its overall strength. As shown in Figure 6a, the proportion of CNTs in the #6 specimen is 0.15%. The probability of the fibers overlapping and agglomerating is greatly increased over that of other specimens. The dispersion in the matrix is further decreased, and the agglomeration and nucleation efficiency are apparent. The bridging effect is weakened, and larger fiber agglomerates occupy a continuous space, which expands the transition zone of the medium. Too many interfacial transition zones cannot fully exert the effect of the fiber inhibiting cracks, and the strength will be weakened. As shown in Figure 6b, the CNT content in eight specimens is 0.05%, the CNT fibers are well distributed and the nucleation and bridging effects are fully exerted. The unevenly distributed CNT fibers constitute interlayer dislocations and defects. In turn, the CNTFC has both a certain strength and damping performance, achieving good compression and splitting strength.

The SEM test is carried out on the #13 specimen with the lowest compressive and splitting tensile strength from the orthogonal test, as shown in Figure 7. At the 2 μm scale, the cracks and pores are more abundant, and the crystal integrity is poor. A large number of very small inert particles are distributed around the colloid without being wrapped, resulting in a low density and strength. In the case of a high FA incorporation rate, high bubble content and low cement content, 0.05% incorporation of CNT fibers is difficult to interlace into a network in the case of excessive foam pores and less gelled hydration products due to the overall structure; therefore, the specimen has a lower density, a lower strength, and a lower specific strength index.

4. Comprehensive Analysis and Determination of the Material Ratio of Buffer for Surrounding Rock Support

Table 4 shows that the 2:1 cylinder strength and splitting tensile strength of the #1, #6 and #8 specimens are the highest. The 2:1 cylinder strength ranges between 12.095 MPa and 18.381 MPa, and the corresponding splitting tensile strength ranges between 1.210 MPa and 1.997 MPa. Taking the surrounding rock support of the transportation lane of the Baiyangling coal mine in Shanxi Province, China, as an example, the maximum supporting force of the high-strength anchor is 150 kN, and the anchoring pallet area is 0.040 m^2, which needs to be achieved when the CNTFC is set under the local stress concentration of the supporting structure. The strength is 3.75 MPa. Considering the influencing factors, such as the stress concentration of the supporting structure, the safety factor is 1.2, and the CNTFC strength should be greater than 4.50 MPa. Considering the mechanical strength, dead weight and economic cost of the material used for surrounding rock support pressure

https://doi.org/10.3390/ma19010184

relief, the densities of the #1, #6 and #8 specimens are all greater than 1300 kg/m^3, although the strengths are sufficient and within the range of lightweight concrete requirements. However, because of its considerable weight, the proportion of FA incorporation is too small, according to Table 6, the overall economics are unfavorable. The #3, #4, #9, #10, #15 and #16 specimens meet the mechanical strength requirements, but the densities are greater than 1000 kg/m^3, the proportion of CNT incorporation is higher and the economics are unfavorable. The #2, #5 and #7 specimens have low incorporation rates of FA, and the economics are unfavorable. The #11 and #12 specimens have an FA mixing ratio of 80% and a CNT incorporation ratio of 0~0.05%. The economics are favorable, and the mechanical indexes also meet the requirements of surrounding rock support and pressure relief. The characteristics of the stress–strain curves suggest the applicability of the pressure-relief material.

Table 6. Price list.

Raw Materials	Specification Attributes	Market Unit Price (Euro/Kilogram, €/kg)	Cost Affects Key Features
Cement	PO42.5ordinary Portland cement	0.15	Gelling core, with a unit price higher than that of fly ash, its proportion directly affects the cost.
Fly ash (FA)	Grade I, fineness 10.8%	0.08	Industrial waste, as a substitute for cement, can reduce gelling costs by 33%
Multi-walled carbon nanotubes (CNTs)	Purity > 97%, surface grafted –COOH/–OH	180.00	The unit price is 1200 times that of cement, and the dosage is extremely sensitive to cost.
Natural sand	Particle size < 2.36 mm, apparent density 2.23 g/cm^3	0.06	The proportion of aggregate cost is low (<5%)
ZT-F50 foam	Active substance 30%, initiation amount 60 mL/g	2.50	Added by volume (50%~150%), with a small total dosage

Cost per cubic meter of CNTFC (€/m^3) = Amount of each raw material × The sum of the corresponding unit prices. Raw material consumption (kg/m^3) = CNTFC measured density (kg/m^3) × Mass fractions of raw materials (such as FA incorporation rate, CNT incorporation rate). Foam is a volume fraction, calculated as "foam volume/mixture volume = 1:1~1:1.5" conversion, with a small amount used and the cost accounting for less than 3%.

The stress–strain data of the #11 and #12 specimens are processed. The stress–strain data of each of the three specimens are controlled by the loading rate and the loading step. The control strain is constant, and the corresponding stress data are averaged and used to draw a stress–strain curve. The 2:1 cylinder compressive stress–strain curve is shown in Figure 12a, and the splitting tensile strength curve is shown in Figure 12b. Figure 12a shows that the peak compressive strength and ultimate strain of the #11 specimen are larger than those of the #12 specimen, and the elastic modulus of the #11 specimen is less than that of the #12 specimen, indicating that the #11 specimen at the early stage has deformation absorption capacity, and the #11 specimen can maintain a large deformation after the peak strength while still providing high resistance, which is a feature required to support the deformation of the surrounding rock. Figure 12b shows that the tensile strength of the #11 specimen is slightly lower, but it is not much different from the #12 specimen, and the ductility is obviously better than that of the #12 specimen. Although the #11 test specimen incorporates 0.05% CNTs, and the cost of the #12 test specimen is high, the mechanical properties are greatly improved while maintaining the same density. Therefore, it is determined that the #11 test specimen reflects the optimal mixing ratio of the roadway surrounding rock support for pressure relief. For the application scenario of the Shanxi Baiyangling Coal Mine roadway, its durability and behavioral risks must be comprehensively evaluated by considering the environments of high humidity, chemical corrosion, long-term static load and cyclic dynamic load. In terms of durability, high humidity can cause pore water penetration and damage the interfacial bonding between

https://doi.org/10.3390/ma19010184

CNTs and hydration products. Acidic mine water and high CO_2 can also cause sulfate expansion, chloride-induced interfacial degradation and carbonation embrittlement. In terms of behavioral risks, high porosity causes creep strain under long-term static load. Cyclic load cycles can cause repeated opening and closing of microcracks and fatigue fracture of CNT bridging structures. Cyclic load cycles cause repeated opening and closing of microcracks and fatigue fracture of CNT bridging structures, thus leading to a decrease in compressive strength and loss of ductility. The root cause of the above problems is the high foam volume fraction and high fly ash content. In engineering, it is necessary to optimize durability by adding waterproofing agents/silica fume, controlling the foam volume fraction, increasing the safety factor and verifying long-term reliability through field exposure tests. For specific engineering cases of surrounding rock support for pressure relief, specific force analysis and further testing between the #11 specimen and the #12 specimen mixing ratios should be carried out to determine the optimal ratio plan.

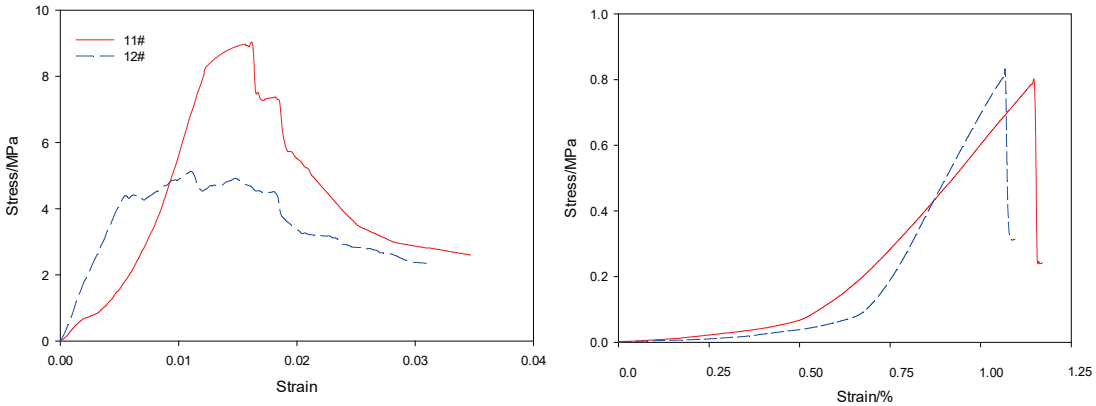

Figure 12. Stress–strain curves. (**a**) Uniaxial compression stress-strain curve; (**b**) Splitting tensile strength curve.

5. Conclusions

Underground mine roadways, tunnels and other soft rock engineering projects have requirements for support and pressure-relief materials: "lightweight, high mechanical properties, low cost". Traditional foamed concrete, though lightweight, environmentally friendly and energy-absorbing, has insufficient mechanical properties, and it is difficult to meet soft rock support requirements. Carbon nanotubes (CNTs) have excellent performance, providing a new direction for improving their performance. This study aims to prepare CNT-modified foamed concrete (CNTFC) suitable for pressure relief in soft rock surrounding rock support. It is hypothesized that microdosage CNTs (0~0.15%, based on the total mass of cementitious materials) can form a nano-network with the hydration products of cement and fly ash while slightly increasing density and enhancing performance, and there exists an optimal dosage. To verify the hypothesis, this study adopts a five-factor, four-level orthogonal test (fly ash content, sand–cement ratio, water–binder ratio, CNT content, foam volume fraction). Combined with mechanical tests, stress–strain analysis and SEM microscopic characterization of specimens after 28 days of curing, the optimal mix ratio was screened out to meet the roadway support requirements of the Baiyangling Coal Mine in Shanxi Province (strength $\geq$ 4.5 MPa). In summary, the study draws the following core conclusions:

(1) The foam volume fraction, water–binder ratio and aggregate–cement ratio are the top three factors affecting the strength of CNTFC. The influence of the CNT incor-

https://doi.org/10.3390/ma19010184

poration rate and the FA incorporation rate on CNTFC strength are the next two most important factors.

(2) Among the five factors of FA incorporation rate, aggregate–cement ratio, water–binder ratio, CNT incorporation rate and foam volume fraction, though fly ash (reducing cementitious material cost by 33%) and foam (accounting for less than 3% of the total cost) can reduce concrete cost, they significantly deteriorate mechanical properties (when fly ash content increases to 100%, the 2:1 cylinder strength decreases by 27.40%; when the foam volume fraction increases to 150%, the strength decreases by 54.2%). Increasing the water–binder ratio also reduces strength. Only the optimal sand–cement ratio and CNT content can improve performance. Among them, the optimal CNT content is 0.05% (compressive strength increases by 15.3%, splitting tensile strength increases by 6.5% and density increases by only 2.0%). The optimal mix ratio adapted to the Baiyangling Coal Mine in Shanxi Province not only meets the engineering strength requirements but also reduces the cost by about 28% compared with the higher-strength mix ratio.

(3) CNTs improve the mechanical properties of a specimen by improving its tensile properties at the nanometer scale. At the optimal dosage of 0.05%, uniaxial compressive strength increases by 15.3%, and splitting tensile strength increases by 6.5%. Specific fracture energy increases from 86 J/m^2 to 128 J/m^2, specific strength reaches 8.9N·m/g, density increases by only 2.0% and ultimate compressive/tensile strains increase by 17.62% and 20.91%, respectively. This effectively inhibits the initiation and expansion of cracks, but excessive blending will decrease the strength and ductility of the foamed concrete.

(4) The optimum proportion of CNTs in CNTFC is 0.05%, with a proper FA, cement and foam blending ratio to fully realize the performance of the CNT fiber.

(5) The specific mixing ratio of a CNTFC used for pressure-relief support of surrounding rock should be considered with the specific engineering conditions and the costs. The paper takes the pressure-relief support of the surrounding rock of the Baiyangling coal mine in Shanxi Province, China, as an example, determining that the #11 CNTFC specimen is optimal: the corresponding FA incorporation rate is 80%, aggregate–cement ratio is 10%, water–binder ratio is 45%, CNT incorporation rate is 0.05% and foam volume fraction is 150%.

Author Contributions: Conceptualization, S.Z. and P.J.; methodology, S.Z.; software, H.W. (Haohao Wang); validation, S.Z., H.W. (Haohao Wang) and D.F.; formal analysis, S.Z.; investigation, D.F. and H.W. (Hao Wang); resources, P.J.; data curation, H.W. (Haohao Wang); writing—original draft preparation, S.Z.; writing—review and editing, P.J.; visualization, H.W. (Haohao Wang); supervision, P.J.; project administration, P.J.; funding acquisition, P.J. All authors have read and agreed to the published version of the manuscript.

Funding: This research was funded by the National Natural Science Foundation of China (Grant No.: 52574168) and the Shandong Provincial Natural Science Foundation (Grant No.: ZR2024ME257).

Data Availability Statement: The original contributions presented in this study are included in the article. Further inquiries can be directed to the corresponding author.

Acknowledgments: The authors acknowledge the support of the National Natural Science Foundation of China 52574168 and the project ZR2024ME257 supported by the Shandong Provincial Natural Science Foundation.

Conflicts of Interest: The authors declare that they have no conflicts of interest.

https://doi.org/10.3390/ma19010184

References

1. Zhang, S.; Wang, L.; Yang, H.; Lu, L. Construction and numerical simulation research of functional supporting in deep roadways. *J. Min. Strat. Control. Eng.* **2023**, *5*, 013012.
2. Krämer, C.; Schauerte, M.; Kowald, T.L.; Trettin, R.H. Three-phase-foams for foam concrete application. *Mater. Charact.* **2015**, *102*, 173–179. [CrossRef]
3. Krämer, C.; Schauerte, M.; Müller, T.; Gebhard, S.; Trettin, R. Application of reinforced three-phase-foams in UHPC foam concrete. *Constr. Build. Mater.* **2017**, *131*, 746–757. [CrossRef]
4. Bai, F.; Davidson, J.S. Analysis of partially composite foam insulated concrete sandwich structures. *Eng. Struct.* **2015**, *91*, 197–209. [CrossRef]
5. Prabha, P.; Palani, G.S.; Lakshmanan, N.; Senthil, R. Flexural behaviour of steel-foam concrete composite light-weight panels. *KSCE J. Civ. Eng.* **2018**, *22*, 3534–3545. [CrossRef]
6. Hájek, M.; Decký, M.; Scherfel, W. Objectification of modulus elasticity of foam concrete poroflow 17-5 on the sub-base layer. *J. CEE* **2016**, *12*, 55–62.
7. Wang, J.; Liang, J.; Hou, W.; Lu, L. Experimental investigation on the compressive behaviour of foam concrete light steel keel composite wall. *J. Asian Archit. Build. Eng.* **2025**, *24*, 3730–3743. [CrossRef]
8. Dong, G. Research Progress and Application of Solid Waste Foam Concrete: A Comprehensive Review. *Adv. Res. Teach.* **2025**, *26*, 418–423. [CrossRef]
9. Tan, X.; Chen, W.; Liu, H.; Chan, A.H.C.; Tian, H.; Meng, X.; Wang, F.; Deng, X. A combined supporting system based on foamed concrete and U-shaped steel for underground coal mine roadways undergoing large deformations. *Tunn. Undergr. Space Technol.* **2017**, *68*, 196–210. [CrossRef]
10. Hu, C.; Li, H.; Liu, Z.; Wang, Q. Research on properties of foamed concrete reinforced with small sized glazed hollow beads. *Adv. Mater. Sci. Eng.* **2016**, *2016*, 5820870. [CrossRef]
11. Jones, M.R.; Ozlutas, K.; Zheng, L. Stability and instability of foamed concrete. *Mag. Concr. Res.* **2016**, *68*, 542–549. [CrossRef]
12. Lim, S.K.; Tan, C.S.; Li, B.; Ling, T.C.; Hossain, M.U.; Poon, C.S. Utilizing high volumes quarry wastes in the production of lightweight foamed concrete. *Constr. Build. Mater.* **2017**, *151*, 441–448. [CrossRef]
13. Nguyen, T.T.; Bui, H.H.; Ngo, T.D.; Nguyen, G.D. Experimental and numerical investigation of influence of air-voids on the compressive behaviour of foamed concrete. *Mater. Des.* **2017**, *130*, 103–119. [CrossRef]
14. Reisi, M.; Dadvar, S.A.; Sharif, A. Microstructure and mixture proportioning of non-structural foamed concrete with silica fume. *Mag. Concr. Res.* **2017**, *69*, 1218–1230. [CrossRef]
15. Mahzabin, M.S.; Hock, L.J.; Hossain, M.S.; Kang, L.S. The influence of addition of treated kenaf fibre in the production and properties of fibre reinforced foamed composite. *Constr. Build. Mater.* **2018**, *178*, 518–528. [CrossRef]
16. Kerienė, J.; Kligys, M.; Laukaitis, A.; Yakovlev, G.; Špokauskas, A.; Aleknevičius, M. The influence of multi-walled carbon nanotubes additive on properties of non-autoclaved and autoclaved aerated concretes. *Constr. Build. Mater.* **2013**, *49*, 527–535. [CrossRef]
17. Zhang, J.; Liu, X. Research on the influence of carbon nanotubes (CNTs) on compressive strength and air-void structure of ultra-light foamed concrete. *Mech. Adv. Mater. Struct.* **2019**, *26*, 2009–2016. [CrossRef]
18. Han, Y.; Zhou, M.; Wang, J.; Tian, Y.; Wang, X. Optimization of coal-based solid waste ceramsite foam concrete mix proportions and performance study. *Constr. Build. Mater.* **2024**, *416*, 135226. [CrossRef]
19. Luo, J.; Li, Q.; Zhao, T.; Gao, S.; Sun, S.; Chen, L. Thermal and electrical resistances of carbon nanotube-reinforced foamed concrete. *Nanosci. Nanotechnol. Lett.* **2014**, *6*, 72–79. [CrossRef]
20. Zhang, J.; Liu, X. Dispersion performance of carbon nanotubes on ultra-light foamed concrete. *Processes* **2018**, *6*, 194. [CrossRef]
21. Zhang, J.; Zhang, X. Interfacial bonding characteristics of multi-walled carbon nanotube/ultralight foamed concrete. *Sci. Eng. Compos. Mater.* **2024**, *31*, 20240028. [CrossRef]
22. Ma, C.; Wang, J.; Zhang, N.; Wang, C.; Zhang, S.; Tao, Y.; Lou, S.; Sun, Q.; Ren, X.; Zhang, H. Shear Strength and Ultimate Bearing Capacity of Silt-Based Foamed Concrete Under Local Vertical Loading. *Buildings* **2025**, *15*, 1914. [CrossRef]
23. Kang, C.; Seo, K.Y.; Park, Y.M.; Kim, T. Characteristics of Lightweight Foam Concrete Manufactured Using Water-Soluble Polymers and Lightweight Aggregates. *Materials* **2025**, *18*, 1881. [CrossRef]
24. Zhang, X.; Luo, T.; Zhong, X.; Zhou, Y.; Peng, X.; Zhao, C. High-performance foam concrete containing multi-wall carbon nanotubes and ssDNA. *Constr. Build. Mater.* **2025**, *458*, 139523. [CrossRef]
25. *GB/T 12960-2019*; Quantitative Determination of Constituents of Cement. State Administration for Market Regulation. Standardization Administration of China: Beijing, China, 2019.
26. Zhang, S.; Wang, Z.; Lu, L.; Feng, D. Preparation and load-deformation characterization of carbon nanotube-reinforced foam concrete. *Constr. Build. Mater.* **2020**, *254*, 119294. [CrossRef]
27. Wang, S.; Han, L.; Zhang, S.; Wang, H. Structure restrengthening process and mechanical properties of damaged weakly cemented mudstone. *Sustainability* **2023**, *15*, 9148. [CrossRef]

https://doi.org/10.3390/ma19010184

28. Wu, X.; Cai, M.; Wu, X.; Li, P.; Zhang, S.; Sun, J. Experimental study on nonlinear failure criterion of HDR under cyclic water-induced thermal shock. *Bull. Eng. Geol. Environ.* **2025**, *84*, 255. [CrossRef]
29. Wang, Q.; Pan, R.; Jiang, B.; Li, S.; He, M.; Sun, H.; Wang, L.; Qin, Q.; Yu, H.; Luan, Y. Study on failure mechanism of roadway with soft rock in deep coal mine and confined concrete support system. *Eng. Fail. Anal.* **2017**, *81*, 155–177. [CrossRef]
30. Wu, X.; Li, P.; Miao, S.; Cai, M.; Liu, Y.; Wang, M.; Xiong, W. Multi-field Coupling Mechanism and Optimization of Heat Transfer in Deep Carbonate Geothermal Reservoirs Based on Acid Fracturing Modification. *Case Stud. Therm. Eng.* **2025**, *73*, 106591. [CrossRef]
31. Li, S.-C.; Wang, H.-T.; Wang, Q.; Jiang, B.; Wang, F.-Q.; Guo, N.-B.; Liu, W.-J.; Ren, Y.-X. Failure mechanism of bolting support and high-strength bolt-grouting technology for deep and soft surrounding rock with high stress. *J. Cent. South Univ.* **2016**, *23*, 440–448. [CrossRef]
32. Tao, Z.; Zhao, F.; Wang, H.; Zhang, H.; Peng, Y. Innovative constant resistance large deformation bolt for rock support in high stressed rock mass. *Arab. J. Geosci.* **2017**, *10*, 341. [CrossRef]
33. Zhang, S.; Jiang, P.; Lu, L.; Wang, S.; Wang, H. Evaluation of compressive geophysical prospecting method for the identification of the abandoned goaf at the Tengzhou Section of China's Mu Shi expressway. *Sustainability* **2022**, *14*, 13785. [CrossRef]
34. Jones, M.R.; Zheng, L. Energy absorption of foamed concrete from low-velocity impacts. *Mag. Concr. Res.* **2013**, *65*, 209–219. [CrossRef]
35. Kim, J.S.; Lim, J.K. Mechanical properties and interfacial compatibility of functionalized carbon nanotubes as fillers for chitosan solid polymer electrolytes. *React. Funct. Polym.* **2021**, *166*, 105013. [CrossRef]
36. Jiang, P.; Zhang, S. Study on the deformation mechanism and application of trench cutting re-mixing deep walls. *Tunn. Undergr. Space Technol.* **2026**, *168*, 107157. [CrossRef]

Disclaimer/Publisher's Note: The statements, opinions and data contained in all publications are solely those of the individual author(s) and contributor(s) and not of MDPI and/or the editor(s). MDPI and/or the editor(s) disclaim responsibility for any injury to people or property resulting from any ideas, methods, instructions or products referred to in the content.

https://doi.org/10.3390/ma19010184

materials

MDPI

Article

Simulation Analysis of Thermal Deformation and Extruded Profile Formability of Al–10Mg–3Zn Aluminum Alloy

Guanmei Niu [1,2,3], Wei Li [3], Kaidi Jiang [2], Yang Yang [3,*], Guojun Wang [3], Cheng Liu [3] and Linzhong Zhuang [2,*]

[1] State Key Laboratory for Advanced Metals and Materials, University of Science and Technology Beijing, Beijing 100083, China; niu_gm133@chinalco.com.cn
[2] Beijing Advanced Innovation Center for Materials Genome Engineering, University of Science and Technology Beijing, Beijing 100083, China
[3] Chinalco Material Application Research Institute Co., Ltd., Beijing 102209, China
* Correspondence: y_yang060@chinalco.com.cn (Y.Y.); linzhongzhuang@163.com (L.Z.)

Abstract

To investigate the hot deformation characteristics of the Al–10Mg–3Zn alloy, a series of hot compression tests was carried out using a Gleeble-3500 simulator. The experimental matrix covered temperatures of 300–450 °C and strain rates from 0.001 to 10 s^{-1}. The true stress–strain curves were obtained and the hot processing map of the alloy was constructed based on the Dynamic Material Model principle. The multi-objective optimization of the extrusion process parameters was performed using the response surface method. The results showed that the flow stress of Al–10Mg–3Zn alloy increased with the increase in the strain rate and decreased with the increase in the deformation temperature, indicating that the alloy had a positive strain rate sensitivity. A strain-compensated Arrhenius constitutive model and a hot processing map of Al–10Mg–3Zn alloy were established based on the temperature-corrected data; here, the optimal temperature range and strain rate range for hot processing were specified. The optimal extrusion process parameters, determined by the response surface method, were as follows: billet temperature of 400 °C, extrusion speed of 0.20 mm/s, and ingot length of 350 mm. With this parameter combination, the simulation predicted an extrusion load of 73.29 MN, a velocity deviation of 24.96%, and a cross-sectional temperature difference of 9.48 °C for the profile. The predicted values from the response surface method were highly consistent with those from the finite element simulation. The optimized process parameters significantly reduced the extrusion load of the profile.

Keywords: Al–10Mg–3Zn alloy; flow stress; hot processing maps; response surface method

1. Introduction

Al–Mg alloys have become pivotal structural materials in the modern transportation industry, including marine, aerospace, and automotive manufacturing; this is due to their exceptional specific strength, excellent toughness, and outstanding corrosion resistance [1,2]. However, with the growing demand for lightweight transportation vehicles, the mechanical properties of traditional Al–Mg alloys (such as those in the 5XXX series) are no longer sufficient to meet the stringent requirements for tough, high-strength materials in next-generation equipment manufacture [3–6]. In the domain of engineering applications, high-magnesium–aluminum alloy extrusions have exhibited considerable potential in the context of rail transportation. In order to address the pressing demand for lightweight materials in next-generation high-speed trains, there is an

urgent need to develop new aluminum alloys that combine high strength (target tensile strength $\geq$ 500 MPa), low density (target density $\leq$ 2.7 g/cm^3), and excellent corrosion resistance and weldability.

As a non-heat-treatable strengthened aluminum alloy, the strength of Al–Mg alloys primarily relies on solid solution strengthening and work hardening. Increasing the Mg content in the alloy is one of the most direct and effective methods for enhancing the strength of Al–Mg alloys [7]. However, when the Mg content exceeds 3.5 wt.%, the β-Al3Mg phase tends to continuously precipitate at grain boundaries. Due to its lower electrochemical potential (-1.15 V) compared to that of the aluminum matrix (-0.82 V), the β phase acts as an anode and preferentially dissolves in corrosive media, reducing the alloy's resistance to intergranular corrosion and limiting the application of high-Mg Al–Mg alloys [8,9]. Precipitation strengthening is one of the most effective strengthening mechanisms in aluminum alloys. In recent years, researchers have found that adding a small amount (less than 1.0 wt.%) of Zn to traditional Al–Mg alloys improves their corrosion resistance [10–15]. Simultaneously, after stabilization treatment, the addition of a small amount of Zn can enhance the yield strength of Al–Mg alloys, which is attributed to the synergistic effects of solid solution strengthening and precipitation strengthening [11,15]. In a study on the hot deformation behavior of Al–Zn–Mg–Cu–Zr series alloys, Maxim G. Khomutov et al. [16] systematically investigated the influence of varying Sc contents (0.05%, 0.1%, and 0.15%) on the deformation behavior of the alloys under conditions of 300–450 °C and 0.1–15 s^{-1} through hot compression experiments. The analysis indicated that the optimal hot processing window for alloys containing 0.05% and 0.1% Sc is 350–400 °C and 0.1–1 s^{-1}; meanwhile, for the alloy with 0.15% Sc, the optimal strain rate within the same temperature range narrows to 0.1 s^{-1}. This optimized processing domain corresponds to a peak power dissipation efficiency of approximately 30–35% and lies within the flow stability region. For an as-cast Al–5Mg–3Zn–1Cu alloy, Lei et al. [17] determined its optimal hot processing parameter window by constructing processing maps and indicated that dynamic recrystallization is the dominant softening mechanism under high-temperature and low-strain-rate conditions; they identified that its flow instability behavior is also highly sensitive to temperature and strain rate. For high-alloyed Al–Mg–Zn alloys containing multiple insoluble phases, the selection of hot deformation parameters requires a critical balance. Yang et al. [18] demonstrated that, for a cast Al–9.7Mg–2.9Zn alloy, rich in Mn and Cr, high strain rates (e.g., 10 s^{-1}) significantly promote dynamic recrystallization; however, this comes at the cost of severe cracking, induced by coarse AlMgMnTiCr particles. Their findings suggest that, for such alloys, a lower strain rate is essential to mitigate cracking; a compositional adjustment can also reduce the presence of crack-inducing elements (Mn, Cr), and this is recommended for improved workability.

High-Mg–aluminum alloys face significant challenges during the extrusion forming process. These include extremely high deformation resistance, which can lead to defects such as 'stalling' (extruder overload shutdown), 'peeling' (surface cracking), and 'waviness' (dimensional fluctuations). In severe cases, extrusion cracking may occur. Currently, systematic research on the extrusion process of Al–Mg alloys (particularly those with high Mg content) remains relatively scarce. Due to the narrow thermal processing window of high-Mg–aluminum alloys, the traditional trial-and-error process development not only takes a long time but also incurs high costs. To address this challenge, the present study employs an advanced approach, combining material characterization with numerical simulation: first, through thermal compression testing (temperature range: 300–450 °C; strain rate range: 0.001–10 s^{-1}), we systematically investigated the high-temperature rheological behavior of an Al–10Mg–3Zn alloy and established an Arrhenius constitutive model based on strain compensation; secondly,

https://doi.org/10.3390/ma19020375

based on the Dynamic Material Model (DMM) theory, we constructed a thermal processing map for the alloy, clearly defining the safe processing zones and instability zones under different strain conditions; finally, using professional finite element (FE) software Qform UK11.0, an FE model of the extrusion process for railway vehicle profiles was established to thoroughly analyze the influence of the extrusion process parameters on forming quality (including temperature field distribution, extrusion load evolution, and metal flow velocity uniformity), thereby determining the optimal process parameter window. This study not only provides theoretical guidance and technical support for the industrial production of high-magnesium–aluminum alloy extrusions but also significantly promotes the application of such advanced materials in high-end equipment manufacturing sectors, such as high-speed train manufacturing.

2. Materials and Simulation Methods

2.1. Materials and Experimental Methods

Al–10Mg–3Zn alloy ingots were prepared in the laboratory, and the chemical composition of the as-cast alloy was analyzed using a direct-reading spectrometer (Germany SPECTRO LAVM11 Direct-Reading Spectrometer). The measurement results are shown in Table 1.

Table 1. Measured chemical composition of the high-magnesium low-density aluminum alloy examined in the present work.

Elements	Mg	Zn	Mn	Cr	Zr	Ti	Fe	Si	Al
Content	9.7	2.9	0.41	0.09	0.14	0.1	$\leq$0.01	$\leq$0.01	Balance

Al–10Mg–3Zn alloy ingots were subjected to a homogenization treatment at 430 °C for a duration of 24 h. A set of ∅10 mm × 15 mm hot compression cylindrical specimens were cut at the midpoint of the radius. They were tested on a Gleeble-3500 thermal simulation testing machine(Dynamic Systems Inc. (DSI) in the United States) at temperatures of 300 °C, 330 °C, 360 °C, 390 °C, 420 °C, and 450 °C with strain rates of 0.001 s^{-1}, 0.01 s^{-1}, 0.1 s^{-1}, 1 s^{-1}, and 10 s^{-1}. Each sample was heated at a rate of 10 °C per minute to the target temperature, held at that temperature for 60 s, and then subjected to thermal compression. The samples were compressed to a total deformation of 60% and then immediately water-quenched.

The test process is presented in Figure 1, while the samples following thermal compression deformation are shown in Figure 2. Figure 2 shows that the hot-compressed specimens exhibit a certain degree of bulging. Although graphite lubricant was used during the hot-compression process to reduce the influence of friction on the test results, it was not possible to completely eliminate friction. Based on a simplified estimation derived from the geometry of the bulged sample after compression, the estimated error in flow stress due to friction is within ±5%. This falls within the typical scatter band of such tests and does not alter the fundamental trends regarding the alloy's sensitivity to temperature and strain rate. The model established in this study is intended for direct input into macroscopic finite element simulations of the extrusion process, where the influence of friction correction on the simulation results remains within an acceptable range. The influence of friction will be considered in future precise studies on material deformation.

https://doi.org/10.3390/ma19020375

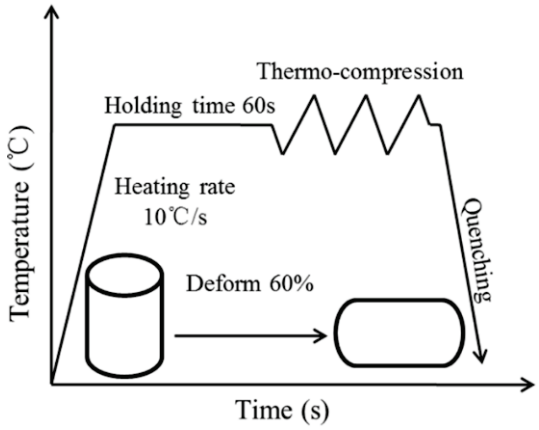

Figure 1. Thermal compression experiment flowchart.

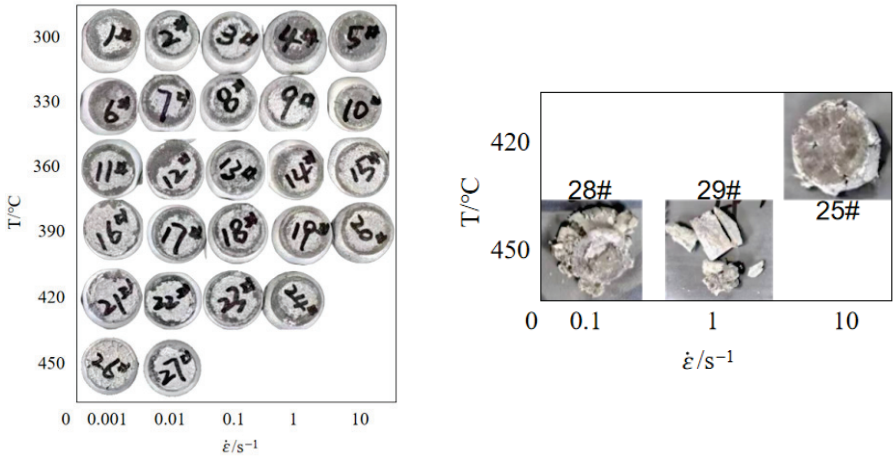

(**a**) (**b**)

Figure 2. Test specimens after heat compression deformation: (**a**) normal sample; (**b**) broken sample.

2.2. Model Establishment and Simulation Plan

In this study, a steady-state extrusion simulation model for rail transit Al–10Mg–3Zn aluminum alloy profiles was established using the Qform finite element software. The simulation employed a Lagrangian–Eulerian method for calculation. The model featured an initial billet of Ø450 mm × 800 mm; the mesh comprised roughly 4.5 million tetrahedral elements. The boundary conditions were set as follows: a shear friction model was applied with a friction factor of 1, and the heat transfer coefficient was set to 30,000 W/(m^2·K), primarily accounting for thermal exchange between the billet and the die, the extrusion container, and the extrusion pad. The billet was heated to 390 °C and extruded at a speed of 0.3 mm/s. Figure 3 presents a cross-sectional view of the profile, while Figure 4 shows the FE model of the extrusion process. A simulation system was utilized to analyze the effects of the billet length, the billet temperature, the extrusion speed, and the friction coefficient on the extrusion formability of the extruded profiles. Detailed simulation schemes are presented in Tables 2 and 3. The effects of the extrusion temperature, extrusion speed, and overall friction coefficient on the properties of the extruded profiles (simulation schemes I–VII) are investigated in Table 2. The effects of billet length and extrusion cylinder friction coefficient on the properties of the extruded profiles (simulation schemes A–E) are investigated in Table 3.

https://doi.org/10.3390/ma19020375

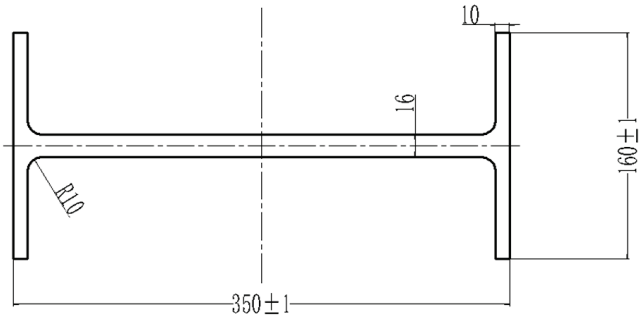

Figure 3. Cross-section diagram of extruded profiles for rail transit.



Figure 4. FE model of the extrusion process for rail transit profiles.

Table 2. Combinations of extrusion temperature, extrusion speed, and overall friction coefficient examined in the present work.

Combination Number	I	II	III	IV	V	VI	VII
Extrusion speed/mm/s	0.3	0.3	0.3	0.1	0.5	0.3	0.3
Billet temperature/°C	360	390	420	390	390	390	390
Friction factor	1	1	1	1	1	0.5	1.5
Ingot length/mm	800	800	800	800	800	800	800

Table 3. Combinations of billet length and friction coefficient of the extrusion cylinder examined in the present work.

Combination Number	A	B	C	D	E
Extrusion speed/mm/s	0.3	0.3	0.3	0.3	0.3
Billet temperature/°C	390	390	390	390	390
Ingot length/mm	800	350	550	800	800
Coefficient of friction of extrusion cylinder	1	1	1	0.1	0.5

3. Results and Discussion

3.1. Stress–Strain Curve and Temperature Correction

Figure 5 presents the true stress–strain curves of the Al–10Mg–3Zn alloy under various hot compression conditions. The curves exhibit a transient stage followed by a steady-state stage [19,20]. Initially, rapid work hardening dominates due to dislocation multiplication. As strain accumulates, the stored deformation energy drives dynamic recovery and recrystallization, which gradually counteract the hardening. Ultimately, a steady-state flow stress is reached when a balance is achieved between these competing mechanisms [21]. Consistently, flow stress decreases with increasing temperature at a fixed strain rate, and increases with strain rate at a constant temperature due to more pronounced work hardening [22].

https://doi.org/10.3390/ma19020375

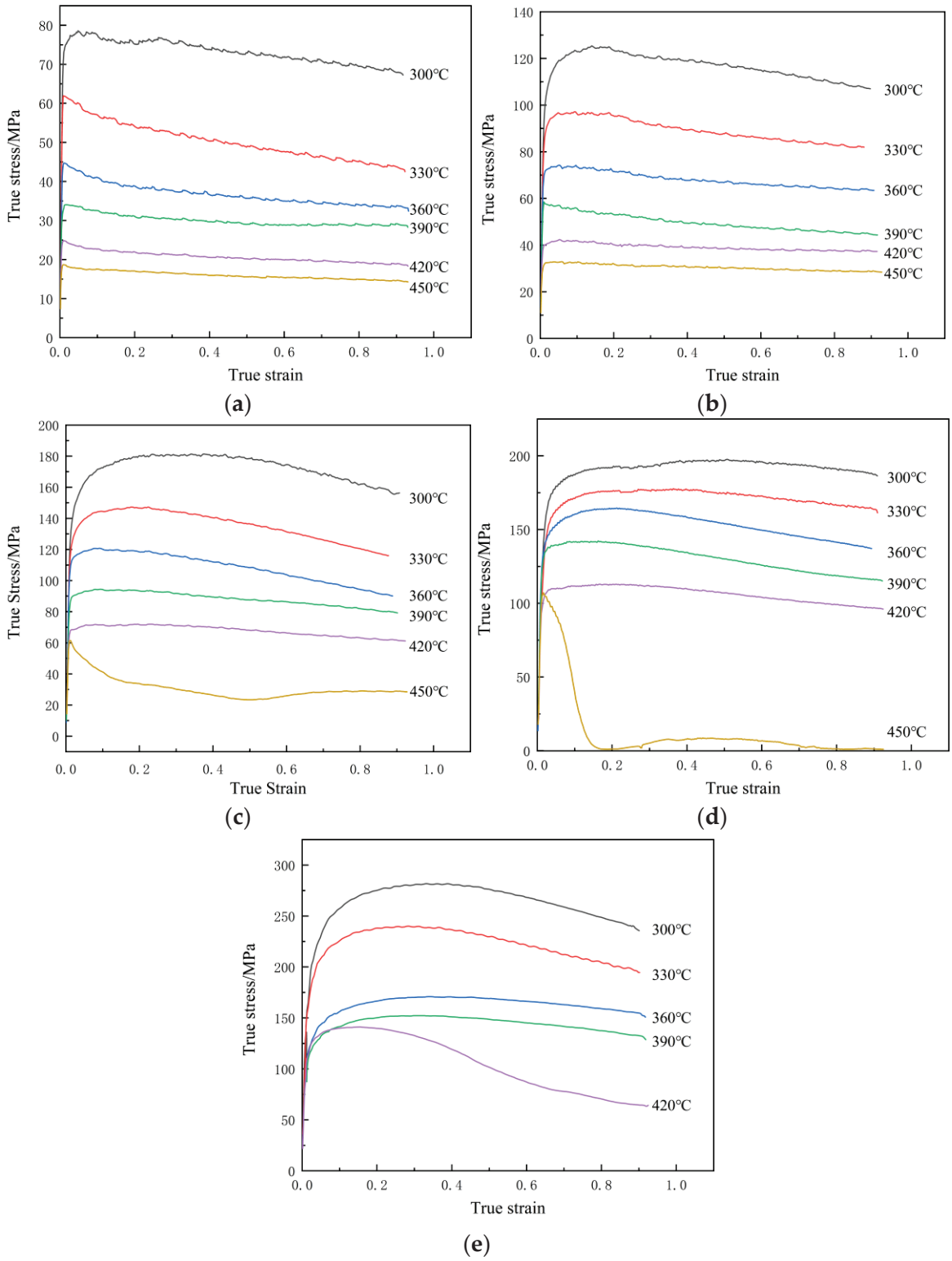

Figure 5. True stress–true strain curves of Al–10Mg–3Zn alloy under different deformation conditions. Each figure refers to a different strain rate: (**a**) 0.001 s^{-1}; (**b**) 0.01 s^{-1}; (**c**) 0.1 s^{-1}; (**d**) 1 s^{-1}; (**e**) 10 s^{-1}.

As illustrated in Figure 5, from the complete dataset, three instances of anomalous behavior were observed in the true stress–strain curves. For the case of a temperature of 420 °C and strain rate of 10 s^{-1} (purple curve in Figure 5e), the stress exhibited a linear decrease after the strain exceeded 0.2. As illustrated in Figure 2b, this sample, 25, exhibited signs of cracking during the compression process. Furthermore, cracking was

https://doi.org/10.3390/ma19020375

also observed in samples subjected to deformation at a temperature of 450 °C and a strain rate greater than 0.1 s^{-1} (samples 28 and 29 in Figure 2b). This finding suggests that thermal plastic instability occurred at elevated temperatures and high strain rates, with dislocation proliferation rates exceeding dynamic recovery rates; this ultimately led to a dislocation pile-up and micro-pore formation. Coupled with insufficient thermal activation energy, this ultimately resulted in intergranular or transgranular cracking [23]. Therefore, the true stress–strain curve data under these conditions are unreliable and are excluded from the subsequent constitutive modeling.

The temperature rise in the sample during hot compression is primarily due to deformation and friction heating; this, coupled with the insufficient responsiveness of the temperature control device (which fails to compensate in real time), leads to a deviation between the actual and preset temperatures.

Figure 6 shows that, at 300 °C, temperature rises of approximately 63 °C, 17 °C, and a negligible increase were observed during compression at strain rates of 10 s^{-1} (blue curve), 1 s^{-1} (red curve), and 0.001 s^{-1} (black curve), respectively. The test results obtained at high strain rates cannot accurately reflect the actual plastic deformation process of the specimen. Therefore, it is necessary to temperature-correct the collected data [24–28]. The overburning point of the homogenized Al-10Mg-3Zn high-magnesium low-density alloy was determined to be 735 K through testing (for details, see Figure 13). A correction was then applied based on the modification method described in [27].

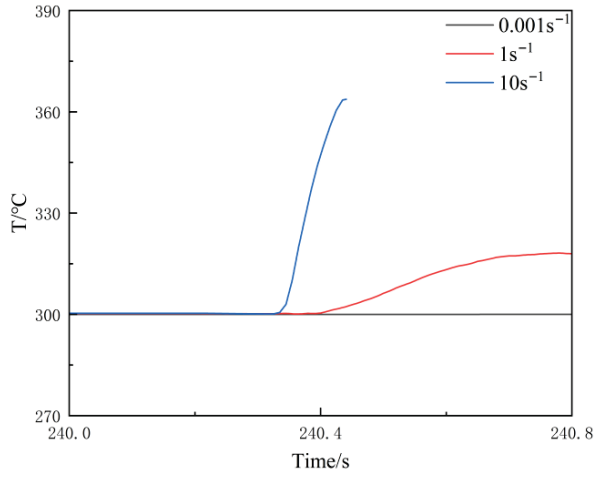

Figure 6. Temperature rise curves during compression processes at identical temperatures but with varying strain rates.

Figure 7 shows a comparison of the true stress–strain curves before and after temperature correction. It can be observed that, during compression at low strain rates (<1 s^{-1}) and different temperatures, almost no temperature rise occurred, and the true stress–strain curves before and after correction are essentially consistent. In contrast, during high-strain-rate (≥1 s^{-1}) compression, a significant temperature rise was observed, with more pronounced effects at lower temperatures and higher strain rates. The difference in flow stress before and after correction was most significant under these conditions. Specifically, during compression at 300 °C and under a strain rate of 10 s^{-1}, the temperature increased by approximately 63 °C; this led to a maximum difference in true stress of up to 100 MPa at the same strain level before and after correction. The measured flow stress is lower than that of its corrected counterpart. This can be attributed to the substantial adiabatic heating induced during high-strain-rate deformation. The elevated temperature softens the material, improving its plasticity and decreasing its flow resistance, which consequently depresses the measured stress value.

https://doi.org/10.3390/ma19020375

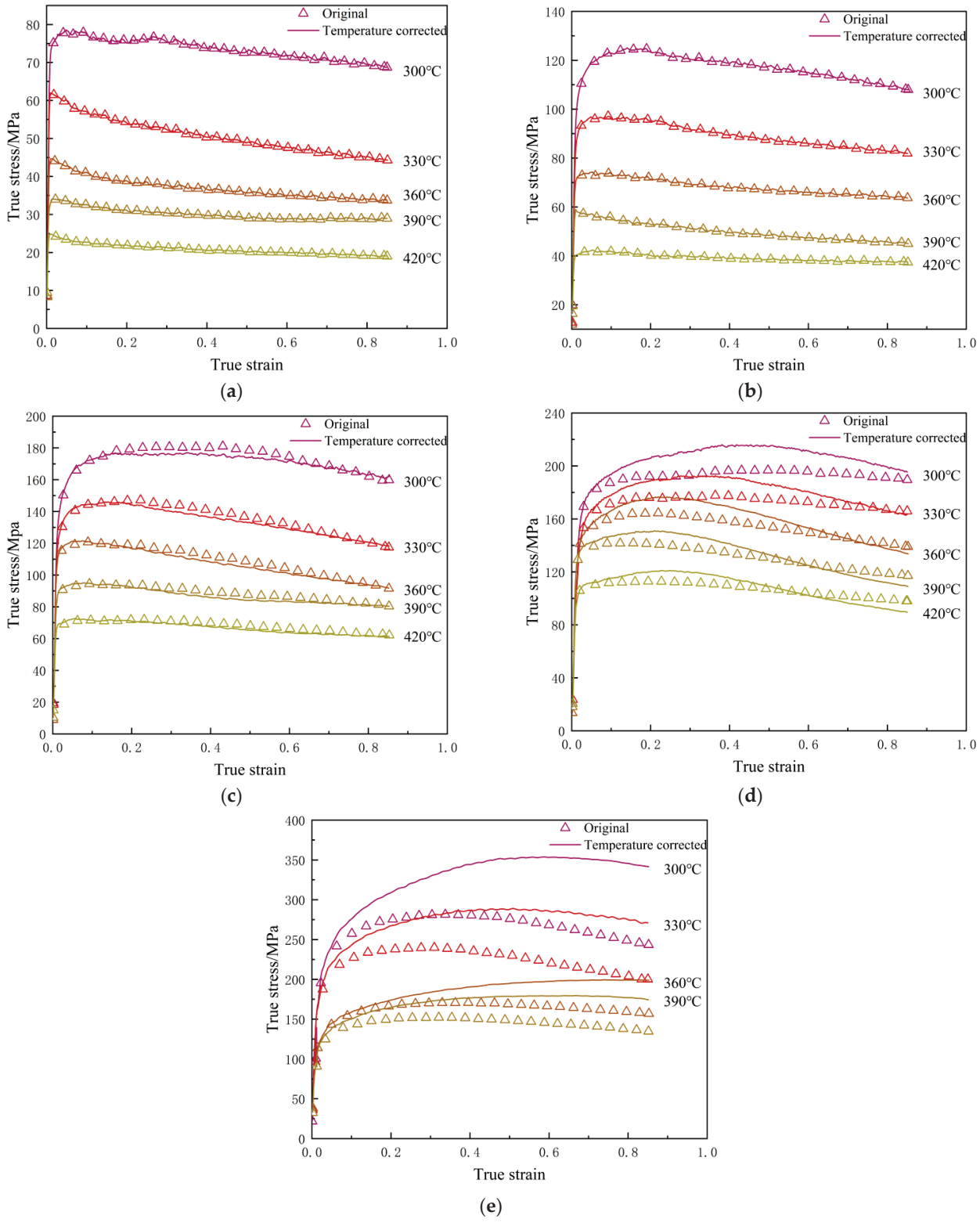

Figure 7. Comparison of the measured true stress–true strain curve with the temperature-corrected curve. Each figure refers to a different strain rate: (**a**) 0.001 s^{-1}; (**b**) 0.01 s^{-1}; (**c**) 0.1 s^{-1}; (**d**) 1 s^{-1}; (**e**) 10 s^{-1}.

3.2. Constitutive Equation

Using the temperature-corrected true stress–strain data, the Arrhenius constitutive equation was employed to establish the relationship between the flow stress and the key deformation parameters (temperature, strain rate, and strain) for the alloy. The effects of

https://doi.org/10.3390/ma19020375

the temperature and strain rate are represented by the Zener–Hollomon parameter, Z. The dependence of flow stress on the Z, expressed by the hyperbolic sine law in the Arrhenius constitutive model [29,30], is given as follows:

$$Z = \dot{\varepsilon} \exp(Q/RT) \tag{1}$$

$$\dot{\varepsilon} = AF(\sigma) \exp[-Q/(RT)] \tag{2}$$

Among these terms, $F(\sigma)$ is a function of stress:

$$F(\sigma) = \begin{cases} \sigma^{n_1} (\alpha\sigma < 0.8) \\ exp(\beta\sigma) (\alpha\sigma > 1.2) \\ \left[sin\mathrm{h}(\alpha\sigma)\right]^n (\text{general validity}) \end{cases} \tag{3}$$

In the above equation, the hyperbolic sine function, $F(\sigma)$, describes the thermal rheological stress, where σ is the flow stress (MPa), $\dot{\varepsilon}$ is the strain rate (s^{-1}), T is the temperature (K), and Q is the activation energy for thermal deformation ($J{\cdot}mol^{-1}$). The parameters R (the ideal gas constant, $J{\cdot}mol^{-1}{\cdot}K^{-1}$), A, α, β, and n_1 are material constants, with the relationship $\alpha = \beta/n_1$ holding among them.

$$\dot{\varepsilon} = A\left[sin\mathrm{h}(\alpha\sigma)\right]^n \exp[-Q/(RT)] \tag{4}$$

By combining Equations (1) and (4), the Zener–Hollomon parameter, Z, is defined as follows:

$$Z = A[sinh(\alpha\sigma)]^n \tag{5}$$

According to the definition of the hyperbolic sine function, the flow stress can be expressed in terms of the Zener–Hollomon parameter, Z.

$$\sigma = \frac{1}{\alpha}\ln\left\{\left(\frac{Z}{A}\right)^{\frac{1}{n}} + \left[\left(\frac{Z}{A}\right)^{\frac{2}{n}} + 1\right]^{\frac{1}{2}}\right\} \tag{6}$$

Next, we take the case in which the strain value is 0.2 as an example to introduce the determination process of material constant solutions under the entire range of stress conditions. Substitute Equation (3) into Equation (4), and take the logarithm of both sides. Then, Equation (7) can be obtained:

$$\begin{cases} ln(\sigma) = \dfrac{1}{n_1} ln(\dot{\varepsilon}) - \dfrac{1}{n_1} ln(B) \\ \sigma = \dfrac{1}{\beta} ln(\dot{\varepsilon}) - \dfrac{1}{\beta} ln(C) \\ ln[sinh(\alpha\sigma)] = \dfrac{Q}{nR}\dfrac{1}{T} + \dfrac{(\ln\dot{\varepsilon} - \mathrm{lnA})}{n} \end{cases} \tag{7}$$

The stress values at a strain of 0.2 were obtained experimentally and extracted from Figure 7 for coefficient calibration. Subsequently, the linear fitting of these data (Figure 8a,b) yielded the parameters $n_1 = 5.631$ and $\beta = 0.056\ MPa^{-1}$, from which $\alpha = \beta/n_1 = 0.010\ MPa^{-1}$ was derived. The parameter n was then determined to be 3.967 from the slope of the $\ln[\sin\mathrm{h}(\alpha\sigma)]$ vs. $\ln\dot{\varepsilon}$ plot (Figure 8c). Finally, from the $\ln[\sin\mathrm{h}(\alpha\sigma)]$ vs. 1/T relationship (Figure 8d), the activation energy, Q, and the material constant, A,

https://doi.org/10.3390/ma19020375

were calculated as 148,900 J/mol and 6.028×10^{10}, respectively. Thus, the constitutive model based on the hyperbolic sine function for $\varepsilon = 0.2$ can be established as follows:

$$\dot{\varepsilon} = 6.038 \times 10^{10}[sinh(0.0100\sigma)]^{3.967}\exp[-148900/(RT)] \quad (8)$$

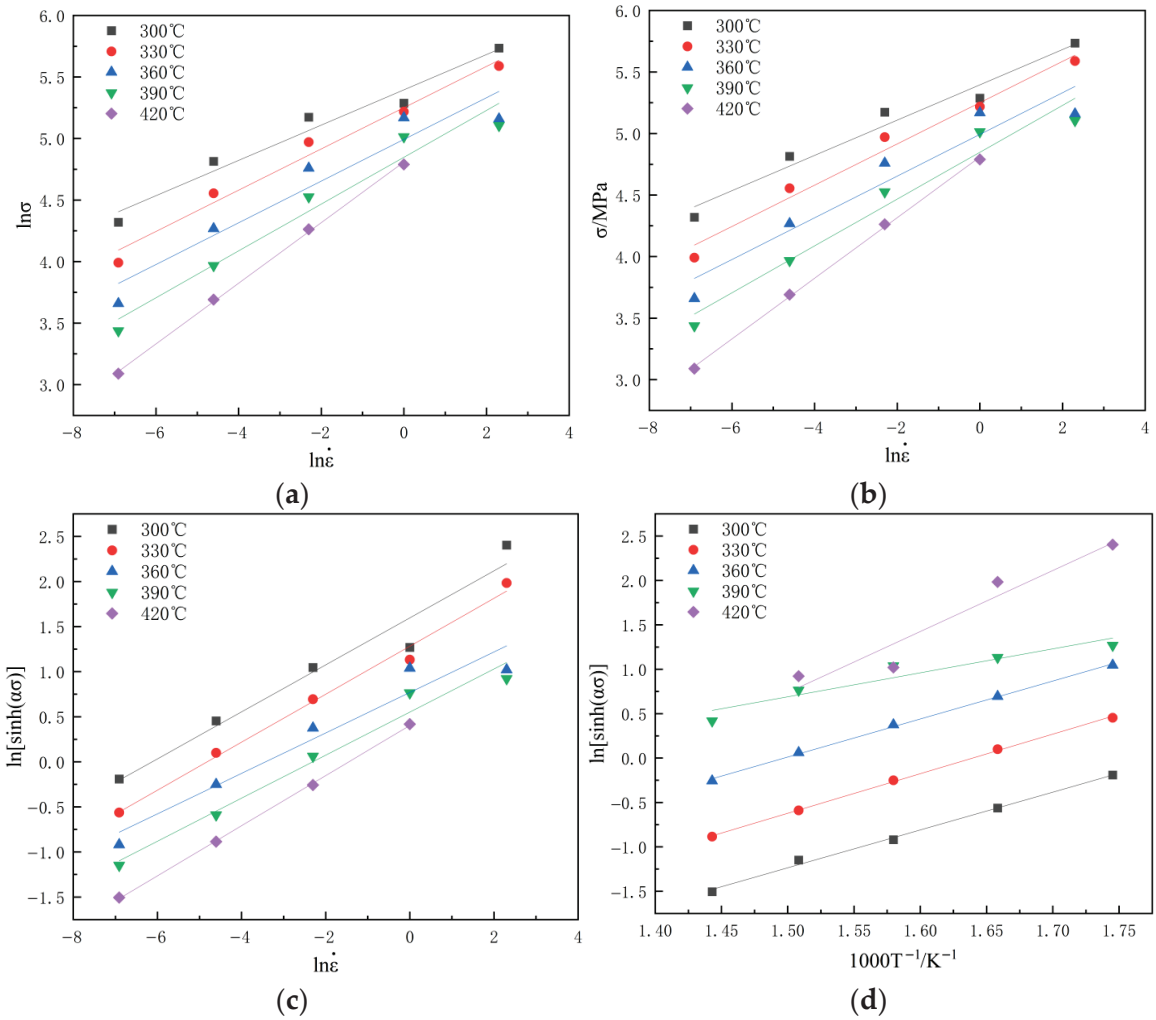

Figure 8. Homogeneous Al–10Mg–3Zn alloy relationship curves: (**a**) $ln\sigma - \ln\dot{\varepsilon}$; (**b**) $\sigma - \ln\dot{\varepsilon}$; (**c**) $ln[sinh(\alpha\sigma)] - \ln\dot{\varepsilon}$; (**d**) $ln[sinh(\alpha\sigma)] - 1/T$.

The formula does not explicitly consider the effect of strain. However, the deformation activation energy, Q, and the material constants α, n, and ln$A$ have been shown to vary with strain [30]. It is assumed that their values are all polynomial functions of the strain ε. To determine this function, parameter values obtained at different strain levels ranging from 0.05 to 0.80 with an interval of 0.05 were used to fit the polynomial function. To ensure greater accuracy in the fitting results, a fifth-order polynomial function was employed to fit the relevant material parameters.

Ultimately, the strain-compensated Arrhenius constitutive model for the Al–10Mg–3Zn alloy was formulated as Equation (9). With the material parameters determined, this model enables the prediction of flow stress for a wide range of deformation conditions.

$$\sigma = \frac{1}{\alpha(\varepsilon)}\ln\{(\frac{\dot{\varepsilon}\exp[Q(\varepsilon)/8.314T]}{A(\varepsilon)})^{\frac{1}{n(\varepsilon)}} + [(\frac{\dot{\varepsilon}\exp[Q(\varepsilon)/8.314T]}{A(\varepsilon)})^{\frac{2}{n(\varepsilon)}} + 1]^{\frac{1}{2}}\} \quad (9)$$

https://doi.org/10.3390/ma19020375

In the equation above, R is the gas constant (8.314 J·mol^{-1}·K^{-1}), and the terms $\alpha(\varepsilon)$, $Q(\varepsilon)$, $\ln A(\varepsilon)$, and $n(\varepsilon)$ are polynomial functions describing the dependence of α, Q, $\ln A$, and n on strain, respectively.The correlation coefficients in the fitted polynomial function (10) were determined by fitting the variation curves of each parameter with strain shown in Figure 9. The coefficients of each calibrated polynomial function are shown in Table 4. Substituting these correlation coefficients yields the calibrated polynomial functions for each parameter, as shown in Formula (10):

$$\begin{aligned} \alpha(\varepsilon) &= 0.01079 - 0.00734\varepsilon + 0.01996\varepsilon^2 - 0.01405\varepsilon^3 - 0.0022\varepsilon^4 + 0.00482\varepsilon^5 \\ Q(\varepsilon) &= 160458 - 75667\varepsilon - 7381\varepsilon^2 + 737554\varepsilon^3 - 1291052\varepsilon^4 + 642526\varepsilon^5 \\ n(\varepsilon) &= 5.74 - 18.09\varepsilon + 76.1\varepsilon^2 - 160.36\varepsilon^3 + 167.69\varepsilon^4 - 67.91\varepsilon^5 \\ A(\varepsilon) &= 3.99 \times 10^{11} - 3.69 \times 10^{12}\varepsilon + 1.4 \times 10^{13}\varepsilon^2 - 2.49 \times 10^{13}\varepsilon^3 + 2.36 \times 10^{13}\varepsilon^4 - 9.7 \times 10^{12}\varepsilon^5 \end{aligned} \quad (10)$$

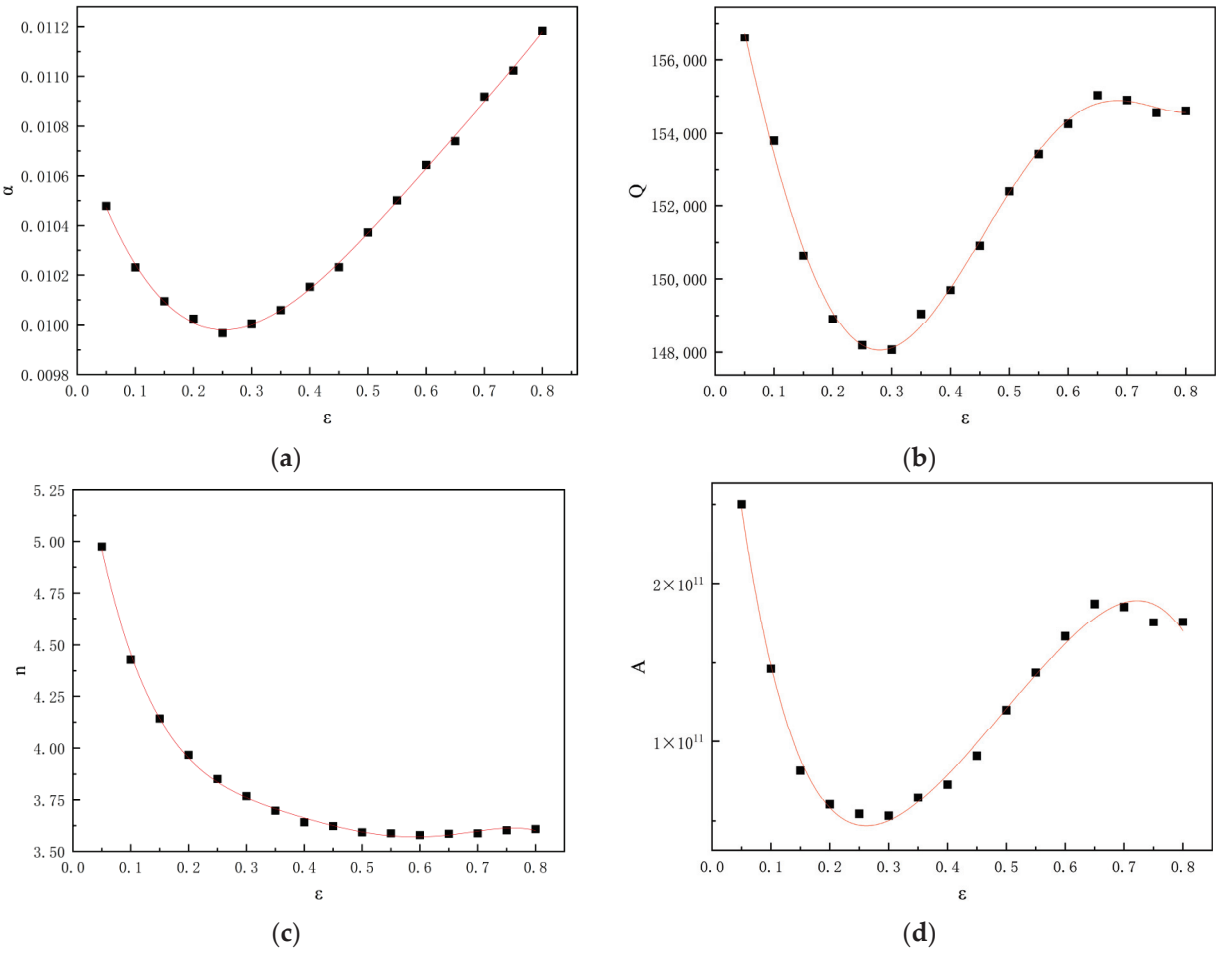

Figure 9. Parameter variation under different strains: (**a**) α-ε; (**b**) Q-ε; (**c**) n-ε; (**d**) A-ε.

Table 4. Al–10Mg–3Zn alloy polynomial fitting parameters.

	α		Q		n		A
α_0	0.0108	Q_0	160,458	n_0	5.74	A_0	3.99×10^{11}
α_1	−0.0073	Q_1	−75,667	n_1	−18.96	A_1	-3.69×10^{12}
α_2	0.0200	Q_2	−7381	n_2	76.1	A_2	1.4×10^{13}
α_3	−0.0141	Q_3	737,554	n_3	−160.36	A_3	-2.49×10^{13}
α_4	−0.0022	Q_4	−1,291,052	n_4	167.69	A_4	2.36×10^{13}
α_5	0.0048	Q_5	642,526	n_5	−67.91	A_5	-9.7×10^{12}

https://doi.org/10.3390/ma19020375

3.3. Hot Processing Map

The Dynamic Material Model (DMM) [31–34] postulates that, during thermal deformation, metals constitute a closed energy dissipation system. The external power input, P, at a given strain rate is accordingly separated into the dissipative component, G, and the co-dissipative component, J, which is expressed mathematically in Equation (11):

$$P = \sigma\dot{\varepsilon} = G + J = \int_0^{\dot{\varepsilon}} \sigma d\dot{\varepsilon} + \int_0^{\sigma} \dot{\varepsilon} d\sigma \tag{11}$$

where G represents the energy dissipated through material deformation (dissipation), and J denotes the energy consumed by microstructural evolution (co-dissipation). The strain rate sensitivity index, m (Equation (12)), quantitatively reflects the competition between these two processes.

$$m = \frac{dJ}{dG} = \frac{\dot{\varepsilon} d\sigma}{\sigma d\dot{\varepsilon}} = \frac{dln\sigma}{dln\dot{\varepsilon}} \tag{12}$$

To quantify the efficiency of power dissipation during the pronounced microstructural evolution, the parameter η is introduced. It attains its specific form under the condition of maximum co-dissipation, i.e., when $m = 1$ and $J = J_{max}$, as follows:

$$\eta = \frac{J}{J_{max}} = \frac{2m}{m+1} \tag{13}$$

The hot processing properties of materials need to be judged in combination with instability maps, which are developed based on the principle of irreversible thermodynamics of fluids. The basis for determining instability is shown in Equation (14):

$$\xi(\dot{\varepsilon}) = \frac{\partial \ln(\frac{m}{m+1})}{\partial \ln \dot{\varepsilon}} + m < 0 \tag{14}$$

In the equation, $\xi(\dot{\varepsilon})$ is the instability parameter. When $\xi(\dot{\varepsilon}) < 0$, the material undergoes thermal deformation in an unstable state; defects will form in the internal structure.

Using Equations (13) and (14), the parameters η and $\xi(\dot{\varepsilon})$ were calculated across different deformation conditions. Two-dimensional contour maps—namely, the power dissipation map (η) and the flow instability map ($\xi(\dot{\varepsilon})$)—were then plotted as functions of strain rate and temperature. Superimposing the flow instability map onto the power dissipation map yields comprehensive hot processing maps.

Figure 10 presents the hot processing maps of the Al–10Mg–3Zn alloy at varying strains. The black line represents the power dissipation contour, the gray shaded area indicates the deformation instability zone, and the green box marks the deformation-safe region. At $\varepsilon = 0.2$, unstable regions (dark grey) appear under two conditions: (i) strain rates > 0.121 s^{-1} with $T \geq 342$ °C; (ii) strain rates between 0.001 and 0.004 s^{-1} with $T \geq 373$ °C. Both of these conditions exhibit strain-rate-sensitive temperature boundaries. As the strain increases to 0.4, the instability zone shifts and shrinks, concentrating at strain rates > 0.271 s^{-1} and $T > 341$ °C; notably, deformation cracking occurred at 420 °C and 10 s^{-1}, consistent with the map's prediction. By $\varepsilon = 0.6$, the instability zone completely disappears.

Therefore, the identified safe processing parameters for the Al–10Mg–3Zn alloy are 360–420 °C and 0.004–0.121 s^{-1}, which corresponds to the green rectangular area shown across Figure 10a–c.

https://doi.org/10.3390/ma19020375

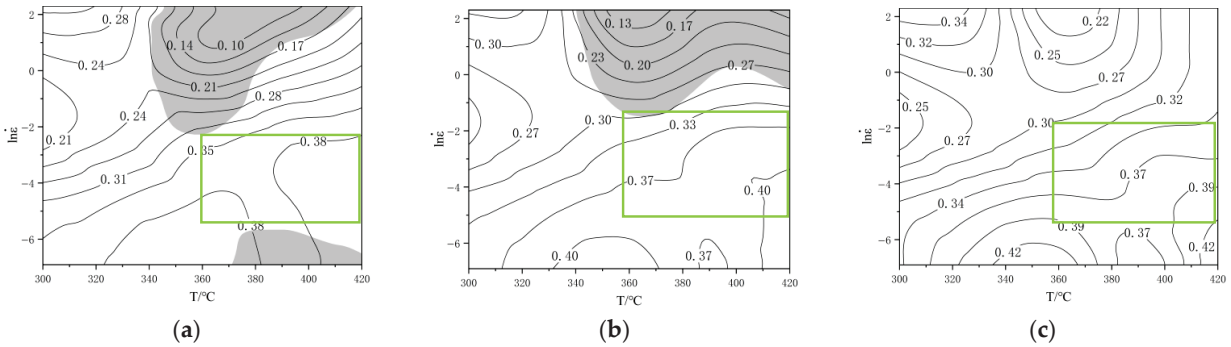

Figure 10. Homogeneous Al–10Mg–3Zn alloy hot processing map: (**a**) ε: 0.2; (**b**) ε: 0.4; (**c**) ε: 0.6.

3.4. Extrusion Simulation Results

3.4.1. Analysis of Simulation Results

Figure 11 shows the prediction of profile formability under the initial process conditions. As shown in the figure, the temperature variation across the profile cross-section is about 11 °C, spanning from a minimum of 427 °C to a maximum of 438 °C. The plastic strain distribution across the profile cross-section is non-uniform, with a surface layer exhibiting a high-strain zone of a certain depth. The maximum strain reaches 91, while the calculated average strain value is 8.36. The velocity deviation across the extruded profile cross-section is approximately 25%, indicating poor flow uniformity. The breakthrough extrusion load for the profile reaches 94 MN; this means that equipment with a capacity of at least 100 MN is required for successful extrusion.

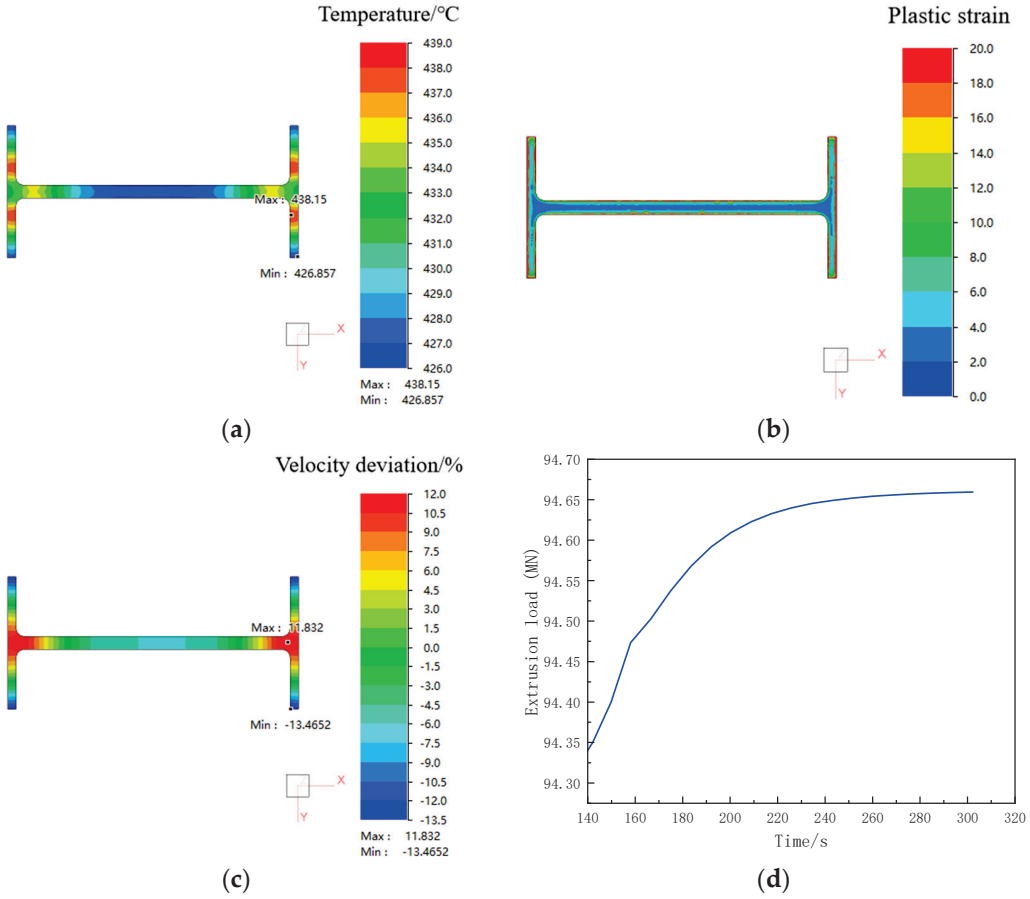

Figure 11. Prediction of profile formability under initial process conditions: (**a**) temperature field; (**b**) plastic strain field; (**c**) velocity deviation; (**d**) extrusion load.

https://doi.org/10.3390/ma19020375

3.4.2. The Effect of Process Parameters on the Forming Temperature of Extruded Profiles

This section will explore the temperature evolution of the Al–10Mg–3Zn alloy during extrusion and its impact on profile quality, grounded in the established thermodynamic and heat transfer theories. Extrusion speed directly influences temperature distribution by affecting the generation rate of deformation heat, while the billet's initial temperature determines the system's thermal baseline. Differential Scanning Calorimetry (DSC) curves are employed to evaluate material thermal stability, particularly overburning temperature, which is a critical parameter for determining the processing limits of extrusion techniques.

Figure 12 shows that increasing both the billet temperature and the extrusion speed will, to some extent, increase the overall extrusion temperature of the profile; Figure 12a indicates that increasing the billet temperature reduces the temperature difference within the profile cross-section, but the reduction is relatively small; Figure 12b shows that increasing the extrusion speed significantly increases the temperature difference within the profile cross-section. In simulation scheme V (extrusion speed 0.5 mm/s), the temperature difference in the profile cross-section is the largest, at approximately 16 °C. The extrusion speed has a greater influence on the extrusion temperature value and uniformity of the profile than the billet temperature. Figure 13 shows the DSC curves of a homogeneous Al–10Mg–3Zn alloy. As shown in Figure 13, the first endothermic peak corresponds to the incipient melting (overburning) temperature of the homogenized Al–10Mg–3Zn alloy, with a value of 462 °C. The maximum temperature of the extruded profile in scheme V is approximately 465 °C, which exceeds the overburning temperature. Therefore, the extrusion speed of 0.5 mm/s has reached the upper limit value.

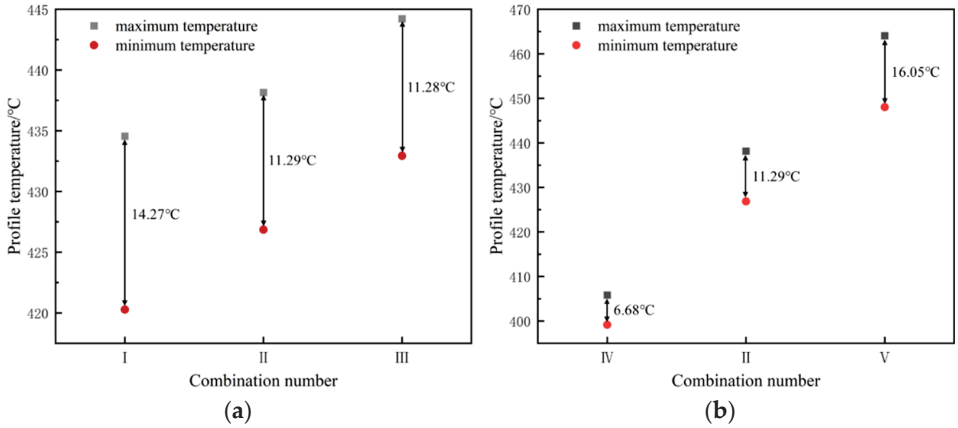

Figure 12. Effect of process parameters on the temperature field at the extrusion die exit: (**a**) billet temperature; (**b**) extrusion speed. In both considered cases, the parameter under investigation in a given figure displays a rise from left to right, see Table 2.

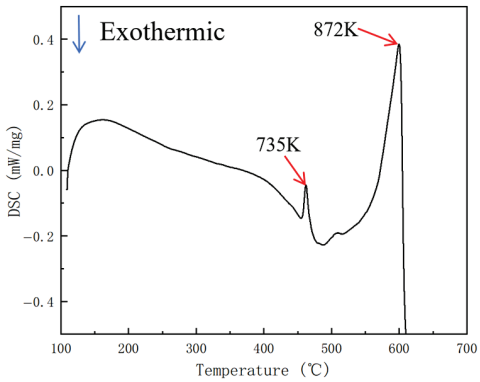

Figure 13. DSC curves of homogeneous Al–10Mg–3Zn alloy.

https://doi.org/10.3390/ma19020375

3.4.3. The Effect of Process Parameters on Extrusion Load

Figure 14 shows the influence of different process parameters on the variation in extrusion load during profile extrusion. When the ingot length, extrusion speed, and friction coefficient increase, the extrusion load generally exhibits an upward trend (Figure 14b–e). This is because, with the growth of these parameters, the energy required to overcome the force of friction and material deformation resistance during the extrusion process escalates correspondingly, driving the extrusion load of the profile to rise. Conversely, when the billet temperature rises, the material's deformation resistance diminishes (Figure 14a). This enhancement in the uniformity of metal flow and deformation during extrusion reduces the additional stresses induced by unevenly coordinated deformation, ultimately causing the extrusion load to decrease as the billet temperature increases.

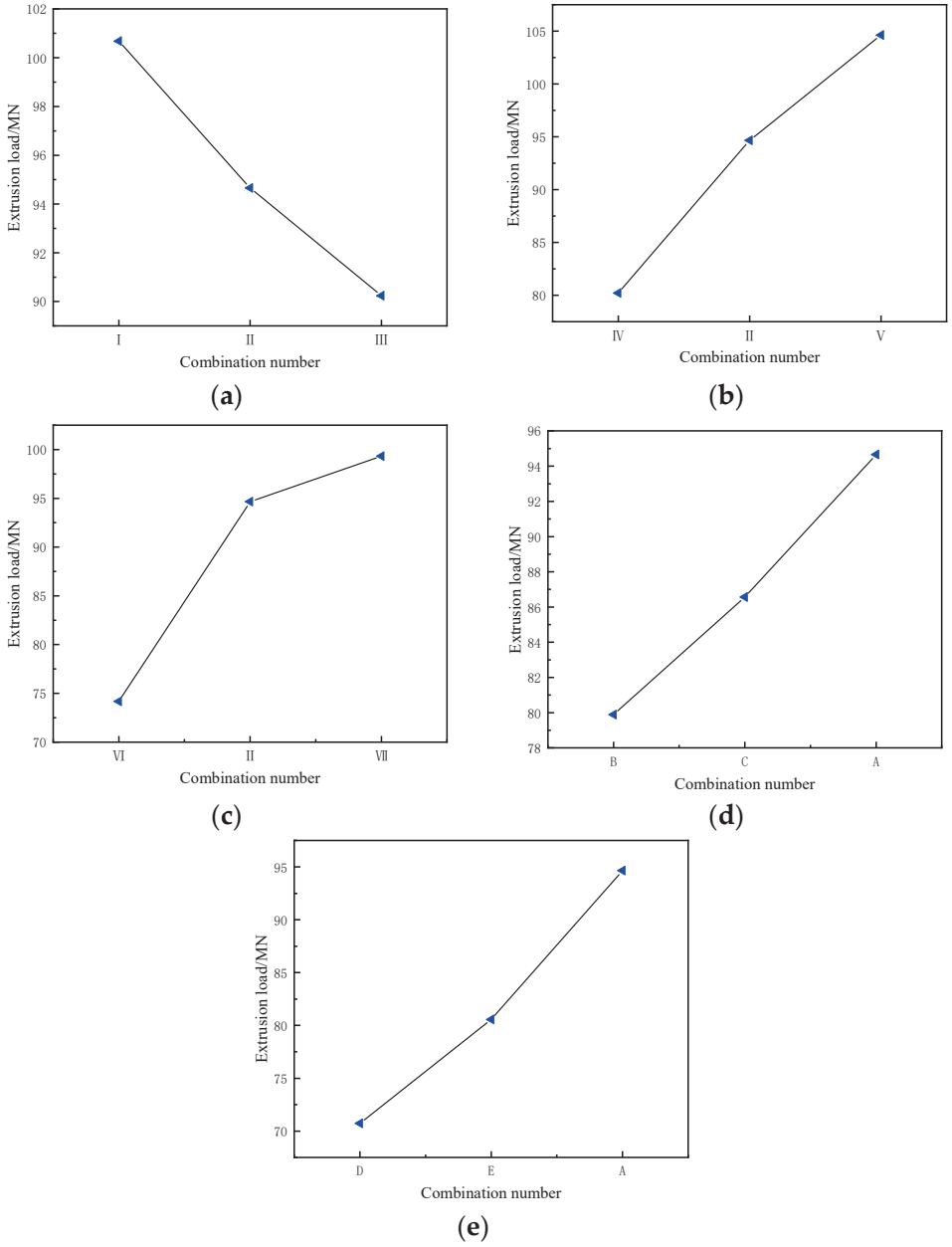

Figure 14. The effect of process parameters on the extrusion load of extruded profiles: (**a**) temperature; (**b**) extrusion speed; (**c**) overall friction coefficient; (**d**) ingot length; (**e**) extrusion cylinder friction coefficient. In all cases considered, the parameter under investigation in a given figure displays a rise from left to right; see Tables 2 and 3.

https://doi.org/10.3390/ma19020375

3.4.4. The Effect of Process Parameters on the Uniformity of Extrusion Flow Rate for Extruded Profiles

This paper adopts the velocity deviation difference (VDD) as an indicator to evaluate the uniformity of the profile's exit speed. The velocity deviation difference is defined as follows:

$$VDD = \left(\frac{v_{max} - v_{min}}{\overline{v}} \right) \%$$

In the formula, v_{max} represents the maximum flow velocity of the nodes on the cross-section of the profile; v_{min} represents the minimum flow velocity of the nodes on the cross-section of the profile; $\overline{v}$ represents the average velocity of all nodes on the cross-section of the profile. The smaller the velocity deviation difference (VDD), the more uniform the velocity distribution on the cross-section of the profile.

Figure 15a shows that, as the billet temperature increases, the VDD of the profile extrusion decreases, and the uniformity of the extrusion flow velocity improves; Figure 15b shows that, as the extrusion speed increases, the VDD decreases. Increasing the extrusion speed results in high-speed shear flow, dominating the deformation process; here, the temperature rise during extrusion compensates for the heat dissipation of the die, eliminating the lag in metal flow velocity at the edges and improving the uniformity of the extrusion flow velocity.

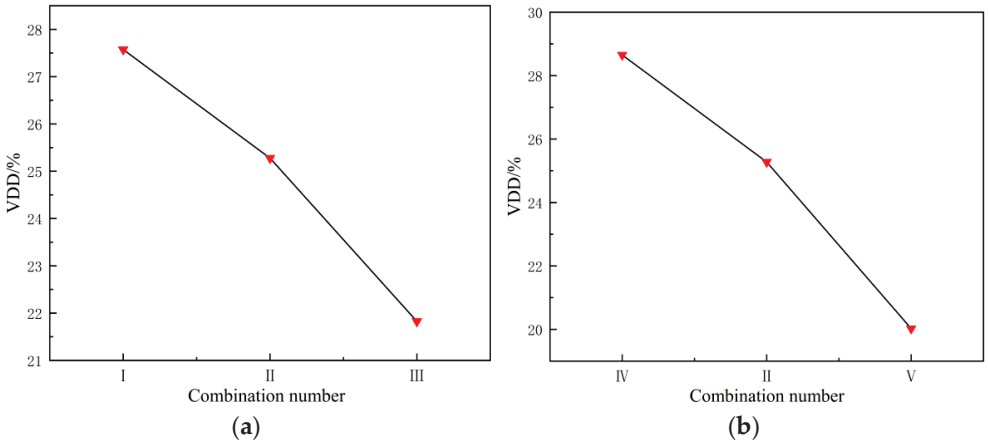

Figure 15. The influence of process parameters on the velocity deviation difference (VDD) in profile extrusion: (**a**) billet temperature; (**b**) extrusion speed.

3.5. Optimization of Extrusion Process Parameters Based on Response Surface Methodology (RSM)

3.5.1. Determination of Design Variables and Optimization Objectives

The billet temperature, extrusion speed, and billet length were selected as design variables for a three-factor, three-level Box–Behnken experimental design [35]. The extrusion load (which F represents), speed deviation (which VDD represents), average strain (which $\overline{\varepsilon}$ represents) of the profile cross-section, and temperature difference (which ΔT represents) of the profile cross-section were chosen as optimization objectives for multi-objective optimization. The synergistic effects of the four process parameters on the extrusion formability of the profile were investigated. The design variables and their ranges are shown in Table 5. Based on the optimal process window determined from the thermal processing diagram (Figure 10), the three levels of the billet temperature, T, were set as 360 °C, 390 °C, and 420 °C. Based on the significant influence of the extrusion speed, v, on the temperature of the extruded profile (Figure 12b), and to prevent a scenario where the overburning temperature was exceeded, three levels of v were designed: 0.1 mm/s, 0.3 mm/s, and 0.5 mm/s. Based on the capacity of the extrusion equipment, the three levels of the billet length, L, design were 350 mm, 575 mm, and 800 mm, respectively.

https://doi.org/10.3390/ma19020375

Table 5. Design variables and value ranges for the three-factor, three-level Box–Behnken experimental design.

Design Variable	Value Ranges
Billet temperature T (°C)	360–420
Extrusion speed v (mm/s)	0.1–0.5
Ingot length L (mm)	350–800

3.5.2. Box–Behnken Experimental Design

This paper selects the Box–Behnken experimental design for response surface analysis. Based on the experimental design results, 15 process parameter modifications and numerical simulations were carried out, with Table 6 presenting the complete calculation results.

Table 6. Calculation results as obtained for the Box–Behnken experimental design. Columns 2–4 show the independent variables of experimental input, and columns 5–8 show the dependent variables of simulation output.

Experiment Number	T (°C)	v (mm/s)	L (mm)	F (MN)	VDD (%)	$\bar{\varepsilon}$	ΔT (°C)
1	360	0.1	575	77.139	26.1029	8.169	6.511
2	420	0.1	575	71.2617	30.4403	8.176	8.341
3	360	0.5	575	104.213	20.95196	8.269	13.457
4	420	0.5	575	91.31	19.16665	8.275	15.525
5	360	0.3	350	86.6928	25.183	8.205	8.891
6	420	0.3	350	75.5111	20.92162	8.45	11.765
7	360	0.3	800	100.682	27.5956	8.276	14.262
8	420	0.3	800	90.2429	21.8673	8.378	11.291
9	390	0.1	350	67.5451	26.7742	8.232	7.843
10	390	0.5	350	88.2312	19.30918	8.388	12.322
11	390	0.1	800	80.7862	28.6261	8.27	6.691
12	390	0.5	800	104.633	19.98956	8.287	15.999
13	390	0.3	575	87.3589	24.773	8.4	9.938
14	390	0.3	575	87.3589	24.773	8.4	9.938
15	390	0.3	575	87.3589	24.773	8.4	9.938

3.5.3. Response Surface Model

The second-order response surface equation fitted by the least squares method is expressed as follows:

$$y = \beta_0 + \sum_{i=1}^{n} \beta_i x_i + \sum_{i=1}^{n} \beta_{ii} x_i^2 + \sum \sum_{p<i} \beta_{pi} x_p x_i + \varepsilon \quad (15)$$

In this equation, x_i is the design variable, ε is the residual error, and β_0, β_i, β_{ii}, and β_{pi} are all the undetermined coefficients.

Based on the data in Table 6 and using Equation (15) as the base expression, the response surface functions of the extrusion load, F, the deviation value, VDD, of the profile cross-sectional velocity, the average strain, $\bar{\varepsilon}$, of the profile cross-section, and the temperature difference, ΔT, of the profile cross-section with respect to each design variable are obtained, as shown in Equations (16)–(19):

$$F = 223.66 - 0.79T + 194.07v + 0.0137L - 0.29Tv + 2.8 * 10^{-5}TL + 0.0176vL + 8.92 * 10^{-4}T^2 - 54.52v^2 + 2.38 * 10^{-6}L^2 \quad (16)$$

$$SD = 40.39 - 0.031T - 20.33v + 0.0033L \quad (17)$$

https://doi.org/10.3390/ma19020375

$$\bar{\varepsilon} = -6.03 + 0.067T + 2.27v + 0.0023L - 4.2 * 10^{-5}Tv - 5.3 * 10^{-6}TL - 7.72 * 10^{-4}vL - 8 * 10^{-5}T^2 - 2.63v^2 - 7.41 * 10^{-9}L^2 \quad (18)$$

$$\Delta T = -45.69 + 0.14T - 1.85v + 0.08L + 0.01Tv - 2.16 * 10^{-4}TL + 0.027vL \quad (19)$$

The above four response surface models were used to predict, respectively, the four optimization objectives, F, VDD, $\bar{\varepsilon}$, and ΔT, under different extrusion process parameters. Figure 16 shows the comparison between the predicted values and actual values of the response surfaces for the various optimization objectives. Squares of different colors in the figure represent distinct actual data points.The results in Figure 16a,d indicate that the predicted values of the extrusion load, F, and the temperature difference, ΔT, of the profile cross-section are in good agreement with the actual values, suggesting that these response surface models are reliable. Figure 16b,c indicate, however, that the predicted values of the velocity deviation difference, VDD, and the average strain, $\bar{\varepsilon}$, of the profile cross-section deviate significantly from the actual values, necessitating a significance test evaluation.

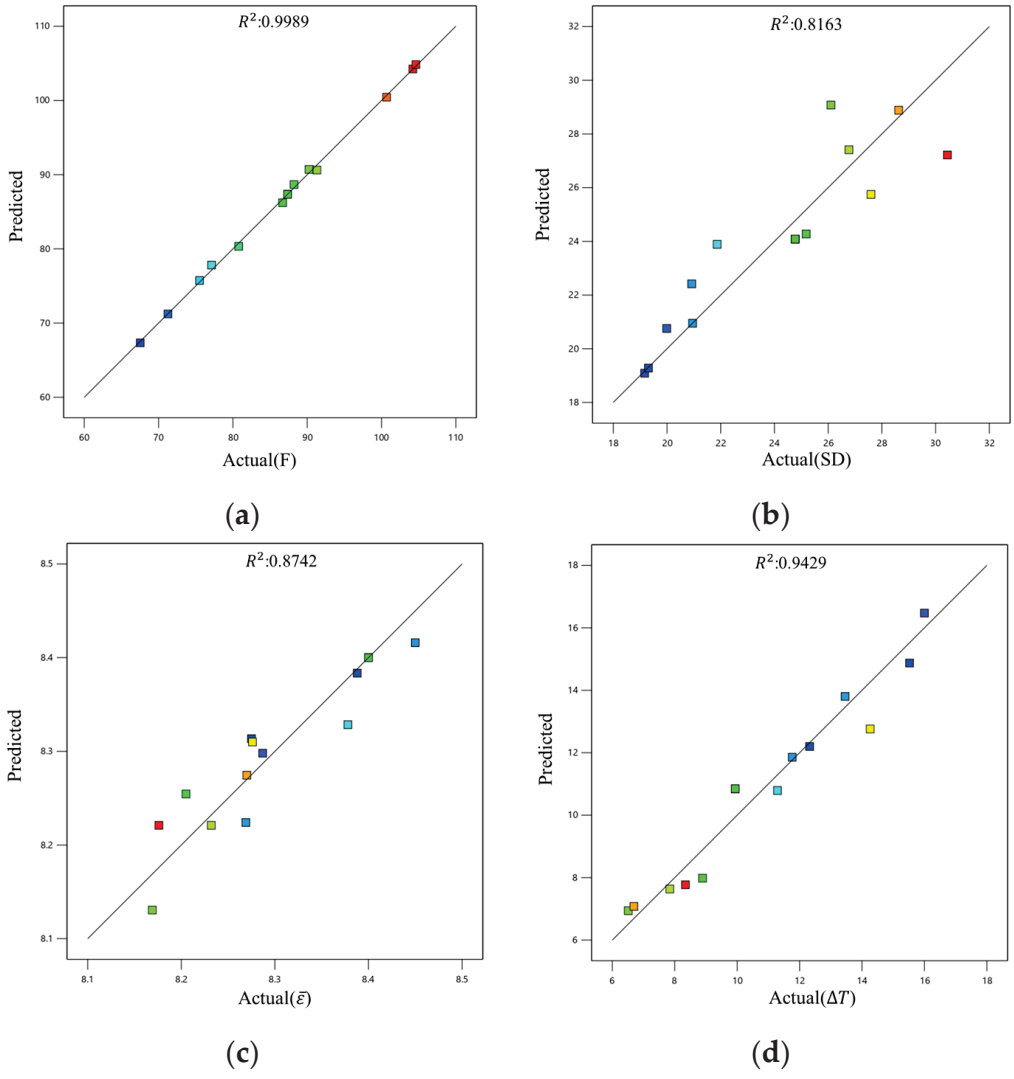

Figure 16. Comparison of actual values and predicted values of the four different response surfaces: (**a**) F; (**b**) VDD; (**c**) $\bar{\varepsilon}$; (**d**) ΔT.

https://doi.org/10.3390/ma19020375

The significance tests were conducted on the response surface models for key response indicators (extrusion load, flow velocity deviation, average strain, and cross-sectional temperature difference). The complete analysis tables are provided in Appendix A. The results indicate the following findings: The model for the extrusion load is highly statistically significant ($F = 488.19$, $p < 0.0001$, $R^2 = 0.9989$). Among the factors, the extrusion speed (v) is the most influential factor affecting the extrusion load. The model for flow velocity deviation is statistically significant ($F = 16.30$, $p = 0.0002$). Its variation is primarily driven by extrusion speed (v). The model for average strain did not pass the significance test ($p = 0.0754 > 0.05$). This indicates that, within the range of process parameters studied, the billet temperature (T), extrusion speed (v), and ingot length (L) have no significant impact on the average strain across the profile cross-section. The model for cross-sectional temperature difference is statistically significant ($F = 22.00$, $p < 0.0001$). Extrusion speed (v) is again the most significant factor contributing to the cross-sectional temperature difference.

3.5.4. Response Surface Analysis

Figure 17 shows the response surface plot for the combined influence of billet temperature, T, and extrusion speed, v, on the extrusion load, F, when the ingot length, L, is 575 mm. The results indicate that the extrusion load is minimal within the high-temperature, low-speed parameter window. As the billet temperature increases, the metal deformation resistance decreases, the plasticity increases, and the extrusion load decreases; at lower extrusion speeds, metal deformation occurs more slowly, internal stresses have time to adjust, the deformation heat effect is not significant, the temperature changes are smooth, and the metal deformation resistance is lower than at high speeds, resulting in reduced extrusion load.

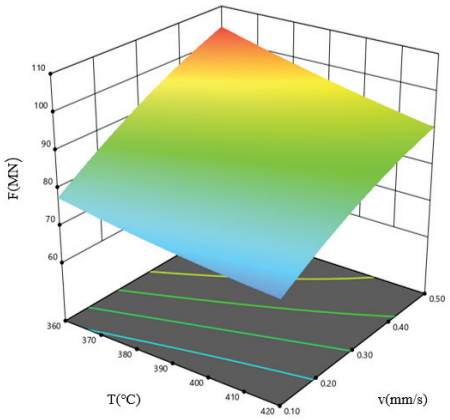

Figure 17. Response surface plot describing how T and v influence F, shown for the case where $L = 575$ mm.

Figure 18 shows the response surface plot for the combined influence of the billet temperature, T, and ingot length, L, on F at an extrusion speed, v, of 0.3 mm/s. The results indicate that the extrusion load is minimal within the high-temperature, short-ingot-length parameter window. As the ingot length increases, the contact area with the extrusion cylinder increases, the friction increases, the metal flow path lengthens, the flow resistance increases, and the pressure required to break through the extrusion increases.

Figure 19 shows the response surface plot for the combined influence of the extrusion speed, v, and the ingot length, L, on F at a billet temperature, T, equal to 390 °C. The results indicate that the extrusion load is minimal within the low-speed, short-ingot-length parameter window.

Figure 20 shows the response surface plot for the combined influence of the billet temperature, T, and the extrusion speed, v, on the speed deviation difference, VDD, when

https://doi.org/10.3390/ma19020375

the ingot length, L, is 575 mm. The results indicate that, within the high-temperature, high-speed parameter window, the speed deviation difference in the extruded profile cross-section is minimal, and the flow velocity is most uniform. As the billet temperature decreases, the metal deformation resistance increases, the plasticity decreases, the deformation becomes uneven, and the velocity deviation difference increases. As the extrusion speed decreases, the metal flow slows down, the flow time increases, and the accumulation of uneven deformation makes the uneven deformation more pronounced, resulting in an increase in the velocity deviation difference.

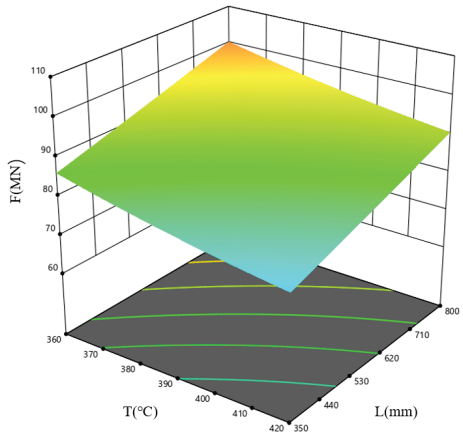

Figure 18. Response surface plot describing how T and L influence F, shown for the case where v = 0.3 mm/s.

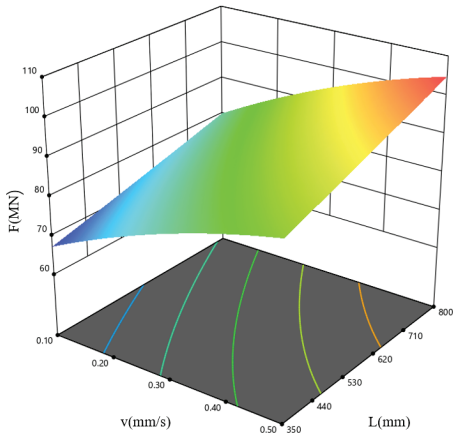

Figure 19. Response surface plot describing how v and L influence F, shown for the case where T = 390 °C.

https://doi.org/10.3390/ma19020375

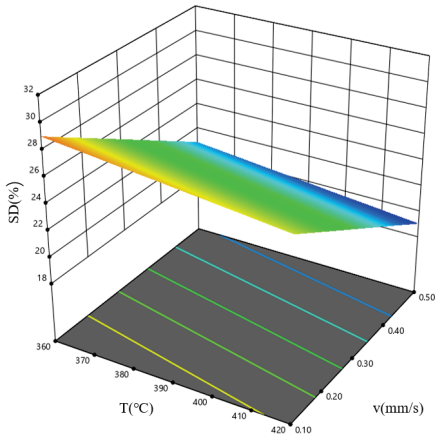

Figure 20. Response surface diagram describing how T and v influence the speed deviation difference, VDD, for the case where L = 575 mm.

Figure 21 presents the response surface diagram for the combined influence of the billet temperature, T, and the extrusion speed, v, on the temperature difference, ΔT, of the extruded profile, when the ingot length, L, is 575 mm. The results indicate that the temperature difference across the extruded profile cross-section is minimal within the high-temperature, low-speed parameter window. As the billet temperature increases, the metal deformation resistance decreases, resulting in less deformation-induced heat generation and a smaller temperature difference across the extruded profile cross-section. Conversely, as the extrusion speed decreases, heat conduction becomes more uniform, leading to more balanced heat distribution and a smaller temperature difference across the extruded profile's cross-section.

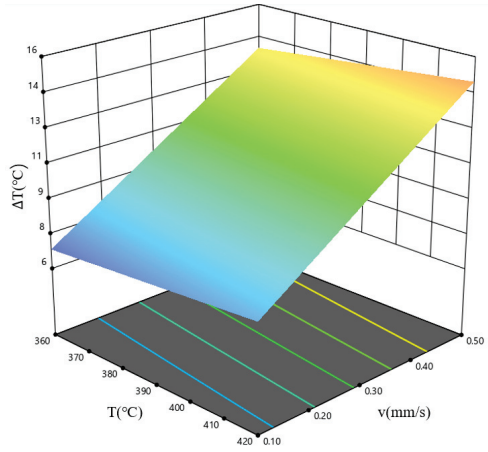

Figure 21. Response surface plots of the interaction between T and v on the profile temperature difference, for the case where L = 575 mm.

Figure 22 shows the response surface plot for the combined influence of the billet temperature, T, and ingot length, L, on ΔT at an extrusion speed, v, of 0.3 mm/s. The results indicate that this temperature difference is minimal within the low-temperature, short-ingot-length parameter window. This is because, as ingot length increases, the distance for heat conduction increases, leading to uneven heat distribution and a larger temperature difference across the profile cross-section; the lower the billet temperature, the lower the heat conduction capacity, resulting in less deformation-induced heat generation and a larger temperature gradient. This leads to the billet length having a more significant influence on the temperature difference across the profile cross-section.

https://doi.org/10.3390/ma19020375

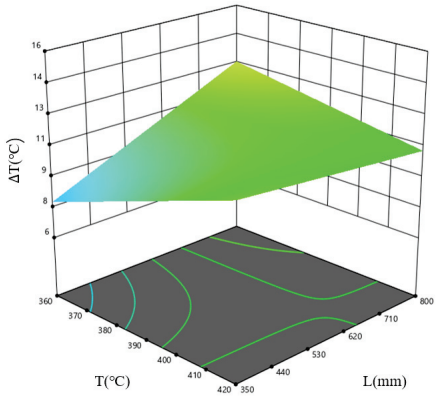

Figure 22. Response surface plots of the interaction between T and L on the profile temperature difference, for the case where v = 0.3 mm/s.

Figure 23 shows the response surface diagram for the combined influence of the extrusion speed, v, and the ingot length, L, on ΔT when the billet temperature, T, is 390 °C. The results indicate that the temperature difference in the cross-section of the extruded profile is minimal within the low-speed, short-ingot-length parameter window, consistent with the previous conclusion.

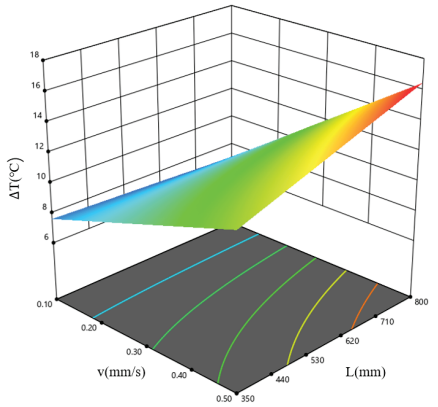

Figure 23. Response surface plots of the interaction between v and L on the profile temperature difference, for the case of 390 °C.

Through multi-objective optimization of the extrusion load for aluminum alloy profiles using response surface methodology (RSM), the optimal parameters were determined: a billet temperature of 400 °C, an extrusion speed of 0.20 mm/s, and an ingot length of 350 mm. Under these conditions, the extrusion load, the profile velocity deviation difference (VDD), and the cross-sectional temperature difference in the extruded profile all reached relatively minimum values. The predicted extrusion load at this point is 73.29 MN, with a VDD of 24.96% and a cross-sectional temperature difference of 9.48 °C. Figure 24 presents the simulation results of the optimized extrusion process parameters based on the RSM model. The optimized parameters yield a VDD of 29.88%, an extrusion load of 73.16 MN, and a cross-sectional temperature difference of 10.06 °C. Notably, the error between the simulated and predicted extrusion load is less than 1%, and the error for the cross-sectional temperature difference is less than 6%, further confirming the significance and reliability of the response surface model. Based on the aforementioned optimization results, a practical extrusion test of the profile was carried out. The extrusion equipment used was an 80 MN extrusion press, with a rated working oil pressure of 320 bar. Figure 24d shows that the actual breakthrough pressure during extrusion was 301 bar. After a proportional calculation, the actual breakthrough extrusion load was 75.25 MN, while the simulated

https://doi.org/10.3390/ma19020375

prediction was 73.29 MN. The prediction error is less than 5%, indicating that the finite element simulation results are reliable.

The use of optimized process parameters significantly reduces the extrusion load, which facilitates the engineering application of high-magnesium low-density aluminum alloy profiles. However, the error between the simulated and predicted VDD is less than 17%, indicating a relatively large discrepancy. In the model, only the extrusion speed is identified as a significant term affecting VDD, while other parameters show no significance. This suggests that improving the uniformity of the extrusion flow velocity requires optimization of the die structure, as the extrusion process parameters have limited influence on the uniformity of extrusion flow velocity.

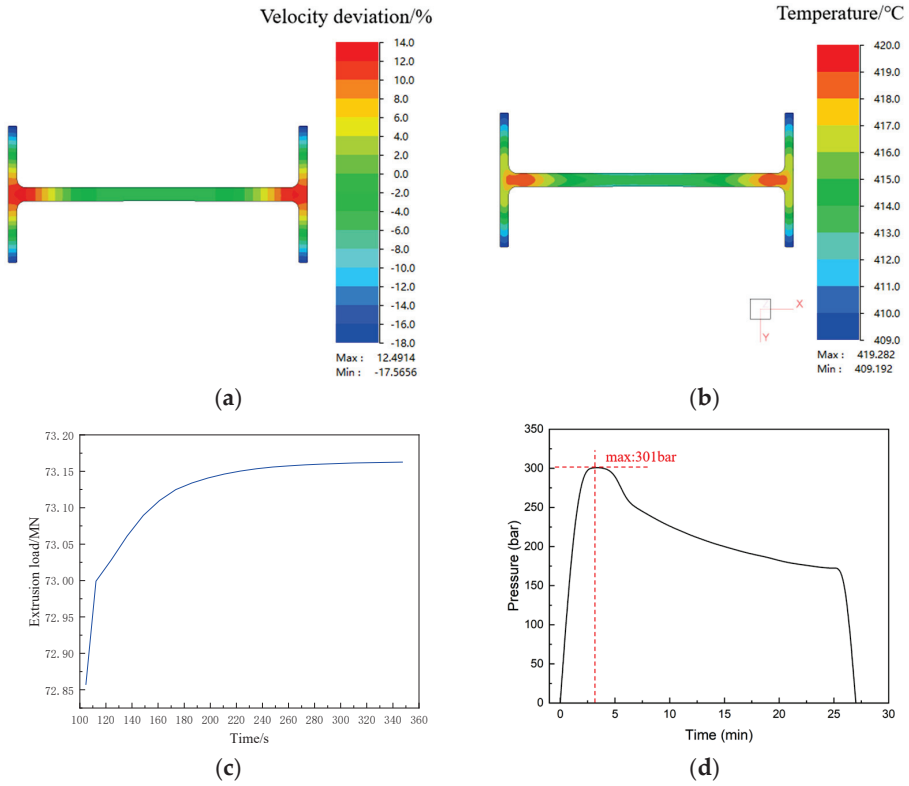

Figure 24. Prediction of the formability of extruded profiles under optimized extrusion process parameters: (**a**) speed deviation cloud chart; (**b**) extruded profile cross-section temperature field cloud map; (**c**) simulated extrusion load; (**d**) actual extrusion load.

4. Conclusions

(1) The flow stress of the Al–10Mg–3Zn alloy increases with increasing strain rate and decreases with increasing deformation temperature, indicating that the alloy exhibits positive strain rate sensitivity. A temperature-corrected true stress–strain curve was used to establish the Arrhenius strain compensation constitutive model for the Al–10Mg–3Zn alloy, which helps us to more accurately describe the rheological behavior of this alloy at elevated temperatures.

(2) The thermal processing diagrams constructed for different strain values can accurately predict the safe processing temperature range and strain rate range for the homogeneous Al–10Mg–3Zn alloy; moreover, the working temperature range of 360–420 °C and the strain rate range of 0.004–0.123 s^{-1} were determined to be optimal for this alloy.

(3) The extrusion speed has a greater influence on the extrusion temperature of the profile and the uniformity of the cross-sectional temperature than the billet temperature.

https://doi.org/10.3390/ma19020375

As the ingot length, extrusion speed, and friction coefficient increase, the extrusion load shows a linear upward trend. As the billet temperature increases, the extrusion load shows a linear downward trend. Increasing the billet temperature and extrusion speed can improve the uniformity of the extrusion flow rate of the profile.

(4) The extrusion process parameters optimized by the response surface method were set at a billet temperature of 400 °C, an extrusion speed of 0.20 mm/s, and a billet length of 350 mm. Under these conditions, the predicted extrusion breakthrough load is 73.29 MN, which deviates by less than 5% from the experimentally measured value. This optimized parameter set effectively lowers the required extrusion load, leading to a significant increase in the trial molding success rate and thereby facilitating the engineering application of high-magnesium, low-density aluminum alloy profiles.

Author Contributions: Software, K.J.; Validation, W.L.; Writing—original draft, G.N.; Writing—review & editing, participated in data analysis and experimental design, C.L. and L.Z.; Supervision, G.W.; Project administration, participated in research design and funding acquisition, Y.Y. All authors have read and agreed to the published version of the manuscript.

Funding: The authors gratefully acknowledge the financial support from the National Key Research and Development Program of China (No.2023YFB3710401).

Data Availability Statement: The original contributions presented in this study are included in the article. Further inquiries can be directed to the corresponding authors.

Conflicts of Interest: Authors Guanmei Niu, Wei Li, Yang Yang, Guojun Wang and Cheng Liu were employed by the Chinalco Material Application Research Institute Co., Ltd. The remaining authors declare that the research was conducted in the absence of any commercial or financial relationships that could be construed as a potential conflict of interest.

Appendix A. Complete Analysis of Significance Tests

Appendix A.1. Test Framework

In the significance testing of the response surface models, a model is considered statistically significant and well-fitted when it has a sufficiently large F-statistic, a *p*-value less than 0.05, a coefficient of determination (R^2) and an adjusted coefficient of determination that are close to 1, and a signal-to-noise ratio that exceeds 4.

Appendix A.2. Extrusion Load Response Model

Table A1. Analysis of variance (ANOVA) for the extrusion load response model.

Factor	Sum of Squares	Degree of Freedom	Mean Square	F-Statistic	*p*-Value
Model	1716.12	9	190.68	488.19	<0.0001
T	204.03	1	204.03	522.38	<0.0001
v	1050.08	1	1050.08	2688.50	<0.0001
L	425.79	1	425.79	1090.15	<0.0001
Tv	12.34	1	12.34	31.59	0.0025
TL	0.1379	1	0.1379	0.353	0.5783
vL	2.50	1	2.50	6.39	0.0526
T^2	2.38	1	2.38	6.09	0.0567
v^2	17.56	1	17.56	44.95	0.0011
L^2	0.0537	1	0.0537	0.1375	0.7259
Residual	1.95	5	0.3906		
Correction	1718.07	14			

Correlation coefficient R^2 = 0.9989, correction factor R^2 = 0.9968, signal-to-noise ratio = 73.4980.

https://doi.org/10.3390/ma19020375

Analysis: The model is highly significant. The extrusion speed (v) has the largest obtained F-value (2688.50), i.e., the most pronounced effect recorded on the extrusion load. The interaction term, Tv, and the quadratic term, v^2, are also significant, while other higher-order terms are not significant.

Appendix A.3. Profile Cross-Sectional Velocity Deviation Response Model

Table A2. Analysis of variance (ANOVA) for the velocity deviation response model.

Factor	Sum of Squares	Degree of Freedom	Mean Square	F-Statistic	*p*-Value
Model	143.50	3	47.83	16.30	0.0002
T	6.91	1	6.91	2.36	0.1530
v	132.24	1	132.24	45.06	<0.0001
L	4.34	1	4.34	1.48	0.2495
Residual	32.28	11	2.93		
Correction	175.78	14			

Correlation coefficient R^2 = 0.8163, correction factor R^2 = 0.7663, signal-to-noise ratio = 11.2938.

Analysis: The model is significant but explains only 81.63% of the variance. Extrusion speed (v) is the significant controlling factor for velocity deviation ($p < 0.0001$), while billet temperature and length have no significant effect.

Appendix A.4. Profile Cross-Sectional Average Strain Response Model

Table A3. Analysis of variance (ANOVA) for the average strain response model.

Factor	Sum of Squares	Degree of Freedom	Mean Square	F-Statistic	*p*-Value
Model	0.1009	9	0.0112	3.86	0.0754
T	0.0162	1	0.0162	5.58	0.0645
v	0.0173	1	0.0173	5.96	0.0585
L	0.0005	1	0.0005	0.1764	0.6919
Tv	2.5×10^{-7}	1	2.5×10^{-7}	0.0001	0.9930
TL	0.0051	1	0.0051	1.76	0.2418
vL	0.0048	1	0.0048	1.66	0.2534
T^2	0.0193	1	0.0193	6.66	0.0493
v^2	0.0410	1	0.0410	14.13	0.0132
L^2	5.192×10^{-7}	1	5.192×10^{-7}	0.0002	0.9898
Residual	0.0145	5	0.0029		
Correction	0.1154	14			

Correlation coefficient R^2 = 0.8742, correction factor R^2 = 0.6479, signal-to-noise ratio = 6.4910.

Analysis: The model p-value is 0.0754 (>0.05), which fails the significance test. None of the investigated process parameters (T, v, L) or their interactions or quadratic terms show stable or significant predictive powers for the average cross-sectional strain.

https://doi.org/10.3390/ma19020375

Appendix A.5. Profile Cross-Sectional Temperature Difference Response Model

Table A4. Analysis of variance (ANOVA) for the temperature difference response model.

Factor	Sum of Squares	Degree of Freedom	Mean Square	F-Statistic	*p*-Value
Model	120.50	6	20.08	22.00	0.0001
T	1.81	1	1.81	1.98	0.1972
v	97.42	1	97.42	106.73	<0.0001
L	6.89	1	6.89	7.54	0.0252
Tv	0.0142	1	0.0142	0.0155	0.9039
TL	8.54	1	8.54	9.36	0.0156
vL	5.83	1	5.83	6.39	0.0354
Residual	7.30	8	0.9128		
Correction	127.80	14			

Correlation coefficient R^2 = 0.9429, correction factor R^2 = 0.9, signal-to-noise ratio = 14.6017.

Analysis: The model is significant. The extrusion speed (*v*) is the most critical factor, inducing the cross-sectional temperature difference (F = 106.73). The interaction terms, *TL* and *vL*, also show some significance, but their effects are far smaller than the main effect, the extrusion speed.

References

1. Deng, Y.; Zhang, X.; Li, J.; Wang, H.; Liu, Z.; Chen, L.; Yang, S.; Zhou, F. Development of aluminum and aluminum alloy. *Chin. J. Nonferrous Met.* **2019**, *29*, 2115–2141.
2. Fang, H.; Liu, H.; Sun, J.; Wang, R.; Xu, Y.; Zhao, L.; Cheng, X.; Li, M. Research Status and Development Trend of 5xxx Series Aluminum Alloys. *Mater. Rep.* **2023**, *37*, 211–220.
3. Wang, Z.T. *Handbook of Aluminum Materials for Aerospace Vehicles*; Central South University Press: Changsha, China, 2015.
4. Qi, Z.; Wu, R.; Wang, G.; Qiang, W.; Legan, H. Application of aluminum alloys in shipbuilding and marine engineering. *Light Alloy Fabr. Technol.* **2016**, *44*, 12–18.
5. Zhu, Z.J. Overview of new aluminum-magnesium and aluminum-zinc-magnesium alloy materials for aerospace applications. *China Strateg. Emerg. Ind.* **2018**, *4*, 75–77.
6. Yang, S.J.; Dai, S.L. Review and prospect of the development of aviation aluminum alloys. *Mater. Rev.* **2005**, *19*, 76–80.
7. Alil, A.; Popović, M.; Radetić, T.; Zrilić, M.; Romhanji, E. Influence of annealing temperature on the baking response and corrosion properties of an Al–4.6 wt% Mg alloy with 0.54 wt% Cu. *J. Alloys Compd.* **2015**, *625*, 76–84. [CrossRef]
8. Zhang, D.; Zhang, Z.; Pan, Y.; Jiang, Y.; Zhuang, L.; Zhang, J.; Zhang, X. Current-driving intergranular corrosion performance regeneration below the precipitates solvus temperature in Al–Mg alloy. *J. Mater. Sci. Technol.* **2020**, *53*, 132–139. [CrossRef]
9. Guo, C.; Zhang, H.; Li, S.; Chen, R.; Nan, Y.; Li, L.; Wang, P.; Li, B.; Cui, J.; Nagaumi, H. Evolution of microstructure, mechanical properties and corrosion behavior of Al-4Mg-2Zn-0.3Ag (wt.%) alloy processed by T6 or thermomechanical treatment. *Corros. Sci.* **2021**, *188*, 109551. [CrossRef]
10. Meng, C.Y. *Corrosion Resistance Mechanism and Sheet Development of Zn-Containing 5xxx Aluminum Alloy for Ship Application*; University of Science and Technology Beijing: Beijing, China, 2016.
11. Meng, C.; Zhang, D.; Cui, H.; Zhuang, L.; Zhang, J. Mechanical properties, intergranular corrosion behavior and microstructure of Zn modified Al–Mg alloys. *J. Alloys Compd.* **2014**, *617*, 925–932. [CrossRef]
12. Meng, C.Y.; Zhang, D.; Liu, P.P.; Zhuang, L.Z.; Zhang, J.S. Microstructure characterization in a sensitized Al-Mg-Mn-Zn alloy. *Rare Met.* **2018**, *37*, 129–135. [CrossRef]
13. Carroll, M.; Gouma, P.; Mills, M.; Daehn, G.; Dunbar, B. Effects of Zn additions on the grain boundary precipitation and corrosion of Al-5083. *Scr. Mater.* **2000**, *42*, 335–340. [CrossRef]
14. Zhao, J.-W.; Luo, B.-H.; He, K.-J.; Bai, Z.-H.; Li, B.; Chen, W. Effects of minor Zn content on microstructure and corrosion properties of Al−Mg alloy. *J. Central South Univ.* **2016**, *23*, 3051–3059. [CrossRef]
15. Meng, C.; Zhang, D.; Zhuang, L.; Zhang, J. Correlations between stress corrosion cracking, grain boundary precipitates and Zn content of Al–Mg–Zn alloys. *J. Alloys Compd.* **2016**, *655*, 178–187. [CrossRef]
16. Khomutov, M.G.; Pozdniakov, A.V.; Churyumov, A.Y.; Barkov, R.Y.; Solonin, A.N.; Glavatskikh, M.V. Flow stress modelling and 3D processing maps of Al4.5Zn4.5Mg1Cu0.12Zr alloy with different scandium contents. *Appl. Sci.* **2021**, *11*, 4587. [CrossRef]
17. Lei, C.; Wang, Q.; Ebrahimi, M.; Li, D.; Tang, H.; Zhang, N.; Cai, H. Hot Deformation Behavior and Processing Maps of an As-Cast Al-5Mg-3Zn-1Cu (wt%) Alloy. *Materials* **2022**, *12*, 4093. [CrossRef] [PubMed]

https://doi.org/10.3390/ma19020375

18. Yang, Y.; Niu, G.; Zhao, P.; Wang, G.; Zou, L. Influence of hot deformation rate on microstructure of Al-Mg-Zn alloy. *Light Alloy Fabr. Technol.* **2025**, *53*, 34–39.
19. Xiao, Y.-H.; Guo, C.; Guo, X.-Y. Constitutive modeling of hot deformation behavior of H62 brass. *Mater. Sci. Eng. A* **2011**, *528*, 6510–6518. [CrossRef]
20. Wu, H.; Wen, S.P.; Huang, H.; Wu, X.L.; Gao, K.Y.; Wang, W.; Nie, Z.R. Hot deformation behavior and constitutive equation of a new type Al-Zn-Mg-Er-Zr alloy during isothermal compression. *Mater. Sci. Eng. A* **2016**, *651*, 415–424. [CrossRef]
21. Zhang, C.; Zhang, L.; Shen, W.; Liu, C.; Xia, Y.; Li, R. Study on constitutive modeling and processing maps for hot deformation of medium carbon Cr–Ni–Mo alloyed steel. *Mater. Des.* **2016**, *90*, 804–814. [CrossRef]
22. Zhou, L.; Zhang, P.; Wang, Q.; Xiao, B.; Ma, Z.; Yu, T. Multi-Scale Study on the Fracture Behavior of Hot Compression B4C/6061Al Composite. *Acta Metall. Sin.* **2019**, *55*, 911–918.
23. Xiang, S.; Liu, D.-Y.; Zhu, R.-H.; Li, J.-F.; Chen, Y.-L.; Zhang, X.-H. Hot deformation behavior and microstructure evolution of 1460 Al–Li alloy. *Trans. Nonferrous Met. Soc. China* **2015**, *25*, 3855–3864. [CrossRef]
24. Chen, G.; Chen, L.; Zhao, G.; Zhang, C.; Cui, W. Microstructure analysis of an Al-Zn-Mg alloy during porthole die extrusion based on modeling of constitutive equation and dynamic recrystallization. *J. Alloys Compd.* **2017**, *710*, 80–91. [CrossRef]
25. Lin, Y.C.; Xia, Y.C.; Chen, X.M.; Chen, M.S. Constitutive descriptions for hot compressed 2124-T851 aluminum alloy over a wide range of temperature and strain rate. *Comput. Mater. Sci.* **2010**, *50*, 227–233. [CrossRef]
26. Peng, N.Q.; Tang, G.B.; Liu, Z.D. Correcting method of flow stress curve for hot compression. *Hot Work. Technol.* **2012**, *41*, 12–15.
27. Zhao, D. Temperature correction in compression tests. *J. Mater. Process. Technol.* **1993**, *36*, 467–471. [CrossRef]
28. Wang, Y.; Zhao, G.; Xu, X.; Chen, X.; Zhang, C. Constitutive modeling, processing map establishment and microstructure analysis of spray deposited Al-Cu-Li alloy 2195. *J. Alloys Compd.* **2019**, *779*, 735–751. [CrossRef]
29. Yang, H.; Bu, H.; Li, M.; Lu, X. Prediction of Flow Stress of Annealed 7075 Al Alloy in Hot Deformation Using Strain-Compensated Arrhenius and Neural Network Models. *Materials* **2021**, *14*, 5986. [CrossRef] [PubMed]
30. Wang, S.-Q.; Zhao, X.; Ren, X.-W.; Zhang, Z.-M.; Tian, X.-D.; He, Y.-Y. Hot Deformation Behavior and Processing Map Considering Strengthening Effect for Al–10.0Zn–3.0Mg–2.8Cu Alloy. *Materials* **2023**, *16*, 1880. [CrossRef] [PubMed]
31. Wu, M.; Wei, W.; Zuo, R.; Wen, S.; Shi, W.; Zhou, X.; Wu, X.; Gao, K.; Huang, H.; Nie, Z. Effect of Zr and Er Addition on the Microstructural Evolution of a Novel Al—Mg—Zn—Er—Zr Alloy during Hot Compression. *Materials* **2023**, *16*, 858. [CrossRef]
32. Jeong, H.; Kim, H.; Kim, W. Processing maps (with flow instability criterion based on power-law breakdown) integrated into finite element simulations for evaluating the hot workability of 7075 aluminum alloy. *Mater. Today Commun.* **2021**, *27*, 102254. [CrossRef]
33. Lakshmi, A.A.; Rao, C.S.; Gangadhar, J.; Srinivasu, C.; Singh, S.K. Review of Processing Maps and Development of Qualitative Processing Maps. *Mater. Today Proc.* **2017**, *4*, 946–956. [CrossRef]
34. Yang, Q.; Liu, W.; Zhang, Z.; Huang, G.; Liu, X. Hot Deformation Behavior and Processing Maps of AA7085 Aluminum Alloy. *Rare Met. Mater. Eng.* **2018**, *47*, 409–415. [CrossRef]
35. Liu, H.; Liu, T.; Chen, Z.; Wang, Y.; Zhang, J.; Li, X.; Zhou, W.; Yang, F.; Xu, S.; Sun, L.; et al. Optimization of Extrusion Process for Large-Sized Thin-Walled Aluminum Profiles with Ribs Based on Experimental Design and Response Surface Methodology. *Forg. Stamp. Technol.* **2022**, *47*, 144–152.

Disclaimer/Publisher's Note: The statements, opinions and data contained in all publications are solely those of the individual author(s) and contributor(s) and not of MDPI and/or the editor(s). MDPI and/or the editor(s) disclaim responsibility for any injury to people or property resulting from any ideas, methods, instructions or products referred to in the content.

https://doi.org/10.3390/ma19020375

materials

MDPI

Article

The Durability Assessment Methodology of Power Engineering Equipment Under Thermo-Mechanical Fatigue Using the Example of the HR6W Alloy

Michał Paduchowicz *, Tomasz Dobosz and Artur Górski

Faculty of Mechanical Engineering, Department of Machine and Vehicle Design and Research, Wrocław University of Science and Technology, 50-370 Wrocław, Poland; tomasz.dobosz@pwr.edu.pl (T.D.); artur.gorski@pwr.edu.pl (A.G.)

* Correspondence: michal.paduchowicz@pwr.edu.pl; Tel.: +48-71-320-39-08

Abstract

This article presents an innovative methodology for assessing the durability of power engineering components under thermo-mechanical fatigue conditions. The approach integrates laboratory low-cycle fatigue tests of alloy specimens at elevated temperatures, measurements of working-medium parameters obtained from operating industrial equipment, and numerical simulations performed using the finite element method. Durability is estimated on the basis of curves describing the relationships between critical parameters such as the Coffin–Manson and Ostergren parameters and the number of cycles to failure. Within the region of the structure identified as the most susceptible to fatigue damage, the orientation of the critical plane is determined with respect to the corresponding criterion functions. This allows the calculated criterion values to be correlated with experimental data, enabling the determination of the incremental durability loss of the component. The proposed methodology is distinguished by its practical applicability and the possibility of incorporating both proprietary fatigue test results and data reported in the literature.

Keywords: high-alloy materials; computer methods in mechanics; Coffin–Manson and Ostergren parameters

1. Introduction

Due to the continuously increasing demand for electric power, ensuring the reliability and continuity of electricity supply has become a matter of critical importance. This, in turn, requires maintaining an adequate technical condition of the engineering systems involved in power generation. In conventional coal-fired power units, whether using hard coal or lignite, the components that largely determine the availability of the entire installation are the thick-walled elements, including the boiler superheater chambers, as well as the valves and casings of steam turbines. These components are exposed to working media characterised by high temperatures, pressures, and mass flow rates.

The failure processes affecting such equipment can be grouped according to the following mechanisms: high-temperature creep, fatigue, low-cycle fatigue at elevated temperatures, thermal fatigue, and thermo-mechanical fatigue.

This article focuses specifically on assessing the impact of thermo-mechanical fatigue on the overall fatigue life of components operating at elevated temperatures. Currently, several methods for assessing the durability of components subjected to low-cycle fatigue

are described in the available literature. These include, among others, the method presented in [1]. The following article proposes a proprietary methodology for predicting life loss resulting from thermo-mechanical fatigue. This methodology integrates laboratory fatigue testing of metal alloys at elevated temperatures, measurements of actual operating parameters of the working fluid flowing through the analysed devices, and numerical calculations using the finite element method. One of the main assumptions of the proposed methodology is the ability to use low-cycle fatigue test results at elevated temperatures instead of thermo-mechanical fatigue results. This approach has been presented in numerous scientific publications, including [2–4]. The above studies, similar to the methodology presented here, assume (supported by research and described in these publications) that the sum of mechanical deformation resulting from simultaneous changes in medium temperature and mechanical loading (e.g., due to fluctuations in working fluid pressure) during actual facility operation is no greater than the range of total deformation assumed during low-cycle fatigue testing at elevated temperatures. This approach also stems from the fact that during actual operation of power plants, the number of possible combinations of simultaneous temperature changes and mechanical loading is so large that it would be very difficult to reflect this in laboratory testing of samples. Furthermore, it is worth noting that conducting low-cycle fatigue testing at elevated temperatures is significantly easier than for thermo-mechanical fatigue, making it easier to obtain results that can then be used in engineering practice for durability assessment. Furthermore, the methodology allows for the simultaneous use of both data from internal fatigue tests and results published in external sources, including publications and relevant standards, which can increase its accuracy. An additional advantage of this methodology is the ability to generate model cyclic hardening curves for temperatures for which fatigue tests have not been conducted, using extrapolation and interpolation of known data from our own studies and those available in the literature.

2. Methodology for Estimating Durability Under Low-Cycle Fatigue at Elevated Temperatures

A novel methodology has been developed for evaluating the durability of power engineering components operating under thermo-mechanical fatigue conditions (Figure 1). The approach is founded on low-cycle fatigue testing of alloy specimens designed for high-temperature applications, in conjunction with measurements obtained from operating industrial installations and numerical simulations performed using the finite element method.

This methodology does not replace TMF with LCF. When the combined mechanical and thermal strains occurring during the operation of power equipment under TMF are significantly smaller than the strains for the LCF specimen tests, this algorithm conducts LCF tests to obtain cyclic hardening curves, which then serve as input data for numerical models of material hardening. The subsequent numerical analysis and the resulting durability assessment are related to the fatigue assessment of TMF.

The first stage of the methodology involves conducting laboratory tests, including uniaxial tensile tests and low-cycle fatigue tests of specimens at elevated temperatures, in order to determine the material's strength and cyclic properties (the monotonic tensile curve and the cyclic hardening curve). In parallel, measurements are carried out on operating industrial equipment to determine the actual thermal and mechanical loads associated with the working-medium flowing through the analysed components (e.g., steam pressure and temperature). The situation is quite different when the above methodology is applied in the design of new power units where the curves of the working medium parameters, such as pressure, temperature, and mass flow, are unknown. In such a situation, these curves

https://doi.org/10.3390/ma19050891

should be designed based on the design and operational assumptions of the new unit and based on analogy to curves derived from actual power units with parameters similar to those of the new power boiler.

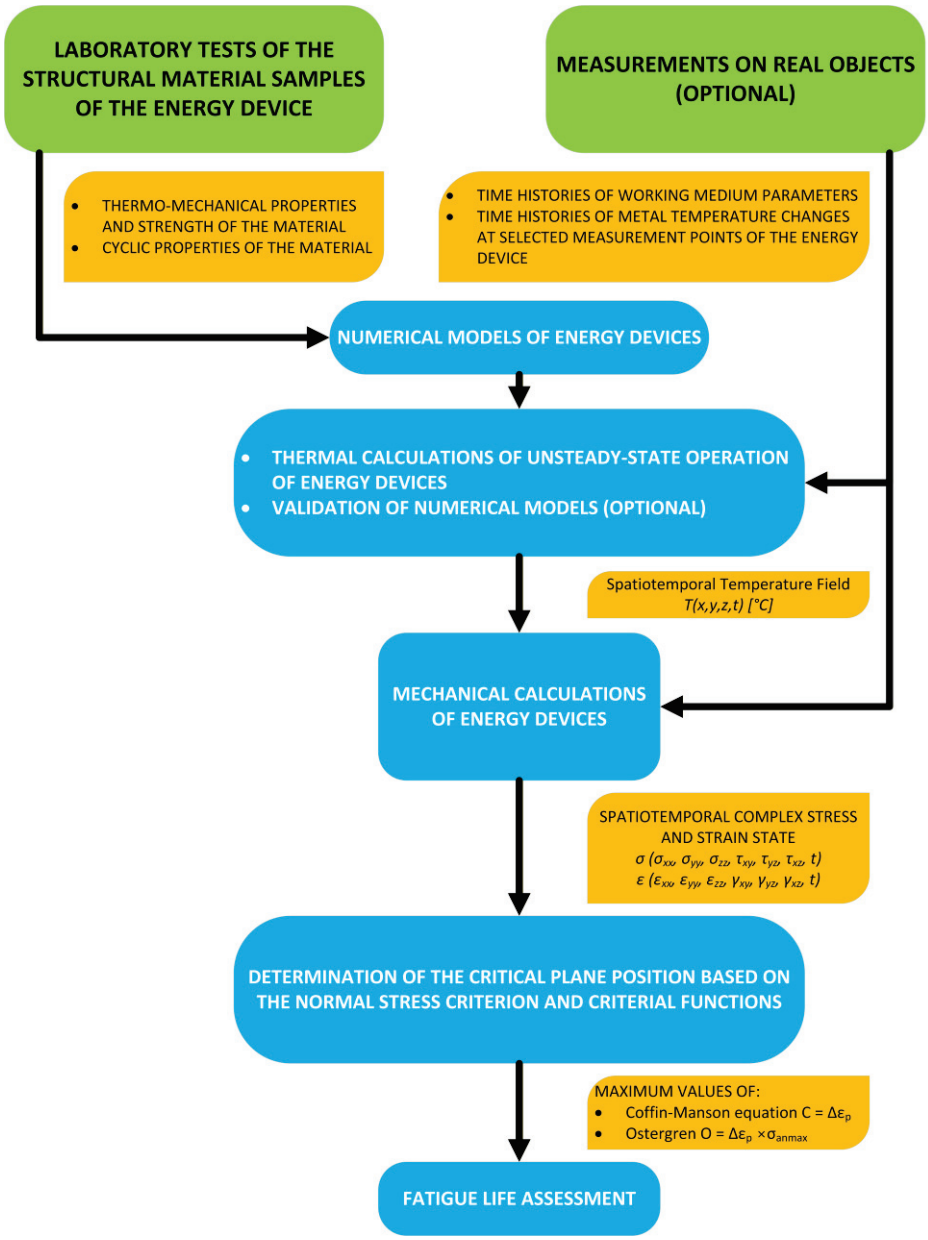

Figure 1. Block diagram of the proposed methodology for assessing the durability of power engineering components under thermo-mechanical fatigue.

The next step in the proposed algorithm is the development of numerical models required for subsequent finite element analyses. At this stage, in addition to generating an appropriate finite element mesh, it is essential to define a suitable material hardening model that incorporates both the monotonic tensile curve and the cyclic hardening curve obtained from laboratory testing at a specified temperature. A significant advantage of the methodology at this stage is the ability to generate missing model cyclic hardening curves for intermediate temperatures.

The subsequent stage consists of performing thermo-mechanical analyses of the investigated component using the finite element method. Boundary conditions are derived from measurements of the working-medium parameters recorded on the actual installation. The

https://doi.org/10.3390/ma19050891

calculations yield the combined stress and strain state of the analysed component. Based on these results, the region of the structure that is most critical from the fatigue-strength perspective is identified, representing the next step of the methodology.

Within this critical location, the orientation of the critical plane is determined using the normal-stress criterion together with the Coffin–Manson and Ostergren parameters. This step is essential for assessing the residual durability of the component on the basis of predefined criterion functions that relate the number of cycles to failure to specific values of the Coffin–Manson and Ostergren parameters. This allows the unit durability loss associated with a single characteristic load cycle to be quantified. Having identified the number of occurrences of this load cycle, and by performing analogous analyses for other load types, the total durability reduction in the component due to thermo-mechanical fatigue can be determined (Figure 1).

The methodology for assessing the durability of power engineering components under thermo-mechanical fatigue conditions, as presented in this article, can be applied both in the design of new installations and in the evaluation of components already in service.

3. Example Application of the Methodology for Assessing the Durability of Power Engineering Components

The proposed methodology is suitable both for the design of new power engineering components and for the evaluation of equipment already in service.

Accordingly, the methodology will be illustrated using the example of a fresh-steam pipeline tee made of HR6W alloy, designed by the authors of publication [2] (Figure 2). It is assumed that the analysed tee will operate as a component of ultra-supercritical boilers, where the maximum temperature of the primary superheated steam is 650 °C and the corresponding pressure is 30.3 MPa.

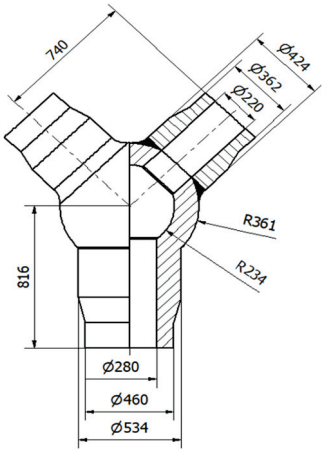

Figure 2. Proposed design of a forked tee made of HR6W material according to the referenced publication.

As part of the presented procedure, strength and fatigue tests of the HR6W alloy conducted at 650 °C were utilised. This nickel-based alloy was selected based on its superior mechanical performance at elevated temperatures, as it is regarded as a candidate structural material for critical components of power units operating under supercritical steam parameters.

To determine the material properties required for developing the material model, a monotonic tensile test was performed on this alloy in accordance with the ISO 6892-2:2018 standard [5]. The tests were carried out at two metal temperature levels: room temperature (22 °C) and an elevated temperature of 650 °C (Figure 3).

https://doi.org/10.3390/ma19050891

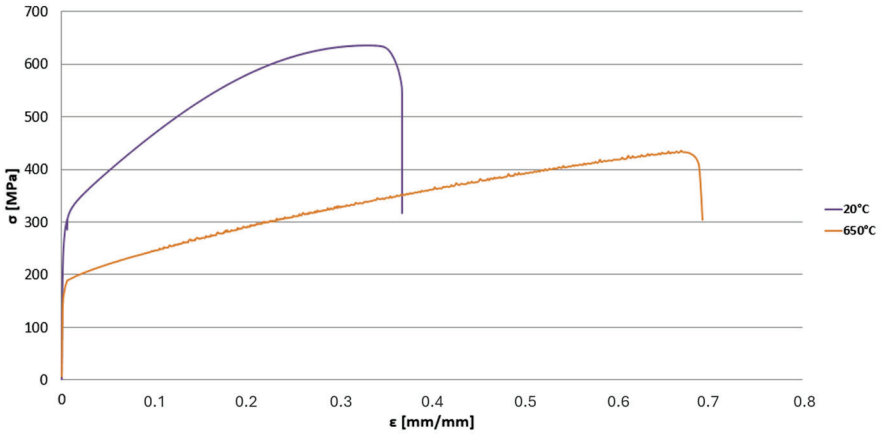

Figure 3. Comparison of monotonic tensile curves for HR6W steel at 20 °C and 650 °C, developed on the basis of averaged results obtained from uniaxial tensile tests performed on five specimens for each temperature in accordance with ISO 6892-2:2018 [5].

The next stage involves conducting thermo-mechanical fatigue tests of the selected alloy in order to obtain its cyclic fatigue characteristics. However, because such tests are time-consuming and costly, low-cycle fatigue (LCF) tests of the HR6W alloy at 650 °C were performed instead. These tests were carried out for several levels of total strain range $\Delta\varepsilon_C$, specifically 0.6%, 0.7%, 0.8%, 0.9%, 1.0%, and 1.2%.

The rationale for replacing thermo-mechanical fatigue testing with elevated-temperature low-cycle fatigue testing is the assumption that, for sufficiently high total strain ranges, LCF tests can reproduce the complex stress–strain state that develops in a specimen subjected to thermo-mechanical fatigue. This simplification has been presented and justified in the relevant literature, for example, in publication [6].

Figure 4 presents an example hysteresis loop obtained for a total strain range $\Delta\varepsilon_C$ of 1.0.

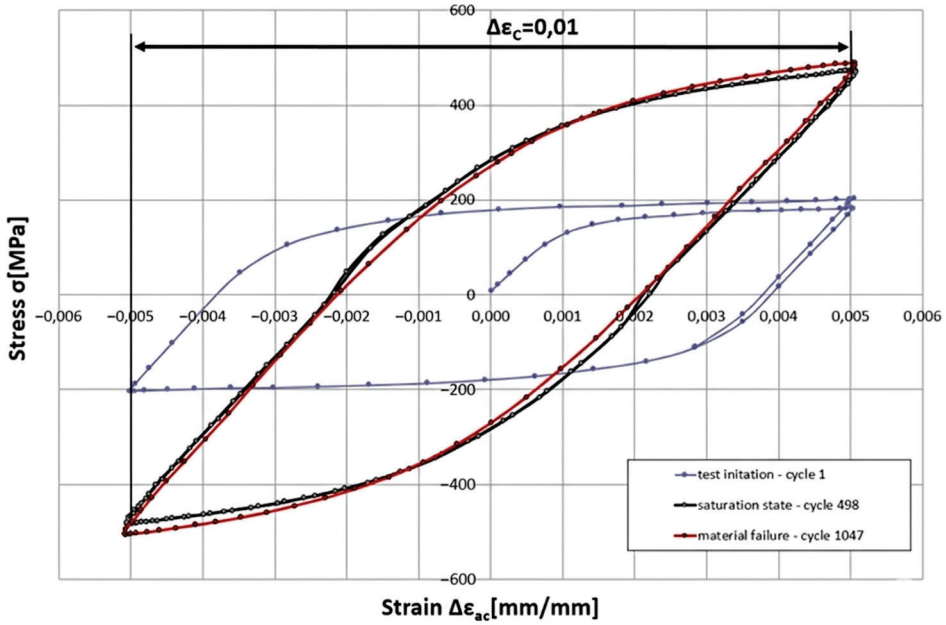

Figure 4. Example hysteresis loop obtained in a low-cycle fatigue test for a total strain range of $\Delta\varepsilon_C$ = 1.0% at a temperature of 650 °C.

At the same time, an increase in the maximum stress value within the hysteresis loops (the loop apex) is observed for the saturation states corresponding to different levels of total strain. This indicates that HR6W steel undergoes cyclic hardening at 650 °C as a result

https://doi.org/10.3390/ma19050891

of repeated deformation. This behaviour was characterised using the cyclic hardening curve shown in Figure 5, which was derived from the hysteresis loops corresponding to the remaining total strain ranges $\Delta\varepsilon_C$.

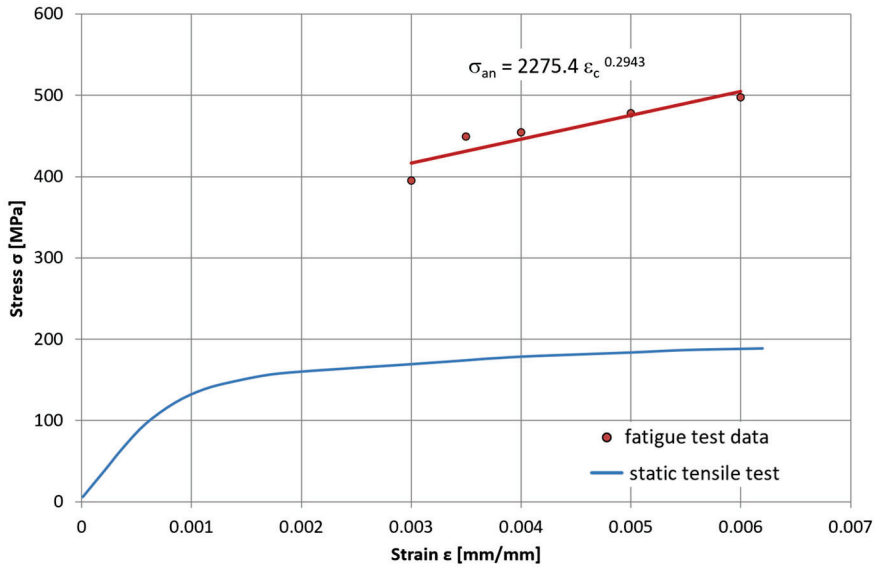

Figure 5. Cyclic hardening curve determined at an elevated temperature of 650 °C, compared with the curve obtained from the monotonic tensile test of the specimen.

Taking into account the obtained results in the context of their further application, particularly in numerical strength calculations, a major limitation may be the insufficient number of cyclic hardening curves. Characteristics for intermediate temperatures up to 650 °C are missing. Therefore, a method for obtaining these curves was developed. First, in the case of the HR6W material, the study reported in Ref. [7] was used for this purpose. From this publication, two additional cyclic hardening curves were obtained for temperatures of 20 °C and 600 °C (Figure 6a,b).

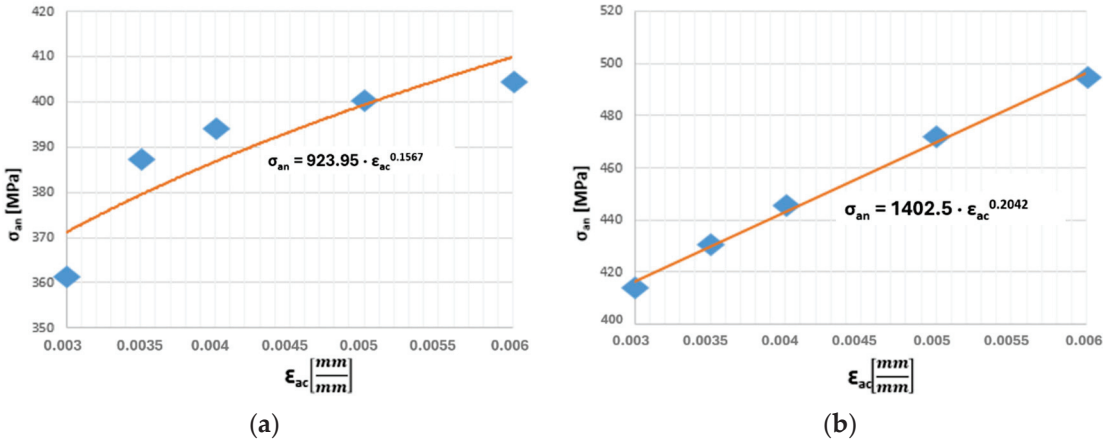

Figure 6. Cyclic hardening curve for the HR6W alloy determined based on literature source [4]: (**a**) at 20 °C, (**b**) at 600 °C.

The methodology for assessing the durability of power engineering equipment presented in this study is, in its fundamental assumptions, based on broadly understood modelling. Consequently, as a next step, the cyclic hardening curves, both those obtained from the authors' own experimental investigations and those acquired from the literature, were used to mathematically determine the cyclic hardening curves for the remaining temperatures of the HR6W material, i.e., in the range between 20 °C and 600 °C.

https://doi.org/10.3390/ma19050891

According to the literature source [8], the cyclic hardening curves take a form that can be described by the following relationship:

$$\sigma_{an} = k \cdot \varepsilon_{ac}{}^{n} \quad (1)$$

where

- k—fatigue strength coefficient for the cyclic strain curve;
- n—cyclic strain hardening exponent for the cyclic strain curve.

Table 1 presents the values of the coefficients k and n for the cyclic hardening curves corresponding to three temperatures: 20 °C, 600 °C (literature data), and 650 °C (experimental data). These values were determined based on our own research described in publication [9] and in an article by other authors [2]. There are no generally available values for the remaining temperatures.

Table 1. Values of the coefficients k and n of the cyclic hardening curves for the HR6W alloy at different temperatures [2,9].

t [°C]	k [MPa]	n [-]
20	923.95	0.1567
600	1402.5	0.2042
650	2275.4	0.2943

In order to improve the accuracy of the calculations, an attempt was made to determine cyclic hardening curves for intermediate temperatures. For this purpose, based on the data summarised in Table 1, plots were constructed showing the dependence of the coefficients k and n on the Young's modulus corresponding to specific temperature values (Figure 7a,b). The Young's modulus was selected as the independent variable for these functions because it influences the stress amplitude σ_{an} and the total strain amplitude ε_{ac}, i.e., the parameters appearing in relation (1). Consequently, the shape of the cyclic hardening curve depends indirectly on the Young's modulus.

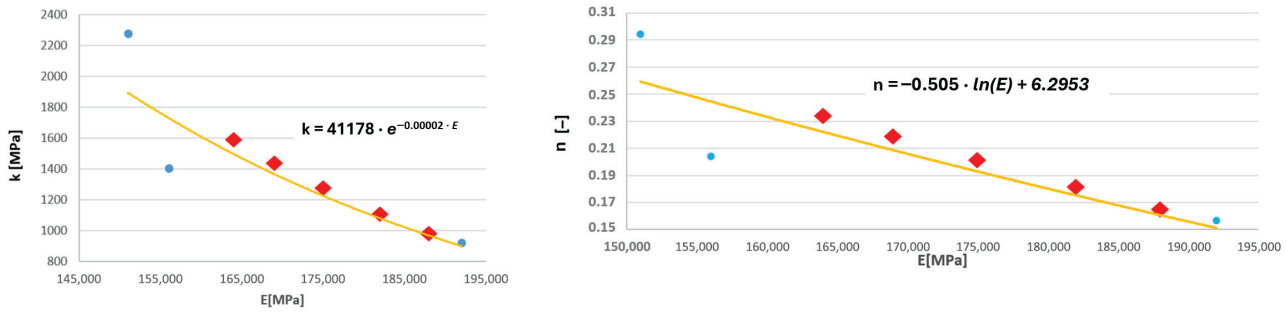

(**a**) (**b**)

Figure 7. Relationships between (**a**) parameter k [MPa] and Young's modulus, and (**b**) parameter n [-] and Young's modulus.

In the above figures, the red markers indicate the values of the coefficients k and n determined on the basis of the proposed relationships obtained through linear regression using the data listed in Table 1 (blue points in Figure 7a,b). The exact values of these coefficients, both the actual ones, i.e., derived from the authors' own experimental results and literature data, as well as the model values calculated using the defined mathematical relationships, are presented in Table 2. These values are listed together with the corresponding Young's modulus values for the respective temperatures. The dependence of the

https://doi.org/10.3390/ma19050891

Young's modulus of the HR6W alloy on temperature was defined based on data from the publication [2] (for temperature values of 100–600 °C) and our own research consisting of carrying out a static tensile test of samples at room temperature of 20 °C and an elevated temperature of 650 °C (Figure 3).

Table 2. Coefficients k and n of cyclic hardening curves for the HR6W alloy determined at different temperatures.

t [°C]	E [MPa]	k [MPa]	n [-]
20	192,000	923.95	0.1567
100	188,000	984.9	0.1652
200	182,000	1110.5	0.1816
300	175,000	1277.3	0.2014
400	169,000	1440.2	0.219
500	164,000	1591.7	0.2341
600	156,000	1402.5	0.2042
650	151,000	2275.4	0.2943

Based on the coefficient values listed in Table 2, model cyclic hardening curves were determined for the remaining temperatures (Figure 8).

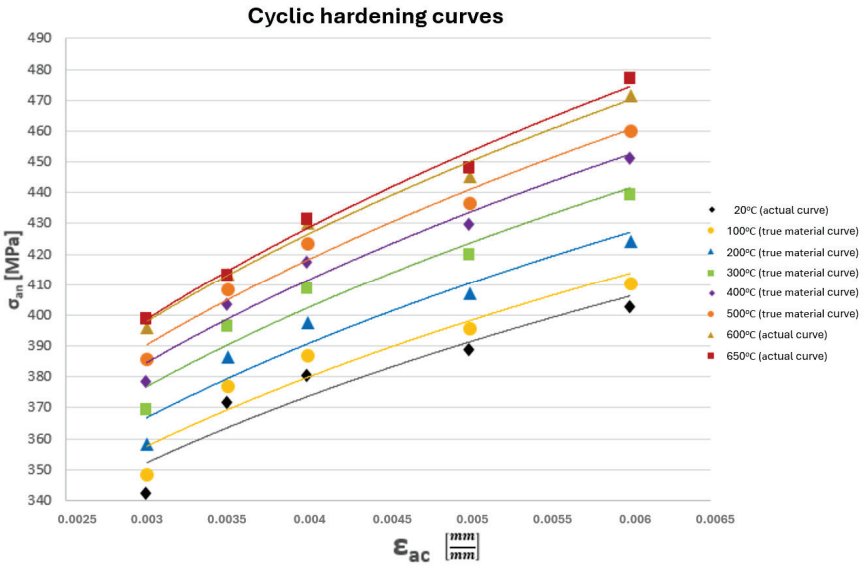

Figure 8. Cyclic hardening curves of the HR6W alloy obtained from laboratory test results on specimens (experimental curves) and approximated using mathematical relationships (model curves).

One way to verify the accuracy of the obtained k and n coefficients is to visually verify the generated model cyclic hardening curves. This involves the shape of these curves (sufficient similarity to the curves obtained from tests) and their spacing (evenness of their position relative to each other). Taking into account the above criteria, the obtained model cyclic hardening curves for the HR6W alloy at temperatures of 100–500 °C are correct.

Subsequently, the operating characteristics of the analysed HR6W alloy tee were determined. This material is not currently used in any components of existing power-generation units. Therefore, the time histories of the working-medium parameters for the analysed pipeline tee were assumed based on similarity to the pressure, temperature, and mass flow rate curves observed in other units operating under comparable conditions (Figure 9).

https://doi.org/10.3390/ma19050891

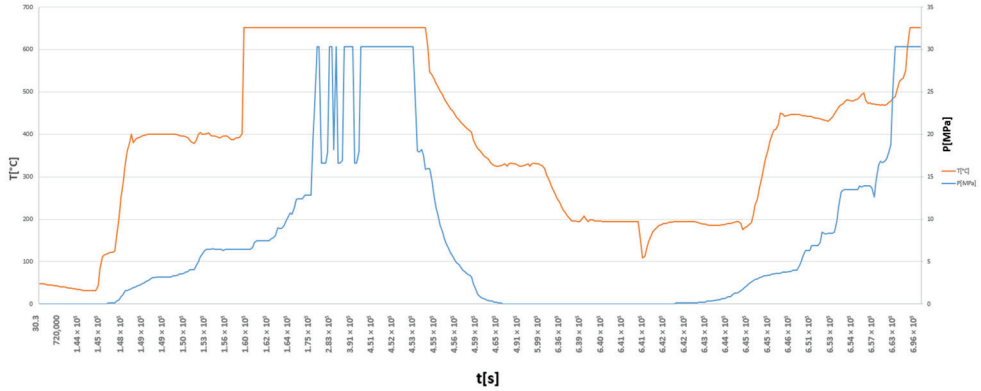

Figure 9. Adopted time-dependent variations in pressure and temperature of fresh steam flowing through the tee of the pipeline made of HR6W material for the reference computational cycle.

The next step of the proposed methodology involves defining an appropriate discrete model of the analysed power engineering component for finite element calculations. Based on the concept of the tee, a CAD model was developed and subsequently discretized using suitable three-dimensional finite elements of the Hexa 20 and Tetra 10 types (Figure 10a). The thus-defined model of a quarter-tee with its thermal insulation consisted of 171,917 finite elements and 373,364 nodes.

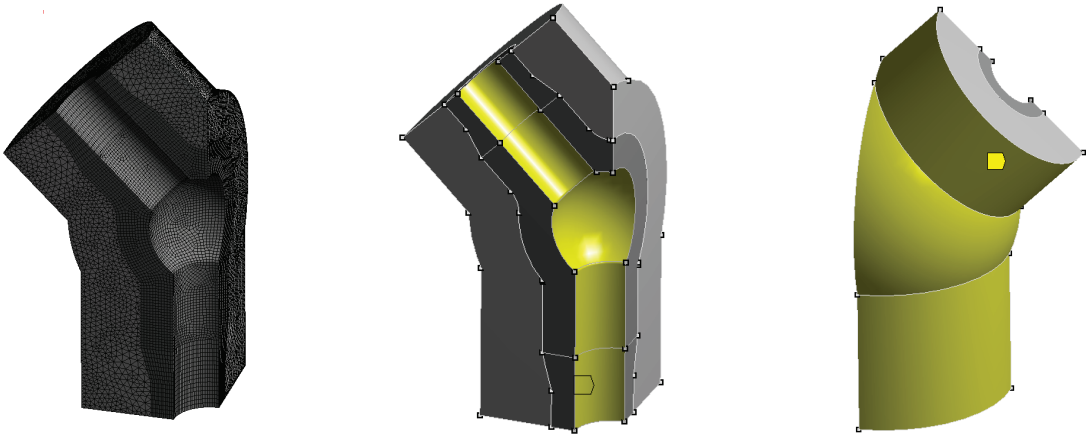

Figure 10. (**a**) Discrete model of the branched tee of the fresh steam pipeline made of HR6W material; (**b**) surfaces of convective heat exchange between the fresh steam and the tee; (**c**) surfaces of heat exchange between the insulation and the environment—natural convection.

Another stage of the procedure is the definition of an appropriate material model. For this purpose, in order to describe the plastic behaviour of the structural material, a suitable hardening model must be adopted.

An analysis of the hysteresis loops obtained at saturation states for specimens subjected to different levels of total strain in the HR6W material, together with the cyclic hardening curves derived from these loops, as well as information available in the literature [10,11] for other alloys used in thermal power engineering, leads to the conclusion that these characteristics describe a kinematic hardening phenomenon. This behaviour occurs between successive saturation states of the material for different levels of total strain amplitude and can be represented using a multilinear kinematic hardening (MKH) model.

Accordingly, the material model incorporates the data listed in Table 3 as well as the coordinates of the points defining the cyclic stress–strain curves shown in Figure 8.

https://doi.org/10.3390/ma19050891

Table 3. Thermo-mechanical properties of the HR6W alloy determined based on reference [1].

	Temperature [°C]							
	20	**100**	**200**	**300**	**400**	**500**	**600**	**650**
Young's modulus E [MPA]	192,000	188,000	182,000	175,000	169,000	164,000	156,000	151,000
Yield strength Re0.2 [MPa]	235	215	185	170	160	155	150	148
Thermal conductivity coefficient $\lambda\left[\frac{W}{m\times K}\right]$	10.8	12.7	15.1	17.4	19.9	23.4	26.1	29.4
Thermal expansion coefficient $\beta\left[\frac{1}{K}\right]$	1.2×10^{-5}	1.36×10^{-5}	1.42×10^{-5}	1.45×10^{-5}	1.49×10^{-5}	1.51×10^{-5}	1.52×10^{-5}	1.536×10^{-5}
Specific heat $Cp\left[\frac{J}{kg\times K}\right]$	442	482	521	549	578	636	665	684.7

The temperature distribution within the material volume of power engineering components has a significant influence on the stress state of their structures and, consequently, on their durability. Of particular importance are thermal shocks, defined as sudden changes in the temperature of metal surfaces in contact with the flowing working medium (e.g., steam) resulting from abrupt changes in the temperature of that medium. Such thermal shocks lead to the formation of large temperature gradients across the thickness of thick-walled components.

As a consequence of the temperature-dependent thermal expansion of the material, the geometric form of the components, and internal constraints (material resistance) or external constraints (such as the method of fixing a given power engineering component, which limits its freedom of movement), these gradients may induce deformations of sufficient magnitude to cause localised plastic deformation. Therefore, from a fatigue perspective, transient operating states of power engineering components, such as start-up and shutdown of power units, are of particular significance.

To determine the temperature distribution occurring during the operation of power engineering components, a transient thermal analysis using the finite element method should be performed [12]. In the case of the tee and steam, the primary mechanism of heat transfer between the working medium and the walls of the thick-walled vessel is convection (Figure 10b). The intensity of this process is characterised by the heat transfer coefficient α [W/(m$^2\cdot$°C)].

For the considered tee made of HR6W steel, the heat transfer coefficient was determined based on the following relationship [13]:

$$\alpha = 0.023\frac{\lambda}{d}\mathrm{Re}^{0.8}\mathrm{Pr}^{\frac{1}{3}}\varepsilon_t \quad (2)$$

where

λ [W/(m·K)]—thermal conductivity coefficient of the fluid,

d [m]—inner diameter of the pipe,

Re [-]—Reynolds number,

Pr [-]—Prandel number,

μf, μs ([kg/(m·s)])—dynamic viscosity coefficient of the fluid for its mean temperature and wall temperature, respectively.

Based on the data presented in Figure 9 and Equation (2), the time history of the heat transfer coefficient for the analysed pipeline tee was obtained for the assumed time period (Figure 11).

https://doi.org/10.3390/ma19050891

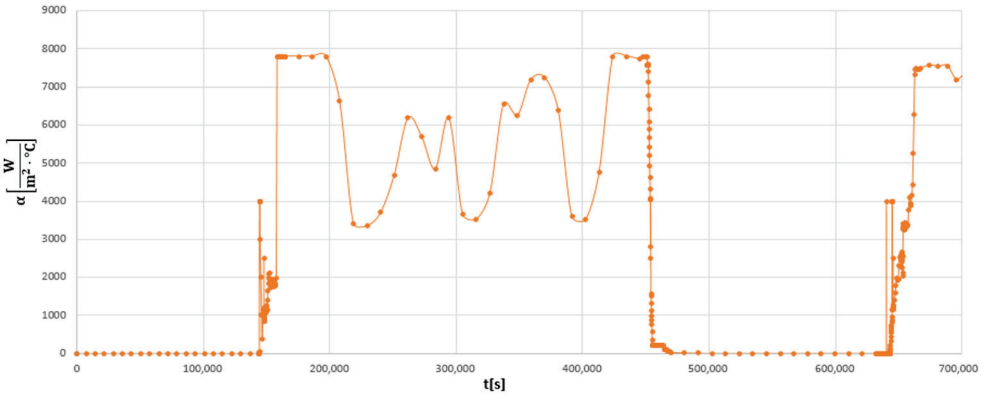

Figure 11. Time variation in the heat transfer coefficient α [W/(m^2·°C)] on the inner surface of the tee made of HR6W material during the considered time period.

Additionally, a heat transfer coefficient of α = 10 W/(m^2·°C) was assumed for the ambient environment at an ambient temperature of 30 °C (Figure 10c).

Below, exemplary temperature contours of the analysed tee obtained during transient thermal analyses are presented (Figure 12).

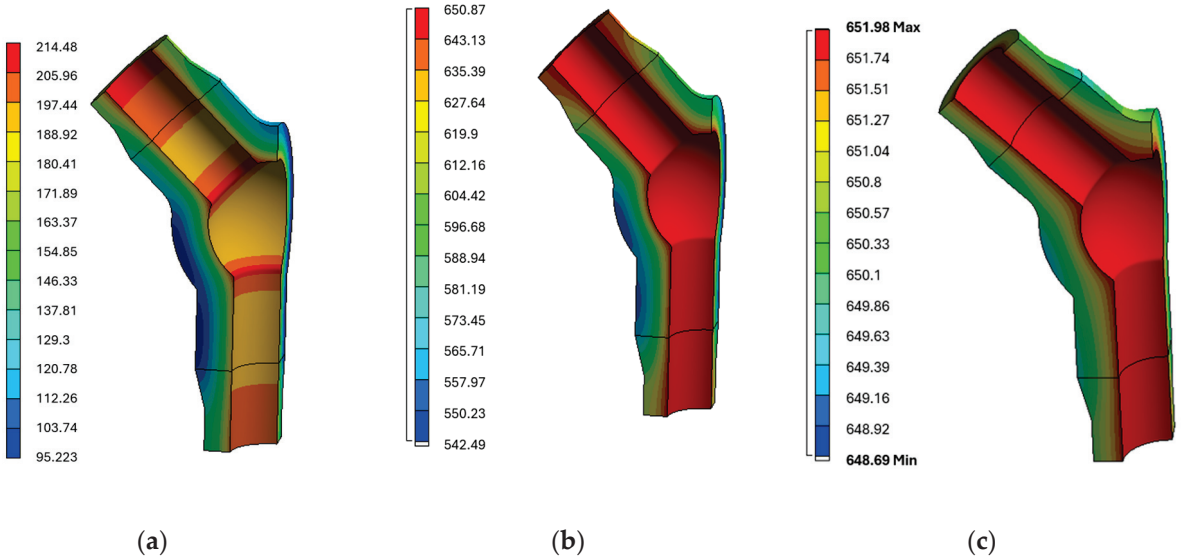

(**a**) (**b**) (**c**)

Figure 12. Temperature contours [°C] in the tee at (**a**) 21.448 s, (**b**) 160.200 s, and (**c**) 261.840 s during thermal analysis for the power unit start-up (**a**,**b**) and steady-state operation (**c**).

The next stage of the methodology for assessing the durability of power engineering components involves performing numerical strength analyses using the finite element method in order to determine the complex strain state of the component structure. To obtain results that are as close to reality as possible, these simulations must take into account the temperature field distributions, the time histories of the working-medium pressure, as well as interaction forces originating from other subsystems directly cooperating with the analysed component. The results are also strongly influenced by the external constraints (boundary conditions) applied to the numerical model, which must accurately reflect the mounting conditions of the real structure.

Figure 13a–c show the areas of the considered tee in which boundary conditions for static, nonlinear numerical calculations were assumed.

https://doi.org/10.3390/ma19050891

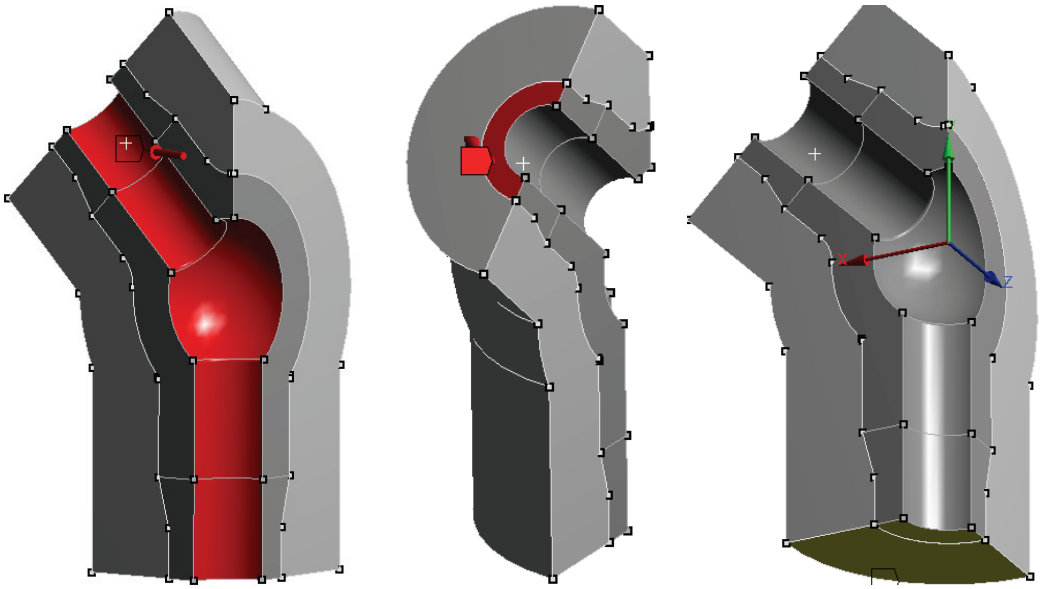

(**a**) (**b**) (**c**)

Figure 13. Graphical representation of the boundary conditions defined for the nonlinear strength analysis of a tee of a live steam pipeline made of HR6W material: (**a**) internal surfaces of the tee to which the live steam pressure was applied, (**b**) the surface separating the tee from the pipeline system to which a force was applied reflecting the effect of the remaining part of it on this branch, (**c**) the surface separating the tee from the pipeline system to which a restraint was applied by taking away vertical displacements from the nodes.

For the tee analysed within the presented methodology, the mechanical properties listed in Table 3 and a multilinear kinematic hardening model based on the cyclic stress–strain curves shown in Figure 8 were used. Selected results of the strength analyses are presented below (Figure 14a–c).

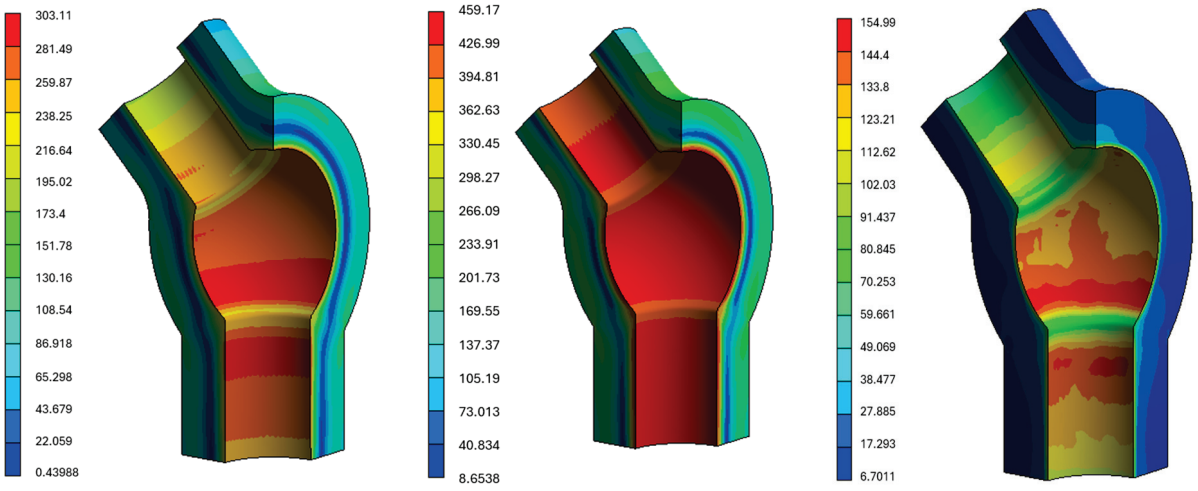

(**a**) (**b**) (**c**)

Figure 14. Equivalent stress contours [MPa] in the tee based on the Huber–Mises criterion at (**a**) 146.100 s, (**b**) 158.400 s during power unit start-up, and (**c**) 361.200 s during steady-state operation.

When analysing the obtained results in the form of contours of equivalent stresses according to the Huber–Mises hypothesis, attention should be paid to whether their magnitudes are sufficiently high to potentially cause plastic deformation.

https://doi.org/10.3390/ma19050891

From the standpoint of both immediate strength and fatigue durability, the potentially most critical region of a power engineering component is the area of the structure where the maximum level of stress occurs, expressed by the highest value of equivalent stress according to the Huber–Mises criterion. In the case of the analysed tee, this critical location corresponds to node number 135,678, situated in the region of the lower nozzle (Figure 15a). It is worth mentioning that a mesh independence analysis was conducted. For this purpose, calculations were performed for three finite element sizes (the first mesh is the one used in the methodology, the other two are 1.3 times denser than the previous one). The results of this analysis, in the form of reduced Huber–Mises stresses in the region of their maximum values (marked in Figure 15a), for three different meshes are very similar (Figure 15b). This indicates that the adopted mesh size is correct, as increasing the mesh density does not significantly change the results.

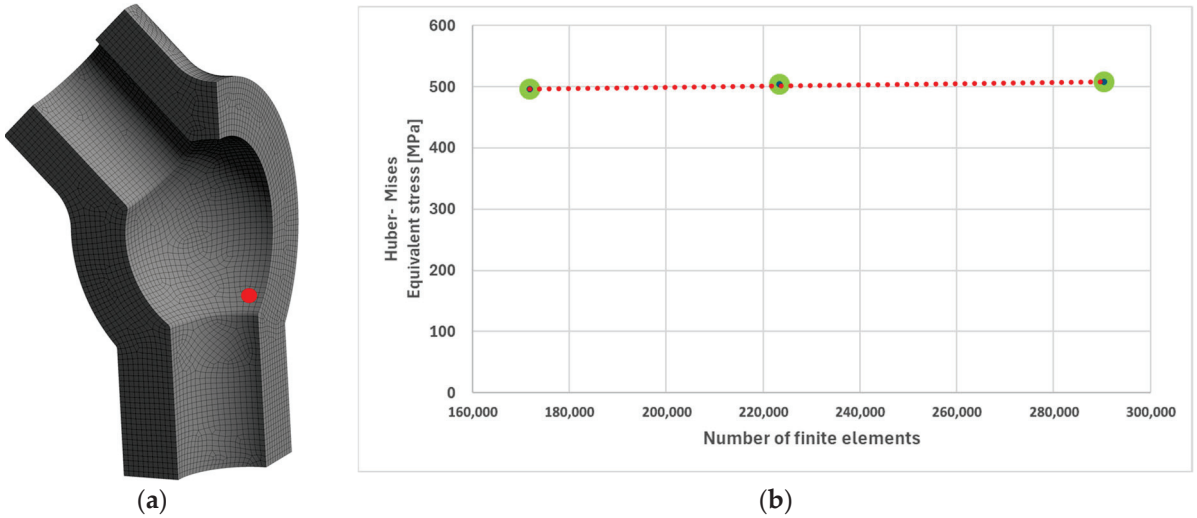

Figure 15. (**a**) Node number 135,678 of the tee made of HR6W material identified as the location of maximum equivalent stress values according to the Huber–Mises hypothesis; (**b**) a graph showing the independence of the results from the mesh size.

For node number 135,678, shown in Figure 15a, the time histories of the normal components of the complex stress state, as well as the equivalent stresses according to the Huber–Mises criterion, are presented (Figures 16 and 17).

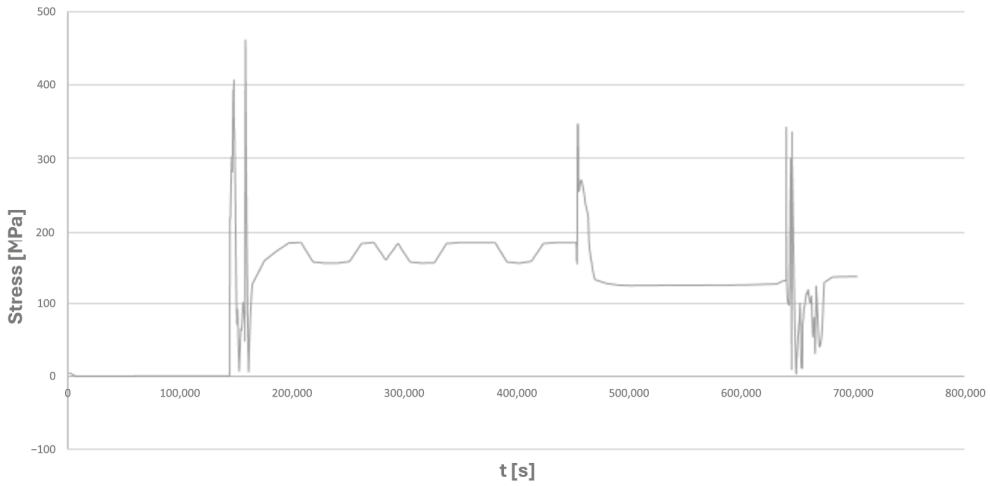

Figure 16. Time history of equivalent stresses according to the Huber–Mises hypothesis for node number 135,678 of the tee made of HR6W material selected for fatigue analysis (Figure 15).

https://doi.org/10.3390/ma19050891

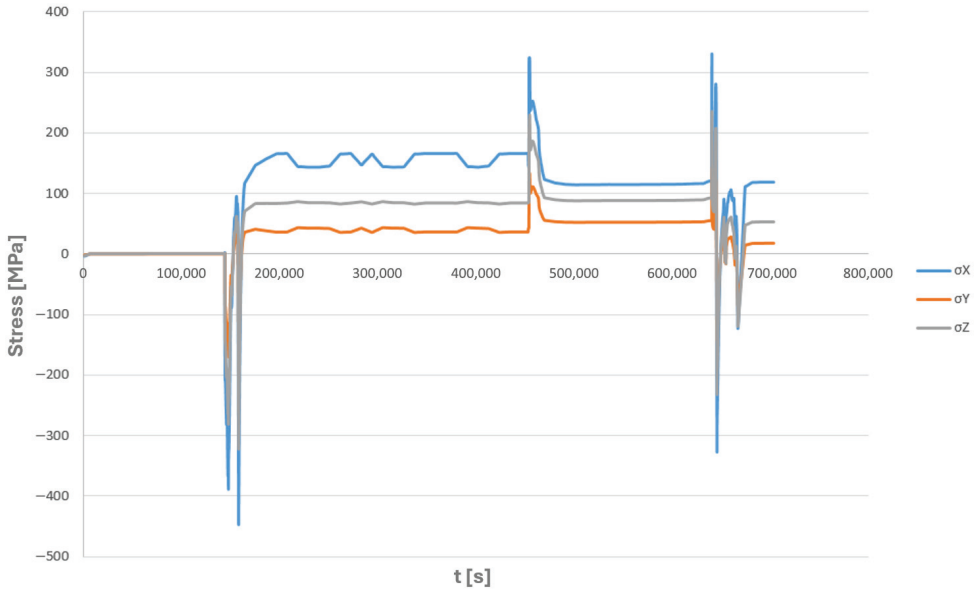

Figure 17. Time history of normal stresses of the assumed stress state for node number 135,678 of the tee made of HR6W material selected for fatigue analysis (Figure 15).

The above results allow for an unambiguous confirmation that the analysed point is subjected to the highest values of equivalent stress, reaching up to 459 MPa. Simultaneously, when considering the strength properties of the HR6W material presented in Table 3, it can be observed that during the operating cycle of the power engineering component, the equivalent stress values exceed, at certain time steps, the yield strength corresponding to the respective metal temperatures. Consequently, it can be concluded that plastic deformation may occur in the tee.

Since the multilinear kinematic hardening material model was defined using data derived from cyclic stress–strain curves, this indicates a high probability of the occurrence of thermo-mechanical fatigue in the analysed power engineering component [3].

Figure 18a–c below present contours of equivalent plastic strains [14].

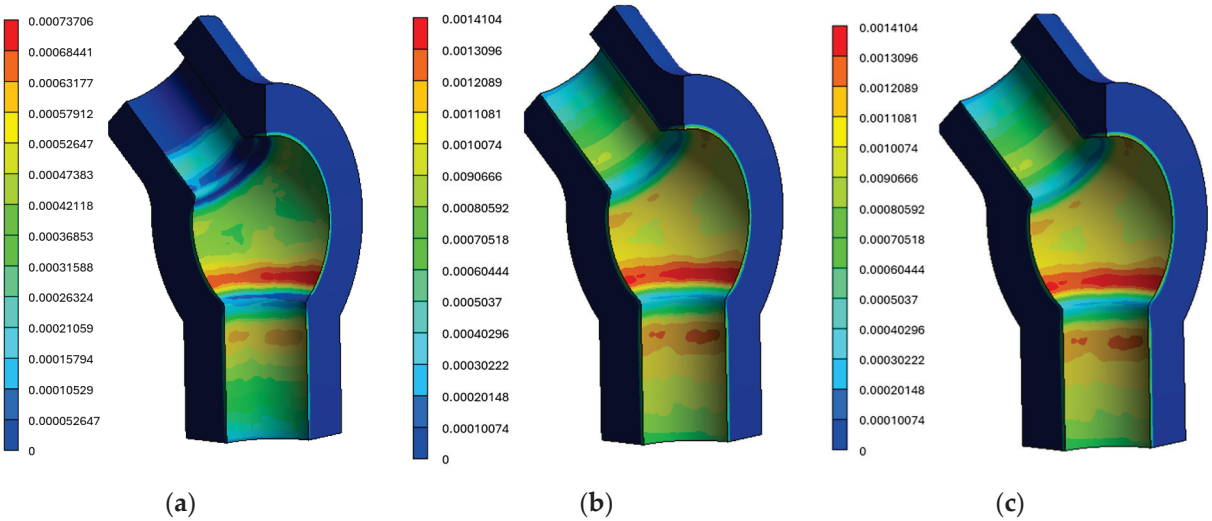

(**a**) (**b**) (**c**)

Figure 18. Equivalent plastic strain contours in the tee at (**a**) 148.020 s, (**b**) 158.400 s during power unit start-up, and (**c**) 361.200 s during the stress state after unit shutdown and temperature stabilisation.

In order to assess the possibility of plastic deformation occurring in each type of operating cycle represented by the finite element simulation, it is necessary to analyse, for a given point of the examined component, a graphical representation of the relationship

https://doi.org/10.3390/ma19050891

between the stress components and their corresponding strains. Figure 19 presents such a stress–strain relationship for the forked tee made of HR6W material at the location indicated in Figure 15a.

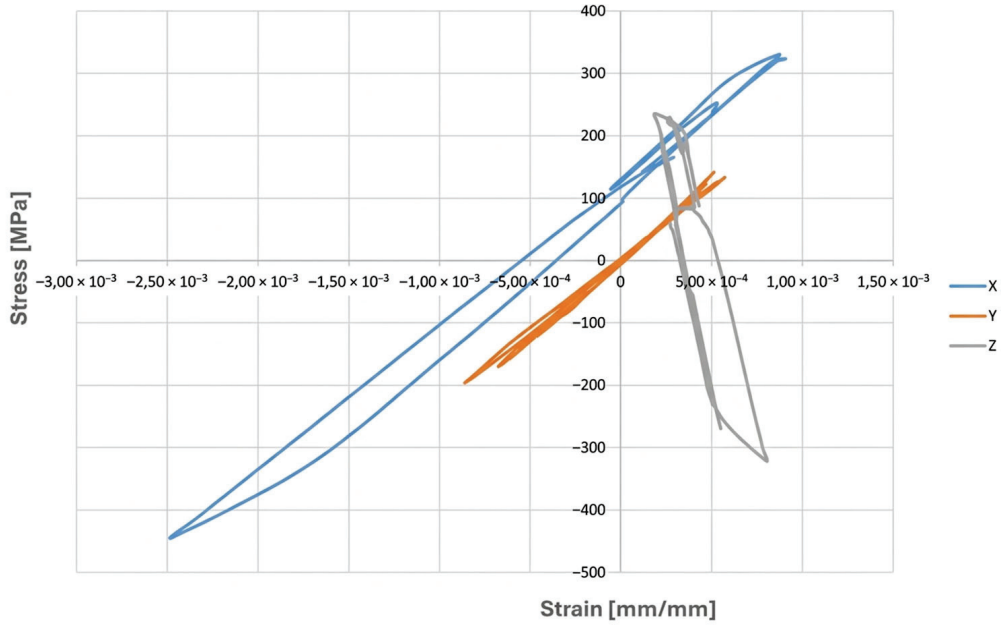

Figure 19. Graphical representation of the relationship between stress state components and strains at a point of the tee made of HR6W alloy, shown in Figure 15a.

An analysis of the above figure indicates that the stress component values in the X and Z directions exceed the yield strength of the material corresponding to the temperatures occurring during the analysed operating cycle. Moreover, the stress–strain relationships in the directions perpendicular to the X and Z axes exhibit hysteresis loop shapes, which indicates the possibility of plastic deformation occurring in each operating cycle examined using the thermo-mechanical simulations described above.

Having at one's disposal the results of low-cycle fatigue tests conducted at elevated temperatures as well as the numerical analysis results for power engineering components, the question arises as to how fatigue durability should be evaluated. In the generally available literature, and particularly in normative documents such as EN 12952-4:2011 [15] and ASME Code Cases—Boilers and Pressure Vessels [16], an approach is adopted that involves identifying load cycles within the load history using the rainflow counting method, followed by counting cycles with the same stress range.

Another approach, described, for example, in Refs. [17,18], involves determining various criterion quantities related to the number of cycles to failure. Since the results of low-cycle fatigue tests at elevated temperatures and, indirectly, thermo-mechanical fatigue tests include hysteresis loops, certain geometric parameters of these loops can be used to define such criterion functions. Of particular importance in this context are the loops corresponding to the saturation state, which, under combined thermal loading (temperature field) and mechanical loading (elongation induced by the testing machine), do not change their position, shape, or size.

It is precisely the geometric parameters determined for these saturation hysteresis loops that are correlated with the number of cycles to failure of specimens tested at a given total strain range and test temperature.

https://doi.org/10.3390/ma19050891

In the scientific literature, criterion values determined on the basis of hysteresis loops corresponding to the saturation state of specimens can be found, such as the Coffin and Ostergren parameters, which are defined by the following relationships:

$$C(N_f) = \Delta\varepsilon_p(\Delta\varepsilon_c, T) \tag{3}$$

$$O(N_f) = \Delta\varepsilon_p(\Delta\varepsilon_c, T)\cdot\sigma_{an_{max}} \tag{4}$$

where

N_f—the number of cycles to failure determined from low-cycle fatigue tests conducted at an elevated temperature for a specimen uniformly heated throughout its entire volume to a temperature T (°C), subjected to fully reversed cyclic loading with a stress ratio of $R = -1$ and a total strain amplitude of $\Delta\varepsilon_c$.

$\Delta\varepsilon_p(\Delta\varepsilon_c, T)$—the plastic strain range obtained for a specimen subjected to a low-cycle fatigue test with a total strain range $\Delta\varepsilon_c$ at a temperature of T degrees Celsius.

$\sigma_{an_{max}}$—the stress amplitude (stress value) for the specimen in the saturation state.

$C(N_f)$—the Coffin parameter as a criterion function used for estimating the fatigue life of components subjected to low-cycle fatigue at elevated temperatures.

$O(N_f)$—The Ostergren parameter, a criterion function used to estimate the fatigue life of components subjected to low-cycle fatigue at elevated temperatures.

Figure 20 illustrates the assumptions adopted for determining the Coffin and Ostergren parameters corresponding to the saturation state of the specimens, based on hysteresis loops obtained from low-cycle fatigue tests carried out up to the saturation condition.

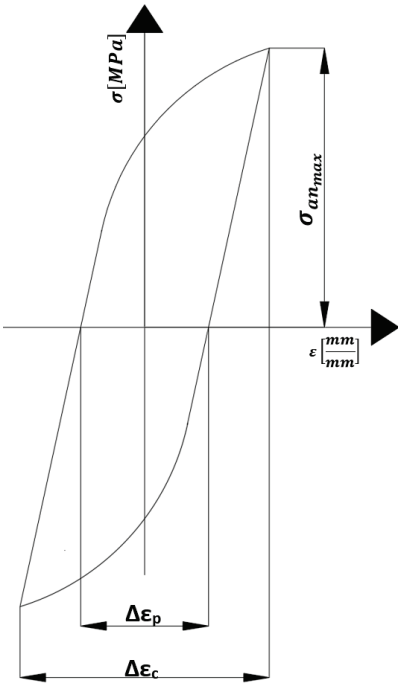

Figure 20. Assumptions for determining the Coffin and Ostergren parameters based on the hysteresis loop corresponding to the saturation state of specimens subjected to low-cycle fatigue tests.

Taking into account the results of the authors' own low-cycle fatigue tests conducted at 650 °C, plots of the Coffin and Ostergren parameters as functions of the number of cycles to failure were prepared (Figures 21 and 22).

https://doi.org/10.3390/ma19050891

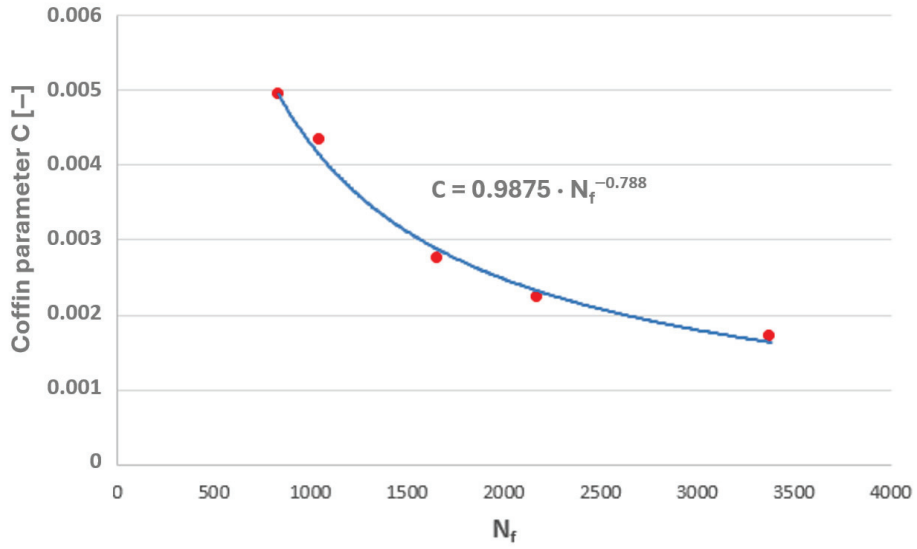

Figure 21. Relationship between the Coffin parameter and the number of cycles to failure (N_f) for the HR6W alloy at 650 °C.

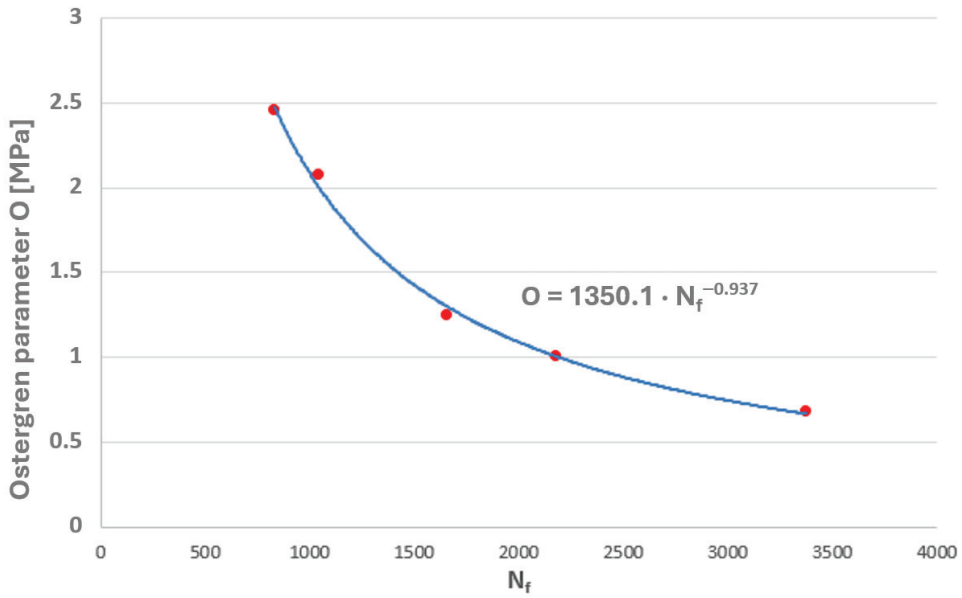

Figure 22. The relationship between the Ostergren parameter and the number of cycles to failure (N_f) for the HR6W alloy at 650 °C.

A power-law character of the distribution of these parameter values as a function of the number of cycles to failure can be observed, which corresponds to the nature of the graphical representation of the plastic strain component of the Manson–Coffin equation. The characteristics presented in Figures 23 and 24 compare the values of the Coffin and Ostergren parameters for several temperature levels, based on data obtained from the authors' own experiments, as well as from the literature.

Considering the two diagrams above, it can be observed that an increase in temperature leads to a reduction in the fatigue life of the HR6W alloy, manifested by a decrease in the number of cycles to failure accompanied by a simultaneous reduction in the values of the Coffin and Ostergren parameters.

At the same time, it is necessary to return to the initial assumption concerning the performance of low-cycle fatigue experimental tests at a constant, elevated temperature in order to describe the phenomenon of thermo-mechanical fatigue. Specifically, it was assumed that by conducting low-cycle fatigue tests at an elevated, constant temperature

https://doi.org/10.3390/ma19050891

for a selected range of total strain amplitudes, it is possible to reflect the influence on the material durability of time-dependent thermal and mechanical strains characteristic of thermo-mechanical fatigue. A similar assumption can be made when determining the fatigue life of the alloy based on the relationships between the Coffin and Ostergren parameters and the number of cycles to failure. This implies that, in order to assess the loss of durability for a specific type of operating cycle of a power-generation component in which thermo-mechanical fatigue occurs, the appropriate relationships of the above criterion functions, determined from low-cycle fatigue tests under isothermal conditions, can be applied. Confirmation of this hypothesis is provided in publications [19,20].

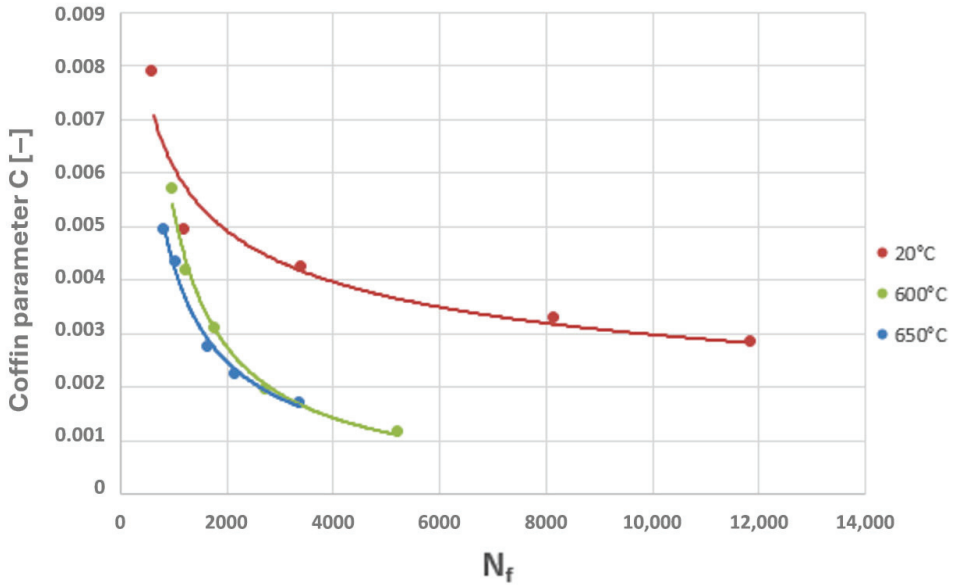

Figure 23. Summary of the relationship between the Coffin parameter and the number of cycles to failure (N_f) for the HR6W alloy at various temperatures.

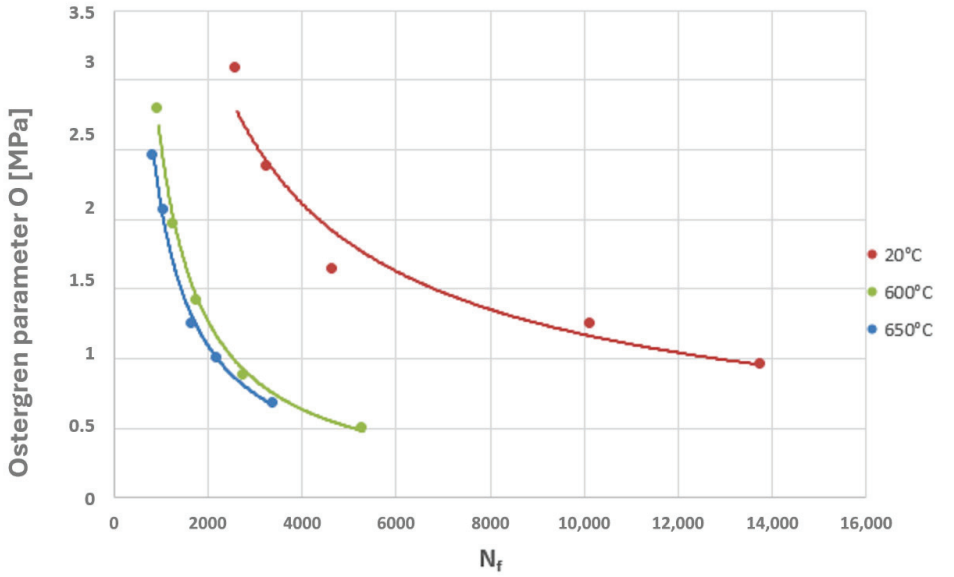

Figure 24. Summary of the relationship between the Ostergren parameter and the number of cycles to failure (N_f) for the HR6W alloy at various temperatures.

In that study, a high degree of agreement was demonstrated between the results obtained from low-cycle fatigue tests and thermo-mechanical fatigue tests for X20CrMoV12-1 steel with respect to the values of the criterion function proposed by the authors, namely

https://doi.org/10.3390/ma19050891

the coefficient P, which is closely related to the quantities $C(N_f)$ and $O(N_f)$, and is described by the following relationship:

$$P(N_f) = \Delta\varepsilon_p(\Delta\varepsilon_c, T)\cdot\sigma_{an_{max}}\cdot T_{max} = O(N_f)\cdot T_{max} = C(N_f)\cdot\sigma_{an_{max}}\cdot T_{max} \quad (5)$$

where T_{max}—the maximum temperature value within the fatigue cycle.

In view of the above, it may be assumed that, also in the case of the Ostergren and Coffin parameters, only a minor difference would occur between the two types of fatigue for the X20CrMoV12-1 alloy.

The values of the criterion functions obtained from low-cycle fatigue tests at an elevated temperature should be compared with those determined for actual power-generation components using the finite element method. In order to assess fatigue life under a complex stress state derived from a thermo-mechanical analysis of a power component, an approach based on the determination of the critical plane may be employed, as described in detail in publications [3,21]. This plane represents the region in which the criterion values, i.e., the Coffin and Ostergren parameters determined from hysteresis loops induced by the normal stresses σ_n acting on this plane, reach their maximum values (Figure 25) [22,23].

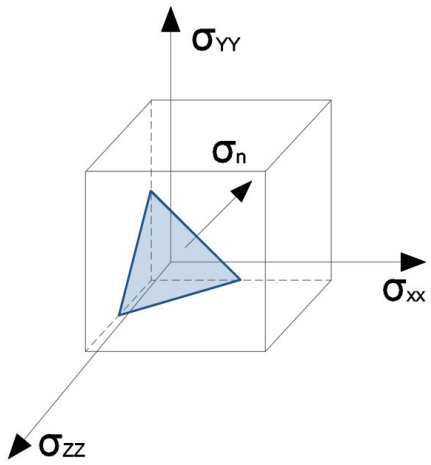

Figure 25. Normal stress vector for determining the critical plane.

For a structural point of a power-generation component analysed in terms of fatigue durability, the procedure for determining life reduction using the critical plane method can be divided into several stages. The first stage involves identifying potential critical planes, defined in three-dimensional space by the angles θ and θR, as illustrated in Figure 26 [24].

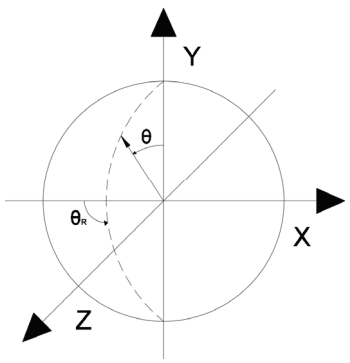

Figure 26. Graphical representation of the definitions of angles θ and θR determining the orientation of potential critical planes.

https://doi.org/10.3390/ma19050891

The coefficients necessary for determining the critical planes can be defined according to the relationships given below:

$$n_Y = -\sin\sin\theta \cdot \cos\cos\theta_R \tag{6}$$

$$n_X = \sin\sin\theta \cdot \sin\sin\theta_R \tag{7}$$

$$n_Z = \cos\cos\theta \tag{8}$$

where $\theta \epsilon \langle 0^\circ, 180^\circ \rangle$ i $\theta_R \epsilon \langle 0^\circ, 180^\circ \rangle$.

For the given ranges of angles, the parameter values expressed by Equations (6)–(8) allow tracing the full set of potentially critical planes due to the properties of trigonometric functions (symmetry of their values). Subsequently, using the above parameters, for each pair of angles θ and θR (defining the plane), the normal stresses and strains on the identified plane must be determined as described by the following equations:

$$\begin{aligned} \sigma_n = \sigma_X \cdot n_X^2 + \sigma_Y \cdot n_Y^2 + \sigma_Z \cdot n_Z^2 + 2 \cdot \tau_{XY} \cdot n_X \cdot n_Y \\ + 2 \cdot \tau_{YZ} \cdot n_Y \cdot n_Z + 2 \cdot \tau_{XZ} \cdot n_X \cdot n_Z \end{aligned} \tag{9}$$

$$\varepsilon_n = \varepsilon_X \cdot n_X^2 + \varepsilon_Y \cdot n_Y^2 + \varepsilon_Z \cdot n_Z^2 + \gamma_{XY} \cdot n_X \cdot n_Y + \gamma_{YZ} \cdot n_Y \cdot n_Z + \gamma_{XZ} \cdot n_X \cdot n_Z \tag{10}$$

where σ_X, σ_Y, σ_Z, τ_{XY}, τ_{YZ}, τ_{XZ}, ε_X, ε_y, ε_z, γ_{XY}, γ_{YZ}, γ_{XZ}—components of the combined stress and strain state at the point of the power device where fatigue life is determined [25,26].

Thus, if the results of numerical analyses in the form of stress and strain state components for specific points of power equipment are functions of computational time, then based on points with coordinates (ε_n, σ_n), hysteresis loops characterising the cyclic behaviour of the structural material can be constructed. By varying the analysed plane through different values of angles θ and θR, a new set of points with coordinates (ε_n, σ_n) is obtained, and consequently, a new hysteresis loop is generated. Among the resulting $\varepsilon_n - \sigma_n$ plots, those for which the Coffin parameter $C(N_f)$ and the Ostergren parameter $O(N_f)$ reach their maximum values must be identified. The pairs of angles θ and θR corresponding to these maxima define the critical planes. Next, the maximum values of the parameters C and O, determined indirectly based on the results of numerical calculations, should be related to the dependencies of these quantities as functions of the number of cycles to failure N_f, established during laboratory tests on specimens (dependencies of the same type as those presented in Figures 21–24) for the temperature equal to the highest temperature occurring in the fatigue cycle. Since experimental test results are usually not available at the exact highest temperature occurring during the analysed period, it is advisable to consider the dependency determined for a temperature as close as possible to, and simultaneously higher than, the temperature used in the calculations. This approach is justified by the fact that the fatigue life of metals decreases with increasing temperature, as shown in the graphs in Figures 23 and 24. Such an approach results in assessing the fatigue life of the power equipment at a conservative (lower than actual) level. Therefore, based on the calculation results, a safe fatigue life limit for the fresh steam pipeline tee has been determined [27,28].

An example hysteresis loop plotted in the $\varepsilon_n - \sigma_n$ coordinate system for the node selected to determine the fatigue life of the analysed tee (Figure 15a) at different potential planes defined by angles θ and θR is shown in Figure 27.

Analysing the cyclic strain curves (Figure 8), hysteresis loops in Figure 19, and the Coffin and Ostergren function plots (Figures 23 and 24), it can be concluded that the

https://doi.org/10.3390/ma19050891

HR6W alloy exhibits a tendency for a significant increase in strength properties (hardening) accompanied by a reduction in ductility, as measured by the hysteresis loop width. This, in turn, explains the high fatigue durability of this steel despite its tendency to develop high thermal stresses caused by thermal shocks [29].

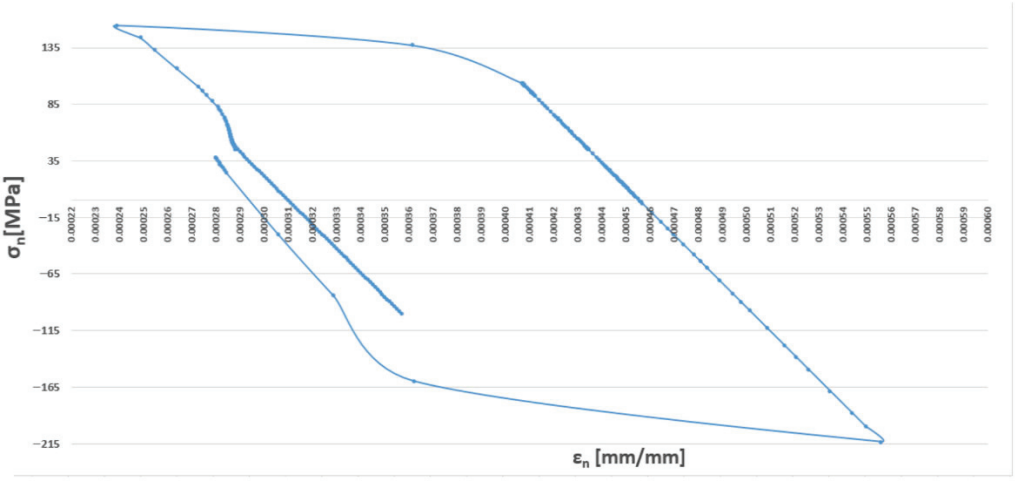

Figure 27. Hysteresis loop obtained from numerical calculations of the analysed tee for node 135,678 selected for fatigue analysis, in the plane defined by angles θ = 90° and θR = 165°.

For the tee point selected for fatigue analysis according to Figure 26, a survey of planes was conducted with respect to the values of the Coffin and Ostergren parameters obtained from the analysis of the resulting hysteresis loops in the $\varepsilon_n - \sigma_n$ coordinate system. The search was performed over the angular ranges of θ and θ_R equal to $\langle 0°, 180° \rangle$, with increments of 15°. The results of these calculations, in the form of 3D plots showing the parameter values as functions of angles θ and θ_R, are presented in Figures 28 and 29 [30,31].

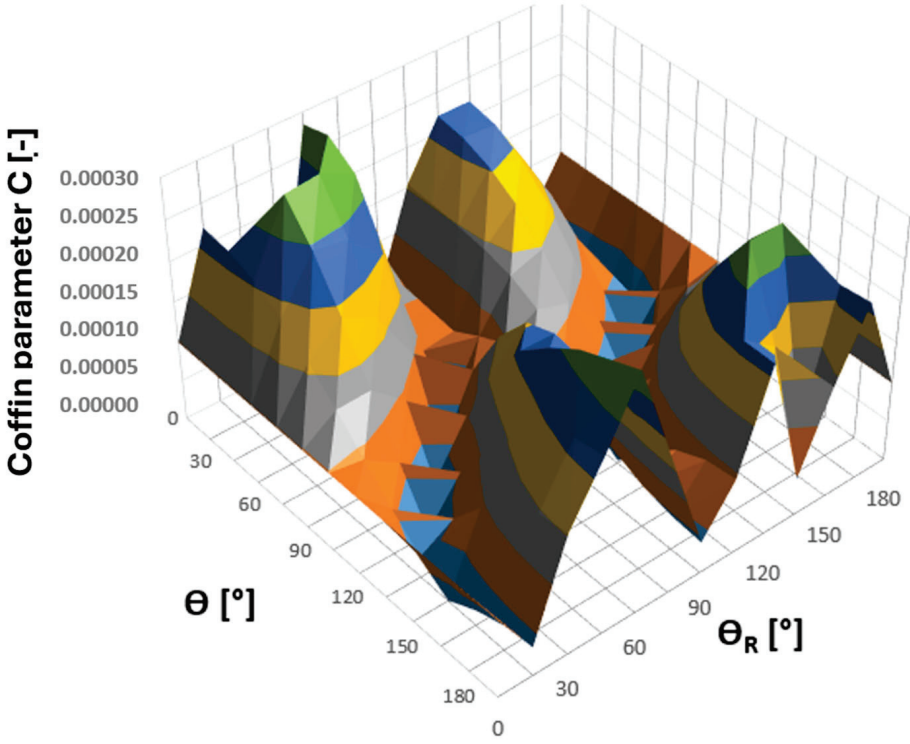

Figure 28. Values of the Coffin parameter C as a function of angles θ and θ_R determined for node 135,678 of the tee made of HR6W material.

https://doi.org/10.3390/ma19050891

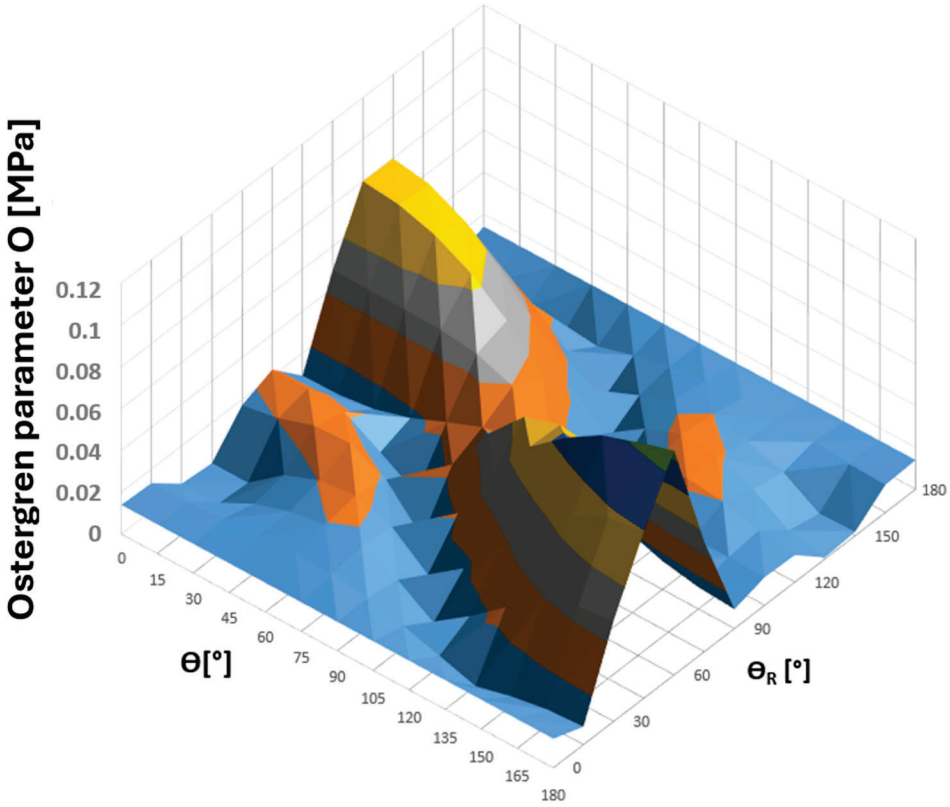

Figure 29. Values of the Ostergren parameter O [MPa] as a function of angles θ and θ_R for node 135,678 of the tee made of HR6W material.

Analysing the above plots, it can be observed that they exhibit a continuous nature, indicating that the Coffin and Ostergren criterion functions were correctly determined based on the components of the combined stress and strain state at node 135,678 of the tee (Figure 30). At the same time, regions of local extrema of these quantities are clearly visible, illustrating their variability across all possible planes. This, in turn, highlights the necessity to identify the critical plane for which the chosen criterion parameters reach their maximum values. Considering the maximum normal stress criterion [21,30], the combined strain state (and consequently the stress) determined in this plane for a precisely defined region of the structure is the most unfavourable from the fatigue life perspective.

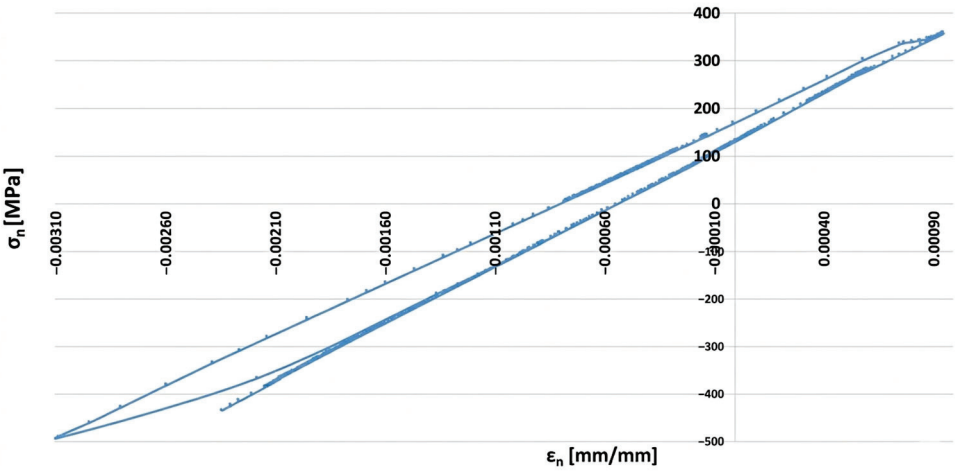

Figure 30. Hysteresis loop obtained from numerical calculations of the tee made of HR6W material for node 135,678 in the critical plane defined by angles θ = 180° and θ_R = 60°.

https://doi.org/10.3390/ma19050891

Considering the above results, both the Coffin and Ostergren parameters reach their maximum values for the same plane defined by the angle pair $\theta = 180°$ and $\theta_R = 60°$, with $C_{max} = 0.000295841$ and $O_{max} = 0.107262268$, respectively. The hysteresis loop corresponding to the identified critical plane is presented in Figure 30 [31,32].

The maximum values of both parameters were plotted on the graphs of these quantities, determined based on laboratory tests on specimens at 650 °C (where the highest temperature obtained on the tee surface during thermal calculations of its operating cycle was approximately 652 °C). The corresponding numbers of cycles to failure were thus determined (Figures 31 and 32).

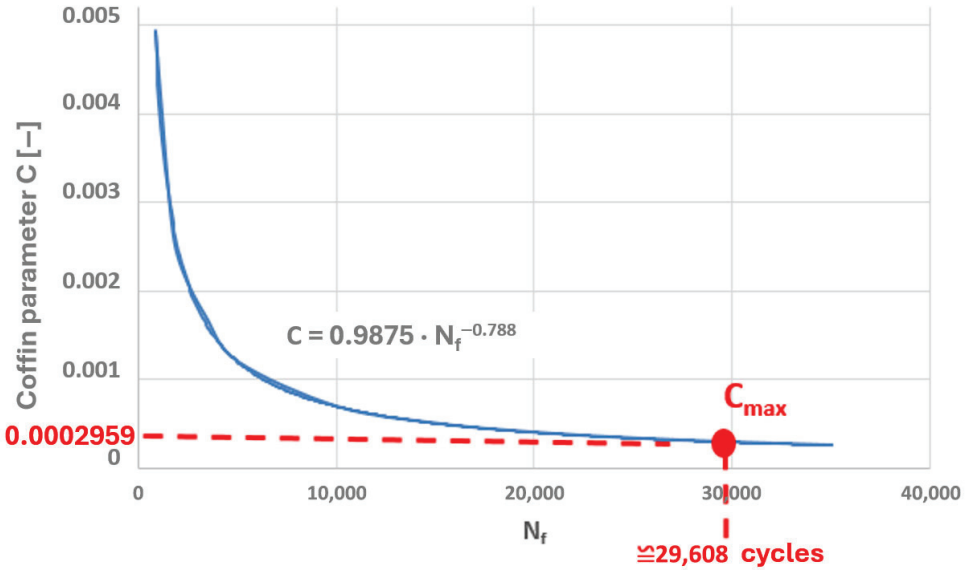

Figure 31. Determination of the number of cycles to failure by plotting the maximum value of the Coffin parameter C_{max} on the graph of this parameter as a function of the number of cycles to failure, established based on low-cycle fatigue laboratory tests conducted at 650 °C.

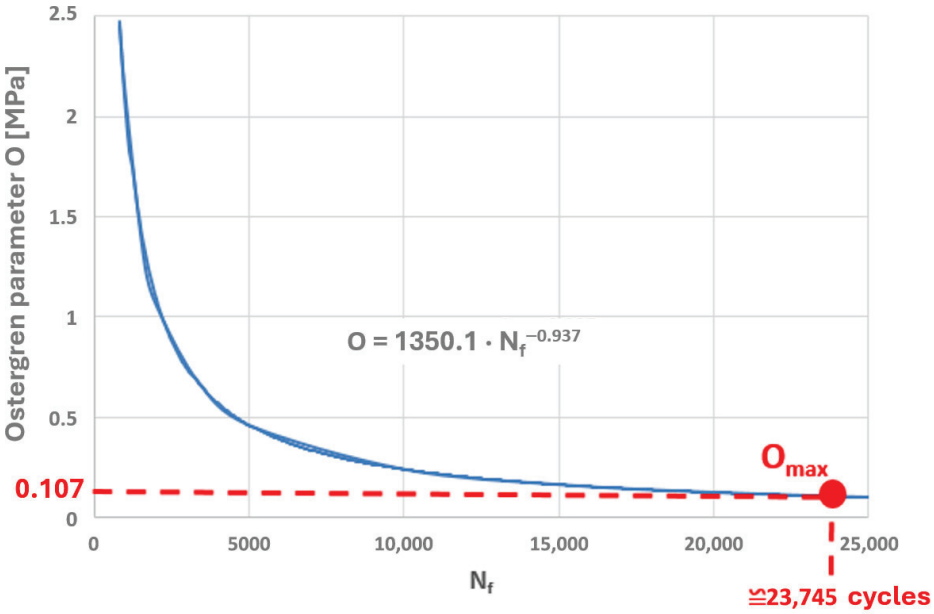

Figure 32. Determination of the number of cycles to failure by plotting the maximum value of the Ostergren parameter O_{max} on the graph of this parameter as a function of the number of cycles to failure, established based on low-cycle fatigue laboratory tests conducted at 650 °C.

https://doi.org/10.3390/ma19050891

Consequently, the determined numbers of cycles to failure for the Coffin and Ostergren parameters are 29,608 and 23,745, respectively. From the perspective of the tee's operational safety, the lower value, i.e., 23,745 (corresponding to the Ostergren parameter), should be adopted for fatigue life calculations. Thus, the unit fatigue damage of the analysed tee made of HR6W material, part of the fresh steam pipeline, caused by a single operation cycle characterised by a cold start-up and normal shutdown of the unit, would be equal to [33,34]:

$$\Delta D_U = \frac{n}{N} = \frac{1}{23,745} \tag{11}$$

4. Conclusions

Based on the content of the above article, the following conclusions can be drawn:

1. The present publication outlines a methodology for assessing the fatigue life of power equipment, which can be applied both during the design process of new power devices and for determining fatigue damage resulting from thermo-mechanical fatigue in already operated installations.
2. The fundamental assumption made in the article is that the evaluation of fatigue life reduction in power equipment operating under thermo-mechanical fatigue conditions can be conducted based on the cyclic properties of materials obtained from low-cycle fatigue tests at elevated temperatures. This hypothesis is grounded in the analysis of results presented in publication [1], where the fatigue lives of specimens made of the material X20CrMoV12-1 subjected to low-cycle fatigue testing at elevated temperatures and thermo-mechanical fatigue tests with similar ranges of total strain $\Delta\varepsilon_c$ were compared. The calculation results confirmed a high correlation in the values of the criterion function describing the fatigue life of the specimens as a function of the number of cycles to failure for both types of fatigue. Consequently, by analogy, it was assumed that the fatigue lives for both phenomena, at the same number of cycles to failure, are comparable.
3. This method allows for the extrapolation or interpolation of data obtained from the literature and laboratory equipment regarding the temperature of metal alloys for the initial values, in order to obtain the emission power at intermediate temperatures. This, in turn, influences the results obtained.
4. The proposed methodology allows for the optimisation of the procedure for changing the operating parameters of power units during operation, with the aim of ensuring greater fatigue life.
5. The above methodology enables the selection of appropriate construction materials for power equipment to ensure adequate fatigue life.

Author Contributions: Conceptualization, M.P. and A.G.; methodology, M.P.; software, M.P.; validation, M.P. and T.D.; formal analysis, M.P.; investigation, M.P.; resources, M.P., T.D. and A.G.; data curation, M.P. and T.D.; writing—original draft preparation, M.P. and T.D.; writing—review and editing, M.P., T.D. and A.G.; visualization, T.D. and A.G.; supervision, A.G.; project administration, M.P.; funding acquisition, M.P. All authors have read and agreed to the published version of the manuscript.

Funding: This research received no external funding.

Data Availability Statement: The original contributions presented in this study are included in the article. Further inquiries can be directed to the corresponding author.

Conflicts of Interest: The authors declare no conflicts of interest.

https://doi.org/10.3390/ma19050891

References

1. Okrajni, J.; Twardawa, M. Description of the Thermo-Mechanical Fatigue of Thick-Walled Pressure Vessels. *Procedia Mater. Sci.* **2014**, *3*, 918–923. [CrossRef]
2. Okrajni, J.; Twardawa, M.; Mutwil, K.; Junak, G. Badania Wytrzymałosci i Trwałosci Elementów Rurociągów Energetycznych. In *Maszyny i Urządzenia Energetyczne Węglowych Bloków na Wysokie Parametry Pary*; Wydawnictwo Politechniki Śląskiej: Gliwice, Poland, 2015; pp. 374–492, ISBN 978-83-7880-286-0.
3. Miller, K.J. The Three Thresholds for Fatigue Crack Propagation. *ASTM Spec. Tech. Publ.* **1997**, *1296*, 267–286. [CrossRef]
4. Bari, S. *Constitutive Modeling for Cyclic Plasticity and Ratcheting*; North Carolina State University: Raleigh, NC, USA, 2001.
5. *ISO 6892-2:2018*; Metallic Materials—Tensile Testing Part 2: Method of Test at Elevated Temperature. ISO: Geneva, Switzerland, 2018.
6. Okrajni, J.; Mutwil, K.; Cieśla, M. Chemical Pipelines Material Fatigue. *J. Mater. Process. Technol.* **2005**, *164–165*, 897–904. [CrossRef]
7. Marek, A.; Okrajni, J.; Junak, G.; Twardawa, M. Research on the Dependence between the Fatigue Life of X20CrMoV12.1 and P91 Steels under the Conditions of the Interactions of Thermo-Mechanical and Isothermal Low-Cycle Fatigue. *Solid State Phenom.* **2015**, *224*, 93–98. [CrossRef]
8. Mroziński, S. Energy-Based Method of Fatigue Damage Cumulation. *Int. J. Fatigue* **2019**, *121*, 73–83. [CrossRef]
9. Junak, G.; Marek, A.; Paduchowicz, M. Impact of Temperature on Low-Cycle Fatigue Characteristics of the HR6W Alloy. *Materials* **2021**, *14*, 6741. [CrossRef]
10. Okrajni, J.; Marek, A. The Attempt of the Low-Cycle Fatigue Life Description of Chosen Creep-Resistant Steels under Mechanical and Thermal Interactions. *Arch. Metall. Mater.* **2017**, *62*, 2349–2353. [CrossRef]
11. Lachowicz, C.T.; Wydawnicza, P.O.O. *Energetyczna Metoda Analizy Zmęczenia Materiałów, Elementów Maszyn i Konstrukcji*; Studia i Monografie—Politechnika Opolska; Oficyna Wydawnicza Politechniki Opolskiej: Opole, Poland, 2013; ISBN 9788364056048.
12. Okrajni, J.; Wacławiak, K. The Impact of Temperature Oscillations and Heat Transfer Conditions in Thick-Walled Elbows and Tubes on the Local Stress-Strain Behaviour during the Fast Start-up of Power Boilers. *Eng. Trans.* **2019**, *67*, 579–591.
13. Okrajni, J.; Junak, G.; Marek, A. Modelling of the Deformation Process under Thermo-Mechanical Fatigue Conditions. *Int. J. Fatigue* **2008**, *30*, 324–329. [CrossRef]
14. Wang, H.; Wan, M.; Wu, X.; Yan, Y. The Equivalent Plastic Strain-Dependent Yld2000-2d Yield Function and the Experimental Verification. *Comput. Mater. Sci.* **2009**, *47*, 12–22. [CrossRef]
15. *EN 12952-4*; Kotły Wodnorurowe i Urządzenia Pomocnicze Część 4: Obliczenia Oczekiwanej Trwałości Kotłów Podczas Eksploatacji. Polski Komitet Normalizacyjny: Warszawa, Poland, 2002.
16. Giglio, M. Fatigue Analysis of Different Types of Pressure Vessel Nozzle. *Int. J. Press. Vessel. Pip.* **2003**, *80*, 1–8. [CrossRef]
17. Miner, M.A. Cumulative Damage in Fatigue. *J. Appl. Mech.* **1945**, *12*, A159–A164. [CrossRef]
18. Ewing, J.A.; Humfrey, J.C.W. The Fracture of Metals under Repeated Alternations of Stress. *Philos. Trans. R. Soc.* **1903**, *A200*, 241–250.
19. Farragher, T.P.; Scully, S.; O'Dowd, N.P.; Leen, S.B. Development of Life Assessment Procedures for Power Plant Headers Operated under Flexible Loading Scenarios. *Int. J. Fatigue* **2013**, *49*, 50–61. [CrossRef]
20. Farragher, T.P.; Scully, S.; O'Dowd, N.P.; Leen, S.B. Thermomechanical Analysis of a Pressurized Pipe Under Plant Conditions. *J. Press. Vessel Technol.* **2012**, *135*, 011204. [CrossRef]
21. Twardawa, M.; Okrajni, J. The Influence of the Grade of Materials and Their State on the Thermo-Mechanical Behaviour of the Chosen Power Plant Components. *Solid State Phenom.* **2016**, *250*, 238–243. [CrossRef]
22. Łagoda, T.; Kurek, M.; Głowacka, K. A Formulation of the Criterion for Multiaxial Fatigue in Terms of Complex Number as Proposed by Macha. *Int. J. Fatigue* **2020**, *133*, 105430. [CrossRef]
23. Mrzygłód, M.W.; Łagoda, T. Numerical Procedures of Multiaxial Fatigue for Structural Design. *AIP Conf. Proc.* **2018**, *2028*, 020012. [CrossRef]
24. Carpinteri, A.; Vantadori, S.; Łagoda, T.; Karolczuk, A.; Kurek, M.; Ronchei, C. Fatigue Assessment of Metallic Components under Uniaxial and Multiaxial Variable Amplitude Loading. *Fatigue Fract. Eng. Mater. Struct.* **2018**, *41*, 1306–1317. [CrossRef]
25. Jacobsson, L.; Persson, C.; Melin, S. Thermo-Mechanical Fatigue Crack Propagation Experiments in Inconel 718. *Int. J. Fatigue* **2009**, *31*, 1318–1326. [CrossRef]
26. Kim, D.; Gerstberger, U.; Asli, M.; Höschler, K. U-Net Driven Semantic Segmentation for Detection and Quantification of Cracks on Gas Turbine Blade Tips. *Results Eng.* **2026**, *29*, 108864. [CrossRef]
27. Barrett, R.A.; Farragher, T.P.; Hyde, C.J.; O'Dowd, N.P.; O'Donoghue, P.E.; Leen, S.B. A Unified Viscoplastic Model for High Temperature Low Cycle Fatigue of Service-Aged P91 Steel. *J. Press. Vessel Technol. Trans. ASME* **2014**, *136*, 021402. [CrossRef]
28. Owsiński, R.; Kowalski, M. Fatigue Performance of Additively Manufactured Ti6Al4V: Effects of Printing Parameters and FEM-Based Residual Stress Analysis. *Measurement* **2025**, *254*, 118004. [CrossRef]
29. Bartošák, M.; Mára, V.; Slaný, M.; Šulák, I. Effect of Phase Angle on Thermo-Mechanical Fatigue Behaviour of Boron-Added 9% Cr Martensitic Steel. *Eng. Fract. Mech.* **2025**, *330*, 111650. [CrossRef]

https://doi.org/10.3390/ma19050891

30. Huang, C.M.; Herrmann, J.W. Durability Distribution Prediction of Thermo-Mechanical Solder Fatigue Failure with Uncertainty Propagation by Eigenvector Dimension Reduction Method. *Microelectron. Reliab.* **2024**, *161*, 115453. [CrossRef]
31. Walat, K.; Łagoda, T. Orientacja Płaszczyzny Krytycznej Przy Wyznaczaniu Trwałości Zmęczeniowej w Funkcji Granic Zmęczenia. *Model. Inżynierskie* **2011**, *10*, 421–428.
32. Purzyńska, H.; Golański, G.; Zieliński, A.; Dobrzański, J.D.; Sroka, M. Precipitation Study in Ti-Stabilised Austenitic Stainless Steel after 207,000 h of Service. *Mater. High Temp.* **2019**, *36*, 296–303. [CrossRef]
33. Mroziński, S.; Golański, G. Study of Influence of Heat Treatment on Cyclic Properties of L21HMF Cast Steel. *J. Mater. Eng. Perform.* **2016**, *25*, 3007–3016. [CrossRef]
34. Dziuba-Kałuża, M.; Zieliński, A.; Dobrzański, J.; Sroka, M.; Urbańczyk, P.; Śliwa, A. Residual Life of Boiler Pressure Parts Made of the 13CrMo4-5 Steel after Long-Term Operation in a Creep Conditions. *Arch. Metall. Mater.* **2018**, *63*, 889–897. [CrossRef]

Disclaimer/Publisher's Note: The statements, opinions and data contained in all publications are solely those of the individual author(s) and contributor(s) and not of MDPI and/or the editor(s). MDPI and/or the editor(s) disclaim responsibility for any injury to people or property resulting from any ideas, methods, instructions or products referred to in the content.

https://doi.org/10.3390/ma19050891

materials

MDPI

Article

Research and Development of Cement-Based Dynamic Water Grouting Material for the CSM Construction Method

Zhigang Yang [1], Fansheng Zhang [1], Yong Chang [2], Xihao Yang [1], Jianjian Li [2], Qiang Feng [1], Hongbo Wang [1,*] and Hao Tong [3]

[1] College of Civil Engineering and Architecture, Shandong University of Science and Technology, Qingdao 266590, China; 13325322936@163.com (Z.Y.); fansheng0228@163.com (F.Z.); 18263820556@163.com (X.Y.); fengqiang@sdust.edu.cn (Q.F.)
[2] The Fifth Engineering Co., Ltd., China Railway First Engineering Group, Baoji 721013, China; changyong202602@163.com (Y.C.); 13354443231@163.com (J.L.)
[3] College of Pipeline and Civil Engineering, China University of Petroleum, Qingdao 266580, China; 15079316585@163.com
* Correspondence: hongbo_wangsdu@163.com; Tel.: +86-18764008288

Abstract

Cutter soil mixing (CSM) is a widely adopted construction technique for forming waterproof diaphragm walls in underground engineering. However, cement slurry is prone to dispersion loss and performance degradation in moving water, making it difficult to meet engineering requirements. In this study, based on the characteristics of the CSM method in dynamic water environments, ordinary Portland cement is used as the main material, and hydroxypropyl methyl cellulose (HPMC), redispersible latex powder, polypropylene fiber and a polyether defoamer are added to improve it. The influence of each component on the performance of the new material is investigated, and a new CSM material suitable for dynamic water environments is developed. The material has good stability and suitable fluidity, controllable setting time, good anti-dispersion performance in dynamic water. The optimal mix ratio is as follows: water–cement ratio of 1; HPMC 1.4%; redispersible latex powder 3%; polypropylene fiber 0.4%; and polyether defoamer 0.8%. Field tests show that the new grouting material applied to CSM waterproof curtain construction results in a leak-free wall with excellent waterproofing performance, which verifies its engineering feasibility and provides a technical reference for the application of the CSM method in dynamic water environments.

Keywords: dynamic water environment; CSM construction method; drouting material; anti-dispersion; impermeability

1. Introduction

With the development of underground space toward more complex hydrogeological conditions, grouting reinforcement technology under dynamic water conditions has become a key problem in foundation treatment, tunnel anti-seepage and other projects. As an efficient cement–soil mixing method, the CSM method can form a large-diameter and high-strength cement–soil curtain, making it suitable for the construction of water-stop curtains in composite strata. However, in dynamic water environment, slurry is susceptible to water erosion, resulting in dispersion loss, uncontrolled setting time and deterioration of mechanical properties, which seriously affect the quality and safety of the project. The anti-dispersion and stability of traditional grouting materials under dynamic water conditions

are insufficient, and it is difficult to meet the CSM method's synergistic requirements for material fluidity, setting time and anti-scouring ability. Developing specialized grouting materials tailored for dynamic water environments is therefore an imperative research and engineering priority.

At present, scholars at home and abroad have made considerable progress in the research and development of dynamic water grouting materials, the study of slurry diffusion laws, and the optimization of construction technologies. In their research on modified cement-based grouting materials, Wu et al. [1] found that for polyacrylate latex-modified cement grouting materials subjected to dynamic water scouring, increasing the polymer–cement ratio can mitigate the deterioration of pore structure and mechanical properties. Wang et al. [2] developed a new type of water-rich grouting material with prominent plastic deformation characteristics by adding setting accelerators, alkali activators and other additives, enabling it to adapt to borehole deformation. Li et al. [3] optimized the performance of water-rich grouting materials via the response surface methodology and identified the water–cement ratio as the most critical factor affecting material performance. Wang et al. [4] prepared a new type of nano-composite cement-based dynamic water grouting material by introducing various additives into the composite material of sulphoaluminate cement and ordinary Portland cement. Wang et al. [5] developed a modified cement–clay grouting material whose scouring retention rate is 30% higher than that of cement slurry at a water flow velocity of 1.2 m/s, with a significantly reduced volume shrinkage rate. Yu et al. [6] developed a red mud-based grouting material using red mud industrial solid waste as the main raw material; this material integrates the advantages of green low-carbon characteristics and high performance and exhibits excellent injectability and diffusivity in water-rich sand layers. In the field of polymer and chemical grouting materials, Li et al. [7] synthesized a superabsorbent expandable polymer grouting material with an expansion ratio of 1:300, which effectively solves the problems of easy dilution and difficult solidification of traditional materials. Feng et al. [8] developed a new type of polyurethane water plugging material that can react normally under the condition of extensive water seepage in fractured coal and rock mass with adjustable gel time, realizing the integration of water plugging and reinforcement in one step. Song et al. [9] clarified the plugging parameters of polyurethane slurry in multi-stratum media under dynamic water conditions through experiments, providing specific technical guidance for the emergency treatment of water inrush in foundation pits.

In the research on slurry performance and mechanical characteristics, Li et al. [10] confirmed that silica fume and fibers can enhance the strength of the slurry, and redispersible polymer powder can improve the erosion resistance of the slurry. Ou et al. [11] systematically analyzed the influence of cellulose ether molecular parameters on the mechanical properties of cement slurry and found that cellulose ether increases the porosity and reduces the strength of cement slurry, with a greater reduction amplitude in compressive strength than in flexural strength. Wang et al. [12] revealed the mechanism of dynamic water scouring-induced attenuation of mechanical properties of cement grouting materials through microscopic experiments, verifying that the increase in water flow velocity leads to a significant rise in the number of micropores in set cement, as well as an obvious decrease in compressive strength and elastic modulus. Zhang et al. [13] determined the optimal mix ratio of cement–fly ash grouting materials for goafs through mix ratio tests, providing a reference for the engineering application of grouting materials with high fly ash content.

In the research on slurry diffusion laws and grouting technologies, Liu et al. [14] developed a new type of grouting material suitable for dynamic water conditions by testing the pumpability, dynamic water retention rate and other indicators of slurry with different water–cement ratios and admixture contents. Zhu et al. [15] established a dynamic

https://doi.org/10.3390/ma19061167

water grouting model based on OpenFOAM (v1812) and found that the slurry diffusion under the action of dynamic water presents obvious asymmetry, and the water flow velocity and grouting rate have a significant impact on the diffusion distance. Gu et al. [16] and Li et al. [17] explored the influencing factors of the diffusion radius of dynamic water grouting in rock mass fractures and the rheological characteristics and diffusion mechanism of cement-based slurry with different water–cement ratios through experiments and theoretical modeling, respectively. They confirmed that the slurry viscosity has time-varying characteristics, which will be weakened with the increase in water–cement ratio. Wang et al. [18] built a visual grouting simulation system for karst straight pipelines, clarified that the dynamic water flow velocity is the external dominant factor affecting the diffusion and plugging distance of the new WIS grouting material, and proposed the action mechanism of the slurry–water velocity ratio. In terms of construction technologies, the dynamic water information-based grouting technology proposed by Yuan et al. [19] effectively improves the guidance and controllability of curtain grouting in karst water-rich tunnels through geological data update, grouting scheme optimization and on-site dynamic control. The ultra-fine cement-based grouting material (EMCG) developed by Sha et al. [20] exhibits excellent diffusivity and reinforcement effect in water-rich sand layers, and its field application has confirmed that it can effectively improve the integrity and stability of the stratum.

In addition, some scholars have developed magnetically driven cement-based grouting materials, erosion-resistant polymer grouting materials and other materials [21–26]. Some of these materials show a significant increase in retention rate under dynamic water erosion, or can harden rapidly with the strength of the consolidated body close to that of wet soil. At the same time, numerous studies have focused on the influence of grouting pressure and slurry type on dynamic water grouting diffusion [27–30], providing theoretical support for the optimization of dynamic water grouting processes.

Although the above research has achieved certain results, it has not yet formed a grouting material suitable for CSM construction under dynamic water conditions. Therefore, in this paper, ordinary Portland cement is used as the main material, and hydroxypropyl methyl cellulose, redispersible latex powder, polypropylene fiber and polyether defoamer are added for modification. The orthogonal test method is used to systematically explore and determine the optimal ratio of slurry materials. Combined with field engineering application, the aim is to solve the problems of easy dispersion and the low retention rate of ordinary Portland cement slurry in dynamic water and to provide technical support for constructing waterproof curtains in dynamic water.

2. Materials Selection

The dynamic water grouting material needs to have both basic performance, economy and environmental protection. Aiming at the problems of the low retention rate of common cement and cement–chemical slurry in dynamic water, poor reinforcement effect, high cost of chemical slurry and the risk of pollution, when developing new grouting materials for CSM underwater construction, ordinary Portland cement with low price, environmental protection and excellent performance is selected as the matrix. Ordinary Portland cement has fast hydration, high strength, controllable setting, wear resistance and frost resistance, and strong engineering adaptability, but it lacks anti-dispersion. Therefore, it is necessary to improve its performance by adding admixtures.

The additives include: hydroxypropyl methyl cellulose, which can improve the anti-dispersion of the slurry and improve the retention rate of dynamic water by reducing the segregation rate and increasing the viscosity; redispersible latex powder, which can enhance waterproof and aggregate bonding and improve impermeability and erosion resistance;

https://doi.org/10.3390/ma19061167

polypropylene fiber, which can enhance the integrity and cohesion of cement structure and optimize crack resistance, impact resistance and other properties; and polyether defoamer, which can reduce bubbles and increase compactness to improve strength and durability. In addition, each component also needs to have good compatibility; that is, after the admixture is added to the slurry, it should not destroy the structure of the cement or cause adverse chemical reactions such as precipitation or decomposition, and the components should remain well coordinated.

3. Test Materials and Methods

3.1. Test Raw Materials

The P.O 42.5 ordinary Portland cement produced by Henan Mengdian Group Cement Co., Ltd., Xinxiang, China was selected for the test, and its basic performance parameters are shown in Table 1. Hydroxypropyl methyl cellulose (HPMC) is a type of mixed cellulose ether and also a polymer surfactant. The test used hydroxypropyl methyl cellulose with a viscosity of 200,000. The redispersible latex powder was produced by Shijiazhuang Chuangsheng Building Materials Technology Co., Ltd., Shijiazhuang, China and its appearance is a white powder. Polypropylene fiber was produced by Shandong Kaiwei New Material Co., Ltd., Tai'an, China and its parameters are shown in Table 2. Polypropylene fibers with this diameter and length can not only effectively fill the internal pores of the structure, but also be uniformly dispersed in the structure. Polyether defoamer is a non-ionic surfactant, which is easily soluble in water. It has not only good compatibility, but also good defoaming performance.

Table 1. Basic properties of cement.

Specific Surface Area (m^2/kg)	Fineness (%)	Setting Time (min)		Flexural Strength (MPa)		Compressive Strength (MPa)	
		Initial Setting	Final Setting	3 d	28 d	3 d	28 d
377	6.4	202	263	5.5	9.8	31.3	49.6

Table 2. Polypropylene fiber parameters.

Diameter (μm)	Length (mm)	Density (g/cm^3)	Tension Strength (MPa)	Elastic Modulus (MPa)	Extension at Break (%)
38	6	0.91	550	3850	28

3.2. Orthogonal Test Program

In this paper, before the start of the orthogonal test, the four influencing factors of the study were examined individually. Slurry fluidity, setting time, strength and anti-dispersion performance were used as indicators to determine the optimal ratio range of the four single factors. It was concluded that the main effect of adding polyether defoamers is to eliminate bubbles in the slurry, which has little effect on the performance of the grouting material. In order to simplify the orthogonal test, the influence of its dosage was not analyzed further. When the content of polyether defoamer is 0.8%, it can not only achieve good defoaming performance, but also effectively improve the fluidity, flexural strength and compressive strength. Therefore, the content of polyether defoamer was 0.8% in the orthogonal test. Next, through the orthogonal test, the multi-factor analysis method was used to study the influence of each component on the anti-dispersion, fluidity, stability, setting time, flexural strength and compressive strength of the slurry, and to regulate

https://doi.org/10.3390/ma19061167

the performance of the grouting material. The optimal level combination of the test was obtained, and the CSM method was applied in the dynamic water grouting project to optimize the ratio of the material to achieve the best performance. For this orthogonal experiment, four key factors affecting the properties of the slurry were selected: water–cement ratio (A), hydroxypropyl methyl cellulose (HPMC) content (B), redispersible latex powder content (C), and polypropylene fiber content (D). Three dosage levels were set for each factor, and a four-factor, three-level orthogonal test (L9 (3^4)) was subsequently conducted. According to the results of the single-factor test, the water–cement ratio was 1, the content of HPMC was 1.4%, the content of redispersible latex powder was 2%, and the content of polypropylene fiber was 0.4%. The adjacent content was selected as the content level of the orthogonal test. The selected content level and orthogonal test scheme are shown in Tables 3 and 4. The contents of various materials in the table are based on the quality of the ordinary Portland cement base.

Table 3. Orthogonal experimental factor level table.

Horizontal	Factors			
	Water–Cement Ratio (A)	**HPMC (B)/%**	**Redispersible Latex Powder (C)/%**	**Polypropylene Fiber (D)/%**
1	0.8	1.3	1	0.3
2	1	1.4	2	0.4
3	1.2	1.5	3	0.5

Table 4. Orthogonal experimental plan.

Test Scheme	A	B/%	C/%	D/%
1	0.8	1.3	1	0.3
2	0.8	1.4	2	0.4
3	0.8	1.5	3	0.5
4	1	1.3	2	0.5
5	1	1.4	3	0.3
6	1	1.5	1	0.4
7	1.2	1.3	3	0.4
8	1.2	1.4	1	0.5
9	1.2	1.5	2	0.3

4. Experimental Results and Analyses

The test results in Table 5 are obtained by testing the fluidity, initial setting time, final setting time, mechanical strength of different ages and retention rate under different flow velocity conditions for each group of orthogonal test schemes.

https://doi.org/10.3390/ma19061167

Table 5. Orthogonal experimental results.

Test Scheme	Fluidity (mm)	Setting Time (min)		Flexural Strength (MPa)			Compressive Strength (MPa)			Retention Rate (%)		
		Initial Setting Time	Final Setting Time	3 d	7 d	28 d	3 d	7 d	28 d	0.2 m/s	0.4 m/s	0.6 m/s
1	190	492	561	2.38	2.61	3.02	9.39	12.27	18.41	98	95	86
2	183	503	573	2.43	2.84	3.23	9.02	12.01	18.92	98	98	89
3	184	512	584	2.51	2.89	3.40	8.42	11.99	18.44	99	99	93
4	218	639	695	1.97	2.25	2.64	5.75	10.36	14.77	94	92	85
5	225	643	711	1.94	2.19	2.56	5.91	10.87	14.93	97	91	88
6	207	635	708	1.88	2.14	2.53	4.13	9.57	14.14	97	93	83
7	247	674	741	1.45	1.49	1.76	3.77	7.59	11.13	90	80	69
8	244	681	742	1.48	1.54	1.81	2.99	7.01	11.02	92	80	64
9	230	693	755	1.41	1.47	1.66	3.17	6.37	10.71	93	81	67

4.1. Stability Analysis

According to the orthogonal test scheme, the water separation rate of the material was tested. No bleeding occurred in each group of schemes, and the slurry had good stability. This is because HPMC and redispersible latex powder have good water retention, which can not only absorb free water in the slurry, but also encapsulate water molecules in the slurry, prevent the loss of water in the slurry, and prevent the segregation and stratification of the slurry. The addition of HPMC and redispersible latex powder in the dynamic water grouting material can greatly improve the stability of the slurry.

4.2. Analysis of Fluidity

The range analysis of the test results for the fluidity in the orthogonal test scheme is shown in Figure 1. From the diagram, it can be seen that the primary and secondary relationships affecting the fluidity of the slurry are the water–cement ratio, hydroxypropyl methyl cellulose, redispersible latex powder, and polypropylene fiber. The combination ratio with better fluidity is A3B1C3D1; that is, the water–cement ratio is 1.2, HPMC is 1.3%, redispersible latex powder is 3%, and polypropylene fiber is 0.3%.

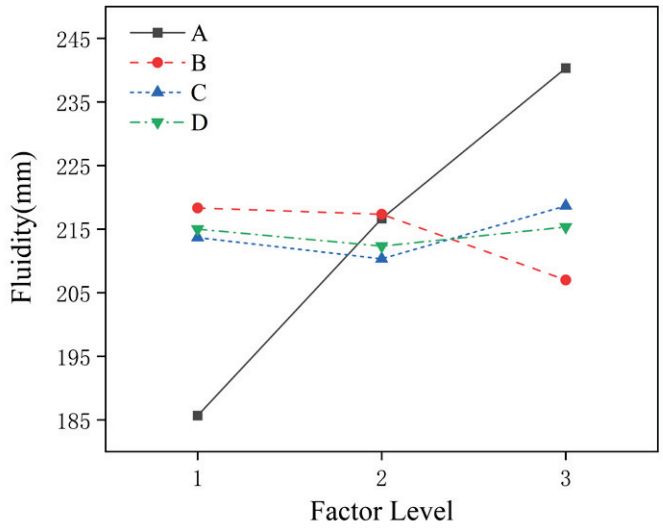

Figure 1. The influence of different factors on the fluidity of the slurry.

https://doi.org/10.3390/ma19061167

The water–cement ratio is the most important factor affecting the fluidity of the slurry. The fluidity of the slurry increases with the increase in the water–cement ratio. The increase in the water–cement ratio increases the content of free water in the slurry, thereby increasing the fluidity of the slurry. The amount of HPMC also has a significant effect on the fluidity of the slurry. HPMC can increase the viscosity of the slurry, reduce the content of free water in the slurry, and reduce the fluidity of the slurry. After the redispersible latex powder is added to the slurry, it can have a lubricating effect on the slurry and increase fluidity. Polypropylene fiber can increase the flow resistance of the slurry and have an adverse effect on fluidity.

4.3. Analysis of Setting Time

According to the range analysis of the condensation time based on the orthogonal test results, Figure 2 is obtained. From the diagram, it can be seen that the primary and secondary relations of the factors affecting the initial setting time of the slurry are the water–cement ratio, hydroxypropyl methyl cellulose, redispersible latex powder, and polypropylene fiber. The primary and secondary factors affecting the final setting time of the slurry are the water–cement ratio, hydroxypropyl methyl cellulose, redispersible latex powder, and polypropylene fiber. The water–cement ratio is the most significant factor affecting the setting time of the slurry, and the setting time of the slurry increases with the increase in the water–cement ratio. HPMC also has an important influence on the setting time of the slurry, and the setting time of the slurry increases with the increase in HPMC content. Although the effect of HPMC content in the ranges of 1.3%, 1.4% and 1.5% on the setting time is not as significant as the water–cement ratio, through the previous single-factor test analysis, it can be concluded that the setting time of the slurry can be significantly prolonged compared with the net slurry after adding HPMC. HPMC can not only form a three-dimensional network structure in the slurry, encapsulate the particles in the slurry, and reduce the contact opportunities between the particles during the hydration process, but also increase the viscosity of the slurry and the movement resistance of the particles during the hydration process, thus prolonging the setting time of the slurry. Therefore, the setting time of the slurry can meet the construction requirements of the CSM method by selecting a reasonable water–cement ratio and HPMC content to ensure that the slurry has excellent working performance.

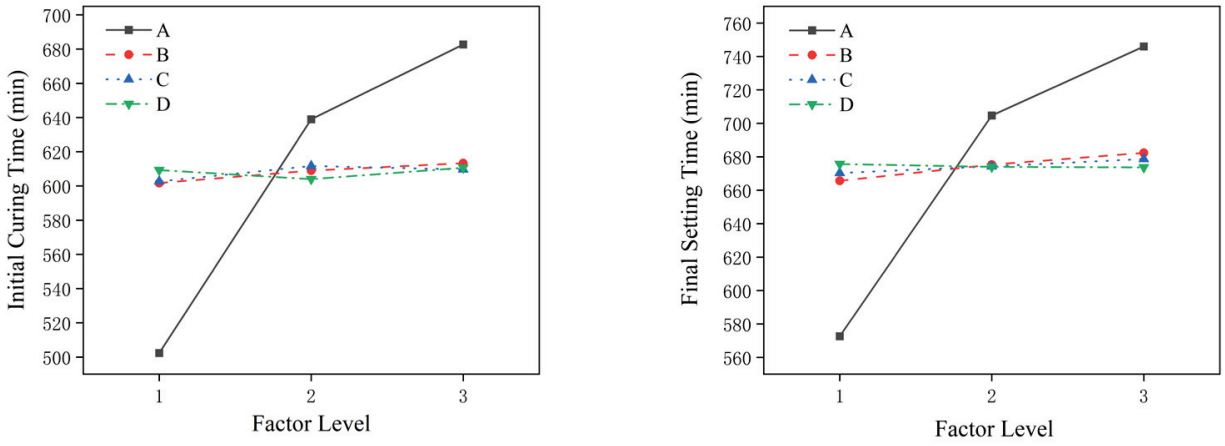

(**a**) Initial curing time (**b**) Final setting time

Figure 2. The influence of different factors on the coagulation time of the slurry.

The setting time of the slurry in the dynamic water grouting project should not be too long. The long setting time will reduce the retention rate due to the long scouring time,

https://doi.org/10.3390/ma19061167

which will affect the effect of grouting. For the CSM construction method, the slurry setting time should not be too short, as setting time that is too short will jam the construction machinery and affect the construction progress. Therefore, a better combination for the initial setting time is A2B2C3D1; that is, a water–cement ratio of 1; HPMC at 1.4%; redispersible latex powder at 3%; and polypropylene fiber at 0.3%. The better combination for the final setting time is A2B2C2D2; that is, a water–cement ratio of 1; HPMC at 1.4%; redispersible latex powder at 2%; and polypropylene fiber at 0.4%.

4.4. Strength Analysis

(1) Flexural Strength

Figure 3 is obtained by range analysis of the flexural strength of different ages (no fewer than three groups, with the average value taken) in the orthogonal test of the slurry. It can be seen from the figure that the primary and secondary factors affecting the flexural strength of the slurry at 3 d, 7 d and 28 d are the water–cement ratio, polypropylene fiber, redispersible latex powder, and hydroxypropyl methyl cellulose. The better combination is A1B2C3D, that is, a water–cement ratio 0.8, HPMC at 1.4%, redispersible latex powder at 3%, and polypropylene fiber at 0.5%.

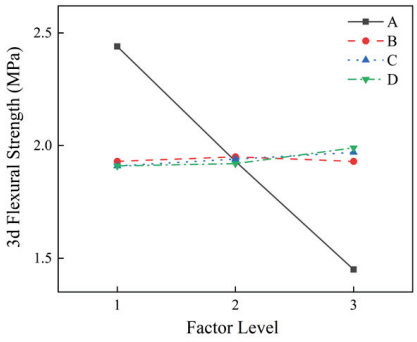

(**a**) 3 d Flexural strength

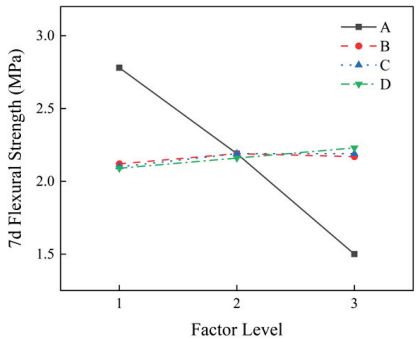

(**b**) 7 d Flexural strength

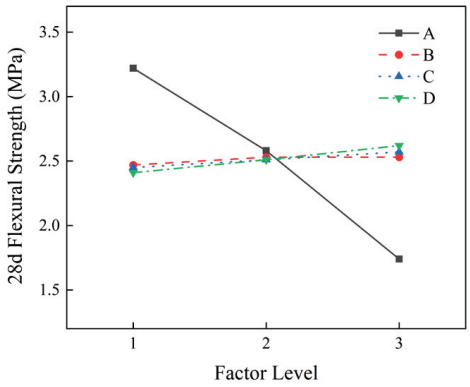

(**c**) 28 d Flexural strength

Figure 3. The influence of different factors on the flexural strength of the slurry.

The most important factor affecting flexural strength is the water–cement ratio, and the flexural strength of the slurry decreases with the increase in the water–cement ratio. The redispersible latex powder and polypropylene fiber also have a significant effect on the flexural strength of the slurry, and flexural strength increases with the increase in their contents. The polypropylene fiber can be uniformly dispersed in the slurry to form a network structure, which increases the traction force inside the stone body and increases the

https://doi.org/10.3390/ma19061167

flexural strength. The redispersible latex powder can improve the viscosity and toughness of the slurry and have a favorable effect on the flexural strength. Due to the addition of a defoaming agent in the orthogonal test, the effect of bubbles on the flexural strength was reduced, so HPMC had no significant effect on the flexural strength.

(2) Compressive Strength

The results of range analysis of compressive strength at different ages (no fewer than three groups, with the average value taken) are shown in Figure 4. It can be seen from the figure that the primary and secondary factors affecting the compressive strength of the slurry at 3 d, 7 d and 28 d are the water–cement ratio, hydroxypropyl methyl cellulose, redispersible latex powder, and polypropylene fiber. The better combination is A1B1C3D3, namely a water–cement ratio 0.8, HPMC at 1.3%, redispersible latex powder at 3%, and polypropylene fiber at 0.5%.

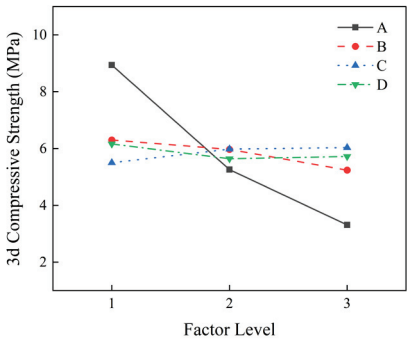

(**a**) 3 d Compressive strength

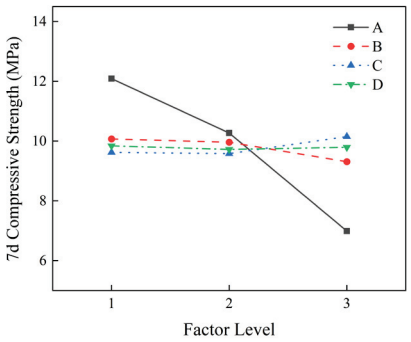

(**b**) 7 d Compressive strength

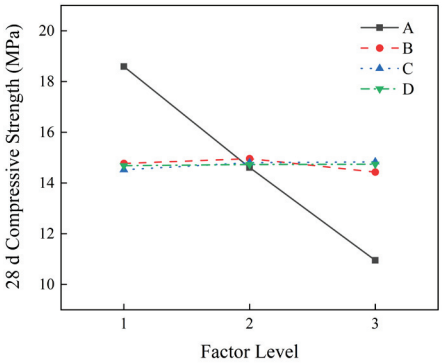

(**c**) 28 d Compressive strength

Figure 4. The influence of different factors on the compressive strength of the slurry.

The water–cement ratio is the most significant factor affecting the compressive strength of the slurry, and the compressive strength decreases with the increase in the water–cement ratio. Although the addition of defoamer to the slurry eliminates some bubbles, it cannot completely eliminate the influence of bubbles on the compressive strength of the slurry. HPMC can increase the number of bubbles in the slurry, reduce the density of the stone body, and lead to a decrease in compressive strength. In addition, after HPMC is added to the slurry, it wraps the cement particles, which is not conducive to the development of the hydration reaction and results in decreased strength. The redispersible latex powder and polypropylene fiber have two effects on the compressive strength of the slurry: on the one hand, they can physically fill the internal pores of the structure and have a beneficial effect on the compressive strength of the slurry; on the other hand, they can increase the toughness of the stone body and adversely affect the compressive strength of the slurry.

https://doi.org/10.3390/ma19061167

4.5. Analysis of Dynamic Water Retention Rate

The most important performance of the grouting material is the anti-dispersion performance of the slurry in moving water. Slurry with good anti-dispersion is not easily lost under moving water and has a high retention rate. Through analysis of the data in the orthogonal test, it can be seen that the slurry also has a high retention rate in dynamic water with a flow rate of 0.6 m/s, indicating that it can resist erosion at a certain flow rate, and has good anti-dispersion performance in dynamic water. The retention rate in moving water shows a downward trend with the increase in flow velocity, which is due to the strong scouring ability of flow with large flow velocity. Range analysis of the test data was carried out, and the results for the slurry retention rate at different flow rates were obtained, as shown in Figure 5. The primary and secondary factors affecting the retention rate of the slurry at a flow rate of 0.2 m/s can be obtained from the figure: water–cement ratio, hydroxypropyl methyl cellulose, polypropylene fiber, and redispersible latex powder. The better combination is A1B3C1D1; that is, a water–cement ratio of 0.8, HPMC 1.5%, redispersible latex powder 1%, polypropylene fiber 0.3%. The primary and secondary factors affecting the retention rate of the slurry at a flow rate of 0.4 m/s are the water–cement ratio, hydroxypropyl methyl cellulose, polypropylene fiber, and redispersible latex powder. The better combination is A1B3C2D2; that is, a water–cement ratio of 0.8, HPMC 1.5%, redispersible latex powder 2%, and polypropylene fiber 0.4%. The primary and secondary factors affecting the retention rate of the slurry at a flow rate of 0.6 m/s are the water–cement ratio, redispersible latex powder, hydroxypropyl methyl cellulose, and polypropylene fiber. The better combination is A1B3C3D3; that is, a water–cement ratio of 0.8, HPMC 1.5%, redispersible latex powder 3%, and polypropylene fiber 0.5%.

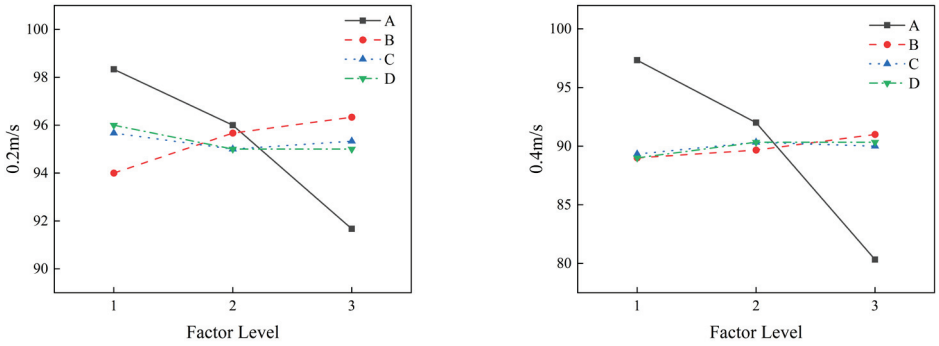

(**a**) Flow velocity 0.2 m/s

(**b**) Flow velocity 0.4 m/s

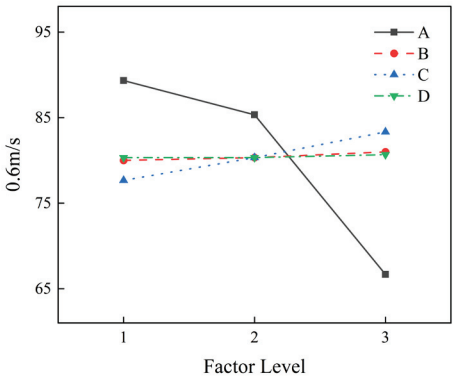

(**c**) Flow velocity 0.6 m/s

Figure 5. The influence of different factors on the retention rate of the slurry.

https://doi.org/10.3390/ma19061167

The most influential factor on the slurry retention rate at different water flow rates is the water–cement ratio. The retention rate of the slurry decreases with the increase in the water–cement ratio, which means that the anti-dispersion of the slurry decreases with the increase in the water–cement ratio. The reason for this phenomenon is that with the increase in water–cement ratio, the content of free water in the slurry increases, which leads to an decrease in the viscosity of the slurry, an increase in the fluidity of the slurry, and the weakening of the resistance to water flow. On the other hand, the content of free water under different water–cement ratios is quite different. Due to the small range of HPMC content selected in the orthogonal test, the ability of HPMC to bind free water within the range of this content does not differ significantly. As the water–cement ratio increases, the effect of HPMC on increasing slurry viscosity gradually decreases, resulting in a decrease in slurry retention rate.

In the process of studying the influencing factors of the retention rate, the influence of water–cement ratio on the retention rate of the slurry was not analyzed. When the flow velocity is less than 0.6 m/s, the main factors affecting the retention rate of the slurry are HPMC and polypropylene fiber. When the water flow rate is greater than 0.6 m/s, the main factor affecting the slurry retention rate is redispersible latex powder. Under the condition of low flow rate, the addition of HPMC and polypropylene fiber can improve the retention rate of the slurry. This is because HPMC is a high-molecular polymer with functional groups that adsorb particles in the slurry. The HPMC molecular chains in the slurry can be interlaced to form a stable three-dimensional network structure, so that the particles are connected and the cohesion is increased. The viscosity of the slurry is improved, and the slurry is not easily dispersed. Polypropylene fiber can interlace into a network structure within the slurry, increasing the integrity of the structure, improving the traction force between the internal structures, and improving the anti-erosion performance of the slurry. Under high-flow rate conditions, the addition of redispersible latex powder can significantly improve the retention rate of the slurry. This is because redispersible latex powder can be uniformly dispersed in the slurry and form a mucosa. As an adhesive, it can play a reinforcing role, increase the bonding performance between the materials, and significantly improve the cohesion of the slurry, enabling it to resist the erosion of high-flow-rate water.

According to the comprehensive analysis, the CSM construction method requires grouting materials with excellent anti-dispersion performance and a high dynamic water retention rate for construction under dynamic water conditions. Additionally, the materials should possess appropriate fluidity and a controllable setting time to facilitate mechanized construction, while their flexural and compressive strengths must be sufficiently high to resist the scouring impact of water flow. Therefore, the ratio of grouting materials in the CSM method under dynamic water is determined to be a water–cement ratio of 1, HPMC1.4%, redispersible latex powder 3%, polypropylene fiber 0.4%, and polyether defoamer 0.8%.

4.6. Analysis of Material Advantages

Compared with ordinary cement materials, the developed dynamic water grouting material has good anti-dispersion performance and high retention rate. Compared with chemical slurry materials, the material is cheap and environmentally friendly; compared with other dynamic water grouting materials, its strength, fluidity and setting time can be adequately applied to the CSM construction method construction projects, without affecting the operation of the mechanical milling wheel, ensuring good performance of the CSM wall. The addition of HPMC improves the dispersion resistance of the material. The addition of redispersible latex powder and polypropylene fiber improves erosion resistance.

https://doi.org/10.3390/ma19061167

In addition, polypropylene fiber also improves the crack resistance and impermeability of the material. The addition of polyether defoamer increases the strength and durability of the material.

5. Engineering Application

5.1. Engineering Situations

The Mangrove Forest Station is the intermediate station of the second phase of Qingdao Metro Line 6 (Qingxi Station~Xintun Road), as shown in Figure 6. It is located in the mangrove parking lot on the west side of the intersection of Binhai Avenue and Jingtaishan Road. The terrain of the station is relatively flat, and the site elevation ranges from 3.78 to 4.97 m. The geomorphic unit is mainly a coastal shoal landform. The foundation pit of Mangrove Station is 220 m long, 20.1–23.8 m wide and 21.85–24.1 m deep. The groundwater is mainly phreatic water and bedrock fissure water, both of which are abundant. The water depth is 2.8–4.6 m. There is no confined water at the station site. The annual variation in groundwater level is 1–2 m. The groundwater level in the coastal environment of the site is significantly affected by tidal action and surface runoff recharge. The stratum is mainly composed of clay layers, sand layers and other composite strata. It has strong permeability and is connected with the water layer, forming an active groundwater flow environment. The traditional waterproof curtain construction faces problems such as groove collapse, cement slurry dilution and erosion, and foundation pit leakage.

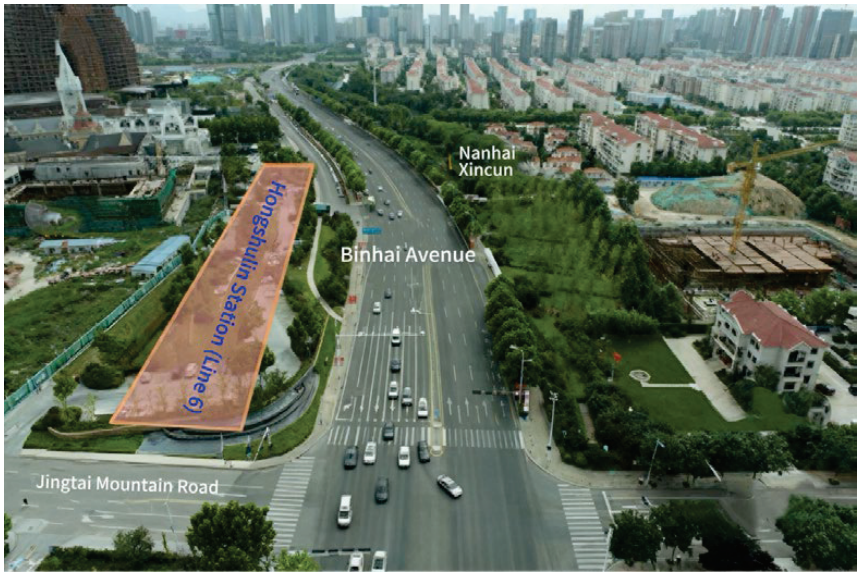

Figure 6. Station location distribution map.

5.2. Test Materials and Ratios

The commonly used construction materials in CSM construction are cutting fluid and curing fluid. The selected materials and ratios should meet not only the requirements of fluidity and setting time, but also of strength and impermeability of the wall. The bentonite slurry was used as the cutting fluid, and the developed dynamic water grouting material was used as the curing fluid. The material ratio was: P.O 42.5 ordinary Portland cement with a water–cement ratio of 1, HPMC at 1.4%, redispersible latex powder at 3%, polypropylene fiber at 0.4%, and polyether defoamer at 0.8%. The cement content of the solidified liquid in the cement soil should be 20%, and the specific content can be adjusted in real time according to the on-site construction situation (Figure 7), and should not be less than 20%.

https://doi.org/10.3390/ma19061167



Figure 7. CSM wall site construction drawing.

5.3. Wall Effect Verification

(1) Core drilling

After 28 days of CSM wall formation, drilling and coring were carried out on the wall to test the effect of wall formation. A total of 12 core samples with a diameter of 80 mm were taken, as shown in Figure 8. The unconfined compressive strength test and permeability coefficient test were carried out on the core samples. The tests were carried out according to 'Technical code for building foundation treatment' JGJ79-2012 [31]. The number of test blocks should not be fewer than three, and the average value should be taken as the strength and permeability coefficient of the test. Through the experimental test, the unconfined compressive strength is greater than 1 MPa and the permeability coefficient is less than 1×10^{-7} cm/s, which meets the requirements of the specification, indicating that the quality of the CSM wall is good.



Figure 8. Drilling and coring results.

(2) High-definition borehole TV detection

In order to intuitively judge the integrity of the CSM wall, high-definition borehole TV is used to observe the surface of the borehole in the wall, and to detect whether there are holes and loose defects in order to verify the wall-forming effect. The inspection using high-definition borehole TV is shown in Figure 9. As can be seen, there are no obvious defects in the wall borehole, and the quality is good.

https://doi.org/10.3390/ma19061167



Figure 9. Drilling TV effect.

(3) Site construction situation

The retaining structure around the foundation pit during excavation is shown in Figure 10. It can be seen from the figure that there is no leakage on the side wall of the foundation pit. During the excavation process, there was no water gushing or sand gushing on the side wall and the bottom of the pit, and the water-stopping effect of the CSM wall was good.



Figure 10. Retaining structure around the foundation pit during excavation (no leakage).

Through a series of measures such as borehole coring, high-definition borehole TV detection and on-site construction observation, the wall-forming effect of the wall was evaluated. The results show that the wall forming effect is good, which verifies the reliability of the research materials mentioned above, ensures the safe construction of foundation pit engineering, and provides a more stable grouting material for CSM construction under dynamic water conditions in the future.

6. Conclusions and Outlook

6.1. Conclusions

The effects of the water–cement ratio, HPMC, redispersible latex powder and polypropylene fiber on the stability, fluidity, setting time, flexural strength and compressive strength at different ages, and retention rate at different water flow rates of dynamic underwater grouting materials were investigated by an orthogonal test. The slurry performance was dynamically regulated, and the experimental formulations under different conditions

https://doi.org/10.3390/ma19061167

were optimized. The influence of different admixtures on the properties of solidified liquid materials was evaluated.

Through orthogonal experimental analysis, the optimal mix proportion of the grouting material for the CSM construction method under dynamic water conditions was determined as follows: a water–cement ratio of 1, a HPMC dosage of 1.4%, a redispersible polymer powder dosage of 3%, a polypropylene fiber dosage of 0.4%, and a polyether defoamer dosage of 0.8%. After optimizing the ratio through the orthogonal test, the R & D material shows good stability, suitable fluidity and controllable setting time under dynamic water conditions. The 28 d compressive strength reaches 14.93 MPa, and the retention rate in dynamic water at a flow velocity of 0.6m/s is more than 90%. The synergistic balance of anti-dispersion, construction and mechanical properties is achieved, meeting the needs of CSM dynamic water grouting project.

Based on the CSM method construction project at Mangrove Station of Qingdao Metro Line 6, engineering application was carried out. Verification of the wall-forming effect shows that the developed material provides good water-stopping performance without leakage, making it suitable for the construction of water-stop curtains using the CSM method in dynamic water environments.

The core innovation of this study is that it specifically addresses the technical challenge posed by the lack of special grouting materials for the CSM construction method in dynamic water environments, and overcomes the limitation of single-performance optimization for traditional dynamic water grouting materials. For the first time, the optimal mix ratio of a special dynamic water grouting material for the CSM construction method with clearly defined component proportions is determined. This fills the technical gap and provides a new material solution for the construction of waterproof curtains in composite strata under dynamic water conditions in underground engineering.

6.2. Outlook

Research on the adaptive optimization of the material for multi-scale complex dynamic water environments should be carried out. For extreme working conditions, including high-velocity dynamic water with a flow rate over 1.0 m/s, coastal tidal fluctuations, dry–wet alternation and salinized dynamic water, the mix ratio of admixtures should be adjusted or new functional admixtures introduced to enhance the material's resistance to scouring and salt corrosion as well as its environmental adaptability.

Research on the green modification and functional upgrading of the material should be conducted. On the premise of ensuring its core performance, industrial solid wastes such as fly ash, slag and silica fume should be used to replace part of the cement, so as to reduce the material's carbon emission and engineering cost and realize the green and low-carbon development of the grouting material.

Author Contributions: Conceptualization, H.W. and F.Z.; methodology, Z.Y., F.Z., H.W., Q.F. and H.T.; validation, Z.Y. and H.W.; formal analysis, F.Z.; investigation, Z.Y., X.Y. and F.Z.; resources, J.L. and Y.C.; writing—original draft, Z.Y. and X.Y.; writing—review and editing, Z.Y., X.Y., F.Z., H.W., Q.F. and H.T.; visualization, F.Z. and Z.Y.; supervision, Y.C. and J.L.; project administration, H.W., Y.C. and J.L.; funding acquisition, H.W., Y.C. and J.L. All authors have read and agreed to the published version of the manuscript.

Funding: This research received no external funding.

Data Availability Statement: The original contributions presented in this study are included in the article. Further inquiries can be directed to the corresponding author.

Conflicts of Interest: Authors Yong Chang and Jianjian Li were employed by the company The Fifth Engineering Co., Ltd. of China Railway First Engineering Group. The remaining authors declare that

https://doi.org/10.3390/ma19061167

the research was conducted in the absence of any commercial or financial relationships that could be construed as a potential conflict of interest.

References

1. Wu, L.; Wu, Z.; Weng, L.; Liu, Y.; Chu, Z.; Xu, X. Investigation on the pore size characteristics and mechanical properties of grouting materials scoured by flow water. *Int. J. Rock Mech. Min. Sci.* **2024**, *183*, 105923. [CrossRef]
2. Wang, B.; Li, B.; Huang, L.; Zhang, J. Study on the mechanical properties and microstructure of a rich-watered grouting material. *Mater. Today Commun.* **2023**, *35*, 106261. [CrossRef]
3. Li, X.; Han, G.; Wang, Y.; Xu, J.; Du, J.; Yang, B.; Zhang, M.; Li, T.; Li, B. Study on Performance Optimization of Water-Rich Grouting Materials Based on Response Surface Methodology. *Processes* **2023**, *11*, 2789. [CrossRef]
4. Wang, S.; Gong, R.; Li, Z.; Yuan, C.; Jiang, G.; Wang, J.; Chen, L.; Ye, C. Water-blocking nano-composite cement-based grouting materials. *Appl. Nanosci.* **2019**, *9*, 1565–1578. [CrossRef]
5. Wang, Z.Q.; Jiang, H.B. Experimental Study on Performance of Modified Cement-Clay Grouting Materials in Dynamic Water Environments. *Renmin Zhujiang* **2025**, *12*, 1–17.
6. Yu, K.P.; Wu, S.T.; Niu, J.D.; Yu, P.; Wan, X.B.; Qiu, L.L. Study on Properties of Red Mud Grouting Materials in Water-Rich Sand Stratum Treatment. *J. Railw. Sci. Eng.* **2025**, *22*, 5364–5378.
7. Li, S.; Ma, C.; Liu, R.; Chen, M.; Yan, J.; Wang, Z.; Duan, S.; Zhang, H. Super-absorbent swellable polymer as grouting material for treatment of karst water inrush. *Int. J. Min. Sci. Technol.* **2021**, *31*, 753–763. [CrossRef]
8. Feng, Z.Q.; Kang, H.P. Development and application of new waterproof grouting materials of polyurethane. *Chin. J. Geotech. Eng.* **2010**, *32*, 375–380.
9. Song, X.S.; Xu, C.; Yang, Z.; Zhang, W.J.; Liu, P.F.; Zhu, J.P. Experimental study on diffusion characteristics and water plugging effect of polyurethane grouting under dynamic water environment. *Mod. Tunn. Technol.* **2024**, *61*, 655–665. [CrossRef]
10. Li, X.; Sun, J.; Chen, W.; Yuan, J.; Liu, J.; Zhang, Q. Strength and anti-washout property of fiber silica fume cement grout. *Rock Soil Mech.* **2018**, *39*, 3157–3163.
11. Ou, Z.H.; Ma, B.G.; Jian, S.W. Effect of cellulose ether molecular parameters on mechanical properties of cement paste. *Bull. Chin. Ceram. Soc.* **2016**, *35*, 2371–2377.
12. Wang, H.L.; Luo, R.; Liu, X.Q. Effect of dynamic water scouring on mechanical properties of cement grouting material. *Bull. Chin. Ceram. Soc.* **2025**, *44*, 417–423.
13. Zhang, H.Y.; Bai, F.W.; Chen, B.K. Experimental Study on the Ratio of Cement-Fly Ash Grouting Material. *Mater. Sci.* **2025**, *15*, 846–853. [CrossRef]
14. Liu, R.; Zhang, L.; Zhang, Q.; Sun, Z.; Zheng, Z.; Wang, H.; Zhang, S. Model test on quick setting slurry diffusion law of crack grouting with dynamic water. *China Civ. Eng. J.* **2017**, *50*, 82–90.
15. Zhu, J.; Chen, J.X.; Zhang, Y.Y. Simulation of dynamic water grouting considering time-varying viscosity of slurry. *J. Zhejiang Univ. Technol.* **2023**, *51*, 180–186.
16. Gu, S.C.; Sun, G.L.; Su, P.L.; Li, J.H. Test of the influence of dynamic water grouting diffusion radius of fractures in rock. *Coal Geol. Explor.* **2019**, *47*, 144–149.
17. Li, L.C.; Wang, Y.T.; Mu, W.Q. Rheological Properties and Diffusion Mechanism of Cement-Based Slurries with Different Water-Cement Ratios. *J. Northeast. Univ.* **2025**, *46*, 104–115.
18. Wang, Z.J.; Zhang, Q.S.; Hui, B. Experimental Study on Diffusion Characteristics of WIS New Grouting Material in Tunnel Karst Conduit. *Mod. Tunn. Technol.* **2024**, *61*, 202–211.
19. Yuan, Y.R.; An, W.H.; Zhang, Y.T. Research on dynamic information-based grouting construction technology for dynamic water. *Mod. Tunn. Technol.* **2012**, *49*, 176–179.
20. Sha, F.; Li, S.C.; Liu, R.T. Performance and engineering application of effective microfine cement-based grout (EMCG) for water-rich sand strata. *Chin. J. Rock Mech. Eng.* **2019**, *38*, 1420–1433.
21. Wang, N.; Deng, Y.; Liu, S.; Chen, L. Study on the performance of new cement-based underwater building crack repair materials based on response surface analysis. *Sci. Rep.* **2025**, *15*, 18499. [CrossRef] [PubMed]
22. Liang, J.; Song, Z.; Fan, Z.; Wang, X. Study and application of a novel high-performance grouting material in the management of karst water inrush disasters. *Front. Earth Sci.* **2025**, *13*, 1556061. [CrossRef]
23. Yang, W.; Zeng, Y.; Bao, H.; Wu, Q.; Gao, H.; Pang, K. Development of cement-based grouting material containing high polymer and high-water resistance. *Constr. Build. Mater.* **2025**, *470*, 140660. [CrossRef]
24. Che, Z.; Wang, T.; Zhou, Z.; Wang, S.; Ma, X. Research on cement-free grouting material for shield tunneling in water-rich karst regions. *Materials* **2025**, *18*, 1192. [CrossRef]
25. Liu, J.; Peng, B.; Liu, S.; Yang, Y.N.; Xiong, M.; Wang, Z.B. Research and development of a new type of cement-based anti-scouring rapid setting grouting material and performance research. *Constr. Build. Mater.* **2025**, *469*, 140480. [CrossRef]

https://doi.org/10.3390/ma19061167

26. Li, S.; Zhang, J.; Li, Z.; Gao, Y.; Qi, Y.; Li, H.; Zhang, Q. Investigation and practical application of a new cementitious anti-washout grouting material. *Constr. Build. Mater.* **2019**, *224*, 66–77. [CrossRef]
27. Liu, X.; Wang, J.; Huang, K.; Li, F. Experimental study on dynamic water grouting of modified water-soluble polyurethane. *KSCE J. Civ. Eng.* **2019**, *23*, 3897–3906. [CrossRef]
28. Liu, R.T.; Li, S.C.; Zhang, Q.S.; Yuan, X.S.; Han, W.W. Experiment and application research on a new type of dynamic water grouting material. *Chin. J. Rock Mech. Eng.* **2011**, *30*, 1454–1459.
29. Wang, H.B.; Zhang, Q.S.; Liu, R.T.; Li, S.; Zhang, L.; Jiang, P. Test and process research of poor geological dynamic water plugging reinforcement material. *Chin. J. Rock Mech. Eng.* **2017**, *36*, 3984–3991.
30. Li, S.; Han, W.W.; Zhang, Q.S.; Liu, R.; Weng, X. Research on time-dependent behavior of viscosity of fast curing grouts in underground construction grouting. *Chin. J. Rock Mech. Eng.* **2013**, *32*, 1–7.
31. *JGJ 79-2012*; Technical Code for Ground Treatment of Buildings. China Architecture & Building Press: Beijing, China, 2012.

Disclaimer/Publisher's Note: The statements, opinions and data contained in all publications are solely those of the individual author(s) and contributor(s) and not of MDPI and/or the editor(s). MDPI and/or the editor(s) disclaim responsibility for any injury to people or property resulting from any ideas, methods, instructions or products referred to in the content.

https://doi.org/10.3390/ma19061167

materials

MDPI

Article

Research on Material Optimization of CSM Method Structures in Highly Weathered Strata

Yifan Xie [1], Haitao Liu [2], Hao Wen [1], Chuangui Sun [1], Yong Chang [2], Qiang Feng [1], Lianzhen Zhang [3] and Hongbo Wang [1,*]

[1] College of Civil Engineering and Architecture, Shandong University of Science and Technology, Qingdao 266590, China; 15865470329@163.com (Y.X.); wh990323@163.com (H.W.); 15020344356@163.com (C.S.); fengqiang@sdust.edu.cn (Q.F.)
[2] China Railway First Group No.5 Engineering Co., Ltd., Baoji 721006, China; 15269391279@163.com (H.L.); changyong202602@163.com (Y.C.)
[3] College of Pipeline and Civil Engineering, China University of Petroleum, Qingdao 266580, China; zhanglianzhen@upc.edu.cn
* Correspondence: hongbo_wangsdu@163.com; Tel.:+86-18764008288

Abstract

To address the challenges of low strength and poor impermeability of soil–cement walls formed with ordinary cement materials when applying the CSM (Cutter Soil Mixing) method in highly weathered strata, this study carried out structural optimization by combining the CSM method with H–section steel. This optimization effectively resolves issues such as low efficiency and high cost associated with the CSM method integrated with cement–filled piles. Meanwhile, using ordinary Portland cement as the base material, basalt fiber, sodium bentonite, and fly ash were added to investigate the influence of each component on the performance of the new composite. A novel CSM material suitable for highly weathered strata was developed, which exhibits excellent mechanical strength and impermeability. The optimal mix proportion of the soil–cement material was determined as follows: basalt fiber 0.5%, fly ash 15%, and sodium bentonite 3%. This research provides a quantitative basis for the efficient and economical application of the CSM method in highly weathered strata.

Keywords: CSM method; highly weathered strata; foundation support; basalt fiber–reinforced soil–cement material; H–section steel

1. Introduction

With the acceleration of urbanization in China, the scale of underground space development and utilization continues to expand, placing higher demands on foundation pit support technologies. Among various support techniques, the CSM (Cutter Soil Mixing) method has been widely applied in engineering fields such as cutoff walls, support structures, and ground improvement, due to its ability to form continuous walls by uniformly mixing in situ soil with cement slurry through a simultaneous cutting and mixing process. However, limited by the insufficient curing strength, poor impermeability, and high cost of ordinary cemented soil walls, the economic efficiency and construction speed of projects have been severely impacted. The current composite process that combines the traditional CSM method with cast–in–place piles struggles to meet the dual demands of modern engineering for both construction efficiency and economic viability, nor can it effectively address the core issues of inadequate mechanical properties and impermeability

of cemented soil walls in foundation pit support. Therefore, there is an urgent need to develop structurally optimized solutions and to research new cementitious materials.

Traditional support techniques, including deep mixing piles and TRD (Trench Cutting Mixed Deep Wall) methods, are frequently associated with limitations such as inadequate strength, inconsistent waterproofing performance, and poor adaptability to heterogeneous rock formations [1–4]. In highly weathered strata, conventional cemented soil mixtures are unable to fulfill both mechanical strength and impermeability requirements concurrently, resulting in elevated construction costs and potential safety risks [5]. Currently, scholars have achieved certain results in research on its design theory, construction technology, structural optimization, effect inspection, and theoretical analysis. Brunner W G introduced the innovative CSM technology for constructing retaining walls and cutoff walls, comparing its advantages over traditional soil mixing methods [6]. Successfully implemented CSM theory in practical engineering applications, with full consideration of the actual project environment [7–9]. In engineering practice, the CSM method was further optimized by introducing section steel [10–12]. It is proposed to replace traditional cast–in–place concrete piles with H–section steel inserted into the TRD cemented soil to form an integrated support structure. This approach not only addresses the issue of insufficient strength of TRD but also enables the recycling of H–section steel, thereby reducing engineering costs [13]. Nevertheless, existing approaches have largely concentrated on structural improvement, with insufficient attention paid to cost–effectiveness, making them unsuitable for cost–sensitive large–scale underground projects.

Building on studies of the solidification mechanism of cement–treated soil and fiber–reinforced cement–treated soil, this research investigates the impact of fiber materials on the physical and mechanical properties of cement–based composites through the incorporation of fibers into the cementitious material [14–17]. Through the investigation of cemented soil, it was found that the solidification mechanism of the improved cemented soil includes the hydration reaction of cement, the bridging and crack resistance effects of fibers, and the aggregate effect and secondary reaction of fly ash [18]. By incorporating bentonite to regulate the impermeability of cement–soil walls, the study found that the minimum permeability coefficient of slag cement–bentonite material can reach 10^{-18} cm/s; furthermore, the addition of bentonite can reduce the permeability coefficient of cement–bentonite consolidations to below 10^{-17} cm/s at 28 days of curing age [19–21]. Using fly ash to replace part of the cement material as grouting material, conducting a feasibility study analyzing its impact on cement compressive strength [22–24]. In a study on the mechanical and hydraulic properties of cement–soil composites reinforced with sisal fiber and fly ash, it was found that the combination of fiber and fly ash significantly improved the peak strength of the cement–soil. Meanwhile, the fiber reduced permeability, whereas the fly ash increased it [25]. In terms of modifying cemented soil materials, existing studies mostly focus on the mechanism of action of single admixtures, which does not align well with complex working conditions.

While previous research has individually demonstrated the structural enhancement potential of the CSM method and the respective contributions of fiber, bentonite, and fly ash to cemented soil performance, no study has yet addressed the collaborative design and systematic optimization of an integrated system combining the CSM–H–section steel support with a basalt fiber–sodium bentonite–fly ash multi–component cementitious material, particularly under the complex geological conditions characteristic of highly weathered strata. Therefore, this paper proposes a CSM structure combined with H–beams, using ordinary Portland cement as the base matrix, adding basalt fiber, sodium bentonite, and fly ash to study the influence rules of each component on the new material, optimize the mix proportion for solidified cement–soil material, and compare the superiority of CSM with

https://doi.org/10.3390/ma19071287

H–beams against bored piles through field engineering tests. It aims to solve the issues of economy, construction efficiency, and the common problems of insufficient solidified strength and poor impermeability of the formed cement–soil walls during construction, providing a practical solution for the efficient and economical application of the CSM method in complex strata.

2. Numerical Simulation

In conventional foundation pit support design, the use of CSM bored piles combined with anchor cables can effectively ensure stability during excavation. However, such temporary support structures are permanently buried upon completion of the foundation pit construction, resulting in neither recyclability nor significant wastage of construction materials, which contradicts the principles of green construction and sustainable development. To address this issue, this study proposes a more economical and environmentally friendly optimization scheme: leveraging the excellent waterproofing performance of the CSM method while replacing traditional bored piles with high–strength recyclable steel sections as the primary load–bearing components. This is combined with a detachable anchor cable system to form a composite support system. This approach not only meets stability requirements during excavation but also enables the recovery of key components such as steel sections and anchor cables upon project completion, facilitating material recycling. This innovative design maintains the reliability of the original support system while significantly reducing engineering costs and minimizing construction waste, offering a more economical, environmentally friendly, and sustainable support solution for foundation pit engineering.

Numerical simulations were conducted using two software packages: COMSOL Multiphysics (Version 6.0, developed by COMSOL AB, Stockholm, Sweden) for the simplified foundation pit model, and Lizheng Deep Foundation Pit Support Structure Design Software (version 7.5, developed by Beijing Lizheng Software Co., Ltd., Beijing, China) for the entire foundation pit.

2.1. Basic Support Parameters

Scheme 1: The foundation pit is supported using bored piles combined with anchor cables and a CSM waterproof curtain. The support schematic is shown in Figure 1a. The embedded depth is 3.5 m, the pile cross–section is circular with a diameter of 1000 mm, and the pile spacing is 1500 mm. The waterproof curtain consists of a 700 mm thick CSM wall, with vertical anchor cables for additional support. The bottom of the CSM waterproof curtain should extend into the weakly permeable rock layer by no less than 1.2 m.

Scheme 2: The foundation pit is supported using the CSM method with embedded H–section steel piles combined with anchor cables. The support schematic is shown in Figure 1b. The CSM wall thickness is 800 mm, and the embedded H–section steel model is HN500 × 200. The steel piles are arranged at equal intervals of 1.0 m, with an embedded depth of 3.5 m. Vertical anchor cables are also installed for additional support.

COMSOL Multiphysics was selected for its suitability for multi–physics coupling, enabling effective simulation of soil–structure interaction. The soil was modeled using the ideal elastic–plastic Mohr–Coulomb model. The boundary conditions were set as follows: the bottom of the model was fixed, the lateral boundaries were constrained in the normal direction, and the top boundary was free.

The simulation primarily analyzed ① horizontal displacement of the support structure (maximum displacement and its location); ② bending moment of the wall/pile; ③ axial force of the struts; ④ overall stability safety factor.

https://doi.org/10.3390/ma19071287

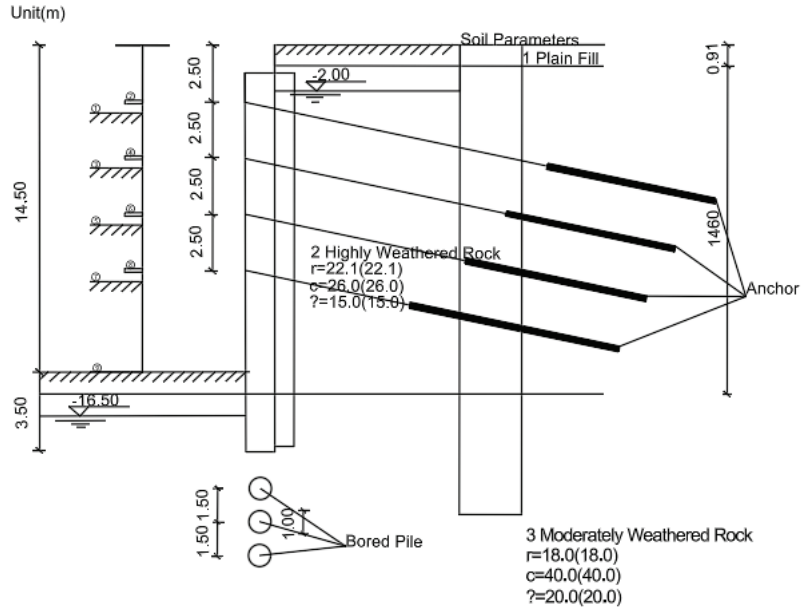

(**a**) Calculation diagram of support structure for Scheme 1

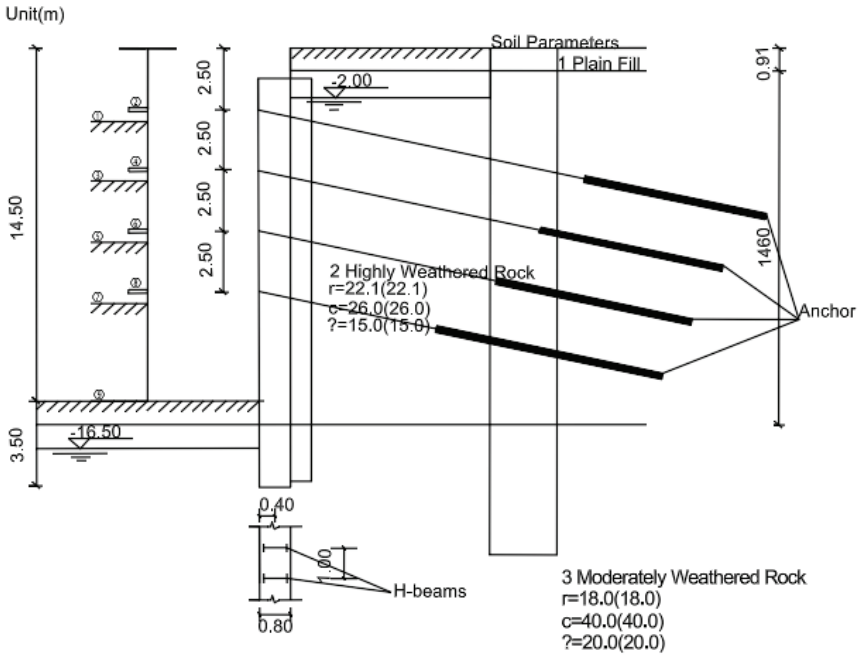

(**b**) Calculation diagram of support structure for Scheme 2

Figure 1. Schematics of support structures.

2.2. Basic Information

The computational model can be simplified as follows: The pit length is 100 m, the width is 25 m, and the excavation depth is 14.5 m. At this support section, four layers of steel waling beams are arranged in a hinged configuration, and four rows of anchor cables are considered in the calculation. Based on the COMSOL Multiphysics software, a comparative study is conducted between the original support scheme and the support scheme using the new CSM construction method. The internal forces in the engineering piles and walls, as well as the displacements of the piles and walls, are compared. A plan view of the internal bracing levels is shown in Figure 2:

https://doi.org/10.3390/ma19071287

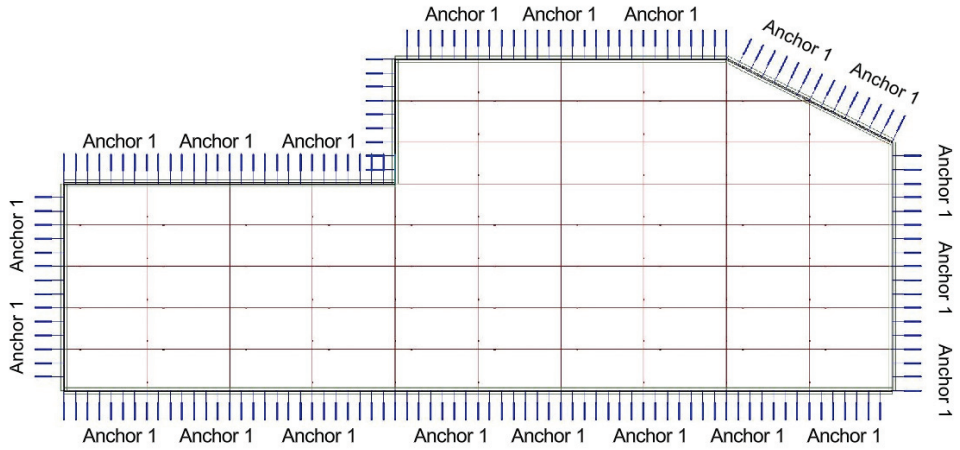

Figure 2. Plan layout of internal bracing system.

The entire foundation pit is reinforced with anchor cables. The anchor cable specifications are detailed in Table 1, and the soil layer properties were determined based on the laboratory soil test results from the detailed investigation report of the Qingdao Metro Haixi Road Station project, as presented in Table 2. The over–excavation depth is 0.5 m. The calculation working conditions are summarized in Table 3.

Table 1. Anchor Cable Parameters of Sectional Support Units.

Anchor Cable ID	Tendon Type	Steel Waling Beam Model	Horizontal Spacing (m)	Inclination Angle (°)	Borehole Diameter (mm)	Effective Length (m)	Free Length (m)	Bond Length (m)	Prestress Lock–Off Value (kN)
Anchor–1	4Φs15.2	2I28b	1.5	15	150	17	10	7	300
Anchor–2	4Φs15.2	2I28b	1.5	15	150	16	9	7	400
Anchor–3	4Φs15.2	2I28b	1.5	15	150	16	8	8	400
Anchor–4	4Φs15.2	2I28b	1.5	15	150	14	7	7	400

4Φs15.2: 4 indicates the number of strands, Φ indicates the diameter symbol, and s15.2 indicates the diameter specification. 2I28b: 2 indicates the number of steel sections, I indicates I–shaped steel, and 28b indicates the model designation of the I–section steel.

Table 2. Soil Layer Information for Sectional Support Units.

Layer No.	Name	Thickness (m)	Unit Weight (kN/m^3)	Buoyant Unit Weight (kN/m^3)	Cohesion (kPa)	Internal Friction Angle (°)	Friction Resistance with Anchor (kPa)	Analysis Method	Total Stress Analysis
1	Plain Fill	0.91	17.9	–	14	18	30	M–Method	Yes
2	Highly Weathered Rock	14.60	22.1	12.1	26	15	300	M–Method	Yes
3	Moderately Weathered Rock	50.00	18.0	8.0	40	20	360	M–Method	Yes

Table 3. Calculation Working Conditions.

Working Condition No.	Excavation Depth (m)	Over–Excavation Depth (m)
1	−3.3	0.5
2	−5.8	0.5
3	−8.3	0.5
4	−10.8	0.5
5	Pit Bottom	0.5

https://doi.org/10.3390/ma19071287

2.3. Calculation Results

(1) Global Displacement

As shown in Figure 3, the variation process of the global displacement of the two support structures during the foundation pit excavation is illustrated.

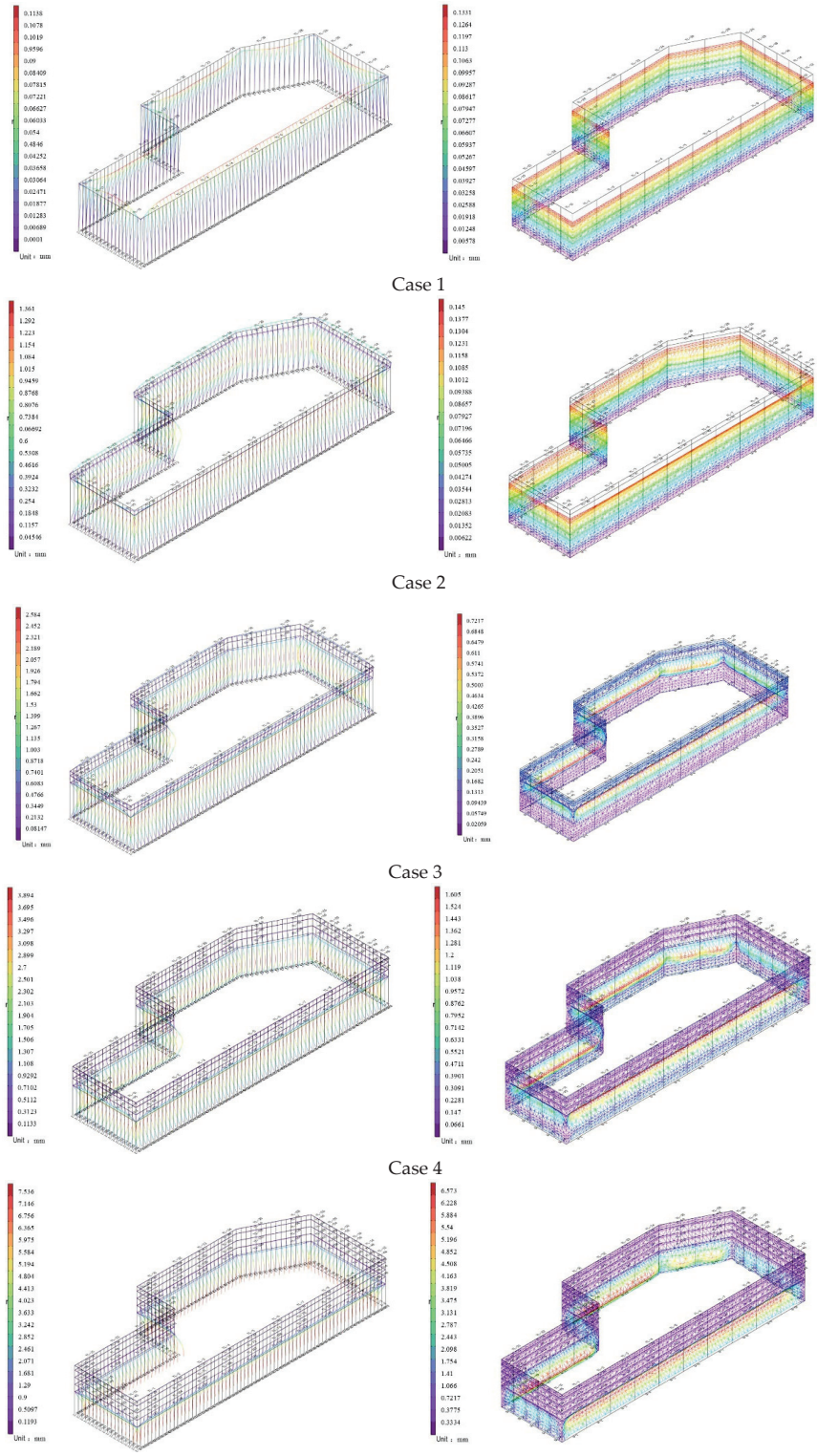

(**a**) Bored pile (**b**) CSM structure

Figure 3. Variation in global displacement for the two support structures.

https://doi.org/10.3390/ma19071287

In Case 1, due to the absence of any constraints and the relatively shallow excavation depth, the displacement of the support structure was most pronounced at the top of the piles and walls, with horizontal displacement directed toward the interior of the foundation pit. As excavation proceeded further, both types of foundation pit support exhibited rigid support behavior; consequently, the wall displacement manifested as triangular horizontal displacement. This differs from flexible walls, which, after the installation of struts or anchor cables, typically show unchanged displacement at the wall top or movement toward the exterior of the pit. As indicated by Case 3, the wall abdomen bulged toward the interior of the pit. By the time excavation reached the pit bottom (Case 5), the inward displacement of the walls or piles gradually decreased from the bottom upward. The variation characteristics of wall displacement during excavation generally conform to the typical patterns observed in foundation pit excavation.

Additionally, due to the release of self–weight stress during soil excavation, the piles and walls exhibited a tendency to heave upward. This upward movement negatively impacts pit stability, surface settlement safety, and the effectiveness of the support structure. This phenomenon was reflected in the pile and wall deformations calculated by Lizheng 7.5, although the changes were not pronounced.

(2) Internal Forces in Retaining Structures

Figure 4 illustrates the development process of internal forces in piles and walls during foundation pit excavation, based on theoretically calculated earth pressure distributions at different depths, and considering the effects of hydrostatic pressure and seepage caused by groundwater level changes on piles and walls.

In the bored pile support structure, as excavation progresses, the location of the maximum bending moment of the pile moves toward the pile bottom. The maximum bending moment on the excavation side is 423.95 kN·m, located near the pile bottom, indicating that earth pressure is concentrated in the deep zone of the retaining side. The maximum bending moment on the retaining side is −653.1 kN·m, directed toward the exterior of the foundation pit, caused by soil rebound after excavation unloading and the constraint effect of the foundation base. As excavation depth increases, the location of the extreme bending moment shifts from the pile top to the pile bottom, reflecting the gradual mobilization of the passive zone soil constraint.

The maximum shear force and axial force also appear at the location of the maximum bending moment, with values of 494.77 kN. At the maximum bending moment on the excavation side, the axial force is 222.29 kN, while on the retaining side it is 155.27 kN, possibly due to uneven distribution of earth pressure on both sides or asymmetric reinforcement of the support structure. The migration of the bending moment location is attributed to the staged excavation effect: in the initial stage, the pile top is free, and the extreme bending moment is located at the pile top; as excavation deepens, the passive resistance of the foundation soil increases, constraining pile bottom displacement, and the extreme bending moment moves downward. The higher modulus of deep soil layers limits pile deformation, exacerbating the bending moment at the pile bottom.

The internal force distribution of foundation pit support piles is jointly influenced by earth pressure, water level changes, and construction sequence. The concentration of bending moment in the deep zone of the retaining side requires optimization through increased pile diameter, reinforcement, and collaborative support. During dynamic construction, the support scheme should be adjusted in real–time based on monitoring data to ensure structural safety.

https://doi.org/10.3390/ma19071287

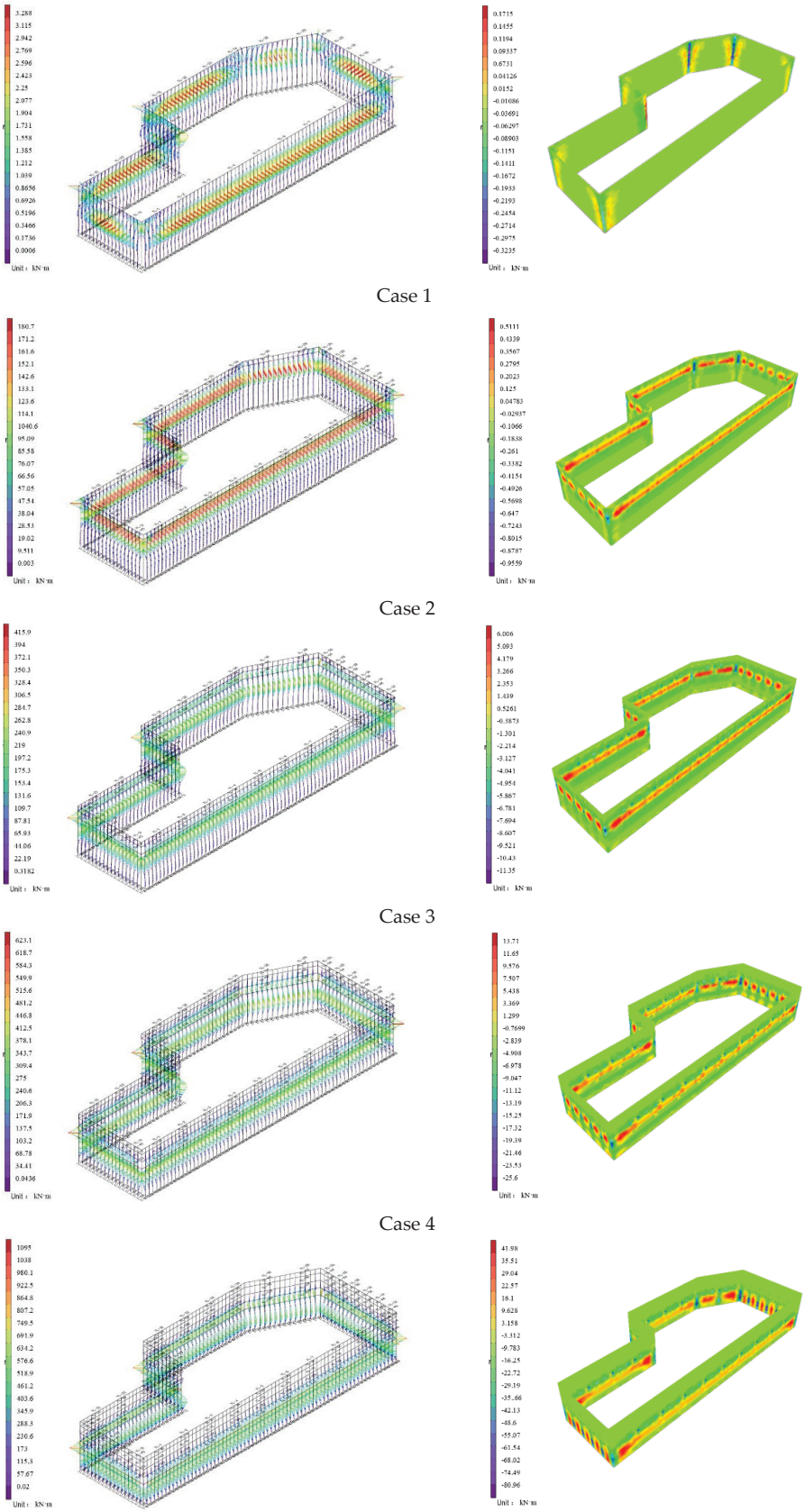

(**a**) Bored pile (**b**) CSM structure

Figure 4. Internal forces in piles and walls during excavation process.

https://doi.org/10.3390/ma19071287

In the CSM method support structure, as the support process progresses, the region of maximum wall bending moment divides the entire wall into three parts: the upper stabilized support zone, the middle stress zone, and the lower unexcavated zone. The location of the maximum bending moment of the wall moves toward the wall bottom. The vertical bending moment is 88.88 kN·m on the excavation side and −166.93 kN·m on the retaining side. The former is mainly caused by active earth pressure, while the latter reflects the constraint effect of the passive zone soil and the concentration of deep earth pressure. The horizontal bending moment is 37.83 kN·m on the excavation side and −64.10 kN·m on the retaining side, indicating the presence of asymmetric loads in the horizontal direction, which arise due to the asymmetric form of the foundation pit. The vertical shear force is 32.45 kN, and the horizontal shear force is 54.47 kN.

During foundation pit excavation, the internal force distribution of the CSM method support structure is jointly influenced by earth pressure, water level, and synergistic effects. The concentration of vertical bending moment on the retaining side requires optimization by improving interfacial shear stiffness and increasing support density. Although the horizontal bending moment is relatively small, attention should be paid to the influence of asymmetric loads. During construction, the support scheme should be adjusted in real–time based on monitoring data to ensure foundation pit stability.

Through the above comparison, the CSM support structure demonstrates good adaptability in design and construction. Future research could further study the mechanism of interface interaction to enhance engineering reliability under complex geological conditions.

(3) Internal Forces (Axial Force) in Top Beam or Waling Beams

As horizontal support members, the top beam or waling primarily bears the horizontal loads transmitted from earth pressure to the retaining piles or diaphragm walls and transfers these loads to the opposing support structures or anchor systems through its axial stiffness. Figure 5 shows the axial force of the waling when the retaining structure is excavated to the pit bottom; the magnitude of this axial force directly reflects the level of earth pressure sustained by the support system.

Figure 5a presents the axial force in the waist beam of the bored pile support system upon excavation to the pit bottom. For waist beams with large spans, bending deformation may occur due to non–uniform earth pressure distribution, construction–induced eccentric loads, or support spacing, while insufficient joint stiffness can induce additional moments. Taking waist beam YL–50 as an example (with compression taken as positive), the maximum axial force is 19.51 kN, indicating that the waist beam is in compression and resists horizontal earth pressure. The relatively low axial force may be attributed to: (1) uniform load sharing within the support system, with the waist beam bearing only localized earth pressure; (2) small support spacing or high beam stiffness leading to load dispersion; or (3) the absence of soil nonlinearity or seepage coupling in the numerical model, potentially underestimating the axial force. The axial force distribution in the piles follows a trend consistent with that in the waist beam (higher at the pile top and lower in the waist beam), confirming effective load transfer and a collaborative load–bearing mechanism.

Figure 5b shows the axial force in the waist beam of the CSM support system at the pit bottom. The maximum axial force reaches 28.65 kN at the wall corner, and the internal force distribution in the wall aligns with the axial force trend in the waist beam, indicating effective load transfer and a collaborative system. Anchor bolts carry the majority of the load, while the waist beam acts as a secondary load transfer path, resulting in lower axial forces. In practice, construction monitoring should be enhanced by installing vibrating–wire axial force gauges at critical sections of the waist beam to track axial force variations in real time and validate design assumptions.

https://doi.org/10.3390/ma19071287

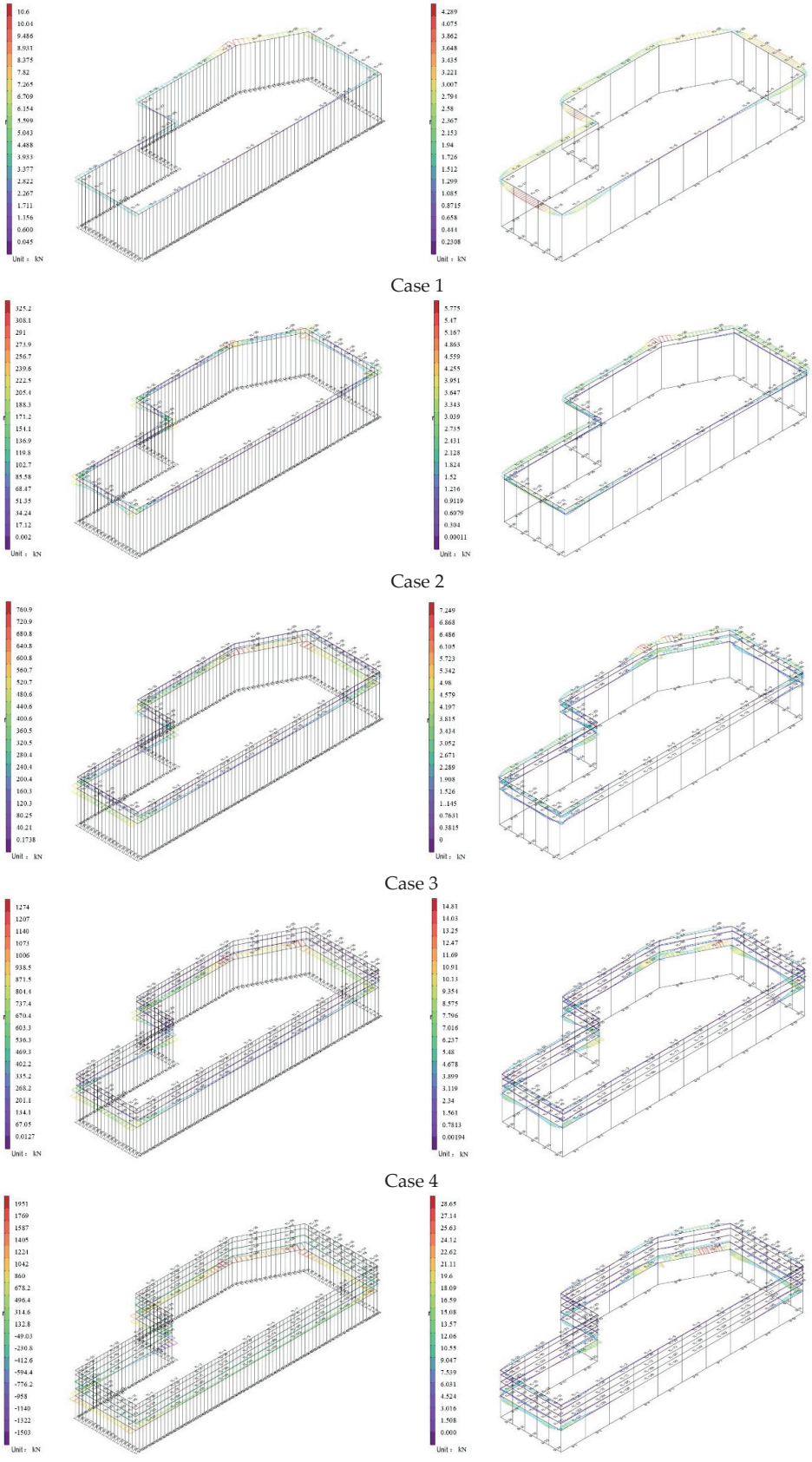

(**a**) Bored pile (**b**) CSM structure

Figure 5. Magnitude of axial force in waling beams for the two support structures.

https://doi.org/10.3390/ma19071287

Through the above comparison, both the bored pile and CSM support structures meet safety requirements under the current working conditions. Future designs could further optimize the load distribution mechanism to enhance the economy and reliability of the support system.

3. Materials Proportioning Study

To address the engineering bottlenecks associated with the CSM (Cutter Soil Mixing) method in highly weathered strata—specifically, the low unconfined compressive strength and high permeability coefficient of the solidified cement soil—this study is based on the principle of material composite modification. Using ordinary Portland cement as the base material, a multi–component synergistic reinforcement system was constructed by incorporating admixtures such as basalt fiber, sodium bentonite, and fly ash. By comparing the influence patterns of different mix proportions, the optimal material combination was determined. The development of this new composite curing agent provides an innovative material solution for improving the quality of CSM diaphragm walls in highly weathered strata.

In concrete, basalt fiber functions as a reinforcing material through micro–reinforcement and crack resistance mechanisms. Fly ash serves as a supplementary cementitious material that predominantly affects later–age strength, durability, and workability. Sodium bentonite is employed as a rheology modifier or waterproofing admixture to control the fluidity of the concrete mixture.

3.1. Raw Materials

(1) Base Material

The cement used in the test was Grade 42.5 ordinary Portland cement produced by Henan Mengdian Group Cement Co., Ltd. (Xinxiang, China). The performance indicators of the cement are shown in Table 4.

Table 4. Performance Indicators of Ordinary Portland Cement.

Specific Surface Area/$m^2 \cdot kg^{-1}$	Setting Time (min)		Flexural Strength (MPa)		Compressive Strength (MPa)	
	Initial Set	Final Set	3 d	28 d	3 d	28 d
≥300	≥45	≤600	≥4.0	≥6.5	≥17.0	≥42.5
355	202	263	5.5	8.2	26.6	50.4

(2) Fiber

The basalt fiber used in the test was chopped fiber produced by Shanghai Chenqi Chemical Technology Co., Ltd. (Shanghai, China), with a specification of 12 mm. Its specific performance is shown in Table 5.

Table 5. Main Performance Parameters of Basalt Fiber.

Name	Specific Gravity	Tensile Strength	Elastic Modulus	Size	Moisture Content	Elongation at Break
Testing Standard for Basalt Fiber	2.8–3.3 g/cm^3	≥1250 MPa	≥40 GPa	12 mm	≤0.2%	≥3.1%
Measured	2.86 g/cm^3	2246 MPa	55 GPa	12 mm	0.1%	3.15%

(3) Additives

The composition of the sodium bentonite used in the test is shown in Table 6.

https://doi.org/10.3390/ma19071287

Table 6. Chemical composition of the Sodium Bentonite.

Type	SiO_2/%	Al_2O_3/%	Na_2O/%	MgO/%	CaO/%	Fe_2O_3/%	Ti_2O_3/%
Content	64.59	17.23	3.26	2.21	1.28	2.65	0.36

Some physics and chemical parameters of fly ash used in the test are shown in Table 7.

Table 7. Some physics and chemical parameters of Fly Ash.

Standard	Loss on Ignition/%	Fineness/%	Moisture Content/%	Water Demand/%	SO_3/%
National Standard	≤5.0	≤12	≤1.0	≤95.0	≤3.0
Measured Data	3.05	10.1	0.34	90	0.26

3.2. Test Scheme

Based on the findings of preliminary tests, the following material proportions were adopted: basalt fiber volume fraction of 0.3–0.5%, fly ash replacement rate of 5–15%, and sodium bentonite content ranging from 3% to 5%—the latter selected to achieve an optimal balance between impermeability and strength loss.

This test adopted the water–cement ratio of 1.0 required by the background project design. The basalt fiber specification was 12 mm with incorporation rates of 0.3%, 0.4%, and 0.5%. Fly ash replaced ordinary Portland cement at the same mass fractions of 5%, 10%, and 15%. Sodium bentonite incorporation rates were set at 3%, 4%, and 5%, respectively. Specimens at ages of 3 d, 7 d, and 28 d were selected as variables. A total of 37 different test conditions were set up. The specific material mix proportions are shown in Table 8. Multiple groups of mixed ratio–related tests were configured for the solidified cement material. The fluidity, bleeding rate, setting time, and other properties of the material's neat paste slurry were tested and recorded, and the results were analyzed. Using relevant test instruments, the compressive strength and flexural strength of the consolidated solid for the solidified cement material under different conditions were tested. The test data were organized and analyzed, and the final results were compared to summarize the influence of material mix proportions on various properties of the solidified cement material under different conditions, ultimately determining the optimal mix proportion for the solidified cement material. A four–factor, three–level orthogonal experiment ($L(3^4)$) was established, with the four factors determined as: basalt fiber (A), fly ash (B), sodium bentonite (C), and a blank column for error (D), orthogonal test scheme is shown in Table 9. Three levels were chosen for each factor. Based on the aforementioned test data results, basalt fiber mass fractions of 0.3%, 0.4%, and 0.5% were selected; fly ash levels of 5%, 10%, and 15% were selected; sodium bentonite levels of 3%, 4%, and 5% were selected.

Table 8. Cementitious materials mix proportion.

No.	Test ID	Basalt Fiber Content	Sodium Bentonite Content	Fly Ash Content
1	BSF–1–1	0.3%	3%	5%
2	BSF–1–2	0.3%	4%	5%
3	BSF–1–3	0.3%	5%	5%
4	BSF–1–4	0.3%	3%	10%
5	BSF–1–5	0.3%	4%	10%
6	BSF–1–6	0.3%	5%	10%

https://doi.org/10.3390/ma19071287

Table 8. *Cont.*

No.	Test ID	Basalt Fiber Content	Sodium Bentonite Content	Fly Ash Content
7	BSF–1–7	0.3%	3%	15%
8	BSF–1–8	0.3%	4%	15%
9	BSF–1–9	0.3%	5%	15%
10	BSF–2–1	0.4%	3%	5%
11	BSF–2–2	0.4%	4%	5%
12	BSF–2–3	0.4%	5%	5%
13	BSF–2–4	04%	3%	10%
14	BSF–2–5	0.4%	4%	10%
15	BSF–2–6	0.4%	5%	10%
16	BSF–2–7	0.4%	3%	15%
17	BSF–2–8	0.4%	4%	15%
18	BSF–2–9	0.4%	5%	15%
19	BSF–3–1	0.5%	3%	5%
20	BSF–3–2	0.5%	4%	5%
21	BSF–3–3	0.5%	5%	5%
22	BSF–3–4	0.5%	3%	10%
23	BSF–3–5	0.5%	4%	10%
24	BSF–3–6	0.5%	5%	10%
25	BSF–3–7	0.5%	3%	15%
26	BSF–3–8	0.5%	4%	15%
27	BSF–3–9	0.5%	5%	15%
28	D–0	0%	0%	0%
29	B–1	0.3%	0%	0%
30	B–2	0.4%	0%	0%
31	B–3	0.5%	0%	0%
32	S–1	0%	3%	0%
33	S–2	0%	4%	0%
34	S–3	0%	5%	0%
35	F–1	0%	0%	5%
36	F–2	0%	0%	10%
37	F–3	0%	0%	15%

Table 9. Orthogonal Test Scheme.

Test ID	A (Basalt Fiber Level)	B (Fly Ash Level)	C (Bentonite Level)	D (Error)
1	1	1	1	1
2	1	2	2	2
3	1	3	3	3
4	2	1	2	3
5	2	2	3	1
6	2	3	1	2
7	3	1	3	2
8	3	2	1	3
9	3	3	2	1

3.3. Research Result

This study prepared 37 groups of solidified cement paste slurries with different mix proportions, including two control groups with water–cement ratios of 1.0 and 0.5, D1.0 and D0.5, which were plain cement paste without any additives. The rest were test groups for solidified cement materials with different mix proportions, details are shown in Table 10.

https://doi.org/10.3390/ma19071287

Table 10. Experimental Results.

Test ID	Initial Set (min)	Final Set (min)	Bleeding Rate (%)	Fluidity (mm)	Compressive Strength (MPa)			Flexural Strength (MPa)		
					3 d	7 d	28 d	3 d	7 d	28 d
BSF–1–1	208	264	6.1	30.1	3.95	6.90	8.54	1.04	1.64	1.96
BSF–1–2	200	240	5.0	28.9	3.84	6.63	7.79	0.96	1.54	1.88
BSF–1–3	196	224	3.9	27.5	3.80	6.11	7.78	0.76	1.46	1.84
BSF–1–4	216	288	5.2	32.5	3.86	7.08	10.18	0.99	1.60	2.48
BSF–1–5	210	276	4.1	31.6	3.82	6.85	10.09	0.85	1.49	2.40
BSF–1–6	204	260	3.0	30.5	3.55	6.23	9.78	0.76	1.45	2.23
BSF–1–7	224	314	4.3	43.0	3.84	7.18	9.46	0.96	1.58	3.09
BSF–1–8	218	286	3.1	39.5	3.77	6.91	9.06	0.76	1.46	3.02
BSF–1–9	210	266	2.4	36.2	3.24	6.70	8.79	0.72	1.27	2.95
BSF–2–1	208	270	5.4	29.1	4.51	7.40	9.23	1.20	1.85	2.24
BSF–2–2	202	248	4.3	28.4	4.28	7.29	9.04	1.13	1.77	2.17
BSF–2–3	196	224	3.4	25.9	4.19	7.20	8.73	1.07	1.75	2.13
BSF–2–4	216	282	4.6	32.1	4.48	7.68	11.44	1.25	1.79	2.98
BSF–2–5	208	276	3.6	31.2	4.21	7.38	11.10	1.17	1.76	2.93
BSF–2–6	204	264	2.3	30.5	4.14	7.23	10.89	1.07	1.65	2.75
BSF–2–7	224	314	3.6	39.5	4.28	7.73	10.15	1.13	1.78	3.50
BSF–2–8	216	284	2.7	36.5	4.20	7.39	10.08	1.08	1.75	3.32
BSF–2–9	210	264	1.9	34.3	4.10	7.30	9.60	1.06	1.65	3.17
BSF–3–1	208	268	4.5	28.8	6.39	9.00	10.13	1.96	2.93	2.75
BSF–3–2	200	242	3.6	27.5	6.12	8.29	9.92	1.47	2.37	2.75
BSF–3–3	196	218	2.5	25.7	4.70	7.75	9.50	1.25	2.02	2.61
BSF–3–4	214	290	3.8	31.3	6.16	9.26	12.26	1.73	2.90	3.17
BSF–3–5	210	276	2.7	30.5	4.88	8.64	11.57	1.44	2.25	3.16
BSF–3–6	204	262	1.6	30.3	4.66	7.90	11.45	1.24	1.97	3.10
BSF–3–7	226	312	2.9	38.2	4.97	9.93	11.24	1.47	2.37	4.33
BSF–3–8	218	282	1.8	35.0	4.75	9.04	11.05	1.26	1.97	3.67
BSF–3–9	212	262	1.2	34.1	4.60	8.29	10.30	1.22	1.86	3.61
D0.5	205	265	11.9	25.0	26.6	50.0	50.40	5.50	9.65	8.20
D1.0	205	265	12.3	25.0	2.02	6.52	8.05	0.45	1.11	1.13
B–1	205	265	13.1	29.0	2.05	5.22	8.11	1.17	2.06	2.77
B–2	205	265	15.1	28.6	2.11	5.68	8.12	1.43	2.32	2.96
B–3	205	265	15.8	27.5	2.17	6.10	8.23	1.58	1.64	3.10
S–1	196	260	5.7	28.4	2.82	6.28	8.25	0.98	1.67	2.66
S–2	184	226	4.2	25.9	3.08	6.62	8.87	1.00	1.63	2.81
S–3	172	206	2.7	24.8	2.78	6.10	8.12	0.93	1.60	2.37
F–1	226	268	6.3	35.0	1.88	5.25	8.10	0.87	1.92	2.14
F–2	238	316	5.4	41.0	2.07	5.47	9.23	0.91	2.00	2.45
F–3	248	318	4.6	45.2	2.10	6.32	9.63	0.98	2.15	2.63

3.3.1. Setting Time Analysis

The setting time of the solidified cement slurry was determined using the Vicat apparatus, following the procedures specified in the Chinese national standard Test methods for water requirement of normal consistency, setting time and soundness of the Portland cement (GB/T 1346) [26].

Setting time serves as a critical parameter for solidified cement slurry materials. An excessively short setting time prevents adequate mixing between the slurry and in situ soil, resulting in non–uniform wall strength distribution and compromised construction quality. Conversely, an overly prolonged setting time promotes slurry segregation, leading to excessive water permeation and increased construction hazards. Consequently, the setting time of solidified cement slurry materials should be designed to be controllable within a specified range while adhering to relevant specifications. The orthogonal experimental design and range analysis for initial setting time and final setting time are shown in Tables 11 and 12.

https://doi.org/10.3390/ma19071287

Table 11. Orthogonal Experimental Design and Range Analysis of Initial Setting Time.

Test No.	A	B	C	D (Error)	Initial Setting Time/min
1	1	1	1	1	208
2	1	2	2	2	210
3	1	3	3	3	210
4	2	1	2	3	202
5	2	2	3	1	204
6	2	3	1	2	224
7	3	1	3	2	196
8	3	2	1	3	214
9	3	3	2	1	218
		Range Analysis			Preferred Combination
K_1	628	606	646	630	
K_2	630	628	630	630	
K_3	628	652	610	626	
k_1	209.3	202	215.3	210	$A_2B_3C_1$
k_2	210	209.3	210	210	
k_3	209.3	217.3	203.3	208.67	
R	0.67	15.3	12	1.3	
		B > C > A			

Table 12. Orthogonal Experimental Design and Range Analysis for Final Setting Time.

Test No.	A	B	C	D (Error)	Final Setting Time/min
1	1	1	1	1	264
2	1	2	2	2	276
3	1	3	3	3	266
4	2	1	2	3	248
5	2	2	3	1	264
6	2	3	1	2	314
7	3	1	3	2	218
8	3	2	1	3	290
9	3	3	2	1	282
		Range Analysis			Preferred Combination
K_1	806	730	868	810	
K_2	826	830	806	808	
K_3	790	862	748	804	
k_1	268.7	243.3	289.3	270	$A_2B_3C_1$
k_2	275.3	276.7	268.7	269.3	
k_3	263.3	287.3	249.3	268	
R	12	44	40	2	
		B > C > A			

Based on the range analysis, the influence on the initial setting time follows the order: fly ash > sodium bentonite > basalt fiber, as indicated by the mean values at each level. The optimal combination ($A_2B_3C_1$) was determined by selecting the level corresponding to the maximum value of k_i was selected for each factor. The initial setting time of the slurry is significantly affected by the material proportions, with fly ash content and sodium bentonite content being the predominant influencing factors.

The primary reactants in cement hydration are cement clinker and water. During the induction period, the addition of fly ash and sodium bentonite partially impedes contact

https://doi.org/10.3390/ma19071287

between cement and water, leading to a slower initial hydration rate. In the acceleration period, a hydration product layer forms on the cement surface. The SiO_2 and Al_2O_3 components in fly ash undergo a secondary hydration reaction with $Ca(OH)_2$—a product of cement hydration—generating calcium silicate hydrate (C–S–H) and other phases that contribute to water retention. As interparticle spacing increases, the time required for hydration products to fill the skeletal pores during setting is prolonged, thereby extending the overall setting time.

In summary, based on the final setting time, the optimal mix design is determined to be $A_3B_3C_1$, corresponding to a basalt fiber content of 0.5%, fly ash content of 15%, and sodium bentonite content of 3%.

3.3.2. Bleeding Rate Analysis

Basalt fiber has a special spatial network structure, giving it good physical properties including electrical insulation and dielectric properties [27]. These properties allow basalt fiber to form a uniform three–dimensional randomly distributed network system in the cement paste, which can slow down water evaporation and migration, thus affecting the bleeding rate of the cement paste. Sodium bentonite has good adsorption and high cation exchange capacity; it can adsorb and inhibit the sedimentation of cement particles, thereby reducing the bleeding rate of the slurry [28]. The main chemical components of fly ash include SiO_2, Al_2O_3, and Fe_2O_3, accounting for over 70% of its total content. These active materials, when mixed with cement, participate in the hydration reaction, thus affecting the stability of the slurry and consequently the bleeding rate of the cement paste.

The degree of influence on slurry bleeding rate is fly ash > sodium bentonite > basalt fiber. Therefore, the material mix proportion $A_1B_1C_1$ has the highest bleeding rate. Considering bleeding rate, the scheme with the highest bleeding rate is $A_1B_1C_1$; the scheme with the lowest bleeding rate is $A_3B_3C_3$. Further comprehensively considering other properties of the cement paste, the better combination is $A_3B_3C_1$, i.e., basalt fiber content 0.5%, fly ash content 15%, sodium bentonite content 3%.

The effect of admixture dosage on bleeding rate is shown in Figures 6–8.

The fluidity of the solidified cement slurry material was tested using the following apparatus: a cement paste mixer, a truncated cone mold (upper diameter: 36 mm, lower diameter: 60 mm), a glass plate (500 mm × 500 mm × 3 mm), and a steel ruler.

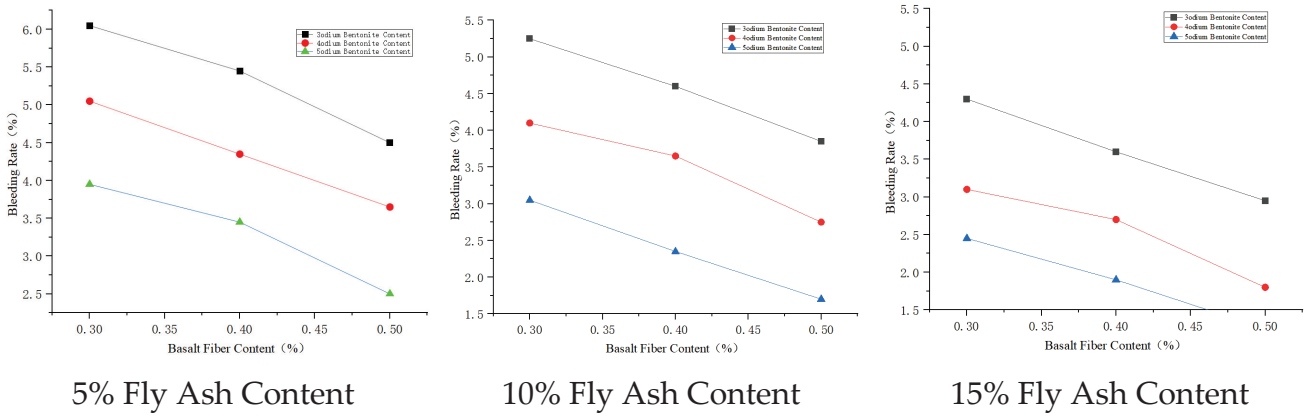

Figure 6. Effects of basalt fiber on bleeding rate.

https://doi.org/10.3390/ma19071287

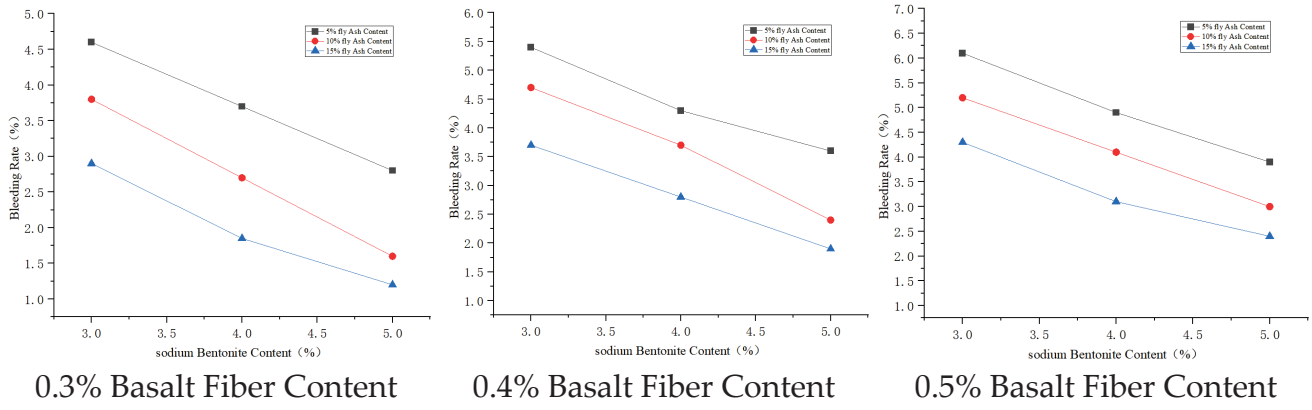

Figure 7. Effects of sodium bentonite on bleeding rate.

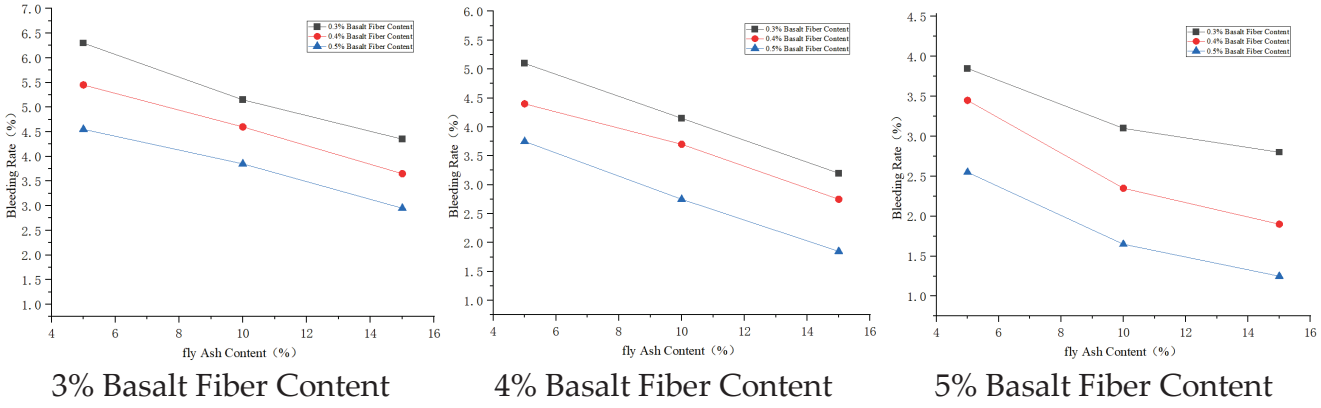

Figure 8. Effects of fly ash on bleeding rate.

3.3.3. Fluidity Analysis

Basalt fiber has stable chemical properties, remaining stable in the slurry, not easily hydrolyzed or chemically decomposed, thus reducing the fluidity of the cement paste. Sodium bentonite, due to its expansibility and adsorbability, forms a uniform three–dimensional randomly distributed network system in the cement paste, which can slow down water evaporation and migration. Due to the particle size and surface positive charge characteristics of cement particles, montmorillonite particles are attached to the surface of relatively larger cement particles under electrostatic attraction and van der Waals forces, reducing the mobility of cement particles and thus decreasing slurry fluidity. Slurry fluidity increases with the increase in fly ash content, and the rate of increase gradually becomes larger. When fly ash particle fineness is less than that of cement particles, it can fill the internal pores of cement particles, enhancing paste fluidity; when the number of glass microbeads in fly ash increases, the microbeads can reduce the slip resistance between cement particles, significantly improving slurry fluidity.

The fly ash content has a significant effect on slurry fluidity. Within the 5~15% content range, the content is positively correlated with slurry fluidity. The influence on slurry fluidity is fly ash content > sodium bentonite content > basalt fiber content. The reason is that the silicon dioxide (SiO_2) and aluminum oxide (Al_2O_3) components in fly ash can undergo secondary hydration reaction with calcium hydroxide ($Ca(OH)_2$) generated during cement hydration. The resulting substances like calcium silicate hydrate have water–retaining functions, not only enhancing the lubricating effect of the ultra–fine cement paste but also achieving excellent fluidity while saving raw materials. For diaphragm wall engineering, which requires high fluidity, the mix proportion $A_2B_3C_1$ is appropriate for the solidified cement material.

https://doi.org/10.3390/ma19071287

While macroscopic mechanical and permeability tests confirm that the combined addition of basalt fiber, fly ash, and bentonite substantially enhances the physical and mechanical properties of cemented soil, this study did not employ microscopic characterization techniques such as scanning electron microscopy (SEM) or mercury intrusion porosimetry (MIP) to directly observe the microstructural evolution. Drawing on findings from the literature, the observed performance improvements are likely attributable to: (1) the bridging and crack–resisting effect of basalt fibers through interfacial bonding with the cement matrix, which inhibits microcrack propagation under load; and (2) the combined pore–filling effect of C–S–H gel from the pozzolanic reaction of fly ash and the gel formed by bentonite upon water absorption and expansion, which reduces the connected porosity. Nevertheless, further microscopic investigation is needed to elucidate the fiber–clay mineral interactions within the interfacial transition zone and the specific influence of multi–component admixtures on the type and morphology of hydration products.

The effect of admixture dosage on fluidity is shown in Figures 9–11.

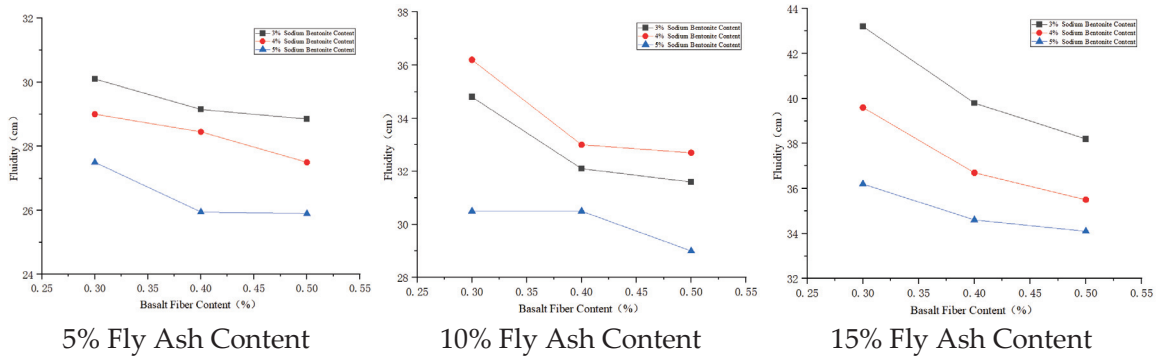

Figure 9. Effects of basalt fiber on fluidity.

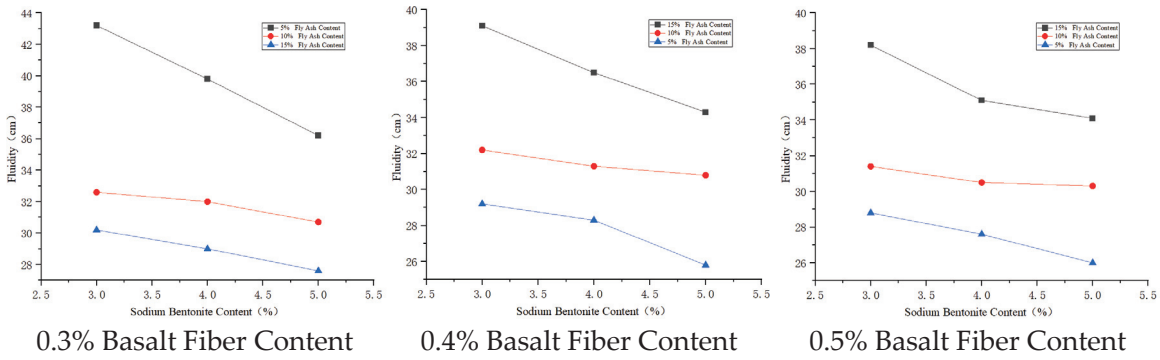

Figure 10. Effects of sodium bentonite on fluidity.

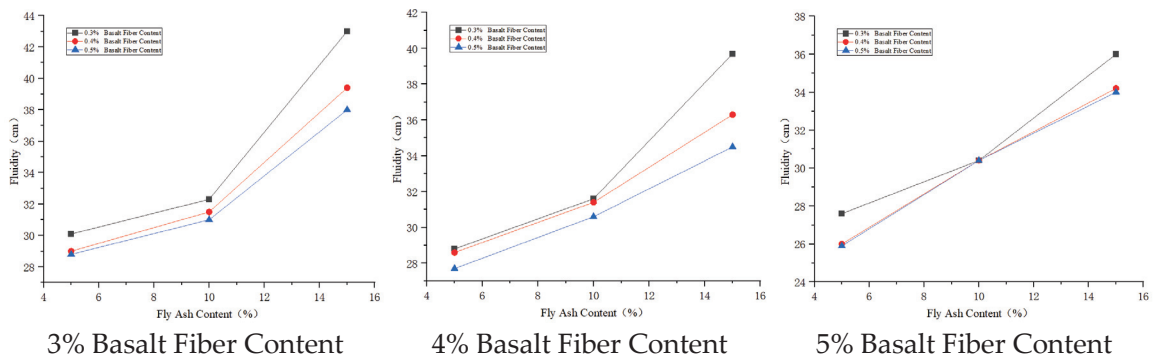

Figure 11. Effects of fly ash on fluidity.

https://doi.org/10.3390/ma19071287

3.3.4. Mechanical Strength Analysis

(1) Flexural Strength

The flexural strength was measured using a CDT1305–2 microcomputer–controlled electronic pressure testing machine via the three–point bending method. A displacement–controlled load was applied at a rate of 0.4 mm/min, and the ultimate load at failure was recorded.

For both tests, if one of three values deviated by more than ±10% from the mean, the mean of the remaining two values was taken; if two values deviated by more than ±10%, the remaining single value was adopted as the result.

Basalt fiber content was found to dominate the early flexural strength of neat paste specimens, with strength increasing as fiber content increased. The relative importance of the three admixtures changed with curing age: at 3 and 7 days, the order of influence was basalt fiber > sodium bentonite > fly ash; at 28 days, however, fly ash became the most significant factor, followed by basalt fiber and then sodium bentonite.

The addition of basalt fiber can improve the microstructure of the cement paste, enhance its crack resistance, thereby increasing flexural strength. However, excessive incorporation will lead to deterioration of fiber dispersion, creating stress concentration weak areas inside the concrete, causing decay in the fiber interface bond strength. The water absorption of sodium bentonite may affect the early strength development of the cement paste, consequently affecting flexural strength. The content of sodium bentonite needs to be determined reasonably to achieve the best balance of flexural strength performance. The addition of fly ash can improve the pore structure of the cement paste, making it denser, thus increasing flexural strength. Increasing fly ash content significantly enhances the 28 d flexural strength of the solidified cement paste, making it an effective reinforcing material. The range analysis of flexural strength is presented in Table 13.

Table 13. Range Analysis for Flexural Strength.

Target	NO.	A	B/%	C/%	D/%
3 d Flexural Strength (MPa)	K1	2.61	3.42	3.9	3.37
	K2	3.33	3.65	3.24	3.23
	K3	4.24	3.11	3.04	3.58
	k1	0.87	1.14	1.3	1.12
	k2	1.11	1.22	1.08	1.08
	k3	1.413	1.04	1.01	1.19
	R	0.54	0.18	0.29	0.12
7 d Flexural Strength (MPa)	K1	4.4	5.43	6.32	3.61
	K2	3.55	4.39	5.23	5.29
	K3	6.89	5.02	3.29	5.94
	k1	1.47	1.81	2.11	1.20
	k2	1.18	1.46	1.74	1.76
	k3	2.30	1.68	1.10	1.98
	R	1.11	0.35	1.01	0.78
28 d Flexural Strength (MPa)	K1	7.31	6.74	8.63	8.38
	K2	8.42	8.32	8.24	8.51
	K3	9.45	10.12	8.31	8.29
	k1	2.44	2.25	2.88	2.79
	k2	2.81	2.77	2.75	2.84
	k3	3.15	3.37	2.77	2.76
	R	0.71	1.13	0.13	0.07

https://doi.org/10.3390/ma19071287

(2) Compressive Strength

Compressive strength was determined using a CDT1305–2 microcomputer–controlled electronic pressure testing machine at a loading rate of 2400 N/s, following GB/T 17671 (ISO method). The water–to–cement ratio was 1.0. Tests were performed on the two halves of specimens obtained from the flexural test, and the average value was reported as the compressive strength.

The order of influence of each factor on the compressive strength of neat paste specimens varied with curing age. At 3 and 7 days, the sequence was basalt fiber > sodium bentonite > fly ash. At 28 days, however, the order shifted to fly ash > basalt fiber > sodium bentonite. Fly ash content significantly influenced later compressive strength; at 28 days, the hydration degree of fly ash was limited, and the specimens were not fully mature. The later strength can still increase by 20–30% at ages of 90 to 180 days.

The addition of basalt fiber can improve the ultimate compressive strength of the specimens. Basalt fiber forms a microskeleton structure inside the concrete, altering the pore structure, making the interior of the specimen denser, which is beneficial for increasing its strength. After bentonite is incorporated, hydration reactions form cementitious products, effectively filling micropores between soil particles and sealing gaps in the aggregate structure, thereby reducing the porosity of the cement paste system. When the bentonite content gradually increases, the filling effect of high incorporation (10%) bentonite plays a major role in improving compressive strength, rather than the cement skeleton [29]. As fly ash content increases, upon contact with $Ca(OH)_2$, it hydrates, and the resulting C–S–H gel products act synergistically with the hydration products of cement clinker, the strength of the solidified cement specimen generally rises, but the increase amplitude is significantly affected by the fiber content. The range analysis of Compressive Strength is presented in Table 14.

Table 14. Range Analysis for Compressive Strength.

Target	NO.	A	B/%	C/%	D/%
3 d Compressive Strength (MPa)	K1	11.01	12.93	14.39	12.84
	K2	12.7	14.12	12.85	12.8
	K3	15.61	12.27	12.08	13.68
	k1	3.67	4.31	4.80	4.28
	k2	4.233	4.71	4.28	4.27
	k3	5.20	4.09	4.027	4.56
	R	1.53	0.62	0.77	0.29
7 d Compressive Strength (MPa)	K1	20.45	21.94	23.89	23.17
	K2	22.25	23.34	23.18	22.33
	K3	26.05	23.47	21.68	23.25
	k1	6.82	7.31	7.96	7.72
	k2	7.42	7.78	7.73	7.44
	k3	8.68	7.823	7.23	7.75
	R	1.87	0.51	0.74	0.31
28 d Compressive Strength (MPa)	K1	27.42	27.08	30.95	30.48
	K2	30.08	33.24	30.18	29.74
	K3	32.81	29.99	29.18	30.09
	k1	9.14	9.03	10.32	10.16
	k2	10.03	11.08	10.06	9.91
	k3	10.94	10.00	9.73	10.03
	R	1.80	2.05	0.59	0.25

Range analysis shows: Basalt fiber content dominates the early flexural strength of the paste specimen, and its content is positively correlated with strength. Basalt fibers are randomly distributed within the cement paste specimen. In the internal space of the specimen, due to their high elastic modulus, they act as distributed reinforcement linking the cement skeleton, bearing external loads. When bearing load, basalt fibers

https://doi.org/10.3390/ma19071287

dissipate externally applied energy through mechanisms like fiber pull–out, fracture, and deformation, effectively enhancing the compressive and flexural strength of the concrete cube. The results indicate that basalt fiber primarily influences early strength, whereas fly ash governs later strength. Considering later compressive strength, the better combination for the slurry material mix proportion is $A_3B_3C_1$.

3.3.5. Solidification Test

The cement content was calibrated based on the stratum parameters to ensure that the wall strength meets the safety threshold for foundation pit excavation. The control value for the 28–day unconfined compressive strength was set at $\geq$0.8 MPa, and the critical cement mixing ratio was taken as 20%. The water–to–cement ratio was optimally selected within the range of 1.0–2.0, and the permeability coefficient was required not to exceed 10^{-7} cm/s.

Specimens for strength testing were prepared using 100 mm cube molds. Permeability test specimens were 50 mm cubes, with at least three specimens per group. All specimens were cured for 24 h in a curing chamber maintained at a temperature of 21 $\pm$ 5 °C and a relative humidity greater than 90%. The test–related content is presented in Table 15.

Table 15. Test–Related Content.

Influencing Factor	Range or Parameter
Cement Material Content	10%, 15%, 20%, 25%, 30%
Cement Material Type	Basalt Fiber Solidified Cement Material
Curing Age	7 d, 28 d, 90 d

(1) Consolidated Solid Compressive Strength

The unconfined compressive strength of the solidified cement soil specimens was measured using a WD–96205 microcomputer–controlled electronic universal testing machine.

The unconfined compressive strength of the cement–soil consolidated solid increases with the increase in cement content. Compared to the control group, the new cement material can enhance the unconfined compressive strength of the cement–soil consolidated solid, and the effect becomes more obvious with increasing age. Through testing, cement–soil consolidated solids with a content above 15% can meet the quality assurance requirements for CSM wall formation. Based on practical engineering needs, a cement content of 20% is suitable for highly weathered stratum conditions. The variation curve of cemented soil strength with cement content is shown in Figure 12.

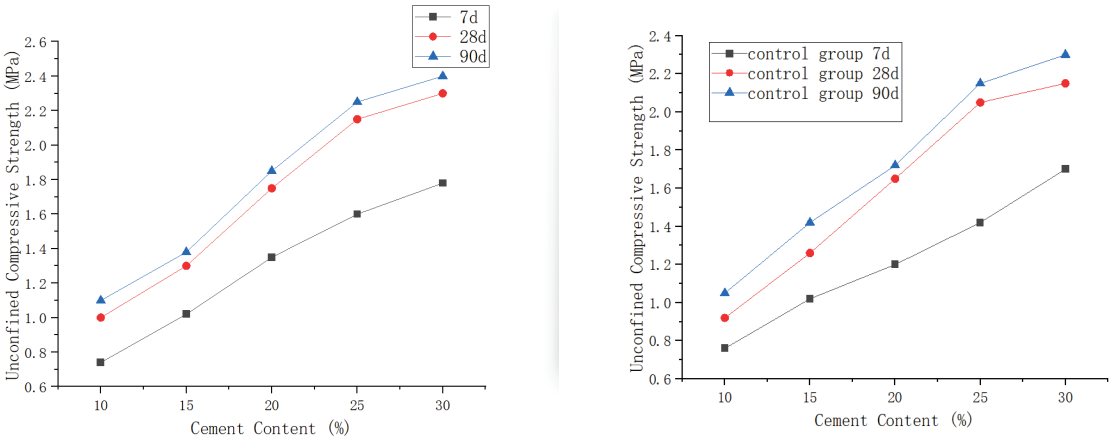

(**a**) Solidified Cement Slurry (**b**) Control Group

Figure 12. Curve of cement–soil consolidated solid strength versus cement content.

https://doi.org/10.3390/ma19071287

(2) Consolidated Solid Permeability Coefficient

The permeability coefficient, which reflects the impermeability of the cemented soil, was determined using a rock permeameter with the constant head method, following Darcy's law.

The influence of solidified cement content on the permeability coefficient of the cement–soil consolidated solid shows that increasing content drives the permeability coefficient negatively correlated. When the content reaches the critical value of 10%, the permeability coefficient of the consolidated solid is significantly higher, unable to meet the seepage prevention threshold requirements for CSM engineering. When the cement content increases further, levels above 15% all meet the requirements. Compared to the control group, the cement content is reduced by 5%. The rate of decrease in permeability coefficient reduces as the cement content increases. Therefore, subsequently increasing cement content to reduce the permeability coefficient will significantly reduce economy. The variation curve of the permeability coefficient of cemented soil with cement content is shown in Figure 13.

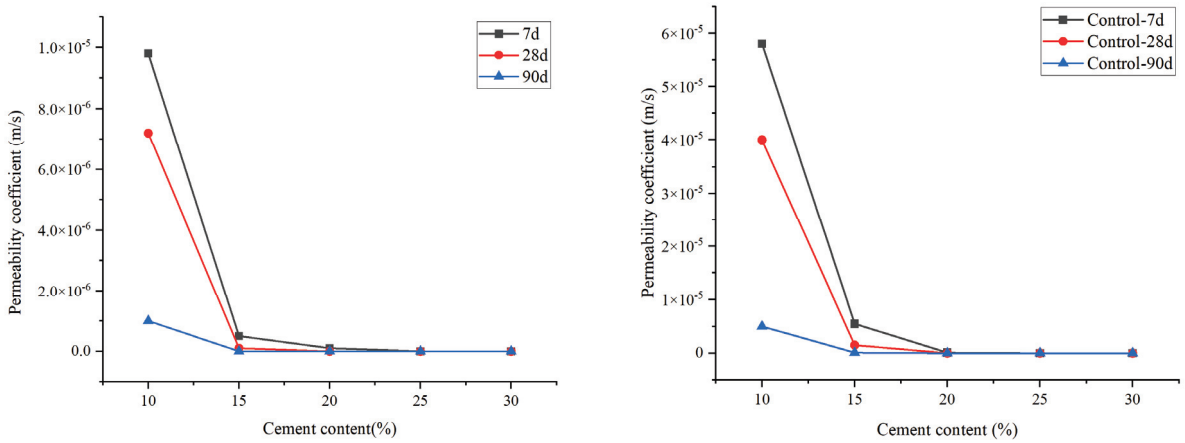

(**a**) Solidified Cement Slurry (**b**) Control Group

Figure 13. Curve of cement–soil consolidated solid permeability coefficient versus cement content.

Basalt fiber provides physical reinforcement through bridging and crack resistance mechanisms, effectively inhibiting the initiation and propagation of microcracks under load, thereby enhancing the toughness and post–peak load–bearing capacity of the matrix. Meanwhile, fly ash contributes chemical reinforcement through its pozzolanic effect, in which reactive SiO_2 and Al_2O_3 consume calcium hydroxide to generate secondary C–S–H gel, densifying the microstructure. Its morphological effect improves workability, while the micro–aggregate effect further fills capillary pores. Sodium bentonite serves as a supplement through physical filling and waterproofing action: upon contact with water, its hydration–induced expansion characteristics can block macroscopic seepage channels, and its fine particles, combined with cation exchange capacity, fill interstitial pores and adsorb onto the surfaces of cement particles, significantly reducing permeability.

Crucially, these mechanisms do not operate in isolation but work synergistically. Fiber reinforcement compensates for the brittleness of the cementitious matrix, while the densifying effect of fly ash pozzolanic reaction provides a stronger interface for fiber anchoring, maximizing reinforcement efficiency. Simultaneously, the expansive filling action of bentonite, combined with the microstructural refinement by fly ash, creates a dual–scale sealing effect, significantly enhancing impermeability and long–term durability.

Ultimately, this ternary system constructs a three–dimensional modification network characterized by "fiber reinforcement–pozzolanic densification–bentonite sealing." The resulting composite material exhibits simultaneous improvements in strength, toughness,

https://doi.org/10.3390/ma19071287

and impermeability, with comprehensive performance far exceeding that achievable by any single additive alone.

4. Field Test

4.1. Project Overview

Haixi Road Station is located between the intersection of Shuangfengshan Road and Haixi Road and the intersection of Shuangfengshan Road and Yujin Road, arranged perpendicular to Shuangfengshan Road from northwest to southeast. The satellite photo is shown in Figure 14. The geological structure pattern of this area is mainly controlled by the regional fault system, belonging to the secondary fault unit of the Cangkou Fault distributed in the NW direction, overall showing a NE extension characteristic. This fault has a strike of 134°, dipping southeast, with a dip angle of 70°, a plane extension length of about 14 km, and a structural fracture zone width of up to 30 m. The excavation is about 101 m long (longitudinal) and about 21.3~49.3 m wide (transverse), with a depth of about 22.4~27.9 m. The upper part of the excavation supporting structure uses the CSM method structural support, with an excavation depth of about 14.5 m. The lower part uses steel pipe piles + anchor cables, with an excavation depth of about 10.4 m. Locally, where the medium and slightly weathered rock surface is higher, a two–level steel pipe pile support type is used.



Figure 14. Satellite photo of Haixi Road Station.

4.2. Engineering Effectiveness

During the actual construction process of the bored pile support structure scheme, due to various factors such as geological conditions and construction techniques, the excavation sidewall may exhibit issues like lack of flatness and water seepage, even noticeable water flow at a few locations. As shown in Figure 15. These problems not only affect the overall stability of the excavation but may also adversely impact subsequent construction and the safety of the structure. The support effect of the CSM method is shown in Figure 16.

The CSM method reduces cement usage, achieves a steel recovery rate of over 85%; shortens the construction period by 30%, reducing machinery rental and labor costs; reduces construction waste and carbon emissions, aligning with sustainable development requirements.

The CSM method structural support scheme uses a dual–wheel cutter device for in situ cutting and mixing of the stratum, coupled with a real–time verticality monitoring system (deviation $\leq 1/300$), ensuring the wall is continuous, vertical, and uniform in thickness, forming a seamless continuous wall (permeability coefficient $\leq 1 \times 10^{-6}$ cm/s), eliminating the seepage paths between piles inherent in bored pile support structures,

https://doi.org/10.3390/ma19071287

thereby reducing the occurrence of the aforementioned problems. The comprehensive cost of the CSM method with embedded steel sections scheme is 19.1% lower than that of bored cast–in–place piles. The CSM method reduces cement usage, achieves a steel recovery rate of over 85%; shortens the construction period by 30%, reducing machinery rental and labor costs; reduces construction waste and carbon emissions, aligning with sustainable development requirements.



(**a**) Insufficient sidewall flatness (**b**) Sidewall water seepage

Figure 15. Common problems of bored pile support structure.



Figure 16. Support effect of CSM method structural support scheme.

The cost of bored piles combined with waterproof curtain and CSM wall with embedded H–beams are shown in Tables 16 and 17.

Table 16. Total Cost of Bored Piles Combined with Waterproof Curtain.

No.	Material Type	Unit	Unit Price (Yuan)	Quantity	Cost (Yuan)
1	Concrete C30	m^3	360	2545.36	916,330
2	HPB300	ton	3570	39.962	142,665
3	HRB335	ton	3870	199.81	773,268
4	Steel Q235	ton	3860	521.42	2,012,682
5	Earthwork	m^3	20	47,850	957,000
Total					4,801,945

Adjusted total project cost = 4,801,945 × 1.00 = 4,801,945 Yuan = 480.195 (10k Yuan).

https://doi.org/10.3390/ma19071287

Table 17. Total Cost of CSM Wall with Embedded H–beams.

No.	Material Type	Unit	Unit Price (Yuan)	Quantity	Cost (Yuan)
1	Concrete C30	m^3	360	130.733	47,064
2	HPB300	ton	3570	2.053	7327
3	HRB335	ton	3870	10.263	39,716
4	Steel Q345	ton	3860	97.665	376,988
5	CSM Method Steel Section	ton	4230	410.194	1,735,121
6	Cement–Soil	m^3	200	3608.273	721,655
7	Earthwork	m^3	20	47,849.984	957,000
Total					3,884,871

Adjusted total project cost = 3,884,871 × 1.00 = 3,884,871 (Yuan) = 388.49 (10k Yuan).

5. Conclusions

To address the technical challenges of low strength and poor impermeability of cemented soil walls when applying the CSM method in highly weathered strata, this study systematically optimized the CSM–H–section steel composite support structure and its associated cement–based material mix proportion through a combination of numerical simulation, orthogonal laboratory tests, and field validation. The main conclusions are as follows:

(1) The proposed CSM structure combined with H–section steel and detachable anchor cables demonstrates superior performance compared to traditional bored pile support systems. Numerical simulation results indicate that the optimized scheme achieves comparable displacement control while reducing the bending moment concentration at the wall toe. Field application at Haixi Road Station confirmed that this method effectively addresses the common issues of sidewall unevenness and water seepage associated with bored piles.

(2) Through orthogonal experiments and range analysis, the optimal mix proportion for the solidified cement–soil material in highly weathered strata was determined as: 0.5% basalt fiber (12 mm), 15% fly ash, and 3% sodium bentonite. This combination achieves the best balance between workability (fluidity, setting time, bleeding rate) and mechanical properties (compressive and flexural strength).

(3) The synergistic mechanism of the ternary additive system was elucidated: basalt fiber provides crack–bridging reinforcement, fly ash contributes pozzolanic densification, and sodium bentonite ensures physical sealing. This multi–level modification network simultaneously enhances strength, toughness, and impermeability, with the optimal cement content identified as 20% for engineering applications in the Huangdao area.

(4) Economic analysis reveals that the CSM method with embedded H–section steel reduces the comprehensive project cost by 19.1% compared to the traditional bored pile scheme, while achieving a steel recovery rate exceeding 85% and a 30% reduction in construction period, aligning with green construction and sustainable development principles.

Despite the achievements described above, this study has certain limitations: the laboratory tests were conducted under standard curing conditions, which cannot fully reflect the complex temperature and humidity variations encountered in the field; the long–term durability of the proposed material under wet–dry cycles and freeze–thaw

https://doi.org/10.3390/ma19071287

cycles—common in weathered strata—has not yet been systematically evaluated; and the numerical simulation assumed a homogeneous stratum without considering the effects of construction disturbances or localized geological anomalies.

It is recommended that future research focus on long–term field monitoring, durability assessment, microstructural characterization, and optimization of construction parameters.

Author Contributions: Author Contributions: Conceptualization, H.W. (Hongbo Wang); Methodology: H.W. (Hao Wen); Validation: Y.X. and Y.C.; Investigation: Y.X., H.L., and C.S.; Resources: Y.X., H.L., L.Z., and H.W. (Hongbo Wang); Writing—Original Draft: Y.X.; Writing—Review and Editing: Y.X., H.W. (Hao Wen), C.S., Q.F., and H.W. (Hongbo Wang); Supervision: Q.F., and L.Z. All authors have read and agreed to the published version of the manuscript.

Funding: This research received no external funding.

Data Availability Statement: The original contributions presented in this study are included in the article. Further inquiries can be directed to the corresponding author.

Conflicts of Interest: Author Haitao Liu was employed by the China Railway First Group No.5 Engineering Co., Ltd. Author Yong Chang was employed by the China Railway First Group No.5 Engineering Co., Ltd. The funding sponsors had no role in the design of the study; in the collection, analyses, or interpretation of data; in the writing of the manuscript; or in the decision to publish the results. The remaining authors declare no conflicts of interest.

References

1. Yan, R.H.; Zhu, M.; Guo, Y.J.; Liu, F. Analysis of the influence of SMW method foundation pit enclosure on adjacent rail viaducts. *Build. Struct.* **2023**, *53*, 2908–2911. (In Chinese)
2. Li, D.J.; Feng, S.; Yang, B.S. Comparison and selection of foundation pit support schemes for the Northern District of the Palace Museum. *Build. Struct.* **2022**, *52*, 111–115+36. (In Chinese)
3. Zhou, J.F. Construction technology and control of retaining pile foundation for deep foundation pits. *Constr. Technol.* **2020**, *49*, 86–89. (In Chinese)
4. Gao, L.L.; Wen, W.G. Application of TRD method in deep foundation pit engineering. *Water Resour. Hydropower Eng.* **2019**, *50*, 92–97. (In Chinese)
5. Sun, Z.Z.; Li, N. Application of TRD method in sandy silty strata of Shanghai Metro. *Constr. Technol.* **2017**, *46*, 1105–1108. (In Chinese)
6. Brunner, W.G.; Fiorotto, R.; Stötzer, E.; Schöpf, M. The innovative CSM–cutter soil mixing for constructing retaining and cut off walls. In *GeoCongress 2006: Geotechnical Engineering in the Information Technology Age*; American Society of Civil Engineers: New York, NY, USA, 2006; pp. 1–6. [CrossRef]
7. Li, C.W.; Liang, Z.R.; Wei, X.; Wang, G.C. Application of CSM method in control of confined groundwater of deep excavations in soft soils. *Chin. J. Geotech. Eng.* **2019**, *41*, 125–128. [CrossRef]
8. Mortazavi, A.; Alavi, F.T. A numerical study of the behavior of fully grouted rockbolts under dynamic loading. *Soil Dyn. Earthq. Eng.* **2013**, *54*, 66–72. [CrossRef]
9. Lu, X.; Mengen, S.; Wang, P. Numerical simulation of the composite foundation of cement soil mixing piles using FLAC3D. *Clust. Comput.* **2019**, *22*, 7965–7974. [CrossRef]
10. Liang, Z.R.; Li, Z.C. Key Problems and New Development of Steel Profile Cement–soil Continuous Wall in Foundation Pit Engineering. *J. Geotech. Eng.* **2010**, *32*, 290–296. (In Chinese)
11. Tan, K.; Wang, W.D.; Di, G.E. Deformation and bearing characteristics of steel cement-soil wall constructed by TRD method. *Chin. J. Geotech. Eng.* **2015**, *37*, 191–196. (In Chinese) [CrossRef]
12. Lu, Y.J.; Liang, S.T.; Zhu, X.J.; Sun, B.W.; Wang, W.K.; Chen, Y.L.; Ji, X. Axial compressive stability of precast H–shaped steel support in foundation pit engineering. *J. Constr. Steel Res.* **2025**, *230*, 109540. [CrossRef]
13. Jiang, P.; Zhang, S. Study on the deformation mechanism and application of trench cutting re–mixing deep walls. *Tunn. Undergr. Space Technol.* **2026**, *168*, 107157. [CrossRef]
14. Wang, Y.; Hu, S.; Sun, X. Experimental investigation on the elastic modulus and fracture properties of basalt fiber–reinforced fly ash geopolymer concrete. *Constr. Build. Mater.* **2022**, *338*, 127570. [CrossRef]
15. Li, Z.X.; Guo, T.T.; Chen, Y.Z.; Fang, C.Z.; Chang, Y.M.; Nie, J.X. Influence of basalt fiber and polypropylene fiber on the mechanical and durability properties of cement–based composite materials. *J. Build. Eng.* **2024**, *90*, 109335. [CrossRef]

https://doi.org/10.3390/ma19071287

16. Cheng, C.M.; He, J.; Li, X.S.; Hong, S.L. Flexural behavior of glass fiber reinforced cement incorporating foam. *J. Eng. Fibers Fabr.* **2024**, *19*, 1–10. [CrossRef]
17. Li, H.; Zhou, W. Hybrid Properties of High–Performance Fiber–Reinforced Cement Composites. *Rom. J. Mater. Rev. Romana Mater.* **2024**, *54*, 29.
18. Tu, Y.L.; Ren, S.Y.; Zhao, L.; Ling, L.; Chai, H.J. Experimental study on the improvement of shear strength of cemented soil with basalt fiber and fly ash. *Mater. Rep.* **2025**, *39*. (In Chinese)
19. Lorenzo, G.A.; Bergado, D.T. Fundamental parameters of cement–admixed clay—New approach. *J. Geotech. Geoenviron. Eng.* **2004**, *130*, 1042–1050. [CrossRef]
20. Opdyke, S.M.; Evans, J.C. Slag–cement–bentonite slurry walls. *J. Geotech. Geoenviron. Eng.* **2005**, *131*, 673–681. [CrossRef]
21. Xu, C.; Huang, L.; Xing, H.F. Effect of Cement–Bentonite Slurry Ratio on Permeability of Seepage Wall. *Rock Soil Mech.* **2010**, *31*, 422–426. (In Chinese)
22. Cho, Y.K.; Jung, S.H.; Choi, Y.C. Effects of chemical composition of fly ash on compressive strength of fly ash cement mortar. *Constr. Build. Mater.* **2019**, *204*, 255–264. [CrossRef]
23. Zhang, C.; Fu, J.; Song, W.D. Mechanical model and strength development evolution of high content fly ash–cement grouting material. *Constr. Build. Mater.* **2023**, *398*, 132492. [CrossRef]
24. Wei, F.L.; Xiao, H.R.; Zhang, J.; He, Z.Q.; Cao, X.H.; Guan, B.W. Feasibility study of magnesium slag, fly ash, and metakaolin to replace part of cement as cementitious materials. *Buildings* **2024**, *14*, 3874. [CrossRef]
25. Lu, L.Y.; Liu, C.H.; Qu, S.Y.; Zhang, M.Z. Experimental study on the mechanical and hydraulic behaviour of Fibre–Reinforced cemented soil with fly ash. *Constr. Build. Mater.* **2022**, *321*, 126374. [CrossRef]
26. *GB/T 1346-2024*; National Technical Committee on Cement of Standardization Administration of China (SAC/TC 184). Test Methods for Water Requirement of Normal Consistency, Setting Time and Soundness of Cement. China Standards Press: Beijing, China, 2024.
27. Chen, P.; Zhang, C.H.; Wang, C.Y.; Shi, K.Y.; Lei, Y.Z. Research Status of Main Characteristics of Basalt Fiber. *Inorg. Salt Ind.* **2020**, *52*, 64–67. (In Chinese) [CrossRef]
28. Fei, Z.H.; Wu, J.G.; Ming, H.J.; Ke, R.; Shi, C.P. Study on the Mixing Proportion and Applicability of Cement–Bentonite Slurry. *J. Three Gorges Univ. (Nat. Sci. Ed.)* **2019**, *41*, 51–54. (In Chinese) [CrossRef]
29. Guo, H.B. Effect of Bentonite Slurry Ratio on the Wall Quality of CSM Cement–soil Mixing Wall in Soft Soil. *Build. Constr.* **2024**, *3*, 317–321. (In Chinese) [CrossRef]

Disclaimer/Publisher's Note: The statements, opinions and data contained in all publications are solely those of the individual author(s) and contributor(s) and not of MDPI and/or the editor(s). MDPI and/or the editor(s) disclaim responsibility for any injury to people or property resulting from any ideas, methods, instructions or products referred to in the content.

https://doi.org/10.3390/ma19071287

materials

MDPI

Article

A Hybrid-Dimensional Iterative Coupled Modeling of Lubrication Flow in Deformable Geological Media with Discrete Fracture Networks

Yue Xu [1,2], Tao You [3] and Qizhi Zhu [1,2,*]

[1] Key Laboratory of Ministry of Education for Geomechanics and Embankment Engineering, Hohai University, Nanjing 210098, China; xuyue_hhu@hhu.edu.cn
[2] College of Civil and Transportation Engineering, Hohai University, Nanjing 210098, China
[3] Department Geoenergy, Montanuniversität Leoben, 8700 Leoben, Austria
* Correspondence: qzhu@hhu.edu.cn

Abstract

Fluid-driven fracture processes are central to the development of subsurface energy systems such as geothermal and hydrocarbon reservoirs. Although phase-field formulations have become a widely used tool for describing fracture initiation and growth, the diffuse representation of cracks makes it difficult to resolve flow behavior accurately inside discrete fracture networks (DFNs) and to represent hydro-mechanical coupling in a sharp-interface sense. This study develops a hybrid-dimensional iterative framework for lubrication-flow simulation in deformable fractured geomaterials. By leveraging phase-field point clouds together with non-conforming discretization schemes for both the solid matrix and fracture domains, the proposed framework enables the dynamic reconstruction of evolving fracture networks. The theoretical formulation and numerical implementation of the coupling strategy are presented in detail. Hydraulic benchmark examples verify the performance of the fluid flow solver under various physical conditions. The classical Sneddon problem and Khristianovic–Geertsma–de Klerk (KGD) model are employed to validate the solid deformation solver, confirming accurate predictions of crack opening displacement and mesh independence in fracture width calculation. Additional simulations with complex pre-existing fracture patterns further demonstrate the applicability of the framework to coupled hydro-mechanical analysis in fractured media.

Keywords: non-conforming discretization; lower-dimensional crack; hybrid-dimensional coupling strategy; fracture width estimation

1. Introduction

Fracture propagation driven by pressurized fluid strongly influences the performance of subsurface energy systems, including shale, petroleum, and geothermal reservoirs [1,2]. For this reason, the numerical simulation of coupled flow-deformation behavior in fractured rocks has become an important approach for investigating fracture growth, fluid migration, and network evolution under different geological settings [3].

Among various computational approaches, phase-field models have attracted considerable attention due to the ability to capture complex fracture nucleation, branching, and coalescence phenomena without the explicit tracking of crack surfaces [4–6]. These methods provide a diffuse approximation of the fracture, allowing robust numerical implementation in continuous solid media. Recent studies have further extended phase-field hydraulic

fracture modeling to porous media, including formulations for fracture nucleation and propagation, hydro-mechanical coupling, and interactions with pre-existing natural fractures [7–9]. However, the diffuse nature brings a significant challenge to accurately resolve fluid flow within discrete fracture networks, where localized aperture and permeability are critical to describing lubrication flow [10]. Moreover, the smeared representation of fractures complicates the modeling of pre-existing natural fracture topology, which governs flow paths in geological reservoirs [11,12]. Owing to the implicit representation of discrete fractures in smeared damage formulations, most phase-field approaches approximate fracture effects by enhancing permeability within damaged regions, while omitting the explicit solution of fluid flow on lower-dimensional DFNs; see the review article [13]. In parallel, recent developments in fractured porous media flow have shown that hybrid-dimensional formulations provide an efficient way to represent fracture–matrix flow exchange while preserving the lower-dimensional nature of discrete fractures [14,15]. Santillán et al. [16] have taken an important step by solving the flow problem on a sharp crack path, but that formulation is not straightforward for complex fracture networks. Zhao et al. [17] have proposed a hydro-mechanical strategy, in which discrete fractures are regularized within a phase-field setting, although the required local mesh refinement near the fracture region may substantially increase computational expense.

To overcome these limitations, a natural alternative is to represent fractures as lower-dimensional manifolds embedded in the surrounding rock matrix, i.e., lines in two dimensions and surfaces in three dimensions [18,19]. To accurately resolve the matrix-fracture interface, the fracture discretization must be sufficiently refined and compatible with the adjacent matrix grid [20–22]. This requirement necessitates the use of locally refined and unstructured meshes to match the explicit geometry of the fractures [23]. However, such mesh refinement leads to several drawbacks, including high computational cost, reduced flexibility and meshing complexity. The hybrid models enable a detailed characterization of the fracture aperture and hydraulic property, and allow for the direct solution of lubrication or Darcy–Stokes flow equations along the fracture domain. However, coupling such DFN representations with the mechanical deformation of the surrounding solid media remains challenging, especially when non-conforming discretization is employed to handle evolving fracture geometries [24,25]. In particular, recent hydro-mechanical studies have emphasized the numerical difficulty of consistently coupling flow, deformation, and fracture evolution under embedded or non-conforming discretizations [26–28]. The iterative schemes capable of exchanging information between the matrix and fractures are therefore essential to ensure consistency in hydro-mechanical coupling and stability in numerical implementation.

In the present study, we introduce a hybrid-dimensional iterative strategy for lubrication flow in deformable media with discrete fracture networks. This framework integrates non-conforming discretization for fractures and reservoirs, enabling independent and flexible mesh optimization. The iterative coupling procedure ensures the consistent transfer of hydraulic pressure and mechanical displacement across the matrix–fracture interface, satisfying equilibrium and mass conservation conditions during the iterative coupling process. The remainder of the paper is organized as follows. Section 2 details the mathematical formulation of the proposed hybrid-dimensional hydro-mechanical system for phase-field fracture. Section 3 describes the numerical procedure of the iterative strategy, as well as employing the fixed-stress split scheme to stabilize the flow equation. Section 4 validates the hydraulic solver and mechanical solver against benchmark cases, illustrating precise crack opening displacement as well as mesh independence in fracture width calculation. Moreover, this section discusses application in discrete fracture networks and demonstrates the model's adaptability for tackling coupled hydro-mechanical processes.

https://doi.org/10.3390/ma19071444

Section 5 provides a brief discussion of the proposed hybrid method, with regard to the current limitations and possible directions for future research. The final section 6 closes the paper with concluding remarks.

2. Methods

2.1. Balance Laws

As illustrated in the left part of Figure 1, consider a cracked brittle solid $\Omega \subset \mathbb{R}^n (n \in \{2,3\})$ with boundary $\partial\Omega$. $\boldsymbol{u}_D$ and $\boldsymbol{t}_\mathrm{N}$ denote the Dirichlet and Neumann boundary conditions, respectively, defined on $\partial\Omega_u$ and $\partial\Omega_t$, which together form a complete partition of the boundary, i.e., $\partial\Omega_u \cup \partial\Omega_t = \partial\Omega$ and $\partial\Omega_u \cap \partial\Omega_t = \varnothing$. Neglecting body forces, the linear momentum balance law reads as Equation (1):

$$\nabla \cdot \boldsymbol{\sigma} = \mathbf{0} \text{ in } \Omega \setminus \Gamma, \tag{1}$$

where $\boldsymbol{\sigma} := \mathbb{C}_\mathrm{e} : \nabla^\mathrm{s}\boldsymbol{u}$, with $\nabla^\mathrm{s}\boldsymbol{u}$ denoting the linearized strain, defined as

$$\nabla^\mathrm{s}\boldsymbol{u} := \frac{\nabla\boldsymbol{u} + (\nabla\boldsymbol{u})^\mathrm{T}}{2}.$$

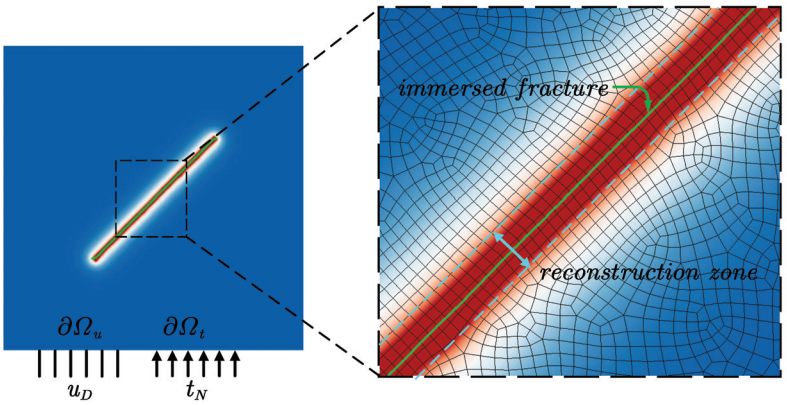

Figure 1. Schematic diagram of phase-field model and the immersed fracture.

The boundary conditions and continuity of stress at the fracture surface yield

$$\begin{cases} \boldsymbol{u} = \boldsymbol{u}_\mathrm{D} \text{ on } \partial\Omega_u \\ \boldsymbol{\sigma} \cdot \boldsymbol{n}_t = \boldsymbol{t}_\mathrm{N} \text{ on } \partial\Omega_t \\ \boldsymbol{\sigma}^\pm \cdot \boldsymbol{n}_{\Gamma^\pm} = -p_\mathrm{f}\boldsymbol{n}_{\Gamma^\pm} \text{ on } \Gamma^\pm \end{cases} \tag{2}$$

By testing Equation (1) with $\boldsymbol{w}_u \in H^1(\Omega \setminus \Gamma)$ and applying integration by parts in conjunction with Equation (2), we obtain

$$\int_{\Omega\setminus\Gamma} \mathbb{C}_\mathrm{e} : \nabla^\mathrm{s}\boldsymbol{u} : \nabla^\mathrm{s}\boldsymbol{w}_u \,\mathrm{d}V = \int_{\partial\Omega_t} \boldsymbol{t}_\mathrm{N} \cdot \boldsymbol{w}_u \,\mathrm{d}S + \int_\Gamma p_\mathrm{f} \left[\!\left[\boldsymbol{w}_u \cdot \boldsymbol{n}_\Gamma\right]\!\right] \mathrm{d}S. \tag{3}$$

where $[\![\cdot]\!]$ denotes a jump quantity over Γ. Given p_f and the crack topology Γ, the weak form in Equation (3) can be interpreted as the first-order optimality condition of the total potential energy functional defined in Equation (4).

$$\mathcal{P} := \int_{\Omega\setminus\Gamma} W(\boldsymbol{u}) \,\mathrm{d}V - \int_{\partial\Omega_t} \boldsymbol{t}_\mathrm{N} \cdot \boldsymbol{u} \,\mathrm{d}S - \int_\Gamma p_\mathrm{f} \left[\!\left[\boldsymbol{u} \cdot \boldsymbol{n}_\Gamma\right]\!\right] \mathrm{d}S, \tag{4}$$

https://doi.org/10.3390/ma19071444

with

$$W(\boldsymbol{u}) := \frac{1}{2}\mathbb{C}_{\mathrm{e}} : \nabla^{\mathrm{s}}\boldsymbol{u} : \nabla^{\mathrm{s}}\boldsymbol{u} \tag{5}$$

being the elastic strain energy density.

2.2. Immersed Fracture Boundary Condition

The presence of discontinuity Γ creates both theoretical and numerical challenges when solving Equation (4). One effective approach to address these issues is to use regularization, i.e., approximating the sharp interface by a diffuse interface, such as the phase-field model [29] as illustrated in Figure 1. However, this diffuse approximation requires reconstructing the pressure that is originally present in a sharp fracture and exhibits a significant gradient perpendicular to the fracture. This process is similar to the immersed boundary method [30], where discontinuities or boundary effects are incorporated into the domain through a smooth transition function.

Accordingly, the last term of Equation (4) can be reformulated as a volume integral over Ω, leading to the regularized energy functional, that is

$$\int_{\Gamma} p_{\mathrm{f}} \left[\!\left[\boldsymbol{u}(x) \cdot \boldsymbol{n}_{\Gamma}\right]\!\right] \mathrm{d}S \approx -\int_{\Omega} p'_f \, \boldsymbol{u}(x) \cdot \nabla d(x) \, \mathrm{d}V, \tag{6}$$

where d is a continuous-order parameter that regularizes the discontinuous fracture as a diffuse interface. p'_f denotes a projected pressure defined as a space- and time-dependent field, which is nonzero only within diffuse regions and can be constructed from the pressure at the nearest point on the fracture.

To approximate the fracture energy within the phase-field framework, we adopt the regularized crack functional proposed in [31,32] given by

$$\Gamma_{\ell}(d) = G_{\mathrm{c}} \int_{\Omega} \gamma(d, \nabla d) \, \mathrm{d}\Omega, \tag{7}$$

where $d \in [0, 1]$ is the phase-field variable, with $d = 0$ corresponding to the undamaged state and $d = 1$ corresponding to the fully broken state. The parameter $G_{\mathrm{c}} > 0$ denotes the critical energy release rate, i.e., the fracture toughness of the material. The crack surface density function $\gamma(d, \nabla d)$ is defined following [31,33] as

$$\gamma(d, \nabla d) = \frac{1}{4c_w}\left(\frac{w(d)}{\ell} + \ell |\nabla d|^2\right). \tag{8}$$

where $\ell > 0$ denotes the regularization length scale governing the width of the diffusive crack zone [33], and $w(d)$ is a degradation function that vanishes in the unbroken state and penalizes the fractured state.

In the phase-field modeling of brittle fracture, the AT1 model is known for producing a compact support profile of the phase-field variable. Unlike the AT2 model, which yields a smooth but infinitely supported profile, the AT1 model leads to a finite-width damage zone, making it particularly suited for simulating crack initiation and fracture localization [34]. In the AT1 model, the degradation function is chosen as

$$w(d) = d, \tag{9}$$

and the normalization constant c_w is set to

$$c_w = \frac{2}{3}, \tag{10}$$

https://doi.org/10.3390/ma19071444

thereby ensuring the convergence of the regularized functional to the classical Griffith fracture energy as $\ell \to 0$.

The phase-field representation can be formulated by solving a homogeneous differential equation as shown in [32].

The diffuse approximation of a sharp fracture also introduces a stiffness degradation to the matrix. For the isotropic phase-field model, the degradation function is taken in the form [32]

$$g(d) = (1-\kappa)(1-d)^2 + \kappa. \tag{11}$$

and then Equation (4) is rewritten as

$$\mathcal{P} := \int_\Omega \frac{1}{2} g(d)\mathbb{C}_\mathrm{e} : \nabla^\mathrm{s}\boldsymbol{u} : \nabla^\mathrm{s}\boldsymbol{u}\,\mathrm{d}V - \int_{\partial\Omega_t} \boldsymbol{t}_\mathrm{N}\cdot\boldsymbol{u}\,\mathrm{d}S + \int_\Omega p_f'\,\boldsymbol{u}\cdot\nabla d\,\mathrm{d}V, \tag{12}$$

where $0 < \kappa \ll 1$ is a constant for numerical robustness.

The Cauchy stress is then expressed as

$$\boldsymbol{\sigma} = g(d)\mathbb{C}_\mathrm{e} : \nabla^\mathrm{s}\boldsymbol{u}. \tag{13}$$

2.3. Flow Equation

In the hybrid-dimensional framework, the fluid flow within lower-dimensional fractures is described using lubrication theory originally introduced by Reynolds [35]. Following the reduced-dimensional fracture flow formulation in [16], the governing equation is written as

$$\frac{\partial w}{\partial t} + C_f w\frac{\partial p_f}{\partial t} = \nabla_s\cdot\Big(K(w)\Big(\nabla_s p_f\Big)\Big) + q. \tag{14}$$

Here, w, p_f, C_f, and q denote the fracture aperture, fluid pressure, fluid compressibility, and source/sink term, respectively. The hydraulic conductivity $K(w)$ is aperture dependent and follows the local cubic law [36]:

$$K(w) = \frac{w^3}{12\mu_f}. \tag{15}$$

Since the phase-field method approximates sharp cracks as smeared interfaces, accurately depicting the crack curve or surface remains challenging. This, in turn, impedes the precise calculation of the crack opening. Accurate representations of discrete fracture networks can be achieved using a crack-path reconstruction method, which will be detailed in the next section. In addition, the crack aperture calculation may also require high computational resources. Despite these limitations, the accurate calculation of crack opening is an essential part of fracture simulation. Similar to the motivation of Shahoveisi et al. [37], the crack opening displacement is estimated using an equation derived from the projection of the strain tensor. Compared with displacement-based crack opening calculations, the proposed approach allows the aperture to be evaluated directly from the local strain field without explicitly tracking crack surfaces. In addition, the formulation is relatively simple compared with more complex aperture evaluation methods, which facilitates efficient implementation within the numerical framework. The aperture can be computed as

$$w = h_e\boldsymbol{\varepsilon}_\mathrm{N}, \tag{16}$$

where h_e is the mesh element size. The normal strain is calculated based on

$$\boldsymbol{\varepsilon}_\mathrm{N} = \boldsymbol{\varepsilon} : (\boldsymbol{n}\otimes\boldsymbol{n}), \tag{17}$$

https://doi.org/10.3390/ma19071444

where $\boldsymbol{n}$ denotes the unit normal vector to the crack, which can be evaluated using the method developed in our previous work [38]. In the present study, only the opening mode relevant to hydraulic fracturing is considered. The sliding mode is not the dominant factor for fracture. Therefore, the aperture perpendicular to the crack path can be used to compute the permeability $K(w)$ based on the cubic law.

2.4. Flow Distribution at Multi-Fracture Intersections

In the treatment of fracture networks, intersection points, such as T-junctions and cross-junctions, are usually treated as connecting nodes of control volumes. At these intersections, the total inflow must be appropriately distributed among the outgoing directions to ensure mass conservation and to reflect the heterogeneity of the geometry. Here we apply a simple general flux allocation algorithm for distributing a total inflow Q_{in} at an intersection into multiple outgoing branches. The method supports both uniform distribution and weighted allocation based on fracture cross-sectional areas. The specific algorithm is described as follows.

Let N denote the number of fracture channels at the intersection, and define A_i as the cross-sectional area of channel i. The outflow flux F_i in each direction is then defined as

$$F_i = \frac{Q_i}{A_i}. \tag{18}$$

If geometric heterogeneity is neglected and all outlet channels are assumed to possess equivalent physical properties, a uniform distribution strategy is adopted as

$$Q_i = \frac{Q_{\text{in}}}{N}. \tag{19}$$

If the cross-sectional areas of the outgoing channels are unequal, an area-weighted strategy is employed, in which the total flux is distributed proportionally to each outlet as

$$Q_i = Q_{\text{in}} \cdot \frac{A_i}{\sum_{j=1}^{N} A_j}. \tag{20}$$

In fracture networks, the fluid outflow at a node along a given fracture segment is governed by the mass conservation principle together with Darcy's law. Along the fracture direction, which is typically one-dimensional, Darcy's law simplifies to

$$Q = u \cdot A = -\frac{k_{\text{f}}}{\mu_{\text{f}}} \cdot \frac{\Delta p}{\Delta x} \cdot A, \tag{21}$$

where u represents the fluid velocity, k_{f} the fracture hydraulic conductivity, μ_{f} the dynamic viscosity of the fluid, and p the pressure field. For each individual node i, the total outflow is the sum of flux along all fracture segments connected to this node with its sign depending on the flow direction:

$$Q_i^{\text{out}} = \sum_{j \in \mathcal{N}(i)} Q_{ij}, \tag{22}$$

where $\mathcal{N}(i)$ represents the set of neighboring nodes connected to node i, and Q_{ij} denotes the flux from node i to node j, computed with a local discretization scheme (such as the two-point flux approximation (TPFA) [39,40] or the multi-point flux approximation (MPFA) [41,42]).

https://doi.org/10.3390/ma19071444

3. Numerical Implementation

This study proposes a hybrid-dimensional framework for staggeredly coupling phase-field fracture in the solid with Reynolds flow in lower-dimensional cracks. It further permits the dynamic reconstruction of two-dimensional discrete fracture networks (DFNs) from phase-field point clouds and accommodates non-conforming discretizations of the solid and fracture domains.

The coupling process in planar conditions is described as follows. As demonstrated in Figure 2, the solid domain is discretized by finite element nodes and the fracture domain is regularized using the phase-field method in the bottom solid layer, which is demonstrated with the red–blue contour. The lower-dimensional fluid domain represented by red paths is discretized by the finite volume method in the top fluid layer. The finite element method (FEM) nodes and finite volume method (FVM) nodes use coordinates defined in different-dimensional spaces. Hence the two models are linked based on the crack-path reconstruction method [38]. According to the concept of phase-field point cloud and the optimized ridge-regression method, the discrete fracture networks can be reconstructed dynamically as shown in bright green. The middle reconstruction layer realizes the bidirectional interplay between the hydraulic and mechanical processes.

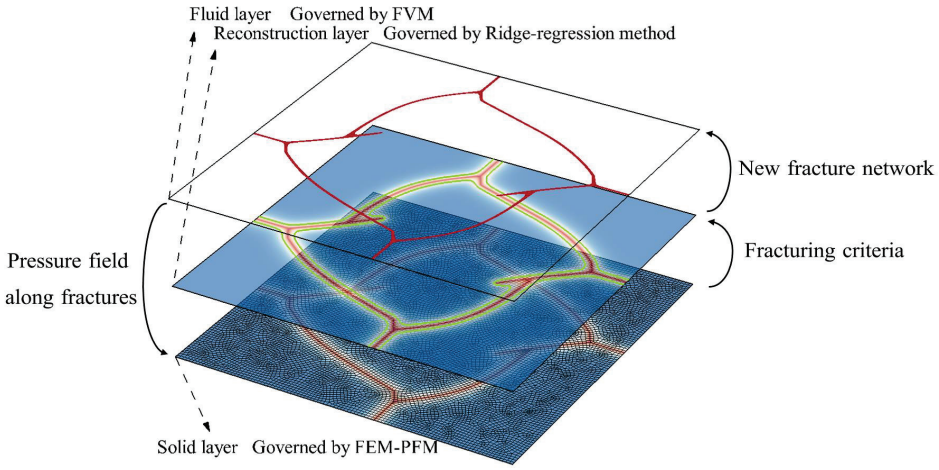

Figure 2. Schematic diagram of the hybrid-dimensional scheme in the coupling process.

The problem is spatially discretized using isoparametric elements, while bilinear shape functions are adopted for interpolation according to the standard finite element framework. This interpolation method provides a balance between computational efficiency and numerical accuracy for two-dimensional problems. Therefore, the discrete approximations of $\boldsymbol{u}$, d, and p are written as

$$\boldsymbol{u} = \boldsymbol{N}_u \hat{\boldsymbol{u}}, \quad \boldsymbol{w}_u = \boldsymbol{N}_u \hat{\boldsymbol{w}}_u, \quad \nabla \boldsymbol{u} = \boldsymbol{B}_u \hat{\boldsymbol{u}}, \quad \nabla \boldsymbol{w}_u = \boldsymbol{B}_u \hat{\boldsymbol{w}}_u \tag{23a}$$

$$d = \boldsymbol{N}_d \hat{d}, \quad w_d = \boldsymbol{N}_d \hat{w}_d, \quad \nabla d = \boldsymbol{B}_d \hat{d}, \quad \nabla w_d = \boldsymbol{B}_d \hat{w}_d \tag{23b}$$

$$p = \boldsymbol{N}_p \hat{p}, \quad w_p = \boldsymbol{N}_p \hat{w}_p, \quad \nabla p = \boldsymbol{B}_p \hat{p}, \quad \nabla w_p = \boldsymbol{B}_p \hat{w}_p \tag{23c}$$

A staggered scheme is employed to solve the d-$(p$-$\boldsymbol{u})$ three-field problem, which is a robust scheme proposed by Miehe et al. [32]. During each time interval $[t_{i-1}, t_i]$, it is assumed that all the variables are known at time t_{i-1}. The time step size is denoted by Δt. The staggered solution procedure for the three-field coupled problem is outlined in Algorithm 1.

https://doi.org/10.3390/ma19071444

Algorithm 1 Staggered scheme for the three-field coupling problem.

Input: d_{i-1}, p_{i-1}, $\boldsymbol{u}_{i-1}$ at time step t_{i-1}
Output: d_i, p_i, $\boldsymbol{u}_i$ at time step t_i
Initialize the d–$(p$–$\boldsymbol{u})$ iteration counter $k = 0$
Set $d_i^k = d_{i-1}$, $p_i^k = p_{i-1}$, $\boldsymbol{u}_i^k = \boldsymbol{u}_{i-1}$
while $err > tol \ \wedge \ k < k_{\max}$ **do**
$k \leftarrow k + 1$
Solve the phase-field equation to obtain d_i^k with fixed p_i^{k-1} and $\boldsymbol{u}_i^{k-1}$
Initialize the p–$\boldsymbol{u}$ iteration counter $j = 0$
Set $p_i^{k,j} = p_i^{k-1}$ and $\boldsymbol{u}_i^{k,j} = \boldsymbol{u}_i^{k-1}$
while $err > tol \ \wedge \ j < j_{\max}$ **do**
$j \leftarrow j + 1$
Solve the fluid flow equation to obtain $p_i^{k,j}$ with fixed $\boldsymbol{u}_i^{k,j-1}$ and d_i^k
Solve the momentum equation to obtain $\boldsymbol{u}_i^{k,j}$ with fixed $p_i^{k,j-1}$ and d_i^k
Compute the error as
$err = \max\Big(\|p_i^{k,j} - p_i^{k,j-1}\|, \|\boldsymbol{u}_i^{k,j} - \boldsymbol{u}_i^{k,j-1}\|\Big)$
end while
Update $p_i^k = p_i^{k,j}$ and $\boldsymbol{u}_i^k = \boldsymbol{u}_i^{k,j}$
Compute the error as
$err = \max\Big(\|d_i^k - d_i^{k-1}\|, \|p_i^k - p_i^{k-1}\|, \|\boldsymbol{u}_i^k - \boldsymbol{u}_i^{k-1}\|\Big)$
end while
Set $d_i = d_i^k$, $p_i = p_i^k$, and $\boldsymbol{u}_i = \boldsymbol{u}_i^k$

3.1. The Equilibrium Equation

The weak form of the momentum balance equation is derived by weighting it with the test function $\boldsymbol{w}_u$ and integrating over the entire domain. Correspondingly, the weak form yields

$$R_u := \int_\Omega \nabla \boldsymbol{w}_u^T \cdot \boldsymbol{\sigma} \, \mathrm{d}V - \int_\Omega \boldsymbol{w}_u^T \cdot p \nabla d \, \mathrm{d}V - \int_{\partial\Omega} \boldsymbol{w}_u^T \cdot \boldsymbol{t} \, \mathrm{d}S. \tag{24}$$

Then the Galerkin approximation (23a) is substituted into Equation (24). The discrete equation yields

$$R_u := \int_\Omega \boldsymbol{B}_u^T \frac{\partial \boldsymbol{\sigma}}{\partial \boldsymbol{\varepsilon}} \boldsymbol{B}_u \hat{\boldsymbol{u}} \, \mathrm{d}V \, \hat{\boldsymbol{w}}_u - \int_\Omega \boldsymbol{N}_u^T \cdot \boldsymbol{N}_p \, \hat{p} \cdot \boldsymbol{B}_d \hat{d} \, \mathrm{d}V \, \hat{\boldsymbol{w}}_u - \int_{\partial\Omega} \boldsymbol{N}_u^T \cdot \boldsymbol{t} \, \mathrm{d}S \, \hat{\boldsymbol{w}}_u \tag{25}$$

$$= \boldsymbol{0}. \tag{26}$$

3.2. The Phase-Field Equation

Likewise, the weak form of the phase-field equation is derived by weighting it with the test function w_d and integrating over the entire domain. Correspondingly, the weak form yields

$$R_d := \int_\Omega w_d \frac{\partial g(d)}{\partial d} \mathcal{H} \, \mathrm{d}V + \int_\Omega w_d \, p \, \boldsymbol{u} \cdot \nabla \, \mathrm{d}V \tag{27}$$

$$+ \int_\Omega w_d \frac{G_c}{4c_\mathrm{n}} \frac{n d^{n-1}}{\ell} \, \mathrm{d}V + \int_\Omega \frac{G_c}{2c_\mathrm{n}} \ell \nabla d \cdot \nabla w_d \, \mathrm{d}V. \tag{28}$$

Substitute the Galerkin approximation (23b) into Equation (28). The discrete equation yields

https://doi.org/10.3390/ma19071444

$$R_d := \int_\Omega \boldsymbol{N}_d^{\mathrm{T}} \frac{\partial g(d)}{\partial d} \mathcal{H}\, \mathrm{d}V\, \hat{w}_d + \int_\Omega \boldsymbol{B}_d^{\mathrm{T}} \boldsymbol{N}_p\, \hat{p}\, \boldsymbol{N}_u\, \hat{\boldsymbol{u}}\, \mathrm{d}V\, \hat{w}_d + \int_\Omega \boldsymbol{N}_d^{\mathrm{T}} \frac{G_c}{4c_{\mathrm{n}}} \frac{n d^{n-1}}{\ell}\, \mathrm{d}V\, \hat{w}_d + \int_\Omega \frac{G_c}{2c_{\mathrm{n}}}\, \ell\, \boldsymbol{B}_d^{\mathrm{T}} \boldsymbol{B}_d\, \hat{d}\, \mathrm{d}V\, \hat{w}_d = \boldsymbol{0}. \tag{29}$$

3.3. The Flow Equation

First the mass-conserving differential equation (14) is integrated for arbitrary control volume Ω in the spatial domain, after which the volume integral is converted into a surface integral by the divergence theorem. The faces of each volume are denoted as $\partial\Omega$. Then the semi-discrete equation is written as Equation (30)

$$\int_\Omega \frac{\partial w}{\partial t}\, \mathrm{d}\Omega + \int_\Omega C_f w \frac{\partial p_{\mathrm{f}}}{\partial t}\, \mathrm{d}\Omega - \int_{\partial\Omega} K(w) \nabla_s p_{\mathrm{f}}\, \mathrm{d}\partial\Omega - \int_\Omega q\, \mathrm{d}\Omega = 0. \tag{30}$$

At time step t_i, application of the Backward Euler scheme for temporal discretization yields

$$\frac{\partial w}{\partial t} = \frac{w^i - w^{i-1}}{\Delta t} \qquad \frac{\partial p_f}{\partial t} = \frac{{p_f}^i - {p_f}^{i-1}}{\Delta t} \tag{31}$$

Substituting Equation (31) into Equation (30) gives

$$\int_\Omega \frac{w^i - w^{i-1}}{\Delta t}\, \mathrm{d}\Omega + \int_\Omega C_f w^i \frac{{p_f}^i - {p_f}^{i-1}}{\Delta t}\, \mathrm{d}\Omega - \int_{\partial\Omega} K(w) \nabla_s p_{\mathrm{f}}\, \mathrm{d}\partial\Omega - \int_\Omega q\, \mathrm{d}\Omega = 0. \tag{32}$$

Inspired by the numerical implementation in [43], here we introduce the fixed-stress split scheme proposed by [44] to ensure the stability of the flow Equation (32). To this end, j is introduced as the coupling iteration index for the u-p system, with the stress fixed at iteration j.

$$k_{\mathrm{n}} w^{i,j}/h_e - p_{\mathrm{f}}^{i,j} = k_{\mathrm{n}} w^{i,j-1}/h_e - p_{\mathrm{f}}^{i,j-1}. \tag{33}$$

k_{n} can be computed as Equation (34)

$$k_{\mathrm{n}}/h_e = \frac{\delta p}{\delta w}, \tag{34}$$

where h_e is the finite element mesh size. δp is a user-defined fluid pressure increment which is much smaller than the real-time pressure in the fracture domain. Then the relevant aperture increment δw can be achieved based on the slight deformation triggered by δp.

For simplicity, k_{n}/h_e is denoted as K_{n}. Thus, $w^{i,j}$ can be written as

$$w^{i,j} = \frac{p_{\mathrm{f}}^{i,j} - p_{\mathrm{f}}^{i,j-1}}{K_{\mathrm{n}}} + w^{i,j-1}. \tag{35}$$

Substituting Equation (35) into Equation (32) gives

$$\int_\Omega \frac{w^{i,j-1} - w^{i-1}}{\Delta t}\, \mathrm{d}\Omega + \int_\Omega \frac{p_f^{i,j} - p_f^{i,j-1}}{K_{\mathrm{n}} \Delta t}\, \mathrm{d}\Omega + \int_\Omega C_f w^{i,j-1} \frac{p_f^{i,j} - p_f^{i-1}}{\Delta t}\, \mathrm{d}\Omega - \int_{\partial\Omega} K(w) \nabla_s p_{\mathrm{f}}^{i,j}\, \mathrm{d}\partial\Omega - \int_\Omega q\, \mathrm{d}\Omega = 0. \tag{36}$$

The fracture flow equation is formulated in a reduced spatial dimension. Following the approach adopted in [16,45], the equation is discretized here using the finite volume

https://doi.org/10.3390/ma19071444

method. It is solved on a one-dimensional mesh generated with our crack reconstruction method. Given the control volume k, the discrete mass-conserving Equation (36) reads

$$\begin{aligned}&\frac{w^{i,j-1}-w^{i-1}}{\Delta t}\delta x+\frac{p_f^{i,j}-p_f^{i,j-1}}{K_{\mathrm{n}}\Delta t}\delta x+C_f w^{i,j-1}\frac{p_{\mathrm{f}}^{i,j}-p_{\mathrm{f}}^{i-1}}{\Delta t}\delta x\\&+\left[-K(w)\frac{\partial p_{\mathrm{f}}}{\partial x}\right]_{k+1/2}-\left[-K(w)\frac{\partial p_{\mathrm{f}}}{\partial x}\right]_{k-1/2}-Q^i=0,\end{aligned}\tag{37}$$

where $K(w)=w^3/(12\mu_{\mathrm{f}})$ and the crack aperture w is updated using Equation (16) before each p solution. Q is the integration of the source q.

The gradient in the diffusion term of Equation (37) can be further rewritten as

$$\begin{aligned}(\frac{\partial p_{\mathrm{f}}}{\partial x})_{k+1/2}&=(\frac{p_{\mathrm{f}}{}_{k+1}^{i}-p_{\mathrm{f}}{}_{k}^{i}}{\delta x})_{k+1/2}\\(\frac{\partial p_{\mathrm{f}}}{\partial x})_{k-1/2}&=(\frac{p_{\mathrm{f}}{}_{k}^{i}-p_{\mathrm{f}}{}_{k-1}^{i}}{\delta x})_{k-1/2}\end{aligned}\tag{38}$$

The proposed finite volume discretization is implemented using the open-source code JFVM [46], which provides a finite volume framework for solving advection–diffusion equations. Further information and examples are available online.

This section presents the overall coupling procedure of the hybrid-dimensional framework. However, in the subsequent numerical verification section, we assume that the fracture topology (or the corresponding phase-field point cloud) is known in advance. The cloud points can be obtained from micro-seismicity or acoustic emission data in practical engineering and laboratory research [47,48].

4. Numerical Verification

In this section, several analytical solutions are employed to validate the proposed fluid–solid coupling scheme. The first three tests assess the hydraulic response of the numerical method, while the fourth tests the mechanical response, that is, the fracture aperture computation in a pre-existing fracture. The final problem assesses the propagation of the hydraulic fracture in the KGD planar model.

4.1. A Steady-State Pressure Distribution with Inhomogeneous Permeability

First we verify the viability of the hydraulic module. Since we have captured the lower-dimensional crack paths in our previous work [38] in two dimensions, the one-dimensional fluid flow problem is all we need to focus on. We start with the 1D steady-state pressure distribution with varying permeability in THMC benchmarking [49]. As illustrated in Figure 3a, the computational domain is a beam of length $L=100\,\mathrm{m}$ aligned with the positive x-axis and discretized into 20 elements. The three-dimensional model is applied here for demonstration, while the problem is computed in a one-dimensional domain. The crack domain is divided by two kinds of permeabilities $k_1=10^{-12}\mathrm{m}^2$ and $k_2=3\times10^{-12}\mathrm{m}^2$ for $x<2L/5$ and $x>2L/5$, respectively. The effect of gravity is neglected. The liquid viscosity is $\mu=1\mathrm{mPa}\cdot\mathrm{s}$. A Dirichlet boundary condition $p_0=1\,\mathrm{MPa}$ is prescribed at $x=0\,\mathrm{m}$, while a Neumann boundary condition $q=-1.5\times10^{-5}\,\mathrm{m/s}$ is applied at $x=L\,\mathrm{m}$. The initial pressure condition is zero for each point on the crack. The analytical solutions to this problem are provided in [49] as

$$p(x)=\begin{cases}\frac{q\mu}{k_1}x+p_0 & for\ \ x\le 2L/5\\ \frac{q\mu}{k_2}x+p_0+q\mu\frac{2L}{5}(\frac{1}{k_1}-\frac{1}{k_2}) & for\ \ x>2L/5\end{cases}\tag{39}$$

https://doi.org/10.3390/ma19071444

In this case, the analysis is restricted to the flow field. As shown in Figure 3b, the numerical pressure distribution agrees well with the analytical solution.

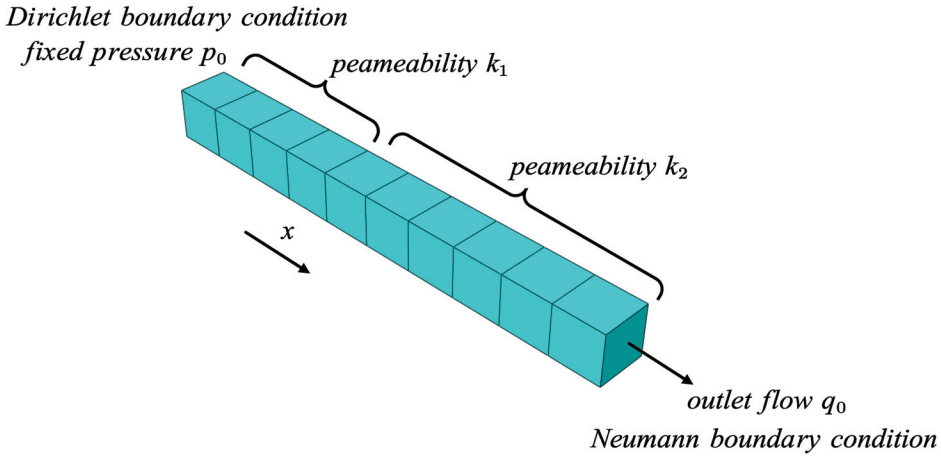

(a) Geometry and boundary conditions

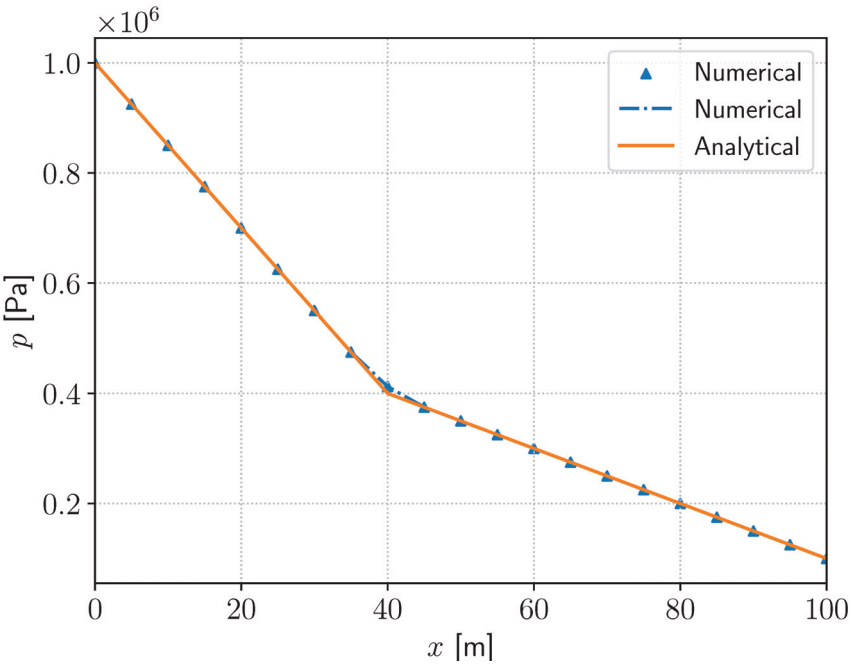

(b) Analytical and numerical results

Figure 3. Steady-state pressure distribution with inhomogeneous permeability.

4.2. A Transient-State Pressure Distribution with Different Boundary Conditions

Next, we investigate the 1D transient-state pressure distribution with non-zero initial pressure in THMC benchmarking [49]. As shown in Figure 4, there are two beams denoted as Beam-1 and Beam-2 extending along the positive x-axis, reflecting two kinds of boundary conditions. Three-dimensional elements are applied here for demonstration, while the problem is computed in the one-dimensional domain actually. Each beam is 100 meters long and divided into 100 elements separately. The whole beam is considered a permeable porous medium filled with liquid of small compressibility. Gravity is neglected. The permeability is assumed to be isotropic with $k = 10^{-14}\,\mathrm{m}^2$, and the fluid viscosity is taken as $\mu = 1.728\,\mathrm{mPa}\cdot\mathrm{s}$. The matrix porosity ϕ and the fluid compressibility κ are combined

https://doi.org/10.3390/ma19071444

as $\phi\kappa = 2 \times 10^{-10}\text{Pa}^{-1}$. The prescribed initial pressure is $p(x, t = 0) = p_0 \cdot f(x)$ with $p_0 = 1\text{MPa}$ and $f(x)$ specified below

$$f(x) = \begin{cases} 0 & for \quad 0 \le x \le 0.1L \\ \frac{10}{3L}x - \frac{1}{3} & for \ 0.1L \le x \le 0.4L \\ 1 & for \ 0.4L \le x \le 0.6L \\ 3 - \frac{10}{3L}x & for \ 0.6L \le x \le 0.9L \\ 0 & for \ 0.9L \le x \le L \end{cases} \tag{40}$$

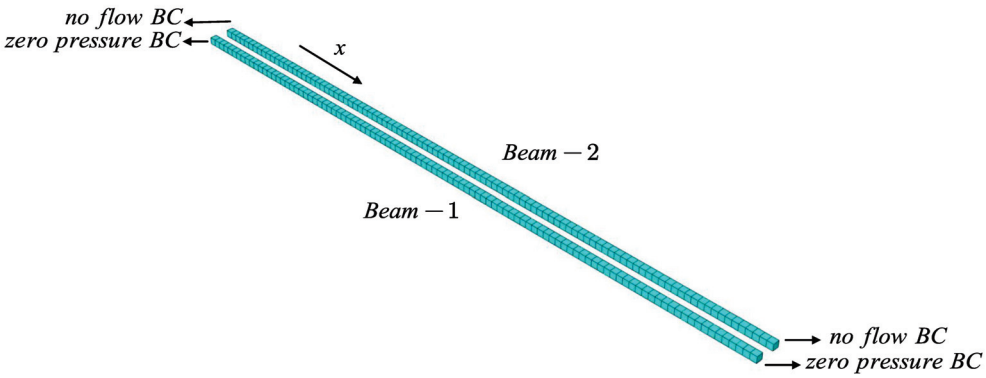

Figure 4. Geometry and boundary conditions of Beam-1 and Beam-2.

The transient pressure field is governed by the fluid diffusion equation derived from the continuity equation and Darcy's law. The governing equation reads

$$\phi\kappa\frac{\partial p}{\partial t} = \frac{k}{\mu}\nabla \cdot \nabla p + q. \tag{41}$$

The zero-pressure boundary condition are prescribed at the ends of Beam-1, while no-flow boundary conditions are imposed at the ends of Beam-2. The analytical solutions of two beams are given in [49,50]. The solutions $p(x, t)/p_0$ take the form

$$p_1(x,t) = \sum_{n=1}^{\infty} \sin\frac{n\pi x}{L} \exp\left(-\frac{k}{\phi\mu\kappa}n^2\pi^2\frac{t}{L^2}\right) \times \frac{80}{3(n\pi)^2} \sin\frac{n\pi}{2} \sin\frac{n\pi}{4} \sin\frac{3n\pi}{20} \tag{42}$$

$$p_2(x,t) = \frac{1}{2} + \sum_{n=1}^{\infty} \cos\frac{n\pi x}{L} \exp\left(-\frac{k}{\phi\mu\kappa}n^2\pi^2\frac{t}{L^2}\right) \times \frac{80}{3(n\pi)^2} \cos\frac{n\pi}{2} \sin\frac{n\pi}{4} \sin\frac{3n\pi}{20} \tag{43}$$

The transient pressure distribution $p(x, t)$ at $t = 1 \times 10^{-5}$, 0.01, 0.1, 0.3, 0.5 and 1.0 days is shown in Figure 5. When the time step is taken as 1×10^{-5} days, the fluid pressure distribution is extremely close to the initial pressure specified by Equation (40). As time proceeds, the pressure in Figure 5a is observed to gradually decrease to 0 under the zero-pressure boundary condition, while the pressure in Figure 5b is found to gradually tend to a constant under the no-flow boundary condition. The simulation results are consistent with the physical expectations. Close agreement is observed between the analytical and numerical pressure distributions.

https://doi.org/10.3390/ma19071444

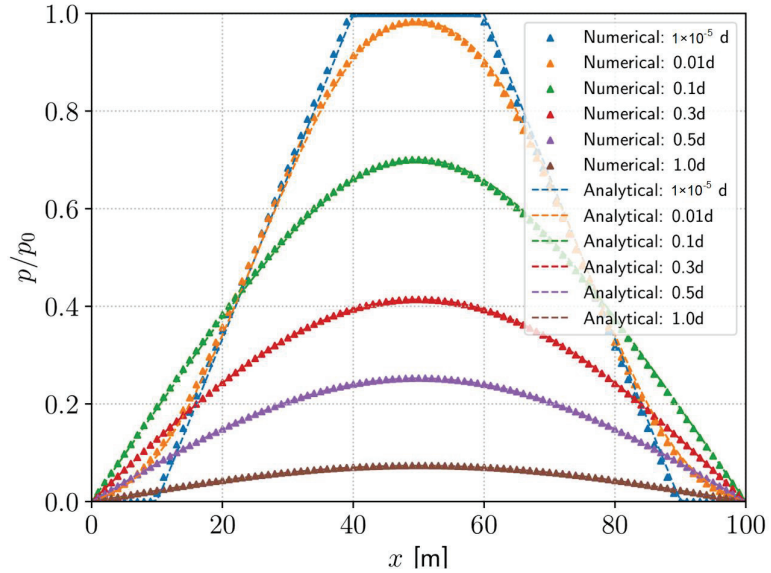

(a) Dirichlet boundary condition

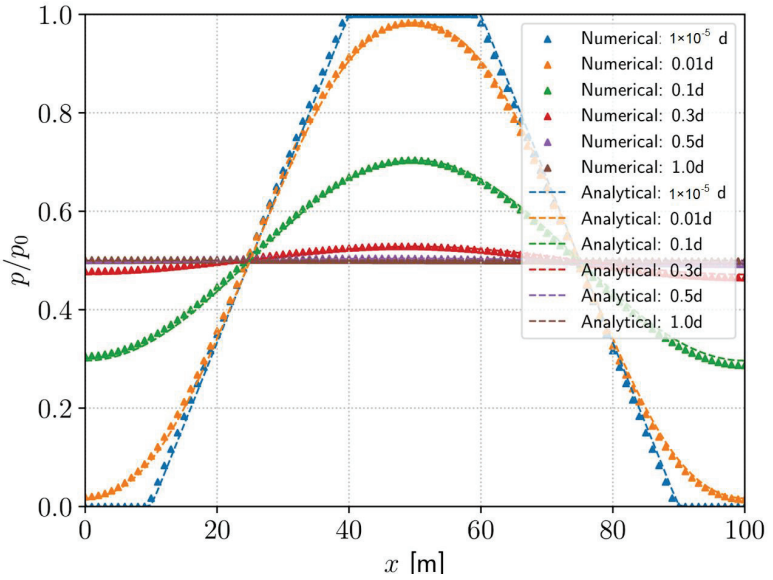

(b) Neumann boundary condition

Figure 5. Analytical and numerical results of transient-state pressure distribution under different boundary conditions.

4.3. Pressure Distribution in a Single-Cracked Path

This section investigates the transient pressure distribution in an impermeable rock specimen containing a single fracture path. You et al. [43] and Song et al. [51] compared the analytical solution of this example with their numerical results. The benchmark parameters adopted in this example are taken from [43]. However, all results are independently computed by the authors using the proposed numerical framework. The geometry and boundary conditions are illustrated in Figure 6a. The left boundary is a Dirichlet condition for $p_0 = 9.5$ MPa, and the right boundary is a no-flow condition. The permeability is $k = 10^{-20}\text{m}^2$ and the fluid viscosity is $\mu = 10^{-3}\text{Pa} \cdot \text{s}$. The fluid compressibility is $C_\text{f} = 4.55 \times 10^{-10}\text{Pa}^{-1}$. By assigning an initial phase-field value $d = 1$ to the fracture do-

https://doi.org/10.3390/ma19071444

main and using the lower-dimensional fracture reconstruction method, a one-dimensional

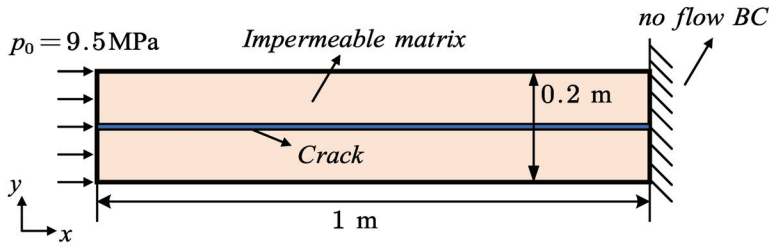

(a) Geometry and boundary conditions

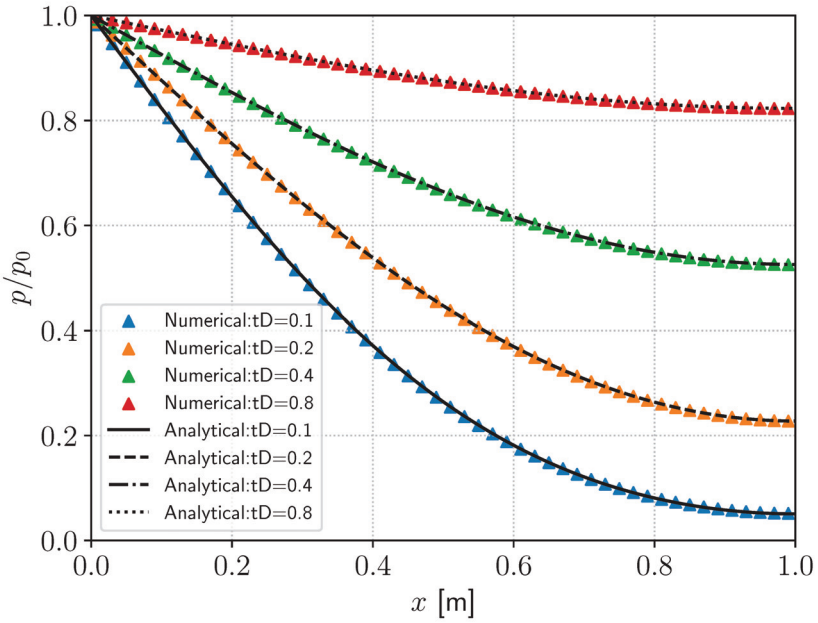

(b) Analytical and numerical results

Figure 6. Transient-state pressure distribution in an impermeable rock sample with a single-cracked path.

The closed form solution of the pressure distribution along the crack [52] is

$$\frac{p(x,t)}{p_0} = 1 + \frac{4}{\pi}\sum_{m=0}^{\infty}\left[\exp\left(-(2m+1)^2(t_D/4)\pi^2\right)\cos\left(\frac{(2m+1)\pi}{2}\zeta\right)\frac{(-1)^{m+1}}{2m+1}\right], \quad (44)$$

where $L = 1$m and $\zeta = \frac{L-x}{L}$.

In this case, t_D is defined as

$$t_D = \frac{w^2 t}{12\mu C_f L^2}, \quad (45)$$

where w denotes the crack aperture. For clarity, the aperture is assumed to be constant and taken as $w = \sqrt{12\mu C_f}$. Figure 6b presents the pressure profiles along the crack at $t_D = 0.1$, 0.2, 0.4, and 0.8. The numerical results show good agreement with the analytical solution given by Equation (44).

https://doi.org/10.3390/ma19071444

4.4. Sneddon Solution for a Pressurized Single Crack

The Sneddon pressurized fracture problem is investigated in this section to verify our crack aperture computation. This problem serves as a classical benchmark for phase-field hydraulic fracture models [16,51,53–58]. However, obtaining an accurate crack aperture remains challenging for some models. The geometry and boundary conditions are shown in Figure 7. A pre-existing crack of length 2.2 m is subjected to a constant fluid pressure $p_0 = 10^5$ Pa, which is imposed by setting the phase-field variable to $d = 1$ within the fracture elements.

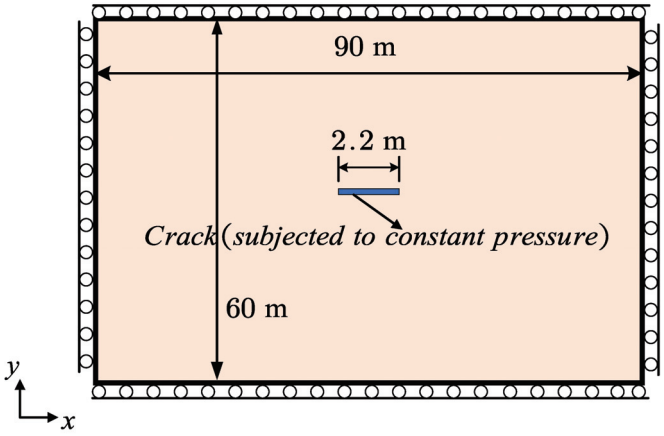

Figure 7. Geometry and boundary conditions of a plate with a single crack under constant internal pressure.

The analytical vertical displacement along the upper crack surface can be evaluated according to [59]

$$u^+(x,0) = \frac{2p_0a_0}{E'}\sqrt{1-\left(\frac{x}{a_0}\right)^2}, \tag{46}$$

where $E' = E/(1-\nu^2)$, a_0 denotes the half-length of the crack, and x is the distance measured from the crack center. The material properties are specified as Young's modulus $E = 1.7 \times 10^{10}$ Pa and Poisson's ratio $\nu = 0.2$. As discussed in [57], the extra energy near the crack tip should be taken into consideration because of the smeared phase-field fracture. Thus the analytical solution Equation (46) is modified with the effective crack length

$$a_{\text{eff}} = a_0\left(1 + \frac{\pi\ell_s/4}{a_0(h/4c_n\ell_s + 1)}\right). \tag{47}$$

The effects of the mesh resolution and the length-scale parameter ℓ_s are then examined. Both the `AT1` and `AT2` models are considered. The numerical results obtained with the `AT2` model are presented in Figure 8. First, the mesh size to length scale ratio is fixed at $h/\ell_s = 1/2$ as shown in Figure 8a. Four mesh sizes are considered, namely $h = 0.1$ m, 0.05 m, 0.025 m, and 0.02 m. In comparison with the analytical solution, the numerical displacement exhibits only a slight sensitivity to mesh refinement. A mesh size of $h = 0.025$ m provides sufficient accuracy and yields results consistent with the analytical solution. Next, the mesh size is fixed at $h = 0.025$ m to assess the effect of the length scale. The parameter ℓ_s is taken as 2 h, 4 h, 6 h, and 8 h. As shown in Figure 8b, a smaller length scale leads to numerical results that more closely match the analytical solution.

Next, we turn to the `AT1` model shown in Figure 9. A similar investigation is conducted for the `AT2` model above. The results indicate that the numerical solutions for the `AT1`

https://doi.org/10.3390/ma19071444

model are more consistent with the theoretical solution in contrast with the other model. Additionally, the AT1 model is less sensitive to the mesh size. The simulation results are in accordance with the standpoint in [57] that AT1 model computes the crack aperture more accurately. Finally, the simulation profiles of the vertical displacement, phase-field and pressure field for AT1 model with $h = 0.025$ m and $\ell_s = 0.05$ m are shown in Figure 10.

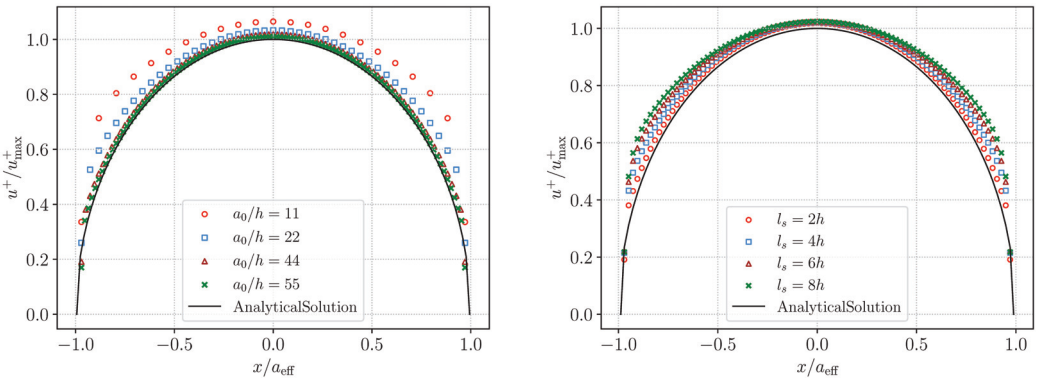

(a) With the ratio $h/\ell_s = 1/2$ fixed (b) With the mesh size $h = 0.025$ m fixed

Figure 8. Analytical and numerical crack opening displacements for the AT2 phase-field model with different mesh sizes and length scale parameters.

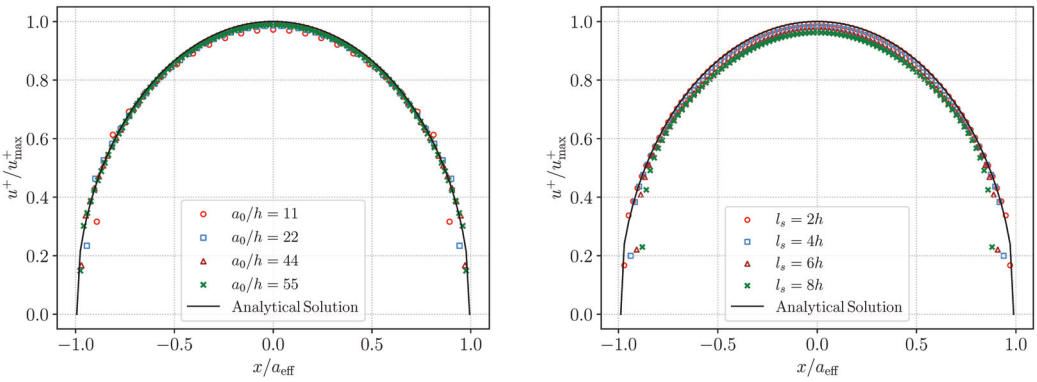

(a) With the ratio $h/\ell_s = 1/2$ fixed (b) With the mesh size $h = 0.025$ m fixed

Figure 9. Analytical and numerical crack opening displacements for the AT1 phase-field model with different mesh sizes and length scale parameters.

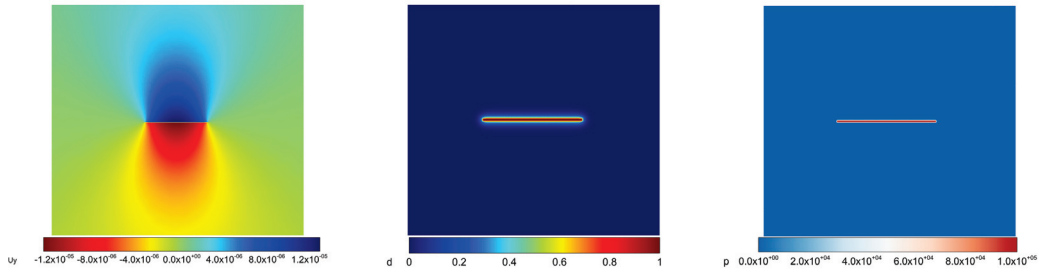

(a) Vertical displacement (b) Phase-field damage (c) Pressure field

Figure 10. Displacement, phase-field damage, and pressure fields for the Sneddon model.

Comparison with Other Crack Aperture Calculation Method

Although the normal strain-based crack opening displacement (COD) calculation method in Equation (17) has been effectively validated within the Sneddon model, it may not be directly applicable to more complex mesh configurations. In particular, when the element orientation is inconsistent with the crack direction or when unstructured mesh

https://doi.org/10.3390/ma19071444

elements are used, the existing COD calculation method requires additional modification to reduce the inaccuracy of the solution due to the element orientation dependence [60].

Therefore, a COD calculation method that is independent of the mesh orientation is required. We introduce a new strain-based method proposed by Fei and Choo [61]:

$$w \approx \frac{(\lambda \mathbf{I} + 2\mu \mathbf{n} \otimes \mathbf{n}) : \boldsymbol{\varepsilon} + p}{\Gamma_d(d, \nabla d)(\lambda + 2\mu)}, \tag{48}$$

where λ and μ denote the Lamé constants, $\mathbf{I}$ is the identity tensor, and $\mathbf{n}$ represents the crack normal vector. Here, $\boldsymbol{\varepsilon}$ is the strain tensor, while p denotes the pressure.

We still employ the Sneddon model to evaluate the mesh sensitivity of the COD calculation methods. As illustrated in Figure 11, three types of structured grids are employed for comparison, with angles between the element orientation and the fracture direction set at $\theta = 0°$, 33.7°, and 45° respectively. Figure 12 presents a comparative analysis of three COD calculation methods against analytical solutions: (1) the direct calculation using the vertical displacement solution, (2) the aperture solution in Equation (48), and (3) the aperture solution derived from the normal strain in Equation (17). It can be observed that when the orientation of the element aligns with the direction of the fracture, namely the angle θ is 0°, the numerical solutions of the three aforementioned methods exhibit good agreement with the analytical solutions. However, when misalignment occurs, the method based on normal strain demonstrates partial deviation from the analytical solution, whereas Fei's methodology remains insensitive to element orientation.

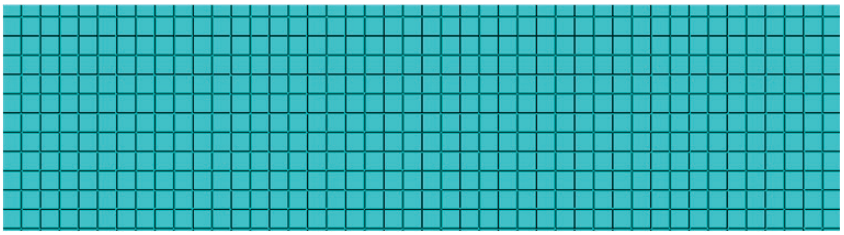

(a) Mesh orientation $\theta = 0°$

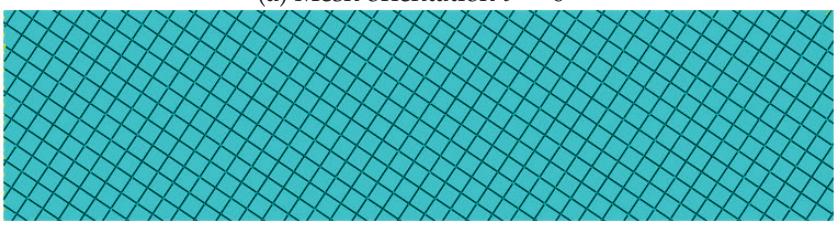

(b) Mesh orientation $\theta = 33.7°$

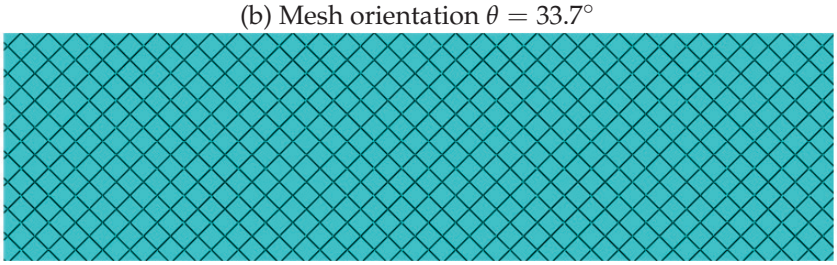

(c) Mesh orientation $\theta = 45°$

Figure 11. Structured meshes with different orientations for the Sneddon model.

This characteristic suggests that Fei's approach could be integrated with the hybrid-dimensional framework proposed in this study. Such a combination may provide a more reliable aperture estimation for unstructured meshes and complex fracture geometries, which will be investigated in future work.

https://doi.org/10.3390/ma19071444

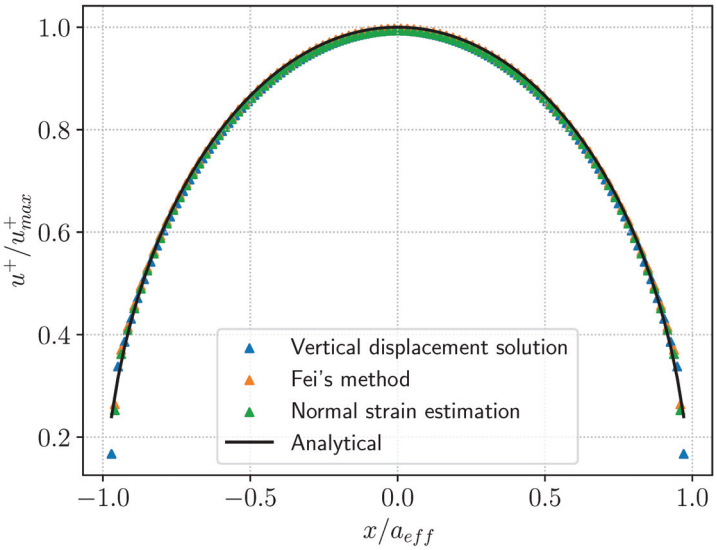

(a) Mesh orientation $\theta = 0°$

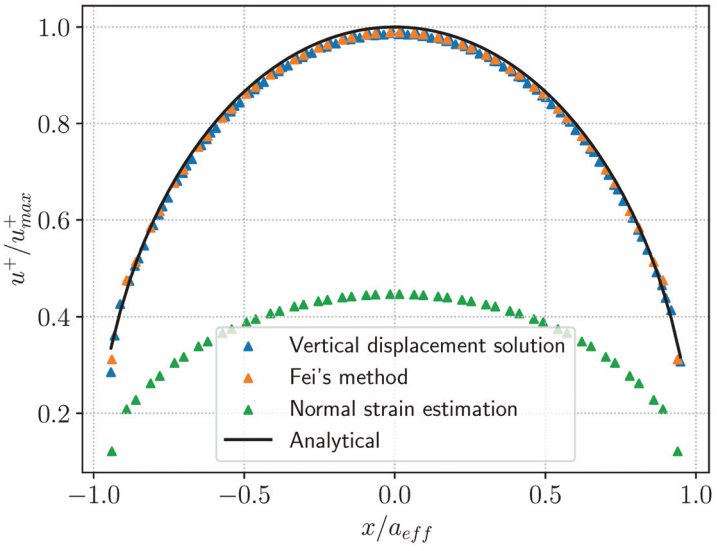

(b) Mesh orientation $\theta = 33.7°$

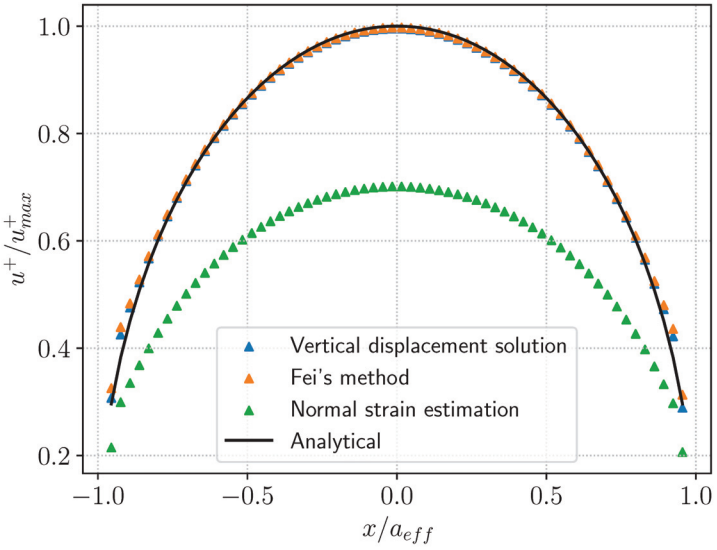

(c) Mesh orientation $\theta = 45°$

Figure 12. Analytical and numerical results of crack opening displacement (COD) obtained using different aperture calculation methods under various mesh orientations.

https://doi.org/10.3390/ma19071444

4.5. KGD Model for Hydraulic Fracture Propagation

In the last section, the KGD (Khristianovic–Geertsma–de Klerk) model [62,63] is investigated to verify our hybrid-dimensional iterative coupling scheme for hydraulic fracture in elastic media. The geometry and boundary conditions are demonstrated in Figure 13. For simplicity, a semi-symmetrical structure is taken here. The domain is 120 m in height and 45 m in width to simulate an infinite plane.

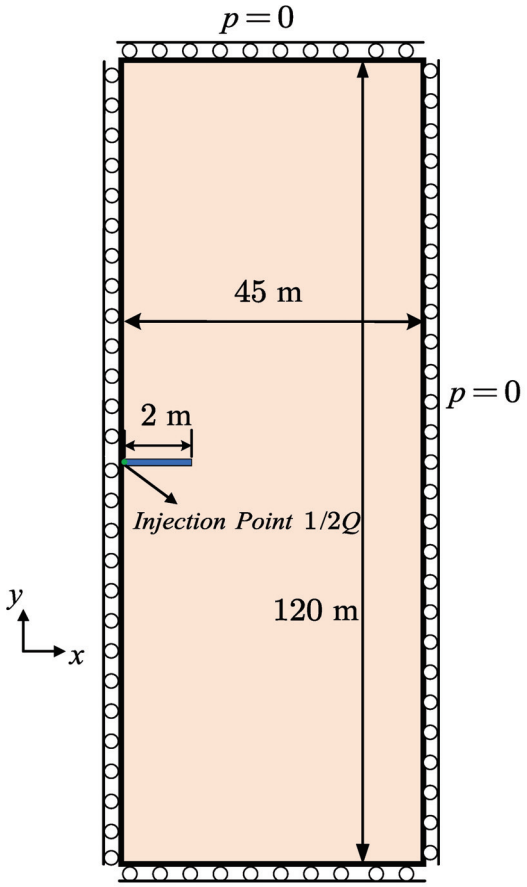

Figure 13. Geometry and boundary conditions of the KGD model.

The initial crack is prescribed by setting the phase-field variable to $d = 1$ over a length of 2 m. The initial crack aperture is taken as $w_0 = 1 \times 10^{-6}$ m, and the injection rate is prescribed as $Q = 2 \times 10^{-3}\,\mathrm{m}^2/\mathrm{s}$. The fluid compressibility C_f is set to zero to reflect the incompressible fluid assumption adopted in the KGD model. The remaining parameters are listed in Table 1.

Table 1. Parameters for the KGD model

Parameter Name	Value	Unit
Young's modulus (E)	1.7×10^9	Pa
Poisson's ratio (ν)	0.2	-
Critical surface energy release rate (G_c)	300	N/m
Fluid viscosity (μ_f)	1×10^{-8}	Pa · s
Injection rate (Q)	2×10^{-3}	m^2/s

In impermeable elastic media under plane-strain conditions, hydraulic fracture propagation is governed by two dominant dissipation mechanisms: viscous dissipation arising from fluid friction within the fracture and toughness-related dissipation associated with the failure of the solid medium [3]. Garagash [64], Garagash and Detournay [65] give the ana-

https://doi.org/10.3390/ma19071444

lytical solution of the toughness-dominated and viscous-dominated regimes respectively. The dimensionless viscosity $\mathcal{M}$, which distinguishes these regimes, is written as

$$\mathcal{M} = \frac{K'}{E'^{3/4}\mu'^{1/4}Q^{1/4}} \tag{49}$$

where Q denotes the injection rate of fluid. The other parameters K', E' and μ' are expressed as

$$K' = 4\sqrt{(\frac{2}{\pi})}K_{\mathrm{IC}},\ K_{\mathrm{IC}} = \sqrt{\frac{EG_{\mathrm{c}}}{1-\nu^2}},\ E' = \frac{E}{1-\nu^2},\ \mu' = 12\mu_{\mathrm{f}} \tag{50}$$

The two kinds of regimes are distinguished as follows:

$$\mathcal{M} > 4.0 \quad \text{toughness-dominated regime} \tag{51}$$

$$\mathcal{M} < 1.0 \quad \text{viscous-dominated regime} \tag{52}$$

The dimensionless viscosity $\mathcal{M}$ with the parameters in this benchmark is calculated as 46.73, indicating a toughness-dominated regime.

4.5.1. Mesh Effect on Numerical Solutions

Now we examine the proposed hybrid-dimensional iterative coupling scheme shown in Figure 2 with varying mesh sizes, types and orientations. Throughout the analysis, the ratio between the crack length scale ℓ_s and the element size h is kept constant at $\ell_s/h = 2$. In the subsequent simulations, the time step is fixed at $\Delta t = 0.1\,\mathrm{s}$. During hydraulic fracture propagation, the pressure and crack aperture at the injection point, together with the crack length, are monitored. Both the `AT1` and `AT2` phase-field models are employed for comparison. It should be noted that, during the initial stage, the numerical curves do not coincide with the analytical solution because the pre-existing crack has not yet propagated, and both the fluid pressure and the fracture aperture increase in an approximately linear manner. Once crack propagation initiates, the numerical results converge and overlap with the analytical solution.

We first consider a structured mesh aligned with the horizontal crack propagation direction to examine the influence of mesh size on the numerical results. The `AT1` model is employed first, owing to its more accurate prediction of crack opening as demonstrated in the previous section. As shown in Figure 14a,c,e, three mesh sizes, namely $h = 0.125\,\mathrm{m}$, 0.1 m, and 0.05 m, are considered. All three meshes capture the crack length, crack opening, and fluid pressure evolution with good accuracy. The phase-field distributions at different times for $h = 0.05\,\mathrm{m}$ are presented in Figure 15. Although the finest mesh yields results for pressure, crack length, and aperture that are closer to the analytical solutions, the mesh size $h = 0.1\,\mathrm{m}$ provides sufficient accuracy while offering higher computational efficiency.

Next we turn to the mesh type effect on the simulation results. According to the previous investigation, the mesh size is fixed as $h = 0.1$ m for accuracy and efficiency. In the structured mesh, both the `AT1` and `AT2` recover the general changes of hydraulic fracture in Figure 14b,d,e. However, the `AT1` model performs better in calculating the crack aperture in Figure 14e. Additionally, this model is better at simulating crack nucleation [34,66], which is verified in Figure 14d. The fracture initiation is delayed for the `AT2` model. Although the `AT2` model is not as precise as the former, it shows better robustness in $\boldsymbol{u} - p$ coupling process mentioned in Section 3.3 while dealing with the unstructured mesh. This phenomenon is due to the `AT2` model possessing a broader phase-field sampling range, which results in smoother fluid pressure reconstruction combined with the proposed hybrid-dimensional scheme. The comparison of the d-profile and sampling range is illustrated in Figure 16. The

https://doi.org/10.3390/ma19071444

bright green dash–dot line is marked as the central axis of the standard crack propagation path. The simulated crack path with `AT1` deviates from the central axis, while the other remains in the middle position, which has a broader sampling range. Therefore, `AT1` is the better choice for structured mesh, while `AT2` is more appropriate for unstructured mesh with our reconstruction method.

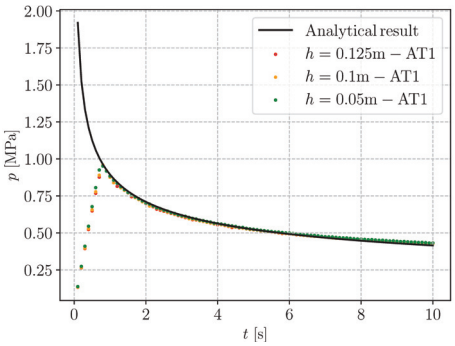

(**a**) Pressure at the injection point with different mesh sizes

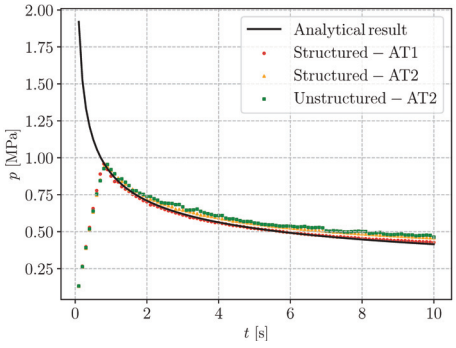

(**b**) Pressure at the injection point with different mesh types

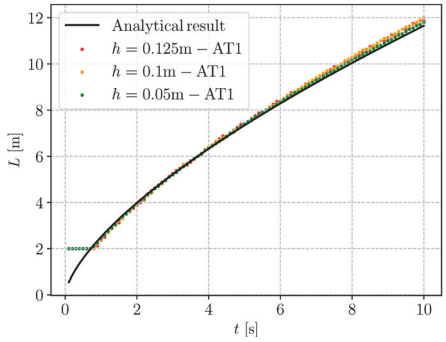

(**c**) Crack length with different mesh sizes

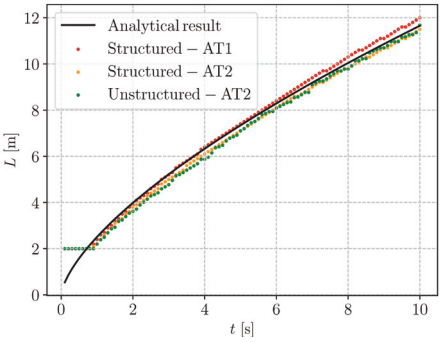

(**d**) Crack length with different mesh types

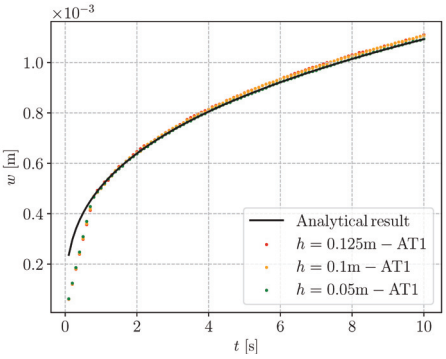

(**e**) Aperture at the injection point with different mesh sizes

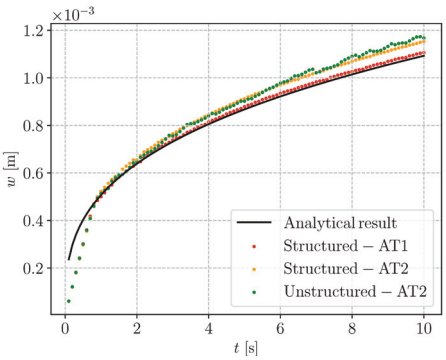

(**f**) Aperture at the injection point with different mesh types

Figure 14. Analytical and numerical results of the KGD model with different mesh sizes and mesh types.

https://doi.org/10.3390/ma19071444

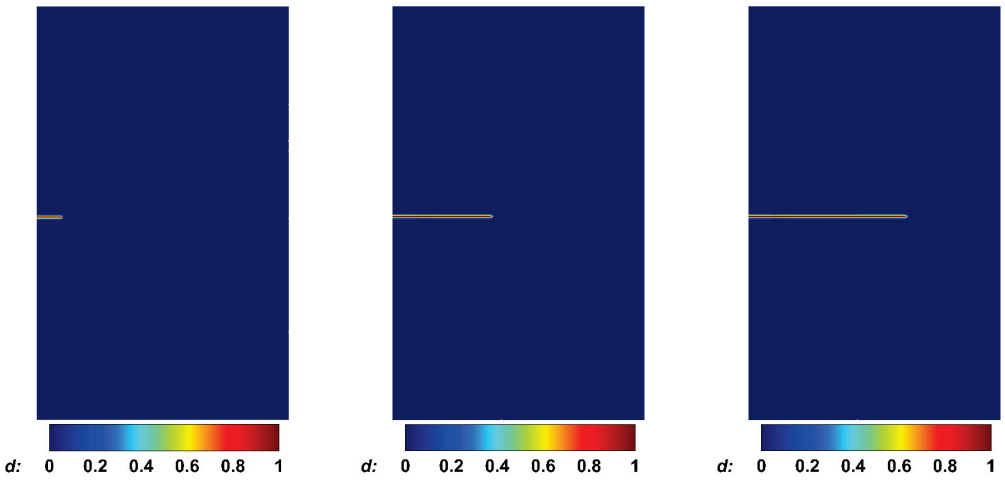

(**a**) Time = 0 s (**b**) Time = 5 s (**c**) Time = 10 s

Figure 15. Phase-field profiles at different times with a mesh size of $h = 0.05$ m for the KGD model.

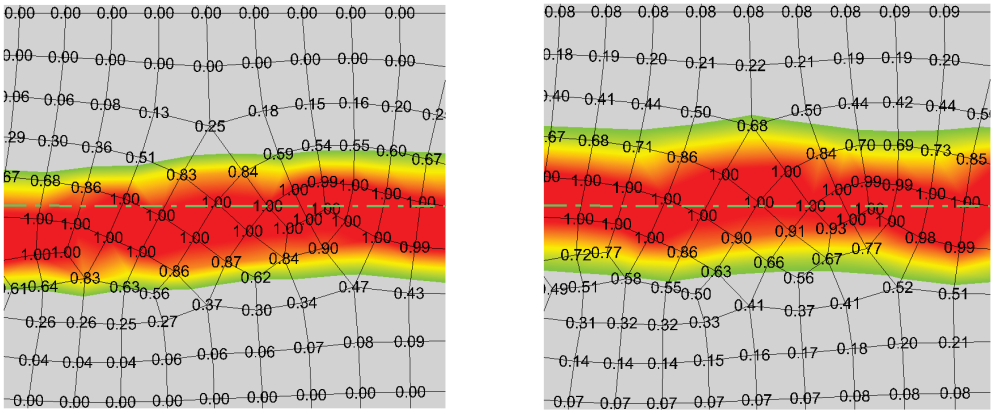

(**a**) The AT1 model (**b**) The AT2 model

Figure 16. Local d-profiles and sampling points for two phase-field models.

Finally, the mesh orientation on the hydraulic fracture simulation is investigated. The structured meshes with fixed element size $h = 0.1$ m and different deflection angles are considered in Figure 17. An unstructured mesh with identical average size is considered as well. The phase-field profiles around the tip of the initial crack, obtained using different meshes for $\alpha = 5°, 10°, 30°$ and an unstructured mesh, are shown in Figure 18. It can be observed that the phase-field profiles with both AT1 and AT2 models are quite sensitive to the orientation for the first two small deflection angles, $\alpha = 5°$ and $\alpha = 10°$. However, the crack propagation results are insensitive to the case of $\alpha = 30°$ and to the unstructured mesh. The crack paths remain in the expected medial axis. The simulation results are in accordance with the findings in [67] on the mesh bias sensitivity of phase-field models. Although the investigation argues that the mesh bias can be eliminated using a very fine mesh or a large length scale, the finer mesh comes with additional computational costs. And the larger length scale may affect the accuracy of crack aperture as verified in the former Section 4.4. Hence the standard structured mesh or unstructured mesh can be acceptable considering the computational efficiency and precision, respectively.

https://doi.org/10.3390/ma19071444

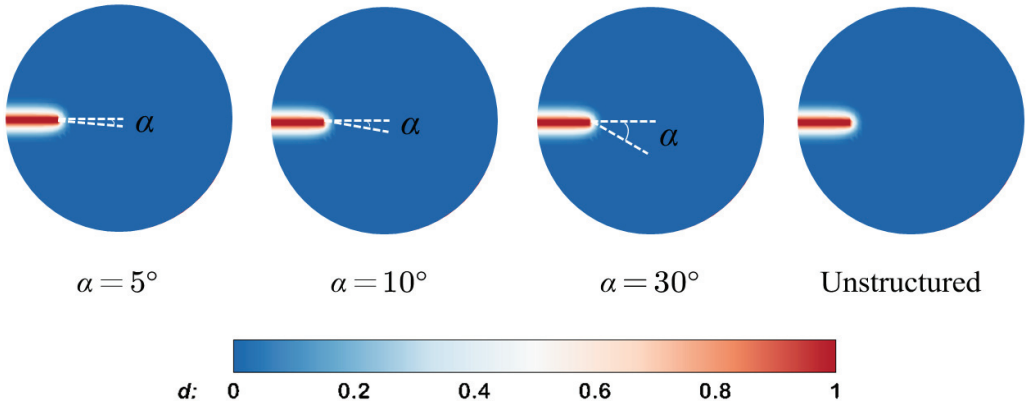

Figure 17. The unaligned mesh with different deflection angle for the KGD model.

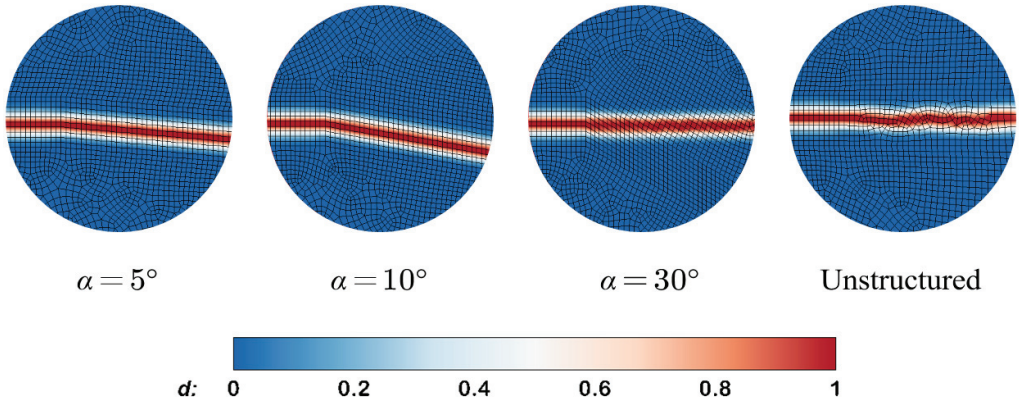

Figure 18. Phase-field distribution near the initial crack tip for different mesh types and orientation.

The aforementioned comparison of the simulation results and the KGD analytical solution demonstrates that our hybrid-dimensional iterative coupling scheme effectively handles the coupling between the mechanical response of impermeable media and fluid flow in fractures.

4.5.2. Discussion of the KGD Numerical Model

In the following, several aspects of the numerical performance are briefly discussed:
Iterative stability. The iterative stability of the coupled KGD model is controlled by the nonlinear interaction between fracture aperture and fluid pressure. In the present benchmark, the iterative process remains overall stable under the adopted time-step size and physical parameters. However, fluctuations may become more likely for larger time steps, higher injection rates, lower material stiffness, or rapid fracture propagation. This stable behavior is mainly attributed to the staggered iterative framework in Algorithm 1 and the fixed-stress algorithm in Section 3.3 used for the flow-mechanics coupling, which together improve the robustness of the coupled solution procedure.
Convergence of the staggered algorithm. The staggered strategy solves the displacement, phase-field, and pressure subproblems separately, and exchanges the field variables through outer iterations. The convergence is monitored by the pressure increment norm, displacement increment norm, and phase-field increment norm. The residual tolerance is set to 10^{-10}, with a maximum of 100 iterations allowed for each time step. Before fracture initiation, the scheme converges rapidly and usually requires fewer than 10 iterations per time step. During fracture propagation, the coupling becomes stronger, and the iteration

https://doi.org/10.3390/ma19071444

count increases accordingly. In the strongly coupled stage, the number of iterations may rise to several tens, but each time step can still be completed within 100 iterations.

Computational cost. The staggered algorithm has the advantages of simple implementation and strong modularity, but compared with a monolithic scheme, it generally requires more outer iterations. For a relatively simple geometry such as the KGD model, the overall computational cost remains controllable. A major difference from many existing studies is that the flow inside the fracture is solved in a reduced-dimensional form, which greatly lowers the computational cost of the flow problem. For this example, a full-domain flow simulation would require solving a two-dimensional problem with the number of elements on the order of 10^5 to 10^6, namely up to about 500,000 elements without local mesh refinement and still about 50,000 elements even with local refinement. After dimensional reduction, the flow problem becomes one-dimensional with only about 500 elements, i.e., on the order of 10^2. This reduction by approximately two to three orders of magnitude leads to a significant improvement in computational efficiency.

Sensitivity of the results to discretization parameters. The numerical results are mainly affected by the mesh size, the phase-field length scale parameter, and the time-step size. The mesh size influences the resolution of the pressure field, displacement field, and phase-field gradient near the fracture. In the present study, local mesh refinement is used to ensure accuracy in the critical region while controlling the overall number of degrees of freedom. As discussed previously, with mesh refinement, key outputs such as the fracture opening, stress peak, and fracture length become closer to the analytical solution, indicating mesh convergence or mesh independence.

The phase-field length scale parameter should be chosen consistently with the mesh size since it controls the width of the diffusive crack zone. Combined with the results in Section 4.4 for the Sneddon model, the numerical results are not very sensitive to this parameter when it is selected in a reasonable range.

The time-step size affects the stability and convergence of the coupled iterations. A large time step may distort the fracture evolution process, while a smaller one usually improves stability and convergence but increases the total computational cost. In the present example, the adopted time-step size provides a satisfactory balance among accuracy, robustness and efficiency.

4.6. Fluid Flow in Discrete Fracture Networks

This part demonstrates the capability of the hybrid-dimensional model to simulate fluid flow within a discrete fracture network. This method reconstructs the DFN topology from phase-field point clouds, which then allows fluid flow on the lower-dimensional DFNs to be computed efficiently.

We take a two-dimensional fracture network as an example. Inspired by Geiger et al. [68], three intersecting fracture patterns are shown in Figure 19, containing two, four, and six fractures, respectively, with modified boundary conditions and material properties. The blue region represents high-permeability fracture network channels, while the gray region denotes impermeable matrix blocks. Natural fractures are represented by prescribing the phase-field variable $d = 1$ within the fracture regions, from which the lower-dimensional fracture network is extracted using the reconstruction procedure. The domain size is $2\,\mathrm{m} \times 2\,\mathrm{m}$. A Dirichlet boundary condition of $p_0 = 9.5\,\mathrm{MPa}$ is imposed on the left boundary, while no-flow conditions are prescribed on the remaining boundaries. For simplicity, the fracture permeability is set to $k = 10^{-20}\,\mathrm{m}^2$, and the fluid viscosity is taken as $\mu = 10^{-3}\,\mathrm{Pa}\cdot\mathrm{s}$. The fluid compressibility is specified as $C_\mathrm{f} = 4.55 \times 10^{-10}\,\mathrm{Pa}^{-1}$. The flow process is modeled as transient single-phase flow governed by the Reynolds equation, Equation (14). The two-point flux approximation is employed for DFN intersections [39].

https://doi.org/10.3390/ma19071444

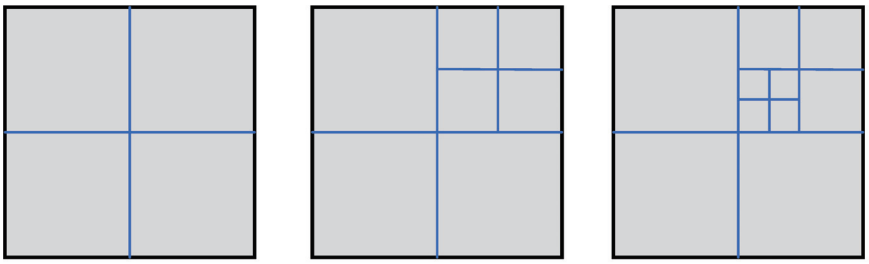

Figure 19. Three idealized 2D grid patterns containing 2, 4, and 6 fractures.

Figures 20–22 illustrate the temporal evolution of the pressure field. The color contours represent the pressure distribution, where blue corresponds to low-pressure regions and red to high-pressure regions. Since the matrix is impermeable, the fluid pressure propagates exclusively through the fracture network from 1 s to 10 s. At the initial stage, the pressure is mainly localized near the left boundary, after which it gradually spreads throughout the fracture system. Eventually, the flow within the fracture network reaches a stabilized state, and the high-pressure regions become fully established.

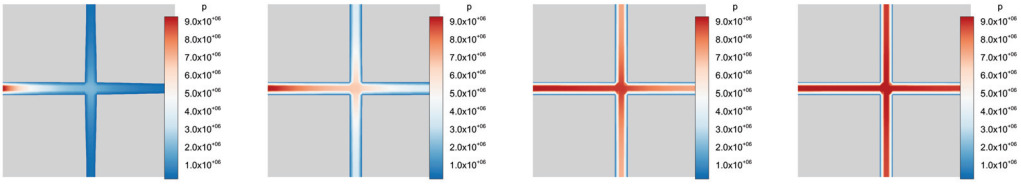

(**a**) Time = 1 s (**b**) Time = 4 s (**c**) Time = 7 s (**d**) Time = 10 s

Figure 20. Fluid flow in a 2D fracture pattern containing two fractures.

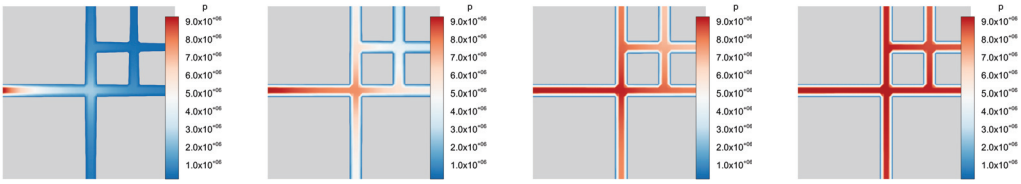

(**a**) Time = 1 s (**b**) Time = 4 s (**c**) Time = 7 s (**d**) Time = 10 s

Figure 21. Fluid flow in a 2D fracture pattern containing four fractures.

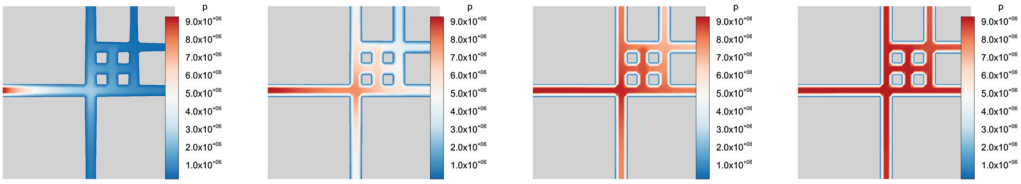

(a) Time = 1 s (b) Time = 4 s (c) Time = 7 s (d) Time = 10 s

Figure 22. Fluid flow in a 2D fracture pattern containing six fractures.

In addition, a hydro-mechanically coupled case with a constant-rate injection boundary condition is considered. A constant injection rate of $q_0 = 10^{-3}\,\mathrm{m}^2/\mathrm{s}$ is prescribed on the left boundary of the model, whereas no-flow boundary conditions are imposed on the remaining boundaries. The initial fracture aperture is set to $w_0 = 10^{-3}\,\mathrm{m}$, and the fluid viscosity is taken as $\mu = 10^{-6}\,\mathrm{Pa}\cdot\mathrm{s}$. The fluid compressibility is specified as $C_\mathrm{f} = 10^{-10}\,\mathrm{Pa}^{-1}$.

https://doi.org/10.3390/ma19071444

The flow process is modeled as transient single-phase flow in the toughness-dominated regime. Figure 23 illustrates the temporal evolution of fluid pressure distribution under an injection boundary condition. At the early stage ($t = 0.1$ s), the pressure field exhibits a significant spatial gradient along the fractures, with clear evidence of fluid injection from the left boundary. As time progresses, the pressure field becomes more uniformly distributed among the fracture network. A quasi-steady state within the fractures confirms that the system behavior remains in the toughness-dominated regime. Owing to the hybrid-dimensional coupling scheme, the proposed method can be readily extended to address more complex hydro-mechanical interactions between the DFNs and the surrounding solid matrix.

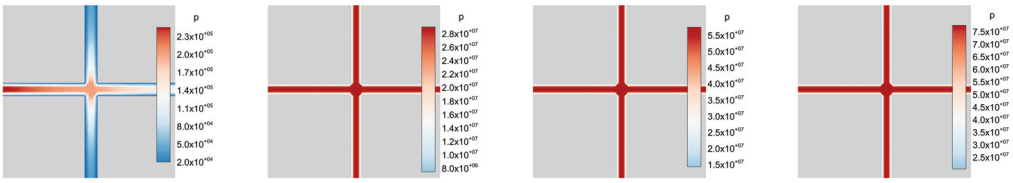

(**a**) Time = 0.1 s (**b**) Time = 0.2 s (**c**) Time = 0.3 s (**d**) Time = 0.4 s

Figure 23. Fluid flow in a 2D fracture pattern containing two fractures under injection boundary conditions.

5. Discussion

This section provides a brief discussion of the proposed hybrid method, with particular attention to current limitations and possible directions for future research.

In the present study, the formulation is restricted to opening-dominated hydraulic fractures. Since the lower-dimensional flow model is governed by the fracture aperture and the associated cubic-law permeability, only the normal opening component is considered in the present implementation. Shear-induced sliding and mixed-mode fracture effects are not included and remain subjects for future work. At the same time, the current fracture aperture estimation is based on strain projection and is subject to certain limitations related to the mesh orientation and element type. By incorporating the estimation method introduced in Section 4.4, the proposed approach can be extended to more complex fracture geometries and mesh elements.

Another limitation of the present framework lies in the fracture reconstruction algorithm. Although the proposed approach can effectively identify and reconstruct evolving fracture paths in the considered two-dimensional examples, its capability for real-time detection of highly complex and dynamically evolving DFN topologies still requires further improvement, especially in cases with multiple crack branching and merging events. The extension of the current reconstruction strategy to fully three-dimensional fracture systems is also challenging, due to the increased complexity of geometric representation, topological tracking, and coupling with lower-dimensional flow models. In addition, although the reduced-dimensional treatment of fracture flow avoids the direct influence of phase-field diffuseness on the local flow field, the flow response may still be indirectly affected through fracture geometry reconstruction. Therefore, further improvements in reconstruction robustness, computational efficiency, and parallel implementation are needed to extend the method to more realistic large-scale geological problems.

https://doi.org/10.3390/ma19071444

6. Conclusions

This paper presents a hybrid-dimensional iterative framework for hydraulic fracturing in deformable geological media with discrete fracture networks. The proposed method combines phase-field based fracture representation, dynamic fracture reconstruction, and lower-dimensional lubrication flow modeling within a staggered coupling scheme. The numerical examples show that the framework can accurately capture fluid pressure, fracture opening, and fracture propagation, while maintaining good numerical performance in terms of stability and convergence. In particular, the benchmark results verify the accuracy of the hydraulic and mechanical solvers, and the DFN examples demonstrate the capability of the method for coupled hydro-mechanical analysis in fractured media. Overall, the proposed framework provides an efficient and flexible approach for simulating fluid-driven fracture processes in complex geological systems. On this basis, we are further developing fluid flow modules to account for different fracture regimes, including toughness-dominated and viscosity-dominated regimes. In future work, improved fracture reconstruction algorithms and iterative coupling frameworks will be developed to address larger-scale and more complex DFN problems.

Author Contributions: Conceptualization, Y.X. and T.Y.; methodology, Y.X. and T.Y.; software, Y.X.; validation, Y.X.; formal analysis, Y.X.; investigation, Y.X.; resources, Q.Z.; data curation, Y.X.; writing—original draft preparation, Y.X.; writing—review and editing, Y.X. and T.Y.; visualization, Y.X.; supervision, Q.Z.; project administration, Q.Z.; funding acquisition, Q.Z. All authors have read and agreed to the published version of the manuscript.

Funding: This research received no external funding.

Data Availability Statement: The data supporting the findings of this study are available from the corresponding author upon reasonable request.

Conflicts of Interest: The authors declare no conflicts of interest.

Abbreviations

The following abbreviations are used in this manuscript:

COD	Crack Opening Displacement
DFN	Discrete Fracture Network
FEM	Finite Element Method
FVM	Finite Volume Method
KGD	Khristianovic–Geertsma–de Klerk
MPFA	Multi-Point Flux Approximation
TPFA	Two-Point Flux Approximation

References

1. Adachi, J.; Siebrits, E.; Peirce, A.; Desroches, J. Computer simulation of hydraulic fractures. *Int. J. Rock Mech. Min. Sci.* **2007**, *44*, 739–757. [CrossRef]
2. Rutqvist, J. Fractured rock stress-permeability relationships from in situ data and effects of temperature and chemical-mechanical couplings. *Geofluids* **2015**, *15*, 48–66. [CrossRef]
3. Detournay, E. Propagation Regimes of Fluid-Driven Fractures in Impermeable Rocks. *Int. J. Geomech.* **2004**, *4*, 35–45. [CrossRef]
4. Miehe, C.; Welschinger, F.; Hofacker, M. Thermodynamically consistent phase-field models of fracture: Variational principles and multi-field FE implementations. *Int. J. Numer. Methods Eng.* **2010**, *83*, 1273–1311. [CrossRef]
5. Borden, M.J.; Verhoosel, C.V.; Scott, M.A.; Hughes, T.J.; Landis, C.M. A phase-field description of dynamic brittle fracture. *Comput. Methods Appl. Mech. Eng.* **2012**, *217-220*, 77–95. [CrossRef]
6. Wu, J.Y.; Nguyen, V.P.; Nguyen, C.T.; Sutula, D.; Sinaie, S.; Bordas, S.P. Phase-field modeling of fracture. *Adv. Appl. Mech.* **2020**, *53*, 1–183.
7. Fei, F.; Costa, A.; Dolbow, J.E.; Settgast, R.R.; Cusini, M. A phase-field model for hydraulic fracture nucleation and propagation in porous media. *Int. J. Numer. Anal. Methods Geomech.* **2023**, *47*, 3065–3089. [CrossRef]

https://doi.org/10.3390/ma19071444

8. Xing, J.; Zhao, C. A hydro-mechanical phase field model for hydraulically induced fractures in poroelastic media. *Comput. Geotech.* **2023**, *159*, 105418. [CrossRef]
9. Kar, S.; Chaudhuri, A.; Singh, A.; Pal, S. Phase field method to model hydraulic fracturing in saturated porous reservoir with natural fractures. *Eng. Fract. Mech.* **2023**, *286*, 109289. [CrossRef]
10. Sahu, A.K.; Roy, A. Evaluating Flow in Fractal-Fracture Networks: Effect of Variable Aperture. *Adv. Geosci.* **2021**, *56*, 117–128. [CrossRef]
11. Karimi-Fard, M.; Durlofsky, L.J.; Aziz, K. An Efficient Discrete-Fracture Model Applicable for General-Purpose Reservoir Simulators. *SPE J.* **2004**, *9*, 227–236. [CrossRef]
12. Hyman, J.D.; Karra, S.; Makedonska, N.; Gable, C.W.; Painter, S.L.; Viswanathan, H.S. dfnWorks: A discrete fracture network framework for modeling subsurface flow and transport. *Comput. Geosci.* **2015**, *84*, 10–19. [CrossRef]
13. Heider, Y. A review on phase-field modeling of hydraulic fracturing. *Eng. Fract. Mech.* **2021**, *253*, 107881. [CrossRef]
14. Aghili, J.; De Dreuzy, J.R.; Masson, R.; Trenty, L. A hybrid-dimensional compositional two-phase flow model in fractured porous media with phase transitions and Fickian diffusion. *J. Comput. Phys.* **2021**, *441*, 110452. [CrossRef]
15. Zhao, J.; Rui, H. Numerical approximation for hybrid-dimensional flow and transport in fractured porous media. *Numer. Methods Partial. Differ. Equ.* **2024**, *40*, e23080. [CrossRef]
16. Santillán, D.; Juanes, R.; Cueto-Felgueroso, L. Phase field model of fluid-driven fracture in elastic media: Immersed-fracture formulation and validation with analytical solutions. *J. Geophys. Res. Solid Earth* **2017**, *122*, 2565–2589. [CrossRef]
17. Zhao, J.; Yin, Q.; McLennan, J.; Li, Y.; Peng, Y.; Chen, X.; Chang, C.; Xie, W.; Zhu, Z. Iteratively coupled flow and geomechanics in fractured poroelastic reservoirs: A phase field fracture model. *Geofluids* **2021**, *2021*, 6235441. [CrossRef]
18. Sandve, T.H.; Berre, I.; Nordbotten, J.M. An efficient multi-point flux approximation method for discrete fracture–matrix simulations. *J. Comput. Phys.* **2012**, *231*, 3784–3800. [CrossRef]
19. Berre, I.; Doster, F.; Keilegavlen, E. Flow in fractured porous media: A review of conceptual models and discretization approaches. *Transp. Porous Media* **2019**, *130*, 215–236. [CrossRef]
20. Geiger, S.; Roberts, S.; Matthäi, S.K.; Zoppou, C.; Burri, A. Combining finite element and finite volume methods for efficient multiphase flow simulations in highly heterogeneous and structurally complex geologic media. *Geofluids* **2004**, *4*, 284–299. [CrossRef]
21. Hægland, H.; Assteerawatt, A.; Dahle, H.K.; Eigestad, G.T.; Helmig, R. Comparison of cell-and vertex-centered discretization methods for flow in a two-dimensional discrete-fracture–matrix system. *Adv. Water Resour.* **2009**, *32*, 1740–1755. [CrossRef]
22. Jin, L.; Zoback, M. Fully coupled nonlinear fluid flow and poroelasticity in arbitrarily fractured porous media: A hybrid-dimensional computational model. *J. Geophys. Res. Solid Earth* **2017**, *122*, 7626–7658. [CrossRef]
23. Mustapha, H.; Dimitrakopoulos, R.; Graf, T.; Firoozabadi, A. An efficient method for discretizing 3D fractured media for subsurface flow and transport simulations. *Int. J. Numer. Methods Fluids* **2011**, *67*, 651–670. [CrossRef]
24. Fumagalli, A.; Keilegavlen, E.; Scialò, S. Conforming, non-conforming and non-matching discretization couplings in discrete fracture network simulations. *J. Comput. Phys.* **2019**, *376*, 694–712. [CrossRef]
25. Berrone, S.; Fidelibus, C.; Pieraccini, S.; Scialò, S. Simulation of the steady-state flow in discrete fracture networks with non-conforming meshes and extended finite elements. *Rock Mech. Rock Eng.* **2014**, *47*, 2171–2182. [CrossRef]
26. Damirchi, B.V.; Bitencourt, L.A., Jr.; Manzoli, O.L.; Dias-da Costa, D. Coupled hydro-mechanical modelling of saturated fractured porous media with unified embedded finite element discretisations. *Comput. Methods Appl. Mech. Eng.* **2022**, *393*, 114804. [CrossRef]
27. Cavalcanti, D.; Mejia, C.; Roehl, D.; de Pouplana, I.; Onate, E. Hydromechanical embedded finite element for conductive and impermeable strong discontinuities in porous media. *Comput. Geotech.* **2024**, *172*, 106427. [CrossRef]
28. Ma, T.; Jiang, L.; Shen, W.; Cao, W.; Guo, C.; Nick, H.M. Fully coupled hydro-mechanical modeling of two-phase flow in deformable fractured porous media with discontinuous and continuous Galerkin method. *Comput. Geotech.* **2023**, *164*, 105823. [CrossRef]
29. Bourdin, B.; Francfort, G.A.; Marigo, J.J. The variational approach to fracture. *J. Elast.* **2008**, *91*, 5–148. [CrossRef]
30. Peskin, C.S. Flow patterns around heart valves: A numerical method. *J. Comput. Phys.* **1972**, *10*, 252–271. [CrossRef]
31. Bourdin, B.; Francfort, G.A.; Marigo, J.J. Numerical experiments in revisited brittle fracture. *J. Mech. Phys. Solids* **2000**, *48*, 797–826. [CrossRef]
32. Miehe, C.; Hofacker, M.; Welschinger, F. A phase field model for rate-independent crack propagation: Robust algorithmic implementation based on operator splits. *Comput. Methods Appl. Mech. Eng.* **2010**, *199*, 2765–2778. [CrossRef]
33. Pham, K.; Amor, H.; Marigo, J.J.; Maurini, C. Gradient damage models and their use to approximate brittle fracture. *Int. J. Damage Mech.* **2011**, *20*, 618–652. [CrossRef]
34. Tanné, E.; Li, T.; Bourdin, B.; Marigo, J.J.; Maurini, C. Crack nucleation in variational phase-field models of brittle fracture. *J. Mech. Phys. Solids* **2018**, *110*, 80–99. [CrossRef]
35. Reynolds, O. On the Theory of Lubrication and Its Application to Mr. Beauchamp Tower's Experiments, Including an Experimental Determination of the Viscosity of Olive Oil. *Philos. Trans. R. Soc. Lond.* **1886**, *177*, 157–234. [CrossRef]
36. Witherspoon, P.A.; Wang, J.S.; Iwai, K.; Gale, J.E. Validity of cubic law for fluid flow in a deformable rock fracture. *Water Resour. Res.* **1980**, *16*, 1016–1024. [CrossRef]

https://doi.org/10.3390/ma19071444

37. Shahoveisi, S.; Vahab, M.; Shahbodagh, B.; Eisenträger, S.; Khalili, N. Phase-field modelling of dynamic hydraulic fracturing in porous media using a strain-based crack width formulation. *Comput. Methods Appl. Mech. Eng.* **2024**, *429*, 117113. [CrossRef]
38. Xu, Y.; You, T.; Zhu, Q. Reconstruct lower-dimensional crack paths from phase-field point cloud. *Int. J. Numer. Methods Eng.* **2023**, *124*, 3329–3351. [CrossRef]
39. Flemisch, B.; Berre, I.; Boon, W.; Fumagalli, A.; Schwenck, N.; Scotti, A.; Stefansson, I.; Tatomir, A. Benchmarks for single-phase flow in fractured porous media. *Adv. Water Resour.* **2018**, *111*, 239–258. [CrossRef]
40. Eymard, R.; Gallouët, T.; Herbin, R. Finite volume methods. In *Handbook of Numerical Analysis*; Elsevier: Amsterdam, The Netherlands, 2000; Volume 7, pp. 713–1018. [CrossRef]
41. Aavatsmark, I. An introduction to multipoint flux approximations for quadrilateral grids. *Comput. Geosci.* **2002**, *6*, 405–432. [CrossRef]
42. Nordbotten, J.M.; Keilegavlen, E. An Introduction to Multi-point Flux (MPFA) and Stress (MPSA) Finite Volume Methods for Thermo-poroelasticity. In *Polyhedral Methods in Geosciences;* Di, P., Daniele, A., Formaggia, L., Masson, R., Eds.; Springer International Publishing: Cham, Switzerland, 2021; pp. 119–158. [CrossRef]
43. You, T.; Yoshioka, K. On poroelastic strain energy degradation in the variational phase-field models for hydraulic fracture. *Comput. Methods Appl. Mech. Eng.* **2023**, *416*, 116305. [CrossRef]
44. Kim, J.; Tchelepi, H.; Juanes, R. Stability and convergence of sequential methods for coupled flow and geomechanics: Fixed-stress and fixed-strain splits. *Comput. Methods Appl. Mech. Eng.* **2011**, *200*, 1591–1606. [CrossRef]
45. Santillán, D.; Juanes, R.; Cueto-Felgueroso, L. Phase field model of hydraulic fracturing in poroelastic media: Fracture propagation, arrest, and branching under fluid injection and extraction. *J. Geophys. Res. Solid Earth* **2018**, *123*, 2127–2155. [CrossRef]
46. Eftekhari, A.A. JFVM.jl: A Finite Volume Tool for Solving Advection-Diffusion Equations. *Zenodo* **2017**. [CrossRef]
47. Hampton, J.; Gutierrez, M.; Frash, L. Predictions of macro-scale fracture geometries from acoustic emission point cloud data in a hydraulic fracturing experiment. *J. Pet. Explor. Prod. Technol.* **2019**, *9*, 1175–1184.
48. Xiong, Q.; Hampton, J.C. A laboratory observation on the acoustic emission point cloud caused by hydraulic fracturing, and the post-pressure breakdown hydraulic fracturing re-activation due to nearby fault. *Rock Mech. Rock Eng.* **2021**, *54*, 5973–5992. [CrossRef]
49. Kolditz, O.; Shao, H.; Wang, W.; Bauer, S. *Thermo-Hydro-Mechanical Chemical Processes in Fractured Porous Media: Modelling and Benchmarking*; Springer: Berlin/Heidelberg, Germany, 2016; Volume 25 .
50. Carslaw, H.S.; Jaeger, J.; Ingersoll, L.R.; Zobel, O.J.; Ingersoll, A.C.; Van Vleck, J. Conduction of Heat in Solids and Heat Conduction. *Phys. Today* **1948**, *1*, 24. [CrossRef]
51. Song, Y.; Cheng, H. Opening-dependent phase field model of hydraulic fracture evolution in porous medium under seepage-stress coupling. *Theor. Appl. Fract. Mech.* **2024**, *129*, 104205.
52. Carslaw, H.; Jaeger, J. *Conduction of Heat in Solids;* Clarendon Press: Oxford, UK , 1959.
53. Bourdin, B.; Chukwudozie, C.; Yoshioka, K. A variational approach to the numerical simulation of hydraulic fracturing. In Proceedings of the SPE Annual Technical Conference and Exhibition San Antonio, TX, USA, 8–10 October 2012; p. SPE-159154-MS.
54. Wheeler, M.F.; Wick, T.; Wollner, W. An augmented-Lagrangian method for the phase-field approach for pressurized fractures. *Comput. Methods Appl. Mech. Eng.* **2014**, *271*, 69–85.
55. Zhou, S.; Zhuang, X.; Rabczuk, T. A phase-field modeling approach of fracture propagation in poroelastic media. *Eng. Geol.* **2018**, *240*, 189–203. [CrossRef]
56. Gerasimov, T.; De Lorenzis, L. On penalization in variational phase-field models of brittle fracture. *Comput. Methods Appl. Mech. Eng.* **2019**, *354*, 990–1026. [CrossRef]
57. Yoshioka, K.; Naumov, D.; Kolditz, O. On crack opening computation in variational phase-field models for fracture. *Comput. Methods Appl. Mech. Eng.* **2020**, *369*, 113210. [CrossRef]
58. Liu, S.f.; Wang, W.; Jia, Y.; Bian, H.b.; Shen, W.Q. Modeling of Hydro-mechanical Coupled Fracture Propagation in Quasi-brittle Rocks Using a Variational Phase-Field Method. *Rock Mech. Rock Eng.* **2024**, *57*, 7079–7101. [CrossRef]
59. Sneddon, I.N.; Lowengrub, M. *Crack Problems in the Classical Theory of Elasticity*; Wiley: New York, NY, USA, 1969.
60. Wilson, Z.A.; Landis, C.M. Phase-field modeling of hydraulic fracture. *J. Mech. Phys. Solids* **2016**, *96*, 264–290. [CrossRef]
61. Fei, F.; Choo, J. Crack opening calculation in phase-field modeling of fluid-filled fracture: A robust and efficient strain-based method. *Comput. Geotech.* **2025**, *177*, 106890. [CrossRef]
62. Khristianovic, S.; Zheltov, Y.P. Formation of vertical fractures by means of highly viscous liquid. In Proceedings of the World Petroleum Congress Proceedings, Rome, Italy, 6–15 June 1955; pp. 579–586.
63. Geertsma, J.; De Klerk, F. A rapid method of predicting width and extent of hydraulically induced fractures. *J. Pet. Technol.* **1969**, *21*, 1571–1581. [CrossRef]
64. Garagash, D.I. Plane-strain propagation of a fluid-driven fracture during injection and shut-in: Asymptotics of large toughness. *Eng. Fract. Mech.* **2006**, *73*, 456–481. [CrossRef]
65. Garagash, D.I.; Detournay, E. Plane-Strain Propagation of a Fluid-Driven Fracture: Small Toughness Solution. *J. Appl. Mech.* **2005**, *72*, 916–928. [CrossRef]

https://doi.org/10.3390/ma19071444

66. Shen, Y.; Mollaali, M.; Li, Y.; Ma, W.; Jiang, J. Implementation details for the phase field approaches to fracture. *J. Shanghai Jiaotong Univ.* **2018**, *23*, 166–174. [CrossRef]
67. Mandal, T.K.; Nguyen, V.P.; Wu, J.Y. Length scale and mesh bias sensitivity of phase-field models for brittle and cohesive fracture. *Eng. Fract. Mech.* **2019**, *217*, 106532. [CrossRef]
68. Geiger, S.; Dentz, M.; Neuweiler, I. A novel multi-rate dual-porosity model for improved simulation of fractured and multi-porosity reservoirs. In Proceedings of the Society of Petroleum Engineers—SPE Reservoir Characterisation and Simulation Conference and Exhibition 2011, Abu Dhabi, United Arab Emirates, 9–11 October 2011; pp. 574–587. [CrossRef]

Disclaimer/Publisher's Note: The statements, opinions and data contained in all publications are solely those of the individual author(s) and contributor(s) and not of MDPI and/or the editor(s). MDPI and/or the editor(s) disclaim responsibility for any injury to people or property resulting from any ideas, methods, instructions or products referred to in the content.

https://doi.org/10.3390/ma19071444

materials

MDPI

Article

Response and Failure of Pillar–Backfill Composite Materials Under Cyclic Loading: The Role of Pillar Width

Qinglin Shan [1], Changrui Shao [1], Hengjie Luan [1,*], Sunhao Zhang [2], Chuming Pang [1], Yujing Jiang [1,2,3] and Lujie Wang [1]

[1] State Key Laboratory of Disaster Prevention and Ecology Protection in Open-Pit Coal Mines, Shandong University of Science and Technology, Qingdao 266590, China; skd995946@sdust.edu.cn (Q.S.); shaochangrui@sdust.edu.cn (C.S.); 201981010010@sdust.edu.cn (C.P.); jiang@nagasaki-u.ac.jp (Y.J.); 19863760029@163.com (L.W.)
[2] Graduate School of Engineering, Nagasaki University, Nagasaki 852-8521, Japan; bb52222191@ms.nagasaki-u.ac.jp
[3] Academician (Expert) Workstation, Inner Mongolia Shanghaimiao Mining Co., Ltd., Ordos 016299, China
* Correspondence: skd995960@sdust.edu.cn

Abstract

In the deep mining of metal mines, the stability of pillar–backfill composite materials (PBCMs) under cyclic loading is crucial for preventing dynamic disasters in goafs. Although previous studies have extensively investigated backfill materials under static loading, the damage evolution mechanism of PBCM under cyclic disturbance—particularly the coupled effects of pillar width and disturbance amplitude—remains insufficiently understood. To address this gap, this study explored the mechanical properties and damage evolution of PBCM under cyclic loading using an indoor testing system. Tests were conducted on composite specimens with varying pillar widths (6, 9, 12, 15 mm) and disturbance amplitudes (3, 4, 5 MPa), combined with acoustic emission (AE), digital image correlation (DIC), and scanning electron microscopy (SEM). Results show that wide-pillar specimens ($\geq$12 mm) exhibit significantly improved bearing strength and deformation modulus, with increases of nearly 90% and over 40%, respectively, compared to narrow-pillar specimens. Notably, wide pillars maintain over 95% strength stability even under 5 MPa cyclic disturbances. Narrow pillars are prone to localized damage concentration with high-frequency AE signals and shear failure, while wide pillars exhibit uniform damage development. Failure morphology confirms that pillar size dictates failure mode: narrow pillars undergo sudden through failure, whereas wide pillars display progressive composite failure, with fewer damage-induced cavities and directional crack propagation along maximum shear stress. These findings provide a theoretical basis for stope structure optimization and dynamic disaster prevention in deep mines.

Keywords: pillar–backfill composite materials (PBCM); low-frequency disturbance; acoustic emission (AE); digital image correlation (DIC); failure mode

1. Introduction

Cemented backfill mining technology has become a key technology for achieving safe and efficient mining in modern metal mines by organically combining cemented backfill with reserved pillars to form a pillar–backfill composite material (PBCM) [1–3]. This technology can not only effectively control the deformation of surrounding rock in goafs but can also significantly improve the recovery rate of mineral resources [4]. As the

core load-bearing body of the mine mining system, the mechanical properties of PBCM directly determine the overall stability of the stope. However, in practical engineering, due to the complexity of geological structures and the dynamics of mining activities, PBCM is often in an inhomogeneous stress field. Especially under deep mining conditions, high in situ stress and complex geological environments make the mechanical response of PBCM more complicated [5–7]. Therefore, an in-depth exploration of the mechanical properties and evolution laws of PBCM is of great theoretical significance and engineering value for optimizing stope structure design and ensuring safe mine production.

In the field of research on the mechanical properties of the PBCM, scholars at home and abroad have made significant progress [8–12]. Among them, Wang et al. [13] studied the mechanical properties and macroscopic fracture characteristics of the composite materials through uniaxial compression, and discussed the crack propagation and energy evolution laws through simulation. Zhao et al. [14] conducted uniaxial compression tests on composite materials samples with different backfill strengths, and analyzed the influence of changes in backfill strength on the mechanical properties of the composite materials. Cui et al. [15] used the digital image correlation (DIC) method to study the deformation characteristics and damage evolution process of six types of composite materials under uniaxial compression conditions. As the main load-bearing unit, changes in the pillar's width will significantly alter the overall mechanical behavior of the composite materials [16]. Wu et al. [17] summarized the pillar stability analysis methods by mechanically dissecting the pillar formation process and explored the influence of pillar size on their mechanical response and stability. Sherizadeh et al. [18] used 3DEC numerical simulation to analyze the influence of pillar size on roof stability. The above studies systematically revealed the evolution laws of mechanical properties and the failure mode characteristics of backfill, especially the key regulatory role of pillar width changes in the overall strength, deformation characteristics, and damage evolution process of backfill. However, in engineering practice, PBCM often bears cyclic loading, such as roof breaking and blasting vibrations (Figure 1), and the progressive damage accumulation caused by such loading is more significant than that under static conditions, leading to the accelerated deterioration of load-bearing performance. Although the research on the mechanical behavior of PBCM under static loading is relatively complete, the research on the synergistic load-bearing mechanism under cyclic loading is still insufficient, which directly affects the accurate evaluation of the long-term stability of backfill in deep mines.

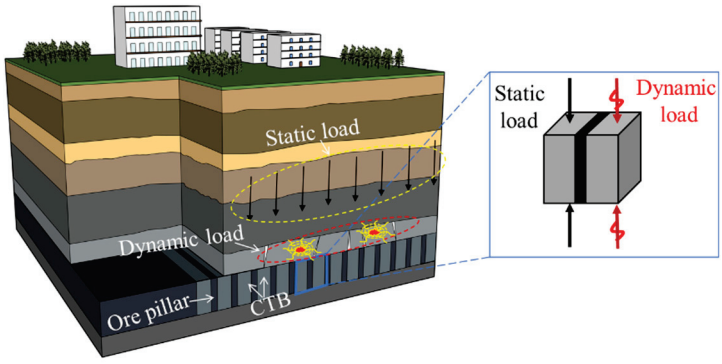

Figure 1. Goaf structure and test model diagram.

During the process of mine exploitation, pillar–backfill composite materials (PBCM) continuously bear periodic loading. Such cyclic stress will induce the progressive accumulation of fatigue damage inside the material, thereby significantly affecting the long-term stability of the structure [19–21]. Zhou et al. [22] conducted indoor cyclic loading tests on rock samples and analyzed the relationship between damage variables and strain rates

https://doi.org/10.3390/ma19081625

under different peak strength ratios in the post-peak stage. Li et al. [23] analyzed the crack propagation process and mechanical properties of rock samples under fatigue loading based on acoustic emission technology, b-value, and the evolution characteristics of AF-RA distribution. Gan et al. [24] performed uniaxial compression tests on backfill samples after cyclic loading, studying the impacts of loading gradient, loading rate, and loading time on their mechanical properties and damage characteristics. Numerous studies have shown that cyclic loading significantly deteriorates the stability of cemented tailings backfill. However, existing research has mainly focused on the mechanical properties and damage evolution of homogeneous materials, while the synergistic load-bearing mechanism of the pillar–backfill composite structure—a heterogeneous material widely applied in mining engineering—under cyclic loading remains poorly understood.

Based on the above background, this study employs a cyclic loading test system to investigate the mechanical response characteristics of pillar–backfill composite structure (PBCM) specimens. The study focuses on examining the effects of disturbance amplitude and pillar width on the strength and deformation behavior of the specimens. By integrating acoustic emission characteristic parameters with the evolution of digital speckle strain fields, the damage development mechanism of the specimens is revealed. Additionally, scanning electron microscopy (SEM) is utilized to observe microscopic features such as microcrack propagation and mineral fragmentation. The research findings provide a theoretical basis and technical support for the optimal design of stope structures and the prevention and control of dynamic disasters in deep mines.

2. Sample Preparation and Test Plan

2.1. Structure Material Composition of PBCM

The pillar–backfill composite samples used in this test consist of pillars and backfill materials. The pillar raw materials were taken from an iron mine in Shandong Province, while the backfill materials were prepared by using tailings as aggregates, mixed with sulphoaluminate cement and tap water. According to the X-ray diffraction (XRD) (Dandong Tongda Technology Co., Ltd., Dandong, China) analysis in Wang's experiment, the main mineral compositions of the pillars are: grunerite (51.1%), hematite (14.3%), magnetite (22.5%), and quartz (8.9%); the main mineral compositions of the tailings are: silicon oxide (67.1%), granite (18.8%), and magnetite (8.2%) [25]. Referencing the actual filling material ratio used in the mine and combining it with previous studies [13], the test ultimately confirmed the ratio scheme of 76% slurry concentration and a 1:4 cement-to-sand ratio (cement:tailing sand:water = 1:4:1.58). This ratio ensures good workability of the slurry while meeting the dual requirements of material strength and economic feasibility in engineering practice.

2.2. Sample Preparation Process

The preparation process of the PBCM samples involves three key steps, as shown in Figure 2. Firstly, the original ore is mechanically processed into standard-sized samples. The pillars are uniformly maintained at a length and height of 100 mm, while their widths are machined into four specifications (6 mm, 9 mm, 12 mm, and 15 mm) according to the test requirements. The surfaces of the pillars are precision-ground to meet the test accuracy requirements. Secondly, backfill slurry is prepared at a cement-to-tailings ratio of 1:4. After fully mixing and stirring tailings, cement, and water, the mixture is poured into a standard cubic mold of 100 mm $\times$ 100 mm $\times$ 100 mm, and vibrated compactly on a shaking table to eliminate internal air bubbles. Finally, the samples are demolded after 48 h of initial curing, then transferred to a standard curing environment (temperature 20 $\pm$ 2 °C, relative humidity $\geq$ 95%) for continuous curing for 28 days. After the curing period, the two end

https://doi.org/10.3390/ma19081625

faces of the samples are finely ground to ensure that the flatness of the contact surfaces meets the test specification requirements.

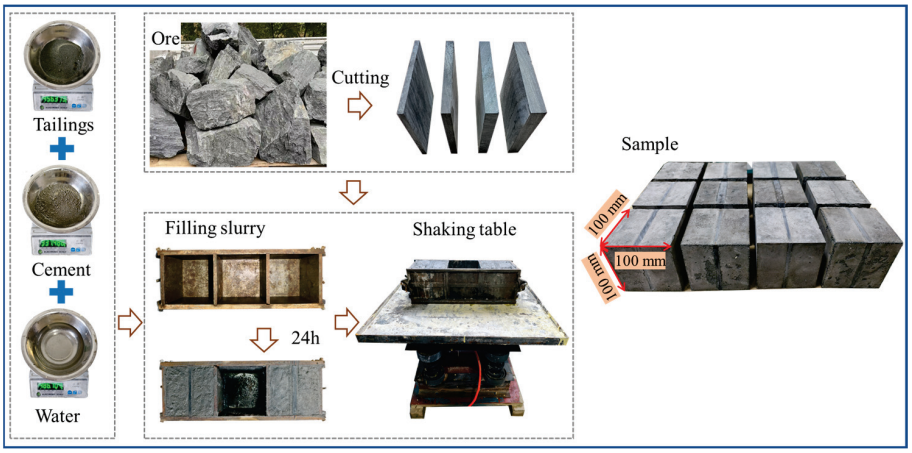

Figure 2. Preparation process of PBCM.

2.3. Test Equipment

The configuration of the test loading and monitoring system is shown in Figure 3. The loading equipment is the rock and soil mass multi-field coupling dynamic and static characteristic test system (Qingdao Qiankunxing Intelligent Technology Co., Ltd., Qingdao, China) from the College of Energy and Mining Engineering, Shandong University of Science and Technology. This system is equipped with a Germanjet1700210200 high-precision displacement sensor (with an accuracy of 0.005% F.S) for real-time monitoring of the axial displacement of the sample. To comprehensively monitor the sample failure process, an acoustic emission monitoring system and a digital image correlation measurement system are configured simultaneously. The acoustic emission monitoring (Beijing Softland Times Technology Co., Ltd., Beijing, China) adopts the DS5 acquisition system with the RS-55A probe. The threshold and sampling rate of acoustic emission acquisition are set to 40 dB and 10 MHz, respectively. Prior to the test, pencil lead break tests were performed for sensor calibration, with each sensor tested three times and localization error controlled within ±5 mm. In this study, a dual-probe symmetric arrangement scheme is adopted, where two acoustic emission probes are accurately installed at the central positions on both sides of the sample. The probes were fixed with adhesive tape using Vaseline as a coupling agent to achieve the comprehensive collection and accurate measurement of acoustic emission signals.

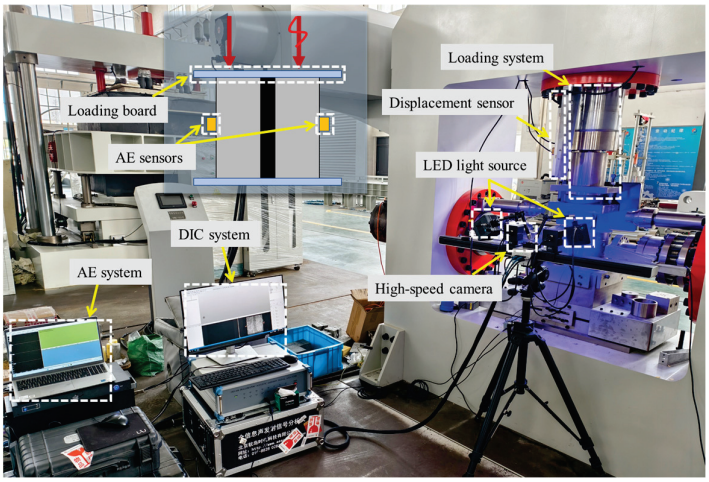

Figure 3. Test equipment diagram.

https://doi.org/10.3390/ma19081625

Meanwhile, the XTDIC (XTOP 3D Technology (Xi'an) Co., Ltd., Xi'an, China) three-dimensional digital speckle dynamic measurement system is used to monitor the surface deformation field of the sample. This system consists of a CCD high-speed camera, a high-brightness LED cold light source, and a professional image processing workstation, and realizes real-time dynamic observation of the surface displacement field of the sample through a non-contact measurement method. Among them, the size of the speckle sub-region is 21 × 21 pixels, the step length is 15 pixels, and the pixel of the CCD high-speed camera is 2048 × 1536. The ZEM18 desktop scanning electron microscope (Anhui ZEION Technology Co., Ltd., Tongling, China) is used to study the microstructure of the sample after failure.

2.4. Test Scheme

Uniaxial compression tests were carried out on the samples of the pillar–backfill composite materials, and the uniaxial compressive strengths of the samples with different pillar widths (6 mm, 9 mm, 12 mm, and 15 mm) were measured, which are 13.21 MPa, 14.86 MPa, 17.11 MPa, and 20.33 MPa, respectively. Based on these values, the initial disturbance value σ was determined [26].

The loading scheme is shown in Figure 4. Firstly, in the static loading stage, the displacement control mode is adopted to apply the load to the predetermined static load σ at a loading rate of 0.1 mm/min. In the cyclic disturbance stage, with the static load σ as the reference stress, a sinusoidal cyclic load with an amplitude A is applied. According to the on-site working conditions, the loading frequency is 5 Hz and the number of cycles is 1000. Finally, in the failure loading stage, the pressure continues to be applied at a loading rate of 0.1 mm/min until the sample is destroyed.

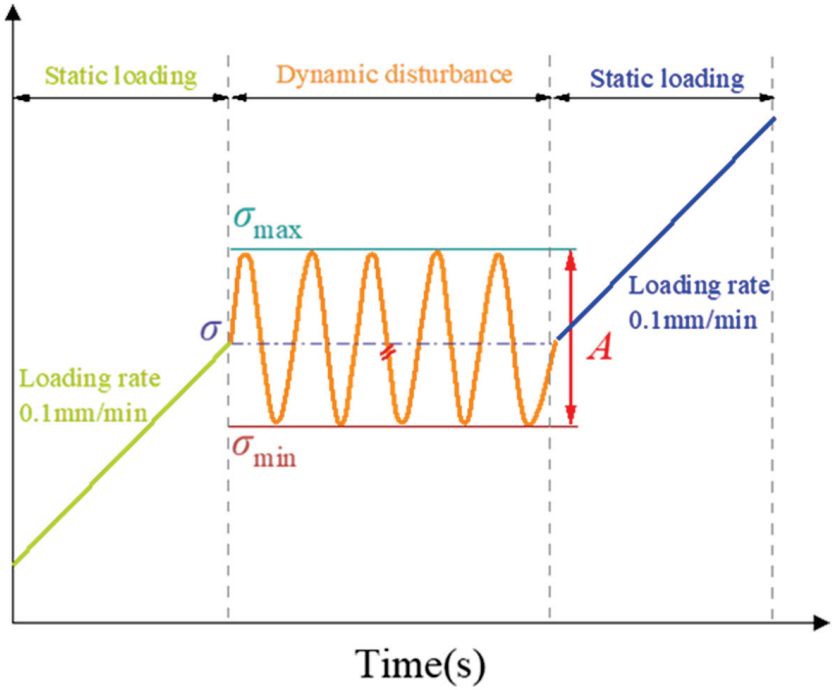

Figure 4. Loading scheme.

The sample number adopts the naming rule of "pillar width–disturbance amplitude". For example, 6-2 represents a sample with a pillar width of 6 mm and a disturbance amplitude of 4 MPa. The specific test parameters are shown in Table 1.

https://doi.org/10.3390/ma19081625

Table 1. Experimental program for low-frequency perturbations.

Sample Name	Pillar Width/mm	Amplitude/MPa	Disturbance Initial Value σ_m/MPa	Disturbance Frequency/Hz	Number of Cycles
6-1	6 mm	3 MPa	6.6 MPa	5 Hz	1000
6-2		4 MPa			
6-3		5 MPa			
9-1	9 mm	3 MPa	7.5 MPa		
9-2		4 MPa			
9-3		5 MPa			
12-1	12 mm	3 MPa	8.5 MPa		
12-2		4 MPa			
12-3		5 MPa			
15-1	15 mm	3 MPa	10.2 MPa		
15-2		4 MPa			
15-3		5 MPa			

3. Analysis of Test Results

3.1. Stress–Strain Curve Characteristics

Figure 5 shows the cyclic load stress–strain curves of the pillar–backfill composite materials under different disturbance amplitudes and pillar widths. Through comparative analysis of the 12 groups of curves, it can be observed that the mechanical response of the composite materials under cyclic loading presents obvious three-stage characteristics: the initial static load stage, the cyclic disturbance stage, and the final failure stage. Among them, disturbance parameters and pillar sizes have significant impacts on the deformation characteristics of each stage.

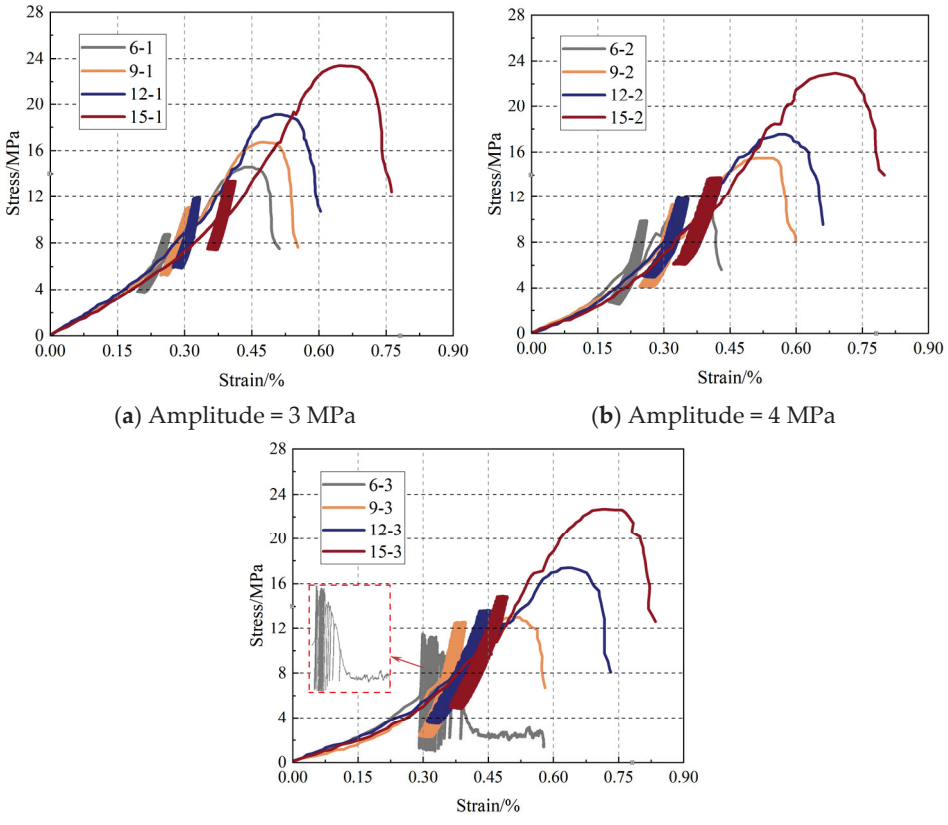

(**a**) Amplitude = 3 MPa (**b**) Amplitude = 4 MPa

(**c**) Amplitude = 5 MPa

Figure 5. Stress–strain curve of PBCM sample under cyclic load.

https://doi.org/10.3390/ma19081625

In the initial static load stage, the stress–strain curves of all samples show significant nonlinear compaction characteristics, and the overall change trend is highly consistent. After entering the cyclic disturbance stage, the curves with different parameter combinations show significant differences. It is worth noting that the sample with a pillar width of 6 mm can only complete 90 cycles under a disturbance amplitude of 5 MPa, and its hysteresis loop shows an obvious "fan-shaped expansion" feature in the later stage, indicating that severe damage accumulation has occurred inside the structure at this time. In contrast, the 15 mm pillar sample can still maintain a relatively regular hysteresis loop shape under the same disturbance conditions, showing better cyclic stability.

In the final failure stage, as the axial stress continues to increase, the microcracks inside the pillar gradually expand and connect with each other, resulting in a significant decrease in its bearing capacity. At this time, the backfill materials begins to play a synergistic bearing role, forming a new bearing system together with the residual pillar to maintain the overall stability of the sample. It is noteworthy that the stress–strain curves of some samples show a short stress platform after reaching the initial strength extreme value, and then the curves rise again. This feature fully reveals the synergistic bearing mechanism between the pillar and the backfill materials. When the load continues to increase to the bearing limit of the backfill materials, the sample finally undergoes overall failure.

3.2. Strength Deformation Characteristics

Figure 6 and Table 2 show the UCS and E of PBCM samples under cyclic loading. The elastic modulus E was determined by linear fitting of the linear elastic portion of the stress–strain curve from the first loading cycle, using a consistent strain interval (10–40% of peak strength) across all specimens. Both the pillar width and disturbance amplitude have significant impacts on the uniaxial compressive strength (UCS) and elastic modulus (E) of the samples. As the pillar width increases, both UCS and E show an upward trend. For example, when the disturbance amplitude is 3 MPa, as the pillar width increases from 6 mm to 15 mm, the UCS of the sample significantly increases from 12.15 MPa to 22.92 MPa, with an increase rate of 88.6%; correspondingly, E increases from 1.78 GPa to 2.54 GPa, with an increase rate of 42.7%. This gradient change in mechanical properties indicates that increasing the pillar width can effectively improve its bearing capacity and deformation resistance.

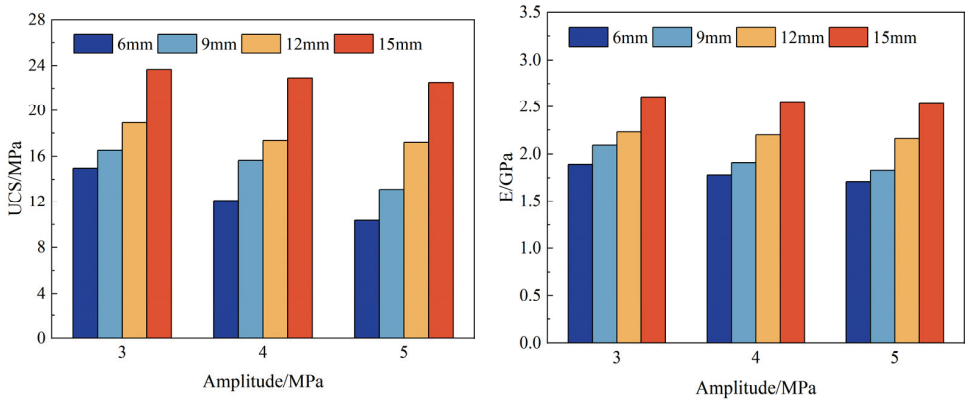

(**a**) UCS (**b**) E

Figure 6. Changes in UCS and E of PBCM samples under cyclic load.

At the same time, the increase in disturbance amplitude will lead to a decrease in the UCS and E of the sample. Taking the 6 mm pillar sample as an example, when the disturbance amplitude increases from 3 MPa to 5 MPa, the UCS decreases from 14.96 MPa to 10.34 MPa, with a decrease rate of 30.9%, and E decreases from 1.89 GPa to 1.71 GPa, with a decrease rate of 9.5%. This phenomenon indicates that dynamic disturbance has an obvious

https://doi.org/10.3390/ma19081625

deteriorating effect on the mechanical properties of the sample, which is attributed to the internal microcrack propagation or cumulative damage effect caused by the disturbance load. It is worth noting that samples with larger pillar widths are less sensitive to the disturbance amplitude. For instance, when the disturbance amplitude increases from 3 MPa to 5 MPa, the UCS of the 15 mm pillar sample only decreases by 4.8%, and the decrease in E is 3.1%, which is much lower than the deterioration degree of the 6 mm pillar sample. This is because the larger-sized pillar can avoid the rapid damage accumulation caused by local stress concentration, indicating that increasing the pillar size can alleviate the adverse effects of dynamic disturbance to a certain extent.

Table 2. The UCS and E values of the samples.

Sample Name	UCS/MPa	E/GPa
6-1	14.96	1.89
6-2	12.15	1.78
6-3	10.34	1.71
9-1	16.52	2.09
9-2	15.65	1.91
9-3	13.11	1.83
12-1	18.92	2.23
12-2	17.36	2.20
12-3	17.21	2.16
15-1	23.67	2.61
15-2	22.92	2.54
15-3	22.53	2.53

3.3. "AE DIC" Characteristics

Figure 7 illustrates the evolution law of acoustic emission energy and the distribution characteristics of digital image correlation (DIC) strain fields for PBCM samples under cyclic loading. Six samples, namely 6-2, 9-2, 12-2, 15-1, 15-2, and 15-3, were selected for analysis. Four characteristic points (Point A: end of compaction stage; Point B: end of cyclic loading stage; Point C: peak point; Point D: final failure point) were chosen from the stress–strain curves to compare the changes in the speckle strain fields.

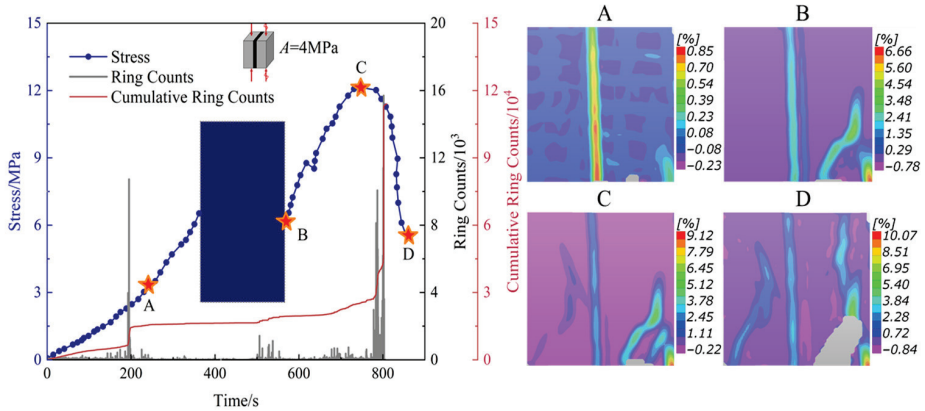

(**a**) 6-2

Figure 7. *Cont.*

https://doi.org/10.3390/ma19081625

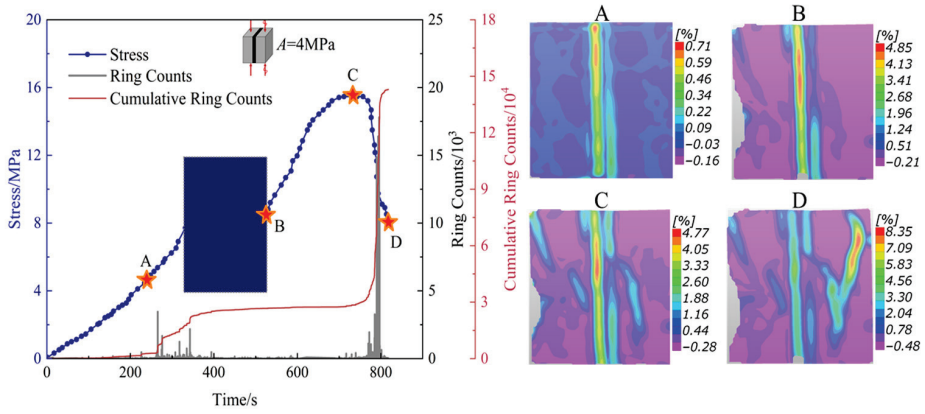

(**b**) 9-2

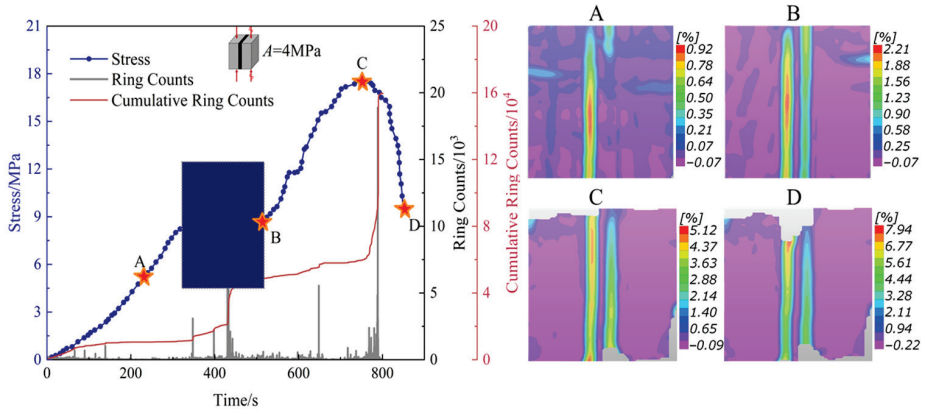

(**c**) 12-2

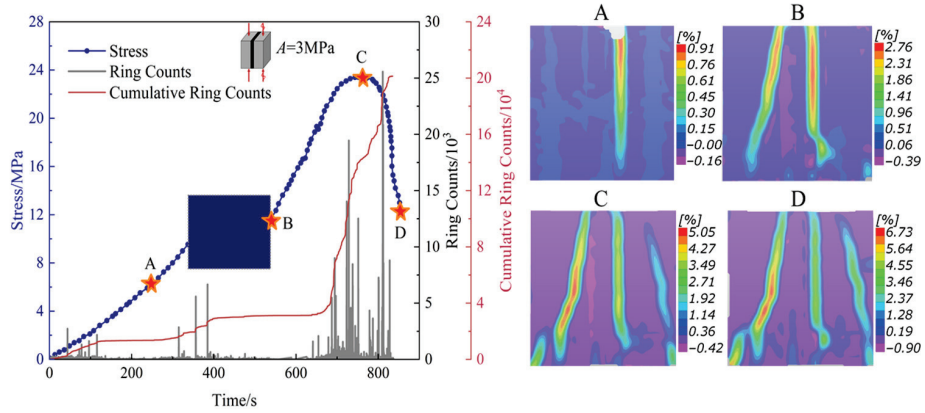

(**d**) 15-1

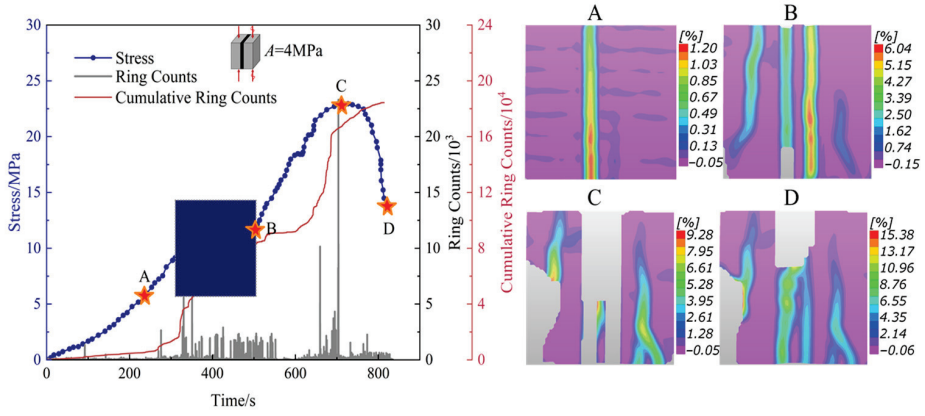

(**e**) 15-2

Figure 7. *Cont.*

https://doi.org/10.3390/ma19081625

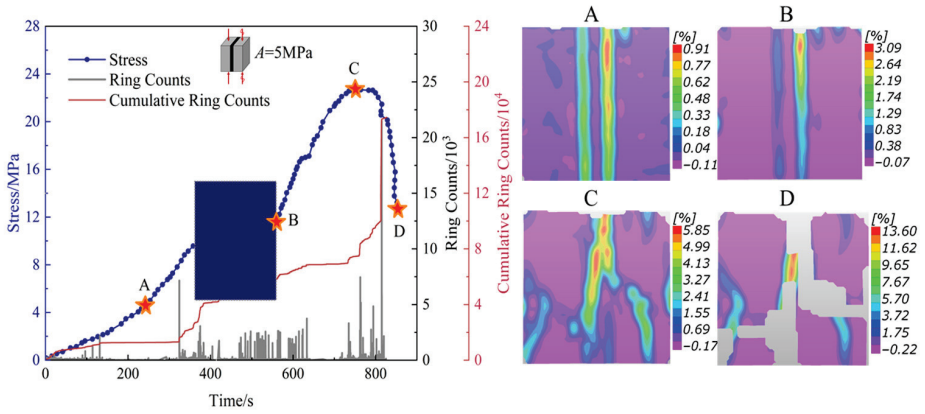

(**f**) 15-3

Figure 7. AE counts and DIC evolution of PBCM.

Through comparative analysis of Figure 7a–c,e, it can be revealed that the pillar width has a significant impact on the damage evolution characteristics under cyclic loading. During the static loading stage, samples with narrower pillars (6 mm and 9 mm) exhibited more active acoustic emission signals, indicating the rapid initiation and propagation of internal microcracks, while those with wider pillars (12 mm and 15 mm) showed weaker acoustic emission activities. At this time, the DIC strain fields indicated that the strain concentration areas of all samples was mainly distributed in the middle of the pillars, showing localization characteristics. After entering the cyclic disturbance stage, the frequency of acoustic emission activities in narrow pillar samples decreased, but sudden high-energy events increased, reflecting that their internal damage entered a stage of unstable expansion. Meanwhile, the strain concentration areas gradually expanded to both ends and formed obvious shear bands. In contrast, the acoustic emission signals of wide pillar samples continued to strengthen, the cumulative energy linearly increased, and the strain fields remained relatively uniformly distributed, with only local areas showing an increase in strain gradient. In the failure stage, the cumulative ringdown counts of samples with pillar widths of 6 mm, 9 mm, 12 mm, and 15 mm were 119,564, 143,755, 161,543, and 189,341, with increases of 20.2%, 12.4%, and 17.2%, respectively. At the same time, the acoustic emission activities of narrow pillar samples (6 mm and 9 mm) continued to strengthen, and the strain fields showed multi-region coordinated deformation, eventually forming a network crack system. For wide pillar samples (12 mm and 15 mm), a significant sudden increase in acoustic emission ringdown counts occurred before macroscopic fracture, accompanied by the penetration of strain concentration areas.

Further analysis of the influence of disturbance amplitude (Figure 7d–f) was conducted using 15 mm pillars as an example. As the disturbance amplitude increased from 3 MPa to 5 MPa, the cumulative acoustic emission energy of the samples increased significantly, especially in the second stage, where acoustic emission activities under a high disturbance amplitude (5 MPa) were more intense. With the increase in disturbance amplitude, the cumulative ringdown counts at sample failure were 203,082, 189,341, and 181,563, with decreases of 6.73% and 4.11% respectively. This indicates that high disturbance loads will accelerate damage concentration, inhibit the progressive expansion of microcracks, and cause the material to fail at a lower cumulative ringdown count. The DIC strain fields showed that under a low disturbance amplitude (3 MPa), the strain concentration areas were mainly distributed at the ends of the pillars, while under a high disturbance amplitude (5 MPa), the strain concentration phenomenon expanded to the interior of the pillars, with local strain values increasing by 30–45%.

https://doi.org/10.3390/ma19081625

A comprehensive comparison shows that pillar width and disturbance amplitude jointly affect the failure mode. Samples with narrow pillars (6 mm and 9 mm) exhibit more uniform damage evolution, while those with wide pillars (12 mm and 15 mm) show stronger anti-disturbance ability but are prone to localized shear failure under cyclic disturbance, with acoustic emission activities concentrated in the pre-failure stage. In addition, the increase in disturbance amplitude will significantly accelerate the rate of damage accumulation inside the pillars, expand the range of strain concentration, and ultimately reduce their overall stability.

3.4. Macroscopic Failure Characteristics

Figure 8 shows the macroscopic damage characteristics of the composite material samples. The annotations highlight the three typical failure characteristics of the specimens: tensile cracks, shear cracks, and spalling. From the perspective of macroscopic failure morphology, samples under different pillar widths and disturbance amplitudes exhibit distinct differences in failure modes. During the failure process of the 6 mm pillar sample (6-2), shear cracks mainly develop in the left backfill, while both dendritic shear cracks and tensile cracks appear in the right backfill, with two significant tensile cracks forming inside the pillar. As the pillar width increases to 9 mm (9-2), the failure characteristics of the sample change: dendritic shear cracks occur in both the left and right backfills, with additional tensile cracks in the left backfill, and the pillar failure is concentrated in the tensile crack at the lower end. The failure of the 12 mm pillar sample (12-2) is relatively localized: shear cracks and upper-end spalling appear in the left backfill, only short tensile cracks form in the right backfill, and spalling occurs at the upper end of the pillar. The 15 mm wide pillar sample (15-2) presents a more complex failure morphology: dendritic shear cracks develop in both side backfills, and the pillar not only has upper-end spalling but also generates multiple long tensile cracks inside.

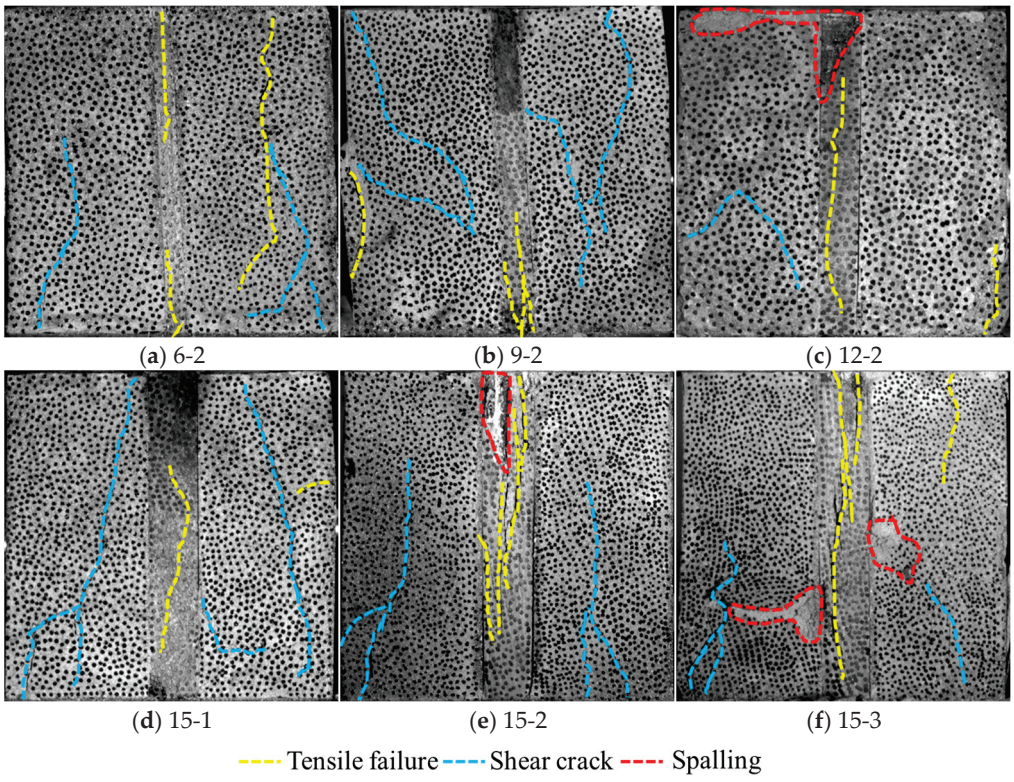

Figure 8. Macroscopic damage characteristics of PBCM samples.

https://doi.org/10.3390/ma19081625

The disturbance amplitude has a significant impact on the failure characteristics of the 15 mm pillar samples. Under the low amplitude of 3 MPa (15-1), only dendritic shear cracks form in the left backfill of the sample, two shear cracks appear on the right side, and a single tensile crack is generated inside the pillar. When the amplitude increases to 4 MPa (15-2), the damage degree intensifies significantly: dendritic shear cracks develop in both side backfills, and the pillar has upper-end spalling with multiple long tensile cracks. When the amplitude further increases to 5 MPa (15-3), the sample suffers the most severe damage: the left backfill has both dendritic shear cracks and spalling, the right backfill generates short shear cracks, tensile cracks, and spalling, and multiple interlaced tensile cracks develop inside the pillar. Under the low amplitude of 3 MPa, the energy input per cycle is limited, mainly leading to the stable propagation of interface microcracks and local shear failure. When the amplitude increases to 4 MPa, the energy input per cycle exceeds the material's critical value, triggering accelerated crack propagation, which manifests as a significant increase in the number and length of cracks. Under the high amplitude load of 5 MPa, the energy input far exceeds the material's fracture toughness, resulting in rapid crack penetration and brittle fracture of the material, with the failure mode showing crushing characteristics. It is worth noting that as the pillar width increases, the energy storage capacity of the sample enhances, enabling it to absorb more energy before failure. This allows wide pillar samples to maintain a certain degree of integrity under high-amplitude loads, with their failure process showing progressive characteristics.

3.5. SEM Image Feature Analysis

To further analyze the damage characteristics of PBCM samples under cyclic loading, the ZEM18 high-resolution desktop scanning electron microscope (SEM) was employed to characterize the microtopography of the fracture surfaces/damaged areas of the samples. These damage-induced cavities, which form during cyclic loading, exhibit irregular shapes and rough surfaces, and are often connected to microcrack networks. By observing microfeatures such as microcrack propagation and mineral fragmentation, SEM technology provides a key basis for establishing a correlation model between materials damage and macroscopic mechanical properties [27–29]. Through analyzing the distribution patterns of damage-induced cavities and fractures, it is found that both pillar width and disturbance amplitude jointly regulate the failure mode of the material, as shown in Figure 9. In samples with narrow pillars (6–9 mm), a large number of damage-induced cavities and intersecting fractures appear in the backfill part, mainly resulting from local stress concentration caused by the end constraint effect. Under cyclic loading, the edge areas of the backfill are subjected to repeated normal stress, which promotes intergranular fracture and forms damage-induced cavities of varying sizes. As the pillar width increases to 12–15 mm, the stress field distribution tends to be uniform, the number of damage-induced cavities decreases significantly, and the fracture morphology changes from intersecting to long fractures extending along the direction of maximum shear stress. This size effect reflects the optimization of the load transfer path by the geometric constraint of the pillar.

The influence of disturbance amplitude on damage characteristics exhibits an obvious threshold effect. When the pillar width is fixed at 15 mm, the backfill suffers the least damage under the 4 MPa disturbance condition, with only a small number of small damage-induced cavities and regular long fractures appearing, indicating that the energy input and material damage dissipation reach a dynamic balance at this point. When the disturbance increases to 5 MPa, the number of damage-induced cavities suddenly increases and the fracture system becomes complicated, revealing that the material has entered the stage of fatigue cumulative damage. This nonlinear response is closely related to the fatigue limit characteristics of the material; high-frequency energy input not only accelerates the

https://doi.org/10.3390/ma19081625

connection of damage-induced cavities but also activates the grain boundary dislocation movement of multiple slip systems.

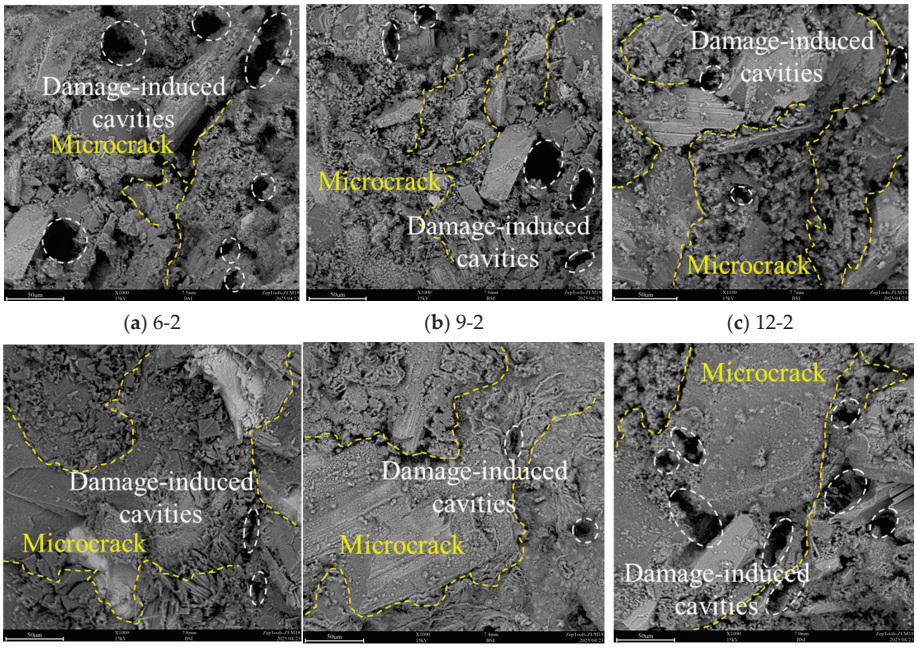

(**a**) 6-2 (**b**) 9-2 (**c**) 12-2

(**d**) 15-1 (**e**) 15-2 (**f**) 15-3

Figure 9. SEM scanning image of the backfill.

The SEM observation results of the pillar part reveal a distinct correlation between its failure characteristics and those of the backfill, as illustrated in Figure 10. For narrower pillars (6–9 mm), the backfill exhibits numerous damage-induced cavities and fractures, while the pillar itself undergoes relatively minor damage, with only a few fractures and localized fragmentation. This indicates that in the case of narrow pillars, most of the load is borne by the backfill, resulting in more severe damage to this area.

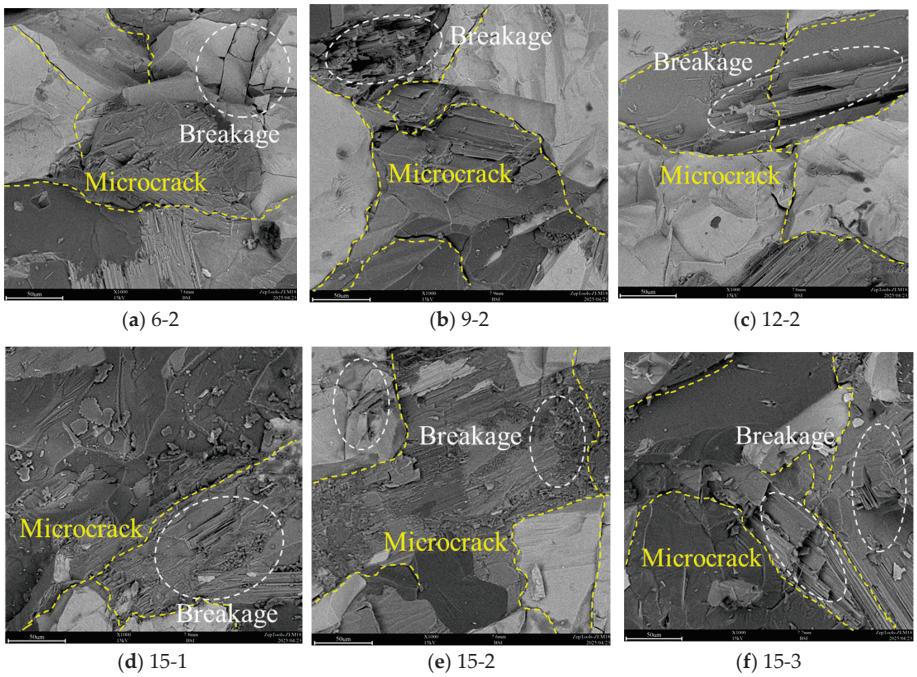

(**a**) 6-2 (**b**) 9-2 (**c**) 12-2

(**d**) 15-1 (**e**) 15-2 (**f**) 15-3

Figure 10. SEM scanning image of the pillar.

https://doi.org/10.3390/ma19081625

As the pillar width increases (12–15 mm), the damage to the pillar itself becomes more severe, with multiple breakage areas and more long fractures observed, while the damage to the backfill is alleviated. This change suggests that wider pillars can share more of the load, thereby reducing the burden on the backfill, but at the same time, the pillars themselves are subjected to greater stress. Under high-disturbance conditions (5 MPa), the pillars develop more complex fracture networks and more breakage areas, indicating that the repeated action of cyclic loading exacerbates the fatigue damage of the pillar material, leading to the gradual deterioration of its internal structure.

3.6. Quantitative Comparison of Mechanical Responses

To systematically assess the coupled effects of pillar width and disturbance amplitude, a quantitative comparison of key parameters is summarized as follows:

(1) Strength Enhancement With Pillar Width: When the disturbance amplitude is fixed at 3 MPa, the UCS increases from 14.96 MPa (6 mm) to 23.67 MPa (15 mm), an increase of 58.2%, while the elastic modulus increases from 1.89 GPa to 2.61 GPa, an increase of 38.1%.
(2) Strength Deterioration Under Higher Disturbance: For the 6 mm wide specimens, increasing the disturbance amplitude from 3 MPa to 5 MPa reduces UCS by 30.9% (from 14.96 MPa to 10.34 MPa). For the 15 mm wide specimens, the same amplitude increase causes only a 4.8% reduction, demonstrating the superior cyclic stability of wider pillars.
(3) Acoustic Emission Characteristics: Under a disturbance amplitude of 4 MPa, the cumulative ringdown counts at failure increase from 119,564 (6 mm) to 189,341 (15 mm), an increase of 58.3%, indicating that wider pillars undergo more extensive microcracking before failure.
(4) Microscopic Damage Features: SEM observations show that when pillar width increases from 6 mm to 15 mm under 4 MPa disturbance, the number of damage-induced cavities in the backfill decreases by approximately 62%, reflecting reduced localized damage concentration.

4. Conclusions

In this study, the mechanical properties and crack evolution mechanism of pillar–backfill composite materials under cyclic loading were investigated using an indoor cyclic loading test system. The main conclusions are as follows:

(1) Pillar width is a key parameter affecting the mechanical properties of PBCM. Samples with wider pillars (12–15 mm) exhibit superior bearing performance, with their uniaxial compressive strength and elastic modulus increasing by 88.6% and 42.7% respectively compared to those with narrower pillars (6–9 mm). It is noteworthy that samples with wider pillars show significantly lower sensitivity to disturbance amplitude; for instance, the UCS of 15 mm pillars only decreases by 4.8% under a 5 MPa disturbance, demonstrating better cyclic stability.
(2) Samples with narrow pillars accumulate damage more rapidly under cyclic loading, characterized by frequent high-energy acoustic emission events, and shear cracks account for over 50% under a 5 MPa disturbance. In contrast, samples with wide pillars exhibit more uniform damage distribution and stronger anti-disturbance capabilities, with their strain field evolution showing progressive characteristics.
(3) Observations of macroscopic failure modes indicate that pillar width directly influences the failure pattern. Samples with narrow pillars mainly undergo tension-dominated failure, where cracks mostly originate from interfaces and propagate rapidly. Samples with wide pillars, however, present shear-tension composite failure with more complex crack propagation paths. Particularly under high-disturbance

https://doi.org/10.3390/ma19081625

(5 MPa) conditions, wide pillars can still maintain partial integrity, showing obvious characteristics of progressive failure.

(4) Given that the present study was conducted on small-scale composite specimens, future work will include large-scale specimens and field-cored samples to further validate the engineering applicability of the findings.

Author Contributions: Methodology, Writing—review and editing: Q.S.; Writing—original draft, Validation: C.S.; Methodology, Writing—review and editing, Funding acquisition: H.L.; Methodology: S.Z.; Investigation: C.P.; Supervision: Y.J.; Writing—original draft, Validation: L.W. All authors have read and agreed to the published version of the manuscript.

Funding: This study is funded by the National Key Research and Development Program Young Scientist Project (No. 2024YFC2911000), the Shandong Provincial Natural Science Foundation (No. ZR2024ME065) and the Ordos City Key Research and Development Project (No. YF20240010). These supports are gratefully acknowledged.

Institutional Review Board Statement: Not applicable.

Informed Consent Statement: Not applicable.

Data Availability Statement: The original contributions presented in this study are included in the article. Further inquiries can be directed to the corresponding author.

Conflicts of Interest: Author Yujing Jiang was employed by the Inner Mongolia Shanghaimiao Mining Co., Ltd. The remaining authors declare that the research was conducted in the absence of any commercial or financial relationships that could be construed as a potential conflict of interest.

Abbreviations

The following abbreviations are used in this manuscript:

PBCM	Pillar–Backfill Composite Materials
AE	Acoustic emission
DIC	Digital image correlation

References

1. Gao, T.; Sun, W.; Liu, Z.; Cheng, H.Y. Investigation on fracture characteristics and failure pattern of inclined layered cemented tailings backfill. *Constr. Build. Mater.* **2022**, *343*, 128110. [CrossRef]
2. Qiu, H.F.; Zhang, F.S.; Liu, L.; Huan, C.; Hou, D.Z.; Kang, W. Experimental study on acoustic emission characteristics of cemented rock-tailings backfill. *Constr. Build. Mater.* **2022**, *315*, 125278. [CrossRef]
3. Gaili, X.; Erol, Y.; Wang, Y.D. Progress and prospects of mining with backfill in metal mines in China. *Int. J. Miner. Metall. Mater.* **2023**, *30*, 1455–1473. [CrossRef]
4. Cheng, A.P.; Zhou, C.S.; Huang, S.B.; Zhang, Y.S.; Pei, M.S. Study on the nonlinear deformation characteristics and constitutive model of cemented tailings backfill considering compaction hardening and strain softening. *J. Mater. Res. Technol.* **2022**, *19*, 4627–4644. [CrossRef]
5. Zhang, C.; Guo, J.; Taheri, A.; Song, W.D.; Wang, X.L.; Xia, W.H. Mechanical characteristics and constitutive model of cemented tailings backfill under temperature-time effects. *J. Build. Eng.* **2024**, *96*, 110630. [CrossRef]
6. Zhang, Y.; Liu, Y.Z.; Lai, X.P.; Cao, S.G.; Yang, Y.B.; Yan, B.X.; Bai, L.C.; Tong, L.; He, W. Transport mechanism and control technology of heavy metal ions in gangue backfill materials in short-wall block backfill mining. *Sci. Total Environ.* **2023**, *895*, 165139. [CrossRef]
7. Hou, Y.Q.; Yin, S.H.; Yang, S.X.; Chen, X.; Du, H.H. Mechanical properties, damage evolution and energy dissipation of cemented tailings backfill under impact loading. *J. Build. Eng.* **2023**, *66*, 105912. [CrossRef]
8. Li, Y.; Fu, J.X.; Wang, K.; He, Z.Q. Influence of shell ash on pore structure and mechanical characteristics of cemented tailings backfill. *Constr. Build. Mater.* **2024**, *411*, 134473. [CrossRef]
9. Zhang, X.Z.; Wu, D.; Lu, H.; Liu, L.; Zheng, S.L. Improvement of tailings gradation on workability and strength of cemented tailings backfill. *Constr. Build. Mater.* **2023**, *387*, 131633. [CrossRef]
10. Song, X.P.; Huang, Y.C.; Wang, S.; Yu, H.G.; Hao, Y.X. Macro-mesoscopic mechanical properties and damage progression of cemented tailings backfill under cyclic static load disturbance. *Compos. Struct.* **2023**, *322*, 117433. [CrossRef]

https://doi.org/10.3390/ma19081625

11. Zhu, T.Y.; Chen, Z.H.; Wang, Z.Y.; Cao, J.; Hao, J.S.; Zhou, Z.H. Experimental and DEM analyses of type I fracture characteristics of waste rock aggregate reinforced cemented tailing backfill. *Theor. Appl. Fract. Mech.* **2025**, *135*, 104764. [CrossRef]
12. Gan, D.Q.; Sun, H.K.; Xue, Z.L.; Liu, Z.Y.; Yang, X. Damage evolution and strength prediction model of soda residue modified cemented tailings backfill under uniaxial compression. *Constr. Build. Mater.* **2023**, *408*, 133709. [CrossRef]
13. Wang, X.L.; Li, Z.F.; Guo, J.P.; Lu, C.W.; Jiang, H.Q.; Mei, J.W. Experimental and numerical investigations on damage mechanical behaviors of surrounding rock-backfill composite under uniaxial compression. *Constr. Build. Mater.* **2024**, *417*, 135210. [CrossRef]
14. Zhao, K.; Huang, M.; Zhou, Y.; Yan, Y.J.; Wan, W.L.; Ning, F.J.; He, Z.W.; Wang, J.Q. Synergistic deformation in a combination of cemented paste backfill and rocks. *Constr. Build. Mater.* **2022**, *317*, 125943. [CrossRef]
15. Cui, B.Q.; Feng, G.R.; Bai, J.W.; Xue, G.L.; Wang, K.; Shi, X.D.; Wang, S.Y.; Wang, Z.H.; Guo, J. Failure characteristics and the damage evolution of a composite bearing structure in pillar-side cemented paste backfilling. *Int. J. Miner. Metall. Mater.* **2023**, *30*, 1524–1537. [CrossRef]
16. Xia, K.Z.; Chen, C.X.; Liu, X.T.; Liu, X.M.; Yuan, J.H.; Dang, S. Assessing the stability of high-level pillars in deeply-buried metal mines stabilized using cemented backfill. *Int. J. Rock Mech. Min. Sci.* **2023**, *170*, 105489. [CrossRef]
17. Wu, S.C.; Li, T.L.; Cheng, H.Y.; Zhang, X.Q.; Zhao, Z.Q. Mechanical response and stability of horizontal pillar size evolution inhigh stress environment. *J. Cent. South Univ.* **2021**, *52*, 1027–1039. [CrossRef]
18. Sherizadeh, T.; Kulatilake, P.H.S.W. Assessment of roof stability in a room and pillar coal mine in the U.S. using three-dimensional distinct element method. *Tunn. Undergr. Space Technol.* **2016**, *59*, 24–37. [CrossRef]
19. Liu, Y.; He, B.; Dai, F.; Zhang, Q.; Liu, Y. Mechanical responses of chemically corroded sandstone under cyclic disturbance: Insights from fatigue properties and macro-micro fracturing mechanism. *Int. J. Rock Mech. Min. Sci.* **2024**, *180*, 105818. [CrossRef]
20. Xu, J.; Xiao, X.C.; Ma, L.; Luo, S.; Jin, J.X.; Wu, B.J. Experimental study of the damage characteristics of rocks containing non-penetrating cracks under cyclic loading. *Int. J. Min. Sci. Technol.* **2024**, *34*, 197–210. [CrossRef]
21. Long, D.Y.; Wang, Y.; Li, C.H.; Wu, Y.F. Macro-meso fatigue fracture and instability of rock-backfill composite structure under increasing-amplitude cyclic loading. *Constr. Build. Mater.* **2024**, *416*, 135187. [CrossRef]
22. Zhou, Y.Q.; Sheng, Q.; Li, N.; Fu, X.D. The relationship between dynamic strength and strain rate and damage to rock materials subjected to dynamic cyclic loading. *Geomech. Geophys. Geo-Energy Geo-Resour.* **2021**, *7*, 88. [CrossRef]
23. Li, J.T.; Shi, Z.M.; Yuan, F.G.; Guo, B.S.; Wang, M.X.; Lin, H.; Han, D.Y.; Li, K.H. Mechanical properties and fracture damage behavior of thermal storage rocks under constant amplitude low cycle fatigue loading. *Eng. Fract. Mech.* **2025**, *321*, 111069. [CrossRef]
24. Gan, D.Q.; Lu, Y.Z.; Sun, H.K.; Liu, Z.Y.; Zhang, Y.J. Mechanical response and damage constitutive model of early-age cemented paste backfill after cyclic loading. *J. Build. Eng.* **2024**, *86*, 108822. [CrossRef]
25. Wang, L.J.; Luan, H.J.; Jiang, Y.J.; Wang, C.S.; Zhang, S.H.; Li, X.P.; Wei, J.L. Study on mechanical properties and damage evolution of pillar-backfill composite under cyclic loading. *Constr. Build. Mater.* **2025**, *492*, 143003. [CrossRef]
26. Liang, B.; Wang, D.; Jiang, Y.J.; Luan, H.J.; Liu, J.K.; Wang, J.L. Analysis of fracture modes and acoustic emission characteristics of low-frequency disturbed coal rock bodies with different cyclic amplitudes. *Fatigue Fract. Eng. Mater. Struct.* **2024**, *47*, 4412–4431. [CrossRef]
27. Zhou, W.; Cheng, J.L.; Zhang, G.K.; Li, H.B.; Cheng, Y.G.; Ma, G.; Ji, X. Effects of Wetting–Drying Cycles on the Breakage Characteristics of Slate Rock Grains. *Rock Mech. Rock Eng.* **2021**, *54*, 6323–6337. [CrossRef]
28. Li, C.X.; Liu, Y.S.; Li, L.S.; Wang, Z.H.; Li, H. Texture-Based Segmentation of SEM Images of Shale Rocks and Estimation of Meso-Scale Elastic Modulus by 2D FEM. *Rock Mech. Rock Eng.* **2025**, *58*, 6475–6491. [CrossRef]
29. Shan, T.C.; Li, Z.H.; Zhang, X.; Wang, X.R.; Jia, H.S.; Wang, E.Y.; Zhang, Q.C.; Niu, Y.; Wang, D.M. Superstatistical approach of electric potential and acoustic emission for investigating damage evolution and precursor of water-bearing sandstone under uniaxial compression. *Int. J. Rock Mech. Min. Sci.* **2025**, *189*, 106063. [CrossRef]

Disclaimer/Publisher's Note: The statements, opinions and data contained in all publications are solely those of the individual author(s) and contributor(s) and not of MDPI and/or the editor(s). MDPI and/or the editor(s) disclaim responsibility for any injury to people or property resulting from any ideas, methods, instructions or products referred to in the content.

https://doi.org/10.3390/ma19081625

MDPI AG
Grosspeteranlage 5
4052 Basel
Switzerland
Tel.: +41 61 683 77 34

Materials Editorial Office
E-mail: materials@mdpi.com
www.mdpi.com/journal/materials



Disclaimer/Publisher's Note: The title and front matter of this reprint are at the discretion of the Guest Editors. The publisher is not responsible for their content or any associated concerns. The statements, opinions and data contained in all individual articles are solely those of the individual Editors and contributors and not of MDPI. MDPI disclaims responsibility for any injury to people or property resulting from any ideas, methods, instructions or products referred to in the content.





Academic Open
Access Publishing

mdpi.com

ISBN 978-3-7258-9186-3